



## Preface

This Activity Report covers scientific and technological activities carried out using the UVSOR-III Synchrotron in FY2018 (April 2018-March 2019). We present scientific examples of how the users study at the UVSOR Synchrotron Facility.

The present UVSOR-III Synchrotron is one of the most advanced low-energy SR facilities of the 3<sup>rd</sup> generation SR in the world and is now one of the

critical resources in doing molecular science. The UVSOR-III Synchrotron has a small electron storage ring but has powerful 6 undulator beamlines (3 VUV and 3 in-vacuum soft X-ray undulators) with 8 dipole beamlines. We never stop improving and upgrading our micro- and nano-scale photoabsorption and photoelectron emission approaches and in situ/operando measurements in the VUV and soft X-ray regions, based on our strategic international collaboration program in molecular science. We are grateful to all the people who use our facility and support our efforts.

UVSOR operates for 40 weeks/year (~ 2,200 h user time), accepts ~ 230 proposals, and ~ 1,300 researchers meaning ca. 100 people/beamline/year and ca. 30 people/week. Most users stay for one or two weeks for doing the experiment. To continue high-level achievements in science and technology at the UVSOR-III Synchrotron, we in-house staff are always working hard to maintain and improve our





high-performance accelerators and beamlines. The FY2019 would be still challenging year for the UVSOR Synchrotron Facility, because of reducing the number of the staff. Prof. Kato who had greatly contributed to develop the UVSOR-III Synchrotron has moved to HiSOR (Hiroshima University). After the two-major upgrade from UVSOR-I to UVSOR-III Synchrotron with his great efforts, now we aim continuously for serving the high-quality light sources and for developing the stability in use. On the experimental side, technology development will not stop, hence we will make a progress on the imaging-related techniques to encourage the advanced molecular science. We have started to construct the new endstation by using effectively two undulator beamlines, BL6U and BL7U. The new apparatus is based on the momentum-resolved photoelectron emission microscope, however the novel function will be uniquely added to our endstation to realize a leading position by having instrumental extensibility in future development over 10 years. The advanced SR-related instrument will offer opportunities to reveal the nature of properties and functions of them. The details on the apparatus will be informing via international workshop related.

We look forward to receiving your feedback and suggestions on the continuing evolution of the UVSOR Synchrotron Facility. And we hope many users will perform excellent work by fully utilizing the UVSOR-III Synchrotron as a unique international hub for the SR research in advanced molecular science.

April 2019

Satoshi Kera

Director of the UVSOR Synchrotron Facility

## 19 Years and 1 month in UVSOR

I moved from KEK Photon Factory to UVSOR in March, 2000. After 19 years and 1 month, I am moving to Hiroshima University in April, 2019.

When I came to UVSOR, the accelerator was very stably operated. However, the machine was already 17 years old. I proposed an upgrade plan and, fortunately, it was approved soon by the efforts of Prof. K. Kaya, Director of IMS and Prof. N. Kosugi, Director of UVSOR at that time. After this upgrade, the emittance was reduced by a factor of 5. The number of straight sections for

insertion devices was increased from three to six. We did not stop. We continued upgrading the machine, introducing new undulators, top-up operation, and so on. By the efforts of the staff members of the facility, particularly those of the technical staff, the accelerator performance has been greatly improved. However, of course, we should not stop. We should step further.

**Masahiro KATOH (UVSOR Synchrotron)**





**2018 Young Scientist Award, The Atomic Collision Society of Japan  
Assist. Prof. Hiroshi Iwayama (UVSOR)****Photoionization and Relaxation Processes of Rare Gas Clusters Irradiated by EUV-FEL Pulses**

Dr. Iwayama has awarded 2018 Young Scientist Award of The Atomic Collision Society of Japan for his pioneering work of interaction of rare gas clusters with intense extreme ultraviolet free electron laser (EUV-FEL) pulses. The Atomic Collision Society of Japan was founded with the goal of promoting the current and future rapid development in atomic, electronic and photonic collision and related science.

Before self-amplified spontaneous-emission FEL succeeded in lasing in EUV regime, the interaction of intense EUV laser pulses with matter is so far only scarcely investigated. To understand the light-matter interaction in the EUV regime, Dr. Iwayama has investigated photoionization and relaxation processes of rare gas clusters irradiated by intense EUV-FEL pulses. Clusters are ideal to investigate the light-matter interaction since their size can be tuned from the molecular to the bulk-like regime and there is no energy dissipation into surrounding media. He measured ions, electrons and photons from the irradiated clusters and found frustration of photoionizations and efficient electron-ion recombination processes. These results are a pioneering works about the interaction of atomic clusters with intense laser pulse in the EUV region.





# Kato Seminar and Farewell Party





# I

## Organization and Staff List

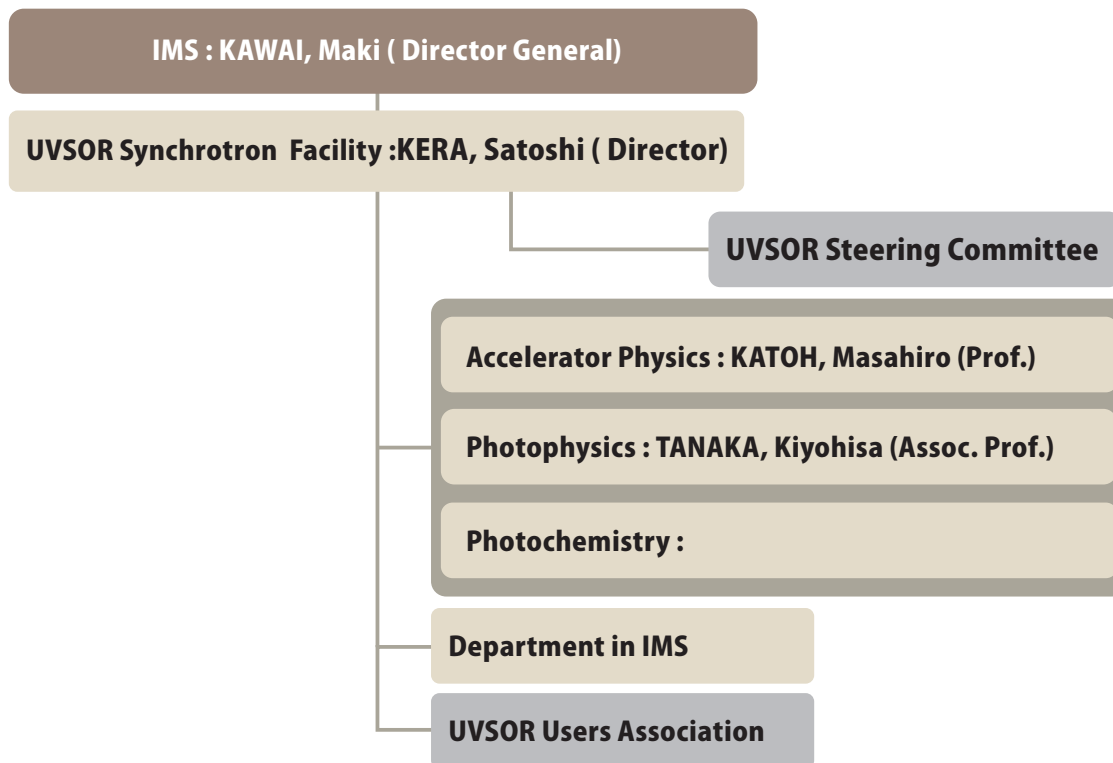






# UVSOR Synchrotron Facility Organization

May 2019



## Staff List

### UVSOR Staff

#### Director

KERA, Satoshi	Professor	kera@ims.ac.jp
---------------	-----------	----------------

#### Light Source Division (Accelerator Physics)

KATOH, Masahiro	Professor	mkatoh@ims.ac.jp	
KANEYASU, Tatsuo	Visiting Associate Professor		
FUJIMOTO, Masaki	Assistant Professor	mfmoto@ims.ac.jp	
MATSUDA, Hiroyuki	Project Research Staff	hmatsuda@ims.ac.jp	(since Apr. 2019)
YAMAZAKI, Jun-ichiro	Unit Chief Engineer	yamazaki@ims.ac.jp	
HAYASHI, Kenji	Unit Chief Engineer	h-kenji@ims.ac.jp	
TESHIMA, Fumitsuna	Assistant Unit Chief Engineer	tetsu@ims.ac.jp	
MINAKUCHI, Aki	Supporting Engineer	minakuchi@ims.ac.jp	

#### Light Source Division (X-ray Imaging Optics)

MATSUI, Fumihiko	Senior Researcher	matui@ims.ac.jp
OHIGASHI, Takuji	Assistant Professor	ohigashi@ims.ac.jp



INAGAKI, Yuichi	Engineer	yinagaki@ims.ac.jp	(until May 2018)
YUZAWA Hayato	Engineer	hayato@ims.ac.jp	

## Beamline Division (Photophysics)

TANAKA, Kiyohisa	Associate Professor	k-tanaka@ims.ac.jp
IDETA, Shin-ichiro	Assistant Professor	idetas@ims.ac.jp
SAKAI, Masahiro	Unit Chief Engineer	sakai@ims.ac.jp

## Beamline Division (Photochemistry)

IWAYAMA, Hiroshi	Assistant Professor	iwayama@ims.ac.jp
NAKAMURA, Eiken	Facility Chief Engineer	eiken@ims.ac.jp
KONDO, Naonori	Assistant Unit Chief Engineer	nkondo@ims.ac.jp
YANO, Takayuki	Assistant Unit Chief Engineer	yano@ims.ac.jp
MAKITA, Seiji	Assistant Unit Chief Engineer	makita@ims.ac.jp
HORIGOME, Toshio	Senior Engineer	horigome@ims.ac.jp

## Secretary

HAGIWARA, Hisayo		hagiwara@ims.ac.jp
INAGAKI, Itsuko		itsuko@ims.ac.jp

## UVSOR Steering Committee (\* Chair)

KERA, Satoshi *	UVSOR, IMS
KATOH, Masahiro	UVSOR, IMS
TANAKA, Kiyohisa	UVSOR, IMS
KANEYASU, Tatsuo	UVSOR, IMS (Kyushu Synchrotron Light Research Center )
MATSUI, Fumihiko	UVSOR, IMS
YOKOYAMA, Toshihiko	IMS
AKIYAMA, Shuji	IMS
MASAOKA, Shigeyuki	IMS
YAMAMOTO, Hiroshi	IMS
KITaura, Mamoru	Yamagata Univ.
KOMORI, Fumio	Univ. of Tokyo
OKABAYASHI, Jun	Univ. of Tokyo
HATSUI, Takaki	JASRI
OKUDA, Taichi	Hiroshima Univ.
KUMIGASHIRA, Hiroshi	KEK-PF
TAKAKUWA, Yuji	Tohoku Univ.

## UVSOR Users Association (\* Chair)

KIMURA, Shin-ichi *	Osaka Univ.
OKABAYASHI, Jun	Univ. of Tokyo

KONDO, Hiroshi	Keio Univ.
ITO, Takahiro	Nagoya Univ.
YAMANE, Hiroyuki	RIKEN

### Graduate Students

HAMADA, Ryo	Nagoya Univ.	(until Sep. 2018)
IKEMOTO, Masashi	Nagoya Univ.	(until Sep. 2018)
KONTANI, Syouta	Nagoya Univ.	(until Sep. 2018)
TAKAHASHI, Kazuyoshi	Nagoya Univ.	(until Sep. 2018)
KIMURA, Keigo	Nagoya Univ.	(since Oct. 2018)
KIMURA, Shinnosuke	Nagoya Univ.	(since Oct. 2018)
NABEHIRA, Naoki	Nagoya Univ.	(since Oct. 2018)
HAYASHI, Naoki	Nagoya Univ.	(since Oct. 2018)
MATSUNAGA, Yukihiro	Nagoya Univ.	(since Oct. 2018)

### Visiting Scientists

PATRICK, Amsalem	Humboldt-Univ. zu Berlin	May 2018
PARK, Soohyung	Humboldt-Univ. zu Berlin	May 2018
THORSTEN, Schultz	Humboldt-Univ. zu Berlin	May 2018
ISMAIL, Mostafa	Univ. of Oulu	Jun. 2018
PATANEN, Minna	Univ. of Oulu	Jun. 2018, Aug. 2018
JUNG, Woobeen	Seoul National Univ.	Jun. 2018
KIM, Younsik	Seoul National Univ.	Jun. 2018
OH, Dong Jin	Seoul National Univ.	Jun. 2018, Mar. 2019
KANAEV, Andrei	CNRS	Jul. 2018
FELDBACH, Eduard	Univ. of Tartu Estonia	Jul. 2018
MUSEUR, Luc	CNRS	Jul. 2018
SCHAAL, Maximilian	Friedrich Schiller Univ. Jena (FSU)	Jul. 2018
CHO, Soohyun	Yonsei Univ.	Jul. 2018
JU, Huanxin	Univ. of Science and Technology of China	Jul. 2018
MA, Jun	Univ. of Science and Technology of China	Jul. 2018
LONG, Ran	Univ. of Science and Technology of China	Jul. 2018
Chen, Shuangming	Univ. of Science and Technology of China	Jul. 2018
CHIU, Chao Wen	National Univ. of Kaohsiung	Jul. 2018
HWANG, Ing-Shouh	Academia Sinica	Jul. 2018
HSU, Wei-Hao	Academia Sinica	Jul. 2018, Feb. 2019
CHUANG, Cheng-Hao	Tamkang Univ.	Jul. 2018, Feb. 2019
LAI, Yu-Ling	NSRRC	Aug. 2018
SHIU, Hung Wei	NSRRC	Aug. 2018
CÉOLIN, Denis	Synchrotron SOLEIL	Aug. 2018
KLAIPHET, Kanchanasuda	Suranaree Univ. of technology	Aug. 2018



SAISOPA, Thanit	Suranaree Univ. of technology	Aug. 2018
YU, Li-Chung	NSRRC	Aug. 2018
RÜHL, Eckart	Freie Univ. Berlin	Sep. 2018, Mar. 2019
FLESCH, Roman	Freie Univ. Berlin	Sep. 2018
REN, Jian	Humboldt-Univ. zu Berlin	Oct. 2018
LABLANQUIE, Pascal	LCP-MR	Oct. 2018
YAO, Jiabin	Sichuan Univ.	Dec. 2018
ZHAI, Tianshu	Soochow Univ.	Dec. 2018
YANG, Jiacheng	Soochow Univ.	Dec. 2018
DUHM, Steffen	Soochow Univ.	Dec. 2018
KIM, Yeongkwan	KAIST	Jan. 2019
HYUN Jounghoon	KAIST	Jan. 2019
LIN, Jack J.	Univ. of Oulu	Jan. 2019
KAMAL, Raj R	Univ. of Oulu	Jan. 2019
MICHAILOUDI, Gerogia	Univ. of Oulu	Jan. 2019
PRISLE, Nønne L.	Univ. of Oulu	Jan. 2019
KIM, Sunghun	KAIST	Jan. 2019
LEE, Gyubin	KAIST	Jan. 2019
LIM, Chan-young	KAIST	Jan. 2019
LEE, Yeonghoon	KAIST	Jan. 2019
SUBACH, Sergey	Forschungszentrum Jülich	Feb. 2019
HAAGS, Anja	Forschungszentrum Jülich	Feb. 2019
DONG, Chung-Li	Tamkang Univ.	Feb. 2019
SALEHI DERAKHTANJANI, Elham	Khatam Univ.	Feb. 2019
YASHINA, Lada V.	Lomonosov Moscow State Univ.	Feb. 2019
GERMER, Gregor	Freie Univ. Berlin	Mar. 2019
LEE, Yeonghoon	Seoul National Univ.	Mar. 2019
PARK, Heonjoon	Seoul National Univ.	Mar. 2019
KIM, Beom Seo	Seoul National Univ.	Mar. 2019
CHANG, Han-Wei	Tamkang Univ.	Mar. 2019
HUANG, Yu-Cheng	National Chiao Tung Univ.	Mar. 2019
USACHOV, Dmitry	St. Petersburg State Univ.	Mar. 2019
TURTURICA, Valter Gabriel	ELI-NP	Mar. 2019
IANCU, Violeta	ELI-NP	Mar. 2019

The background is a vibrant teal color. It features several abstract geometric elements: a large, semi-transparent circular graphic on the right side, composed of concentric rings and a dotted outer edge; several diagonal lines of varying thickness and opacity crossing the frame; and a dense grid of small, light-colored dots in the lower-left quadrant.

# II

## Current Status of Light Sources and Beamlines





# Light Source in 2018

## 1. Status of UVSOR Accelerators

In the fiscal year 2018, we had scheduled to operate UVSOR-III from May to March, for 36 weeks for users. We had several machine troubles as described later. In July we had a trouble in the linac and we could not operate the machine in the top-up mode almost for one week, in adding to 12 hour loss. In cases of other minor troubles, we extended the operation time for compensation. We had a scheduled shutdown period in April and May for about 6 weeks. This was mainly for the scheduled maintenance works. We had one week shut down period in August and October, two week one around the New Years day and one week one at the end of March. We had 2 weeks for machine and beamline conditioning in May after the spring shut down. In addition, we had 4 weeks for machine conditionings and studies, in October, November, January and March. The machine study week in November was mainly for the machine conditioning after the annual planned power outage.

We operated the machine for 34 weeks in the multi-bunch top-up mode at 300 mA, and 2 weeks in the single-bunch top-up mode at approximately 40 mA. The monthly statistics of the operation time and the integrated beam current are shown in Fig. 1.

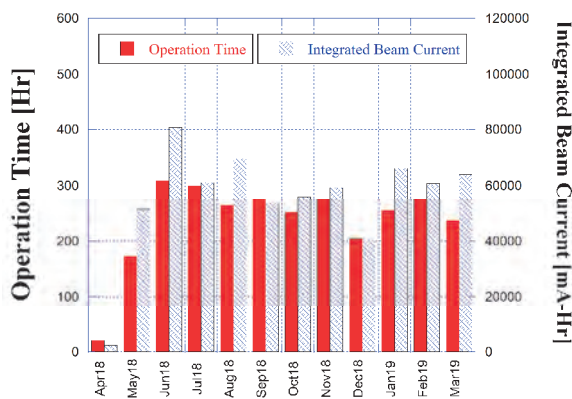


Fig. 1. Monthly statistics in FY2018.

The weekly operation schedule is as follows. On Monday, from 9 am to 9 pm, the machine is operated for machine conditionings and studies. On Tuesday and Wednesday, from 9am to 9pm, the machine is operated for users. From Thursday 9am to Friday 9pm, the machine is operated for 36 hours continuously for users. Therefore, the beam time for users in a week is 60 hours. In the single bunch operation weeks, the machine is operated for 12 hours per day from Tuesday to Friday.

We had a trouble in the high voltage power supplies and the cooling water system for the linac in July. The

former case, it took about several days to completely repair the power supply. In the latter, the chilling water unit was malfunctioned. We gave up to use it and alternatively we started supplying the chilling water to the linac from the cooling water system for other part of accelerator system. It has been working well without any trouble.

In February 2018, a cooling water leakage was found at a sextupole coil wound on a pole face of a multipole (quadrupole/sextupole) magnet. After about one year, we have found similar leakage on nine of same coils. The hollow conductor used for these coils has relatively thin wall. It is supposed that, after the installation in 2003, the walls have been eroded by the water flow. In the spring shutdown 2019, we are applying liquid sealant for all the coils for life prolonging. In parallel, we have started constructing coils for replacement.



Fig. 2. The sextupole main coil wound on the pole face of a quadrupole magnet.

## 2. Improvements and Developments

In the UVSOR accelerator system, there are still some components which have been used since the construction of the facility early in 1980's. This year, after more than 35 year operation, the pulse transformer for the klystron modulator of the linac was replaced (Fig. 3). The cooling water system for the RF cavity in the booster synchrotron was also replaced with the one which has a good temporal stability of 0.1 degree C. The control system of the undulator U6 was replaced after 15 year operation. The signal generator as the master oscillator of the accelerator complex was also replaced this year.

The chilling water system for the linac had troubles several times in the past, which were mainly due to the unstable cooling water supply from the facility. This system provided 20 degree chilling water to the temperature control system of the linac. We tried to use about 25 degree water from the facility instead of



the 20 degree chilling water and found that the linac could be operated stably without any problem. We stopped using the chilling water system.

II



Fig. 3 New pulse transformer for the klystron modulator of the linac.



Fig. 4. New Control system for the undulator U6

### *Light Source Developments and Beam Physics Studies*

We continue the efforts to develop novel light sources technologies and their applications such as free electron lasers, coherent harmonic generation, coherent synchrotron radiation, laser Compton scattering gamma-rays, intense polarized and vortex UV radiation at the source development station BL1U, which was constructed under the support of Quantum Beam Technology Program by MEXT/JST. In these years, we continued studying the generations of structured light beam from undulators in collaboration with Hiroshima U., Nagoya U. and other institutes. Since the UVSOR electron beam is diffraction-limited in the UV range, we could precisely investigate the optical properties of the vortex beams from undulators using conventional optical components. Moreover, we succeeded in producing optical vector beam which has a tailored distribution of the polarization in the transverse plane.

The laser Compton scattering gamma-rays are powerful tools for nuclear science and technologies. By using various external lasers, we have demonstrated generating quasi-monochromatic gamma-rays in the energy range from 1MeV to around 10MeV. We continue the experiments in collaboration with Kyoto U., AIST and QST towards imaging applications. We started new experiments on positron lifetime spectroscopy experiments in collaboration with Yamagata U., Nagoya U. and AIST.

**Masahiro KATOH**  
(UVSOR Synchrotron Facility)

## UVSOR Accelerator Complex

### Injection Linear Accelerator

Energy	15 MeV
Length	2.5 m
Frequency	2856 MHz
Accelerating RF Field	$2\pi/3$ Traveling Wave
Klystron Power	1.8 MW
Energy Spread	$\sim 1.6$ MeV
Repetition Rate	2.6 Hz

### UVSOR-III Storage-Ring

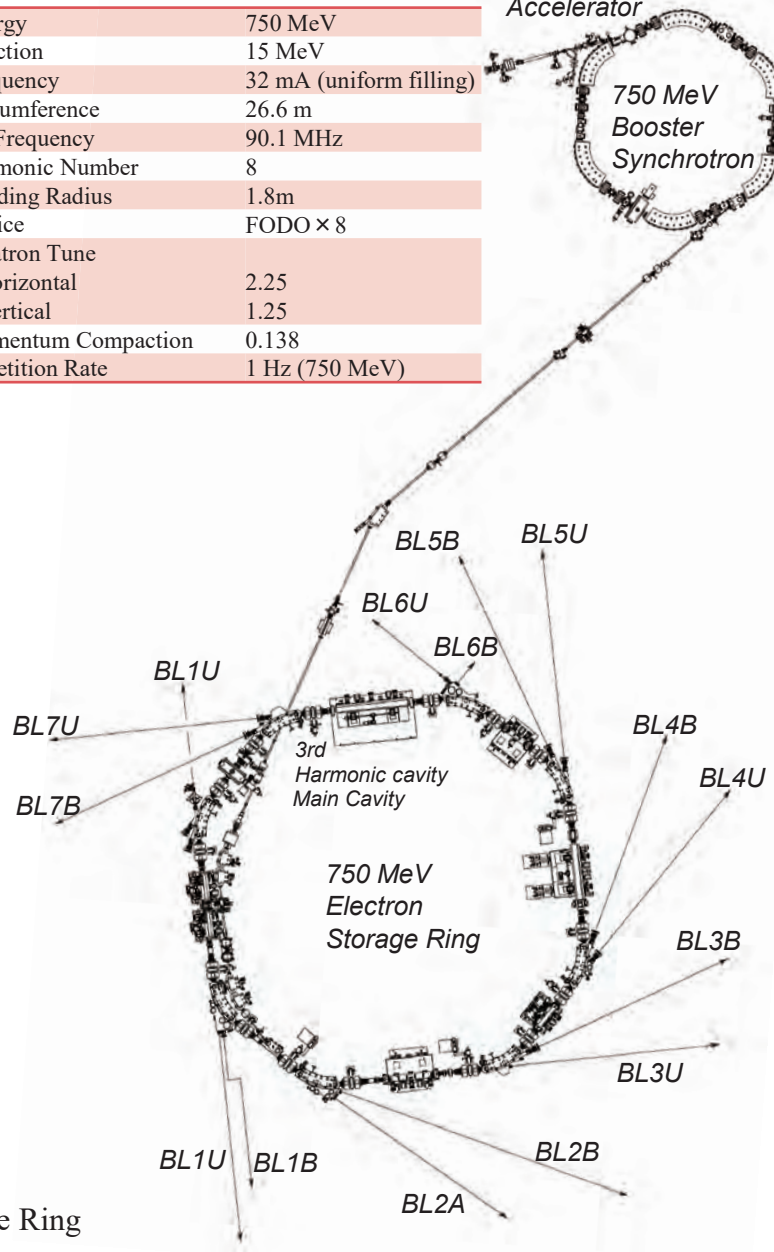
Energy	750 MeV
Injection Energy	750 MeV
Maximum Storage Current	500 mA (multi bunch) 100 mA (single bunch)
Normal operation current (Top-up mode)	300 mA (multi bunch) 50 mA (single bunch)
Natural Emittance	17.5 nm-rad
Circumference	53.2 m
RF Frequency	90.1 MHz
Harmonic Number	16
Bending Radius	2.2 m
Lattice	Extended DBA $\times 4$
Straight Section	(4 m $\times$ 4)+(1.5 m $\times$ 4)
RF Voltage	120 kV
Betatron Tune	
Horizontal	3.75
Vertical	3.20
Momentum Compaction	0.030
Natural Chromaticity	
Horizontal	-8.1
Vertical	-7.3
Energy Spread	$5.26 \times 10^{-4}$
Coupling Ratio	1%
Natural Bunch Length	128 ps

### Booster Synchrotron

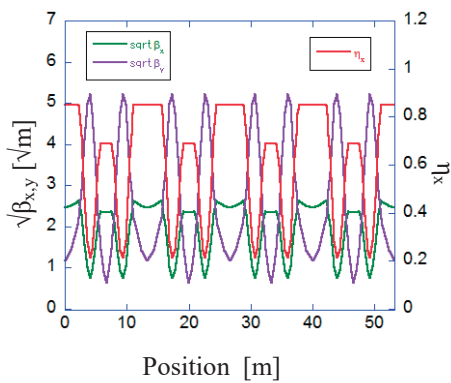
Energy	750 MeV
Injection	15 MeV
Frequency	32 mA (uniform filling)
Circumference	26.6 m
RF Frequency	90.1 MHz
Harmonic Number	8
Bending Radius	1.8m
Lattice	FODO $\times 8$
Betatron Tune	
Horizontal	2.25
Vertical	1.25
Momentum Compaction	0.138
Repetition Rate	1 Hz (750 MeV)

15 MeV  
Linear  
Accelerator

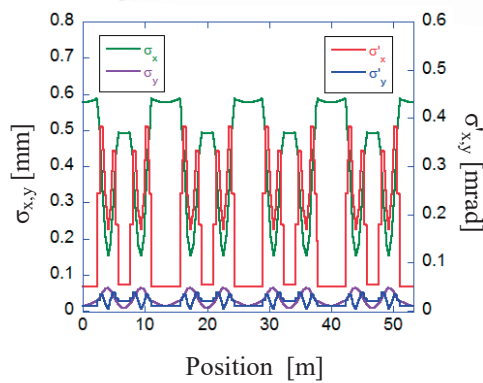
750 MeV  
Booster  
Synchrotron



### Electron Beam Optics of UVSOR-III Storage Ring



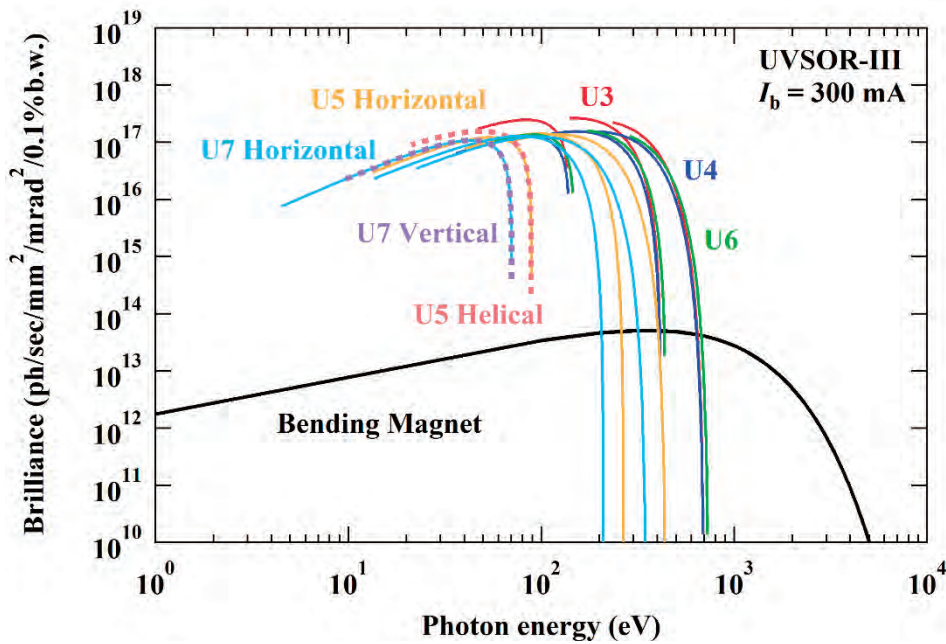
Horizontal/vertical betatron functions and dispersion function



Horizontal/vertical electron beam size and beam divergences



## Insertion Device



Brilliance of radiation from the insertion devices (U3, U4, U5, U6 and U7) and a bending magnet of UVSOR-III

### U1 Apple-II Undulator /

#### Optical Klystron

Number of Periods	10+10
Period length	88 mm
Pole Length	0.968 m + 0.968 m
Pole Gap	24-200 mm
Deflection Parameter	7.36 (Max. Horizontal) 4.93 (Max. Vertical) 4.06 (Max. Helical)

### U3 In-vacuum Undulator

Number of Periods	50
Period length	38 mm
Pole Length	1.9 m
Pole Gap	16.5-40 mm
Deflection Parameter	1.8-0.24

### U4 In-vacuum Undulator

Number of Periods	26
Period length	38 mm
Pole Length	0.99 m
Pole Gap	13-40 mm
Deflection Parameter	2.4-0.19

### U5 Apple-II

#### Variable Polarization Undulator

Number of Periods	38
Period length	60 mm
Pole Length	2.28 m
Pole Gap	24-190 mm
Deflection Parameter	3.4 (Max. Horizontal) 2.1 (Max. Vertical) 1.8 (Max. Helical)

### U6 In-vacuum Undulator

Number of Periods	26
Period length	36 mm
Pole Length	0.94 m
Pole Gap	13-40 mm
Deflection Parameter	1.78 - 0.19

### U7 Apple-II

#### Variable Polarization Undulator

Number of Periods	40
Period length	76 mm
Pole Length	3.04 m
Pole Gap	24-200 mm
Deflection Parameter	5.4 (Max. Horizontal) 3.6 (Max. Vertical) 3.0 (Max. Helical)

### Bending Magnets

Bending Radius	2.2 m
Critical Energy	425 eV

## Beamlines in 2018

Kiyohisa TANAKA

*UVSOR synchrotron Facility, Institute for Molecular Science*

Among the synchrotron radiation facilities with electron energies of less than 1 GeV, UVSOR is one of the highest-brilliance light sources in the extreme-ultraviolet region. The natural emittance of the UVSOR-III storage ring is as low as 17.5 nm-rad after the successful completion of the storage ring upgrade project (the UVSOR-III project) in 2012.

Eight bending magnets and six insertion devices are available as synchrotron light sources at UVSOR. As of 2017 there are a total of fourteen operational beamlines, which are classified into two categories. Twelve of them are the so-called “Open beamlines”, which are open to scientists from universities and research institutes belonging to the government, public organizations, private enterprises and also those from foreign countries. The remaining two beamlines are the “In-house beamlines”, and are dedicated to the use of research groups within Institute for Molecular Science (IMS).

There is one soft X-ray station equipped with a double-crystal monochromator, seven extreme ultraviolet and soft X-ray stations with grazing incidence monochromators, three vacuum ultraviolet (VUV) stations with normal incidence monochromators, two infrared (IR) stations equipped with Fourier-Transform interferometers, and one direct radiation station located after two undulators installed in tandem, as shown in the appended table (next page) for all available beamlines at UVSOR in 2018. The details of the updates for several beamlines are the followings.

BL1U, which is one of the in-house beamlines, has been partially open for general users from Oct. 2018. Users can use UV/VUV light and gamma rays for irradiation experiments.

In BL3B, a new sample stage has been developed. Samples can be heated up to ~500 K during the VIS-VUV photoluminescence and reflection/absorption spectroscopy measurements.

BL5U has been officially opened for users from 2016 as high energy resolution angle-resolved photoemission spectroscopy (ARPES) beamline. Using a new mirror located close to the sample

position, the beam spot size is successfully focused to ~23 x 40  $\mu\text{m}$ , which make users possible to perform measurements on small samples or inhomogeneous samples. A new software to precisely control the sample position has been developed, and users can easily take intensity image from sample with 10  $\mu\text{m}$  step and move to some particular position of the sample in the obtained image.

In BL6U, which is one of the in-house beamlines, the latest version of ARPES analyzer was installed (MB Scientific AB, A-1 analyzer Lens#5). Manipulator was modified so that a mesh can be set in front of the sample and the sample can be biased voltages. By applying bias voltages to the sample, the wider acceptance angle (~ 60 deg.) with  $h\nu = 40\text{-}60$  eV is available. We also have performed *in situ* cleaning of mirrors by exposure to oxygen at a pressure of  $1 \times 10^{-2}$  Pa under irradiation of non-monochromated synchrotron radiation (SR). As a result, the photon intensity around 280 eV has greatly been improved.


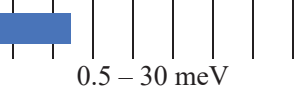



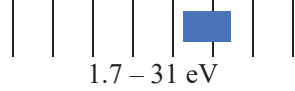
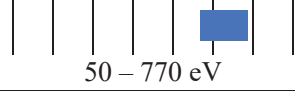

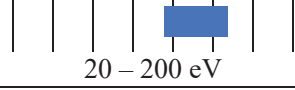

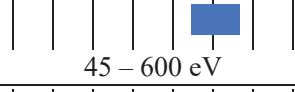
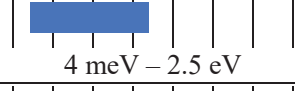
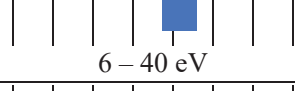
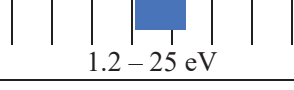
In BL7U, a high energy resolution ARPES beamline with low energy of photons, a new low temperature 6-axis manipulator was developed and installed from FY2018. Samples can be cooled down to 4.5 K with tilt angle -15 ~ 50 deg. and azimuth angle  $\pm 120$  deg..

UVSOR is now planning to introduce so-called “Momentum microscope (MM)”, which is an electronic spectroscopy with both the real space and momentum space resolution. The original plan has been modified and MM will be installed at BL6U. Tender process for MM analyzer has been concluded and it will be installed in FY2019.

All users are required to refer to the beamline manuals and the UVSOR guidebook (the latest revision in PDF format uploaded on the UVSOR web site in June 2018), on the occasion of conducting the actual experimental procedures. Those wishing to use the open and in-house beamlines are recommended to contact the appropriate beamline master (see next page). For updated information on UVSOR, please see <http://www.uvsor.ims.ac.jp>.

## Beamlines at UVSOR

II

Beamline	Monochromator / Spectrometer	Energy Range	Targets	Techniques	Contact
BL1U	Free electron laser	 1.6 – 13.9 eV		(Irradiation)	M. Fujimoto mfmoto@ims.ac.jp
BL1B	Martin-Puplett FT-FIR	 0.5 – 30 meV	Solid	Reflection Absorption	K. Tanaka k-tanaka@ims.ac.jp
BL2A	Double crystal	 585 – 4 keV	Solid	Reflection Absorption	K. Tanaka k-tanaka@ims.ac.jp
BL2B	18-m spherical grating (Dragon)	 23 – 205 eV	Solid	Photoemission	S. Kera kera@ims.ac.jp
BL3U	Varied-line-spacing plane grating (Monk-Gillieson)	 40 – 800 eV	Gas Liquid Solid	Absorption Photoemission Photon-emission	M. Nagasaka nagasaka@ims.ac.jp
BL3B	2.5-m off-plane Eagle	 1.7 – 31 eV	Solid	Reflection Absorption Photon-emission	K. Tanaka k-tanaka@ims.ac.jp
BL4U	Varied-line-spacing plane grating (Monk-Gillieson)	 50 – 770 eV	Gas Liquid Solid	Absorption (Microscopy)	T. Ohigashi ohigashi@ims.ac.jp
BL4B	Varied-line-spacing plane grating (Monk-Gillieson)	 25 eV – 1 keV	Gas Solid	Photoionization Photodissociation Photoemission	H. Iwayama iwayama@ims.ac.jp
BL5U	Spherical grating (SGM-TRAIN <sup>†</sup> )	 20 – 200 eV	Solid	Photoemission	K. Tanaka k-tanaka@ims.ac.jp
BL5B	Plane grating	 6 – 600 eV	Solid	Calibration Absorption	K. Tanaka k-tanaka@ims.ac.jp
BL6U*	Variable-included-angle varied-line-spacing plane grating	 45 – 600 eV	Gas Solid	Photoionization Photodissociation Photoemission	F. Matsui matui@ims.ac.jp
BL6B	Michelson FT-IR	 4 meV – 2.5 eV	Solid	Reflection Absorption IR microscope	K. Tanaka k-tanaka@ims.ac.jp
BL7U	10-m normal incidence (modified Wadsworth)	 6 – 40 eV	Solid	Photoemission	S. Ideta idetas@ims.ac.jp
BL7B	3-m normal incidence	 1.2 – 25 eV	Solid	Reflection Absorption Photon-emission	K. Tanaka k-tanaka@ims.ac.jp

Yellow columns represent undulator beamlines.

\* In-house beamline.



# BL1U

## Light Source Development Station

### ▼ Description

BL1U is dedicated for developments and applications of various novel photon sources including free electron laser in the range from visible to deep UV, coherent harmonic generation in the deep UV and VUV, laser Compton scattering gamma-rays and undulator radiation with various polarization properties including optical vortex beam and optical vector beam.

The beam-line is equipped with a dedicated twin polarization variable undulator system with a buncher section, which can be used for a FEL oscillator and a VUV CHG. It is also equipped with a femto-second laser system synchronized with the accelerator, which is used for CHG, slicing, LCS and coherent THz radiation generation.

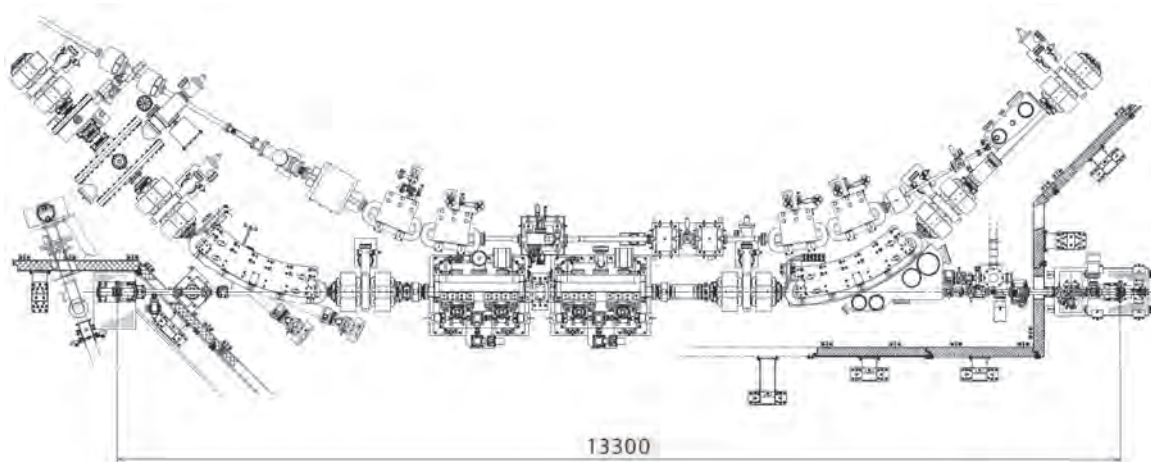


Fig. 1. Configuration of the free electron laser (under reconstruction)



Fig. 2. Twin Apple-II Undulator

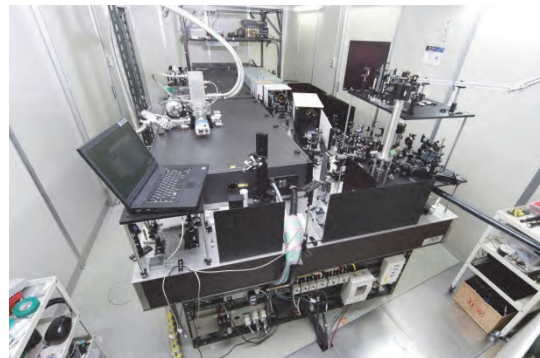


Fig. 3. Accelerator synchronized Laser System

### ▼ Technical Data of FEL

Wave Length	199-800 nm
Spectral Band Width	$\sim 10^{-4}$
Polarization	Circular/Linear
Pulse Rate	11.26 MHz
Max. Ave. Power	$\sim 1W$

### ▼ Technical Data of Ti:Sa Laser

Wave Length	800 nm
Pulse Length	130 fsec
Oscillator	90.1 MHz
Pulse Energy	2.5mJ    10mJ    50mJ
Repetition Rate	1kHz    1kHz    10Hz

# BL1B

## Terahertz Spectroscopy Using Coherent Synchrotron Radiation

II

### ▼ Description

Coherent synchrotron radiation (CSR) is a powerful light source in the terahertz (THz) region. This beamline has been constructed for basic studies on the properties of THz-CSR. However, it can be also used for measurements of reflectivity and transmission spectra of solids using conventional synchrotron radiation.

The emitted THz light is collected by a three-dimensional magic mirror (3D-MM, M0) of the same type as those already successfully installed at BL43IR in SPring-8 and BL6B in UVSOR-II. The 3D-MM was installed in bending-magnet chamber #1 and is controlled by a 5-axis pulse motor stage ( $x$ ,  $z$  translation;  $\theta_x$ ,  $\theta_y$ ,  $\theta_z$  rotation). The acceptance angle was set at 17.5-34 degrees (total 288 mrad) in the horizontal direction. The vertical angle was set at  $\pm 40$  mrad to collect the widely expanded THz-CSR.

The beamline is equipped with a Martin-Puplett type interferometer (JASCO FARIS-1) to cover the THz spectral region from 4 to 240  $\text{cm}^{-1}$  ( $h\nu = 500 \mu\text{eV}$ -30 meV). There is a reflection/absorption spectroscopy (RAS) end-station for large samples ( $\sim$  several mm). At the RAS end-station, a liquid-helium-flow type cryostat with a minimum temperature of 4 K is installed.

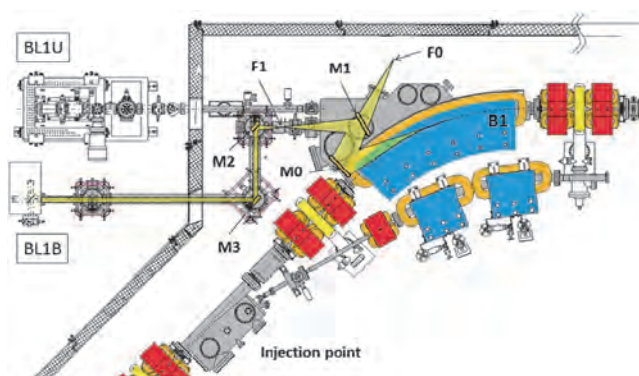


Fig. 1. Schematic top view of the beam extraction part of the THz-CSR beamline, BL1B. The three-dimensional magic mirror (3D-MM, M0) and a plane mirror (M1) are located in the bending-magnet chamber. A parabolic mirror (M2) is installed to form a parallel beam. The straight section (BL1U) is used for coherent harmonic generation (CHG) in the VUV region.

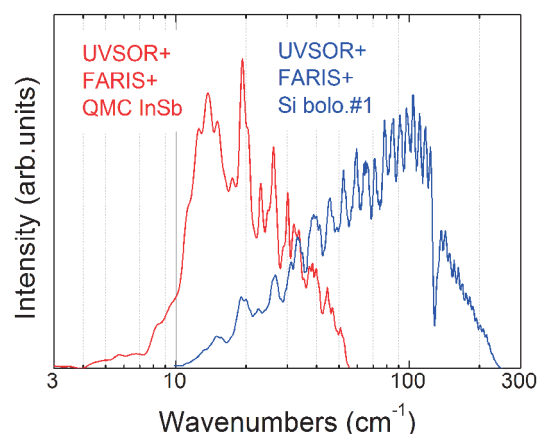


Fig. 2. Obtained intensity spectra with the combination of a light source (UVSOR), interferometer (FARIS-1), and detectors (Si bolometer and InSb hot-electron bolometer).

### ▼ Technical Data

Interferometer	Martin-Puplett (JASCO FARIS-1)
Wavenumber range (Energy range)	4-240 $\text{cm}^{-1}$ (500 $\mu\text{eV}$ -30 meV)
Resolution in $\text{cm}^{-1}$	0.25 $\text{cm}^{-1}$
Experiments	Reflection/transmission spectroscopy
Miscellaneous	Users can use their experimental system in this beamline.

# BL2A

## Soft X-Ray Beamline for Photoabsorption Spectroscopy

### ▼ Description

BL2A, which was moved its previous location as BL1A in 2011, is a soft X-ray beamline for photoabsorption spectroscopy. The beamline is equipped with a focusing premirror and a double-crystal monochromator [1]. The monochromator serves soft X-rays in the energy region from 585 to 4000 eV using several types of single crystals, such as  $\beta$ - $\text{Al}_2\text{O}_3$ , beryl, KTP ( $\text{KTiOPO}_4$ ), quartz, InSb, and Ge. The throughput spectra measured using a Si photodiode (AXUV-100, IRD Inc.) are shown in Fig. 1. The typical energy resolution ( $E / \Delta E$ ) of the monochromator is approximately 1500 for beryl and InSb.

A small vacuum chamber equipped with an electron multiplier (EM) detector is available. Photoabsorption spectra for powdery samples are usually measured in total electron yield mode, with the use of the EM detector. A silicon drift detector is also available for measuring partial fluorescence yields from solid samples.

[1] Hiraya *et al.*, Rev. Sci. Instrum. **63** (1992) 1264.

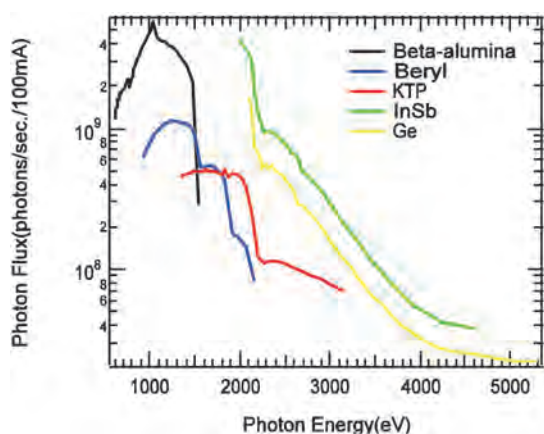


Fig. 1. Throughput spectra of the double-crystal monochromator at BL2A.



Fig. 2. Side view of BL2A.

### ▼ Technical Data

Monochromator	Double crystal monochromator
Monochromator crystals: (2 $\theta$ value, energy range)	$\beta$ - $\text{Al}_2\text{O}_3$ (22.53 $\text{\AA}$ , 585–1609 eV), beryl (15.965 $\text{\AA}$ , 826–2271 eV), KTP (10.95 $\text{\AA}$ , 1205–3310 eV), quartz (8.512 $\text{\AA}$ , 1550–4000 eV), InSb (7.481 $\text{\AA}$ , 1764–4000 eV), Ge (6.532 $\text{\AA}$ , 2094–4000 eV)
Resolution	$E/\Delta E = 1500$ for beryl and InSb
Experiments	Photoabsorption spectroscopy (total electron yield using EM and partial fluorescence yield using SDD)



# BL2B

## Photoelectron spectroscopy of molecular solids

II

### ▼ Description

This beamline previously dedicated for experiments in the field of gas phase photoionization and reaction dynamics. Then, the beamline has been reconstructed for photoelectron spectroscopy of molecular solids with a new end station, and experiments can be performed from May 2014. The monochromator is a spherical grating Dragon type with 18-m focal length. High throughput ( $1 \times 10^{10}$  photons  $s^{-1}$ ) and high resolution ( $E/\Delta E = 2000 - 8000$ ) are achieved simultaneously under the condition of the ring current of 100 mA [1]. The optical system consists of two pre-focusing mirrors, an entrance slit, three spherical gratings (G1 - G3), two folding mirrors, a movable exit slit, and a refocusing mirror [2]. The monochromator is designed to cover the energy range of 23–205 eV with the three gratings: G1 (2400 lines  $mm^{-1}$ ,  $R = 18$  m) at 80–205 eV; G2 (1200 lines  $mm^{-1}$ ,  $R = 18$  m) at 40–100 eV; G3 (2400 lines  $mm^{-1}$ ,  $R = 9.25$  m) at 23–50 eV. The percentage of the second-order light contamination at  $h\nu = 45.6$  eV is 23% for G2 or 7% for G3.

A UHV chamber is placed downstream of the refocusing mirror chamber and equipped silicon photodiode, sapphire plate Au mesh and filters for absolute photon flux measurement, monitor the photon-beam position, relative photon flux measurements and attenuate higher order light, respectively.

The new end station consists of a main chamber with a hemispherical analyzer (SCIENTA R3000) and a liquid-He-cooled cryostat (temperature range of 15–400 K) with 5-axis stage, a sample preparation chamber with a fast-entry load-lock chamber and a cleaning chamber with LEED, ion gun for sputtering and IR heating unit.

[1] M. Ono, H. Yoshida, H. Hattori and K. Mitsuke, Nucl. Instrum. Meth. Phys. Res. A **467-468** (2001) 577.

[2] H. Yoshida and K. Mitsuke, J. Synchrotron Radiation **5** (1998) 774.



Fig. 1. 18 m spherical grating monochromator at BL2B.

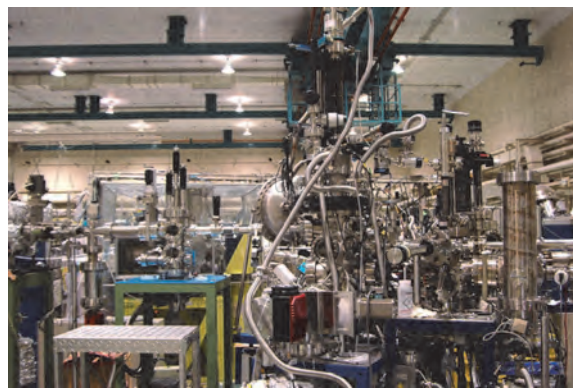


Fig. 2. End station of BL2B for photoelectron spectroscopy of molecular solids.

### ▼ Technical Data

Monochromator	18 m spherical grating Dragon-type
Wavelength Range	23–205 eV
Resolution	2000–8000 depending on the gratings
Experiments	Angle-resolved ultraviolet photoelectron spectroscopy

# BL3U

## Varied-Line-Spacing Plane Grating Monochromator for Molecular Soft X-Ray Spectroscopy

### ▼ Description

The beamline BL3U is equipped with an in-vacuum undulator composed of 50 periods of 3.8 cm period length. The emitted photons are monochromatized by the varied-line-spacing plane grating monochromator (VLS-PGM) designed for various spectroscopic investigations in the soft X-ray range. Three holographically ruled laminar profile plane gratings are designed to cover the photon energy range from 40 to 800 eV. The beamline has liquid cells for soft X-ray absorption spectroscopy (XAS) in transmission mode as shown in Fig. 1. The liquid cell is in the atmospheric helium condition, which is separated by a 100 nm thick  $\text{Si}_3\text{N}_4$  membrane with the window size of  $0.2 \times 0.2 \text{ mm}^2$  from the beamline in an ultrahigh vacuum condition. The thin liquid layer is assembled by using two 100 nm thick  $\text{Si}_3\text{N}_4$  membranes. The thickness of the liquid layer is controllable from 20 to 2000 nm by adjusting the helium pressures around the liquid cell in order to transmit soft X-rays. Liquid samples are exchangeable *in situ* by using a tubing pump. The liquid cell has two types of windows: one is the liquid part to obtain the soft X-ray transmission of liquid ( $I$ ), and the other is the blank part to obtain the transmission without liquid ( $I_0$ ). We can obtain the reliable XAS spectra based on the Lambert-Beer law  $\ln(I_0/I)$ . Since the liquid cell is in the atmospheric condition, we can measure XAS of liquid samples in the real environment. *Operando* XAS observation of several chemical reactions such as catalytic, electrochemical reactions are also possible by using our liquid cells developed for these purposes.

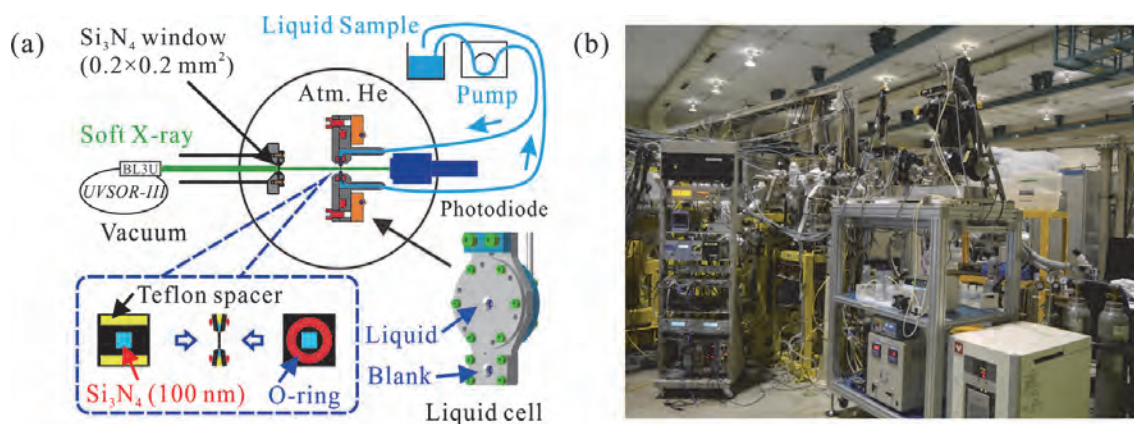


Fig. 1. (a) Schematics of a liquid cell for XAS in transmission mode settled in BL3U. The blowup shows a thin liquid layer assembled by two  $\text{Si}_3\text{N}_4$  membranes with the thickness of 100 nm. (b) Photograph of a XAS measurement system for liquid samples at the end station of BL3U.

### ▼ Technical Data

Monochromator	Varied-line-spacing plane grating monochromator
Energy Range	40-800 eV
Resolution	$E / \Delta E > 10\,000$
Experiments	Soft X-ray absorption spectroscopy of liquid in transmission mode

# BL3B (HOTRLU)

## VIS-VUV Photoluminescence and Reflection/Absorption Spectroscopy

II

### ▼ Description

BL3B has been constructed to study photoluminescence (PL) in the visible (VIS) to vacuum ultraviolet (VUV) region. This beamline consists of a 2.5 m off-plane Eagle type normal-incidence monochromator, which covers the VUV, UV, and VIS regions, i.e., the energy (wavelength) region of 1.7-31 eV (40-730 nm), with three spherical gratings having constant grooving densities of 1200, 600, and 300 l/mm optimized at the photon energies of  $\sim 20$ ,  $\sim 16$ , and  $\sim 6$  eV, respectively. The schematic side view and top view layouts are shown in Figs. 1(a) and 1(b), respectively. The FWHM of the beam spot at the sample position is 0.25 mm (V)  $\times$  0.75 mm (H). Low energy pass filters (LiF, quartz, WG32, OG53) can be inserted automatically to maintain the optical purity in the G3 (300 l/mm) grating region (1.7–11.8 eV). Figure 2 shows the throughput spectra (photon numbers at a beam current of 300 mA) for each grating with entrance and exit slit openings of 0.1 mm (resolving power  $E / \Delta E$  of  $\sim 2000$  (G3,  $\sim 6.8$  eV)). Since both slits can be opened up to 0.5 mm, a monochromatized photon flux of  $10^{10}$  photons/s or higher is available for PL measurements in the whole energy region.

The end station is equipped with a liquid-helium-flow type cryostat for sample cooling and two detectors; one of which is a photomultiplier with sodium salicylate and the other a Si photodiode for reflection/absorption measurement. For the PL measurements in the wide energy region from VIS to VUV, two PL monochromators, comprising not only a conventional VIS monochromator but also a VUV monochromator with a CCD detector, are installed at the end station.

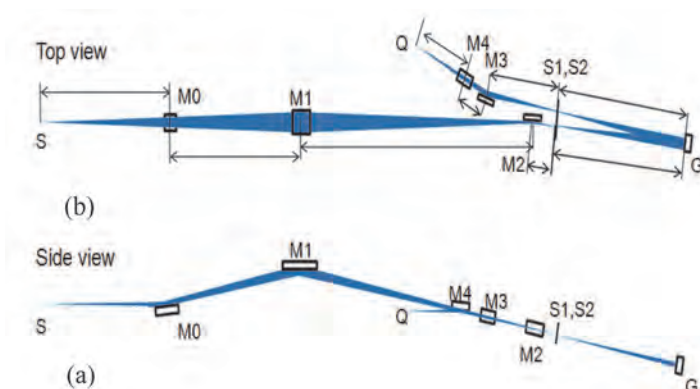


Fig. 1. Schematic layout of the BL3B (a) side view and (b) top view.

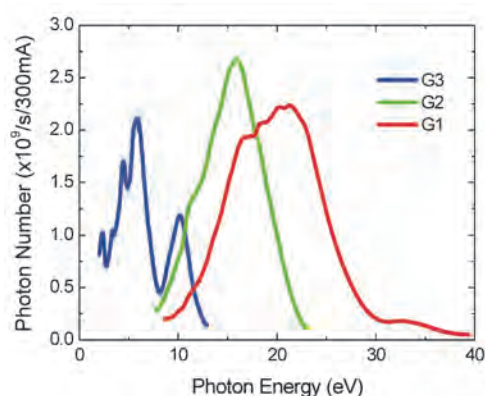


Fig. 2. Throughput spectra for each grating (G1:1200 l/mm, G2:600 l/mm and G3:300 l/mm) with  $S1 = S2 = 0.1$  mm.

### ▼ Technical Data

Monochromator	-2.5 m normal-incidence monochromator
Energy range	1.7-31 eV (40~730 nm)
Resolution ( $\Delta h\nu / h\nu$ )	$\geq 12000$ (at $\sim 6.9$ eV, 0.02 mm slits, G1 (1200 l/mm))
Experiments	Photoluminescence, reflection, and absorption spectroscopy, mainly for solids



# BL4U

## Scanning Transmission X-ray Microscopy in the Soft X-ray Region

### ▼ Description

In the soft x-ray region, there are several absorption edges of light elements and transition metals. The near edge X-ray absorption fine structure (NEXAFS) brings detailed information about the chemical state of target elements. A scanning transmission X-ray microscope (STXM) in the soft X-ray region is a kind of extended technique of the NEXAFS with high spatial resolution. The STXM has a capability of several additional options, for example, in-situ observations, 3-dimensional observation by computed tomography and ptychography, by utilizing the characteristics of the X-rays. The STXM can be applied to several sciences, such as polymer science, material science, cell biology, environmental science, and so on.

This beamline equips an in-vacuum undulator, a varied-line-spacing plane grating monochromator and a fixed exit slit. The soft X-ray energy range from 50 to 770 eV with the resolving power ( $E/\Delta E$ ) of 6,000 is available. The aperture size of the fixed exit slit determines not only the resolving power but also the size of a microprobe. A Fresnel zone plate is used as a focusing optical device through an order select aperture and its focal spot size of ~30 nm is available at minimum. An image is acquired by detecting intensities of the transmitted X-rays by a photomultiplier tube with scintillator with scanning a sample 2-dimensionally. By changing the energy of the incident beam, each 2-dimensional NEXAFS image is stacked. A main chamber of STXM is separated from the beamline optics by a silicon nitride membrane of 50-nm thickness; therefore, sample folders can be handled in vacuum or in helium.

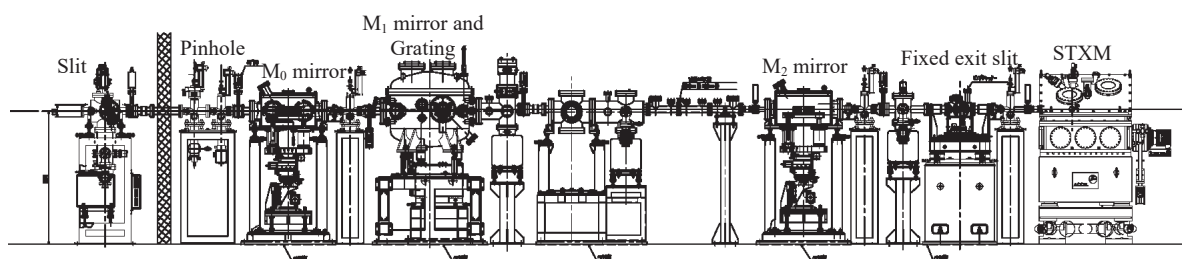


Fig. 1. Schematic image of BL4U

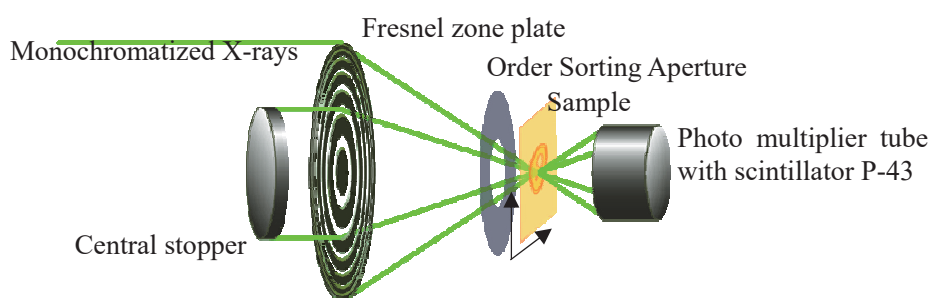


Fig. 2. Schematic image of STXM

### ▼ Technical Data

Energy range (E)	50 -770 eV
Resolving power ( $E/\Delta E$ )	~6,000
Focusing optical element	Fresnel zone plate
Spatial resolution	~30 nm
Experiments	2-dimensional absorption spectroscopy
Measurement environment	standard sample folder in vacuum or in helium, specially designed sample cell in ambient condition

# BL4B

## *Varied-Line-Spacing Plane Grating Monochromator for Molecular Soft X-Ray Spectroscopy*

### ▼ Description

The beamline BL4B equipped with a varied-line-spacing plane grating monochromator (VLS-PGM) was constructed for various spectroscopic investigations in a gas phase and/or on solids in the soft X-ray range. Three holographically ruled laminar profile plane gratings with SiO<sub>2</sub> substrates are designed to cover the photon energy range from 25 to 800 eV. The gratings with groove densities of 100, 267, and 800 1/mm cover the spectral ranges of 25–100, 60–300, and 200–1000 eV, respectively, and are interchangeable without breaking the vacuum. Figure 1 shows the absolute photon flux for each grating measured using a Si photodiode (IRD Inc.), with the entrance- and exit-slit openings set at 50 and 50 μm, respectively. The maximum resolving power ( $E/\Delta E$ ) achieved for each grating exceeds 5000.

There is no fixed endstation on this beamline. A small vacuum chamber equipped with an electron multiplier (EM) detector is available. Soft X-ray absorption spectra of solid samples are usually measured by means of the total electron yield method using EM, and the partial fluorescence yield method using a silicon drift detector (SDD).

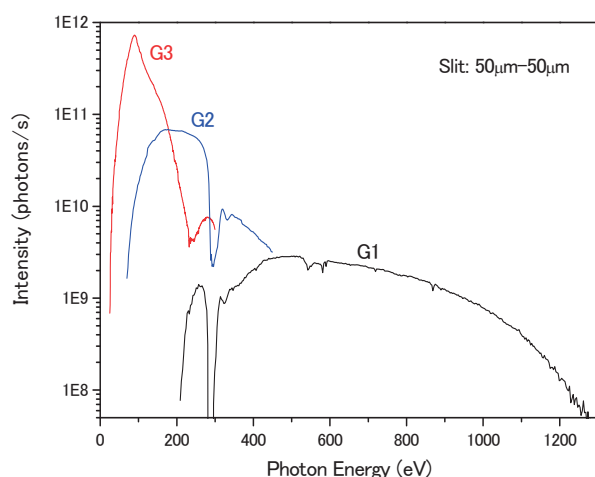


Fig. 1. Throughput from the VLS-PGM monochromator on BL4B.

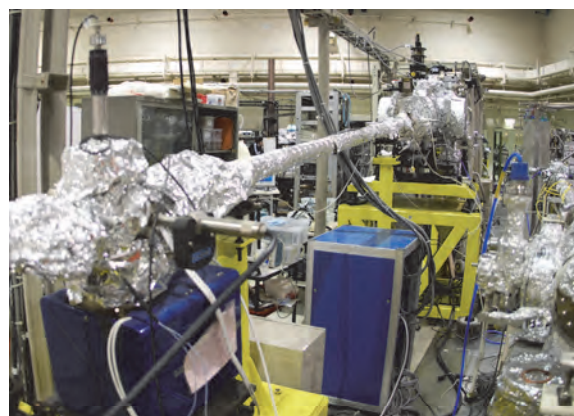


Fig. 2. Photo of BL4B.

### ▼ Technical Data

Monochromator	Varied-line-spacing Plane Grating Monochromator
Energy range	25–1000 eV
Resolution	$E / \Delta E > 5000$ (at maximum)
Experiments	Soft X-ray spectroscopy (mainly, photoabsorption spectroscopy for solid targets by means of total electron yield method using EM and partial fluorescence yield method using SDD)

# BL5U

## Photoemission Spectroscopy of Solids and Surfaces

### ▼ Description

Since the monochromator of BL5U was an old-style spherical grating type SGMTRAIN constructed in 1990s and the throughput intensity and energy resolution were poor, the whole beamline has been replaced to state-of-the-art monochromator and end station. The new beamline has been opened to users from FY2016 as high-energy resolution ARPES beamline. Samples can be cooled down to 3.8 K with newly developed 5-axis manipulator to perform high energy resolution measurements. Users can also obtain spatial-dependence of the electronic structure of solids using micro-focused beam ( $\sim 50 \mu\text{m}$ ). The new electron lens system makes it possible to obtain ARPES spectra without moving samples. This beamline will also have new capability to perform high-efficient spin-resolved ARPES in the future.

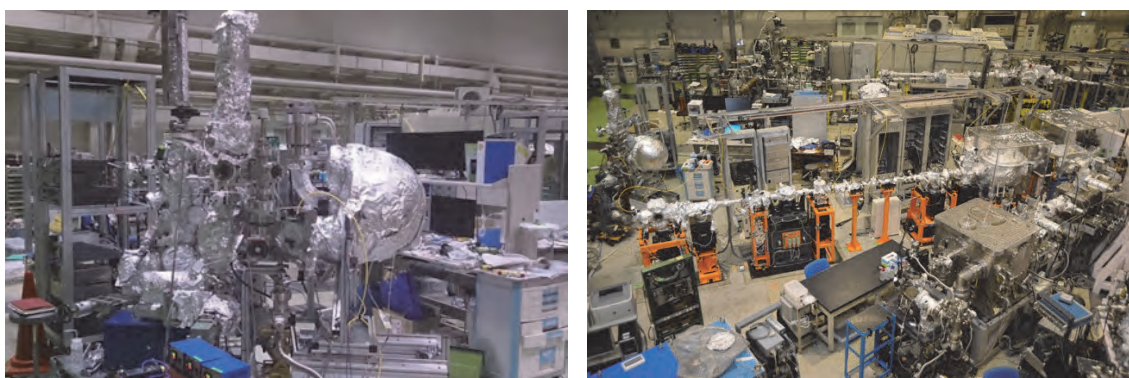


Fig. 1. Pictures of BL5U.

### ▼ Technical Data (Expected Performance)

Light source	APPLE-II type undulator ( $\lambda_u = 60 \text{ mm}$ , $N = 38$ ) vertical/horizontal, right/left circular (depending on $h\nu$ )
Monochromator	Monk-Gillieson VLS-PGM
Energy Range	20-200 eV
Resolution	$h\nu / \Delta E > 10,000$ for $< 10 \mu\text{m}$ slits
Experiment	ARPES, Space-resolved ARPES, Spin-resolved ARPES
Flux	$< 10^{12}$ photons/s for $< 10 \mu\text{m}$ slits (at the sample position)
Beam spot size	23 (H) x 40 (V) $\mu\text{m}$
Main Instruments	Hemispherical photoelectron analyzer with deflector scan (MBS A-1 Lens#4), Liq-He flow cryostat with 5-axis manipulator (3.8 K-350 K)



# BL5B

## Calibration Apparatus for Optical Elements and Detectors

II

### ▼Description

BL5B has been constructed to perform calibration measurements for optical elements and detectors. This beamline is composed of a plane grating monochromator (PGM) and three endstations in tandem. The most upstream station is used for the calibration measurements of optical elements, the middle one for optical measurements for solids, and the last for photo-stimulated desorption experiments. The experimental chamber at the most downstream station is sometimes changed to a chamber for photoemission spectroscopy. The calibration chamber shown in Fig. 2 is equipped with a goniometer for the characterization of optical elements, which has six degrees of freedom, X-Y translation of a sample, and interchanging of samples and filters. These are driven by pulse motors in vacuum. Because the polarization of synchrotron radiation is essential for such measurements, the rotation axis can be made in either the horizontal or vertical direction (s- or p-polarization).

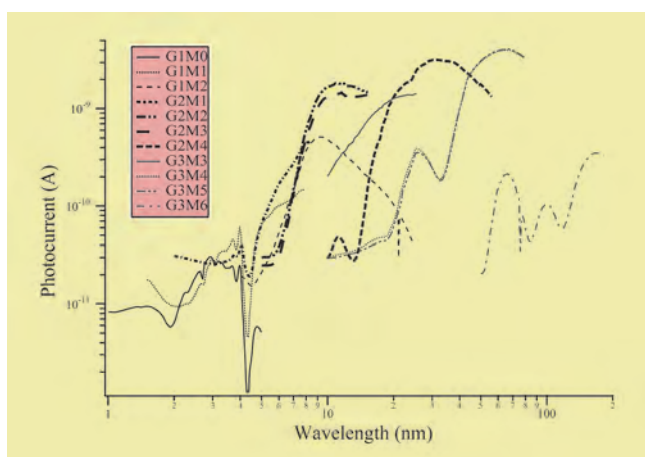


Fig. 1. Throughput spectra for possible combinations of gratings and mirrors at BL5B measured by a gold mesh.

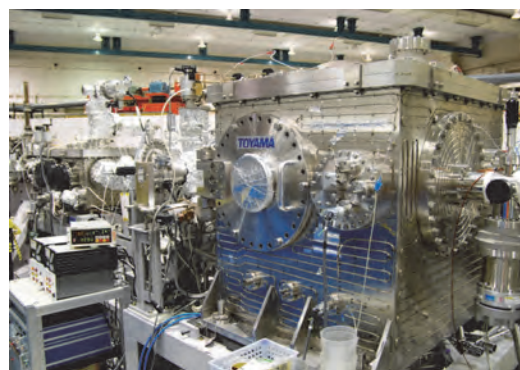


Fig. 2. A side view of the experimental chamber for calibration measurements.

### ▼Technical Data

Monochromator	Plane Grating Monochromator
Energy range	6-600 eV (2-200 nm)
Resolution	$E / \Delta E \sim 500$
Experiments	Calibration of optical elements, reflection and absorption spectroscopy mainly for solids

# BL6U

## Variable-Included-Angle / Variable-Line-Spacing Plane Grating Monochromator for Soft X-Ray photoelectron Spectroscopy

### ▼ Description

The beamline BL6U equipped with a variable-included-angle Monk-Gillieson mounting monochromator with a varied-line-spacing plane grating was constructed for various spectroscopic investigations requiring high-brilliance soft X-rays on solid surfaces. Through a combination of undulator radiation and sophisticated monochromator design (entrance slit-less configuration and variable-included-angle mechanism), using a single grating, the monochromator can cover the photon energy ranging from 40 to 500 eV, with resolving power of greater than 10000 and photon flux of more than  $10^{10}$  photons/s. Figure 1 shows an example of the monochromator throughput spectra measured using a Si photodiode, with the exit-slit opening set at 30  $\mu\text{m}$ , which corresponds to the theoretical resolving power of 10000 at 80 eV.

The end station is equipped with an electron energy analyzer for angle-resolved photoelectron spectroscopy (MB Scientific AB, A-1 analyzer Lens#5). This spectrometer consists of a hemispherical electron analyzer with a mechanical deflector and a mesh electrostatic lens near the sample to make the acceptance cone tunable. A constant energy angular distribution of the valence band dispersion cross section in the large  $k$  range can be efficiently obtained by applying a negative bias voltage to the sample and using the mechanical deflector.

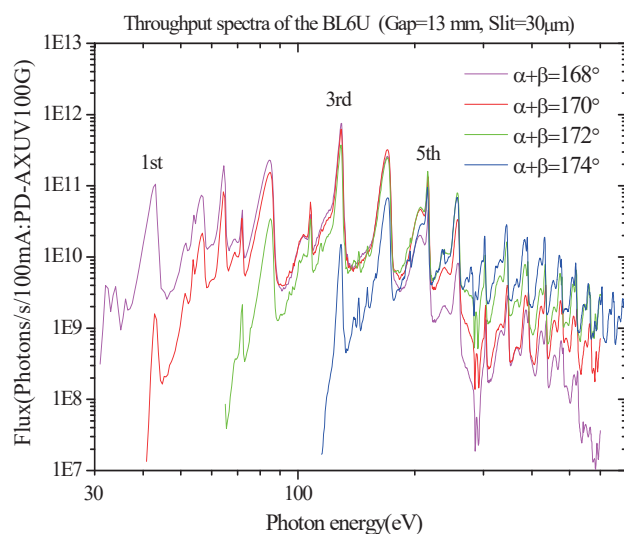


Fig. 1. Throughput spectra of the BL6U monochromator at various included angles.



Fig. 2. Photograph of BL6U end station.

### ▼ Technical Data

Monochromator	Variable-included-angle Varied-line-spacing Plane Grating Monochromator
Energy range	45-600 eV(practical)
Resolution	$E / \Delta E > 10000$ (at maximum)
Experiments	High-resolution soft X-ray spectroscopy (photoelectron spectroscopy for solid surfaces)

# BL6B

## Infrared and Terahertz Spectroscopy of Solids

II

### ▼ Description

Synchrotron radiation (SR) has good performance (high brilliance and high flux) not only in the VUV and soft X-ray (SX) regions but also in the infrared (IR) and THz regions. BL6B covers the IR and THz regions. The previous beamline, BL6A1, which was constructed in 1985, was the pioneer in IRSR research. The beamline was deactivated at the end of FY2003 and a new IR/THz beamline, BL6B (IR), was constructed in FY2004. The front-end part including bending duct #6 was replaced with a new part having a higher acceptance angle ( $215 (H) \times 80 (V) \text{ mrad}^2$ ) using a magic mirror, as shown in Fig. 1.

There are two Michelson type interferometers in this endstation; with first one (Bruker Vertex70v), which covers a wide spectral region from 30 to 20,000  $\text{cm}^{-1}$  ( $h\nu = 4 \text{ meV}-2.5 \text{ eV}$ ), reflection/absorption spectroscopy measurements of large samples (up to several mm) and IR/THz microscopy measurements of tiny samples (up to several tens of  $\mu\text{m}$ ) can be performed. For reflection/absorption spectroscopy measurements, a liquid-helium-flow type cryostat with a minimum temperature of 4 K is installed. The other interferometer (Jasco FT/IR-6100), which covers 350 to 15,000  $\text{cm}^{-1}$  ( $h\nu = 45 \text{ meV}-1.8 \text{ eV}$ ), has been available for IR microscopy imaging measurements from FY2014. One can also perform ATR measurements using diamond ATR prism.

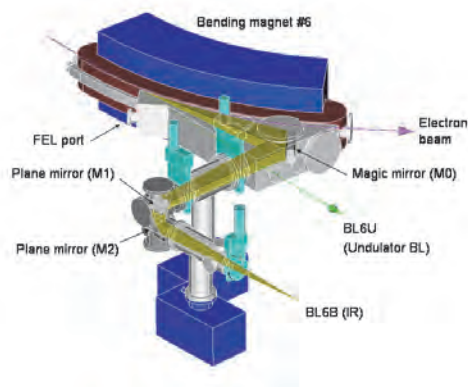


Fig. 1. Design of the optics and front end of BL6B.

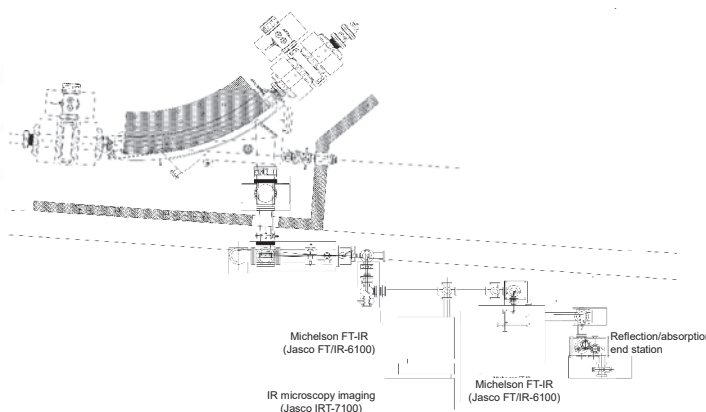


Fig. 2. Schematic top view of BL6B.

### ▼ Technical Data

Interferometer	Michelson (Bruker Vertex70v)	Michelson (Jasco FT/IR-6100)
Wavenumber Range (Energy range)	30-20,000 $\text{cm}^{-1}$ (4 meV-2.5 eV)	350-15,000 $\text{cm}^{-1}$ (45 meV-1.8 eV)
Resolution in $\text{cm}^{-1}$	0.1 $\text{cm}^{-1}$	0.5 $\text{cm}^{-1}$
Experiments	Reflectivity and transmission spectroscopy THz Microspectroscopy	IR microscopy imaging (JASCO IRT-7000) ATR spectroscopy



# BL7U (SAMRAI)

## Angle-Resolved Photoemission of Solids in the VUV Region

### ▼ Description

Beamline 7U, named the Symmetry- And Momentum-Resolved electronic structure Analysis Instrument (SAMRAI) for functional materials, was constructed to provide a photon flux with high energy resolution and high flux mainly for high-resolution angle-resolved photoemission spectroscopy, so-called “ARPES”, of solids [1]. An APPLE-II-type variable-polarization undulator is installed as the light source. The undulator can produce intense VUV light with horizontal/vertical linear and right/left circular polarization. The undulator light is monochromatized by a modified Wadsworth type monochromator with three gratings (10 m radius; 1200, 2400, and 3600 lines/mm optimized at  $h\nu = 10, 20,$  and  $33$  eV). The energy resolution of the light ( $h\nu/\Delta h\nu$ ) is more than  $10^4$  with a photon flux of  $10^{11}$ - $10^{12}$  ph/s or higher on samples in the entire energy region. The beamline has a photoemission end-station equipped with a 200 mm-radius hemispherical photoelectron analyzer (MB Scientific AB, A-1 analyzer) with a wide-angle electron lens and a liquid-helium-cooled cryostat with 6-axis pulse motor control. The main function of the beamline is to determine the electronic structure of solids and its temperature dependence in order to reveal the origin of their physical properties.

[1] S. Kimura, T. Ito, M. Sakai, E. Nakamura, N. Kondo, K. Hayashi, T. Horigome, M. Hosaka, M. Katoh, T. Goto, T. Ejima and K. Soda, Rev. Sci. Instrum. **81** (2010) 053104.

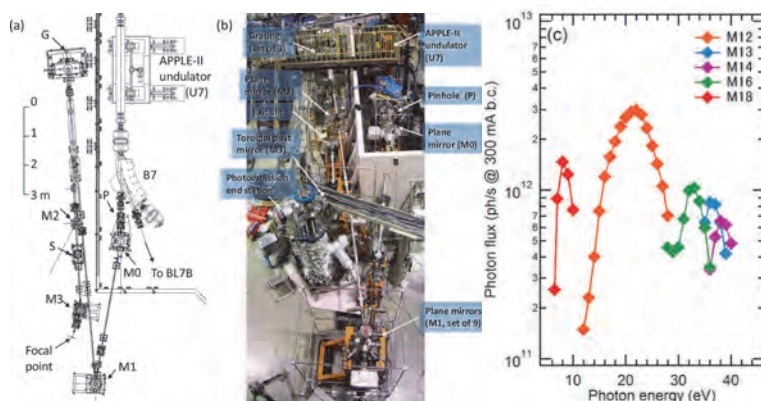


Fig. 1. SAMRAI beamline [(a), (b)] consisting of an APPLE-II type undulator (U7), a modified Wadsworth type monochromator (M0-S), and a high-resolution photoemission analyzer at the focal point. The monochromator has five major optical components: two plane mirrors (M0 and M1) with water cooling, one set of three spherical gratings (G), an exit slit (S), and one toroidal refocusing mirror (M3). (c) Example of flux intensity versus photon energy [1]

### ▼ Technical Data

Light source	APPLE-II type undulator ( $\lambda_u = 76$ mm, $N = 36$ ) vertical/horizontal, right/left circular (depending on $h\nu$ )
Monochromator	10 m normal-incidence monochromator (modified Wadsworth type)
Photon energy range	6 – 40 eV ( $\lambda = 30 - 200$ nm)
Resolution ( $h\nu/\Delta h\nu$ )	$E / \Delta E > 10000$ -50000
Photon flux on sample	$\geq 10^{11}$ - $10^{12}$ ph/s (depending on $h\nu$ )
Beam size on sample	200 (H) $\times$ 50 (V) $\mu\text{m}^2$
Experiments	Angle-resolved photoemission of solids (MV Scientific A-1 analyzer, acceptance angle: $\pm 18$ deg)

# BL7B

## 3 m Normal-Incidence Monochromator for Solid-State Spectroscopy

II

### ▼ Description

BL7B has been constructed to provide sufficiently high resolution for conventional solid-state spectroscopy, sufficient intensity for luminescence measurements, wide wavelength coverage for Kramers–Kronig analyses, and minimum deformation to the polarization characteristic of incident synchrotron radiation. This beamline consists of a 3-m normal incidence monochromator, which covers the vacuum ultraviolet, ultraviolet, visible, and infrared, i.e., the wavelength region of 50–1000 nm, with three gratings (1200, 600, and 300 l/mm). Two interchangeable refocusing mirrors provide two different focusing positions. For the mirror with the longer focal length, an LiF or a MgF<sub>2</sub> window valve can be installed between the end valve of the beamline and the focusing position. Figure 1 shows the absolute photon intensity for each grating with the entrance and exit slit openings of 0.5 mm. A silicon photodiode (AXUV-100, IRD Inc.) was utilized to measure the photon intensity and the absolute photon flux was estimated, taking the quantum efficiency of the photodiode into account.

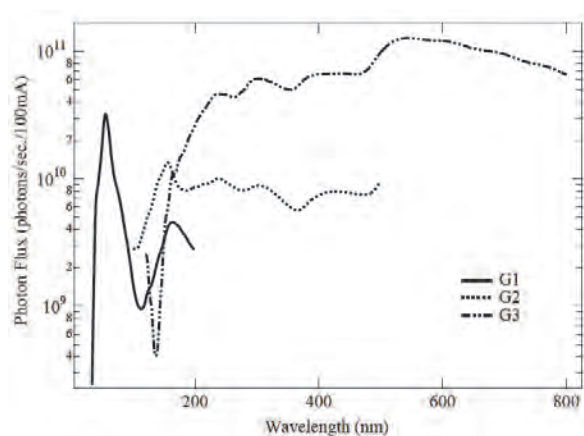


Fig. 1. Throughput spectra of BL7B measured using a silicon photodiode.

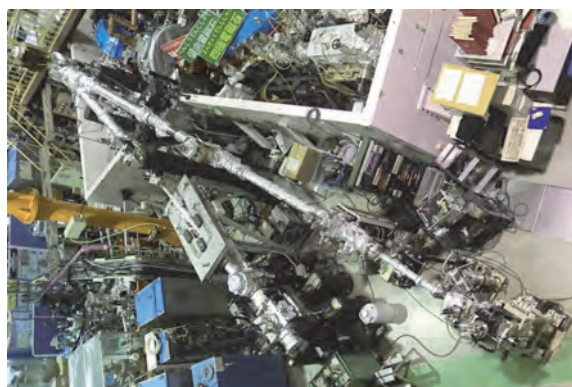


Fig. 2. Photo of BL7B.

### ▼ Technical Data

Monochromator	3 m Normal-Incidence Monochromator
Wavelength Range	50-1000 nm (1.2-25 eV)
Resolution	$E / \Delta E = 4000-8000$ for 0.01 mm slits
Experiments	Absorption, reflection, and fluorescence spectroscopy, mainly for solids

The background is a vibrant blue with a complex geometric design. A large, semi-transparent circular graphic is centered on the right side, featuring concentric rings and a dotted border. Diagonal lines and a grid of small dots are also visible, creating a sense of depth and movement.

# III-1

Accelerators and  
Instruments





BL1U

## Generation of Vector Beam with Tandem Helical Undulators at BL1U

S. Matsuba<sup>1</sup>, K. Kawase<sup>1</sup>, A. Miyamoto<sup>1</sup>, S. Sasaki<sup>1</sup>, M. Fujimoto<sup>2</sup>, T. Konomi<sup>2</sup>,  
N. Yamamoto<sup>3</sup>, M. Hosaka<sup>3</sup> and M. Katoh<sup>2</sup>

<sup>1</sup>Hiroshima Synchrotron Radiation Center, Hiroshima University, Higashi-hiroshima 739-0046, Japan

<sup>2</sup>UVSOR Synchrotron Facility, Institute for Molecular Science, Okazaki 444-8585, Japan

<sup>3</sup>Nagoya University Synchrotron Radiation Research Center, Seto 489-0965, Japan

Some sorts of lights which have spatially structured in intensity, polarization, and/or phase, called "structured light", have stimulated significant interests for a range of applications. Optical vortices and vector beams which have a donuts-shaped intensity with spiral phase structure or spatially dependent polarization that direction rotates around its beam axis have long been interest in laser community [1, 2]. Figure 1 shows schematic illustration of vector beams.

In accelerator-based light sources, several ways to generate optical vortices has been proposed and demonstrated [3]. In addition, edge radiation and transition radiation belong a category of vector beam. In these situations, we devise a scheme to produce a vector beam based on synchrotron radiation technology, which enables the generation of vector beams in the VUV or x-ray range [4]. The scheme is similar to the idea of "cross undulator" [5] but we expanded it into two dimensions to superpose second harmonics from tandem helical undulators at their polarizations were opposite to each other. It was well known in the laser community that the vector beams can be generated by superposing optical vortices.

The experiment was carried out at the BL1U. The first harmonic of the undulators light was set to 496 nm, and the second harmonic to 248 nm. The intensity was monitored with a CCD camera 7.5 m downstream from the center of the downstream undulator after through the band-pass filter with a center wavelength of  $248 \pm 1$  nm and rotatable linear polarizer for analysis of polarization direction.

The experimental results and the numerical simulations results done by using the Synchrotron Radiation Workshop [6] are shown in the Fig. 2. In the vicinity of the center, distributions of polarization are well approximated as a vector beams of Fig.1. Obtained degree of linear polarization is distributing in the range of 60-80%. This scheme may form the basis of generating vector beam in diffraction-limited synchrotron light sources in future.

In the next machine time, Stokes parameters of undulator radiation including vector beams will be measured for obtaining all polarization parameters.

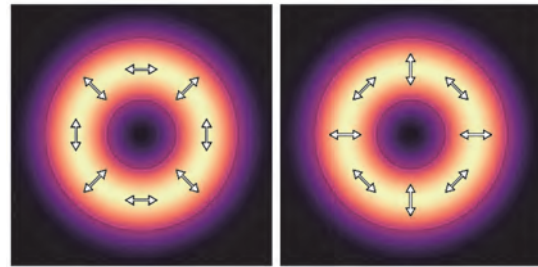


Fig. 1. Schematic illustration of intensity and polarization structure of vector beams.

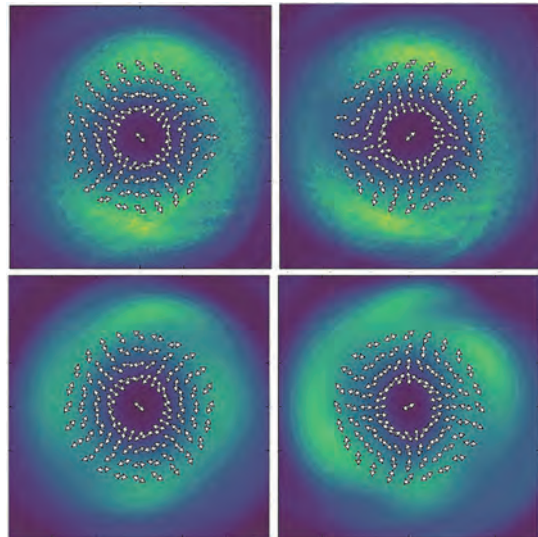


Fig. 2. Distribution of direction of linear polarization on the observed plane. The observed area is 6 mm × 6 mm square. Top and bottom rows show experimental and simulation results respectively. The experimental condition of results in right column have relative phase retardation of downstream undulator radiation from the condition of left column. The relative phase retardation is controlled approximately 180° by buncher magnets between undulators.

[1] H. Rubinsztein-Dunlop *et al.*, *J. Opt.* **19** (2017) 013001.

[2] Q. Zhan, *Adv. Opt. Photon.* **1** (2009) 1.

[3] M. Katoh *et al.*, *Sci. Rep.* **7** (2017) 6130.

[4] S. Matsuba *et al.*, *Appl. Phys. Lett.* **113** (2018) 021106.

[5] K. J. Kim, *Nucl. Instrum. Meth. Phys. Res.* **219** (1984) 425.

[6] O. Chubar *et al.*, *Nucl. Instrum. Meth. Phys. Res. A* **435** (1999) 495.

## The Performance Evaluation of Nuclear Emulsion

T. Takao<sup>1</sup>, T. Fukuda<sup>1,2</sup> and M. Nakamura<sup>1,2</sup>

<sup>1</sup>Graduate School of Science, Nagoya University, Nagoya 464-8602, Japan

<sup>2</sup>Institute of Materials and Systems for Sustainability, Nagoya University, Nagoya 464-8601, Japan

Nuclear emulsion is a kind of photographic film having sensitivity for ionization. The film is made by coating emulsion gel, consisting mainly of silver bromide crystals and gelatin, on plastic base (Fig. 1). When a charged particle passes through the film, its track is recorded by silver grains, for the particle runs in the film with silver bromides around it ionized. Our group uses the film to find neutrino interactions. It is not easy because the tracks we try to find are very fine. Nuclear emulsion resolves this difficulty. Because the silver bromide crystal's diameter is 200 nm, we can detect them. We produced the films by ourselves and checked their performance.

Grain density (GD) is a reference index of its sensitivity. This value is counts of silver grains per 100  $\mu\text{m}^2$ . The larger the value is, the thicker the track is. Then, I use the films exposed electron beam at UVSOR which has equivalent energy with minimum ionizing particle. Figure 2 shows the difference of grain densities by product batches. These values are not extraordinary and it suggests that the films can be used safely.

The film has accumulated tracks since it is produced. It means the film keep on recording cosmic ray, natural radiation, and so on. These tracks recorded before an experiment become noise. We want to fade noise tracks because our targets contain fine tracks. Then, we make the films "refresh". Refresh is a process to fade tracks in the film. The film is filled with silver bromide crystals. If a charged particle flies near them, they are ionized and become silvers. The reaction that silver bromide turns to be silver is reversible. It suggests that the tracks may fade away. We call this phenomenon "fading", and try to inhibit it. Refresh uses the characteristics of fading. I checked that refresh is effective for our films to use in the neutrino experiment. Then, I use the films exposed electron beam at UVSOR. I make the film refresh and measure grain density. Figure 3 shows the result. It is recognized that electron tracks and cosmic ray tracks faded after refresh.

We check the film's performance by using electron beam at UVSOR. After figuring out it, we use the film in experiments.

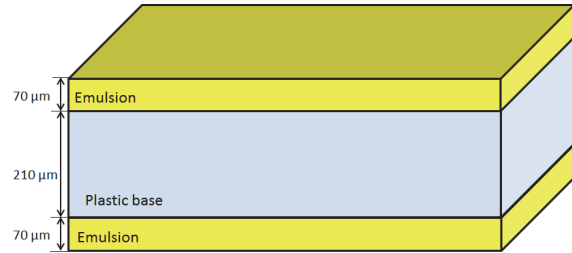


Fig. 1. The structure of nuclear emulsion



Fig. 2. The difference of GD by product batches

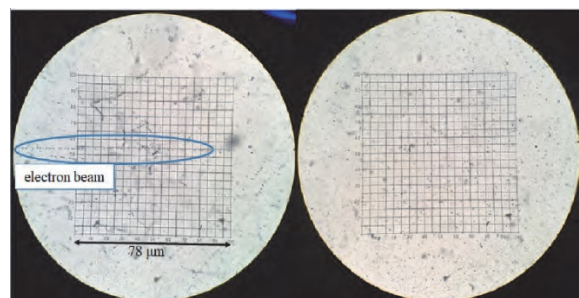


Fig. 3. microscope views of films (left: unrefreshed film, right: refreshed film)

BL1U

## Laser Compton Scattering Gamma-ray Generation for Nonlinear Effect in QED

T. Hayakawa<sup>1,2</sup>, K. Kawase<sup>1</sup>, T. Shizuma<sup>1</sup>, J. K. Koga<sup>3</sup>, H. Zen<sup>4</sup>, T. Kii<sup>4</sup>, H. Ohgaki<sup>4</sup>,  
M. Fujimoto<sup>5</sup> and M. Katoh<sup>5</sup>

<sup>1</sup>Tokai Quantum Beam Science Research Center, National Institutes for Quantum and Radiological Science and Applications, Tokai 319-1106, Japan

<sup>2</sup>National Astronomical Observatory of Japan, Mitaka 181-8588, Japan

<sup>3</sup>Kansai Photon Science Institute, National Institutes for Quantum and Radiological Science and Applications, Kizugawa 619-0215, Japan

<sup>4</sup>Institute of Advanced Energy, Kyoto University, Uji 611-0011, Japan

<sup>5</sup>UVSOR Synchrotron Facility, Institute for Molecular Science, Okazaki 444-8585, Japan

Although QED is considered to be established yet, QED predicted unresolved nonlinear effects, such as photon-photon interactions. However, because their cross sections are extremely small, the interactions have not been well studied [1,2]. Recently, the scattering of virtual photon – virtual photon scattering has been measured for the first time [1]. One of the photon- photon interactions is Delbrück scattering. Delbrück scattering, in which a gamma-ray interacting with a Coulomb field creates an electron-positron pair, which subsequently annihilates to generate a gamma-ray whose energy is almost identical with the incident gamma-ray, is one of important phenomena to study nonlinear effects by QED and vacuum polarization. However, there was a critical problem that one cannot derive only the amplitude of Delbrück scattering by the interference with other elastic scattering such as nuclear Thomson scattering and Giant Dipole Resonance.

Koga and Hayakawa [3] have presented that it is possible to measure selectively the amplitude of Delbrück scattering using linearly polarized gamma-ray beams. Furthermore, if one uses a linearly polarized beam with energies lower than 1.022 MeV, which is the threshold of the pair creation, it is possible to measure only the virtual process of Delbrück Scattering, namely vacuum polarization. For such a purpose, we have developed a laser Compton scattering (LCS) gamma-ray beam with a CO<sub>2</sub> laser having a wavelength of 10.6  $\mu\text{m}$  at the UVSOR-III synchrotron radiation facility, in which the energy of the electron beam stored in top-up mode is approximately 750 MeV. We have demonstrated the 1-MeV LCS gamma-ray beam generation using a random polarization CO<sub>2</sub> laser [4].

We newly installed a linearly polarized CW CO<sub>2</sub> laser with power of up to 130 W in order to generate linearly polarized LCS gamma-ray beam (see Fig. 1). We measured the energy spectra of the generated LCS gamma-ray beam using 3.5"  $\times$  4" LaBr<sub>3</sub>(Ce) scintillation detector. Figure 2 shows the measured energy spectra. The LCS gamma-ray intensity increases with increasing laser power.

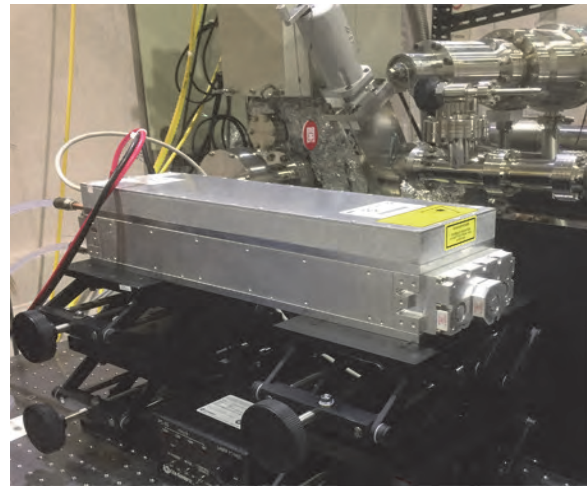


Fig. 1. Photo of the newly installed high power linearly polarized CO<sub>2</sub> laser.

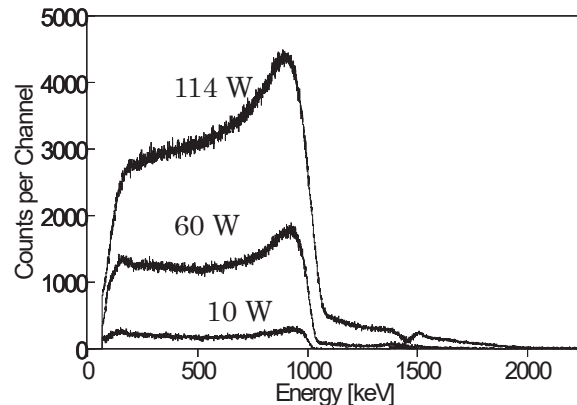


Fig. 2. Measured energy spectra of the generated LCS gamma-ray beam. The gamma-ray intensity increases with increasing laser power.

[1] ATLAS Collaboration, *Nature Physcs* **13** (2017) 852.

[2] T. Inada *et al.*, *Phys. Lett. B* **732** (2014) 356 .

[3] J. K. Koga and T. Hayakawa, *Phys. Rev. Lett.* **118** (2017) 204801.

[4] H. Zen *et al.*, *J. Phys.: Conf. Ser.* **1067** (2018) 092003.



BL1U

## Study on Isotope 3D Imaging Using NRF Absorption Method in UVSOR-BL1U

H. Ohgaki<sup>1</sup>, H. Zen<sup>1</sup>, T. Kii<sup>1</sup>, K. Ali<sup>1</sup>, T. Hayakawa<sup>2</sup>, T. Shizuma<sup>2</sup>, H. Toyokawa<sup>3</sup>, Y. Taira<sup>3</sup>, V. Iancu<sup>4</sup>, V. G. Turturica<sup>4</sup>, M. Fujimoto<sup>5</sup> and M. Katoh<sup>5</sup>

<sup>1</sup>Institute of Advanced Energy, Kyoto University, Kyoto 611-0011, Japan

<sup>2</sup>Tokai Quantum Beam Science Center, National Institutes for Quantum and Radiological Science and Technology, Tokai 319-1106, Japan

<sup>3</sup>National Institute of Advanced Industrial Science and Technology (AIST) Tsukuba Central 2-4, Tsukuba 305-8568, Japan

<sup>4</sup>Extreme Light Infrastructure - Nuclear Physics, s/ Horia Hulubei National Institute for R&D in Physics and Nuclear Engineering, Bucharest-Magurele, Judet Ilfov, RO-077125, Romania

<sup>5</sup>UVSOR Synchrotron Facility, Institute for Molecular Science, Okazaki 444-8585, Japan

A Nuclear Resonance Fluorescence (NRF) method is a powerful tool for investigation not only of the nuclear physics, but also of isotope imaging inside the spent nuclear fuel canisters and nuclear wastes. We have been developing an isotope imaging technique by using NRF [1]. The absorption can be measured by sample material and “witness target”[2].

A demonstration experiment of the NRF-CT imaging by using LCS gamma-ray beam has been carried out at the LCS gamma-ray beamline, BL1U (Fig. 1), at UVSOR-III where 5.4 MeV LCS gamma-rays with a flux of  $1 \times 10^7$  photons/s can be available [3]. In 2018, we upgraded the energy of LCS gamma-rays up to 5.5 MeV and about 10 times higher flux by replacing the IR fiber laser.

By using NRF absorption method a NRF-CT image has been taken for a sample target consists of aluminum, stainless steel, and lead rods (shown in Fig. 2 (a)). The NRF signals from the witness target (natural lead) were measured by a Ge detector. At the same time, transmission gamma-rays have been measured by a LaBr<sub>3</sub>(Ce) detector which gives a density distribution of the sample target. The segmented CT reconstruction method has been developed and we obtained clear <sup>208</sup>Pb distribution as shown in Fig. 2 (b) [4].

After the upgrade of the UVSOR-III BL1U beamline, we have been trying to take a real isotope image by using enriched targets, <sup>206</sup>Pb and <sup>208</sup>Pb. The experiment has been performed and the isotope CT image reconstruction is under processing. To obtain a high resolution image and 3D CT have also been planned.

[1] N. Kikuzawa *et al.*, Appl. Phys. Express **2** (2009) 036502.

[2] H. Ohgaki *et al.*, Proceedings of IPAC2016, Busan, Korea, 2007-2010 (2016).

[3] H. Zen *et al.*, Energy Procedia **89** (2016) 335-345.

[4] H. Zen *et al.*, AIP Advanced **9** (2019) 35101.

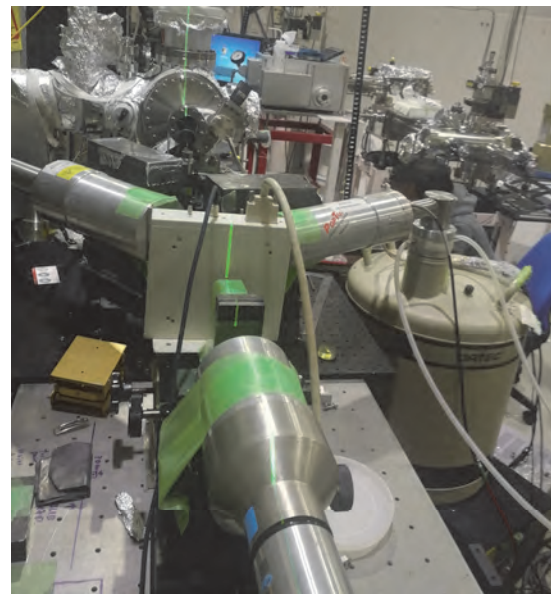


Fig. 1. BL1U LCS gamma-ray beamline with the setup for NRF-CT measurement.

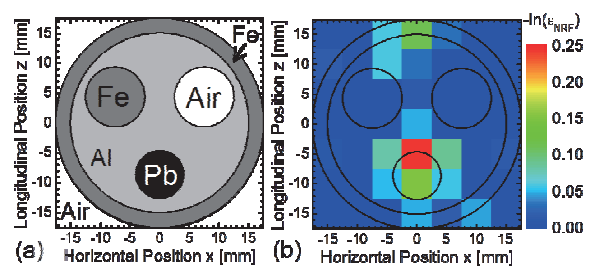


Fig. 2. (a) Arrangement of the sample target. (b) Result of NRF-CT measurement.

BL1U

## Study on Oxygen Vacancy in TiO<sub>2</sub> Using Photon Induced Positron Annihilation Spectroscopy at UVSOR-BL1U

H. Toyokawa<sup>1</sup>, S. Dohshi<sup>2</sup>, T. Ehiro<sup>2</sup>, K. Maeda<sup>2</sup>, Y. Taira<sup>1</sup>, T. Hirade<sup>3</sup>,  
M. Fujimoto<sup>4</sup> and M. Katoh<sup>4</sup>

<sup>1</sup>National Institute of Advanced Industrial Science and Technology  
Tsukuba Central 2-4, Tsukuba 305-8568, Japan

<sup>2</sup>Osaka Research Institute of Industrial Science and Technology, Izumi 594-1157, Japan

<sup>3</sup>Nuclear Science and Engineering Center, Japan Atomic Energy Agency, Tokai 319-1195, Japan

<sup>4</sup>UVSOR Synchrotron Facility, Institute for Molecular Science, Okazaki 444-8585, Japan

Titanium dioxide (TiO<sub>2</sub>) is one of the most important catalysts and catalyst supports for industrial use. It is sometimes used under harsh chemical or physical conditions, such as in water or chemical vapors under high temperature and pressure. We have been interested in a mechanism of catalytic activity of TiO<sub>2</sub> to improve its performance.

Our recent studies showed formation of oxygen vacancies and titanium ions (Ti<sup>3+</sup>) gave strong effect on the surface wettability and catalytic activity of TiO<sub>2</sub> under irradiation of UV light or gamma-rays [1]. It is also recently reported that very high oxidative decomposition activity for organic molecules such as toluene was observed by an excitation of valence electrons with applying heat, instead of light or ionizing radiation [2]. While these mechanisms are not understood in detail yet, we believe oxygen vacancy plays an important role.

Our research proposal is to study the mechanism of the catalytic activity of TiO<sub>2</sub> under heat application, by an observation of oxygen vacancy concentration as a function of temperature of sample material. In this study, a contactless and noninvasive material analysis method, so called the photon induced positron annihilation spectroscopy method was applied [3]. The method is based on a positron annihilation gamma-ray spectroscopy, triggered by a high-energy photon beam incident on a sample material.

When photons of a few MeV or higher are incident on a sample material, a part of them decays into electron-positron pair (pair creation), and intense monochromatic gamma-rays of 511 keV are emitted following to the positron annihilation with their counterpart electrons (positron annihilation). In the present research study, we measured an energy spread of annihilation gamma-rays, which contains information on the atomic vacancy concentration of the sample material.

While the energy of the annihilation gamma-rays is simply monochromatic, it slightly shifts as the momentum of the counterpart electrons with which the positrons annihilate. It is called the doppler broadening of the annihilation gamma-rays. When a momentum of the counterpart electrons was large, the energy spread of the annihilation gamma-rays is also large, and it is small when the momentum was small. The energy

spread is usually small, typically on the order of keV, and it can be measured with high energy-resolution gamma-ray spectrometer, such as high-purity germanium detector (HPGe).

We have set up a gamma-ray spectroscopy system at the laser-Compton scattering (LCS) beamline of BL1U at UVSOR-III [4], and measured the energy spectra of the annihilation gamma-rays as we changed the sample temperature, from room temperature to 600 degree Celsius. The data acquisition was successful, and their analysis is being undergone. We also prepare for the experiment of the positron lifetime measurement in next fiscal year, to study the mechanism in detail.

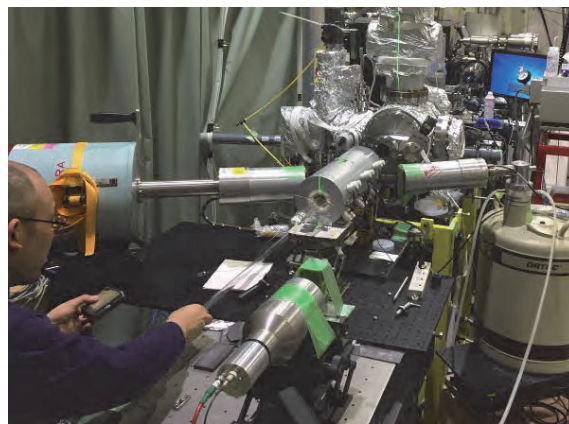


Fig. 1. Measurement system for doppler broadening spectroscopy at LCS beamline at BL1U in UVSOR-III.

- [1] S. Dohshi *et al.*, Top Catal. **35** (2005) 327.
- [2] H. Nishikawa, Appl. Surf. Sci. **225** (2009) 7468.
- [3] H. Toyokawa *et al.*, Proc. AccApp'07 (2007) 331.
- [4] H. Zen *et al.*, Energy Procedia **89** (2016) 335.

BL2A

## Unprecedented Data of the Solar Corona Taken by a High-Speed X-ray CMOS Camera aboard FOXSI-3 Sounding Rocket

 N. Narukage<sup>1</sup> and S. Ishikawa<sup>2</sup>
<sup>1</sup>National Astronomical Observatory of Japan, Mitaka 181-8588, Japan

<sup>2</sup>Institute for Space-Earth Environmental Research (ISEE), Nagoya University, Nagoya 464-8601, Japan

The solar corona is full of dynamic phenomena. They are accompanied by interesting physical processes, namely, magnetic reconnection, particle acceleration, shocks, waves, flows, evaporation, heating, cooling, and so on. The understandings of these phenomena and processes have been progressing step-by-step with the evolution of the observation technology in EUV and X-rays from the space. But, there are fundamental questions remain unanswered, or haven't even addressed so far. Our scientific objective is to understand underlying physics of dynamic phenomena in the solar corona, covering some of the long-standing questions in solar physics such as particle acceleration in flares and coronal heating. In order to achieve these science objectives, we identify the imaging spectroscopy (the observations with spatial, temporal and energy resolutions) in the soft X-ray range (from  $\sim 0.5$  keV to  $\sim 10$  keV) is a powerful approach for the detection and analysis of energetic events [1]. This energy range contains many lines emitted from below 1 MK to beyond 10 MK plasmas plus continuum component that reflects the electron temperature.

The soft X-ray imaging spectroscopy is realized with the following method. We take images with a short enough exposure to detect only single X-ray photon in an isolated pixel area with a fine pixel Silicon sensor. So, we can measure the energy of the X-ray photons one by one with spatial and temporal resolutions. When we use a high-speed soft X-ray camera that can perform the continuous exposure with

a rate of more than several hundred times per second, we can count the photon energy with a rate of several 10 photons / pixel / second. This high-speed exposure is enough to track the time evolution of spectra generated by dynamic phenomena in the solar corona, whose lifetimes are about from several ten seconds to several minutes.

For the first imaging spectroscopic observation of the solar corona in soft X-ray range, we launched a NASA's sounding rocket (FOXSI-3) on September 7<sup>th</sup>, 2018 [2] and successfully obtained the unprecedented data (see Fig. 1) [3] using a high speed X-ray camera with a back-illuminated CMOS sensor [4].

The performances (especially, the photon counting capability) of this CMOS sensor was evaluated at UVSOR BL2A [5]. We deeply thank Mr. Kondo, Mr. Nakamura and Dr. Tanaka for their kind help.

[1] N. Narukage *et al.*, White paper of the "soft X-ray imaging spectroscopy", arXiv:1706.04536 (2017).

[2] Web Release:

<https://hinode.nao.ac.jp/en/news/topics/foxsi-3-180907/>

[3] Web Release:

<https://hinode.nao.ac.jp/en/news/topics/foxsi-3-data-release-en-20190115/>

[4] S. Ishikawa *et al.*, Nucl. Instrum. Methods Phys. Res. Sec. A **912** (2018) 191.

[5] N. Narukage and S. Ishikawa, UVSOR Activity Report **45** (2017) 33.

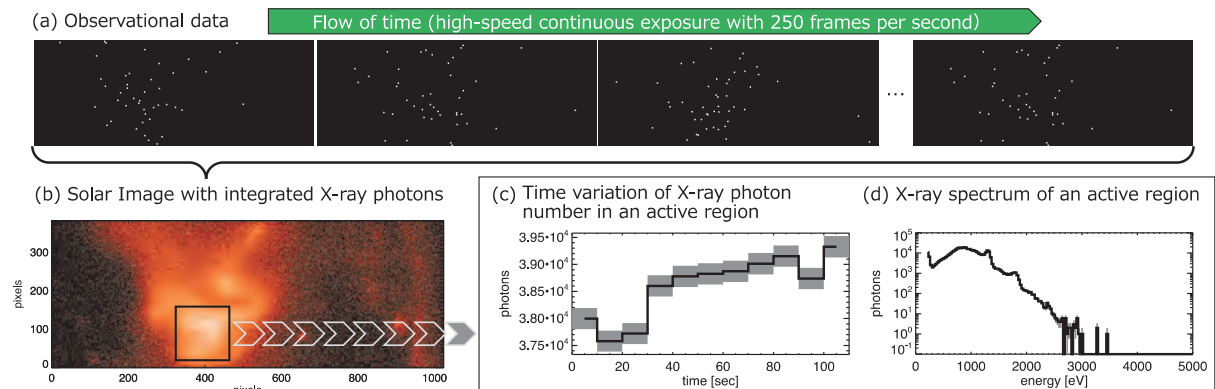


Fig. 1. Focusing imaging spectroscopic data in soft X-rays obtained by the FOXSI-3 sounding rocket. Panel (a) shows real FOXSI data. Each white dot in these images is an individual X-ray photon. From these images, we can simultaneously obtain information about the position, timing, and energy of each X-ray photon. Using this information, we can construct a solar corona image (see Panel (b)). We can also investigate the temporal evolution and spectrum of the X-ray photons, as shown in Panels (c) and (d), respectively.



BL4U

## Development of a Secondary Electron Detector for a Scanning Transmission X-ray Microscope

T. Ohigashi<sup>1,2</sup> and H. Yuzawa<sup>1</sup><sup>1</sup>UVSOR Synchrotron Facility, Institute for Molecular Science, Okazaki 444-8585, Japan<sup>2</sup>School of Physical Sciences, The Graduate University for Advanced Studies (SOKENDAI), Okazaki 444-8585, Japan

Analysis of interactions of X-ray with matters, such as absorption, scattering, fluorescence, photoemission, phase transition, photo- and secondary electron etc., brings unique information according to its mechanism. Basically, a scanning transmission X-ray microscope (STXM) uses X-ray absorption to acquire integrated information of a sample along its optical axis (i.e. bulk information) and sometimes uses X-ray fluorescence or photo- and secondary electron to obtain additional information simultaneously. Detection of the electrons is useful to analyze near surface information of the sample since escape depth of the electrons is limited to a few nm. Furthermore, the detection of the electrons also enables to measure a thick sample which cannot be penetrated by the X-rays. STXM beamline BL4U can use low energy region from 50 to 770 eV [1] so that the detection of the secondary electrons is more suitable than that of X-ray fluorescence in regard to their yields. Therefore, we have been developing an optical system for STXM with using a channeltron to detect the secondary electrons.

A schematic image of an optical system of STXM with a channeltron (C4831, Photonis Inc.) is shown in Fig. 1. Typically, the channeltron for STXM is placed downstream of the sample in parallel with a detector for a transmitted X-ray [2] because gap between an order select aperture (OSA) and the sample is not enough to set the channeltron to detect the electrons from top surface of the sample. Even though, in this report, the channeltron was placed upstream of the sample, set toward between the sample and OSA, to analyze front-surface of the sample. A focusing element, a Fresnel zone plate, with outermost zone width of 45 nm and diameter of 240  $\mu\text{m}$  was used for longer focal length instead of higher spatial resolution. Then, the gap between the OSA and the sample was about 1 mm at the X-ray energy of 400 eV.

An ultra thin section of blended polymer supported by a copper grid was used as a test sample. The sample was tilted about 30° towards the channeltron. 50 V for input end and 2000 V for output end were applied to the channeltron. Degree of vacuum was  $\sim 3 \times 10^{-6}$  mbar. A secondary electron image by the channeltron and an X-ray transmission image were obtained simultaneously (shown in Fig. 2). Then, energy of the X-ray was 400 eV and dwell time per a pixel was 500 ms. From edge

profiles of the copper grid in each image, spatial resolutions are almost similar. In the secondary electron image in Fig. 2 (b), open space shown by a dashed circle, where signals should be zero, produces some signals more than the polymer. This result is under discussion.

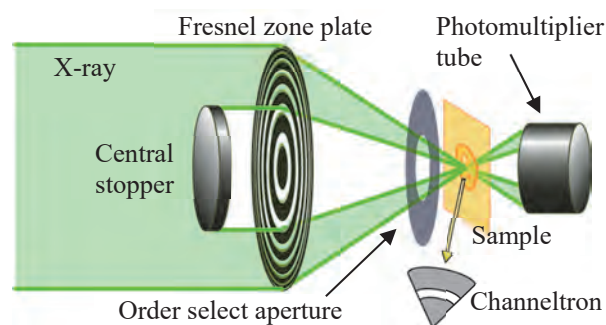


Fig. 1. A schematic image of a optical system of STXM with a channeltron.

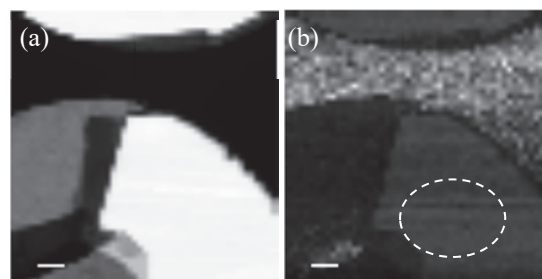


Fig. 2. (a) An X-ray transmission and (b) a secondary electron images of a thin section of blended polymer on a copper grid. White color shows more signals. Scale bars are 5  $\mu\text{m}$ .

- [1] See beamline section of this activity report  
 [2] C. Hub, W. Wenzel, J. Raabe, H. Ade and R. H. Fink, Rev. Sci. Instrum. **81** (2010) 033704.



BL7B

### Pre-flight Verification of CLASP2 Throughput

D. Song<sup>1</sup>, R. Ishikawa<sup>1</sup>, R. Kano<sup>1</sup>, M. Yoshida<sup>2</sup> and K. Shinoda<sup>1</sup>

<sup>1</sup>National Astronomical Observatory of Japan, Mitaka 181-8588, Japan

<sup>2</sup>Department of Astronomical Science, Graduate University for Advanced Studies (SOKENDAI), Mitaka 181-8588, Japan

We have developed a high precision (<0.1%) UV spectro-polarimeter called Chromospheric LAYER Spectro-Polarimeter (CLASP2), and it is in a final step for the launch whose expected date is on April 1<sup>st</sup>, 2019. CLASP2 is a NASA sounding rocket experiment, which aims to advance our knowledge of the magnetic fields in the upper solar chromosphere by spectro-polarimetric observations at the Mg II h & k lines (near 280 nm) and imaging observation with high cadence at the Lyman-alpha line (121.6 nm) [1]. For this, the high throughput of the instrument in both the UV lines is required.

To obtain the high throughput of CLASP2, we had carried out a dual-band pass “cold mirror” coating targeting at both the lines to the primary mirror of the telescope, and also performed the high reflectivity (R) mirror coating (Al+MgF<sub>2</sub>) to other mirrors. After coating, we have frequently checked its coating performance at UVSOR [2], and monitored their reflectivity by using the witness samples (WSs) which are 1-inch flat mirrors coated simultaneously with the flight mirrors.

On November, 2018, we moved our instrument from Japan to USA for the final preparation of the launch. At that time, we attached six WSs on our instrument to monitor the contamination during the transportation and experiment. We brought the monitored WSs back to Japan, and carried out the pre-flight verification of the healthiness of the CLASP2 flight mirrors at the UVSOR BL7B by using the WSs. In particular, we measured the reflectivity of each WS not only near 280 nm (G3 grating) but also at 121.6 nm (G2 grating). Finally, we compared the results with those of previous UVSOR measurements and derived the final throughput of CLASP2.

Figure 1(a) shows one of the results of our reflectivity measurement of the primary mirror (M1) from the 115 nm to the 850 nm wavelengths. The measured reflectivity is 50% at the 121.6 nm and 71% near the 280 nm wavelengths, both of which meet the specification. The average reflectivity in the visible light is about 5%. The difference between this measurement and the previous measurement is only about 1% near the 280 nm and about 3% at the 121.6 nm wavelengths. It indicates that the dual-band pass cold mirror coating performed on the M1 still keeps sufficient performance even 15 months after the coating.

We also confirmed that the coating performance of other flight mirrors is well maintained as our required specification. Figure 1(b) presents results of reflectivity of each mirror, and Table 1 represents the results in detail.

Finally, we calculated throughput of the spectro-polarimeter and updated the radiometry of CLASP2 based on our measurements at the UVSOR. From the

calculation of radiometry, we confirmed that our minimum required time for the observations of each target is still less than the planned observing time.

In summary, we have measured the reflectivity of WSs which were simultaneously coated with flight mirrors and accompanied with the instrument during the integration in Japan and shipment from Japan to USA through the UVSOR experiment. From this experiment, we confirmed: (1) There is no significant degradation of the coating performance of all the flight mirrors. (2) The final throughput of SP is satisfied for the solar observations we required.

Recently, we moved our instrument of CLASP2 to the launch site "US White Sands Missile Range" in New Mexico. It is ready for the launch.

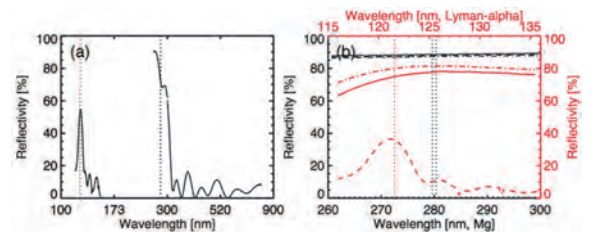


Fig. 1. Measured reflectivity of witness samples of (a) the primary mirror (M1) and (b) other mirrors: M3 - Off-axis parabolic mirror (black solid line), M4 - Hyperbolic Mirror (black dashed line), M5 - Folder mirror (black dot-dashed line), Grating (black three dots-dashed line), Slit mirror (red solid line), Slit-jaw cold coating mirror (red dashed line), and M2 – Secondary mirror of telescope (red dot-dashed line). Red dotted lines represent the Lyman-alpha line and black dotted lines show the Mg II line near 280 nm wavelength.

Table 1. Reflectivity of CLASP2’s flight mirrors: Spec.: specification, Prev.: previous UVSOR measurements, and U#38: pre-flight measurements (M1 & M2 are flight mirrors of telescope, From M3 to M5 and Grating are SP mirrors, SM and SC represent a slit mirror and a slit-jaw cold mirror). Note that, black color indicates the value of reflectivity at 280 nm and red color represents the values of reflectivity at 121.6 nm

	M1	M2/M3	M4	M5	SM	SC	Grating
Spec.	>70%	>80%	>80%	>80%	>75%	>35%	-
Prev.	72%	89%	87%	87%	78%	36%	89%
U#38	50%	80%	88%	87%	76%	36%	84%

[1] N. Narukage *et al.*, SPIE **9905** (2016) 99052U.  
 [2] D. Song *et al.*, UVSOR Activity Report 2017 **45** (2018) 36.

BL7B

## The Composite Type Measurement System for VIS-VUV Complex Refractive Index

D. Imai<sup>1</sup>, S. Takashima<sup>1</sup>, K. Fukui<sup>1</sup>, K. Yamamoto<sup>2</sup>, T. Saito<sup>3</sup> and T. Horigome<sup>4</sup>

<sup>1</sup>Department of Electrical and Electronics Engineering, University of Fukui, Fukui 910-8507, Japan

<sup>2</sup>Far-infrared region Development Research Center, University of Fukui, Fukui 910-8507, Japan

<sup>3</sup>Department of Environment and Energy, Tohoku Institute of Technology, Sendai 982-8577, Japan

<sup>4</sup>UVSOR Synchrotron Facility, Institute for Molecular Science, Okazaki 444-8585, Japan

Since the ultraviolet (UV) - vacuum UV (VUV) region generally has strong absorption, for example, the correct complex refractive index (CRI) of the photodetector material is necessary, for example, for the design of the UV - VUV region photodetector. Based on the instrument designed by Saito *et al.* [1], we have developed a synchrotron radiation (SR) dedicated visible (VIS) - VUV spectroscopic ellipsometer (SE) which is installed at BL7B. Although this type of SE has an advantage in obtaining not only optical constants of the sample, but also Stokes parameters of the incident beam [2], but in principle the wavelength continuous complex refractive spectrum can not be measured. Furthermore, ellipsometry requires a layered model of the sample to calculate the CRI from the measured ellipsometric parameters. Another way to obtain the wavelength continuous CRI spectrum is the Kramers - Kronig transformation method applied to the reflectance spectrum (KK method). In this method, it is not difficult to measure the wavelength continuous reflectance spectrum and KK method does not require the layered model, but it is not so easy to measure the reflectance spectrum quantitatively. In short, it can be seen that the SE method and KK method are complementary to each other. Then, we have been reconstructing our VIS-VUV SE to the composite type measurement system for VIS - VUV CRI. In this report, we will discuss the mechanical remodeling in our VIS - VUV SE by the incorporating a reflectometer. Specifically, in addition to the insertion of the reflectometer, the sample alignment mechanism was redesigned that does not interfere with the reflectometer rotation.

Figure 1 shows the schematic layout of VIS - VUV SE with the incorporated reflectometer. In order to cancel the wavelength sensitivity dependence of the photodiode, both light source and reflected light from the sample must be measured with the same photodiode. The 3D layout of the reflectometer considering the above condition is shown in fig. 2a. All parts of this reflectometer are equipped on one ICF203 flange. The renewed sample position adjustment mechanism with the sample holder is shown in fig. 2b. Precise rotation and translation adjustments of the sample can be made with the rotary ball spline device (red color part). Figure. 2c represents the positional relationship in the main chamber of our SE among the reflectometer, the sample alignment mechanism with the sample holder, and the  $\beta$  rotation mechanism. Figures 3a and 3b shows the

experimental results of the ellipsometric parameters and the reflectivity under the same experimental conditions (without the incidence angle) after reconstruction, respectively. Since sample is 1  $\mu\text{m}$  AlN thin film, interference is clearly observed at the lower photon energy side of fig. 3b. We are currently working on the establishment of analytical methods for deriving the CRI from the measurement results of ellipsometry and reflection measurement.

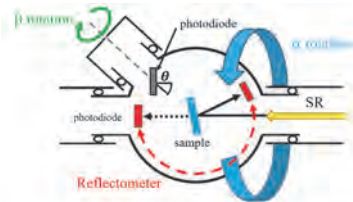


Fig. 1. Schematic layout of VIS-VUV SE.

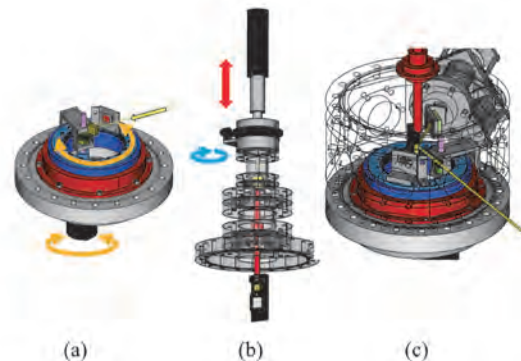


Fig. 2. 3D layouts of reflectometer (a), sample mechanism (b), and their relationship (c).

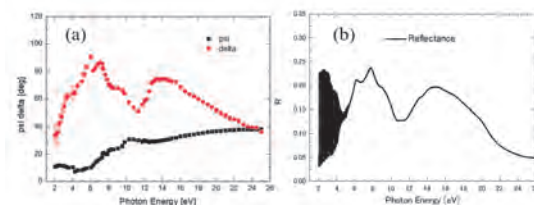


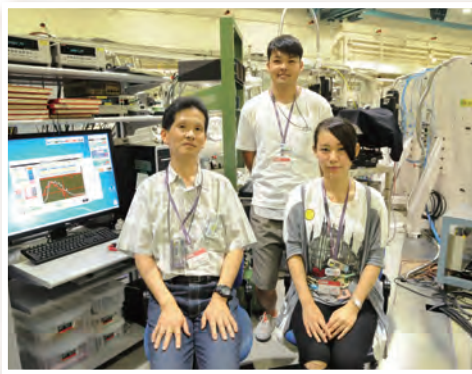
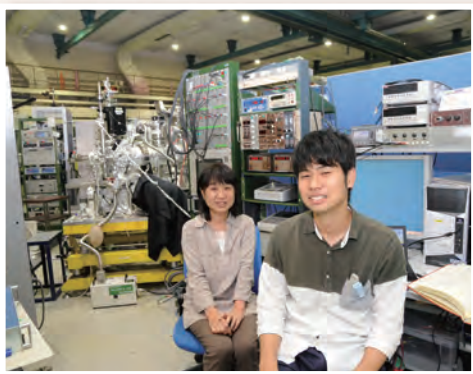
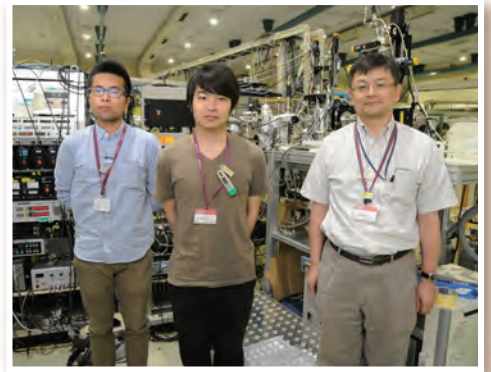
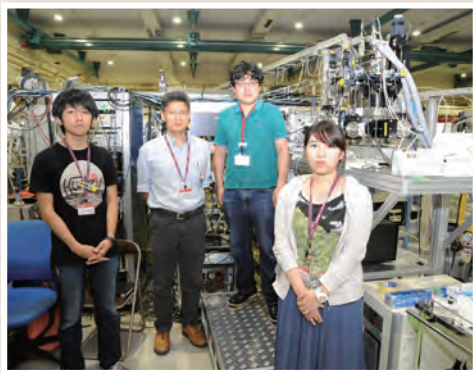
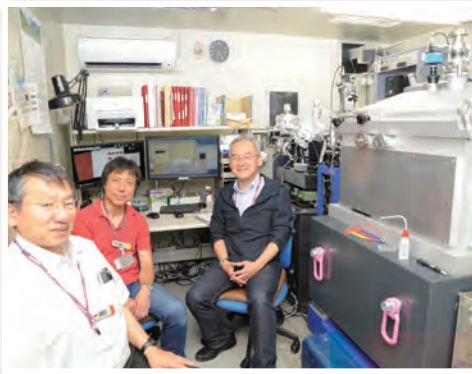
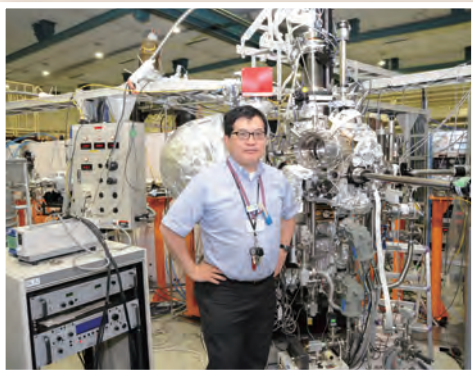
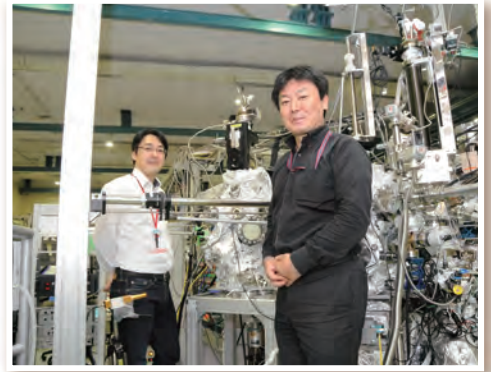
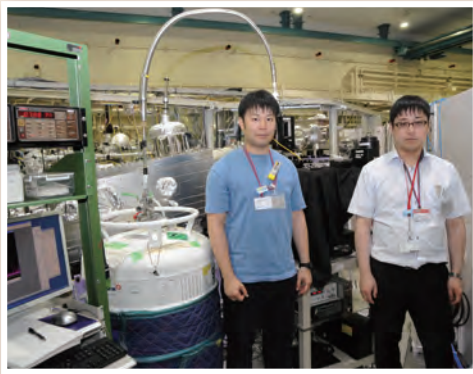
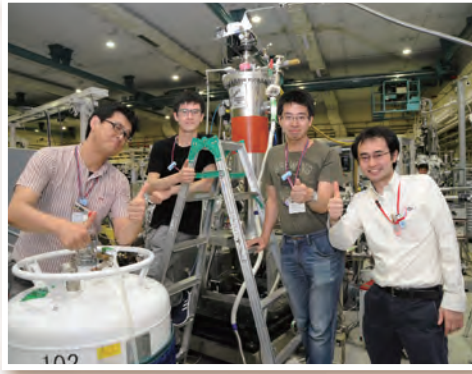
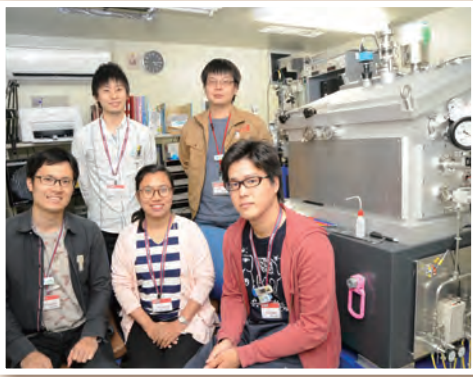
Fig. 3. Experimental results. (a) ellipsometric parameters, (b) reflectance

[1] T. Saito, M. Yuri and H. Onuki, Rev. Sci. Instrum. **66** (1995) 1570.

[2] F. Sawa *et al.*, UVSOR Activity Report 2017 **45** (2018) 37.



# UVSOR User 2



# III-2

Materials Sciences





BL5U

## Detwinned Electronic Structure of $\text{Ba}_{0.82}\text{K}_{0.18}\text{Fe}_2\text{As}_2$ Observed by ARPES

S. Ideta<sup>1,2</sup>, M. Nakajima<sup>3</sup> and K. Tanaka<sup>1,2</sup>

<sup>1</sup>National Institutes of Natural Science, Institute for Molecular Science, Okazaki, 444-8585, Japan

<sup>2</sup>The Graduate University for Advanced Studies (SOKENDAI), Okazaki, 444-8585, Japan

<sup>3</sup>Department of Physics, Graduate School of Science, Osaka University, Toyonaka 560-0043, Japan

Iron-based superconductors have an interesting phase diagram with the antiferromagnetic (AFM) transition and the structural phase transition. Recently, nematicity, defined as broken rotational symmetry [a trigonal( $C_4$ )-to-orthorhombic ( $C_2$ ) structural transition], has shed light on the understanding of the mechanism on the iron-based superconductivity [1-4]. In hole-doped  $\text{BaFe}_2\text{As}_2$  (Ba122) system,  $\text{Ba}_{1-x}\text{Na}_x\text{Fe}_2\text{As}_2$  and  $\text{Ba}_{1-x}\text{K}_x\text{Fe}_2\text{As}_2$  (K-Ba122) have shown the magnetic order without  $C_4$  symmetry breaking [5, 6] and the moment's direction would be swapped from in-plane to out-of-plane [7]. Besides, the superconductivity is suppressed between the superconductivity and the  $C_4$ -magnetic phase. The electronic structure at the  $C_4$  magnetic phase has been unclear yet, and it would give us a great interest to elucidate the mechanism of the hole-doped Ba122.

Here, in order to compare with results obtained from the previous study [8], we have demonstrated a temperature dependent angle-resolved photoemission spectroscopy (ARPES) experiment to elucidate the electronic structure of detwinned underdoped K-Ba122 ( $x = 0.18$ ) with the orthorhombic ( $C_2$ ) phase transition below the structural and AFM transition temperatures ( $T_{N,S} \sim 100$  K). In hole-doped Fe-SCs, it has been known that the anisotropic resistivity disappears in contrast with the electron-doped Fe-SCs [9]. However, we have clearly observed the orbital anisotropy corresponding to the two-fold symmetry at the  $C_2$  phase in the hole-doped Fe-SC.

High-quality single crystals of  $\text{Ba}_{0.82}\text{K}_{0.18}\text{Fe}_2\text{As}_2$  ( $T_c \sim 10$  K) were grown by self-flux technique. ARPES experiments were carried out at BL5U of UVSOR-III Synchrotron using the linearly  $s$  polarized light of  $h\nu = 60$  eV. Temperature was set at  $T = 6$  K-150 K and clean sample surfaces were obtained for the ARPES measurements by cleaving single crystals *in-situ* in an ultrahigh vacuum better than  $1 \times 10^{-8}$  Pa.

Figures 1(a) and 1(b) show the second-derivative ARPES intensity plots along the Z-X and Z-Y directions, respectively, corresponding to the Z points. In Figs. 1(a) and 1(b), the direction of the uniaxial pressure is perpendicular or parallel to the  $s$  polarization vector respectively [4] as shown by photos, and both band dispersions are considered to be the electronic structure from the strain free single domain. In Fig.1(c), we also measured twinned single crystals and found that two dispersions simultaneously corresponding to the  $d_{xz}$  and  $d_{yz}$  orbitals shown in Figs. 1(a) and 1(b), respectively. In future work, we focus on the  $d_{yz}$  and  $d_{xz}$  orbitals as shown in Figs. 1(a) and

1(b) and will analyze the temperature dependent ARPES spectra and compare with the previous ARPES study [8]. In the electronic structure of the Z-X and Z-Y directions, we expect that the occupation of the  $d_{yz}$  and  $d_{xz}$  orbitals might be the same above  $T_{s,N}$ .

In summary, we have performed an ARPES study of detwinned K-Ba122 ( $x = 0.18$ ) and measured the electronic structure in the Z-X, Z-Y, and Z-X/Y directions. We found that the electronic structure in the Z-X and Z-Y directions shows different band dispersions, reflecting the electronic structure from the single domain due to the uniaxial pressure. We will analyze the detailed temperature dependence of the ARPES spectrum of  $d_{yz}$  and  $d_{xz}$ .

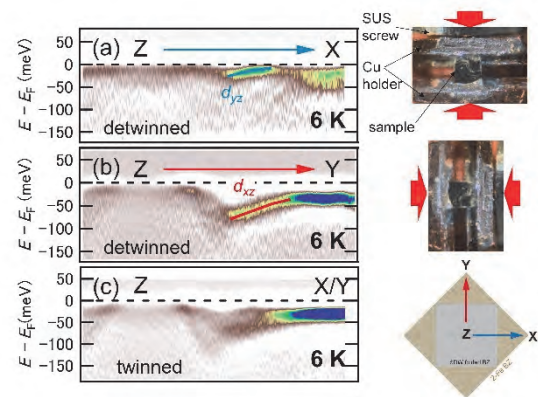


Fig. 1. Electronic structure of underdoped K-doped Ba122. (a), (b), (c) Second-derivative ARPES intensity plots for detwinned (Z-X and Z-Y directions) and twinned  $\text{Ba}_{0.82}\text{K}_{0.18}\text{Fe}_2\text{As}_2$  taken at  $h\nu = 60$  eV. The  $d_{yz}$  and  $d_{xz}$  bands are clearly observed differently. Photos of the sample setup and schematic Brillouin Zone are shown on the right side. Red arrows indicate the direction of uniaxial pressure.

- [1] R. M. Fernandes *et al.*, Nat. Phys. **10** (2014) 97.
- [2] R. M. Fernandes *et al.*, Phys. Rev. Lett. **111** (2013) 127001.
- [3] T. Shimojima *et al.*, Phys. Rev. B **90** (2014) 12111(R).
- [4] Y. Ming *et al.*, PNAS **108** (2011) 6878.
- [5] L. Wang *et al.*, Phys. Rev. B **93** (2016) 014514.
- [6] A. E. Böhrer *et al.*, Nat. Commun. **6** (2015) 7911.
- [7] D. D. Khalyavin *et al.*, Phys. Rev. B **90** (2014) 174511.
- [8] S. Ideta *et al.*, Activity Report **45** (2017) 77.
- [9] E.C. Blomberg *et al.*, Nat. Commun. **4** (2014) 1914.

BLIU

## Photon Induced Positron Annihilation Lifetime Spectra of Ce:GAGG Crystals Measured Using Ultrashort Laser-Compton-Scattered Gamma Ray Pulses

K. Fujimori<sup>1</sup>, M. Kitaura<sup>1</sup>, Y. Taira<sup>2</sup>, M. Fujimoto<sup>3</sup>, Y. Okano<sup>4</sup>, H. Zen<sup>5</sup>, M. Katoh<sup>3,8</sup>, M. Hosaka<sup>6</sup>, J. Yamazaki<sup>3</sup>, K. Kamada<sup>7</sup> and A. Ohnishi<sup>1</sup>

<sup>1</sup>Faculty of Science, Yamagata University, Yamagata 990-8560, Japan

<sup>2</sup>National Institute of Advanced Industrial Science and Technology, Tsukuba 305-8568, Japan

<sup>3</sup>UVSOR Synchrotron Facility, Institute for Molecular Science, Okazaki 444-8585, Japan

<sup>4</sup>Center for Mesoscopic Sciences, Institute for Molecular Science, Okazaki 444-8585, Japan

<sup>5</sup>Institute of Advanced Energy, Kyoto University, Uji 611-0011, Japan

<sup>6</sup>Synchrotron radiation Research Center, Nagoya University, Nagoya 464-8603, Japan

<sup>7</sup>New Industry Creation Hatchery Center, Tohoku University, Sendai 980-8579, Japan

<sup>8</sup>Hiroshima Synchrotron Radiation Center, Hiroshima University, Higashi-hiroshima, 739-0046, Japan

Ce<sup>3+</sup>-doped Gd<sub>3</sub>Al<sub>2</sub>Ga<sub>3</sub>O<sub>12</sub> (Ce:GAGG) is known as an inorganic scintillator with high light yield and good energy resolution. It has been demonstrated that, in this material, antisite Gd<sup>2+</sup> ions adjacent to oxygen vacancies are responsible for shallow electron traps [1]. Such electron traps cause the occurrence of phosphorescence with long lifetime and the lowering of light yield, and thus they have to be suppressed in the process of crystal growth. It was pointed out that the antisite Gd<sup>3+</sup> ions and oxygen vacancies are introduced in Al/Ga deficient compositions. In order to improve scintillation properties of Ce:GAGG crystals, it is important to find out the best way to suppress Al/Ga deficiency.

The existence of cation vacancies has been investigated by positron annihilation lifetime spectroscopy, because positrons are attractive for negative charged cation vacancies. The position annihilation lifetime spectroscopy (PALS) generally requires radioisotope such as <sup>22</sup>Na as a positron source. In this case, positrons are injected from the outside of a crystal, so that pair annihilation gamma rays generate not only from the inside of the crystal but also from the outside. The latter has to be removed to analyze the positron annihilation lifetime at the cation vacancy site, because it is responsible for the uncertainty of the lifetime. This problem is to be solved to perform the lifetime analysis more accurately.

Photon induced PALS (PIPALS) is the only solution that can solve the above-mentioned problem [2]. This method utilizes ultrafast laser Compton-scattered (LCS) gamma ray pulses generated by the normal collision of electron beam and ultrashort laser pulses. The advantage is that positrons can be created inside the crystal through the pair creation process. PIPALS allows us to clarify the existence of cation vacancies in Ce:GAGG crystals. For this purpose, we performed PIPALS experiment using ultrashort LCS gamma ray pulses at the BLIU beamline of UVSOR synchrotron facility.

The size of the Ce:GAGG crystal used in our experiment was 10×10×10 mm<sup>3</sup>. The details of PIPALS experiment have been reported elsewhere. The photon energy, pulse width, and repetition rate of the LCS gamma ray pulses were 6.6 MeV, 2 ps, and 1 kHz,

respectively. The pair annihilation gamma ray from the Ce:GAGG crystal was detected with two photomultiplier tubes attached BaF<sub>2</sub> crystals, which were faced each other. The waveforms were stored in the memory of a digital storage oscilloscope, when the output signals from two photomultiplier tubes coincided with each other. The PIPALS spectrum of a Ce:GAGG crystal was obtained from the distribution of the time half the maximum intensity.

The PIPALS spectrum of a Ce:GAGG crystal is shown in Fig. 1. Solid circles indicate experimental data. Apparently, the PIPALS spectrum is of a single decay component. A solid line indicates the result of curve fitting analysis, and it reproduces the experimental data. From the fit, the lifetime is determined 178 ± 14 ps. This value is almost agreement with the lifetime of the pair annihilation of a positron with an electron in the bulk. A longer lifetime component is slightly observed in the tail of the main component. The higher statistical accuracy for experimental data is needed for detail lifetime analysis.

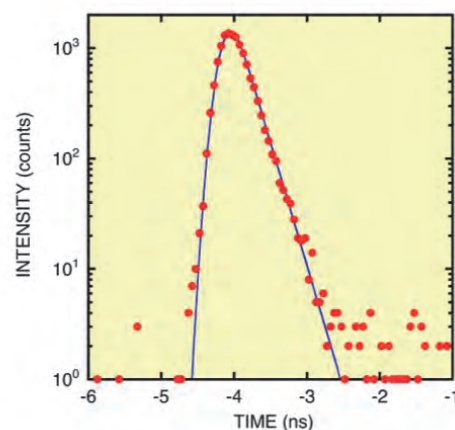


Fig. 1. PIPALS spectrum of a Ce:GAGG crystal measured at room temperature.

[1] M. Kitaura *et al.*, Appl. Phys. Lett. **113** (2018) 041906.

[2] Y. Taira *et al.*, Rev. Sci. Instrum. **84** (2013) 053305.

BL1B

## Polarized Terahertz Reflectivity Spectra of $\text{Ca}_3\text{TaGa}_3\text{Si}_2\text{O}_{14}$ Piezoelectric Crystals with Ordered Langasite Structure

 M. Kitaura<sup>1</sup>, K. Kamada<sup>2</sup>, Y. Yokota<sup>2</sup>, Y. Ohashi<sup>2</sup>, S. Watanabe<sup>3</sup> and A. Ohnishi<sup>1</sup>
<sup>1</sup>Faculty of Science, Yamagata University, Yamagata 990-8560, Japan

<sup>2</sup>New Industry Creation Hatchery Center, Tohoku University, Sendai 444-8585, Japan

<sup>3</sup>Graduate School of Engineering, Nagoya University, Nagoya 464-8603, Japan

Langasites are expressed by the chemical formula of  $\text{A}_3\text{BC}_3\text{D}_2\text{O}_{14}$ , and are composed of four cations A-D. These materials belong to the trigonal system of the space group P321, and are known piezoelectric materials with high electromechanical coupling factors. They are classified into two categories: order-type and disorder-type. In order-type langasites, each cation site is occupied by different element. In disorder-type, one element occupies multi cation sites. Order-type langasites are preferred, because they present better thermal stability of piezoelectric properties.  $\text{Ca}_3\text{TaGa}_3\text{Si}_2\text{O}_{14}$  (CTGS) is one of such order-type langasites. CTGS exhibits a higher electrical resistivity which is advantage to high-temperature use of sensor applications [1]. Despite such an industrial key material, the fundamental optical functions such as dielectric constant and refractive index in the terahertz region have not yet been studied so far. In order to determine terahertz optical functions of CTGS, we have measured polarized terahertz reflectivity spectra of CTGS crystals at 9 K.

A typical result is shown in Fig. 1 by using dotted curves. One can see remarkable dichroism between the spectra for  $E\perp c$  and  $E//c$  configurations, which reflects the crystal structure of CTGS. According to the consideration based on group theory [2], the E and  $A_2$  modes are IR-active for  $E\perp c$  and  $E//c$  configurations, respectively. Thus, it is likely that the two bands are assigned to E and  $A_2$  modes for  $E\perp c$  and  $E//c$  configurations, respectively.

We determined the complex dielectric function from the fit of Eq. (1) with experiment data.

$$\hat{\epsilon} = \epsilon_\infty \frac{\omega_{\text{LO}}^2 - \omega^2 - i\omega\gamma_{\text{LO}}}{\omega_{\text{TO}}^2 - \omega^2 - i\omega\gamma_{\text{TO}}}, \quad (1)$$

where  $\epsilon_\infty$  is the high-frequency dielectric constant,  $\omega$  is the frequency of terahertz wave, and  $\omega_{\text{TO}}(\omega_{\text{LO}})$  and  $\gamma_{\text{TO}}(\gamma_{\text{LO}})$  are frequencies and damping factors of TO (LO) phonons, respectively. The parameters determined from the fit of Eq. (1) are listed in Table 1. The reflectivity spectra calculated using the complex dielectric function are indicated by broken curves. In Fig. 1, the calculated reflectivity spectra reproduce the experimental ones. The lowest frequency bands exhibit the high-reflectivity plateau in the high frequency side of  $\omega_{\text{TO}}$  and the dip at the position of  $\omega_{\text{LO}}$ . These features imply that phonon polaritons are

formed in CTGS. The phonon polariton dispersion curves obtained are drawn in Fig. 2.

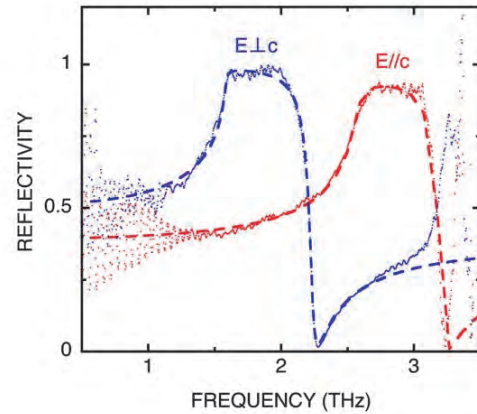


Fig. 1. Polarized terahertz reflectivity spectra of CTGS for  $E\perp c$  and  $E//c$  configurations, measured at 9K. Dotted and broken curves indicate experimental and calculated results, respectively.

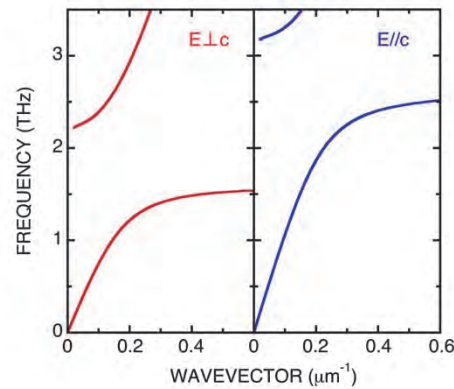


Fig. 2. Phonon polariton dispersion curves of CTGS for  $E\perp c$  and  $E//c$  configurations, calculated on the basis of Fig. 1.

Table1: Parameters obtained from the fit of Eq. (1) with experimental data.

	$\epsilon_\infty$	$\omega_{\text{TO}}$ (THz)	$\gamma_{\text{TO}}$ (MHz)	$\omega_{\text{LO}}$ (THz)	$\gamma_{\text{LO}}$ (MHz)
$E\perp c$	16.3	1.58	15.5	2.32	53.9
$E//c$	9.6	2.57	68.6	3.34	26.9

[1] X. Fu *et al.*, J. Ceram. Soc. Jpn. **124** (2016) 523.

[2] J. Lan *et al.*, Phys. Stat. Sol. **242** (2005) 1996.



BL1B, BL7B

## Extremely Sharp Structure of the Vibration Modes Derived from Hydrogen Bonds of Single-crystalline L-alanine

Z. Mita<sup>1</sup>, H. Watanabe<sup>1,2</sup> and S. Kimura<sup>1,2</sup><sup>1</sup>Graduate School of Frontier Biosciences, Osaka University, Suita 565-0871, Japan<sup>2</sup>Department of Physics, Graduate School of Science, Osaka University, Toyonaka 560-0043, Japan

Amino acids are the most basic molecules, which compose proteins in vivo. Since almost all amino acids have chiral molecule structure, the crystal structures as well as the optical properties are expected to be anisotropic. One of amino acids with optical isomers, alanine [CH<sub>3</sub>CH(COOH)NH<sub>2</sub>] has orthorhombic molecular structure [1]. Many spectroscopic measurements have been performed for alanine so far [2,3,4]. To clarify the thermal effect of molecular vibrations of different origins, we have measured polarization and temperature dependences of optical conductivity spectra using single crystalline alanine.

We have grown the single crystalline L-alanine by using the solvent evaporation method and confirmed to be orthorhombic structure by taking X-ray Laue diffraction pattern. Anisotropic optical reflectivity spectra from the terahertz (THz) to vacuum-ultraviolet (VUV) regions have been measured by using BL1B and BL7B of UVSOR-III and laboratorial equipments. The obtained spectra were converted to optical conductivity [ $\sigma(\omega)$ ] spectra by the Kramers-Kronig analysis. Temperature dependence of anisotropic  $\sigma(\omega)$  spectrum in the THz region is shown in Fig. 1. To reveal its temperature dependence, each peak was fitted with the function of the Lorentz model [5]. As shown in Fig. 1, there are 18 peaks originating from molecular vibrations. The spectra are strong anisotropy and all peaks have very large temperature dependence. Specifically, the peak positions shift to the high energy side and the widths become narrow significantly with decreasing temperature. However, the peak areas of all peaks were approximately constant. In comparison of the obtained peak energy with a previous investigation [2], peaks of number 1 to 12 originate from the vibration of hydrogen bond. Figure 2 shows the peak widths of all peaks as a function of peak energy at 10 K. Red (blue) bars indicate the vibration with (without) the contribution of hydrogen bond. The peaks originating from hydrogen bond have extremely sharp structure, so hydrogen bond is a vibration where thermal fluctuation effects mainly appear. Therefore, to compare the peak width with one another at a very low temperature may become one of useful methods to identify the origin of the peaks, hydrogen bonds or not. In addition, at 10 K, the peak widths originating from hydrogen bonds become almost constant near the resolution limit of the spectrometer, suggesting the possibility of the quantum fluctuations.

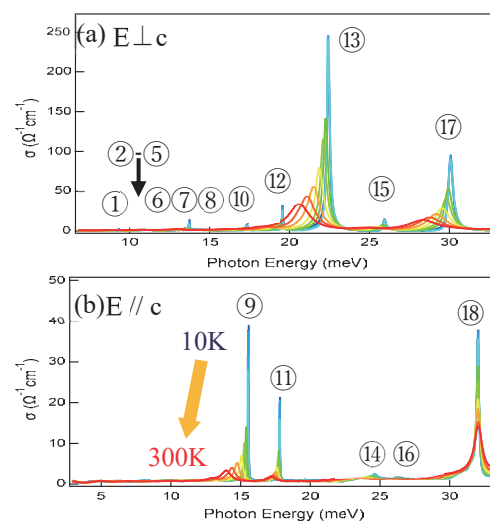


Fig. 1. Anisotropic optical conductivity [ $\sigma(\omega)$ ] spectra at temperatures from 10 to 300 K in the THz region perpendicular to the c-axis (a) and parallel to the c-axis (b).

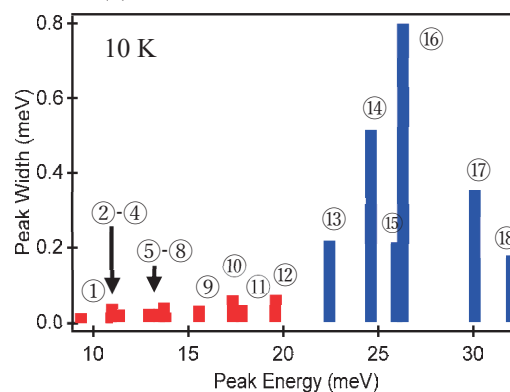


Fig. 2. Peak widths of all peaks in Fig. 1 at 10 K in THz region. Red (blue) bars show the vibrations with (without) the contribution of hydrogen bonds.

[1] M. Fleck and A. M. Petrosyan, *Salts of Amino Acids-Crystallization Structure and Properties* (Springer, 2014) p.26.

[2] J. Bandekar *et al.*, *Spectrochimica Acta Part A: Molecular Spectroscopy* **39** (1983) 357.

[3] M. Yamaguchi *et al.*, *Appl. Phys. Lett.* **86** (2005) 053903.

[4] V. S. Minkov *et al.*, *J. Struct. Chem.* **51** (2010) 1052.

[5] F. Wooten, *Optical Properties of Solids* **82** (Academic Press, 1972) 42.

BL1B

## Ground State of Ultrashallow Thermal Donors in Silicon

A. Hara and T. Awano

Faculty of Engineering, Tohoku Gakuin University, Tagajo 985-8537, Japan

We discovered ultrashallow thermal donors (USTDs) in carbon- and hydrogen-doped Czochralski silicon (CZ Si) crystals [1, 2]. To the best of our knowledge, these are the shallowest energy levels among those of currently reported donors in Si crystals. In addition, the ground (1S) state of USTDs was found to be split into two states [3, 4]. This is direct evidence that the ground state of USTDs consists of a linear combination of the wave functions of the conduction band minimum. However, electron spin resonance measurements have shown nearly isotropic spectra with slight anisotropy, thus indicating  $T_d$  symmetry. If  $T_d$  symmetry is correct, the ground state must split into three levels [5, 6]. To evaluate another ground state, we measured the optical absorption spectra at a region of low wavenumbers using BL1B.

Carbon-doped CZ Si samples were doped with hydrogen by annealing in wet oxygen at 1300 °C for 60 min. The samples were then cooled to room temperature by rapid exposure to air. For carbon doping, the Si melt used to prepare the ingot was doped with carbon powder during CZ Si crystal growth. Transmittance spectra were obtained using a BL1B beamline with a flowing cryostat.

Figure 1 shows  $\text{Trans. (40 K)}/\text{Trans. (8 K)}$ , where  $\text{Trans. (T K)}$  represents the transmittance at T K [3, 4]. According to our previous research using BL6B [3, 4], the two broad dips observed at approximately 100 and 150  $\text{cm}^{-1}$  at 40 K originate in the transition from the upper ground state to the  $2P_0$  and  $2P_{+-}$  states. The upper ground states are occupied by thermal excitation of electrons from the ground state.

Figure 2 shows  $\text{Trans. (40 K)}/\text{Trans. (5 K)}$  at a region of 20–100  $\text{cm}^{-1}$ . No clear difference was observed between the two transmittance spectra.

These indicate that the ground state of USTDs were split into two levels but not three. Thus, symmetry of USTDs was concluded not to be  $T_d$ .

In summary, the ground-state splitting of USTDs was evaluated at a low-wavenumber region. However, new peaks were not observed at 20–100  $\text{cm}^{-1}$ . This indicates possibility that the ground state of USTDs are split into two and that symmetry of USTDs is not  $T_d$ .

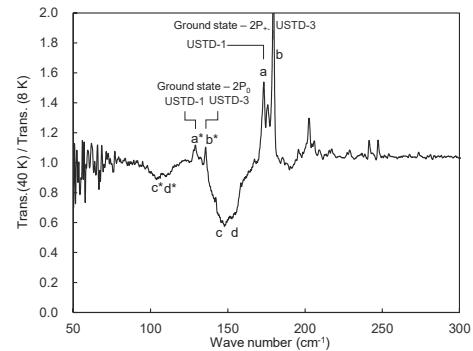


Fig. 1.  $\text{Trans. (40 K)}/\text{Trans. (8 K)}$  of USTDs [4].

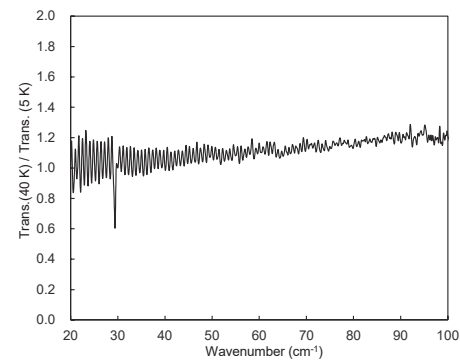


Fig. 2.  $\text{Trans. (40 K)}/\text{Trans. (5 K)}$  of USTDs.

- [1] A. Hara, T. Awano, Y. Ohno and I. Yonenaga, *Jpn. J. Appl. Phys.* **49** (2010) 050203.
- [2] A. Hara and T. Awano, *Jpn. J. Appl. Phys.* **54** (2015) 101302.
- [3] A. Hara and T. Awano, *Jpn. J. Appl. Phys.* **56** (2017) 068001.
- [4] A. Hara and T. Awano, *Jpn. J. Appl. Phys.* **57** (2018) 101301.
- [5] W. Kohn, in *Solid State Physics*, ed. F. Seitz and D. Turnbull (Academic Press, New York, 1957) Vol. **5**, p. 257.
- [6] R. L. Aggarwal and A. K. Ramdas, *Phys. Rev.* **140** (1965) A1246.

BL2A

## XAFS Measurement for Alloying Element in Tempered Nitrogen Martensite

M. Sato and T. Murata

*Institute for Materials Research, Tohoku University, Sendai 980-8522, Japan*

It is well known that the martensite phase obtained by rapid quenching is hard but brittle. Therefore the balance between hardness and toughness is adjusted by the subsequent tempering treatment. At that time, cementite is precipitated in case carbon steel, and  $\text{Fe}_{16}\text{N}_2$  or  $\text{Fe}_4\text{N}$  is precipitated in case of nitrogen steel [1, 2].

From the experimental results, the  $\text{Fe}_{16}\text{N}_2$  precipitates in the temperature range between 100 °C and 250 °C, and transition to  $\text{Fe}_4\text{N}$  occurs at tempering temperature around 300 °C. In addition, it has been found that precipitation of alloy nitride also occurs because the substitutional element can be diffused [3].

Although the alloying elements are known to partially dissolve as solid solutions in these precipitates, there is no data of Si and Mo in iron nitrides. The solid solution of alloying elements into iron nitrides greatly affect the stability of iron nitrides and also affect the subsequent precipitation of alloy nitride. Therefore, in order to understand the hardness change associated with tempering, it is important to clarify the solid solution state of such substitutional elements.

In this study, changes in the chemical state of the substitutional elements such as Si and Mo in the precipitates formed during tempering were investigated by XAFS measurement.

Fe-1mass%Si and Fe-1mass%Mo alloys were used as starting materials. They were homogenized at 1523 K for 24h and furnace-cooled until room temperature. The Fe-1Si-0.3N and Fe-1Mo-0.3N alloys were prepared by nitriding and quenching (N-Q) process using  $\text{NH}_3/\text{H}_2$  mixed gas at 1273 K for 1 h. Then obtained these alloys were tempered at 773 K, and precipitated  $\text{Fe}_4\text{N}$  generated during tempering were extracted using Iodine-alcohol procedure. The Si K-edge and Mo L3-edge XANES spectra were corrected by fluorescence method using InSb double crystal monochromator and silicon drift detector (SDD) at BL2A in UVSOR, respectively. Obtained data were analyzed using Athena software.

Figure 1 shows Si K-edge XANES spectra of extracted  $\text{Fe}_4\text{N}$  powders. As shown in this figure, pure Si,  $\text{SiO}_2$  and  $\text{Si}_3\text{N}_4$  were used as references.

The obtained XANES spectra are different for each samples, and the extracted residue from the tempered sample at 200 °C had a peak around 1847 eV, while the that obtained from the sample tempered at 500 °C showed double peaks around 1844 eV and 1847 eV, respectively. From the comparison with the reference sample, the peak at 1847 eV is presumed to be due to the oxidation that occurred during extraction or storage. On the other hand, it can be seen that the peak around

1844 eV shows similar shape to  $\text{Si}_3\text{N}_4$ . From the TEM observation, since the precipitation of the Si-nitrides has not been observed in this sample, it is considered that the Si makes a solid solution into  $\text{Fe}_4\text{N}$  and the local structure of Si in  $\text{Fe}_4\text{N}$  has similar to that of  $\text{Si}_3\text{N}_4$ .

Similar results were obtained in the case of Fe-1Mo-0.3N alloy. In the future, detailed examination of solid solution state of alloying element in iron nitrides should be carried out by combination of N K-edge and O K-edge measurement of these samples at BL4B and prediction of XANES spectra from calculation.

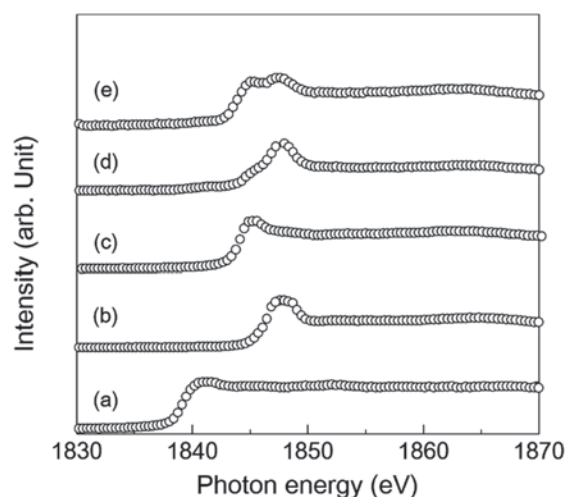


Fig. 1. Si K-edge XANES spectra of references and extracted precipitates. (a) Pure Si, (b)  $\text{SiO}_2$ , (c)  $\text{Si}_3\text{N}_4$ , (d) extracted residue from tempered sample at 200 °C for 1 h, and (e) extracted residue from tempered sample at 500 °C for 1h.

[1] L. Cheng and E. J. Mittemeijer, *Met. Trans. A* **21A** (1990) 13.

[2] L. Cheng, A. Bottger and E. J. Mittemeijer, *Met. Trans. A* **23A** (1992) 1129.

BL2A

## Mo L<sub>3</sub>-edge XANES Study of Active and Durable Mo-Carbide Species on H-MFI for Methane Dehydroaromatization Catalysts

H. Aritani<sup>1</sup>, K. Kuramochi<sup>2</sup>, R. Yamazaki<sup>2</sup>, H. Miyanaga<sup>1</sup>, S. Sato<sup>1</sup> and A. Nakahira<sup>3</sup>

<sup>1</sup>Graduate School of Engineering, Saitama Institute of Technology, Fukaya 369-0293 Japan

<sup>2</sup>Advanced Science Research Laboratory, Saitama Institute of Technology, Fukaya 369-0293 Japan

<sup>3</sup>Graduate School of Engineering, Osaka Prefecture University, Sakai 599-8531 Japan

As an innovative GTL (Gas-To-Liquid) process, methane dehydroaromatization (methane-to-benzene reaction; MTB) has been studied for its potential in the direct conversion of methane into liquid fuels. It has been investigated intensively that Mo-modified H-MFI (Mo/H-MFI) zeolite catalysts show high activity for methane dehydroaromatization. Since the MTB reaction is revolutionary for direct conversion of natural gas, deactivation due to coking over the catalyst cannot be avoided during the methane conversion. It is a serious problem for development of MTB reaction, and thus, clarification of the deactivation process over the catalysts is one of the important points for development of highly active and durable MTB catalysts. Not only carbon deposition on acid sites of H-MFI but also excess carbonization of active Mo species causes the deactivation of MTB. It is widely accepted that addition of hydrogen to methane reactant is effective for inhibiting the deactivation. In the present study, Mo L<sub>3</sub>-edge XANES study is introduced to characterize the active Mo-carbide species on H-MFI after the MTB reaction.

Mo/H-MFI and Mo-V/H-MFI catalysts were prepared by impregnation of H-MFI (Si/Al<sub>2</sub>=30-50) support with MoO<sub>2</sub>(acac)<sub>2</sub>-CHCl<sub>3</sub> or MoO<sub>2</sub>(acac)<sub>2</sub>-VO(acac)<sub>2</sub>-CHCl<sub>3</sub> solution (5.0wt% as MoO<sub>3</sub>; Mo/V=10), and followed by drying overnight and calcination at 773 K. H-MFI supports were synthesized hydrothermally at 413 K for a week, and followed by ion-exchanging with NH<sub>4</sub>Cl and calcination at 873 K. The catalytic activity of MTB was evaluated by means of fixed bed flow reaction, as described in a separate paper.[1] The reactant gas is CH<sub>4</sub>(20%)+H<sub>2</sub>(0-3%)+He(base) at the flow rate of 30 mL/min, and the reactivity was evaluated at 1023 K by using the 0.25 g of each Mo/H-MFI catalyst. Mo L<sub>III</sub>-edge XANES spectra were obtained in BL2A of UVSOR-IMS in a total-electron yield mode using InSb double-crystal monochromator. Photon energy was calibrated by using Mo metal-foil at Mo L<sub>III</sub>-edge, and normalized XANES spectra are presented by using REX-2000 (Rigaku) software.

Figure 1 shows the Mo L<sub>3</sub>-edge XANES spectra of Mo/H-MFI and Mo-V/H-MFI catalysts (Si/Al<sub>2</sub>=30 and 40) after MTB reaction at 1023 K. For Mo/H-MFI in Si/Al<sub>2</sub>=40, partially carbonized Mo species (MoC<sub>x</sub>O<sub>y</sub>) were possibly formed. By H<sub>2</sub> co-feed, reduction of Mo species advanced. In case of Mo-V/H-MFI (Si/Al<sub>2</sub>=40), the Mo species were deeply carbonized and formed MoC<sub>x</sub> (x>0.5) species. Since

the catalyst showed high MTB reactivity, it is suggested that the deeply carbonized species relate to the highly active one. For Mo/H-MFI (Si/Al<sub>2</sub>=30), the Mo species are different from those of Mo/H-MFI in Si/Al<sub>2</sub>=40 even in H<sub>2</sub> co-feed and/or V co-modification. Deeply reduced Mo species on H-MFI (Si/Al<sub>2</sub>=30) support have been invisible, and α-Mo<sub>2</sub>C like species were formed in any cases. Because the Mo/H-MFI (Si/Al<sub>2</sub>=30) catalysts showed durable reactivity for MTB, the correlation between the reactivity and the active Mo-carbide species is still unclear. It is now in progress.

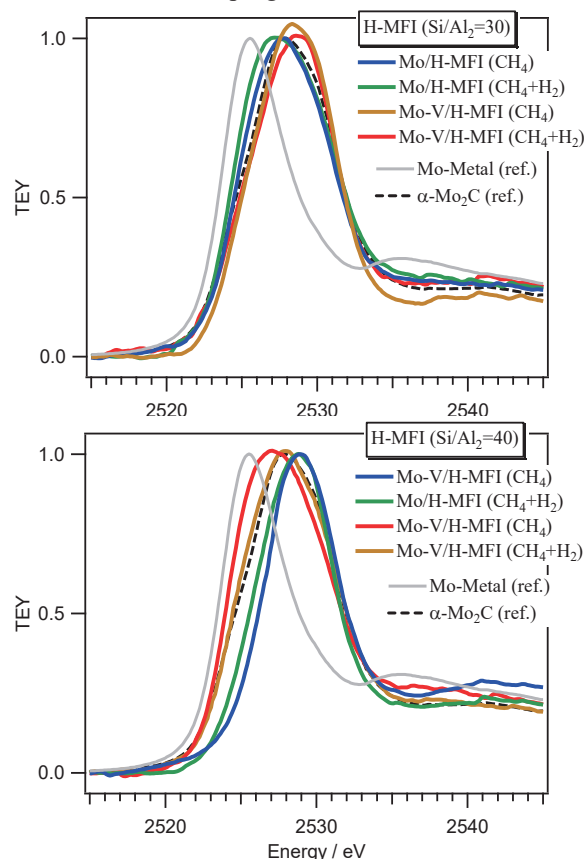


Fig. 1. Mo L<sub>3</sub>-edge XANES of Mo/H-MFI and Mo-V/H-MFI catalysts (Si/Al<sub>2</sub>=30 and 40) after MTB reaction at 1023 K.

- [1] H. Aritani *et al.*, J. Environm. Sci. **21** (2009) 736.  
 [2] H. Aritani *et al.*, UVSOR Activity Report 2016 **44** (2017) 52.  
 [3] H. Aritani *et al.*, UVSOR Activity Report 2017 **45** (2018) 44.



BL2A

## Local Environment Analysis of Sr Ions in Octacalcium Phosphate

K. Arakawa<sup>1</sup> and T. Yamamoto<sup>1,2,3</sup><sup>1</sup>Faculty of Science and Engineering, Waseda University, Tokyo 169-8555, Japan<sup>2</sup>Institute of Condensed-Matter Science, Waseda University, Tokyo 169-8555, Japan<sup>3</sup>Kagami Memorial Research Institute for Materials Science and Technology, Waseda University, Tokyo 169-0051, Japan

Calcium phosphate basis bioceramics have been widely studied because of their efficient medical applications. Among these bioceramics, octacalcium phosphate (OCP) has a great attention, since it is a precursor of the hydroxyapatite (HAp), which can change into the natural bone in human body. It was reported that the existence of the trace elements such as Zn and Mg can enhance the speed of bone reconstruction [1]. However, the mechanism of such enhancement has not yet been understood. To understand the mechanism, it is essential to know the local environment of doped ions. For such purpose, we have studied wide variety of the functional materials by using the X-ray absorption near edge structure (XANES) and the first-principles calculations within a density functional theory (DFT), which could successfully determine the local environment of the trace elements in  $\beta$ -tricalcium phosphate [2-6]. In the current study, local environment of Sr ions in OCP has been investigated by the above strategy, i.e., combined use of XANES measurements and DFT calculations.

Sr-doped OCPs were synthesized with precipitation method changing the concentration of doped Sr ions. Crystal structures of these Sr-doped OCPs were examined by the powder X-ray diffraction, which showed all the samples are single phased and no secondary phase could be observed. Elemental analysis was also carried out with Energy Dispersive X-ray (EDX) analyzer equipped with the scanning electron microscope (SEM) to confirm the concentration of Sr ions in OCP. For the local environment analysis of Sr ions in OCP, Sr-L<sub>3</sub> XANES spectra were observed at BL2A, UVSOR, in a total electron mode. Sample powders were settled on the carbon adhesive tape, which was put on the first dinode of the electron multiplier. The synchrotron radiations from the storage ring was monochromatized with the InSb(111) double-crystal monochrometer. Observed Sr-L<sub>3</sub> XANES spectra are shown in Fig. 1. Although it can be determined that Sr is divalent from this comparison, we cannot get any further information on local environment of Sr ions in OCP only from these experiments. To get more information, theoretical XANES spectra for the models of Sr-doped OCP were constructed by the all-electron linearized augmented wave plus local orbital package, WIEN2k [7], with core-hole effect. Furthermore solution energy for these models were also calculated with same package.

Considering the above experimental and theoretical XANES and theoretical solution energy the local environment of Sr ions in OCP could be determined.

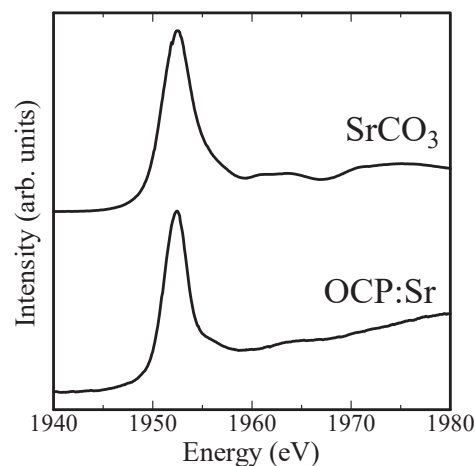


Fig. 1. Observed Sr-L<sub>3</sub> XANES spectra of SrCO<sub>3</sub> and Sr-doped OCP.

- [1] H. Kawamura, A. Ito, S. Miyakawa, P. Layrolle, L. Ojima, H. Naito, N. Ichinose and T. Tateishi, *J. Biomed. Mater. Res.* **50** (2000) 184.
- [2] K. Kawabata, H. Sato and T. Yamamoto, *J. Ceram. Soc. Jpn.* **116** (2008) 108.
- [3] K. Kawabata, T. Yamamoto and A. Kitada, *Physica B* **406** (2011) 890.
- [4] K. Kawabata, T. Yamamoto and A. Kitada, *Mater. Trans.* **56** (2015) 1457.
- [5] K. Kawabata, H. Sato and T. Yamamoto, *UVSOR Activity Report 2007* **35** (2008) 108.
- [6] K. Kawabata and T. Yamamoto, *UVSOR Activity Report 2010* **38** (2011) 110.
- [7] P. Blaha, K. Schwarz, G.K.H. Madse, D. Lvasnicka, J. Luiz, WIEN2k (Wien, Austria, Univ. Vienna, 2001).

BL2A

## P-K XANES Study for Hydration Reaction of $\alpha$ -Tricalcium Phosphate in Aqueous Solutions with Various Ions

H. Murata, R. Hashii and A. Nakahira

Department of Materials Science, Osaka Prefecture University, Sakai 599-8531, Japan

A number of biomaterials which are used in human bodies have been developed in order to improve quality of life (QOL) for a long time. Calcium phosphates are promising biomaterials which is used as alternative materials of human bones and teeth.  $\alpha$ -tricalcium phosphate ( $\text{Ca}_3(\text{PO}_4)_2$ ,  $\alpha$ -TCP) is one of main components of bone cements which are hydrated and hardened in human bodies.[1] Hydration of  $\alpha$ -TCP usually forms hydroxyapatite ( $\text{Ca}_5(\text{PO}_4)_3\text{OH}$ , HAp) of which human bones and teeth are composed. It is known that coexistent ions and molecules in aqueous solutions affects hydration reaction of  $\alpha$ -TCP. Since it is considered that hydration reaction starts on surface of  $\alpha$ -TCP, it is essential to investigate surface and bulk states of  $\alpha$ -TCP hydrated with various kinds of environments.

X-ray absorption near edge structure (XANES) is a powerful tool to investigate local structures. In soft X-ray region, XANES analyses can reveal both of surface and bulk states using methods with different attenuation length, electron yield and fluorescent yield. [2] In detail, electron yield method collects information around several nano-meters below the surface while fluorescent yield done around several micro-meters below it. In this study, we investigated surface and bulk structures of hydrated  $\alpha$ -TCP in aqueous solutions which contains various kinds of ions with P-K XANES.

$\alpha$ -TCP powders were purchased from Taihei Chemical Industrial Co., Ltd. They were soaked in aqueous solutions with various kinds of ions. P-K XANES spectra were collected at BL2A in UVSOR by a total electron yield (TEY) mode with a drain current method and a partial fluorescent yield (PFY) mode with a silicon drift detector (SDD). Samples were mounted using carbon tapes on Cu plates. X-ray beam was monochromated using InSb double crystals.

Figure 1 shows typical P-K XANES spectra of  $\alpha$ -TCP samples hydrated in 0.1 mol/L  $\text{NH}_3$  aqueous solution at different temperature for 24 h and reference materials. P-K XANES of  $\alpha$ -TCP has different features from those of HAp and we can distinguish from each other. P-K XANES of samples shows that  $\alpha$ -TCP hydrated at 70 °C and 80 °C were transformed to HAp while  $\alpha$ -TCP hydrated at 37 °C still remained.

Co-existent ions, such as  $\text{Zn}^{2+}$ , disturb hydration reaction of  $\alpha$ -TCP. We investigated  $\alpha$ -TCP samples hydrated in aqueous solutions which contains  $\text{Zn}^{2+}$ . Both of TEY and PFY results indicated that samples

soaked in the solution for 12 h remained while samples were transformed to HAp in the aqueous solution without  $\text{Zn}^{2+}$ . Powder X-ray diffraction analyses gave the same tendencies to that of P-K XANES. These results means that hydration of  $\alpha$ -TCP to HAp does not occur even on the surface. Therefore, It is implied that hydration reaction of  $\alpha$ -TCP to HAp do not simply occur on the surface but relate solution-precipitation process.

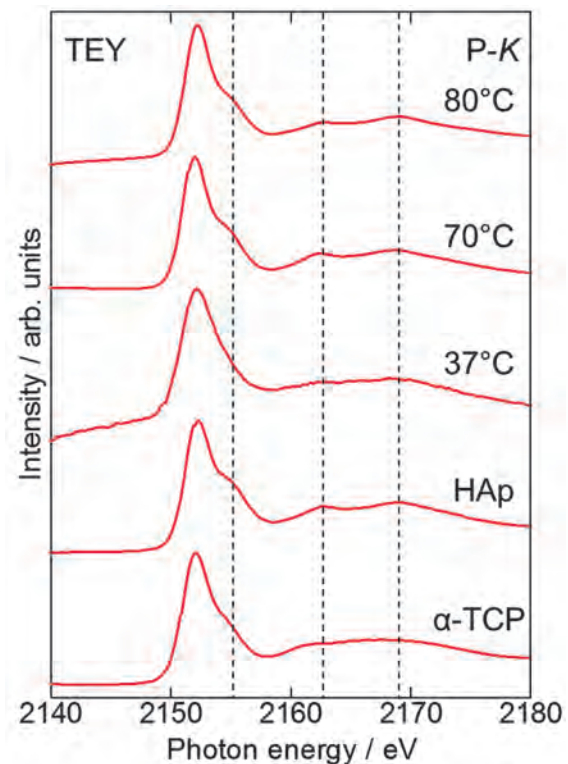


Fig. 1. Typical P-K XANES spectra of  $\alpha$ -TCP hydrated in different temperature for 24 h and reference materials.

[1] R.G. Carrodegua and S. De Aza, *Acta Biomater.* **7** (2011) 3536.

[2] M. Kasrai *et al.*, *Appl. Surf. Sci.* **99** (1996) 303.

BL2A

## Ga L<sub>3</sub>-edge XAFS Analysis of Ga<sub>2</sub>O<sub>3</sub> Loaded Al<sub>2</sub>O<sub>3</sub> Photocatalysts

T. Yoshida<sup>1</sup>, R. Ito<sup>2</sup>, M. Akatsuka<sup>2</sup>, Y. Kato<sup>2</sup>, A. Ozawa<sup>2</sup>, M. Yamamoto<sup>1</sup> and T. Tanabe<sup>1</sup>

<sup>1</sup>Advanced Research Institute for Natural Science, Osaka City University, Osaka 558-8585, Japan

<sup>2</sup>Graduate School of Engineering, Osaka City University, Osaka 558-8585, Japan

Recently Ga<sub>2</sub>O<sub>3</sub> has attracted a lot of interests as a photocatalyst for water splitting and CO<sub>2</sub> reduction with water, and various efforts have been paid to improve its photocatalytic activity. Yamamoto et al. have reported improvement of photocatalytic activity for CO<sub>2</sub> reduction with water under UV irradiation using Ag as a co-catalyst. In the present study, we have focused to geometrical or morphological effects of Ga<sub>2</sub>O<sub>3</sub> particles supported on Al<sub>2</sub>O<sub>3</sub> (referred as Ga<sub>2</sub>O<sub>3</sub>/Al<sub>2</sub>O<sub>3</sub>, hereafter) for water splitting and CO<sub>2</sub> reduction under UV light irradiation without using the Ag cocatalyst. The reasons of utilization of Al<sub>2</sub>O<sub>3</sub> as the support are twofold, (1) to increase surface area of Ga<sub>2</sub>O<sub>3</sub>, as evidenced by the observation that Ga<sub>2</sub>O<sub>3</sub>/Al<sub>2</sub>O<sub>3</sub> was used for the removal of NO<sub>x</sub>, and (2) that Al<sub>2</sub>O<sub>3</sub> hardly show the photocatalytic activity for both water splitting and CO<sub>2</sub> reduction.

Ga<sub>2</sub>O<sub>3</sub>/Al<sub>2</sub>O<sub>3</sub> photocatalyst samples were prepared by an impregnation method. Ga(NO<sub>3</sub>)<sub>3</sub>·8H<sub>2</sub>O (Kishida Chemical Co. Ltd. purity 99.0%) and 1.0 g γ-Al<sub>2</sub>O<sub>3</sub> (Sumitomo Chemical Co. Ltd. purity 99.99%) were added to 200 mL of distilled water and stirred with a magnetic stirrer in air and dried up, followed by calcination at 823 K for 4h, resulting the Ga<sub>2</sub>O<sub>3</sub>/Al<sub>2</sub>O<sub>3</sub> samples. The loaded amounts of Ga<sub>2</sub>O<sub>3</sub> were 5, 10, 20, 40 and 60 wt%. Pure Al<sub>2</sub>O<sub>3</sub> and unsupported Ga<sub>2</sub>O<sub>3</sub> samples (referred as 0 and 100 wt%, respectively) were also prepared in the similar procedure. Ga L<sub>3</sub>-edge XANES were measured with the beam line of BL5S1 at Aichi Synchrotron Radiation Center and BL2A at UVSOR, Institute for Molecular Science in Japan, respectively.

Photocatalytic CO<sub>2</sub> reduction with H<sub>2</sub>O under UV light irradiation was tested for 0.1 g of one of the samples set in a fixed-bed flow reactor cell under CO<sub>2</sub> gas flow. The UV light intensity was 35 mW/cm<sup>2</sup> in the range of 254 ± 10 nm. Before the test, the sample was irradiated with a 300 W Xe lamp for 1h under CO<sub>2</sub> gas flow with the flow rate of 20.0 mL/min. Then the reduction test was started introducing a NaHCO<sub>3</sub> aqueous solution (1.0M) of 10.0 mL and CO<sub>2</sub> gas with a flow rate at 3.0 mL/min under the UV light irradiation. The reaction products (CO, H<sub>2</sub> and O<sub>2</sub>) were analyzed by a gas chromatograph equipped with a thermal conductivity detector (GC-TCD).

All prepared Ga<sub>2</sub>O<sub>3</sub>/Al<sub>2</sub>O<sub>3</sub> samples have shown significantly higher photocatalytic activity compared to that of pure Ga<sub>2</sub>O<sub>3</sub> (non-supported Ga<sub>2</sub>O<sub>3</sub>). The cause of the improvement is discussed considering detailed characterizations by Ga L<sub>3</sub>-edge XAFS

measurements.

Figure 1 shows Ga L<sub>3</sub>-edge XANES spectra. A peak appeared near 1123 eV is caused by a Ga-O-Al bond. [1-3] For lower Ga<sub>2</sub>O<sub>3</sub> loaded samples, this peak was relatively high compared to other peaks. This indicates that some interaction between Ga<sub>2</sub>O<sub>3</sub> and Al<sub>2</sub>O<sub>3</sub> occurred in lower loaded samples. For higher Ga<sub>2</sub>O<sub>3</sub> loaded samples, the peak intensity at 1123 eV became less and the spectrum transformed to that of Ga<sub>2</sub>O<sub>3</sub> indicating loaded Ga<sub>2</sub>O<sub>3</sub> well crystallized. The result of XANES analysis was quite consistent with that of our separate EXAFS and XPS analyses.

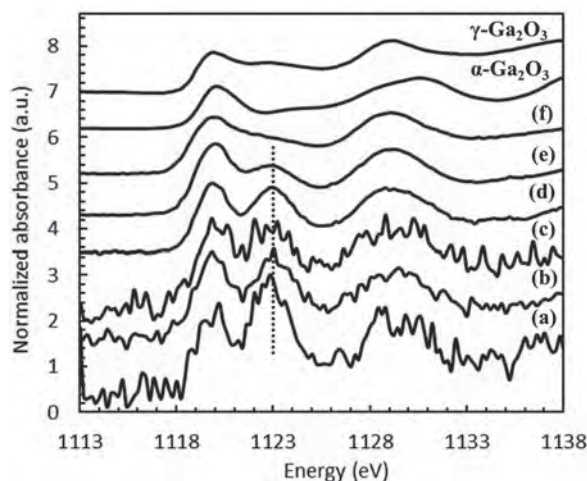


Fig. 1. Ga L<sub>3</sub>-edge XANES spectra of all prepared samples. The spectrum of β-Ga<sub>2</sub>O<sub>3</sub> is also given for comparison. (a) 0.15 vol% Ga<sub>2</sub>O<sub>3</sub>/Al<sub>2</sub>O<sub>3</sub> (b) 0.32 vol% Ga<sub>2</sub>O<sub>3</sub>/Al<sub>2</sub>O<sub>3</sub> (c) 0.73 vol% Ga<sub>2</sub>O<sub>3</sub>/Al<sub>2</sub>O<sub>3</sub> (d) 2.6 vol% Ga<sub>2</sub>O<sub>3</sub>/Al<sub>2</sub>O<sub>3</sub> (e) 4.2 vol% Ga<sub>2</sub>O<sub>3</sub>/Al<sub>2</sub>O<sub>3</sub> (f) 100 vol% Ga<sub>2</sub>O<sub>3</sub>/Al<sub>2</sub>O<sub>3</sub>. Peaks appeared at 1123 eV is assigned to be caused by Ga-O-Al bond formation.

[1] K. Shimizu, M. Takamatsu, K. Nishi, H. Yoshida, A. Satsuma, T. Tanaka, S. Yoshida and T. Hattori, *J. Phys. Chem. B* **103** (1999) 1542.

[2] X. T. Zhou, F. Heigl, J. Y. P. Ko, M. W. Murphy, J. G. Zhou, T. Regier, R. I. R. Blyth and T. K. Sham, *Phys. Rev. B* **75** (2007) 125303.

[3] N. H. Tran, R. N. Lamb, L. J. Lai and Y. W. Yang, *J. Phys. Chem. B* **109** (2005) 18348.



BL2A

## Removal of Elastic Scattering for Partial Fluorescence Yield XANES Measurements

H. Murata

Department of Materials Science, Osaka Prefecture University, Sakai 599-8531, Japan

X-ray absorption near edge structure (XANES) is a powerful tool for materials science since its targets are widely varied. For example, ultra-dilute dopants ( $\sim$  ppm), thin films, amorphous materials can be analyzed. In soft X-ray region, it is difficult to use transmission mode due to low transparency. Instead, electron yield and fluorescent yield method were often adapted for XANES measurements. Although there are some problems such as “self-absorption effect”, a number of beamlines for soft X-ray absorption introduced fluorescence yield method. In the case of UVSOR, a silicon drift detector (SDD) for partial fluorescent yield (PFY) method are available at BL2A and BL4B. [1, 2] Using SDD, elastic scattering of incident X-ray was sometimes observed. Since energy of incident X-ray scans from low to high, usual “region of interest” (ROI) sampling cannot remove elastic scattering. In this study, energy variable fitting method was developed to removal elastic scattering for PFY XANES measurements.

PFY XANES measurements were performed at BL2A in UVSOR. X-ray beam was monochromated by beryl, KTP and InSb double crystals. Conversion of SDD channel to X-ray energy were estimated using linear function. Its factors were determined using several energy of incident X-ray. It was noted that rather strong elastic scattering was observed in several cases. Amorphous materials and samples containing nano-particles gave strong elastic scattering due to their broad X-ray diffraction pattern, halo pattern. In addition to this, ultra-dilute dopants also done since SDD are moved close to samples to improve detection efficiency of fluorescent X-ray. Therefore  $\text{SiO}_2$  was diluted by  $\text{TiO}_2$  nanopowder for model samples.

Figure 1 shows typical X-ray fluorescence spectra of  $\text{SiO}_2$  diluted by  $\text{TiO}_2$  nano-powders. Elastic scattering of incident X-ray was also detected. As energy of incident X-ray increase, peaks of elastic scattering were shifted. Figure 2 shows XANES spectra estimated by  $\text{Si-K}_\alpha$  and elastic scattering of incident X-ray. It was note that the elastic scattering have intensities below  $\text{Si-K}$  absorption edge. Elastic scattering have small peak at the white line of  $\text{SiO}_2$  due to overlapping of  $\text{Si-K}_\alpha$  and the elastic scattering. Therefore it behave as background. We also measured more diluted samples, the background caused by the elastic scattering were well reduced using this method. Therefore, this method were useful for samples of which fluorescent X-ray was overlapped.

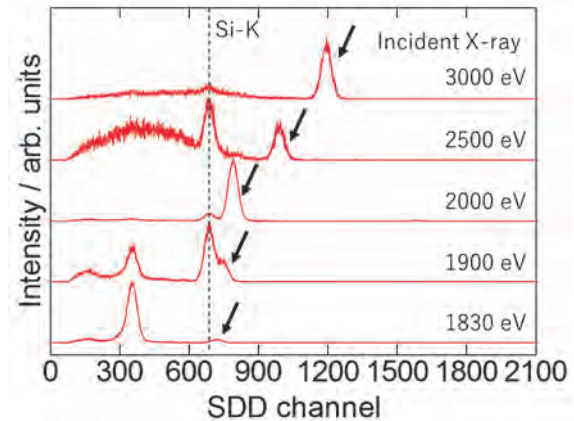


Fig. 1. Typical fluorescent X-ray spectra of  $\text{SiO}_2$  diluted by  $\text{TiO}_2$  nano-powders with different incident X-ray energy. Arrows indicates elastic scattering of incident X-ray.

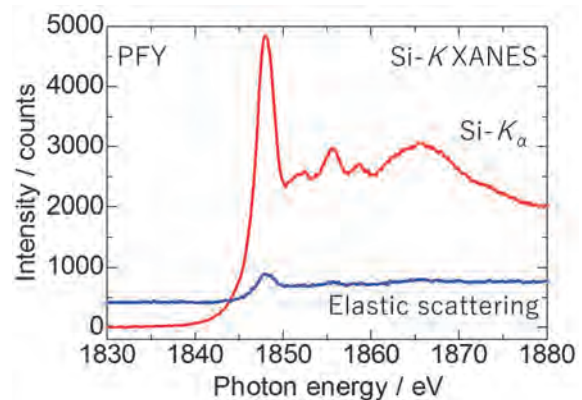


Fig. 2. Si-K XANES of  $\text{SiO}_2$  diluted by  $\text{TiO}_2$  nano-powders. Red and blue lines indicates spectra measured by  $\text{Si-K}_\alpha$  X-ray and elastic scattering of incident X-ray.

[1] H. Murata *et al.*, UVSOR Activity Reports 2013 41 (2014) 52.

[2] H. Murata *et al.*, UVSOR Activity Reports 2013 41 (2014) 56.

BL2A

## Local Environment of Multivalent Cations in Ion-Exchanged Layered Titanate and Titanate Nanotubes

A. Fujimoto, H. Murata and A. Nakahira

Department of Materials Science, Osaka Prefecture University, Sakai 599-8531, Japan

Titanate nanotubes have attracted many researchers due to their unique structures.[1] They consist of  $\text{TiO}_6$  octahedra linked by sharing edges, which is considered to be based on structures of layered titanate. Titanate nanotubes and layered titanates have cation-exchange ability. Since they have variable-length interlayers, various kinds of cations can be incorporated. Generally, univalent cations,  $\text{M}^+$ , are easily ion-exchanged into them. On the other hand, multivalent cations are slightly difficult to introduce into them. In this study, we tried to synthesize ion-exchanged titanate nanotubes and layered titanates with multivalent cations, and investigated their local environments by X-ray absorption near edge structure (XANES).

Layered titanate samples were prepared with a solid-state reaction method.  $\text{Na}_2\text{CO}_3$  and  $\text{TiO}_2$  were used as starting materials. They were mixed and ground in an agate mortar. Then, they were calcined at  $1000^\circ\text{C}$  for 8 h. Titanate nanotubes samples were synthesized by the hydrothermal method based on Kasuga *et al.* [2]. Anatase-type  $\text{TiO}_2$  nano-powders and 10 mol/L of NaOH aqueous solution were sealed into Teflon-lined autoclave and they were heated at  $150^\circ\text{C}$  for 24 h. Obtained samples were ion-exchanged in aqueous solutions of HCl,  $\text{MgCl}_2$  or  $\text{AlCl}_3$ .

XANES spectra were measured at BL2A in UVSOR. Partial fluorescent yield method with a silicon drift detector (SDD) were adapted. X-ray beam was monochromated using beryl double crystals for Na-K and Mg-K edge, and KTP double crystals for Al-K edge. Samples were mounted by a carbon tape on Ti plates. It was noted that X-ray fluorescence from ion-exchanged titanate nanotubes gave rather weak signals. For example, only 10 cps for Al-K were observed at the peak top that the incident photon energy was 1570 eV. Therefore, we set maximum 15 second/points for dwell time.

As an example of results, fig.1 shows typical Al-K XANES spectra of  $\text{Al}^{3+}$ -exchanged samples and references.  $\text{Al}^{3+}$ -exchanged titanate nanotubes and  $\text{Na}_2\text{Ti}_3\text{O}_7$  have similar spectra to each other. This means local environments of  $\text{Al}^{3+}$  in them were also similar. When titanate nanotubes and  $\text{Na}_2\text{Ti}_3\text{O}_7$  are soaked in aqueous solutions, pH usually increase because of  $\text{H}^+$  incorporation into them, which often forms hydroxides. But our samples have different spectra from those of hydroxide and starting materials.

These results implied that  $\text{Al}^{3+}$  were incorporated into titanate nanotubes and layered titanates. Detail analyses of local environments for  $\text{Al}^{3+}$  in titanate nanotubes and layered titanates have been in progress using XANES simulation by first-principles manner.

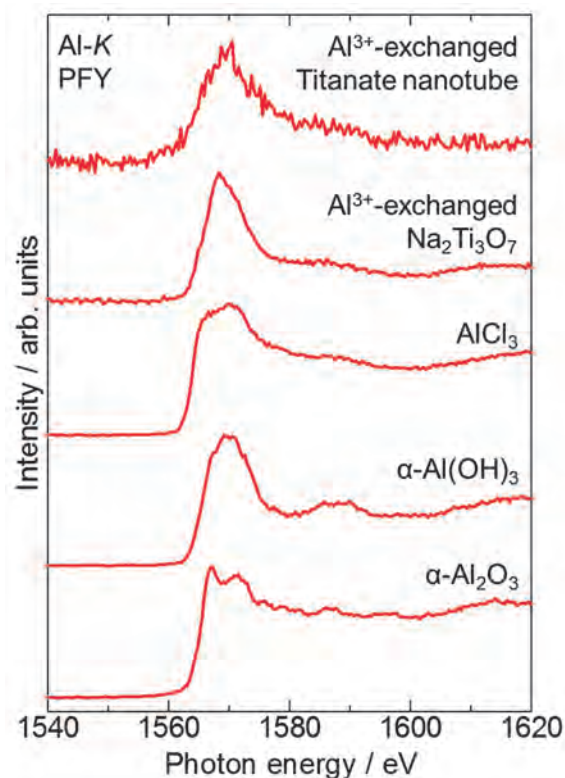


Fig. 1. Typical Al-K XANES spectra of titanate nanotubes and layered titanate which were ion-exchanged in  $\text{AlCl}_3$  aqueous solutions. Spectra of reference samples were also shown.

[1] D. V. Bavykin *et al.*, Adv. Mater. **18** (2006) 2807.

[2] T. Kasuga *et al.*, Langmuir **14** (1998) 3160.

BL2A

## Local Structure Investigations of $Y_3Al_5O_{12}$ Induced by Swift Heavy Ions Irradiations

S. Yoshioka<sup>1</sup>, K. Yasuda<sup>1</sup>, S. Matsumura<sup>1</sup>, N. Ishikawa<sup>2</sup>, K. Kobayashi<sup>3</sup> and K. Okudaira<sup>4</sup>

<sup>1</sup>Department of Applied Quantum Physics and Nuclear Engineering, Kyushu University, Fukuoka 819-0395, Japan

Nuclear Science and Research Center, Japan Atomic Energy Agency (JAEA), Tokai 319-1184, Japan

<sup>3</sup>Kyushu Synchrotron Light Research Center (SAGA-LS), Tosu 841-0005, Japan

<sup>4</sup>Graduate School of Advanced Integration Science, Chiba University, Chiba, 263-8522, Japan

Yttrium aluminum garnet ( $Y_3Al_5O_{12}$  or YAG) is considered as an important material for laser optical application. Ion irradiations are currently used to tailor materials properties. In particular, for garnet structure materials, swift heavy ion irradiations, produce amorphous tracks that can change the microstructure and the magnetic or magneto-optical properties[1]. In the present study, we made a combined study of NEXAFS measurements and first principles calculations on  $Y_3Al_5O_{12}$  with special interests on the local environment of Y and Al after irradiated with swift heavy ions (SHI).

Synthetic single crystals of  $Y_3Al_5O_{12}$  were used in this study. The crystals were cut into sheets with a (111) plane surface and were polished to a mirror finish. The specimens were irradiated with 340 MeV Au ions to fluences of  $3 \times 10^{11}$  and  $1 \times 10^{12}$   $cm^{-2}$  at the HI beamline of the tandem ion accelerator facility at the Japan Atomic Energy Agency (JAEA) in Tokai. Al  $K$ -edge and Y  $L_3$ -edge XANES measurements were performed at the BL2A beamline of UVSOR Okazaki, Japan, using the total electron yield method (TEY). A Beryl and an InSb double crystal monochromators defined Al  $K$  and Y  $L_3$  absorption edges, respectively. The samples were set with their surface perpendicular to the incident X-ray beam. All measurements of XANES spectra were carried out in vacuum of  $1 \times 10^{-5}$  Pa at room temperature. To interpret the local structure from the experimental spectra, we used theoretical spectra by the full-potential linearized augmented plane wave (APW) plus local orbitals technique as implemented in WIEN2k code.

Figure 1 shows the XANES spectra with the Al  $K$ -edge acquired from the  $Y_3Al_5O_{12}$  samples before and after irradiation with 340 MeV Au ions with fluences of  $3 \times 10^{11}$  and  $1 \times 10^{12}$ . The Al  $K$ -edge spectrum features of the irradiated sample show significant change with increasing SHI irradiation fluences. On the other hand, the Y  $L_3$ -edge spectrum features of the irradiated samples are very similar to that the pristine sample, as shown in Fig. 2. These results suggest that the SHI irradiations to the  $Y_3Al_5O_{12}$  sample preferentially induced the local structure changes of Al, compared to Y.

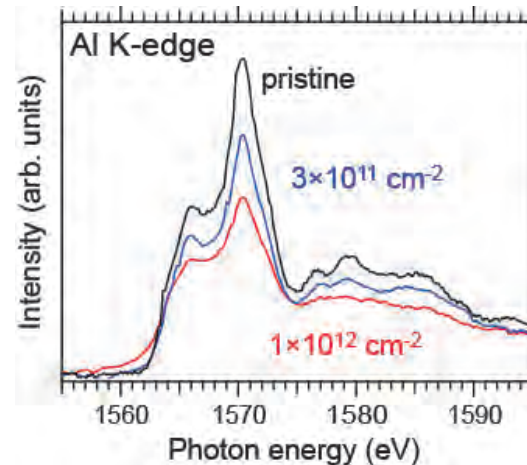


Fig. 1. Al  $K$ -edge XANES spectra of pristine and irradiated  $Y_3Al_5O_{12}$  with 340 MeV Au ions to fluences of  $3 \times 10^{11}$  and  $1 \times 10^{12}$   $cm^{-2}$ .

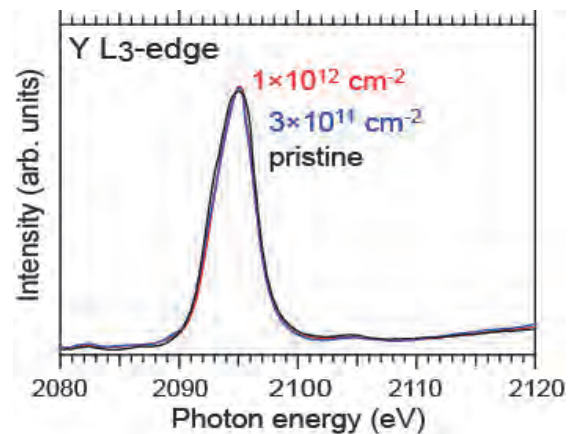


Fig. 2. Y  $L_3$ -edge XANES spectra of pristine and irradiated  $Y_3Al_5O_{12}$  with 340 MeV Au ions to fluences of  $3 \times 10^{11}$  and  $1 \times 10^{12}$   $cm^{-2}$ .

[1] J. M. Costantini, S. Miro, F. Beuneu and M. Toulmonde, *J. Phys.: Condens. Matter* **27** (2015) 496001.



BL2B

## Excitation Energy Dependent UPS of Solution-processed Perovskite Film

A. Mirzehmet<sup>1</sup> and H. Yoshida<sup>2,3</sup>

<sup>1</sup>Graduate School of Advanced Integration Science, Chiba University, Chiba 263-8522, Japan

<sup>2</sup>Graduate School of Engineering, Chiba University, Chiba 263-8522, Japan

<sup>3</sup>Molecular Chirality Research Center, Chiba University, Chiba 263-8522, Japan

In the perovskite solar cell, the interfaces play crucial roles in the charge extraction, transfer and recombination. The general chemical formula for the perovskite is  $ABX_3$ . The most commonly used working layer is the solution-processed film of methylammonium lead iodide ( $MAPbI_3$ ) where A, B, and X are methylammonium (MA), lead (Pb) and iodine (I), respectively. The electronic properties of the interface involving the perovskite  $ABX_3$  should be strongly affected by the elements of the surface termination layer being either A, B, or  $X_3$ .

Previously, we have examined the uppermost surface elements of the solution-processed  $MAPbI_3$  perovskite film by comparing the valence band spectra measured with different probing depths using ultraviolet photoelectron (UPS) and metastable-atom electron (MAES) spectroscopies [1]. In this work, we have measured the excitation energy dependent UPS in the range between 24.3 eV and 110 eV to confirm our peak assignment.

Figure 1 shows the energy dependent UPS. Based on the reported DFT calculations [2, 3], we tentatively assigned the peak at 3.3~3.6 eV to the I 5p derived-states, and the peak at 4.7 eV to the Pb 6s and 6p derived-states. The features at 8.8 and 10.8 eV are dominated by MA molecular states, with additional Pb 6s states at 8.8 eV.

The intensities of the peaks vary with the excitation energy as shown in Fig. 1. The features of I 5p shows strong intensity on the low energy and decreased as the increases of the photon energy. Pb 6p and 6s, however, always shows lower intensity compared with I 5p. The features of MA (N 2p and C 2p) show strong intensity and decreased on the high energy.

The observations are fully consistent with the photoionization cross-section [4] (Fig. 2) confirming our peak assignment.

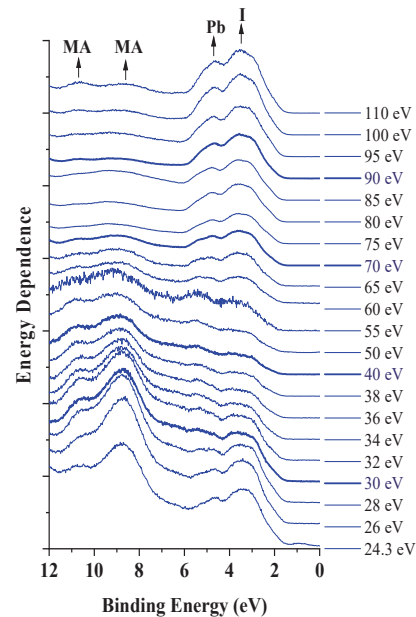


Fig. 1. Energy dependent UPS spectra of  $MAPbI_3$  film.

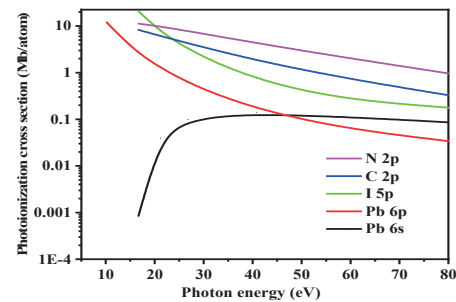


Fig. 2. Photoionization cross-section of  $MAPbI_3$  elements.

[1] M. Abduheber, *et al.*, The 79<sup>th</sup> JSAP Autumn Meeting (2018).

[2] W-J. Yin *et al.*, *Appl. Phys. Lett.* **104** (2014) 063903.

[3] J. Endres *et al.*, *J. Phys. Chem. Lett.* **14** (2016) 2722.

[4] J-J. Yeh, *Atomic calculation of photoionization cross-sections and asymmetry parameters* (Gordon and Breach Science, Publishers, 1993).

BL3B

## Correlation between Intrinsic Luminescence Intensity and Structure in $(\text{Ca}_{1-x}\text{Sr}_x)_2\text{Al}_2\text{SiO}_7$ and $(\text{Ca}_{1-x}\text{Sr}_x)_2\text{MgSi}_2\text{O}_7$ Melilite Crystals

N. Kodama, H. Kubota, T. Uematsu and T. Takahashi

Graduate School of Engineering Science, Akita University, Akita 010-8502, Japan

Crystals with a layered structure are expected to exhibit strong luminescence from peculiar two-dimensional excitons resulting from their large binding energy.  $(\text{Ca}_{1-x}\text{Sr}_x)_2\text{Al}_2\text{SiO}_7$  and  $(\text{Ca}_{1-x}\text{Sr}_x)_2\text{MgSi}_2\text{O}_7$  melilite crystals have a tetragonal sheet structure, which consists of five-membered rings of  $\text{TO}_4$  ( $T = \text{Al}, \text{Si}, \text{Mg}$ )  $\text{AlO}_4^{5-}$ ,  $\text{SiO}_4^{4-}$ , or  $\text{MgO}_4^{6-}$  oxoanions, resulting in self-trapped excitons (STEs) under band-to-band (interband) excitation or molecular transitions in the VUV region. The formation energy and the luminescence properties of excitons are considered to depend on the nature of the oxoanion-linked structure, such as the dimensionality (intra-layer distance) or two-dimensional modulation. To date, very little research has focused on the formation of self-trapped excitons in the dimensionality and modulation of the structure. We examined the correlation between the intrinsic luminescence intensity and the two-dimensionality and structure modulation (superstructure) in  $(\text{Ca}_{1-x}\text{Sr}_x)_2\text{Al}_2\text{SiO}_7$  and  $(\text{Ca}_{1-x}\text{Sr}_x)_2\text{MgSi}_2\text{O}_7$  ( $x = 0, 0.25, 0.5$ ) melilite crystals. We report intrinsic luminescence from self-trapped excitons (STEs). In addition, we discuss the structural correlation of the intrinsic luminescence intensity from STEs.

Luminescence and excitation spectra of STEs in  $(\text{Ca}_{1-x}\text{Sr}_x)_2\text{Al}_2\text{SiO}_7$  and  $(\text{Ca}_{1-x}\text{Sr}_x)_2\text{MgSi}_2\text{O}_7$  ( $x = 0, 0.25, 0.5$ ) crystals were measured in the temperature range of 14–293 K using the undulator beamline BL3B at the UVSOR facility. Under VUV excitation at 160 and 70 nm, intrinsic luminescence from self-trapped excitons (STE) was observed in these crystals.

The dependence of the intrinsic luminescence intensity on the Sr fraction  $x$  was examined for these crystals. In  $(\text{Ca}_{1-x}\text{Sr}_x)_2\text{Al}_2\text{SiO}_7$ , one luminescence band with a peak at 271–300 nm associated with STE appears at temperatures of 14–293 K. The luminescence spectra of  $(\text{Ca}_{1-x}\text{Sr}_x)_2\text{MgSi}_2\text{O}_7$  with  $x = 0.0, 0.25$ , and  $0.5$  consisted of two broad bands with peaks at 238–246 nm and 340–350 nm associated with STEs in the range of 14–293 K.

Figures 1(a) and 1(b) show the luminescence spectra for  $(\text{Ca}_{1-x}\text{Sr}_x)_2\text{Al}_2\text{SiO}_7$  and  $(\text{Ca}_{1-x}\text{Sr}_x)_2\text{MgSi}_2\text{O}_7$  ( $x = 0.0, 0.25, 0.5$ ) excited at 160 nm at 14 K.

In  $(\text{Ca}_{1-x}\text{Sr}_x)_2\text{Al}_2\text{SiO}_7$ , the crystal with  $x = 0.5$  exhibited one intense STE luminescence band, and the STE luminescence intensity decreases rapidly at  $x = 0.25$ . No significant luminescence was observed at  $x = 0.0$ . On the other hand, in  $(\text{Ca}_{1-x}\text{Sr}_x)_2\text{MgSi}_2\text{O}_7$ , the intensity of STEs passes through a maximum at intermediate fraction  $x = 0.25$ , as  $x$  increases. For the dependence of luminescence intensity on the Sr fraction,  $x$ , two possibilities are plausible: one is a two-

dimensional effect and the other is a structural modulation effect (superstructure).

First, the intra-layer distance increases with increasing  $x$ , because of the larger ionic radius involved in substituting  $\text{Sr}^{2+}$ . One possible explanation for such an intense luminescence at  $x = 0.5$  in  $(\text{Ca}_{1-x}\text{Sr}_x)_2\text{Al}_2\text{SiO}_7$  and  $(\text{Ca}_{1-x}\text{Sr}_x)_2\text{MgSi}_2\text{O}_7$  ( $x = 0.0, 0.25, 0.5$ ) is that a larger two-dimensional effect, i.e., the intra-layer distance increases with increasing Sr fraction  $x$ , which leads to larger two-dimensionality. However, the enlargement of intra-layer distance is not very large even at  $x = 0.5$  (a few percent). The second possible explanation is that a modulation effect of commensurate or incommensurate structure leads to an increase in local sites with larger distortion potentials. The formation of STEs and the luminescence intensity may be strongly affected by whether the crystals form a modulated structure (commensurate or incommensurate phase) and by the amplitude of modulation. We found that a  $(\text{Ca}_{1-x}\text{Sr}_x)_2\text{Al}_2\text{SiO}_7$  crystal with 0.5, which shows the most intense luminescence among the three  $x$  fractions (0.0, 0.25, and 0.5), exhibited commensurate modulation with two-fold periodicity along the  $c$ -axis by X-ray diffraction. Moreover, incommensurately and two-dimensionally modulated structures with Sr fractions,  $x$ , ranging from 0.04 to 0.32 have been observed in  $(\text{Ca}_{1-x}\text{Sr}_x)_2\text{MgSi}_2\text{O}_7$  [1]. Based on these structural changes with Sr composition, the intense luminescence at  $x = 0.5$  is considered to be due mainly to a structural modulation effect.

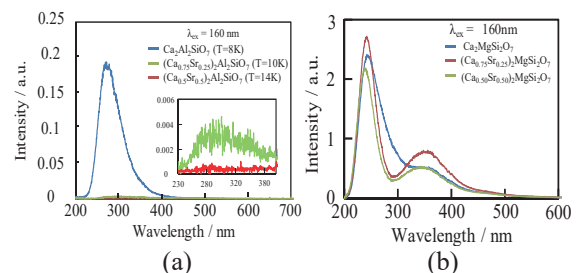


Fig. 1. Dependence of intrinsic luminescence on Sr fraction  $x$  in (a)  $(\text{Ca}_{1-x}\text{Sr}_x)_2\text{Al}_2\text{SiO}_7$  and (b)  $(\text{Ca}_{1-x}\text{Sr}_x)_2\text{MgSi}_2\text{O}_7$  ( $x = 0.0, 0.25, 0.5$ ) at 14 K under excitation at 160 nm. The inset shows the enlarged luminescence spectra in the range from 230 to 390 nm.

[1] J. C. Jiand, M. Schosnig, A. K. Schapaer, K. Ganster, H. Ragaer and L. Toth, *Phys. Chem. Minerals* **26** (1998) 128.

BL3B

## Evaluation of Fluorescence Lifetimes of Scintillation Fibers

H. Oikawa, M. Kitaura, A. Ohnishi, Y. Tajima and H. Y. Yoshida  
 Yamagata University, yamagata 990-8560, Japan

In high-energy physics experiments, particle detectors with fast time response are absolutely imperative. Especially, plastic scintillators are the first choice for radiation converter, because they have fluorescence with short decay time of nanosecond range. This feature is necessary for successive detection of particles at high count rates. In order to develop plastic scintillators, it is indispensable to evaluate fluorescence lifetimes with the use of a short pulse light source in the wide range from visible to vacuum ultraviolet. In the present study, we have measured fluorescence spectra and decay curves for some polystyrene-based plastic scintillators.

Samples used in our experiment can be available commercially, and they are labelled as Y-8, Y-11, B-3, O-2, R-3, and SCSF-78. As an example, the fluorescence spectrum of SCSF-78 is shown in Fig. 1. This spectrum was obtained under excitation at 200 nm. Two bands peaking at 335 nm and 435 nm appear in Fig. 1. Fluorescence decay curves were measured under single bunch operation by adopting time-correlated single photon counting method. The decay curve for the 335 nm band is shown in Fig. 2. The blue line indicates experimental data.

Lifetimes were analyzed by using the data analysis framework named "ROOT" [1]. For the lifetime analysis, we adopted the equation

$$I(t) = \int_{-\infty}^{\infty} P(t') G(t-t') \theta(t'-T_0) dt', \quad (1)$$

where

$$P(t) = \sum_i \exp(-t/\tau_i), \quad (2)$$

and

$$G(t-t') = A \exp\left(-\frac{(t-t'-\mu_1)^2}{2\sigma_1^2}\right) + B \exp\left(-\frac{(t-t'-\mu_2)^2}{2\sigma_2^2}\right). \quad (3)$$

$I(t)$  represents the fluorescence decay curve observed.  $P(t)$  represents the superposition of fluorescence decay curve functions.  $G(t-t')$  represents the resolution of the experimental system, the time structure of the beam, and so on. A sum of two Gaussians (3) successfully describes the measurement of the  $G(t-t')$  in this analysis.  $\theta(t'-T_0)$  is assumed a step function to reproduce the origin of time  $T_0$ . Table 1 shows fluorescence lifetimes of samples determined in the present study, together with the excitation and emission wavelengths. Decay curves for the 355 nm and 435 nm bands of SCSF-78 are reproduced by two or three exponential decay functions. Such complicated decay

curves suggest the existence of plural relaxation pathway under excitation in the fundamental absorption region of host polystyrene.

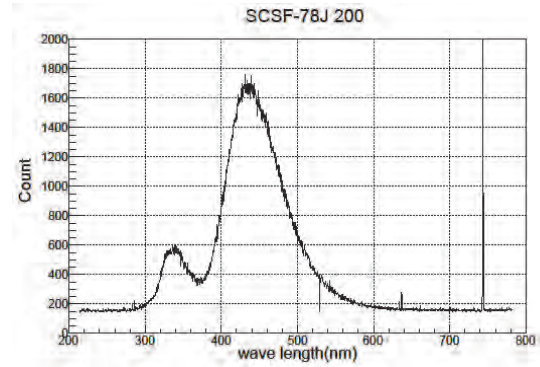


Fig. 1. Emission spectrum of SCSF-78, measured at room temperature under excitation at 200 nm.

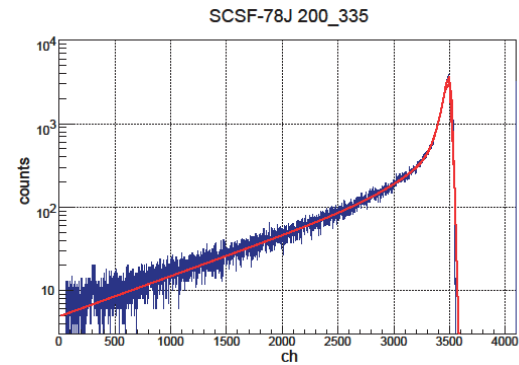


Fig. 2. Fluorescence decay curve for the 335 nm band of SCSF-78, measured at room temperature under excitation at 200 nm.

Table 1. Fluorescence peak-wavelengths and lifetimes determined in the present study.

sample	$\lambda_{EX}$ (nm)	$\lambda_{EM}$ (nm)	$\tau_1$ (ns)	$\tau_2$ (ns)	$\tau_3$ (ns)
SCSF78	200	335	0.934	4.68	17.4
	200	435	3.33	14.7	
	277	335	0.694		
	277	435	2.10		
	351	435	2.01		
Y11	430	495	6.92		
Y8	455	526	7.24		
B3	351	442	2.04		
O2	535	577	5.32		
R3	550	606	6.70		

[1] R. Brun and F. Rademakers, Nucl. Instrum. Methods Phys. Res. A **389** (1997) 81.

BL3B, BL7B

## Effect of Ce and Mg Concentration Ratio on the Properties of $\text{Gd}_3\text{Al}_2\text{Ga}_3\text{O}_{12}$ Single Crystal Scintillators

K. Bartosiewicz<sup>1</sup>, A. Yoshikawa<sup>1,2,3</sup>, S. Kurosawa<sup>2,4</sup>, A. Yamaji<sup>1</sup> and M. Nikl<sup>5</sup><sup>1</sup>Institute for Material Research, Tohoku University, Sendai 980-8577, Japan<sup>2</sup>New Industry Creation Hatchery Center, Tohoku University, Sendai 980-8579, Japan<sup>3</sup>C&A corporation, T-Biz, Sendai 980-8579, Japan<sup>4</sup>Facility of Science, Yamagata University, Yamagata 990-8560, Japan<sup>5</sup>Institute of Physics, Academy of Sciences of the Czech Republic, Na Slovance 1999/2, Prague 8, 18221, Czech Republic

In gadolinium gallium aluminum garnets ( $\text{Gd}_3\text{Al}_2\text{Ga}_3\text{O}_{12}$ , GAGG), efficient luminescence is dependent on dopants to create a radiative transition within the forbidden band [1]. In medical imaging,  $\text{Ce}^{3+}$  is commonly used due to fast and bright  $5d \rightarrow 4f$  transition with the emission wavelength that is suitable also for semiconductor photodetectors [2]. The  $\text{Ce}^{3+}$  activated GAGG is considered as a promising candidate for the next generation Positron Emission Tomography material due to its high light yield value ( $\sim 58,000$  ph/MeV), fast scintillation response ( $\sim 100$  ns), and high density ( $\sim 6.2$  g/cm<sup>3</sup>). However, this material suffers from the contribution of the undesired slow component in the scintillation response and long rise time [3]. Recently, the divalent ( $\text{Me}^{2+}$ ) codoping strategy has been used in order to mitigate the degraded scintillation properties that result from charge carrier traps and have been shown to improve light yield and decay times in some scintillators [4].

The  $\text{Mg}^{2+}$  codoping in GAGG:Ce single crystal significantly accelerates the scintillation decay time, but at the same time the light yield become strongly reduced [4]. To deeper understand the effect of  $\text{Mg}^{2+}$  codoping content on the scintillation characteristics of GAGG:Ce, we recorded thermally stimulated luminescence (TSL), see Fig.1. The results show that increasing  $\text{Mg}^{2+}$  concentration creates new peaks within the whole recorded temperature range. This means that  $\text{Mg}^{2+}$  codoping increases the number of metastable levels, which act as electron traps. Due to the transformation of  $\text{Ce}^{3+}$  to  $\text{Ce}^{4+}$  crystal lattice become perturbed. Consequently, many defects arise, which can significantly diminish scintillation performances. Moreover, a rich pattern of TSL peaks over RT is due to the presence of the deep electron traps, which are associated with oxygen vacancies. To conclude, TSL measurements revealed that  $\text{Mg}^{2+}$  codoping reduces the quality of the crystal lattice due to the creation of many defects acting as electron traps.

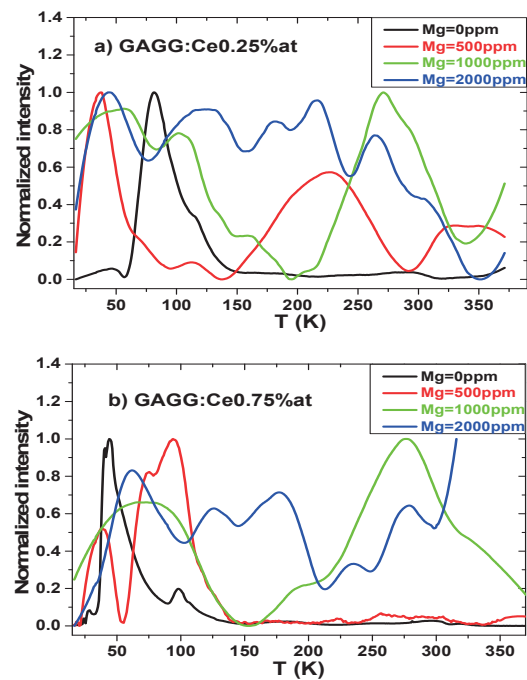


Fig. 1. Normalized TSL glow curves (measured in the 10-3800 K temperature range for the for  $\text{Mg}^{2+}$  free and  $\text{Mg}^{2+}$  codoped GAGG:Ce single crystals. Nominal content of  $\text{Ce}^{3+}$  was (a) 0.25% and (b) 0.75% at, irradiated at 10 K by UV radiation (12.4 eV)

[1] M. Nikl and A. Yoshikawa, *Adv. Optical Mater.* **3** (2015) 463.

[2] C. Ronda, *J. Solid State Sci. Technol.* **5** (2016) R3121.

[3] M. Lucchini *et al.*, *Instr. Meth. Phys, Research A* **852** (2017) 1.

[4] C. Foster *et al.*, *J. Cryst. Growth*, in press (10.1016/j.jcrysgro.2018.01.028).



BL3B

## Estimation of Optical Properties of RE<sub>2</sub>Si<sub>2</sub>O<sub>7</sub> Sintered Compacts Using the UVSOR Synchrotron Facility

T. Horiai<sup>1</sup>, S. Kurosawa<sup>2</sup>, A. Yamaji<sup>1</sup>, S. Kodama<sup>1</sup>, S. Yamato<sup>1</sup>, Y. Shoji<sup>1,4</sup>, M. Yoshino<sup>1</sup>, H. Sato<sup>2</sup>, Y. Ohashi<sup>2</sup>, K. Kamada<sup>2,3</sup>, Y. Yokota<sup>2</sup> and A. Yoshikawa<sup>1,2,3</sup>

<sup>1</sup>Institute for Materials Research, Tohoku University, Sendai 980-8577, Japan

<sup>2</sup>New Industry Creation Hatchery Center (NICHe), Tohoku University, Sendai 980-8579, Japan

<sup>3</sup>C&A Corporation, Aramaki, Sendai 980-8579, Japan

Scintillation crystals convert energy of ionizing radiation such as gamma-ray and X-ray into multiple photons of energy 2~8 eV, and are used in many fields, as radiation detectors [1-3]. The Ce-doped RE<sub>2</sub>Si<sub>2</sub>O<sub>7</sub> (RE= rare-earth ions) scintillators have been reported to have a high light yield, short decay time and good thermal stability. Here, the crystal system of RE<sub>2</sub>Si<sub>2</sub>O<sub>7</sub> are changed by rare-earth ions [4]. In addition, the emission and excitation spectra of Ce<sup>3+</sup> 5d-4f transition are strongly depend on the host crystal structure of RE<sub>2</sub>Si<sub>2</sub>O<sub>7</sub> due to the involved Ce<sup>3+</sup> 5d orbital are not shielded by outer electrons. Therefore, it is important to estimate the influence of crystal structure of RE<sub>2</sub>Si<sub>2</sub>O<sub>7</sub> and the ionic radii of rare-earth ions on optical properties of Ce-doped RE<sub>2</sub>Si<sub>2</sub>O<sub>7</sub>. In addition, the bandgap energy of RE<sub>2</sub>Si<sub>2</sub>O<sub>7</sub> is also affected when the rare-earth ion changes. In this study, we estimated the bandgap energy of RE<sub>2</sub>Si<sub>2</sub>O<sub>7</sub> (RE=La, Gd, Y and Lu) to investigate the change in bandgap energy due to the ionic radii of rare-earth ions.

We prepared (Ce<sub>0.01</sub> RE<sub>0.99</sub>)<sub>2</sub>Si<sub>2</sub>O<sub>7</sub> (RE=La, Gd, Y and Lu) sintered compacts.; As starting materials, we used La<sub>2</sub>O<sub>3</sub>, CeO<sub>2</sub>, Gd<sub>2</sub>O<sub>3</sub>, Y<sub>2</sub>O<sub>3</sub>, Lu<sub>2</sub>O<sub>3</sub> and SiO<sub>2</sub> powders the purities of which were at least 99.99%. After weighing, the powders were well wet-blended, and they were molded into pellets using a hydraulic press, and the pellets were pre-sintered at 1550 °C for 12 hours under air. Finally, we sintered the pellets at 1600 °C for over 24 hours under air. The emission spectra of these sintered compacts were measured with a spectrometer (spectropro-300i, Acton research), and the excitation spectra were measured with a photo diode (IRD, AXUV 100) at BL3B of UVSOR.

Figure 1 shows the emission spectra of Ce-doped RE<sub>2</sub>Si<sub>2</sub>O<sub>7</sub> (RE=La, Gd, Y, Lu). From this figure, the emission peak due to Ce<sup>3+</sup> 5d<sub>1</sub>-2f<sub>5/2</sub> was changed with changes in the ion radii of rare-earth ions. The excitation spectra of Ce-doped RE<sub>2</sub>Si<sub>2</sub>O<sub>7</sub> (RE=La, Gd, Y, Lu) is shown in Fig. 2. The result of estimating the host excitation band peak showed that the bandgap energies of La<sub>2</sub>Si<sub>2</sub>O<sub>7</sub>, Gd<sub>2</sub>Si<sub>2</sub>O<sub>7</sub>, Y<sub>2</sub>Si<sub>2</sub>O<sub>7</sub> and Lu<sub>2</sub>Si<sub>2</sub>O<sub>7</sub> were approximately 7.0, 6.9, 7.2 and 6.9 eV, respectively. All samples were found to have high bandgap energy of over 7.0 eV.

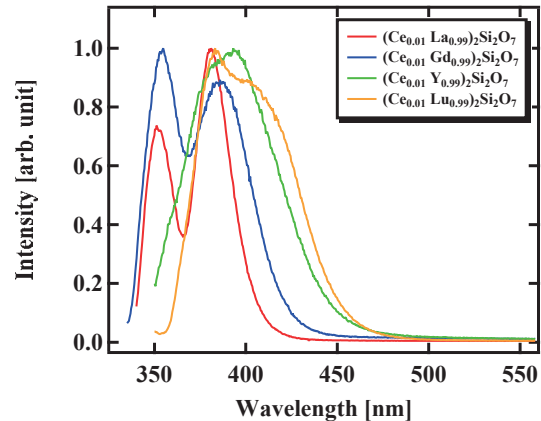


Fig. 1. Emission spectra of Ce-doped RE<sub>2</sub>Si<sub>2</sub>O<sub>7</sub> (RE=La, Gd, Y and Lu) at 6 K

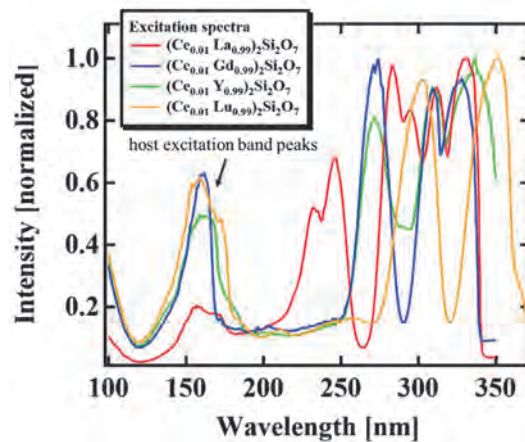


Fig. 2. Excitation spectra of Ce-doped RE<sub>2</sub>Si<sub>2</sub>O<sub>7</sub> (RE=La, Gd, Y and Lu) at 6 K

- [1] C. Rozsa, R. Dayton, P. Raby, M. Kusner and R. Schreiner, IEEE Trans. Nucl. Sci. **37** (1996) 966.
- [2] A. Baberdin, A. Dutova, A. Fedorov, M. Korzhik, V. Ligoun, O. Missevitch, V. Kazak, A. Vinokurov and S. Zagumenov, IEEE Trans. Nucl. Sci. **55** (2008) 1170.
- [3] C.L. Melcher, J.S. Schweitzer, R.A. Manente and C.A. Peterson, J. Crystal Growth **109** (1991) 37.
- [4] J. Felsche, Journal of the Less Common Metals **21** (1970) 1.

BL3B

## Temperature Dependence of PL Spectra of p-terphenyl and 1,4-bis(2-methylstyryl)benzene (bis-MSB) at 6-300 K

S. Yamato<sup>1</sup>, S. Kurosawa<sup>2,3</sup>, A. Yamaji<sup>1</sup>, T. Horiai<sup>1</sup>, S. Kodama<sup>1</sup>, M. Abe<sup>3</sup>, M. Yoshino<sup>1</sup>, Y. Ohashi<sup>2</sup>, K. Kamada<sup>2,4</sup>, Y. Yokota<sup>2</sup> and A. Yoshikawa<sup>1,2,4</sup>

<sup>1</sup>Institute for Materials Research (IMR), Tohoku University, Sendai 980-8577, Japan

<sup>2</sup>New Industry Creation Hatchery Center (NICHe), Tohoku University, Sendai 980-8579, Japan

<sup>3</sup>Faculty of science, Yamagata University, Yamagata 990-8560, Japan

<sup>4</sup>C&A Corporation, Sendai 980-8577, Japan.

Neutron detectors can be used in several fields such as neutron diffraction for crystal structure analysis, social infrastructure maintenance and nuclear fusion physics [1-3]. Here, nuclear fusion technology is expected as next effective energy generation technology. In fusion reactors, neutrons are emitted from nuclear fusion reactions, and the monitoring these particles is an important technology to control fusion reactors and generate energy effectively.

Among several nuclei, the neutron cross section of hydrogen nucleus is the largest in higher energy range. <sup>1</sup>H has relatively higher cross section for the fast neutron than other materials. We focused on organic scintillators which contains many <sup>1</sup>H and have low detection efficiency for gamma rays as background noise.

Although the neutron detectors in fusion reactors can be exposed on high temperature of about from 400 to 600 K, conventional organic scintillators cannot be used at high temperature. Plastic scintillators melt at around 230 K. Liquids evaporate at high temperature and are difficult to handle. Even crystals, only low-melting-point materials were developed. As a first step, we aimed to develop the organic scintillators which can be used at over 270 K. Also, I considered high-melting-point crystal have a potential to meet this demand.

We grew pure p-terphenyl crystal and pure 1,4-bis(2-methylstyryl)benzene (bis-MSB) crystal by the self-seeding vertical Bridgman method using an enclosed chamber [4]. Pulling down rate for growth was ~1 mm/h. The melting point of p-terphenyl and bis-MSB are 485 and 352 K, respectively.

We measured the photoluminescence (PL) emission spectra of the samples at 6-300 K with the beamline BL3B at UVSOR facility. The spectra of p-terphenyl excited by 245 nm photons and bis-MSB excited by 260 nm photons were shown in Fig. 1 and Fig. 2, respectively.

At 300 K the emission peaks of 375 and 390 nm were observed for p-terphenyl. As temperature decreased, the ratio of peak of 375 nm for 390 nm became smaller and new peak of 350 nm appeared. For bis-MSB, the emission peak of 484 nm became weaker and several peaks were appeared in shorter wavelength range as temperature decreased.

Since the molecular vibration was suppressed at lower temperature, emission peaks were split clearly. As future works, we study on the relationship between

these results and temperature dependence of photoluminescence decay time.

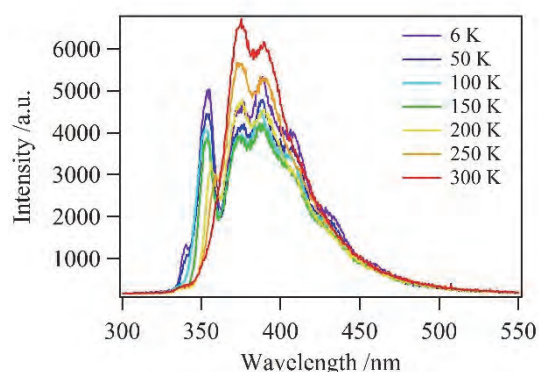


Fig. 1. Emission spectra of p-terphenyl crystal excited by 245 nm photons at 6-300 K.

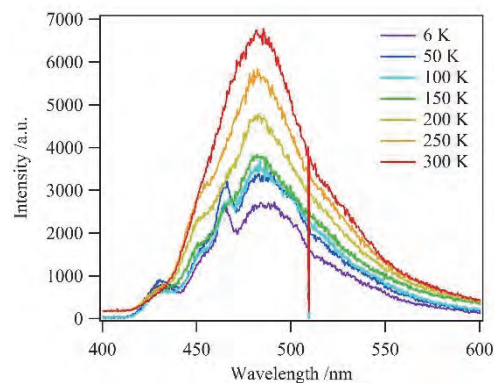


Fig. 2. Emission spectra of bis-MSB crystal excited by 260 nm photons at 6-300 K.

- [1] P. Zhang *et al.*, Cement and Concrete Research **108** (2018) 152.
- [2] H. K. Lee *et al.*, J. Supercond. Novel Magn. **31** (2018) 1677.
- [3] Y. K. Kim *et al.*, J. Instrum. **7** (2012) C06013.
- [4] A. Arulchakkaravarthi *et al.*, J. Crystal Growth **234** (2002) 159.

BL3B

## Low-temperature Photoluminescence Spectra of Cs<sub>2</sub>HfI<sub>6</sub>

S. Kodama<sup>1</sup>, S. Kurosawa<sup>2,3</sup>, M. Ohno<sup>1</sup>, A. Yamaji<sup>1</sup>, M. Yoshino<sup>1</sup>, H. Sato<sup>2</sup>,  
Y. Ohashi<sup>1</sup>, K. Kamada<sup>2,4</sup>, Y. Yokota<sup>2</sup> and A. Yoshikawa<sup>1,2,4</sup>

<sup>1</sup>Institute for Materials Research (IMR), Tohoku University, Sendai 980-8577, Japan

<sup>2</sup>New Industry Creation Hatchery Center (NICHe), Tohoku University, Sendai 980-8579, Japan

<sup>3</sup>Faculty of Science, Yamagata University, Yamagata 990-8560, Japan

<sup>4</sup>C&A Corporation, Sendai 980-8577, Japan.

A<sub>2</sub>HfX<sub>6</sub> (A: monovalent cation, X: halogen ion) compounds are host-emitting materials originated from self-trapped exciton (STE) [1]. Since the crystal lattice of A<sub>2</sub>HfX<sub>6</sub> compounds can be a well-ordered and high symmetry cubic structure (space group: *Fm-3m*), producing a transparent single crystal is easy. Actually, Our research group has developed a Cs<sub>2</sub>HfI<sub>6</sub> (CHI) single crystal as a noble red-emitting (around 650 nm) scintillator with a high light output of ~64,000 photons/MeV [2,3]. As mentioned above, the luminescence mechanism of CHI could be STE around [HfI<sub>6</sub>]<sup>2-</sup>, however, the detail of emission mechanism was still unclear. In this year, we evaluated the temperature dependence of CHI photoluminescence properties to study the luminescent origin.

A single-crystalline CHI specimen was synthesized from 99%-pure HfI<sub>4</sub> and 99.999%-pure CsI using the vertical Bridgman growth method in our laboratory. We measured photoluminescence emission spectra of CHI at from 10 K to 300 K cooled by liquid Helium in a cryostat chamber of UVSOR BL3B. The light source was a synchrotron light.

Figure 1 indicate the photoluminescence emission spectra of CHI. When the sample was excited by 400 nm at 300 K in Fig. 1 (a), the typical broad emission spectrum around 650 nm was observed. At 150 K one additional peak appeared at 550 nm, and as temperature decrease, the 550-nm-peak became very intense, while the intensity of 650-nm-peak decreased. The 550-nm-peak intensity leached the maximum at 10 K. CHI room temperature (300 K) emission excited 460 nm showed the different temperature dependence. To 8 K, the peak intensity increased, and wavelength shifted towards 700 nm.

Based on above temperature dependence, CHI was considered to have several excitation-emission bands. Moreover, the major band could change as temperature changes. Since the typical STE emission intensity increases at low temperature, the low temperature emission peak at 550 nm could be one STE band which thermally quenches above 150 K. Further study should be needed to understand the energy transfer between room temperature emission band and low temperature band. For the direct evaluation of STE center, electron paramagnetic resonance technique would be available.

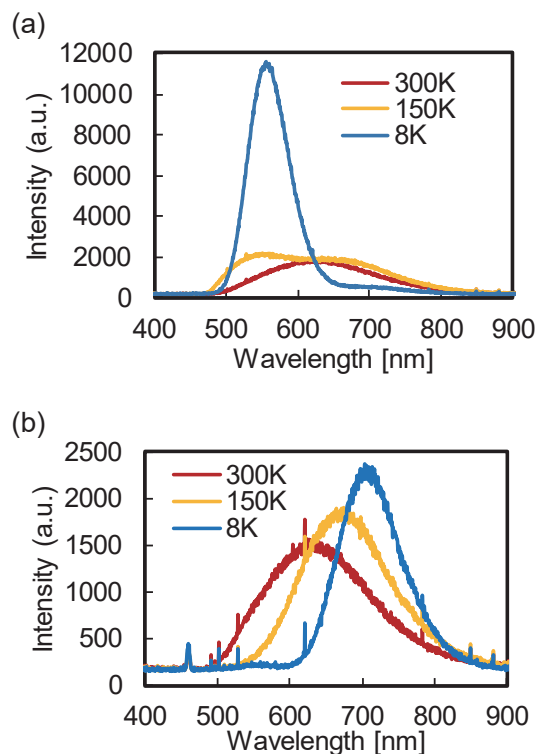


Fig. 1. Photoluminescence emission spectra of CHI crystal. (a) and (b) are spectra excited by 400 nm and 460 nm, respectively.

[1] B. Kang and K. Biswas, *J. Phys. Chem. C* **120** (2016) 12187. doi:10.1021/acs.jpcc.6b02496.

[2] S. Kodama, S. Kurosawa, M. Ohno, A. Yamaji, M. Yoshino, J. Pejchal, R. Král, Y. Ohashi, K. Kamada, Y. Yokota, M. Nikl and A. Yoshikawa, *Radiat. Meas.* in print (2019).

[3] S. Kodama, S. Kurosawa, A. Yamaji, J. Pejchal, R. Král, Y. Ohashi, K. Kamada, Y. Yokota, M. Nikl and A. Yoshikawa, *J. Cryst. Growth* **492** (2018) 1.

BL3B

## Photoluminescence upon Vacuum Ultraviolet Excitation in Pr<sup>3+</sup> Ion Doped Alkaline–Earth Phosphates

Y. Inaguma<sup>1</sup>, R. Horiguchi<sup>1</sup>, S. Sasaki<sup>1</sup>, M. Yaname<sup>1</sup>, D. Mori<sup>1</sup>, K. Ueda<sup>1</sup> and T. Katsumata<sup>2</sup>

<sup>1</sup>Department of Chemistry, Faculty of Science, Gakushuin University, Tokyo 171-8588, Japan

<sup>2</sup>Department of Chemistry, School of Science, Tokai University, Hiratsuka 259-1292, Japan

Pr<sup>3+</sup> ion doped inorganic materials have been extensively investigated in connection with various applications [1]: laser materials utilizing visible emission corresponding to <sup>3</sup>P<sub>0</sub> → <sup>3</sup>H<sub>4</sub> and <sup>1</sup>D<sub>2</sub> → <sup>3</sup>H<sub>4</sub> transitions (blue-green and red emission, respectively), or infrared emission from the <sup>1</sup>G<sub>4</sub> state of Pr<sup>3+</sup>, field emission display (FED) devices utilizing red <sup>1</sup>D<sub>2</sub> emission, scintillators or tunable ultraviolet (UV) lasers utilizing UV emission from the 4f5d state. Since the emission color or energy in Pr<sup>3+</sup> ion doped phosphors is closely related to the electronic structure of host materials, the choice of host materials is a matter of vital importance to control the emission color/energy [2].

Recently phosphor materials emitting UV light upon vacuum ultra violet (VUV) excitation are desired as the substitutes of mercury lamp due to the toxicity of mercury. Pr<sup>3+</sup> ion doped compounds are candidates of the UV phosphors because the UV emission from the 4f5d state in Pr<sup>3+</sup> can be expected. The UV emission from the 4f5d state would be observed if the band gap energy of the host material corresponds to the VUV region. We then chose Pr<sup>3+</sup> ion doped alkaline-earth phosphates with the band gap energy in the VUV region and investigated their luminescence properties. In our previous report[3], we presented the results of UV photoluminescence upon VUV excitation of Ca<sub>3</sub>(PO<sub>4</sub>)<sub>2</sub>:Pr. Herein, we report on the UV photoluminescence of Pr-doped alkaline–earth phosphates A<sub>3</sub>(PO<sub>4</sub>)<sub>2</sub>:Pr (A = Sr, Ba) in addition to Ca<sub>3</sub>(PO<sub>4</sub>)<sub>2</sub>:Pr.

The polycrystalline samples were synthesized by a solid state reaction. The mixture of starting materials: alkaline-earth carbonate ACO<sub>3</sub> (A = Ca, Sr, Ba), (NH<sub>4</sub>)H<sub>2</sub>PO<sub>4</sub> and Pr nitrate solution were calcined at 1000 °C in air. The calcined powder was pressed into pellets and sintered at 1000-1200 °C in air. The phase identification for the samples was carried out by the laboratory powder X-ray diffraction (XRD) using a Rigaku RINT 2100 diffractometer or a PANalytical X'Pert3 Powder diffractometer with a Bragg Brentano geometry (CuKα radiation). The emission and excitation spectra were recorded in the beamlines BL3B and BL7B at the UVSOR facility.

Figure 1 displays the emission(right side) and excitation(left side) spectra for A<sub>3</sub>(PO<sub>4</sub>)<sub>2</sub>:Pr5% (A = Ca, Sr, Ba) at room temperature. As seen in Fig.1, the UV emission peaks corresponding to the transitions from the 4f5d state to the 4f<sup>2</sup> (<sup>3</sup>H<sub>J</sub>, <sup>3</sup>F<sub>J</sub>) states of Pr<sup>3+</sup> were observed. In the excitation spectra, the peaks in the

range of 150-220 nm were observed. The shorter and longer wavelength regions correspond to the host absorption band, *i.e.* the intra charge transfer of PO<sub>4</sub><sup>3-</sup> [4] and the transition from the ground state of 4f<sup>2</sup> (<sup>3</sup>H<sub>4</sub>) to the 4f5d state of Pr<sup>3+</sup>, respectively. The emission and excitation peaks for A<sub>3</sub>(PO<sub>4</sub>)<sub>2</sub>:Pr (A = Sr, Ba) appears at the shorter wavelength than those for Ca<sub>3</sub>(PO<sub>4</sub>)<sub>2</sub>:Pr, which is attributable to the difference in covalency of Pr-O bonding.

Consequently, we found that A<sub>3</sub>(PO<sub>4</sub>)<sub>2</sub>:Pr (A = Sr, Ba) as well as Ca<sub>3</sub>(PO<sub>4</sub>)<sub>2</sub>:Pr exhibits the UV emission corresponding to the transition from the 4f5d state of Pr<sup>3+</sup> upon the VUV excitation and the Pr<sup>3+</sup> ion doped alkaline–earth phosphates are candidates of UV phosphors.

The authors thank Mr. M. Hasumoto, Mr. T. Yano for their experimental supports.

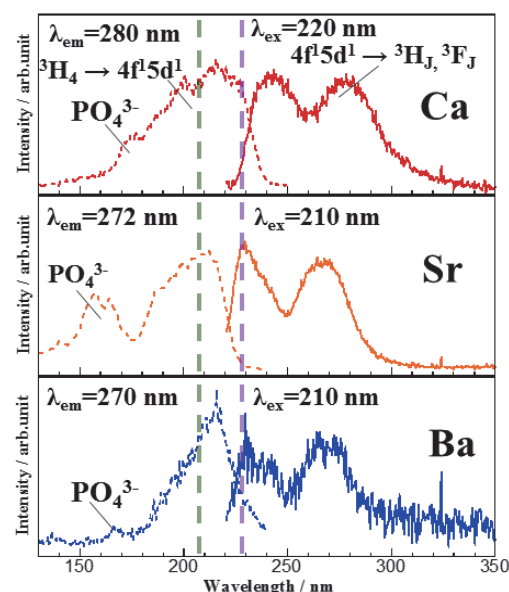


Fig. 1. Emission spectra (right side) and excitation spectra emission (left side) for A<sub>3</sub>(PO<sub>4</sub>)<sub>2</sub>:Pr5% (A = Ca, Sr, Ba) at room temperature.

[1] E. Van der Kolk *et al.*, Phys. Rev. B. **64** (2001) 195129.

[2] Y. Inaguma *et al.*, Inorg. Chem. **50** (2011) 5389.

[3] Y. Inaguma *et al.*, UVSOR activity report 2011 **39** (2012) 129.

[4] H. Liang *et al.*, J. Solid State Chem. **177** (2004) 901.



BL3B

### Emission Spectra of Pr-doped BaZrO<sub>3</sub>

M. Yoshino, J. Sugiyama, T. Kuyama and S. Watanabe

Graduate School of Engineering, Nagoya University, Nagoya 464-8603, Japan

In this study, the excitation spectra and emission spectra of Pr<sup>3+</sup> in BaZrO<sub>3</sub> crystal have been measured and changes in the spectra with doping of Yttrium and hydration are examined. The samples are synthesized by solid state reactions followed by annealing in N<sub>2</sub>-H<sub>2</sub> atmosphere in order to reduce Pr<sup>4+</sup> to Pr<sup>3+</sup>. The oxygen vacancies are created in Y-doped BaZrO<sub>3</sub> and protons are incorporated by hydration of the vacancies. The concentration of Pr is 0.5 mol% and that of Y are 5 mol% and 15 mol%. The Y-doped samples are hydrated at 523 K in humidified N<sub>2</sub>.

The emission spectra of BaZrO<sub>3</sub>:Pr and BaZrO<sub>3</sub> host at 265 nm excitation are shown in Fig. 1. The sharp peaks of BaZrO<sub>3</sub>:Pr around 500 nm and 600-650 nm originate from 4*f*-4*f* transitions of Pr<sup>3+</sup>. Since the broad emission peaks around 350-550 nm appear in both BaZrO<sub>3</sub>:Pr and BaZrO<sub>3</sub> samples, these originate from electron transitions in host rather than from 4*f*-5*d* transitions of Pr<sup>3+</sup>. The emission spectra of BaZrO<sub>3</sub>:Pr and Y-doped BaZrO<sub>3</sub>:Pr shown in Fig. 2. The intensities of Pr<sup>3+</sup> emissions increase with 5 mol% doping of Y, but they do not increase monotonically and become smaller in 15 mol%. It is supposed that Y substituted for Zr and oxygen vacancy promote the radiative transition in Pr<sup>3+</sup> by decreasing the site symmetry of the Pr<sup>3+</sup>, but oxygen vacancy prevent the transition with creation of defect level in the bandgap in high doping concentration. The excitation spectrum of Y15mol%-doped samples monitored at 490 nm and 616 nm are shown in Fig. 3 and Fig. 4. It is found that the changes in the emission intensity with hydration around 265 nm excitation is larger in 490 nm than in 616 nm as is the case in the change with increasing Y concentration in Fig. 2. The intensities around 220-250 nm decrease in both 490 nm and 616 nm. These two characteristic changes may be due to the defect levels of oxygen vacancy and hydrogen, respectively.

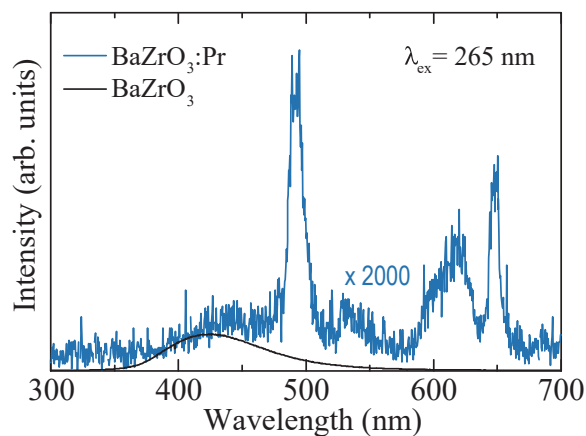


Fig. 1. Emission spectra of BaZrO<sub>3</sub>:Pr and BaZrO<sub>3</sub>. ( $\lambda_{\text{ex}} = 265 \text{ nm}$ ).

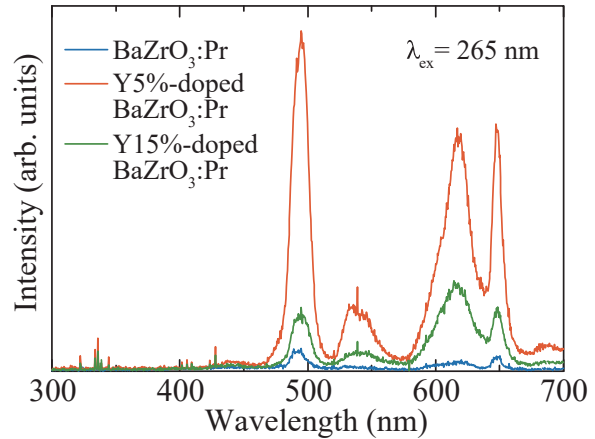


Fig. 2. Emission spectra of BaZrO<sub>3</sub>:Pr and Y-doped BaZrO<sub>3</sub>:Pr. ( $\lambda_{\text{ex}} = 265 \text{ nm}$ ).

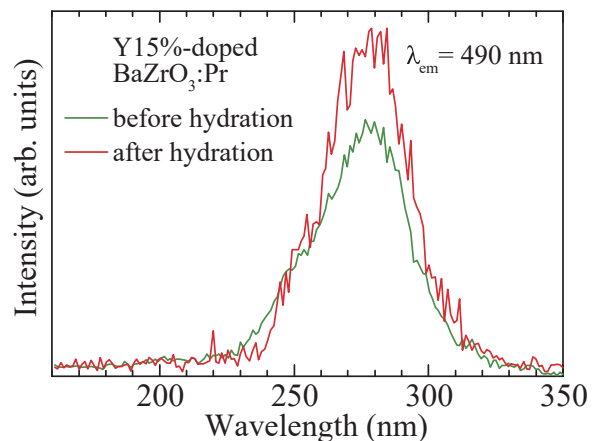


Fig. 3. Change in excitation spectra of Y-doped BaZrO<sub>3</sub>:Pr with hydration. ( $\lambda_{\text{em}} = 490 \text{ nm}$ ).

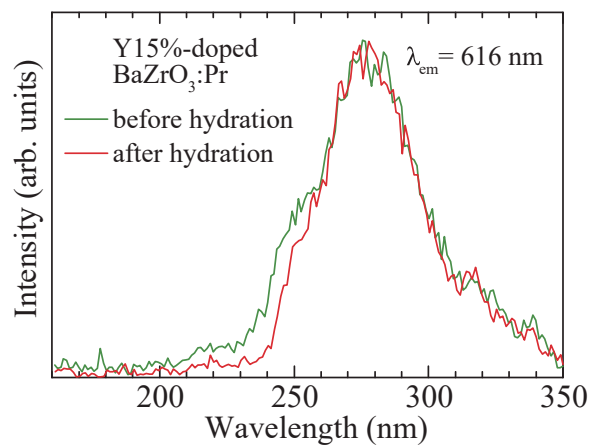


Fig. 4. Change in excitation spectra of Y-doped BaZrO<sub>3</sub>:Pr with hydration. ( $\lambda_{\text{em}} = 616 \text{ nm}$ ).

BL3B

## Temperature Dependence of Dielectric Function in Widegap Oxide Epilayer

T. Makino, T. Takeuchi and T. Asai

Department of Electrical and Electronics Engineering, University of Fukui, Fukui 910-8585, Japan

Oxide-based strongly electron correlated materials are important from both fundamental and applied perspectives, due to their potential in the optoelectronic and electronic devices.

A detailed understanding of the bulk and surface optical properties of these materials is essential in order to make the best selection. However, in spite of its significance, very little work has been done on the optical properties of oxide-based strongly electron correlated materials, especially in the case of rare-earth compounds [1].

$\epsilon\text{-Ga}_2\text{O}_3$  has various advantages as a wide band-gap semiconductor, and it is expected to be applied to power devices such as high frequency devices by taking advantage of this. In this way, it is essential for the detailed understanding of the bulk and surface optical properties of this material for the best choice. In recent years, its crystal symmetry has been identified; therefore little has been reported on the optical properties of  $\epsilon\text{-Ga}_2\text{O}_3$  at present. In this research, we aim to elucidate the interaction between electrons and phonons in  $\epsilon\text{-Ga}_2\text{O}_3$  and report on the temperature dependence of its dielectric function.

Figure 1 shows temperature dependence of the dielectric functions taken for  $\text{Ga}_2\text{O}_3$  thin film. Only the real part is shown. The situation in the case of double layer (thin films grown on substrates) becomes very complicated. In case of bulk crystals free from their substrates, the conversion is rather simple. Although both the transmissivity and reflectivity can be analytically represented by using Fresnel's effective coefficient method with dielectric functions and thickness of the thin film, the dielectric functions cannot be represented with transmissivity and reflectivity. In our case, some model dielectric functions were adopted for this purpose.

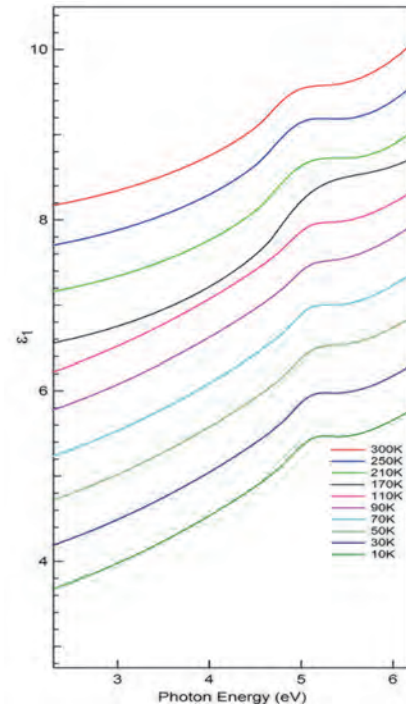


Fig. 1. Temperature dependence of real parts of dielectric function for  $\epsilon\text{-Ga}_2\text{O}_3$  thin film.

- [1] R. Roy, V. G. Hill, E. F. Osborn, *J. Am. Chem. Soc.* **74** (1952) 719.
- [2] H. Playford *et al.*, *Chem. Eur. J.* **19** (2013) 2803.
- [3] F. Mezzadri *et al.*, *Inorgan. Chem.* **55** (2016) 12079.
- [4] H. Nishinaka *et al.*, *Jpn. J. Appl. Phys.* **55** (2016) 1202BC.
- [5] T. Uchida *et al.*, *Appl. Phys. Express* **7** (2014) 021303.
- [6] J. C. Lu *et al.*, *J. Cryst. Growth* **299** (2007) 1.
- [7] Y. P. Varshni, *Physica (Utrecht)* **34** (1967) 149.
- [8] H. Qi *et al.*, *J. Quant. Spectros. Rad. Transfer* **112** (2011) 2507.
- [9] M. A. Ordal *et al.*, *Appl. Opt.* **22** (1983) 1099.

BL3B

## Appearance of the Luminescence Band due to $\text{Ag}^-$ Centers by VUV Irradiation at Room Temperature in Co-doped $\text{NaCl}:\text{I}^-,\text{Ag}^+$ Crystals

T. Kawai and O.Yagi

Graduate School of Science, Osaka Prefecture University, Sakai 599-8531, Japan

Since silver (Ag) atoms are normally present as cation impurities in ionic crystals,  $\text{Ag}^-$  centers are not naturally existed in alkali halide crystals. The  $\text{Ag}^-$  centers in alkali halides are created by the electrolytic coloration, additive coloration, and/or X- and  $\gamma$ -ray irradiation [1, 2]. In general, the  $\text{Ag}^-$  centers are not created by irradiation of light in the vacuum ultra violet (VUV) region. We found that the irradiation of a VUV light on co-doped  $\text{NaCl}:\text{I}^-,\text{Ag}^+$  crystals leads to the appearance of the A' luminescence due to the  $\text{Ag}^-$  centers through the experiment with the BL3B beam line.

Figure 1 shows the typical luminescence and absorption spectra of  $\text{NaCl}:\text{Ag}^-$  and  $\text{NaCl}:\text{I}^-,\text{Ag}^+$  crystals at room temperature (RT). The A' luminescence and the C absorption bands due to the  $\text{Ag}^-$  center in  $\text{NaCl}:\text{Ag}^-$  are observed at 2.81 and 4.46 eV, respectively. In co-doped  $\text{NaCl}:\text{I}^-,\text{Ag}^+$  crystals, the absorption and luminescence bands are observed at 6.78 and 5.02 eV, respectively. The absorption and luminescence bands due to the  $\text{I}^-$  center are located at the same energy positions as those due to the  $\text{Ag}^+$  center [2, 3]. Thus, the absorption and luminescence bands observed in the co-doped  $\text{NaCl}:\text{I}^-,\text{Ag}^+$  crystals consist of the sum of both bands due to respective impurity centers.

Figure 2 shows the appearance and enhancement of the A' luminescence band obtained under excitation at 4.5 eV by prolonged irradiation of 6.74 eV light at RT. The 6.74 eV light corresponds to the absorption bands due to the  $\text{I}^-$  and  $\text{Ag}^+$  centers. The enhancement of the A' luminescence intensity is plotted as a function of irradiation time of VUV light at 6.74 eV in the insert of Fig. 2.

The appearance and enhancement of the A' luminescence imply that the  $\text{Ag}^-$  centers are created by the irradiation of VUV light at 6.74 eV; that is to say, the conversion from the  $\text{Ag}^+$  to  $\text{Ag}^-$  ions occurs in NaCl host lattice at RT. When the VUV light corresponding to the absorption band due to the  $\text{Ag}^+$  centers is irradiated to single-doped  $\text{NaCl}:\text{Ag}^+$  crystals, the A' luminescence does not appear. Thus, the appearance of the A' luminescence in the co-doped  $\text{NaCl}:\text{I}^-,\text{Ag}^+$  crystals would be related with the existence of the  $\text{I}^-$  center band.

In our recent study [4], the photoexcitation on the  $\text{I}^-$  center band at RT induces the creation of the electrons and the  $\text{V}_\text{K}$  centers in NaCl host crystals. The electrons and the  $\text{V}_\text{K}$  centers migrate through the host lattice at RT and are trapped at impurity centers. Though the detailed mechanism is unknown, the electrons and the

$\text{V}_\text{K}$  centers created under photo-excitation at the  $\text{I}^-$  center would play an important role on the conversion from the  $\text{Ag}^+$  to  $\text{Ag}^-$  ions. Such valence change processes might lead to the potential for producing the uncommon anions such as  $\text{Au}^-$  and  $\text{Pt}^{2-}$ .

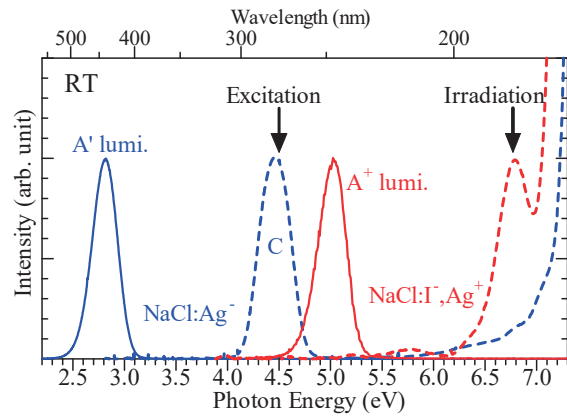


Fig. 1. Typical luminescence (solid curves) and absorption (broken curves) spectra of  $\text{NaCl}:\text{Ag}^-$  (blue) and  $\text{NaCl}:\text{I}^-,\text{Ag}^+$  (red) crystals at RT.

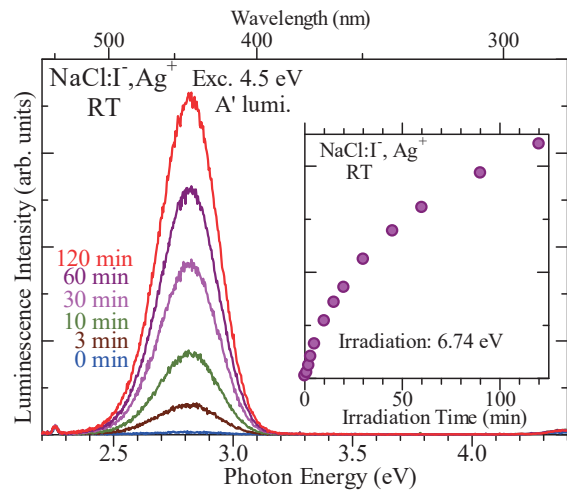


Fig. 2. Appearance and enhancement of the A' luminescence in  $\text{NaCl}:\text{I}^-,\text{Ag}^+$  by prolonged irradiation of 6.74 eV light at RT.

- [1] K. Kojima *et al.*, J. Phys. Soc. Jpn. **28** (1970) 1227.
- [2] T. Kawai *et al.*, Opt. Mater. **77** (2018) 30.
- [3] I. Akimoto *et al.*, Phys. Status Solidi C **6** (2009) 342.
- [4] T. Kawai and A. Iguchi, J. Lumin. **207** (2019) 58.

BL3B

## Optical Properties of Tl<sup>+</sup>-doped CsCaCl<sub>3</sub> Single Crystals

K. Kubota and T. Kawai

Graduate School of Science, Osaka Prefecture University, Sakai 599-8531, Japan

Though optical properties of alkali halide crystals doped with metal ions of  $ns^2$  electron configuration such as Tl<sup>+</sup>, In<sup>+</sup>, and Ag<sup>+</sup> have been studied for a long time, there have been few reports on the  $ns^2$  centers in other crystals [1]. In this study, we focused on Tl<sup>+</sup> centers in ternary compound CsCaCl<sub>3</sub>. The CsCaCl<sub>3</sub> crystals attract attention as a host crystal for scintillator materials and the optical properties of the CsCaCl<sub>3</sub> crystals doped with various kind of impurity ions have been investigated [2]. However, the optical properties of the CsCaCl<sub>3</sub> crystal doped with  $ns^2$  ions are considerably less studied. Thus, we have investigated the optical properties of the CsCaCl<sub>3</sub> crystals doped with the Tl<sup>+</sup> ions.

CsCaCl<sub>3</sub>:Tl<sup>+</sup> crystals were grown by the Bridgman method from CsCl, CaCl<sub>2</sub> and TlCl powders. The optical measurements were performed at various temperatures from 8 K to 300 K at the BL3B line of UVSOR.

The absorption spectrum of a CsCaCl<sub>3</sub>:Tl<sup>+</sup> crystal at 8 K is shown in Fig. 1. The A, B, and C absorption bands due to the Tl<sup>+</sup> ion were observed around 5.6, 6.7, and 7.1 eV, respectively. These absorption bands are attributed to the intra-ionic transitions from the ground <sup>1</sup>S<sub>0</sub> state to the excited <sup>3</sup>P<sub>1</sub>, <sup>3</sup>P<sub>2</sub>, and <sup>1</sup>P<sub>1</sub> states in the Tl<sup>+</sup> ion. The intensity ratio among the A, B, and C absorption bands in CsCaCl<sub>3</sub>:Tl<sup>+</sup> is similar to that of the Tl<sup>+</sup> centers in alkali halide crystals, while these energy positions are located at the higher energy region than that of the Tl<sup>+</sup> centers in alkali chloride crystals. The difference of the energy positions might come from that of the lattice arrangement around the Tl<sup>+</sup> ion between CsCaCl<sub>3</sub> and alkali halide crystals.

Figure 2 shows the temperature change of the A absorption band between 8 K and 300 K. As the temperature rises, the bandshape of the A absorption band broadens and the peak position shifts to the higher energy side up to around 150 K. On the other hand, above 150 K, the peak position shifts to the low energy side. The change of the shift of the peak energy would come from a slight change of the lattice arrangement related with the tetragonal to cubic phase transition in CsCaCl<sub>3</sub>.

Figure 3 shows the temperature dependence of the half-width of the A absorption band. The temperature dependence of the half-width can be fitted by the following theoretical formula considering the electron lattice interaction,

$$H(T) = H(0) \sqrt{\coth\left(\frac{hv}{2k_B T}\right)},$$

where  $H(0)$  and  $hv$  are the half-width at 0 K and the effective phonon energy, respectively. From the fitting result, the values of 0.17 eV and 29.7 meV were obtained as  $H(0)$  and  $hv$ , respectively.

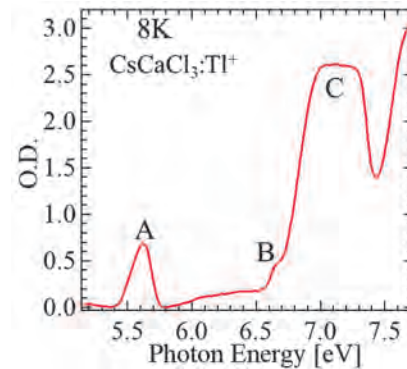


Fig. 1. Absorption spectrum of CsCaCl<sub>3</sub>:Tl<sup>+</sup> at 8 K.

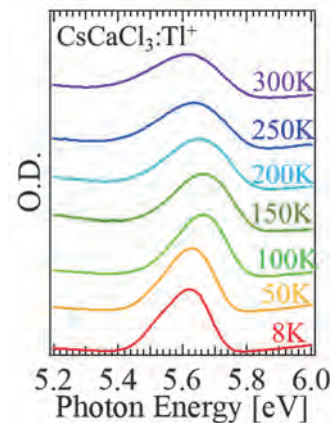


Fig. 2. Temperature change of the A absorption band in the CsCaCl<sub>3</sub> crystal at 8 K-300 K.

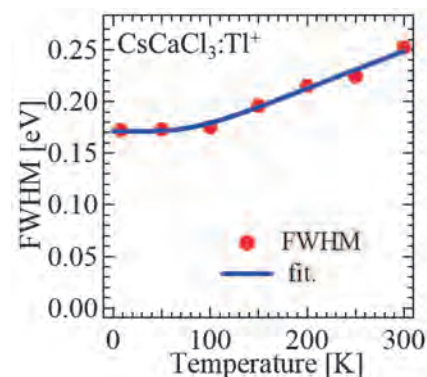


Fig. 3. Temperature dependence of the half-width of the A absorption band in the CsCaCl<sub>3</sub> crystal.

[1] A. Ranfagni *et al.*, *Advances in Physics* **32** (1983) 823.

[2] M. Tyagi *et al.*, *J. Appl. Phys.* **113** (2013) 203504.



BL3B

## UV-visible Spectroscopy of $\gamma$ -Si<sub>3</sub>N<sub>4</sub>

L. Museur<sup>1</sup>, E. Feldbach<sup>2</sup>, A. Zerr<sup>3</sup>, M. Kitaura<sup>4</sup> and A. Kanaev<sup>3</sup>

<sup>1</sup>Laboratoire de Physique des Lasers, CNRS, Université Paris 13, 93430 Villetaneuse, France

<sup>2</sup>Institute of Physics, University of Tartu, 1 W. Ostwald str., 50411, Tartu, Estonia

<sup>3</sup>Laboratoire des Sciences des Procédés et des Matériaux, CNRS, Université Paris 13, 93430 Villetaneuse, France

<sup>4</sup>Faculty of Science, Yamagata University, Yamagata 990-8560, Japan

Compounds having spinel structure have been predicted to exhibit a very high tolerance to irradiation with fast neutrons resulting in low swelling even at high doses [1]. In this connection, the understanding of their electronic band structure and defects induced by ionized radiation is of paramount importance for the development of novel optical materials stable in the environments of a fusion reactor. We performed the study of a polycrystalline  $\gamma$ -Si<sub>3</sub>N<sub>4</sub> with spinel structure by means of photoluminescence (PL) spectroscopy.

The sample of  $\gamma$ -Si<sub>3</sub>N<sub>4</sub> was synthesized according to the earlier reported procedure [2]. The starting powder of  $\alpha$ -Si<sub>3</sub>N<sub>4</sub> with oxygen content <2 wt.%, compacted into a Pt capsule, was compressed to 14 GPa and heated to 1700 °C for ~30 minutes. The sample irradiation with He-ions of total dose 10<sup>17</sup> cm<sup>-2</sup> was performed in the Ion Beam Lab of Helsinki University. The PL experiments were carried out at the BL3B beamline of UVSOR facility with synchrotron-radiation (SR) excitation in the UV-visible spectral range. The samples were mounted on a LHe flow-type cryostat, which permitted stabilizing the sample temperature in the range between 300 and 8K. The vacuum in the samples chamber was ~3·10<sup>-7</sup> Pa. The measured spectra were corrected for the detector sensitivity and optical line transmission.

The PL and PL-excitation (PLE) spectra of the pristine and irradiated  $\gamma$ -Si<sub>3</sub>N<sub>4</sub> are respectively shown in Fig. 1 and Fig. 2. According to Museur et al. [3], the dominant PL band in Fig. 1a excited with photons of energy above band gap  $E_g=5.05$  eV belongs (in Kröger-Vink notation) to  $X^*Si^X_{Si}$  exciton bound to neutral defects. No significant PL of excited metastable paramagnetic nitrogen anion radical at 450 nm was observed. The absence of the self-trapped exciton emission at 312 nm (4.0 eV) may be explained by a structural quenching. After He<sup>+</sup> irradiation and excitation with photons of energy  $h\nu \geq E_g$ , the PL strongly weakened and exhibited red shift indicating structural modifications; simultaneously, a new near-IR PL band appeared at ~700 nm. In contrast, no modification was observed for the PL spectra excited with  $h\nu < E_g$ . The PLE spectra of the bound exciton (Fig. 2) evidenced red shift after the He<sup>+</sup> irradiation. Moreover, interband transitions above 5.05 eV ( $\lambda < 250$  nm) did not appreciably contribute to PL and a new band with the maximum at 530 nm was intensified with the lower-energy excitation. Apparently, the

related radiation-induced structural defects have different origins. The excitonic origin may be proposed for the near-IR PL, which has no allowed sub-band gap transitions. The shifted visible PL band apparently belongs to modified structural defects  $Si^X_{Si}$ .

This work has been carried out within the framework of the EUROfusion Consortium and French Research Federation for Fusion Studies and has received funding from the Euratom research and training programme 2014–2018 under grant agreement No. 633053. The views and opinions expressed herein do not necessarily reflect those of the European Commission.

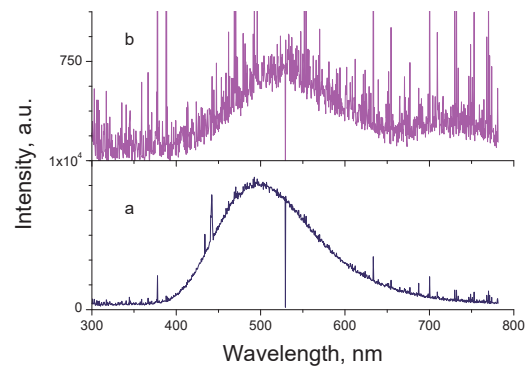


Fig. 1. PL spectra of fresh (a) and irradiated (b)  $\gamma$ -Si<sub>3</sub>N<sub>4</sub> excited at 230 nm.

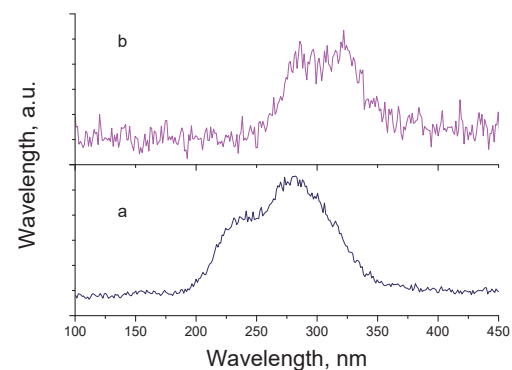


Fig. 2. Excitation spectra of PL at 500 nm of fresh (a) and irradiated (b)  $\gamma$ -Si<sub>3</sub>N<sub>4</sub>.

- [1] K. E. Sickafus *et al.*, *Science* **289** (2000) 748.
- [2] N. Nishiyama *et al.*, *Sci. Rep.* **7** (2017) 44755.
- [3] L. Museur *et al.*, *Sci. Rep.* **6** (2016) 18523.

BL3B

## UV-visible Spectroscopy of MgAl<sub>2</sub>O<sub>4</sub> Spinel Single Crystal

L. Museur<sup>1</sup>, E. Feldbach<sup>2</sup>, M. Kitaura<sup>3</sup> and A. Kanaev<sup>4</sup>

<sup>1</sup>Laboratoire de Physique des Lasers, CNRS, Université Paris 13, 93430 Villetaneuse, France

<sup>2</sup>Institute of Physics, University of Tartu, 1 W. Ostwald str., 50411, Tartu, Estonia

<sup>3</sup>Faculty of Science, Yamagata University, Yamagata 990-8560, Japan

<sup>4</sup>Laboratoire des Sciences des Procédés et des Matériaux, CNRS, Université Paris 13, 93430 Villetaneuse, France

Spinel or MgAl<sub>2</sub>O<sub>4</sub> is well known material, which electronic band and defect structures are not yet understood. In the same time, this material has a strong practical interest because of the predicted high tolerance to ionized radiation [1]. The knowledge of its electronic and optical properties in connection with radiation-induced defects will help to develop novel optical materials for extreme environments. In this study, we performed the spectroscopic analysis of MgAl<sub>2</sub>O<sub>4</sub> single crystals by means of energy resolved photoluminescence (PL) spectroscopy.

The experiments were carried out at the BL3B beamline [2] of UVSOR facility with synchrotron radiation (SR) excitation in the UV-visible spectral range. The samples were mounted on the cold finger of a LHe flow type cryostat, which permitted stabilizing the sample temperature in the range between 300 and 8K. The vacuum in the samples chamber was  $\sim 3 \cdot 10^{-7}$  Pa. In the complement to PL and PL-excitation (PLE) spectra, transmission and reflection spectra were recorded. The measured spectra were corrected on the detector sensitivity and optical line transmission. The single crystal (S1) from Alineason was (100) oriented and both sides polished of size 5x5x0.5 mm<sup>3</sup>. Another crystal (S2) with (100) oriented surface, was available from the Tartu group. The irradiation of the spinels with He<sup>+</sup> ions of total dose 10<sup>17</sup> cm<sup>-2</sup> was performed in the Accelerator Lab of Helsinki University.

The PL spectra of the pristine crystals S1 and S2 are quite similar. The most long-wavelength structured near-IR emission at  $\sim 700$  nm (1.8 eV) belongs to the well-known R-lines of Cr<sup>3+</sup> impurity. According to previous interpretations, the strongest PL band at 5.4 eV belongs to the recombination of conduction-band electrons with holes captured at the nearby oxygen ions (e/h), and bands at 3.8 eV and 3.0 eV were respectively assigned to F (two electrons trapped at an oxide-ion vacancy) and F<sup>+</sup> (one electron trapped at an oxide-ion vacancy) centers (see in [3]). The PLE spectra of different PL bands for pristine samples are shown in Fig. 1. All PL bands (except for that of Cr<sup>3+</sup> impurity) show up upon the band gap excitation, which energy  $E_g \approx 8.3$  eV can be suggested. The He<sup>+</sup> irradiation weakened PL and strongly modified PLE spectra of all bands, except for that of Cr<sup>3+</sup> impurity (Fig. 2). In particular, the interband transitions do not significantly contribute to these spectra and the intraband transitions shift to longer wavelengths. The common excitation band of e/h, F and F<sup>+</sup> emissions at

7.2 eV may be connected to antisite defects. The work is in progress to interpret radiation-induced damage of the spinel structure.

This work has been carried out within the framework of the EUROfusion Consortium and French Research Federation for Fusion Studies and has received funding from the Euratom research and training programme 2014–2018 under grant agreement No. 633053. The views and opinions expressed herein do not necessarily reflect those of the European Commission.

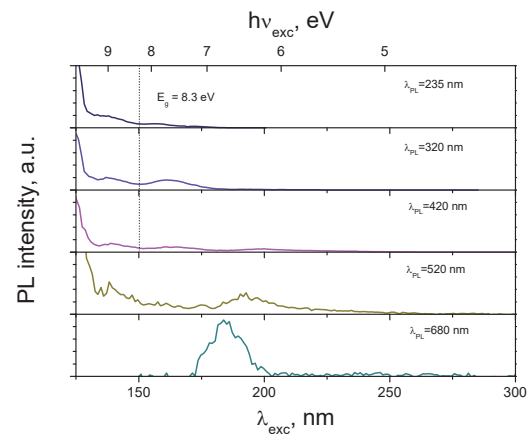


Fig. 1. PLE spectra of S1 crystal (T=8 K).

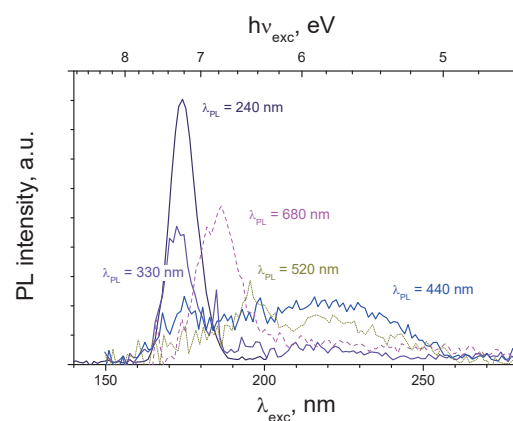


Fig. 2. PLE spectra of irradiated S2 crystal (T=8 K).

[1] K. E. Sickafus *et al.*, *Science* **289** (2000) 748.

[2] M. Kitaura *et al.*, *J. Lum.* **172** (2016) 243.

[3] A. Pille *et al.*, *Ceram. Int.* **45** (2019) 8305.

BL3B

## Construction of Vacuum Referred Binding Energy Diagram of YSiO<sub>2</sub>N Doped with Lanthanoid Ions for Persistent Luminescence

Y. Kitagawa, J. Ueda and S. Tanabe

Graduate School of Human and Environment Studies, Kyoto University, Kyoto 606-8501, Japan

Lanthanoid ions doped in inorganic materials form localized energy levels in the host bandgap. The relative positions of these levels play a very important role for the carrier trapping process of persistent luminescence. From the view point of developing novel persistent phosphors, it is necessary to investigate the electronic structure of  $Ln^{3+/2+}$ -doped compounds. Dorenbos proposed the method to construct the vacuum referred binding energy (VRBE) diagram of  $Ln^{3+/2+}$  in compounds based on spectroscopy [1,2]. In this work, the VRBE diagram of YSiO<sub>2</sub>N, which has characteristic Y<sup>3+</sup> sites coordinated by six oxide and two nitride ions [3], was constructed. Since Ce<sup>3+</sup> ions in oxynitrides show  $5d-4f$  luminescence with low energy because of the stronger nephelauxetic effect by N<sup>3-</sup> than O<sup>2-</sup> [4], oxynitrides activated with Ce<sup>3+</sup> have the potential to be a characteristic persistent phosphor with longer luminescent wavelength. To obtain some parameters for construction of the VRBE diagram, photoluminescence excitation (PLE) spectra of Ce<sup>3+</sup>- or Eu<sup>3+</sup>-doped YSiO<sub>2</sub>N samples were measured at UVSOR BL3B.

Figure 1 shows the PLE spectra of Ce<sup>3+</sup>- or Eu<sup>3+</sup>-doped YSiO<sub>2</sub>N samples. In both spectra, a small band was observed at around 210 nm. This band is assigned to the host exciton creation band. Considering the binding energy between an electron and a hole, the optical bandgap of YSiO<sub>2</sub>N was estimated to be 6.34 eV, which is smaller than that of pure oxide materials with the same Y/Si ratio. This is because for oxynitride compounds, energy of the valence band top increases due to N 2*p* orbitals. For the YSiO<sub>2</sub>N:Ce<sup>3+</sup> sample, several overlapped excitation bands, which are derived from the  $4f-5d$  transition of Ce<sup>3+</sup>, were observed at around 260 nm ( $4f-5d_{4,5}$ ) and around 360 nm ( $4f-5d_{1,2,3}$ ). In the case of the YSiO<sub>2</sub>N:Eu<sup>3+</sup> sample, another broad excitation band was observed in the range of 250-350 nm. This band is attributed to the charge transfer (CT) transition from the coordinating anions to Eu<sup>3+</sup> ions. Although for many Eu<sup>3+</sup>-activated oxides the CT band is located at around 250 nm, the CT band of the Eu<sup>3+</sup>-activated oxynitride sample has lower energy. Therefore, this band is due to the CT transition from not O<sup>2-</sup> but N<sup>3-</sup> to Eu<sup>3+</sup>.

Based on the measured spectroscopic data, the VRBE diagram of YSiO<sub>2</sub>N was constructed and shown in Fig. 2.  $E_C$  and  $E_V$  mean the bottom of the conduction band and the top of the valence band, respectively. The red and blue zigzag curves indicate the ground level of divalent and trivalent lanthanoid ions, respectively. Lanthanoid ions with energy levels below  $E_C$  have the potential to be an electron trap. For YSiO<sub>2</sub>N:Ce<sup>3+</sup>, Sm<sup>3+</sup>

and Tm<sup>3+</sup> is predicted to be the suitable co-dopant ions for persistent luminescence at room temperature because they have appropriate activation energy, the difference between  $E_C$  and levels of divalent lanthanoid ions.

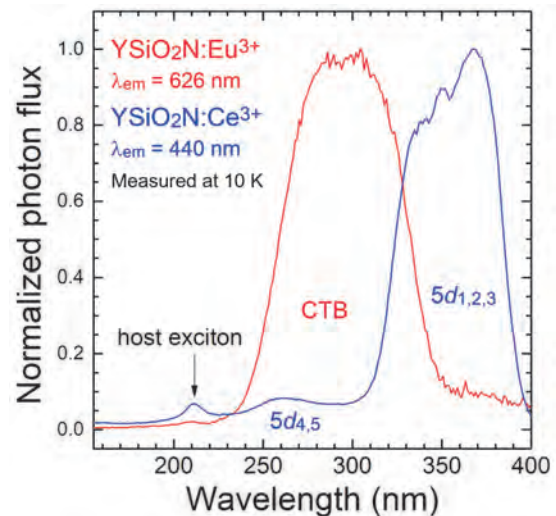


Fig. 1. PLE spectra of YSiO<sub>2</sub>N samples doped with  $Ln^{3+}$  ( $Ln = Ce$  or  $Eu$ ). Both spectra were measured at 10 K.

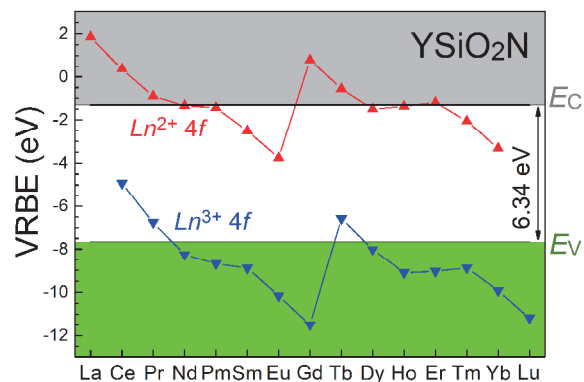


Fig. 2. The constructed VRBE diagram of YSiO<sub>2</sub>N.

- [1] P. Dorenbos, Phys. Rev. B **85** (2012) 1.
- [2] P. Dorenbos, J. Solid State Sci. Technol. **2** (2012) R3001.
- [3] L. Ouyang *et al.*, Phys. Rev. B **69** (2004) 094112.
- [4] J. W. H. van Krevel *et al.*, J. Alloys Compd. **268** (1998) 272.

BL4U

## STXM Study of Nanowire Cathode Materials for Li-Ion Batteries

D. Asakura<sup>1,2</sup>, K. Akada<sup>3</sup>, Y. Harada<sup>2,3,4</sup>, H. Yuzawa<sup>5</sup>, T. Ohigashi<sup>5</sup> and E. Hosono<sup>1,2</sup>

<sup>1</sup>Research Institute for Energy Conservation, National Institute of Advanced Industrial Science and Technology (AIST), Tsukuba 305-8568, Japan

<sup>2</sup>AIST-UTokyo Advanced Operando-Measurement Technology Open Innovation Laboratory (OPERANDO-OIL), AIST, Kashiwa 277-8565, Japan

<sup>3</sup>Institute for Solid State Physics, The University of Tokyo, Kashiwa 277-8581, Japan

<sup>4</sup>Synchrotron Radiation Research Organization, The University of Tokyo, Sayo 679-5148, Japan

<sup>5</sup>UVSOR Synchrotron Facility, Institute for Molecular Science, Okazaki 444-8585, Japan

Li-ion battery (LIB) is a key energy-storage device to realize a low-carbon society. Particularly, for electric vehicles, LIBs with high energy density and high power density are necessary. To develop such high-performance LIBs, improving the performances of the cathodes and designing novel cathode materials are inevitable.

Nanowire materials are promising to enhance the rate performance because of the short Li-diffusion path, which should contribute to the power density of LIB. For nanowire cathode materials, it is important to investigate how the Li diffusion proceeds in the nanowire and to visualize the distribution of electronic structure upon the charge/discharge. Thus, X-ray microscopy should be powerful to clarify those issues. In this study, we demonstrate *ex situ* scanning transmission X-ray microscopy (STXM) for LiMn<sub>2</sub>O<sub>4</sub> (LMO) nanowire.

The LMO nanowire made by our group [1] was mixed with carbon additive and a binder. The slurry was dropped on Au(5 nm)/Ti(5 nm)/Si<sub>3</sub>N<sub>4</sub>(150 nm) membrane window and dried. The thickness of the coated film was thin enough to transmit soft X-rays. This film as a working electrode was assembled as a three-electrode cell with Pt counter electrode, Ag/AgCl reference electrode and 1 M LiNO<sub>3</sub>/H<sub>2</sub>O electrolyte solution. Cyclic voltammetry experiments with a scan speed of 0.5 mV/s were performed before the soft X-ray measurements. The voltage range was set to 0.01 V (vs. Ag/AgCl) and 1.0 V. *Ex situ* Mn *L*<sub>2,3</sub>-edge X-ray absorption spectroscopy (XAS) and STXM were carried out for the initial and charged LMO samples at BL4U of UVSOR.

Figure 1(a) shows the Mn *L*<sub>2,3</sub>-edge XAS for the total area of the charged LMO nanowire. The profile is almost attributed to a Mn<sup>4+</sup> state according to a multiplet calculation. Figures 1(b-1) and 1(b-2) are the STXM images for the nanowire measured with the photon energies of A and B shown in Fig. 1(a). Figure 1(b-1) for which the Mn<sup>3+</sup> character is enhanced are not uniform compared to Fig. 1(b-2). A difference between the optical density image of Fig. 1(b-1) and that of Fig. 1(b-2) is displayed in Fig. 1(c), showing inhomogeneous distribution of Mn<sup>3+</sup> states remaining in the nanowire after partial and insufficient oxidation, which is hardly found by the XAS without imaging.

For the initial LMO, mixed Mn<sup>3+</sup> and Mn<sup>4+</sup> states were confirmed (not shown here). Thus, the utility of

STXM to nanostructured electrode materials for LIBs is extremely high. In the near future, we will develop an *operando* STXM measurement system to monitor charge distribution dynamics during charge-discharge reaction of LIBs.

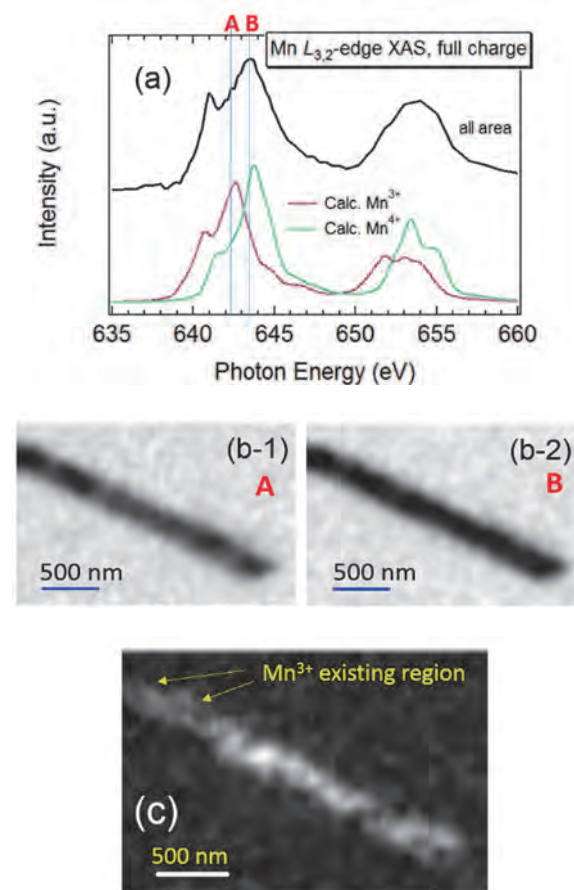


Fig. 1. (a) Mn *L*<sub>2,3</sub>-edge transmission XAS for the whole area of a nanowire. Charge-transfer multiplet calculations for Mn<sup>3+</sup> and Mn<sup>4+</sup> are also shown [2]. (b-1) and (b-2) STXM images for the photon energies A and B in panel (a). (c) Difference between the optical density of (b-2) and that of (b-1).

[1] E. Hosono *et al.*, Nano Lett. **9** (2009) 1045.

[2] E. Stavitski and F. M. F. de Groot, Micron **41** (2010) 687.



BL4U

## STXM Imaging of Water Surrounding Air Bubbles

Y. Harada<sup>1,2</sup>, T. Ohdaira<sup>1</sup>, K. Akada<sup>1</sup> and T. Ohgashi<sup>3</sup>

<sup>1</sup>*Institute for Solid State Physics, The University of Tokyo, Kashiwa 277-8581, Japan*

<sup>2</sup>*Synchrotron Radiation Research Organization, The University of Tokyo, Sayo 679-5148, Japan*

<sup>3</sup>*UVSOR Synchrotron Facility, Institute for Molecular Science, Okazaki 444-8585, Japan*

Hydrogen bond network of liquid water is spatiotemporally uniform on average, while the local and instantaneous coordination of individual water molecules is of course heterogeneous. Many discussions have been made on the nature of the microscopic heterogeneity. In the past 15 years we have studied liquid water using synchrotron soft X-rays aiming at an essential understanding of this heterogeneity and obtained a lot of experimental results which supported the existence of two characteristic moieties that constitute liquid water [1, 2].

When the subject is extended to solid-liquid, liquid-liquid and liquid-gas interfaces, we must consider a connection between the bulk water having heterogeneous hydrogen bond network and water at the solid-liquid, liquid-liquid and liquid-gas interfaces which we simply refer to as interfacial water [3]. In the case of micro/nano bubbles liquid-gas interface is formed, and the presence of interfacial water surrounding the micro/nano bubbles can be considered. However, the thickness and hydrogen bond network of the interfacial water has yet to be systematically explored. Moreover, the electrostatic charge around micro/nano bubbles and their stabilization mechanism are still under debate [4]. In this work, we performed chemical state imaging of water surrounding micro/nano bubbles using O K-edge X-ray absorption spectroscopy to elucidate the electronic state and network structure of water molecules forming the micro/nano bubbles by taking advantage of the experience cultivated in the analysis of bulk water.

Water sample filled up with plus charged nano bubbles with the maximum  $\zeta$ -potential of +23 mV, the averaged diameter of 180 nm and the number density around  $1 \times 10^8$  particles/ml were prepared, all estimated by using a ZetaView Particle Tracking Analyzer. A drop of the micro/nano bubble water was sandwiched in between two 150 nm-thick SiN membranes. During the limited beamtime we could find only micrometer sized bubbles due to better possibility to find them than 100 nm order nano bubbles. Prior to the O K-edge imaging we obtained N K-edge image to confirm that the particle is indeed an air bubble that has stronger N K-edge absorption inside than outside.

Figure 1 shows O K-edge STXM image of a micro bubble obtained at (a) 532.04 eV and (b) 536.44 eV excitations, respectively. At 532.04 eV, enhancement of the signal inside the micro bubble occurred by the resonance to the  $\pi^*$  state of an O<sub>2</sub> gas (around 1 eV

above the typical absorption peak). At 536.44 eV excitation which is close to the pre-edge resonance of liquid water (around 1.5 eV above the typical absorption peak), we found surrounding water has specific chemical state in a micrometer region from the bubble surface compared to the bulk region far from the bubble. The origin of the appearance of different chemical state of water is yet unknown. A possible explanation is that water in this region is under the electric dipole layer around the bubble and influenced by the interaction with the dipole moment of a water molecule, although the thickness of the dipole layer could be the micrometer size only in an ultrapure water, which is not expected in the present experimental protocol. An additional bright region was found in Fig. 1(b) indicated by the black arrow. This sphere was not observed in Fig. 1(a) and we believe this is due to radiation induced damage of the bubble interacting with both sides of the SiN membranes. In the near future we need to trace the cause of the occurrence of the additional structure and realize the imaging of real nanobubbles.

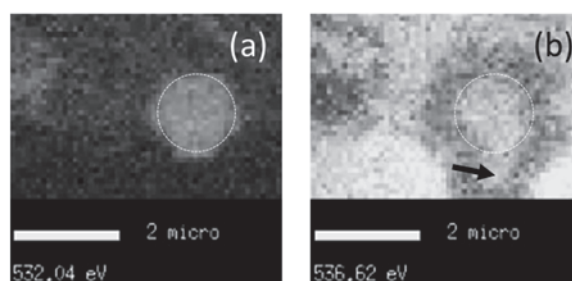


Fig. 1. O K-edge transmission XAS images of a microbubble obtained (a) at 532.04 eV excitation (around 1 eV above the  $\pi^*$  state of typical O<sub>2</sub> gas) and (b) at 536.62 eV excitation (around 1.5 eV above the pre-edge resonance of typical liquid water).

[1] T. Tokushima *et al.*, Chem. Phys. Lett. **460** (2008) 387.

[2] A. Nilsson and L. G. M. Pettersson, Nat. Commun. **6** (2015) 8998.

[3] K. Yamazoe *et al.*, Langmuir **33** (2017) 3954.

[4] M. Alheshibri, J. Qian, M. Jehannin, and V. S. J. Craig, Langmuir **32** (2016) 11086.

BL4U

## STXM Studies on Vapor-assisted Quasi-2D Perovskite Solar Cells

H. W. Shiu<sup>1</sup>, M. S. Li<sup>2</sup>, L. C. Yu<sup>1</sup>, Y. L. Lai<sup>1</sup>, T. Ohigashi<sup>3</sup>, N. Kosugi<sup>3</sup>, P. Chen<sup>2</sup> and Y. J. Hsu<sup>1</sup>

<sup>1</sup>National Synchrotron Radiation Research Center, Hsinchu 300, Taiwan

<sup>2</sup>Department of Photonics, National Cheng Kung University 701, Tainan, Taiwan

<sup>3</sup>Institute for Molecular Science, Okazaki 444-8585, Japan

Organic hybrid perovskite is one of the most attractive emerging photovoltaic devices due to its high optical absorption coefficient, long carrier diffusion lengths and low manufacturing costs. Although the power conversion efficiency (PCE) of 3D perovskite has been reported to reach a high record of 23 % for a small area device [1], how to improve the stability of organic hybrid perovskite in high humid condition is an important issue. Recent study indicated that a hybrid structured low dimensional perovskites formed by replacing the cation with large planar organic cation exhibits much more resistant to humidity than the 3D perovskite devices.

In order to investigate the device performance and electronic properties, we synthesized a bunch of dimensional tunable quasi-2D perovskite by mixing stoichiometric quantities of lead iodide ( $\text{PbI}_2$ ) and PEAI ( $\text{C}_8\text{H}_9\text{NH}_3$ ) to yield a series of compounds with different PEAI/ $\text{PbI}_2$  ratio on mp- $\text{TiO}_2/\text{SiN}$  substrate. With further treatment of vapor-assisted MAI ( $\text{CH}_3\text{NH}_3\text{I}$ ), a series of compact crystalline layer of  $(\text{PEA})_2(\text{MA})_{n-1}\text{Pb}_n\text{I}_{3n+1}$  were formed. As a results, a remarkable PCE of 19.1% has been successfully achieved with PEAI/ $\text{PbI}_2 = 0.05$  ( $n = 40$ ) which showed better performance than the pristine 3D perovskite of  $\text{MAPbI}_3$  (PCE = 17.31%) [2]. However, at high PEAI/ $\text{PbI}_2$  ratio, for example PEAI/ $\text{PbI}_2 = 1$  or 2, poor PCE of 5.85% and 0.02 % were observed. Besides, the SEM and KPFM results suggest that the grain size and surface potential of PEAI modified perovskite play an important role for the photovoltaic performance. In order to understand the quasi-2D materials in a microscopic point of view, we systematically studied the layer number dependent behavior of  $(\text{PEA})_2(\text{MA})_{n-1}\text{Pb}_n\text{I}_{3n+1}$  perovskite by scanning transmission X-ray microscopy (STXM) and Near-edge X-ray absorption fine structure (NEXAFS).

Two different substrates with low and regular mp- $\text{TiO}_2$  concentration were prepared for study the interplay between PEAI modified-perovskite and mp- $\text{TiO}_2$ . Herein, we mainly focus on the high PEAI/ $\text{PbI}_2$  ratio perovskite on regular substrate to understand the correlation between PEAI and the  $\text{MAPbI}_3$ . Figure 1 shows the STXM carbon map of (a) PEAI/ $\text{PbI}_2 = 2$  ( $n = 1$ ) without MAI treatment and (b) PEAI/ $\text{PbI}_2 = 1$  ( $n = 2$ ) with MAI treatment. Only weak contrasts were observed in Fig. 1 (a), however there is no chemical difference between dark and bright regions after detail examined by NEXAFS (not show here). The results implied that for high PEAI/ $\text{PbI}_2$  ratio, the hybrid perovskite performed morphologically and chemically uniform.

Figure 2 shows STXM carbon map and the corresponding micro-spectroscopy of PEAI/ $\text{PbI}_2 = 2$  ( $n = 1$ ) extracted from 3D images after MAI treatment.

Compare with the result without MAI treatment (Fig.1 (a)), clear bubble like structures with nearly  $5 \mu\text{m}$  size domain were observed. For pure  $(\text{PEA})_2\text{PbI}_4$  ( $n = 1$ ), the characteristic carbon signal is  $\text{C}=\text{C} \pi^*$  resonance at 285 eV, in contrast with pure  $\text{MAPbI}_3$  ( $n = \infty$ ), the characteristic signal is  $\text{C}-\text{H}$  and  $\text{C}-\text{N} \sigma^*$  resonance at 288.5 and 290 eV. As shown in Fig. 2 (b), the shape of red and blue spectrum is similar, however the ratio of  $\text{C}=\text{C} \pi^*$  to  $\text{C}-\text{N} \sigma^*$  resonance exhibits opposite behavior between which indicated the phase separation behavior is presented in PEAI/ $\text{PbI}_2$  mixtures. It is another evidence for the formation of multiphase quasi-2D perovskite with  $n = 1, 2, 3$  and else.

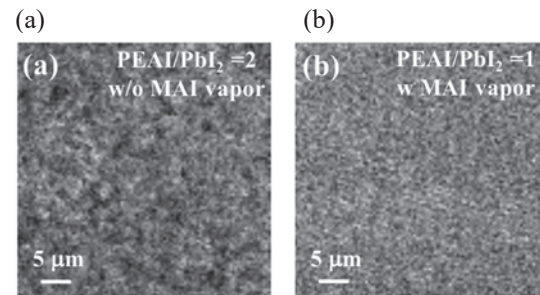


Fig. 1. STXM carbon map of (a) PEAI/ $\text{PbI}_2 = 2$  without MAI vapor treatment and (b) PEAI/ $\text{PbI}_2 = 1$  with MAI vapor treatment on mp- $\text{TiO}_2/\text{SiN}$  substrate. The mapping are obtained by the imaging subtraction between 285 eV and the pre-edge.

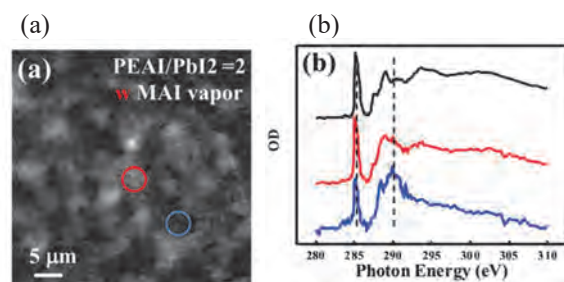


Fig. 2. (a) STXM carbon map of PEAI/ $\text{PbI}_2 = 2$  with MAI vapor treatment and (b) the corresponding micro-spectroscopy before (dark line) and after (red and blue line) MAI treatment.

[1] Y. Rong, Y. Hu, A. Mei, H. Tan, M. I. Saidaminov, S. Seok, M. D. McGehee, E. H. Sargent and H. Han, *Science* **361** (2018) eaat8235.

[2] M.-H. Li, H.-H. Yeh, Y.-H. Chiang, U.-S. Jeng, C.-J. Su, H.-W. Shiu, Y.-J. Hsu, N. Kosugi, T. Ohigashi, Y.-A. Chen, P.-S. Shen, P. Chen and T.-F. Guo, *Adv. Mater.* **30** (2018) 1801401.

BL4U

## In Depth Qualitative Structural Analysis of Nanocellulose Hybrid Materials

M.Y. Ismail<sup>1</sup>, M. Huttula<sup>2</sup>, M. Patanen<sup>2</sup>, H. Liimatainen<sup>1</sup>, T. Ohigashi<sup>3</sup>, H. Yuzawa<sup>3</sup> and N. Kosugi<sup>3</sup>

<sup>1</sup>Fibre and Particle engineering unit, University of Oulu, P.O. Box 3000, 90014 University of Oulu, Finland

<sup>2</sup>Nano and Molecular Systems unit, University of Oulu, P.O. Box 3000, 90014 University of Oulu, Finland

<sup>3</sup>UVSOR Synchrotron Facility, Institute for Molecular Science, Okazaki 444-8585, Japan

Hybrid materials are high strength and modulus materials that consist of an organic-inorganic blend. We have fabricated such kind of hybrid films using cellulose nanofibrils (CNF) and nanosilica (5 - 30% wt) embedded in a chitosan (Chi) biopolymer matrix using a slow evaporation method, and characterized various mechanical, chemical and structural aspects of these films [1]. The combination of these constituents can result in a sustainable packaging material with tailored characteristics such as microbial resistance with the help of chitosan, high strength and stiffness and biodegradability and with the aid of CNF and nanosilica. The inorganic filler plays a major role in the mechanical, thermal and UV absorption properties. The interaction between the constituents is a key factor in affecting the hybrid's properties.

Microscale structural properties of hybrids are commonly investigated using field emission scanning electron microscopy (FESEM) and transmission electron microscopy. However, those techniques do not give the chemical distribution of the structure. Therefore, synchrotron radiation techniques are needed in order to complement the FESEM imaging. Scanning Transmission soft X-ray Microscopy (STXM) was used to investigate the spatial distribution of the chemical components of the studied hybrids, verifying the agglomerates of silica in the hybrid.

The STXM experiment was carried out at BL4U beamline at UVSOR. The imaging was performed at energies spanning over the C K-edge (280 and 320 eV) and Si L<sub>2,3</sub>-edge (100 to 130 eV). The samples were "sandwiched" between resin blocks for ultramicrotome sectioning, a reference spectrum of resin was collected to ensure that the main material between the resin has not been affected by the embedding. The reference X-ray absorption spectra (XAS) at C K-edge of pure cellulose nanofibers and chitosan were recorded and matched with previous references [2].

Figure 1 shows examples of the obtained results for 10 wt% nanosilica hybrid film. Upper panels show examples how the spectral information of STXM can be used to differentiate the silica-rich regions from the CNF-chitosan film. The RGB images have been constructed using a "stack fit" procedure of aXis2000 software [3]. In short, the XAS (shown in Figs. 1 b & d) of indicated regions (shown with circles in Figs. 1 a & c) are extracted and they are fitted to each pixel of the image. The final color of a pixel depends on the weight of each RGB component spectra in that specific pixel. In Fig. 1 b, the red XAS is a resin spectrum, extracted

from right lower corner of Fig. 1 a. The blue XAS resembles both cellulose and chitosan spectra. Green shows strong XAS with cellulose-type features. At Si L<sub>2,3</sub>-edge (Figs. 1 c & d), the regions in red show a typical XAS for SiO<sub>2</sub> [4], whereas blue and green regions do not exhibit as strong resonance behavior. The optical density images are shown in the lower panels (Figs. 1 e and f) and corresponding average C K-edge XAS of the whole imaged region is shown in Fig. 1 g. Figures 1 e and f represent the sum stacks below the C K-edge (280-284 eV) and on the top of the C K-edge (288.2-300 eV). Figure 1 e shows strongly absorbing white band and spots, which effectively disappear on the top of the C K-edge resonance region (Fig. 1 f). Instead, thin (width <150 nm) lines are clearly highlighted. This indicates that the white regions below the C K-edge are SiO<sub>2</sub> agglomerates, whereas the thinner stripes showing up at the C K-edge are bundles of nanocellulose fibers aligned with the direction of cutting or wrinkles in the CNF-chitosan film.

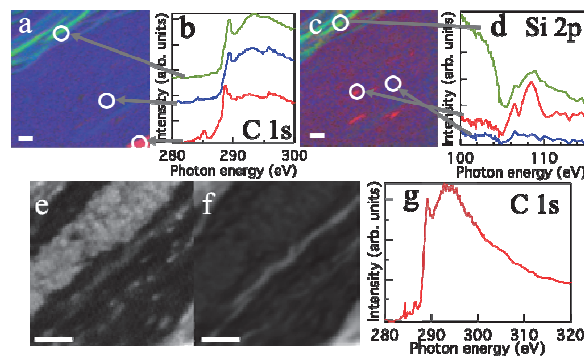


Fig. 1. Upper panels: RGB maps at a) C K-edge with b) corresponding XAS of indicated regions, and c) at Si L<sub>2,3</sub>-edge with d) XAS of indicated regions. Lower panels: Optical density images e) below and f) on the top of the C K-edge, and g) the average XAS showing the energy regions used to construct images e and f (grey shadowed areas). Scale bar 1  $\mu\text{m}$ .

[1] M. Y. Ismail *et al.*, submitted to Carbohydrate Polymers.

[2] C. Karunakaran *et al.*, PLOS ONE **10** (2015) e0122959.

[3] <http://unicorn.mcmaster.ca/aXis2000.html>

[4] D. Li *et al.*, Am. Miner. **70** (1994) 622.



BL4U

## Chemical and Spatial Identification for Gas-Dependent Nanobubbles Sandwiched in Graphene Liquid Cells

C. H. Chuang<sup>1</sup>, W. H. Hsu<sup>2</sup>, I. S. Huang<sup>2</sup>, W. F. Pong<sup>1</sup>, T. Ohigashi<sup>3</sup> and N. Kosugi<sup>3</sup>

<sup>1</sup>Department of Physics, Tamkang University, Tamsui 251, Taiwan

<sup>2</sup>Institute of Physics, Academia Sinica, Taipei 115, Taiwan

<sup>3</sup>UVSOR Synchrotron Facility, Institute for Molecular Science, Okazaki 444-8585, Japan

Since 2004, graphene retains the crown among the most studied two-dimensional materials for numerous applications, not only due to the promising electric and thermal conductivity but also due to the true two-dimensionality of single layer graphene. The idea of replacing Si<sub>3</sub>N<sub>4</sub> window by graphene in liquid cells is under development, which will provide in-situ conditions and real-time control [1]. X-ray source used in scanning transmission X-ray microscopy (STXM) can provide the X-ray absorption spectrum with the element-specific determination and chemical bonding information, even at the nanoscale resolution. Using the combined ability of X-ray spectral feature in STXM microscopes, in-situ detection is achieved in various investigation [2]. Although the use of graphene sheet as ultra-thin window has been proposed due to physical enhancement, it is rarely seen in the utilization in STXM owing to the limited knowledge in the solid-liquid interface and electrochemical ability. In the energy materials research, the catalytic activity on the external surface and active site is of prime importance which will provide space-resolved information.

In this work, we observed structure formed by gas molecules within the confinement of few-layers graphene sheets by STXM experiment which was carried out at the BL4U. The left inset in Fig. 1(a) shows the C 1s mapping image of graphene by STXM which reveal an elliptical dark-shade region at the center, corresponding to gas-formed structure surrounded by multi-layer graphene. The transmission image through a variety of piece of graphene sheet demonstrates the variation in mapping intensity. The absorption intensity inside the elliptical shape at the center area is much higher than the signal of the graphene sheets, which is the characteristic of the cross-section absorption of gas region and was also identified as the gas-formed structure area by transmission electron microscopy (TEM) experiments prior to this experiment. Individual x-ray absorption spectrum (XAS) at the carbon near edge corresponding to the selected area are shown in Fig. 1(a). The C1s spectra collected from outside of the gas-formed structure exhibit a flat anisotropy of graphene layer, while it is strongly based on the incident polarization of X-ray beam and its directional dipole-transition selection rule. The inside area of elliptical gas-formed structure is divided into three areas and features owing to the spectral features around photon energy 284 ~ 287 eV. It is indicative of the interface bonding coordination and gas-filled contribution, and also the relative ratios of  $\pi^*/\sigma^*$  state at 285.5 and 291.7

eV are one of the spectral evidence as for the position dependence [3].

Figure 1(b) displays the N1s mapping image and relative XAS. At the corresponding area as Fig. 1(a), the graphene region outside the gas-formed structure has the low edge jump at the N K-edge absorption due to the unnoticed nitrogen content owing to the large-area signal integration. Relatively, the intensity of N K-edge absorption is verified for the higher absorption in the gas-formed region. The features at 398.9 and 400.5 eV are mostly assigned to pyridinic/pyrrolic N-related groups and  $-C \equiv N$  triplet state [3]. Both the features reflect the evidence of nitrogen bonding configuration inside the structure, different from the outside surface absorption. Thus, our STXM result for graphene materials and its application show the interior phase of gas as for the combination and absorption. It provides valuable insights into the possible mechanism of gas absorption at the graphene interface as well as the observation of gas-condensed phase at solid-liquid interface [4].

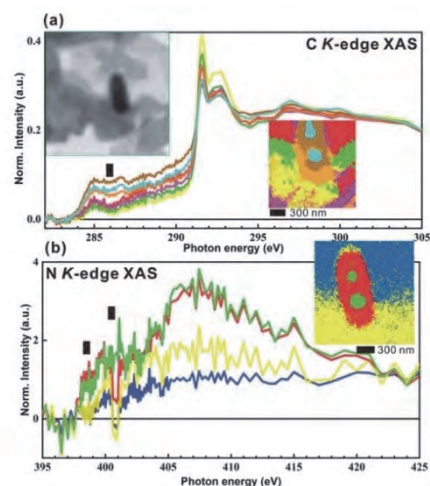


Fig. 1. (a) Individual XAS at carbon K-edge, selected from the STXM mapping image (inset). (b) XAS at N k-edge obtained from STXM mapping image (inset).

[1] S. Nemsak *et al.*, *J. Am. Chem. Soc.* **139** (2017) 18138.

[2] T. Ohigashi *et al.*, *AIP Conference Proceedings* **1741** (2016) 050002.

[3] C. H. Chuang *et al.*, *Scientific Report* **7** (2017) 42235.

[4] C.-K. Fang *et al.*, *Scientific Reports* **6** (2016) 24651.



BL4U

## Effect of Defect on Perovskite Hydroxide for Oxygen Evolution Reaction

Y. R. Lu<sup>1</sup>, C. H. Chuang<sup>1</sup>, C. L. Dong<sup>1</sup>, W. F. Pong<sup>1</sup>, T. Ohgashi<sup>2</sup>, N. Kosugi<sup>2</sup>,  
Y.-S. Liu<sup>3</sup> and J. Guo<sup>3</sup>

<sup>1</sup>Department of Physics, Tamkang University, Tamsui 251, Taiwan

<sup>2</sup>UVSOR Synchrotron Facility, Institute for Molecular Science, Okazaki 444-8585, Japan

<sup>3</sup>Advanced Light Source, Lawrence Berkeley National Laboratory, Berkeley, CA 94720

Perovskite-based materials have been largely investigated for using as promising electrocatalysts for oxygen evolution reaction. Control of oxygen vacancies can modulate the electronic structure of perovskite and is beneficial for enhancing OER activity [1]. To further promote the oxygen evolution reaction performance, metal cation vacancies are proposed in addition to oxygen vacancies [2]. However, it is challenging to create the cation vacancies in perovskites owing to the fact that the formation energy of metal cation vacancies are too high. Herein, SnCoFe perovskite hydroxide was prepared by a simple coprecipitation, and then treated with Ar plasma to obtain the defective SnCoFe-Ar. An advanced SnCoFe hydroxide for efficient oxygen evolution reaction is developed recently [3]. The electrochemical properties and the x-ray absorption spectroscopic studies have revealed the correlation between the defective structures and the catalytic activities. Yet, the details of these defective structures are not fully understood. In this study, the SnCoFe perovskite hydroxide and that treated with Ar have been investigated by scanning transmission X-ray microscopy (STXM) which provides regional atomic/electronic structure information.

Figures 1(a) and (b) present the Fe L-edge STXM images and its stack mappings of selected region of SnFeCo and SnFeCo-Ar perovskite hydroxides. The stack mappings display red, yellow, and green areas, corresponding to the different areas which are associated with various thickness and the different electronic structures are revealed for these two samples. The spectral variations between SnFeCo and SnFeCo-Ar suggest there are more defective site formed after Ar treatment, and the chemical states of Fe are quite different in the exterior and interior region in the sample. Similarly, Figs 1(c) and (d) show the Co L-edge STXM. Interestingly, the Co is distributed more homogeneously in SnFeCo-Ar than in the one without Ar treatment. This suggest the Ar treatment has greater effect on the Co site in SnFeCo.

Further O K-edge and Sn M-edge will be performed in order to reveal the correlation between the OER activity and the defective structures in these perovskite hydroxides.

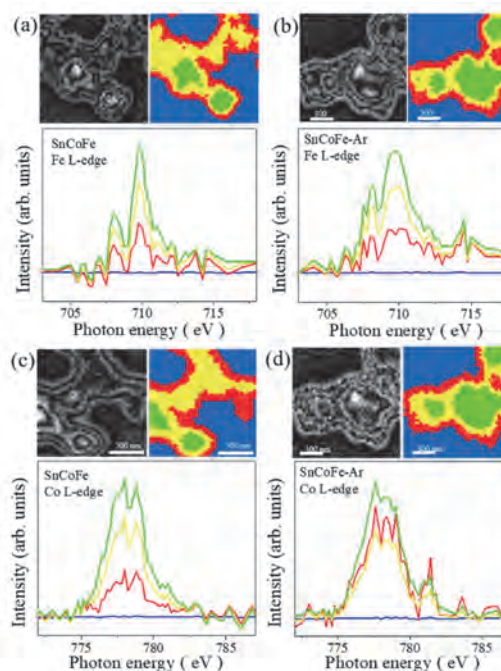


Fig. 1. Fe L-edge ((a) and (b)) and Co L-edge ((c) and (d)) scanning transmission X-ray microscopy image and its corresponding stack mappings of selected region of SnFeCo and SnFeCo-Ar.

- [1] J. A. Koza *et al.*, Chem. Mater. **24** (2012) 3567.  
[2] C. Yang *et al.*, J. Phys. Chem. Lett. **8** (2017) 3466.  
[3] D. Chen *et al.*, Angew. Chem. Int. Ed. **57** (2018) 8691.

BL4U

## Characterization of Two-phase Network Structure of Sulfur Cross-linked Isoprene Rubber

K. Miyaji<sup>1</sup>, T. Nakajima<sup>1</sup>, Y. Sakaki<sup>1</sup>, J. Preeyanuch<sup>2</sup> and Y. Ikeda<sup>3</sup>

<sup>1</sup>Graduate School of Science and Technology, Kyoto Institute of Technology, Kyoto 606-8585, Japan

<sup>2</sup>Research Strategy Promotion Center, Kyoto Institute of Technology, Kyoto 606-8585, Japan.

<sup>3</sup>Faculty of Molecular Chemistry and Engineering, Kyoto Institute of Technology, Kyoto 606-8585, Japan

The cross-linking reaction to form a three-dimensional network structure in rubber is necessary to give a good rubber elasticity for rubber products. Among the conventional cross-linking reactions, a sulfur cross-linking (vulcanization) is the most important cross-linking reaction which has been widely used in rubber industries. However, the rubber network formations are generally very complicate. The controls of network structures are not easy because many cross-linking reactions proceed heterogeneously, depending on various factors such as cross-linking reagents, fillers, processing methods, and so on. Because the network structures of rubber materials significantly influence their mechanical properties, the evaluation of the rubber network structures is an important for development of rubber science and technology. In 2009, our research group found the two-phase network structure of sulfur cross-linked isoprene rubber composed of network domain and mesh network using small-angle neutron scattering. The network domains with high network-chain densities embedded in mesh network was proposed. [1] This specific morphology was found to be controlled by changing the amount of cross-linking reagents. There are several analytical methods to investigate the morphology of rubber vulcanizates. Scanning transmission X-ray microscopy (STXM) is one of methods which provides chemical mapping in nanometer scales. Also, both spatial and compositional chemical information are provided at the same time. In this study, STXM was used to confirm the two-phase network morphology of isoprene rubber vulcanizate in terms of the distribution of sulfur, and an existence of network domain in the isoprene rubber vulcanizates was confirmed.

The rubber compound was prepared by conventional mixing at room temperature on a two-roll mill with a water cooling system; isoprene rubber was mixed with zinc oxide, *N*-(1,3-benzothiazol-2-ylsulfanyl)cyclohexanamine (CBS), and sulfur. Rubber vulcanizate was prepared by conventional pressing method. This rubber vulcanizate was extracted by tetrahydrofuran (THF) to remove the unreacted sulfur. The vulcanized rubber sheet after THF extraction was cut by an ultra-microtome to prepare a smooth and flat surface with a thickness of approximately 100 nm for STXM measurement.

Figure 1 shows the STXM image of the vulcanized isoprene rubber at 165.4 eV. The bright and dark regions

indicate the strong and weak absorptions by sulfur, respectively. Thus, the brighter regions shown in Fig. 1 are possibly the clusters of sulfur in the vulcanized isoprene rubber. As predicted by the SANS results, the network domains were formed by the absorption of sulfur and the accelerator, CBS on the ZnO clusters, and followed by sulfur cross-linking on the surface of ZnO clusters [1].

This STXM image successfully confirmed the inhomogeneous two-phase network morphology in the vulcanized isoprene rubber from the view point of sulfur distribution. The localized sulfur cluster is one of the evidences for the network domain formation.

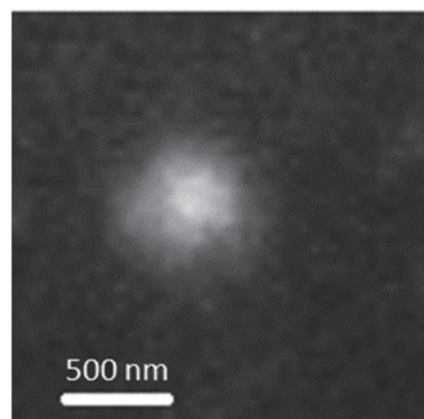


Fig. 1. STXM image of the vulcanized isoprene rubber at 164.5eV.

[1] Y. Ikeda *et. al.*, *Macromolecules* **42** (2009) 2741.

BL4B

## Chemical State Investigation of Nitrogen in Nitrided Steels by Soft X-ray Absorption Spectroscopy

M. Sato and S-W. Young

*Institute for Materials Research, Tohoku University, Sendai 980-8522 Japan*

Machinery structural materials such as gears, shafts and molds are required to have high surface hardness and high toughness because of the severe friction and/or abrasion at the surface.

Nitriding is a surface hardening technique widely used industrially and flows nitrogen from the surface and combining with strong nitride forming elements (for example, Al, Cr, V, Ti, etc.) contained in steel to precipitate clusters and alloy nitrides at near the surface. Compared to other surface hardening methods such as carburizing and shot peening, the nitriding has advantages of less strain because it does not involve phase transformation and deformation during treatment [1, 2]. Therefore, the importance of nitriding process is increasing in recent high-precision materials. In the nitriding treatment, a sufficient amount of nitrogen flows in the vicinity of the surface to precipitate the alloy nitride at the initial stage of nitriding, whereas precipitation is delayed at the inside of the sample because it takes long time for the nitrogen diffusion. As a result, the concentration gradient of nitrogen is formed in a sample.

In this research, we aimed to investigate whether such gradient change of nitrogen can be captured by XAFS method. Since this measurement is our first beam time at BL4B, it is also an important object to acquire how to use the devices and to obtain the correct data.

A sample with a nitrogen concentration gradient from the surface to the inside was prepared by plasma nitriding treatment at 550 °C for 16 hours using the Fe-0.5V-1.5Al alloy. In addition, nitrogen martensite steel including 0.3, 0.5 and 2 mass% N prepared by nitriding and quenching (N-Q) treatment using the pure iron, and the  $\gamma'$ -Fe<sub>4</sub>N and the BN powder were used as reference materials.

XAFS measurement was carried out at the beam line BL4B, and the N-K edge (380 ~ 450 eV) XANES spectra were collected by the total electron yield method, respectively. The measurement for the low concentration sample was performed a plurality of times, and the obtained spectrum was merged.

Figure 1 shows the N-K edge XANES spectra of nitrided Fe-0.5V-1.5Al samples at different depth. The shape and intensity of the obtained spectrum were different at the distance from the surface of the sample. In the case of nitriding, the reaction proceeds by diffusion of nitrogen from the surface to the inside of the sample, so the amount of nitrogen becomes thinner as it becomes inside of the sample. Obtained spectra showed such a concentration gradient of nitrogen well.

In addition, since the spectral shape is different between the sample surface and the inside, it is understood that the chemical state of nitrogen is different inside the sample. At the inside of the sample, VN clusters are precipitated mainly. On the other hand, at the sample surface, AlN and Fe<sub>4</sub>N or Fe<sub>16</sub>N<sub>2</sub> are precipitated in addition to VN clusters, and supersaturated nitrogen also exists. In the future, detailed analysis of the obtained spectrum will be performed by combining simulations.

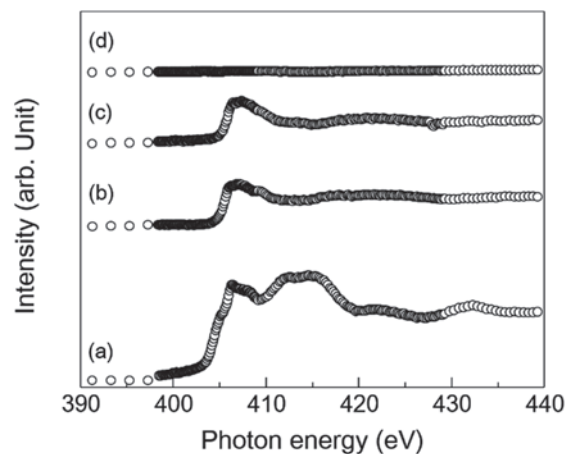


Fig. 1. N K-edge XANES spectra of nitride Fe-0.5V-1.5Al samples obtained at different depth. (a) 50  $\mu\text{m}$  (b) 200  $\mu\text{m}$  (c) 400  $\mu\text{m}$  and (d) 600  $\mu\text{m}$ , respectively.

[1] Tekkou Zairyou, The Japan Institute of Metals and Materials, 1985.

[2] K. Kawasaki, M. Okumiya and S. Uchida, NETSUSHORI **50** (2010) 305.

BL4B

## Charge State Analysis of Fe Ions in Cr-doped $\text{Y}_3\text{Fe}_5\text{O}_{12}$

K. Shimazu<sup>1</sup> and T. Yamamoto<sup>1,2,3</sup><sup>1</sup>Faculty of Science and Engineering, Waseda University, Tokyo 169-8555, Japan<sup>2</sup>Institute of Condensed-Matter Science, Waseda University, Tokyo 169-8555, Japan<sup>3</sup>Kagami Memorial Research Institute for Materials Science and Technology, Waseda University, Tokyo 169-0051, Japan

Thermochromism is a phenomenon to change the color due to a change in temperature. There are wide variety of organic materials, which show thermochromism. However, few inorganic ones show such thermochromism. Among such inorganic thermochromic materials, rare-earth (RE) iron garnet,  $\text{RE}_3\text{Fe}_5\text{O}_{12}$ , shows such color change [1]. Although it was reported that red-shift occurs by Cr-doping in one of the rare-earth iron garnet,  $\text{Y}_3\text{Fe}_5\text{O}_{12}$  [2], the mechanism in such red-shift has not yet been clearly understood. In the current study, we focused upon the change in electronic structure of the Cr-doped  $\text{Y}_3\text{Fe}_5\text{O}_{12}$  garnet. Especially, change in charge state of Fe ions as a function of doped Cr concentration was investigated by the Fe- $L_3$  X-ray absorption spectra (XAS) measurements in this report.

Cr-doped  $\text{Y}_3\text{Fe}_5\text{O}_{12}$  garnet was synthesized with conventional solid state reaction method changing the concentration of doped Cr ions. Crystal structures of the synthesized powders were examined by the powder X-ray diffraction, which showed all the samples are single phased and no secondary phase could be observed. From the observed XRD patterns, we obtained the volumes of cells as a function of Cr concentration, which are shown in Fig. 1. Volumes decrease as increase of Cr concentration, which suggests Cr ions substitute at Fe site as trivalent ions. These results can be explained by the difference in ionic radii, i.e., ionic radius of  $\text{Cr}^{3+}$  ion is smaller than that of  $\text{Fe}^{3+}$  ion [3].

Fe- $L_3$  XAS spectra were observed at BL4B, UVSOR, in a total electron mode by collecting the drain current. Sample powders were settled on the carbon adhesive tape, which was put on the Cu plate. Incident beams were irradiated perpendicular onto the plate, which was monochromatized with a varied-space grating (800 l/mm). Observed Fe- $L_3$  XANES spectra are shown in Fig. 2. All the spectral profile of Fe- $L_3$  XAS of Cr-doped  $\text{Y}_3\text{Fe}_5\text{O}_{12}$  garnet is independent from the concentration of doped Cr and shows similar profile as that of  $\text{Fe}_3\text{O}_4$ . From these results we can safely conclude that valence state of Fe ions do not change in all samples with different Cr concentration from the mixture of 2+ and 3+ as in  $\text{Fe}_3\text{O}_4$ . The red-shift is under investigation by the calculated electronic density of states within a density functional theory.

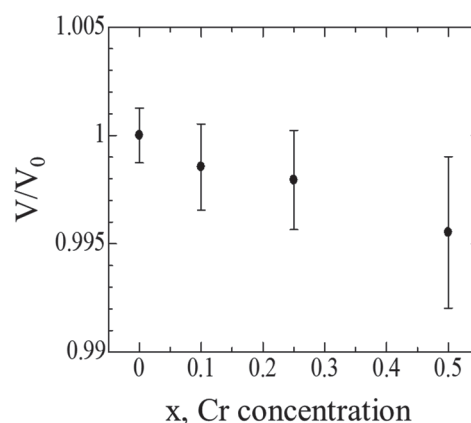


Fig. 1. Relative volume ( $V/V_0$ ) of Cr-doped  $\text{Y}_3\text{Fe}_5\text{O}_{12}$  ( $\text{Y}_3\text{Fe}_{5-x}\text{Cr}_x\text{O}_{12}$ ) garnet as a function of Cr concentration.

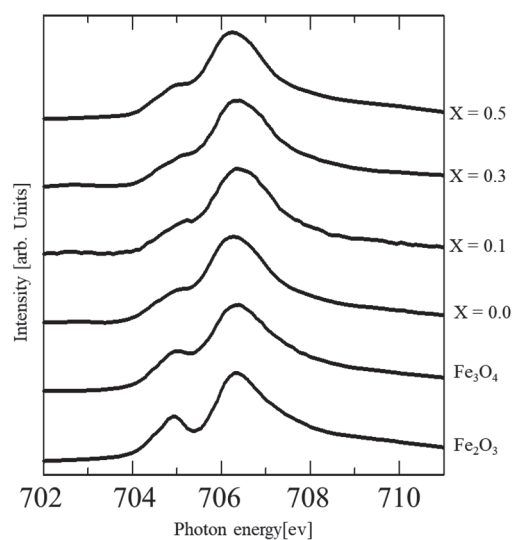


Fig. 2. Observed Fe- $L_3$  XANES spectra of Cr-doped  $\text{Y}_3\text{Fe}_5\text{O}_{12}$  ( $\text{Y}_3\text{Fe}_{5-x}\text{Cr}_x\text{O}_{12}$ ) with those of the standard iron oxides.

- [1] S. C. Parida *et al.*, *J. Phase Equil.* **24** (2012) 5.
- [2] H. Lu *et al.*, *J. Mater. Chem.* **C44** (2016) 15981.
- [3] R. D. Shanon, *Acta Cryst.* **A32** (1976) 751.



BL4B

## Applications of Soft X-ray Spectroscopy to the Analysis of Nitrogen Implanted TiO<sub>2</sub> Photocatalysts

T. Yoshida<sup>1</sup>, M. Yamamoto<sup>1</sup>, Y. Kato<sup>2</sup>, A. Ozawa<sup>2</sup> and T. Tanabe<sup>1</sup>

<sup>1</sup>Advanced Research Institute for Natural Science, Osaka City University, Osaka 558-8585, Japan

<sup>2</sup>Graduate School of Engineering, Osaka City University, Osaka 558-8585, Japan

Photocatalytic reactions at the surface of titanium dioxide (TiO<sub>2</sub>) under UV light irradiation have been attracting much attention in view of their practical applications to environmental cleaning such as self cleaning of tiles, glasses, and windows.[1] It has been reported that the doping of nitrogen into TiO<sub>2</sub> contributes to band gap narrowing to provide visible-light response.[2, 3] In the present study, nitrogen doped TiO<sub>2</sub> photocatalysts were prepared by nitrogen implantation method, and investigated the chemical states of the surface of the samples mainly by soft X-ray absorption and photoelectron spectroscopies.

Nitrogen ions were implanted into TiO<sub>2</sub> at 5 or 50 keV at room temperature. Photocatalytic activity of the N<sup>+</sup>-implanted sample was evaluated by the decomposition reaction of methylene-blue solution under visible-light irradiation. The photocatalytic activity changed with the amount of implanted nitrogen, and the photocatalytic active and inactive N<sup>+</sup>-implanted samples were obtained.

As shown in Fig. 1, O K-edge and Ti L<sub>2,3</sub>-edge of XANES analysis exhibited the formation of Ti<sup>3+</sup> species in both photocatalytic active and inactive samples (A-cat and I-cat). The Ti<sup>3+</sup> species would be formed by the displacement effect of oxygen atoms during the N<sup>+</sup> implantation. On the other hand, in N K-edge XANES spectra, a double-peak structure

around 400 eV was observed for the photocatalytic active sample while the XANES spectrum of the photocatalytic inactive sample showed a distinct single peak around 401 eV. These results suggested two types of chemical states of nitrogen, i.e., the photocatalytic active N substituting the O sites and the inactive NO<sub>2</sub> species. In the valence band photoelectron spectrum of the photocatalytic active sample, the additional electronic states were observed just above the valence band edge of a TiO<sub>2</sub>. The electronic state would be originated from the substituting nitrogen and be responsible for the band gap narrowing, i.e., visible light response of TiO<sub>2</sub> photocatalysts. On the other hand, the resonant photoemission spectra of the active sample under X-ray excitation around N K-edge were almost the same regardless of X-ray energy, while those of the inactive sample showed an additional sharp peak in valence band under the X-ray excitation around 401 eV.

[1] A. Fujishima, X. Zhang and D. A. Tryk, *Surf. Sci. Rep.* **63** (2008) 515.

[2] R. Asahi, T. Morikawa, T. Ohwaki, K. Aoki and Y. Taga, *Science* **293** (2001) 269.

[3] R. Asahi and T. Morikawa, *Chem. Phys.* **339** (2007) 57.

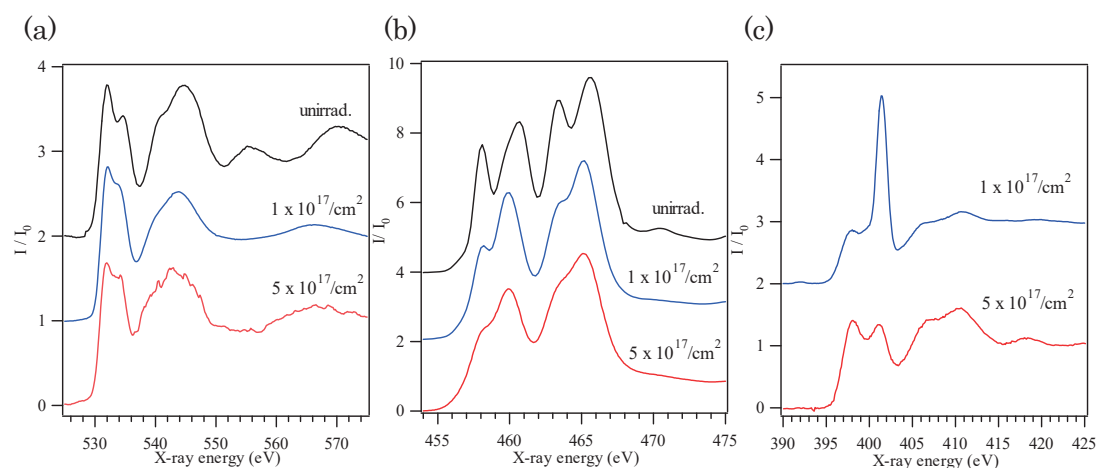


Fig. 1. (a) O K-edge XANES spectra of active sample (A-cat), inactive sample (I-cat) and a bare sample. (b) Ti L<sub>2,3</sub>-edge XANES spectra of active sample (A-cat), inactive sample (I-cat) and a bare sample. (c) N K-edge XANES spectra of active sample (A-cat) and inactive sample (I-cat).

BL4B

## N *K*-edge XAS Spectroscopy on 3*d* Transition Metal Doped AlN Films

N. Tatemizo and S. Imada

Faculty of Electrical Engineering and Electronics, Kyoto Institute of Technology, Kyoto, 606-8585, Japan

For the last two decades, wide-band gap semiconductors heavily doped with 3*d* transition metals (3*d*-TM) have been extensively investigated in order to realize devices with new functionality [1, 2]. To confer photoconversion of sun light as an intermediate band (IB) material [1], we have been exploring the possibility of heavy 3*d*-TM doping to AlN, which is in the family of III-nitrides [3-5]. For IB material, Fe is thought not to be effective because an Fe ion in an Al site of AlN have 5 3*d* electrons, that is, half-filled electronic structure. However, from the view point of chemical trend study of 3*d*-TM in AlN, Fe is an interesting dopant; the additional band mainly consisting of 3*d* states of Fe are formed very near to the valence band (VB) of AlN according to our theoretical band structure calculation, while those of Ti, V and Cr are formed in the middle of the band gap [6]. To investigate the band structures of the Fe-doped AlN (AlFeN), we synthesized AlFeN with various Fe concentration between 0-30% [7] and carried out N *K*-edge XAS measurements.

The films were deposited on SiO<sub>2</sub> glass substrates by RF sputtering from an AlN target with Fe metal chips on it. Results of XRD and TEM showed that the films have wurtzite structures [7]. N *K*-edge XAS measurements for the films in fluorescence-detection mode at room temperature. The electric field vectors of the X-rays were parallel to the film plane.

Figure 1 shows the N *K*-edge XAS spectra of AlFeN (7.8%) and Ti-doped AlN (AlTiN, Ti: 8.3%) films [3]. The energies of the 3 main peaks indicated black arrows A, B, and C for the both films coincided with those of un-doped AlN [3]. Regarding the relative intensities of the peaks, there is a difference at the peak C. This is thought to be due to the difference in the orientation axis of the films; the AlTiN film has a *c*-axis orientation [3], while the AlFeN film has an *a*-axis orientation [7]. In both spectra, pre-edge peaks were clearly observed. Reflecting the large number of un-occupied *d*-states (9 or 10 states [3]) hybridized with N *p*-states just below the bottom of the conduction band, AlTiN film had a large pre-edge peak near the main peak. On the contrary, that of AlFeN was small and far from the main peak A. According to the result of Fe *K*-edge XANES analyses (not showing here), Fe ions have an oxidation state of 3+ (3*d*<sup>5</sup>). It is reasonable that the spectrum of AlFeN had smaller pre-edge peak than that of AlTiN. As intensities of pre-edge peaks reflect not only un-occupation of 3*d* states but also symmetry around N, further study on the symmetries around N (Fe/Ti) should be necessary.

The difference of the peak energies of the pre-edge peak and the main peak A is about 5 eV in the spectrum of AlFeN. This indicates that the un-occupied states were formed near the VB of AlN. This is consistent with our calculation of the band structure of AlFeN.

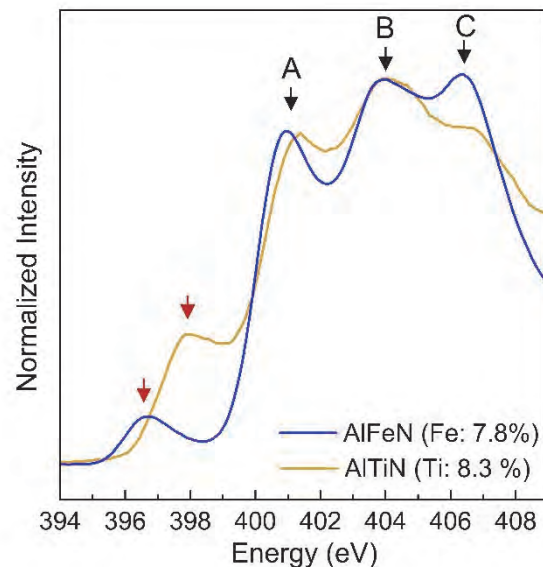


Fig. 1. N *K*-edge XAS of AlTiN (Ti: 8.3%) and AlFeN (Fe: 7.8%) films deposited on SiO<sub>2</sub> glass substrates.

- [1] A. Luque *et al.*, Phys. Rev. Lett. **78** (1997) 5014.
- [2] T. Dietl *et al.*, Science **287** (2000) 1019.
- [3] N. Tatemizo *et al.*, J. Mater. Chem. A **5** (2017) 20824.
- [4] N. Tatemizo *et al.*, J. Appl. Phys. **123** (2018) 161546.
- [5] N. Tatemizo *et al.*, J. Phys.: Condens Matter **29** (2017) 085502.
- [6] N. Tatemizo *et al.*, Materials Science Forum **924** (2018) 322.
- [7] N. Tatemizo *et al.*, AIP advances **8** (2018) 115117.

BL4B

## Local Structure Investigation of Alloy Nitrides Precipitated by Interface Precipitation during Ferrite Transformation

M. Sato and T. Murata

<sup>1</sup>Institute for Materials Research, Tohoku University, Sendai 980-8522, Japan

The pro-eutectoid ferrite formed from austenite is the most frequently appearing morphology in steel. In general, it is known that grain boundary allotriomorph ferrite are formed when the degree of supercooling from the Ae<sub>3</sub> line is low, and the widmanstatten ferrite is formed as the degree of supercooling increases [1, 2]. In addition, in carbon steel, when the strong carbide-forming elements such as Ti, Nb, V, Cr and Mo are added, the interface precipitation occurs and alloy carbides are periodically generated on the  $\gamma/\alpha$  interface during ferrite transformation.

Although there are many reports on the ferrite transformation behavior in carbon steel, there are very few reports on nitrogen steel. Under such circumstances, we have found that the interface precipitation of CrN occurs in the ferrite transformation of Fe-1Cr-0.3N austenite.

In this study, the change in chemical states of Cr and N during the ferrite transformation with interface precipitation in Fe-1Cr-0.3N austenite.

Fe-1mass%Cr alloy were used as starting materials. They were homogenized at 1523 K for 24h and furnace-cooled until room temperature. The Fe-1Cr-0.3N alloy were prepared by nitriding and quenching (N-Q) process using NH<sub>3</sub>/H<sub>2</sub> mixed gas at 1273 K for 1 h. The obtained alloys were isothermally treated at 973 K for several time of periods and then quenched into iced brine. The N K-edge and Cr L-edge XANES spectra were corrected by fluorescence method using silicon drift detector (SDD) at BL4B in UVSOR, respectively. Obtained data were analyzed using Athena software.

Calculation of XANES spectrum was performed by FDMNES software and the crystal structural data was corrected from NIMS web site [3].

Figure 1 shows Cr L-edge XANES spectra of samples. In the L<sub>3</sub> edge peak, intensity around 588 eV increased with increasing holding time due to the increasing the volume fraction of CrN precipitate.

Figure 2 shows N K-edge XANES spectrum of sample isothermally treated at 750 °C for 10 min. and calculated XANES spectrum of Fe<sub>4</sub>N and CrN. It is thought that the obtained spectra are consisted from the combination of Fe<sub>4</sub>N and CrN. Further detailed analysis will be performed using this kind of calculations.

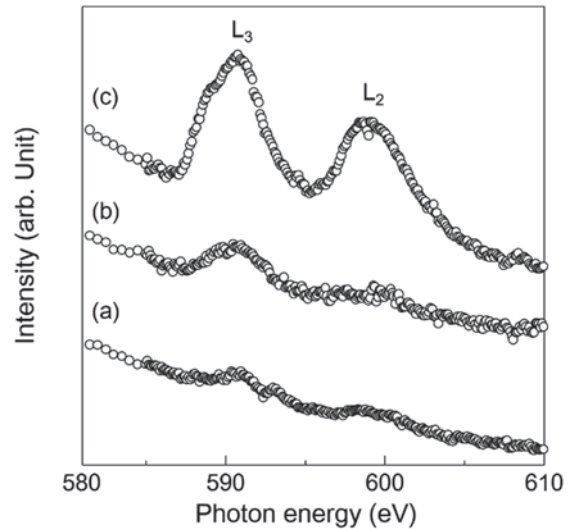


Fig. 1. Cr L-edge XANES spectra of samples (a) As quenched, (b) heat treated at 750 °C for 10 min. and (c) heat treated at 750 °C for 1 h.

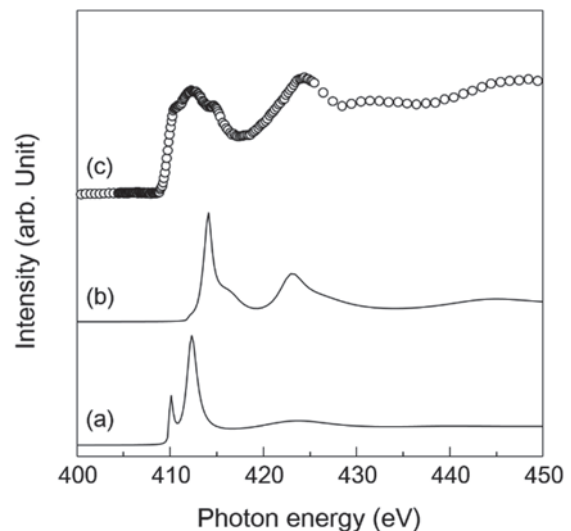


Fig. 2. Calculated and measured N K-edge XANES spectra. (a) Fe<sub>4</sub>N (calc.), (b) CrN (calc.) and (c) heat treated at 750 °C for 10 min.

[1] Dube' C. A., H. I. Aaronson and R. F. Mehl, *Re'v.met.* **55** (1958) 201.

[2] H. B. Aaron and H. I. Aaronson: *Metall. Trans.* **2** (1971) 23.

[3] <https://crystdb.nims.go.jp/>

BL5U

## ARPES Study of Iron-chalcogenide High- $T_c$ Superconductors

K. Nakayama<sup>1</sup>, G. N. Phan<sup>1</sup>, H. Oinuma<sup>1</sup>, D. Takane<sup>1</sup>, K. Sugawara<sup>1,2</sup>, T. Takahashi<sup>1,2,3</sup>,  
F. Nabeshima<sup>4</sup>, T. Ishikawa<sup>4</sup>, T. Shikama<sup>4</sup>, A. Maeda<sup>4</sup> and T. Sato<sup>1,3</sup>

<sup>1</sup>Department of Physics, Tohoku University, Sendai 980-8578, Japan

<sup>2</sup>Center for Spintronics Research Network, Tohoku University, Sendai 980-8577, Japan

<sup>3</sup>WPI Research Center, Advanced Institute for Materials Research, Tohoku University, Sendai 980-8577, Japan

<sup>4</sup>Department of Basic Science, the University of Tokyo, Tokyo 153-8902, Japan

Iron chalcogenides  $FeCh$  ( $Ch$ : S, Se, Te) have long been attracting considerable attention as the structurally simplest iron-based superconductors. These materials show rich physical properties such as superconductivity, antiferromagnetism, structural transition, and electronic nematicity. Intriguingly, these physical properties exhibit gigantic pressure effects, as exemplified by a marked increase in a superconducting transition temperature ( $T_c$ ) from 8 K to 37 K in pressurized FeSe [1]. Understanding the origin of such pressure-induced  $T_c$  enhancement would provide a key to resolving the high- $T_c$  mechanism in iron-based superconductors.

Recent successful fabrication of  $FeSe_{1-x}Te_x$  thin films allows us to control the lattice parameters by tuning the lattice mismatch with substrate. Such strain engineering has great capability for manipulating various physical properties. For example, the application of compressive strain enhances the  $T_c$  value up to 12 K in FeSe on  $CaF_2$  [2, 3] and further up to 23 K in  $FeSe_{0.8}Te_{0.2}$  on  $CaF_2$  [4]. In addition, strain-induced drastic changes in the structural, magnetic, and nematic properties have been discovered in  $FeSe_{1-x}Te_x$  [5]. These findings have provided a rare opportunity for investigating the interplay between the physical properties and the lattice parameters at ambient pressure.

In this study, we have performed high-resolution angle-resolved photoemission spectroscopy (ARPES) of compressive-strained and strain-free  $FeSe_{1-x}Te_x$  thin films at BL5U, and determined their band structure in the three-dimensional momentum space. Our systematic ARPES measurements revealed the strain-induced evolution of Fermi surface and electronic nematicity as well as their relationship with  $T_c$  variation.

High-quality compressive-strained  $FeSe_{1-x}Te_x$  thin films with the thicknesses of approximately 300 monolayers were grown on  $CaF_2$  substrate by pulsed laser deposition. Figure 1 shows the representative ARPES results in the normal state of  $FeSe_{0.8}Te_{0.2}$  ( $T_c = 23$  K) measured with circularly-polarized 40-eV photons. We observed several dispersive bands near the Fermi level ( $E_F$ ), which mainly originate from Fe  $3d$  orbitals. Fermi surfaces consist of hole-like and electron-like small pockets at the Brillouin-zone center ( $\Gamma$  point) and corner (M point), respectively (see Fig. 1). Similar size of these Fermi surfaces supports the semimetallic nature of  $FeSe_{0.8}Te_{0.2}$ . We have also performed ARPES measurements on several different

samples such as strain free and different compositions, and found strain- and Te-substitution-induced changes in the semimetallic band overlap and the nematicity. Our observations provide important insights into the interplay between  $T_c$  enhancement and lattice parameters.

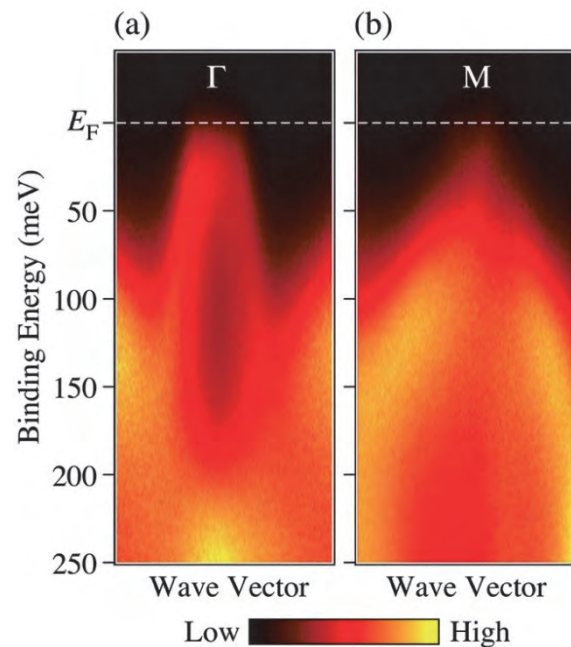


Fig. 1. (a) and (b) ARPES intensity plot as a function of binding energy and wave vector measured around the Brillouin-zone center and corner, respectively, on  $FeSe_{0.8}Te_{0.2}$  ( $T_c = 23$  K) at  $T = 30$  K. The data were obtained with circularly-polarized 40-eV photons.

- [1] S. Medbedev *et al.*, *Nature Mater.* **8** (2009) 630.
- [2] F. Nabeshima *et al.*, *Appl. Phys. Lett.* **103** (2013) 172602.
- [3] G. N. Phan *et al.*, *Phys. Rev. B* **95** (2017) 224507.
- [4] Y. Imai *et al.*, *Proc. Natl. Acad. Sci. USA* **112** (2015) 1937.
- [5] Y. Imai *et al.*, *Sci Rep.* **7** (2017) 46653.



BL5U

## Observation of Fermi-arc Surface States in CoSi

D. Takane<sup>1</sup>, Z. Wang<sup>2</sup>, S. Souma<sup>3,4</sup>, K. Nakayama<sup>1</sup>, T. Nakamura<sup>1</sup>, H. Oinuma<sup>1</sup>, K. Hori<sup>1</sup>,  
K. Sugawara<sup>1,3</sup>, T. Takahashi<sup>1,3,4</sup>, Y. Ando<sup>2</sup> and T. Sato<sup>1,3</sup>

<sup>1</sup>Department of Physics, Tohoku University, Sendai 980-8578, Japan

<sup>2</sup>Physics Institute II, University of Cologne, 50937 Köln, Germany

<sup>3</sup>Center for Spintronics Research Network, Tohoku University, Sendai 980-8577, Japan

<sup>4</sup>WPI Research Center, Advanced Institute for Materials Research, Tohoku University, Sendai 980-8577, Japan

The search for new fermionic particles, which has long been an important research target in elementary-particle physics, is now becoming an exciting challenge in condensed-matter physics to realize exotic fermions, as highlighted by the discovery of two-dimensional (2D) Dirac fermions in graphene and helical Dirac fermions at the surface of three-dimensional (3D) topological insulators. The recent discovery of 3D Dirac semimetals and Weyl semimetals hosting massless Dirac-Weyl fermions further enriches the category of exotic fermions. While all these fermions could manifest themselves in elementary-particle physics, recent theories have predicted new types of massless fermions in condensed-matter systems that have no counterparts in elementary particles. These fermions appear in the crystals with specific space groups, such as CoSi, as exemplified by the spin-1 chiral fermion and the double Weyl fermion showing multifold band degeneracies at the band-crossing point (node) protected by the crystal symmetry [1-3] [Fig. 1(a)]. While a well-known spin-1/2 Weyl fermion shows a Weyl-cone energy band dispersion with twofold degeneracy at the node that carries the topological charge (Chern number)  $C$  of  $\pm 1$ , these novel fermions carry topological charge of  $\pm 2$ , and hence produce multiple (double) Fermi-arc surface states.

In this study, we performed angle-resolved photoemission spectroscopy (ARPES) of CoSi at BL5U. By utilizing energy-tunable photons from synchrotron radiation, we found first experimental evidence for unconventional Fermi-arc surface states that strongly support the presence of spin-1 chiral fermion and double Weyl fermion in the bulk [4].

High-quality single crystals of CoSi were grown by a chemical vapor transport method. To search for the predicted Fermi-arc surface states, we selected  $h\nu = 67$  eV, which corresponds to  $k_z \sim 0.75\pi$  at  $k_x \sim 0$  to avoid a possible complication from the bulk bands. As shown in the upper left panel of Fig. 1(b), the ARPES intensity at the Fermi level ( $E_F$ ) is elongated toward two of four adjacent  $\bar{M}$  points, resulting in a  $C_2$ -symmetric “Z”-shaped intensity pattern. This feature is commonly observed at other  $h\nu$ 's [Fig. 1(b)] despite a sizable change in the  $k_z$  value [0.3- 0.95 $\pi$ ]. We found that the energy dispersion of the  $E_F$ -crossing band that produces the Z-shaped Fermi contour seems to be unchanged against a variation of  $h\nu$ . These results

strongly suggest the surface origin of the Fermi contour in Fig. 1(b). This Fermi contour is attributed to the predicted Fermi-arc surface states, since the calculated surface states are  $C_2$  symmetric and connect with the bulk FSs at the  $\bar{\Gamma}$  and  $\bar{M}$  points, consistent with the present ARPES results. The present study strongly supports the existence of chiral topological fermions beyond Dirac and Weyl fermions in condensed-matter systems.

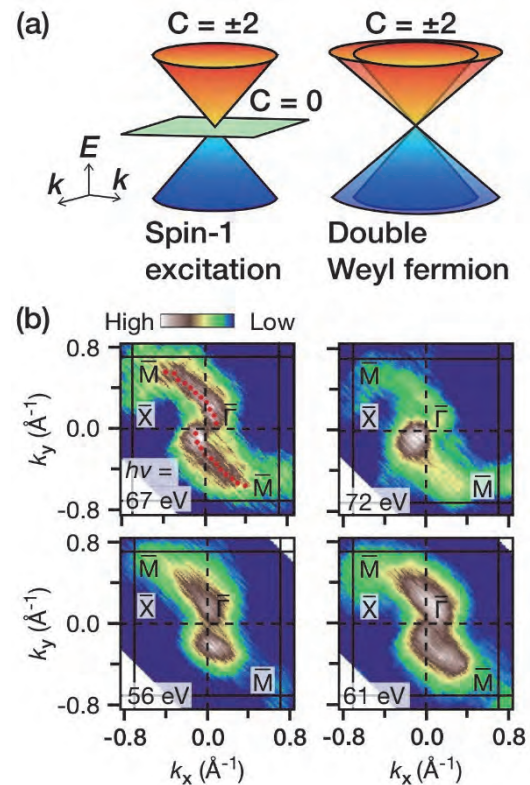


Fig. 1. (a) Spin-1 chiral fermion (left), and double Weyl fermion (right). (b) Fermi-surface mapping of CoSi at  $h\nu = 67$  eV which indicates the existence of Fermi-arc surface states.

- [1] B. Bradlyn *et al.*, *Science* **353** (2016) aaf5037.
- [2] G. Chang *et al.*, *Phys. Rev. Lett.* **119** (2017) 206401.
- [3] P. Tang *et al.*, *Phys. Rev. Lett.* **119** (2017) 206402.
- [4] D. Takane *et al.*, *Phys. Rev. Lett.* **122** (2019) 076402.

BL5U

## Investigating Electronic Structures of the Strained Transition Metal Dichalcogenide Monolayers

D. J. Oh<sup>1,2</sup>, B. Kim<sup>1,2</sup>, K. Tanaka<sup>3</sup>, S. R. Park<sup>4</sup> and C. Kim<sup>1,2</sup>

<sup>1</sup>Department of Physics and Astronomy, Seoul National University (SNU), Seou 088261, Republic of Korea

<sup>2</sup>Center for Correlated Electron Systems, Institute for Basic Science (IBS), Seoul 08826, Republic of Korea

<sup>3</sup>UVSOR Synchrotron Facility, Institute for Molecular Science, Okazaki 444-8585, Japan

<sup>4</sup>Department of physics, Incheon National University, Incheon 406-772, Korea

Transition metal dichalcogenides (TMDs) monolayer (ML) such as MoS<sub>2</sub> and NbSe<sub>2</sub> have recently drawn a lot of attentions because of their novel properties distinguished from their bulk formed materials [1, 2]. It is desired to manipulate the electronic structures and materials properties of TMDs ML by applying external field or strain. Uniaxial strained MoS<sub>2</sub> ML was recently realized by a special method using a flexible substrate and exhibit a interesting property [3]. The electronic structure of monolayer MoS<sub>2</sub> can be modified by uniaxial strain. When the current was applied to the sample, strained monolayer MoS<sub>2</sub> can have valley polarization. In addition, the direction of the valley polarization can be controlled by the direction of the current [3].

We bought the MoSe<sub>2</sub> single crystal from the HQ graphene. We exfoliated the thick MoSe<sub>2</sub> flakes from single crystal on the viscoelastic substrate [4]. Then we applied the uniaxial strain using a mechanical translation stage [3]. Finally, we transferred a MoSe<sub>2</sub> flake onto the degenerately doped Si substrate. Samples were annealed at 700K for 2h in UHV to cleaning the surface before ARPES measurements. ARPES spectra were acquired by hemispherical photoelectron analyzer (MBS A-1) equipped with deflectors that enable momentum space mapping. The base pressure is better than  $5 \times 10^{-11}$  torr. We used linearly polarized light with 80eV photon energy.

We have tried to measure the electronic structure of strained MoSe<sub>2</sub> by angle resolved photoemission in UVSOR BL5U. Figure 1(a) is the constant energy cut obtained at -2.4 eV binding energy. There are two hole pockets at  $\Gamma$  and K-point. In Fig. 1(b), there are band splitting induced by spin-orbit coupling and it was coincident with previous work [5]. Due to the small spin-orbit coupling in MoSe<sub>2</sub>, it is hard to measure the size of splitting. And we couldn't measure any modified electronic structure induced by uniaxial strain. We assume that the applied uniaxial strain is too small to modify the electronic structure. Or the applied uniaxial strain was released during the annealing process. Furthermore, we have checked the charging effect. We measure the energy distribution curve (EDC) with two different entrance slit size. In Fig. 2, measured EDC is shifted to higher binding energy when we use larger entrance slit. It is a general tendency when there is a charging effect. It seems to be caused from poor electrical

contact between Si substrate and MoSe<sub>2</sub> flake or the presence of SiO<sub>2</sub> layer on the Si substrate.

Based on these results, we were able to identify the problems to be solved. We will try to make better electrical contact or use another conducting substrate. And we will try to apply uniaxial strain using another method which can maintain the uniaxial strain during ARPES measurement.

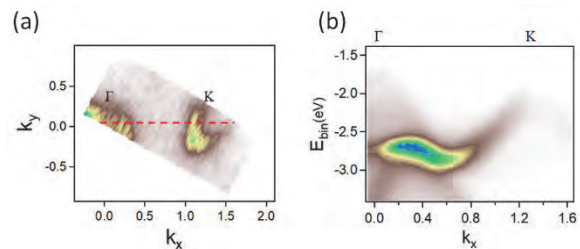


Fig. 1. (a) Constant energy cut obtained at the -2.4 eV binding energy (b) Measured dispersion along the red dashed line in Fig. 1 (a).

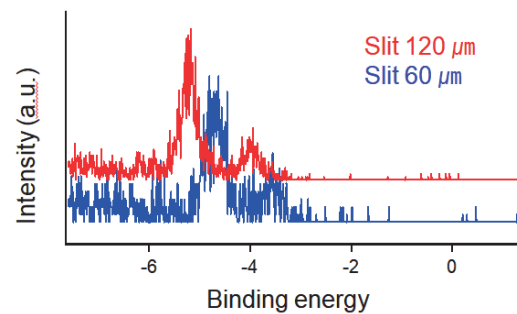


Fig. 2. Measured energy distribution curves using two different slit size.

- [1] D. Xiao *et al.*, Phys. Rev. Lett **108** (2012) 0196820.
- [2] M. Ugeda *et al.*, Nature Physics **12** (2016) 92.
- [3] J. Lee *et al.*, Nat. Materials **16** (2017) 887.
- [4] A. Castellanos-Gomez *et al.*, 2D Mater. **1** (2014) 011002.
- [5] B. S. Kim *et al.*, Sci. Rep. **6** (2016) 36389.

BL5U

## Angle-Resolved Photoemission Spectroscopy Study of Fermi Surface and Superconducting Gap in NdFeAs<sub>0.4</sub>P<sub>0.6</sub>(O,F)

 Z. H. Tin<sup>1</sup>, T. Adachi<sup>1</sup>, A. Takemori<sup>1</sup>, S. Ideta<sup>2,3</sup>, K. Tanaka<sup>2,3</sup>, S. Miyasaka<sup>1</sup> and S. Tajima<sup>1</sup>
<sup>1</sup>Department of Physics, Graduate School of Science, Osaka University, Toyonaka 560-0043, Japan

<sup>2</sup>UVSOR Synchrotron Facility, Institute for Molecular Science, Okazaki 444-8585, Japan

<sup>3</sup>School of Physical Sciences, The Graduate University for Advanced Studies (SOKENDAI), Okazaki 444-8585, Japan

The discovery of IBSSs has bestowed us an alternative direction to investigate the origin of superconductivity. Amongst the various type of families in Fe-based superconductors, 1111-system such as NdFeAs(O,F) achieves the highest  $T_c$ , which is 55K. In spite of highest  $T_c$ , 1111-system is not well-researched. The reasons behind are the difficulty of synthesizing single crystal and no cleaved surface with electrical neutrality. In our previous study, we are able to observe the evolution of Fermi surfaces and  $T_c$  accordance to isovalent doping of As site to P. [1] In addition, we had measured the superconducting gap of NdFeAs(O,F) by using ARPES method. In this report, we show the ARPES result of NdFeAs<sub>0.4</sub>P<sub>0.6</sub>(O,F).

The single crystals of NdFeAs<sub>0.4</sub>P<sub>0.6</sub>(O,F) were grown by self-flux method under high pressure using a cubic anvil press machine. [1, 2]  $T_c$  of the single crystal was about 11 K. The ARPES data were measured at BL5U of UVSOR facility.

The in-plane mapping of Fermi surfaces (FSs) in  $P$  and  $S$ -polarized photon configurations at 60eV were shown in Fig. 1. In these mappings, three hole FSs and two electron FSs can be clearly seen in  $\Gamma(0,0)$  and  $M(1,-1)$  points, respectively.

The  $k_z$  dependence of all FSs were measured by changing the energy of the incident photon and the results were shown in Fig. 2. All the FSs showed less dispersive feature along the  $k_z$  direction. The largest hole FS (arrow mark) remains around zone center even by 60% P-doping. This largest FS is treated as surface state from polar-cleaved surface of the 1111-type superconductors.  $\Gamma$  points determined to be around 64 eV with inner potential of 18 eV.

The superconducting gap measurement was carried out on the FSs around the  $\Gamma$  and  $M$  points in  $P$ -polarized photon configuration. Figure 3 shows the symmetrized energy-distribution curves (EDCs) at the various  $k$  point on the inner and outer hole FSs around the  $\Gamma$  point, and on the inner electron FS around  $M$  point. In the symmetrized EDCs at 5 K, the coherence peaks or the shoulder like structures can be observed around 10 meV, suggesting the superconducting gap  $\sim 10$  meV. However, these peaks or the shoulder like structure do not diminish at 19 K. This behavior suggests that the peak and the shoulder like features are due to pseudogap, which was often observed in the Fe-based superconductors.

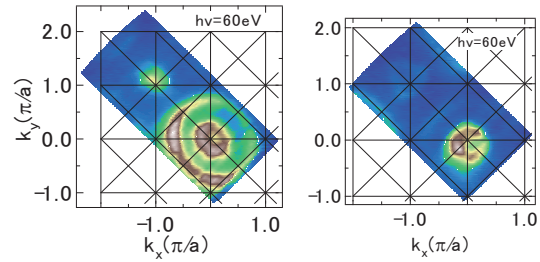


Fig. 1. FS mapping of NdFeAs<sub>0.4</sub>P<sub>0.6</sub>(O,F) in  $P$  and  $S$ -polarized configurations (left and right panels) at 60eV.

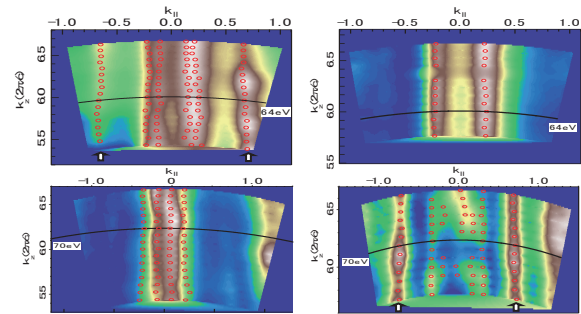


Fig. 2.  $k_z$  dependence of FSs of NdFeAs<sub>0.4</sub>P<sub>0.6</sub>(O,F) in  $P$  and  $S$ -polarized configuration (left and right panels). Top and bottom panels show the results of hole and electron FSs, respectively.

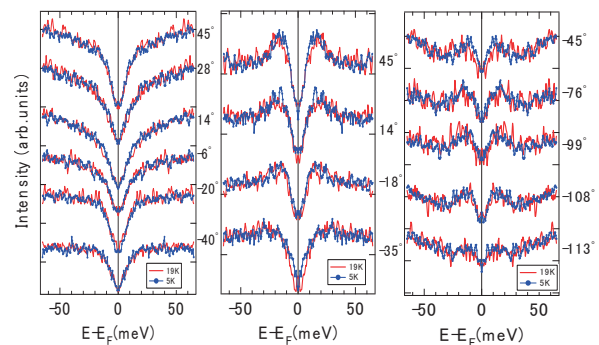


Fig. 3. Symmetrized EDC of inner (left), outer (middle) hole bands and inner electron band (right) at 5 K (blue) and 19 K (red).

[1] A. Takemori *et al.*, Phys. Rev. B **98** (2018) 100501(R).

[2] A. Takemori *et al.*, JPS Conf. Proc. **1** (2014) 012111.



BL5U, BL7U

## Study on Interaction between Charge Density Wave Collective Modes and Electrons

Y. Lee, J. Hyun, C.-Y. Lim, G. Lee, S. Kim and Y. Kim

Korea Advanced Institute of Science and Technology (KAIST), Daejeon, 34141, Republic of Korea

Among atomic-layer materials, transition-metal dichalcogenides (TMDs) have been an attractive system to research due to their various physical properties such as superconductivity, charge-density wave (CDW), magnetic ordering, etc. Amongst various properties, competition between CDW phase and superconductivity provides an important playground to study the possible connection between CDW fluctuation and superconductivity. The suitable system for such study is 2H-TaSe<sub>2</sub>. It shows superconducting transition  $T_c \sim 0.15$  K. Also, there exists two CDW transitions: from normal phase to incommensurate CDW phase at 122 K and from incommensurate CDW phase to commensurate CDW phase at 90 K [1].

In our previous work and other early studies, kink near Fermi level is observed along M-K high symmetry direction in 2H-TaSe<sub>2</sub> [2, 3] which shows clear temperature dependence across the CDW transition. It is not expected behavior of ordinary kink produced through electron-phonon interaction. Instead, such temperature dependence implies a possible role of CDW fluctuation on the observed renormalization. If we can clearly demonstrate that the kink develops below CDW transition temperature apart from the band folding and disappears after CDW relaxation, we can conclude that the coupling between collective excitation mode of CDW and electron is responsible for the kink. It will be the first step towards the understanding on the relationship between CDW and superconductivity.

In this study, we have performed high-resolution angle-resolved photoemission spectroscopy (ARPES) on 2H-TaSe<sub>2</sub> single crystals grown by chemical vapor transport (CVT) method [4]. ARPES experiments were conducted on Beamline 5U and 7U at UVSOR, using linearly horizontal polarized photon of  $h\nu = 50$  eV. Total energy resolution was set to 20 meV. Samples were cleaved *in situ* in the condition of pressure lower than  $1 \times 10^{-8}$  Pa at temperature 10 K. In order to observe temperature evolution of kink, we measured the electronic band structure at 10 K, 70 K, 110 K, 150 K respectively.

Figure 1(a) shows the band dispersion of 2H-TaSe<sub>2</sub> along M-K direction taken at 10 K. Dispersion also M-K is free from band folding due to symmetry lowering. We observed the kink at binding energy around 10 meV near M point. Figure 1(b) shows the kink (upper) and corresponding peak positions of momentum distribution curve (MDC) fitting at four different temperatures (lower). We observed that kink

disappears above 70K. Therefore, the present result clearly suggests that the kink is weakened as CDW phase transition occurs at 90 K, and thus it is originated from electron-CDW coupling.

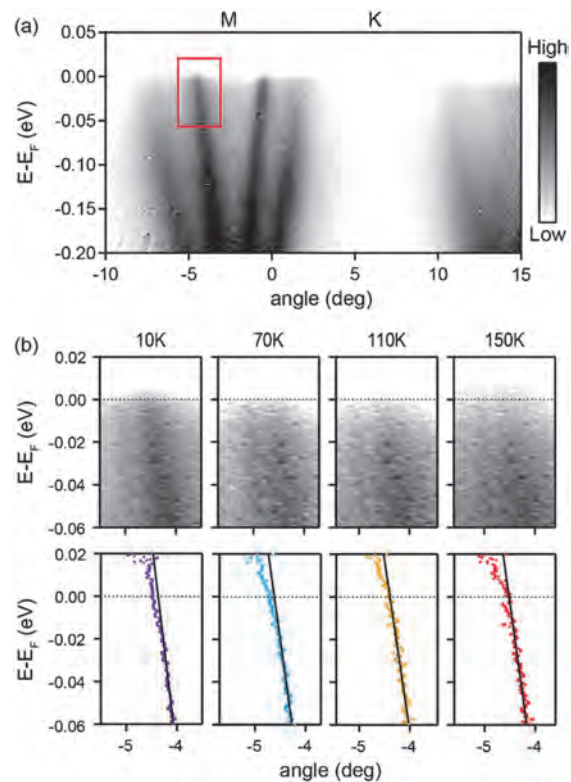


Fig. 1. (a) Band dispersion of 2H-TaSe<sub>2</sub> along M-K direction of BZ taken at 10 K. Kink structure is shown in the red box. (b) Temperature evolution of kink structure and corresponding peak positions of MDC fitting of 2H-TaSe<sub>2</sub> (in the red box of (a)).

- [1] D. E. Moncton *et al.*, Phys. Rev. B **16** (1977) 801.
- [2] T. Valla *et al.*, Phys. Rev. Lett. **85** (2000) 4759.
- [3] K. Rossnagel *et al.*, Phys. Rev. B **72** (2005) 121103(R).
- [4] L. H. Brixner *et al.*, J. Inorg. Nucl. Chem. **24** (1962) 257.



BL5U

## Polarization-dependent Angle-resolved Photoemission Study of MAX Phase compound $Ti_2SnC$

 T. Ito<sup>1,2</sup>, M. Ikemoto<sup>2</sup>, D. Pinek<sup>3</sup>, M. Nakatake<sup>4</sup>, S. Ideta<sup>5,6</sup>, K. Tanaka<sup>5,6</sup> and T. Ouisse<sup>3</sup>
<sup>1</sup>Nagoya University Synchrotron radiation Research center (NUSR), Nagoya University, Nagoya 464-8603, Japan

<sup>2</sup>Graduate School of Engineering, Nagoya University, Nagoya 464-8603, Japan

<sup>3</sup>Grenoble Alpes, CNRS, Grenoble INP, LMGP, F-38000 Grenoble, France

<sup>4</sup>Aichi Synchrotron Research Center, Seto 489-0965, Japan

<sup>5</sup>UVSOR Synchrotron Facility, Institute for Molecular Science, Okazaki 444-8585, Japan

<sup>6</sup>The Graduate University for Advanced Studies, Okazaki 444-8585, Japan

MAX phase compounds, i.e.,  $M_{n+1}AX_n$  where M is a transition metal, A belongs to groups 13-16 and X is the C or N element, have recently been attracted much attention due to their possible application for new class of two-dimensional systems called MXenes by removing A atoms [1]. On the other hand, the bulk electronic structure of MAX phase has been studied mostly by calculations, mainly because of lack of well-established single crystalline samples. In this study, we have performed angle-resolved photoemission spectroscopy (ARPES) on MAX phase compound  $Ti_2SnC$  [2] to directly investigate the electronic structure of this system.

ARPES measurements were performed at the UVSOR-III BL5U. Data were acquired at  $T = 25$  K with  $h\nu = 71.5$  eV which enables us to trace around the  $\Gamma$ KM plane with inner potential of  $V_0 = 10.7$  eV estimated from the photon energy dependent measurement (not shown). With using linear horizontally (LH), vertically (LV) and circularly right (CR), left (CL) polarized photons, we have obtained the orbital and orbital-angular-momentum (OAM) dependent ARPES images. It should be noted that each ARPES images were obtained without changing the photon incident angle relative to the sample surface by utilizing two-dimensional mapping lens mode of MBS A-1 analyzer.

Figure 1 shows the obtained Fermi surface (FS) image on the  $\Gamma$ KM plane (a) compared with the FS topologies calculated by DFT method (b, c). The band structure along the  $\Gamma$ M and  $\Gamma$ K line is shown in Fig. 2 (a) together with the DFT calculation [2]. Six-fold symmetry of hole-pockets  $\alpha$  and  $\beta$  has clearly been observed in consistent with the DFT calculations. In addition, three-fold symmetry around the M point of the small FS  $\gamma$  formed by the electron and hole dispersive feature crossing below the Fermi level along the  $\Gamma$ K line has also been elucidated in Fig.1 (a). Furthermore, we have found that the  $\gamma$  branch has been formed by the Dirac-cone-like dispersive feature along  $k_y$  axis (Figs. 2 (b), (c)). More interestingly, the  $\gamma$  branch shows opposite OAM sign without changing orbital symmetry with respect to the  $\Gamma$ M line. The results indicate the change of chirality of OAM between the two  $\gamma$  branches in Fig. 2 (c). To elucidate the relation between the observed anomalies and the spin-orbit coupling effect, further studies are intended.

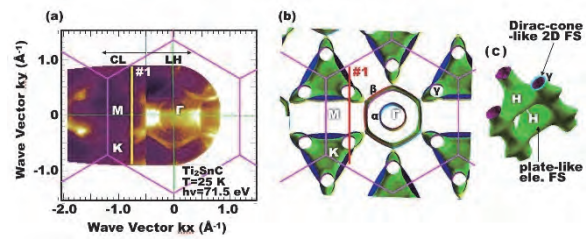


Fig. 1. Fermi surface (FS) image on  $\Gamma$ KM plane of  $Ti_2SnC$  (a). (b,c) FS calculated by DFT shown as projection along the  $[001]$  axis (b) and enlarged FS around the KH axis (c).

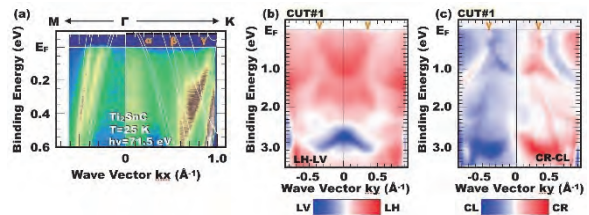


Fig. 2. (a) Band structure along the  $\Gamma$ M and  $\Gamma$ K line of  $Ti_2SnC$  obtained by LH polarized photons. Solid lines are DFT calculation. (b, c) orbital (b) and OAM (c) dependent ARPES image of  $Ti_2SnC$  along the cut#1 ( $k_x = -0.7 \text{ \AA}^{-1}$ ) in Fig. 1., which is obtained by subtracting the ARPES results of linearly (LH–LV) and circularly (CR–CL) polarized photons, respectively.

[1] M. Basoum, MAX phases (Wiley, Weinheim 2013).

[2] J. Y. Wu, Y. C. Zhou, J. Y. Wang, Mat. Sci. Eng. A **422** (2006) 266.

BL5B

## Study on Optical Properties of Metallic Sodium by Vacuum Ultra Violet in UVSOR

M. Kawaguchi<sup>1</sup>, J. Saito<sup>1</sup>, H. Daido<sup>2</sup> and T. Suemoto<sup>3</sup>

<sup>1</sup>Sodium Technology Development Group, Japan Atomic Energy Agency, Tsuruqa 919-1279, Japan

<sup>2</sup>Institute of Laser Engineering, Osaka University, Suita 565-0871, Japan

<sup>3</sup>Toyota Physical and Chemical Research Institute, Nagakute 480-1192, Japan

Metallic sodium (Na) is well-known as a typical alkali metal and very reactive material with oxygen and/or moisture. The physical properties of Na have been researched experimentally and theoretically for a long time [1, 2]. Recently, the paper entitled on “Demonstration of partially transparent thick metallic sodium in the vacuum ultraviolet spectral range [3]” was published by one of the authors (H. D.), and it demonstrated vacuum ultraviolet light (Wave length: 115-180 nm) penetrates in several millimeters of Na with high transmittance for the first time. To elucidate theoretically this mysterious and novel phenomenon, the aim of this research is to obtain the accurate spectrum using BL5B in UVSOR.

Figure 1 shows the outline of the Na sample which was fabricated in glove box of argon gas atmosphere (O<sub>2</sub> concentration: less than 1.0 ppm, Dew point: less than -76 °C) in Sodium Engineering Research Facility (SERF) [4] in Japan Atomic Energy Agency where the R&D programs on the advanced sodium handling technology have been conducted. The Na sample which consisted of the inner and safety cells was designed to improve the safety for the chemical reactivity and to prevent from oxidizing Na surface. The inner and safety cells functioned correctly during transportation from SERF to UVSOR, and Na sample maintained metallic luster. The gas conditions in the both cells were inert argon gas. The ER grade of Na (Na: 99.98%, Ca and K: less than 10 ppm) which was provided from Metaux speciaux was filled between MgF<sub>2</sub> windows in the inner cells by immersion in the liquid Na for high quality. Figure 2 shows the Na sample set up in the chamber of BL5B in UVSOR. The chamber was vacuumed by turbo-molecular pumps during measuring the transmittance.

Now, we started the measurement of the transmittance for the four Na samples using 100-200 nm in wave length: (1) clean MgF<sub>2</sub> windows, (2) MgF<sub>2</sub> windows after immersion in liquid Na, (3) MgF<sub>2</sub> windows + Na (thickness: 0.2 mmt) and (4) MgF<sub>2</sub> windows + Na (thickness: 5 mmt). From the difference of each spectrum, we recognized possibility to occur the intransparent layer for vacuum ultraviolet light on the MgF<sub>2</sub> windows. In the near future, we will improve the Na sample to solve the problems and conduct the measurement again.

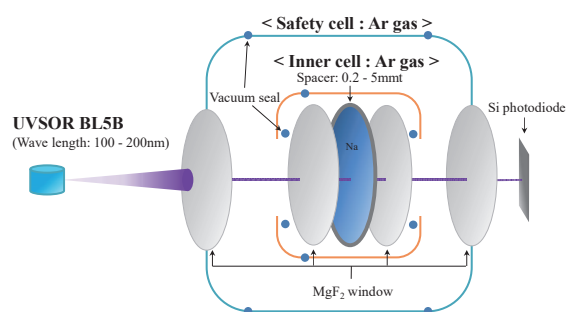


Fig. 1. Outline of the inner and safety cells to prevent oxidizing sodium surface.

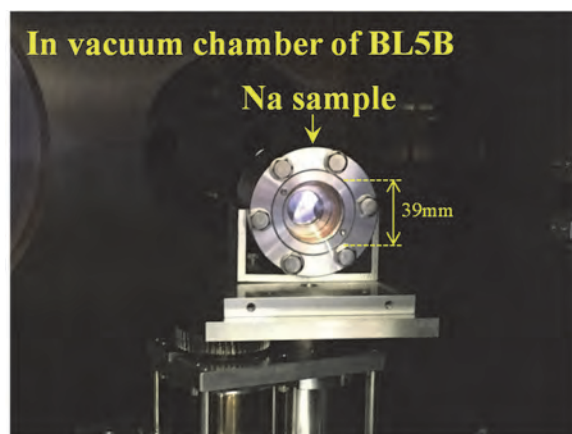


Fig. 2. Na sample (inner and safety cells) set up in the vacuum chamber of BL5B in UVSOR.

[1] J. C. Sutherland *et al.*, Optical properties of sodium in the vacuum ultraviolet (ORNL-TM-1776, Oak Ridge National Laboratory, 1967).

[2] R. W. Wood, Phys. Rev. **44** (1933) 353.

[3] H. Daido *et al.*, Optics express **21** (2013) 28182.

[4]

<https://www.jaea.go.jp/04/turuga/center/fpc/index.htm>.

BL6U

## Orbital Mapping of One-dimensionally Ordered Picene Film on Ag(110)

Y. Yamada<sup>1</sup>, M. Iwasawa<sup>1</sup>, N. Sumi<sup>1</sup>, M. Meissner<sup>2,3</sup>, T. Yamaguchi<sup>3</sup>, S. Kera<sup>2,3</sup> and F. Matsui<sup>2</sup><sup>1</sup>Faculty of Pure and Applied Sciences, University of Tsukuba, Tsukuba 305-8573, Japan<sup>2</sup>UVSOR Synchrotron Facility, Institute for Molecular Science, Okazaki 444-8585, Japan<sup>3</sup>School of Physical Sciences, The Graduate University for Advanced Studies, Okazaki 444-8585, Japan

For an establishment of the state-of-art orbital mapping and orbital tomography, a well-defined molecular layer is surely required for a model system. Especially, the molecular layer with single-domain structure is preferred for the detailed analysis of the angular distribution of the photoelectrons. However, such a film of the small organic semiconductor molecules has been rare, because they usually forms rotational domains even on the single crystalline substrate.

We have recently shown that, by using small organic semiconductor molecules with strong intermolecular interaction such as picene, nicely ordered molecular films can be realized [1, 2]. We have further demonstrated that, using anisotropic surface of Ag(110), a nearly single-domain film of picene can be fabricated [3]. Here, we tried to measure angular dependence of the photoelectron intensity of the single-domain, multilayer film of picene on Ag(110).

The single-domain film of picene were formed by supplying approximately 10 nm of picene on the clean on Ag(110). The thickness of the film was monitored with the quartz microbalance and the film structure were examined in situ by scanning tunneling microscopy (STM) and low-energy electron diffraction (LEED). Photoemission experiments were done at BL6U of UVSOR, equipped with A1 analyzer (MB Scientific) which enables the mechanical deflector scan in the direction perpendicular to the analyzer slit. The intensity mapping was measured with increasing acceptance angle of photoelectrons, by applying potential of 400eV to the mesh electrode in front of the sample. Sample temperature was 15 K.

Figure 1 (a) shows the STM image of the multilayer picene film on Ag(110). It is seen that the multilayer film consists of one-dimensional molecular rows only along [1 -10] direction of the substrate. It is found that the molecular long axis of picene in the 1D row structure is also along [1-10] direction, from the detailed STM image of the row, shown in Fig.1 (b). Therefore, it is considered that the picene film on the Ag(110) surface is suitable for orbital mapping because of the fact that the molecular axis is aligned in one direction. However, we also have to note that the detailed molecular arrangement in the present structure have yet been fully clarified.

Figure 2(a) shows the UPS spectrum of the multilayer picene film on Ag(110). It is seen that HOMO, HOMO-1 and HOMO-2 are close to each other and difficult to distinguish in the spectrum, consistent to the previous reports. However, in the

photoelectron intensity mapping shown in Fig. 2(b), HOMO and HOMO-1 can be well separated; HOMO maxima comes in the direction perpendicular to the molecular axis, while that of HOMO-1 comes direction along the molecular axis. This behavior is consistent with the simple simulation of the photoelectron distribution, by means of FFT of the molecular orbitals as shown in the inset, suggesting that the film is indeed consist of the single domain of picene and that the system is suitable for further detailed measurements and analysis.

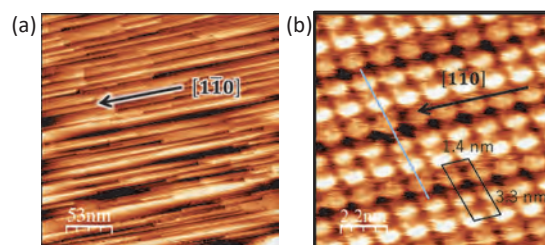


Fig. 1. (a) STM image of picene multilayer film on Ag(110), 200 nm x 200 nm, and (b) a detailed scan.

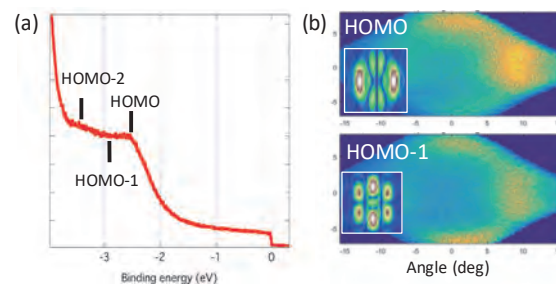


Fig. 2. (a) UPS spectrum of the picene multilayer film on Ag(110) (b) Intensity mapping of HOMO and HOMO-1. FFT of the molecular orbitals are displayed in the inset.

[1] Y. Hasegawa, Y. Yamada, T. Hosokai, Y. Wakayama, K. Rasika, M. Yano and M. Sasaki, *J. Phys. Chem. C* **120** (2016) 21536.

[2] C. Zhang, H. Tsuboi, Y. Hasegawa, M. Iwasawa, M. Sasaki, Y. Wakayama, H. Ishii and Y. Yamada, *ACS Omega*, (in press).

[3] 長谷川友里, 山田洋一, 佐々木正洋, 表面と真空, 2018年61巻6号 p. 366-371.



BL6B

## Analogy of Trapped Electron Centers in Ce:GGG and Ce:LuGG Crystals

T. Yagihashi<sup>1</sup>, M. Kitaura<sup>1</sup>, K. Kamada<sup>2</sup>, S. Kurosawa<sup>2</sup>, S. Watanabe<sup>3</sup>, A. Ohnishi<sup>1</sup> and K. Hara<sup>4</sup>

<sup>1</sup>Faculty of Science, Yamagata University, Yamagata 990-8560, Japan

<sup>2</sup>New Industry Creation Hatchery Center, Tohoku University, Sendau 980-0845, Japan

<sup>3</sup>Graduate School of Engineering, Nagoya University, Nagoya 464-8603, Japan

<sup>4</sup>Research Institute of Electronics, Shizuoka University, Hamamatsu 432-8011, Japan

The nature of shallow electron traps in Ce:Gd<sub>3</sub>Al<sub>5-x</sub>Ga<sub>x</sub>O<sub>12</sub> crystals has been studied so far. Grigorjeva *et al.* have performed luminescence spectroscopy, and tentatively attributed the origin of shallow traps to Ga<sup>2+</sup> ions perturbed by the nearest neighboring Ce<sup>3+</sup> ions [1]. We have carried out infrared absorption spectroscopy, and found two types of shallow electron traps [2]. The one is the antisite Gd<sup>2+</sup> ion adjacent to oxygen vacancies, which is formed in the range of  $x < 3.5$ . The other is of an unknown origin, which is formed in the range of  $x > 3.5$ . The existence of two types of electron traps is likely, because the main component of the conduction band minimum (CBM) is varied from the Gd<sup>3+</sup> 5d state to the Ga<sup>3+</sup> 3s state with increasing  $x$  [3]. The Ga<sup>3+</sup> 3s character in the CBM is common among REGa<sub>5</sub>O<sub>12</sub> (RE=Y, Gd, and Lu). Therefore, it is expected that the electron trap in Ce:GGG is of the same origin as that in Ce:LuGG.

In the present study, we have measured infrared absorption spectra of undoped GGG, Ce:GGG, and Ce:LuGG crystals under irradiation and unirradiation with UV-light. The crystals of Ce:GGG and Ce:LuGG were grown from high-temperature melt by the micro pulling down method. The concentration of cerium ions was set 0.5 mol%. Experiment was performed at the beamline BL6B. The photon energy of the UV-light was 3.31 eV.

Figure 1 shows UV-induced infrared absorption spectra of (a) Ce:GGG and (b) Ce:LuGG crystals, measured at 12 K. The data were obtained by subtracting unirradiated spectra from irradiated spectra. In Fig. 1(a), a mid-infrared (MIR) band appears in the region below 4000 cm<sup>-1</sup>. This band was enhanced by high-temperature annealing under hydrogen atmosphere. In undoped GGG, the MIR band disappeared completely, in contrast with undoped GAGG. These facts suggest that Ce<sup>3+</sup> ions play an important role on the occurrence of the MIR band. In Fig. 1(b), one can see the MIR band below 4000 cm<sup>-1</sup>, almost the same as that in Fig. 1(a). From this result, it is evident that electron traps in Ce:GGG and Ce:LuGG are associated with Ga<sup>3+</sup> ions, but not with Gd<sup>3+</sup> and Lu<sup>3+</sup> ions.

As mentioned above, the CBM is mainly of Ga<sup>3+</sup> 3s state. Generally, the electronic structure of electron traps reflects the CBM character. On this basis, Ga<sup>2+</sup> ions are the most plausible candidate for electron traps in Ce:GGG and Ce:LuGG crystals. As suggested by Grigorjeva *et al.*, the formation of such electron traps

may require the perturbation by Ce<sup>3+</sup> ions in the vicinity of them. This is supported by missing of the MIR band in undoped GGG. The enhancement of the MIR band by high-temperature annealing under hydrogen atmosphere is also explained by the increase in the concentration of Ce<sup>3+</sup> ions. In order to clarify the origin of shallow electron traps responsible for the MIR band, further data by spectroscopy experiment and theoretical calculations are needed.

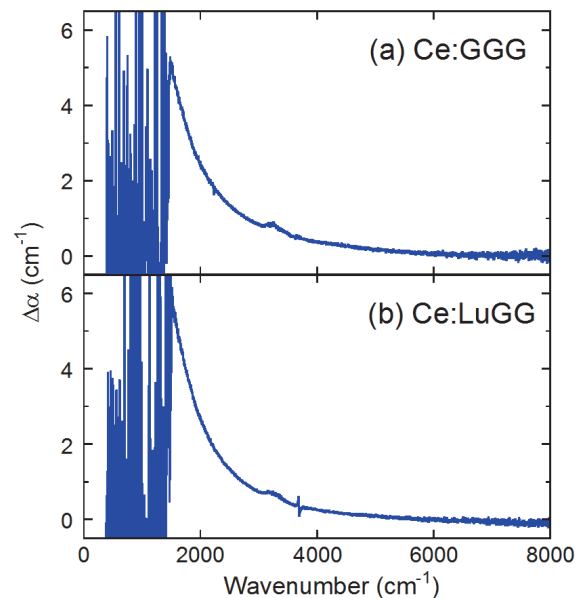


Fig. 1. UV-induced infrared absorption spectra of (a) Ce:GGG and (b) Ce:LuGG crystals measured at 12K.

- [1] L. Grigorjeva *et al.*, *Opt. Mater.* **75** (2018) 331.  
 [2] M. Kitaura *et al.*, *Appl. Phys. Lett.* **113** (2018) 041906.  
 [3] P. Dorenbos, *J. Lumin.* **134** (2013) 310.



BL6B

## Far-Infrared Reflective Analysis for Unipolar Fatigued Piezoelectric Ceramics

H. Nishiyama, D. Xie, R. Hasegawa, S. Maeda, Y. Ito, R. Kimata, N. Nagamatsu, H. Hashimoto and K. Kakimoto

Graduate School of Engineering, Nagoya Institute of Technology, Nagoya 466-8555, Japan

Piezoceramics is widely used in the industry to convert electric energy to mechanical energy. As generally accepted, piezoelectric effect is caused by lattice expansion and domain orientation. The piezoelectric property deteriorates through repeated use, and some researchers attribute this cyclic fatigue to pinning of the domain structure. However, there have been no investigation for the change of the lattice vibration. Although far-infrared reflective (FIR) analysis reveals the lattice vibration and many researchers investigated for single crystal, nobody reports for ceramics due to its complexity of vibration-mode assignment. We have measured FIR spectra for lead-free piezoceramics including alkali niobate perovskite. In this study, we next investigated for BaTiO<sub>3</sub> which has already reported in single crystal [1].

BaTiO<sub>3</sub> ceramics was prepared by conventional solid state sintering. For comparing as-sintered and fatigued samples, unipolar cyclic *E*-field of 100 Hz with a maximum field of 3 kV/mm was applied up to 10<sup>5</sup> cycles. FIR measurement was conducted by a FT-IR spectrometer (Bruker, VERTEX 70v). A beam splitter and a detector used in this measurement were a Mylar 6 μm and a Si bolometer, respectively. Note that aperture diameter was 6 mm and then these were hundred thousands of grains in the spotted area.

Figure 1 shows lattice vibration modes of BaTiO<sub>3</sub> ceramics. From the FIR spectra shown in Figs. 1a and d, imaginary part of permittivity (Figs. 1b and e) was calculated with Drude-Lorentz model [2]. Infrared-active vibration modes of tetragonal perovskite are explained as  $4E + 3A_1$ , but we cannot fit with seven vibration modes for ceramics well because of not only the ratio of the polarization on its surface but also the distribution of the domain width, which can make a deviation of the locations due to internal stress caused by surrounding domain structure. This is why we used plenty number (23 waves) of Lorentz functions for fitting. Imaginary part of permittivity calculated with Drude-Lorentz model was fitted again with Voigt functions to separate overlapping of each peaks (Figs. 1c and f). According to the fitting result for crystal [1], these three peaks were identified *Last*, *Slater*, and *Axe* modes, respectively. Moreover, *Slater* mode in 10<sup>5</sup> cycles shifted higher by 32.2 cm<sup>-1</sup> comparing to the as-sintered one. Here, *Slater* mode locates 34 cm<sup>-1</sup> in a-axis and 280 cm<sup>-1</sup> in c-axis oriented single crystal [1]. Considering a polarization ratio of as-sintered sample should be 2/3 for a-axis and 1/3 for c-axis due to its randomness, the amount of c-axis oriented domain should be increased. In other words, 10<sup>5</sup> cycles applied

BaTiO<sub>3</sub> ceramics became more like c-axis oriented single crystal. In these ways, the change of lattice vibration for unipolar fatigued piezoceramics can be evaluated with FIR analysis.

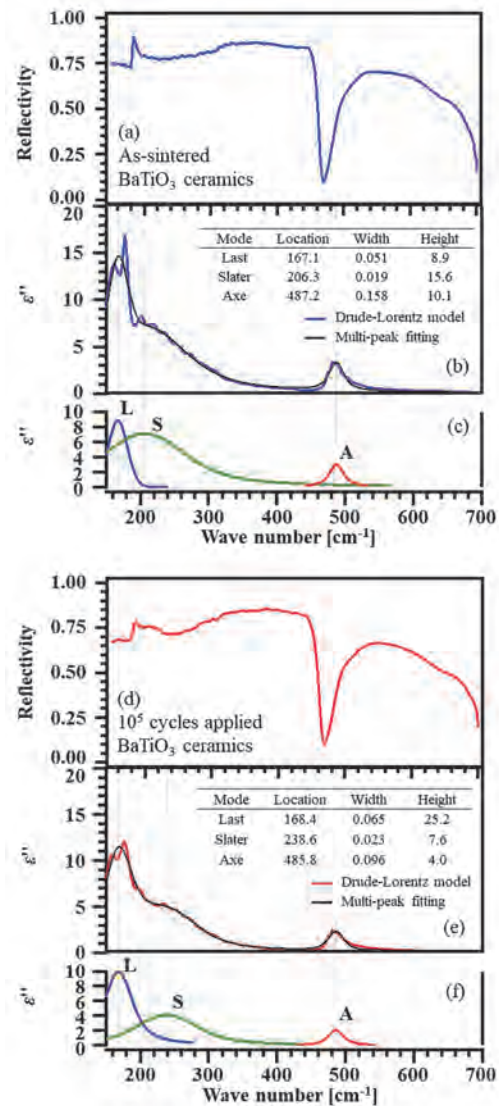


Fig. 1. Lattice vibration modes calculated from FIR spectra of BaTiO<sub>3</sub> ceramics.

[1] T. Hoshina *et al.*, Jpn. J. Appl. Phys. **53** (2014) 09PD03.

[2] H. Nishiyama *et al.*, UVSOR Activity Report 2016 **44** (2017) 84.

BL6B

## Material Control by High Intensity THz Wave and Physical Property Evaluation by Infrared Spectroscopy

A. Irizawa

*The Institute of Science and Industrial Research, Osaka University, Ibaraki 567-0047, Japan*

Optical study is one of the most powerful techniques for investigating electronic states on solids. We can obtain direct of information about the electronic states, a band structure, a symmetry of crystal structure, and a dielectric response of materials. In view of experimental affinity, the optical study is extremely compatible with extreme conditions such as low temperature, high magnetic field, and high pressure, excited state by pumping light, and their combinations. The observation of electronic states can be concluded with only optical operations in contrast with e.g. photoemission spectroscopy. Additionally small sample area and/or convoluted mixed-phase have need of microscopic technique, in such view optical study including infrared spectroscopy is one of the best choice for determining electronic states of materials. Beamline 6B in UVSOR is adjusted for the investigations for optical study in a low-energy region of infrared, i.e. FIR and MIR. In this report, we have performed the optical transmittance measurements in the longest wavelength region. The introduced dry-air system is investigated by check the absorption lines of gas components in the air.

The experiments are performed by using Michelson-type interferometer in MIR region with infrared microscope. Before this experiment, this system was operated in the air without closed atmospheric condition. Otherwise we can get the best condition by using N<sub>2</sub> gas flow with rather quantity, one compressed gas cylinder for 2 days. This time, active-dry air system has been installed for this beamline and the performance was checked by IR spectroscopy. Figure 1 shows the spectra of black-body light source with the atmospheric conditions of open in the air, flowing dried air, and flowing N<sub>2</sub> gas from compressed cylinder with a fine resolution of  $\Delta=1\text{ cm}^{-1}$ . Between 1000 and 2000 cm<sup>-1</sup>, 3000 and 4000 cm<sup>-1</sup>, and 5000 and 6000 cm<sup>-1</sup>, there shows clustered fine absorption lines of the vapor in the air. The atmospheric condition of humidity was around 15 % in the beamline which was not wet condition, but the MIR light was strongly absorbed by vapor in these regions. In case of dried air flow and N<sub>2</sub> gas flow are better than this, except for the absorption line of CO<sub>2</sub> around 2300 cm<sup>-1</sup>, the obtained light source spectra are applicable for estimating the ratio of spectra, i.e. absorptance, transmittance, and reflectance. This improvement must be the advantage for microscopic spectroscopy under extreme conditions including the experiments using organic materials that have absorption lines in an infrared region.

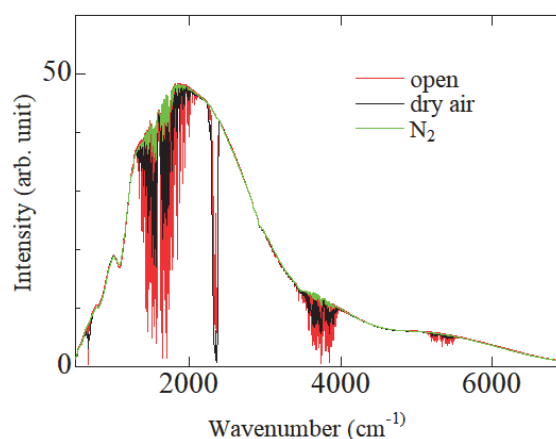


Fig. 1. Spectra of light source with different atmospheric conditions.

BL7U

## High-resolution ARPES Study of Nodal Fermion Materials

T. Sato<sup>1,2</sup>, Z. Wang<sup>3</sup>, K. Nakayama<sup>1</sup>, S. Souma<sup>2,4</sup>, D. Takane<sup>1</sup>, Y. Nakata<sup>1</sup>, K. Hori<sup>1</sup>,  
H. Oinuma<sup>1</sup>, T. Takahashi<sup>1,2,4</sup> and Y. Ando<sup>2</sup>

<sup>1</sup>Department of Physics, Tohoku University, Sendai 980-8578, Japan

<sup>2</sup>Physics Institute II, University of Cologne, 50937 Köln, Germany

<sup>3</sup>Center for Spintronics Research Network, Tohoku University, Sendai 980-8577, Japan

<sup>4</sup>WPI Research Center, Advanced Institute for Materials Research, Tohoku University, Sendai 980-8577, Japan

The search for new types of topological materials hosting nodal fermions is one of the emergent topics in condensed-matter physics. One of the effective strategies to search for nodal fermions is to utilize the point-group symmetries of crystal, i.e., mirror reflection, rotation, and inversion symmetries in addition to time-reversal symmetry, as highlighted by the discovery of topological crystalline insulators hosting the surface nodal fermions protected by mirror reflection symmetry. Recent theoretical studies also predicted that nonsymmorphic space-group symmetry combining point-group symmetry and the fractional translation further enriches the category of nodal fermions. This is demonstrated by the prediction/observation of nodal loops protected by the glide mirror (mirror reflection plus translational) symmetry [1-3], as well as the Weyl nodes in trigonal Te and the nodal lines in ZrSiS, both of which are protected by the screw (rotation plus translational) symmetry [2, 4, 5].

Recently, it was theoretically proposed that the layered ternary telluride Ta<sub>3</sub>SiTe<sub>6</sub> hosts nodal fermions protected by nonsymmorphic glide mirror symmetry [6]. This material crystallizes in the orthorhombic structure with the space group No. 62 (*Pnma*). As shown in Fig. 1(a), the basic structural unit of Ta<sub>3</sub>SiTe<sub>6</sub> is a Te trigonal prismatic slab with Ta atoms located around the center of this prism. Each unit cell contains two such slabs which are overlaid with each other by the inversion operation. First-principles band-structure calculations [6] show that, when the spin-orbit coupling (SOC) is neglected, Ta<sub>3</sub>SiTe<sub>6</sub> displays a fourfold-degenerate nodal line on the SR line in the bulk Brillouin zone [see Fig. 1(b)] due to the protection by glide mirror symmetry. It is also suggested that when the SOC is included, the fourfold degeneracy is slightly lifted and as a result hourglasslike dispersions appear. To examine such intriguing predictions, it is highly desirable to experimentally establish the electronic band structure of Ta<sub>3</sub>SiTe<sub>6</sub>.

In this study, we performed low-energy high-resolution ARPES measurements of Ta<sub>3</sub>SiTe<sub>6</sub> at BL7U, and found a signature of Dirac-like band dispersion protected by the glide mirror symmetry.

Figure 1(c) shows a representative ARPES intensity in the valence-band region of Ta<sub>3</sub>SiTe<sub>6</sub> measured at  $T = 40$  K with  $h\nu = 26$  eV photons. We find several highly dispersive bands within 1 eV of the Fermi level. These

bands mainly originate from the Ta 5*d* orbitals hybridized with the Te 4*p* orbitals. We have also performed detailed three-dimensional *k*-space mapping by tuning photon energy and observed the band degeneracy that which supports the existence of nodal fermions predicted by the calculation.

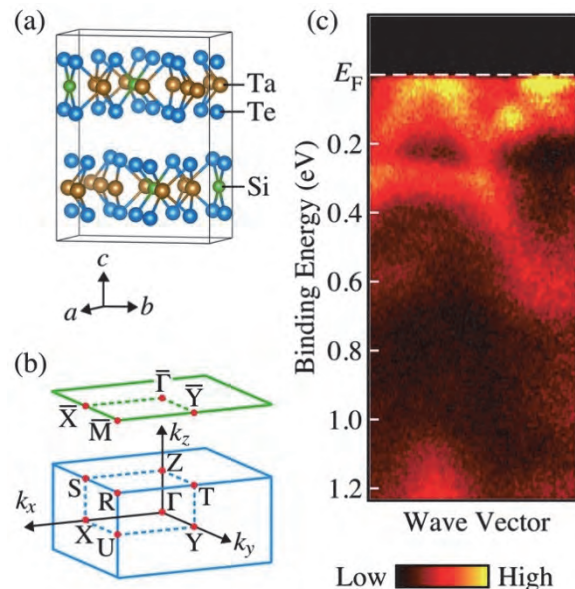


Fig. 1. (a) Crystal structure of Ta<sub>3</sub>SiTe<sub>6</sub>. (b) Bulk orthorhombic BZ (blue) and corresponding surface BZ projected onto the (001) plane (green). (c) ARPES intensity as a function of binding energy and wave vector measured at  $T = 40$  K with linearly polarized 26-eV photons.

- [1] Q. Xu *et al.*, Phys. Rev. B **92** (2015) 205310.
- [2] L. M. Schoop *et al.*, Nat. Commun. **7** (2016) 11696.
- [3] D. Takane *et al.*, Phys. Rev. B **94** (2016) 121108(R).
- [4] C. Chen *et al.*, Phys. Rev. B **95** (2017) 125126.
- [5] K. Nakayama *et al.*, Phys. Rev. B **95** (2017) 125204.
- [6] S. Li *et al.*, Phys. Rev. B **97** (2018) 045131.



BL7U

## Electronic State of the Two-dimensional Transition Metal Chalcogenide Ferromagnets Studied by ARPES

M. Suzuki<sup>1</sup>, B. Gao<sup>2</sup>, K. Koshiishi<sup>1</sup>, C. Lin<sup>1</sup>, Y. X. Wan<sup>1</sup>, M. Kobayashi<sup>3,4</sup>, S. Ideta<sup>5</sup>, K. Tanaka<sup>5</sup>, S.-W. Cheong<sup>2</sup> and A. Fujimori<sup>1</sup>

<sup>1</sup>Department of Physics, The University of Tokyo, Tokyo 113-0033, Japan

<sup>2</sup>Rutgers Center for Emergent Materials and Department of Physics and Astronomy, Rutgers University, Piscataway, New Jersey 08854, USA

<sup>3</sup>Center for Spintronics Research Network, The University of Tokyo, Tokyo 113-0033, Japan

<sup>4</sup>Department of Electrical Engineering and Information Systems, The University of Tokyo, Tokyo 113-8656, Japan

<sup>5</sup>UVSOR Synchrotron Facility, Institute for Molecular Science, Okazaki 444-8585, Japan

Since the discovery of graphene, there has been tremendous interest in the development of new two-dimensional (2D) materials and their functionalities [1]. The materials have layered crystal structures and the layers are bonded to each other through van der Waals (vdW) forces. In addition to graphene and transition-metal dichalcogenides, vdW ferromagnets have recently attracted much attention as candidate materials for new types of spintronic devices.

$\text{Cr}_2\text{Ge}_2\text{Te}_6$  (CGT) and  $\text{Cr}_2\text{Si}_2\text{Te}_6$  (CST) are representative vdW ferromagnets, and along with other vdW ferromagnets, e.g.,  $\text{CrI}_3$ , their electronic and magnetic properties have been studied theoretically and experimentally [2, 3]. The magnetism of CGT nanosheets shows soft behaviors and is well described by the 2D Heisenberg model [4].

To unveil the origin of the ferromagnetism in 2D materials, understanding the physical properties from the electronic structure points of view is important. For both fundamental understanding and potential applications of 2D vdW ferromagnets, the knowledge of the electronic structure of CGT related to the ferromagnetism is indispensable. Therefore, we have conducted angle-resolved photoemission spectroscopy (ARPES) in order to clarify the electronic structure of CGT and CST.

Figures 1(a) and 1(b) show ARPES spectra of CGT obtained by using p- and s-polarizations. The center of the cuts corresponds to the  $\Gamma$  point. One can see that a hole-like band centered at  $\Gamma$  is located at  $\sim 0.2$  eV below the Fermi level and the valence-band maximum does not reach the Fermi level, indicating a semiconducting property, consistent with the electric transport properties [2, 5]. In addition, a similar hole band exists at  $\sim 0.5$  eV below the upper hole band. Photoemission spectra of CGT are shown in Fig. 1(c). Difference between s- and p-polarizations has been clearly observed. Especially, the position of the main peak around 2 eV is shifted between the two polarizations. Since Cr 3d electrons are supposed to form partial density of states (PDOS) around the binding energy of  $\sim 2$  eV, according to first-principle calculation, we consider that the PDOSs of different Cr 3d orbitals have been observed.

On the other hand, for CST, we could not observe any differences as shown in Fig. 1(d). Moreover, its spectral line shape is completely different from that of CGT. However, it is not natural that electronic states of the Cr 3d electrons is dramatically changed by only substituting Si for Ge. Therefore, we consider that the results for CST maybe due to extrinsic effects.

In order to reveal the origin of the ferromagnetism in these materials, further studies are required.

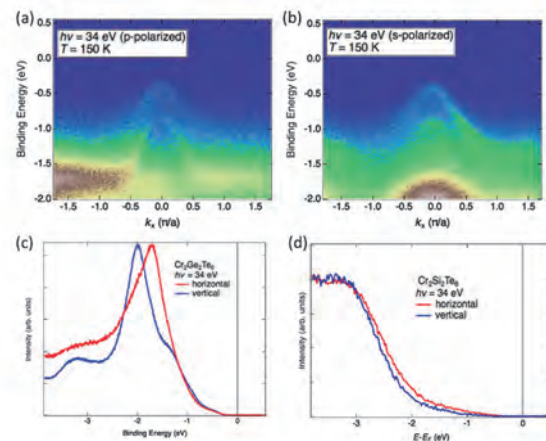


Fig. 1. ARPES spectra of van der Waals ferromagnets. (a), (b) Energy-momentum plots of  $\text{Cr}_2\text{Ge}_2\text{Te}_6$  using p- and s-polarizations. (c) Comparison of the valence-band photoemission spectra of  $\text{Cr}_2\text{Ge}_2\text{Te}_6$  between p- and s-polarizations. (d) Photoemission spectra of the valence band of  $\text{Cr}_2\text{Si}_2\text{Te}_6$ .

- [1] K. S. Novoselov *et al.*, Science **306** (2004) 666.
- [2] X. Zhang *et al.*, Jpn. J. Appl. Phys. **55** (2016) 033001.
- [3] G. T. Lin *et al.*, Phys. Rev. B. **95** (2017) 245212.
- [4] C. Gong *et al.*, Nature **546** (2017) 265.
- [5] H. Ji *et al.*, J. Appl. Phys. **114** (2013) 114907.



BL7U

## Angle-resolved Photoemission Study of Ullmannite NiSbS with the Cubic Chiral Crystal Structure

T. Ito<sup>1,2</sup>, T. Hosoya<sup>2</sup>, M. Nakatake<sup>3</sup>, S. Ideta<sup>4,5</sup>, K. Tanaka<sup>4,5</sup>, M. Kakihana<sup>6</sup>, D. Aoki<sup>7</sup>,  
A. Nakamura<sup>7</sup>, T. Takeuchi<sup>8</sup>, H. Harima<sup>9</sup>, M. Hedo<sup>10</sup>, T. Nakama<sup>10</sup> and Y. Onuki<sup>10</sup>

<sup>1</sup>Nagoya University Synchrotron radiation Research center (NUSR), Nagoya University, Nagoya 464-8603, Japan

<sup>2</sup>Graduate School of Engineering, Nagoya University, Nagoya 464-8603, Japan

<sup>3</sup>Aichi Synchrotron Research Center, Seto 489-0965, Japan

<sup>4</sup>UVSOR Synchrotron Facility, Institute for Molecular Science, Okazaki 444-8585, Japan

<sup>5</sup>The Graduate University for Advanced Studies, Okazaki 444-8585, Japan

<sup>6</sup>Graduate School of Engineering and Science, University of the Ryukyus, Okinawa 903-0213, Japan

<sup>7</sup>Institute for Materials Research, Tohoku University, Ibaraki 311-1313, Japan

<sup>8</sup>Low Temperature Center, Osaka University, Osaka 560-0043, Japan

<sup>9</sup>Graduate School of Science, Kobe University, Kobe 657-8501, Japan

<sup>10</sup>Faculty of Science, University of the Ryukyus, Okinawa 903-0213, Japan

Non-centrosymmetric compounds have attracted much attention due to their interesting phenomena relating with inversion symmetry breaking. The ullmannite type NiSbS with the non-centrosymmetric cubic chiral structure has recently been suggested to be a possible candidate of Weyl semimetal [1]. Indeed, split Fermi surface topologies reflecting the cubic chiral crystal structure and the spin-orbit interactions have been reported [2]. In this study, we have performed angle-resolved photoemission spectroscopy (ARPES) on NiSbS to directly investigate the electronic band structure of this system.

ARPES measurements were performed at the UVSOR-III BL7U. Data were acquired at  $T = 25$  K with  $h\nu = 32$  eV which enables us to trace around the XMR plane with inner potential of  $V_0 = 24.7$  eV estimated from the photon energy dependent measurement (not shown). Clean surfaces were obtained by *in situ* cleaving on (001) plane.

Figure 1(a) shows the obtained Fermi surface (FS) image on the XMR plane compared with the reported FS topologies [2]. The band structure along the XM line is shown in Fig. 2 together with the band calculation [2]. From the present ARPES study, it has been found that the electronic structure of NiSbS seems to be well reproduced by the calculation along the XMR plane. For example, an electron pocket around the X point which touches the Fermi level and then disperses to 0.5 eV around the R point has clearly been observed in Fig. 2. On the other hand, we found non-negligible contributions of the  $\Gamma$ XM plane and the surface states. The bands due to electron (hole) -like FS branch  $\alpha$  ( $\epsilon$ ) appear and merge with the bands along the XR line. This might originate from a large  $k_z$ -broadening effect [3]. In addition, narrow dispersion around 0.5 eV should be assigned as surface states. The results suggest the applicability of ARPES to pursue the Weyl points and node features originating in the chiral crystal structure with great care about bulk sensitivity as well as spin (orbital) -polarizations at the electronic structure.

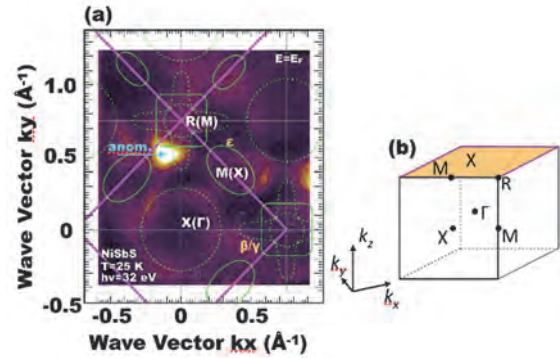


Fig. 1. (a) Fermi surface (FS) image on the XMR plane of NiSbS. Solid and dashed green lines are FS topologies on the XMR and  $\Gamma$ XM plane reported in ref. [2], respectively. (b) Cubic Brillouin zone shown with the momentum axis.

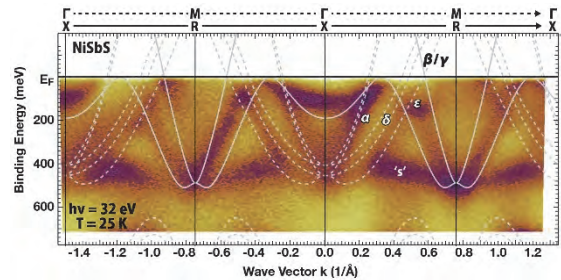


Fig. 2. Band structure image along the XM line of NiSbS. Solid and dashed lines are band calculation along the XR and  $\Gamma$ M lines, respectively [2].

- [1] A. Furusaki, Sci. Bulletin **62** (2017) 788.  
 [2] M. Kakihana *et al.*, J. Phys. Soc. Jpn. **84** (2015) 084711.  
 [3] T. Mitsuhashi *et al.*, Phys. Rev. B **94** (2016) 125148.

BL7U, BL5U

## Direct Observation of the Energy Gap Generation of Ruthenium mono-arsenide RuAs

Y. Nakajima<sup>1</sup>, T. Nakamura<sup>1</sup>, Y. Ohtsubo<sup>2,1</sup>, H. Kotegawa<sup>3</sup>, H. Sugawara<sup>3</sup>, H. Tou<sup>3</sup>  
and S. Kimura<sup>1,2</sup>

<sup>1</sup>Department of Physics, Osaka University, Toyonaka 560-0043, Japan

<sup>2</sup>Graduate School of Frontier Biosciences, Osaka University, Suita 565-0871, Japan

<sup>3</sup>Department of Physics, Kobe University, Kobe 657-8501, Japan

Ruthenium mono-pnictides RuPn ( $Pn = P, As, Sb$ ) have been recently noted in the relation to iron pnictide superconductors. Actually, Rh-doped RuP and non-doped RuSb become superconductor at low temperatures [1]. Other interesting properties are the charge-density wave in RuP [2] and the metal-to-insulator transition (MIT) in RuAs [1]. These phenomena are believed to be related to the origin of the superconductivity, but it is under debate at present [3].

RuAs, which is one of the RuPn family, is being well investigated. The MIT originates from the formation of a superlattice of  $3 \times 3 \times 3$  of the original unit cell [4]. However, the origin of the superlattice formation has not been clarified yet. One possibility is the electronic instability, and the other the lattice distortion owing to the zigzag-chain of Ru site. To clarify the origin of MIT, we are investigating the electronic and the phonon structure as a function of temperature.

According to the electronic band calculations, the density of states (DOS) within the energy of about 0.2 eV from the Fermi level ( $E_F$ ) decreases in the low-temperature insulating (LT) phase from the high-temperature metallic (HT) phase as shown in Fig. 1, even though the finite DOS at  $E_F$  still remains in the LT phase, i.e., no energy gap is expected. However, the optical conductivity spectra as well as the electrical resistivity have suggested that a clear energy gap appears in the LT phase [5]. Then, we have performed the temperature-dependent angle-integrated photoelectron spectroscopy (AIPES) of RuAs to investigate whether the energy gap can be realized at low temperatures or not.

Figure 2 shows the temperature-dependent AIPES spectra divided by the Fermi-Dirac distribution functions for each temperature, which can be compared with DOS. The intensity at  $E_F$  at 280 K (in the HT phase) is almost flat suggesting the constant DOS near  $E_F$ , but it slightly decreases with decreasing temperature to 13 K in the LT phase. The energy at which the divergence starts with decreasing temperature is about 0.15 eV, which corresponds to the energy where DOS changes from the HT phase to the LT phase. Therefore, the change of electronic structure was clearly observed in the AIPES spectra.

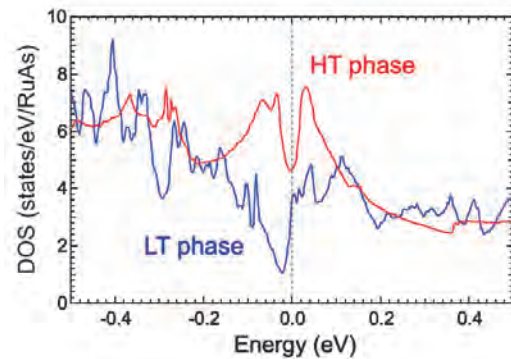


Fig. 1. Density of states (DOS) of RuAs as high-temperature (HT) and low-temperature (LT) phases. The zero energy was set as the Fermi level ( $E_F$ ). The intensity in the energy region within 0.15 eV below and above  $E_F$  decreases from the HT phase to the LT phase, but finite DOS remains even at the LT phase.

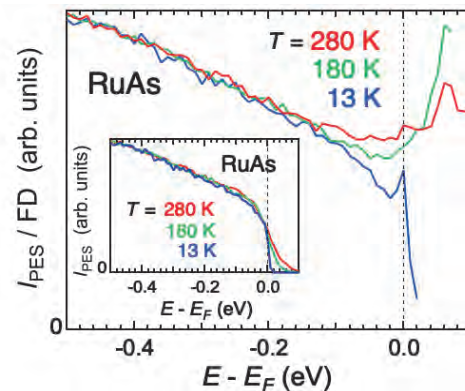


Fig. 2.

Temperature-dependent angle-integrated photoelectron spectra of RuAs divided by the Fermi-Dirac distribution functions (FDs) for each temperature convoluted with a Gaussian function of  $\sigma$  of 10 meV. The excitation photon energy was 20 eV. (Inset) Same as the main figure but without the division of FDs.

- [1] D. Hirai *et al.*, Phys. Rev. B **85** (2012) 140509(R).
- [2] R. Y. Chen *et al.*, Phys. Rev. B **91** (2015) 125101.
- [3] Y. Kuwata *et al.*, J. Phys. Soc. Jpn. **87** (2018) 073703.
- [4] H. Kotegawa *et al.*, Phys. Rev. Mater. **2** (2018) 055001.
- [5] Y. Nakajima *et al.*, UVSOR Activity Report 2017 **45** (2018) 84.

BL7U

## Measurement for the Dispersion of the Excited States in NbSe<sub>2</sub> by Using the Photon-Energy-Dependent ARPES

 S. Tanaka<sup>1</sup> and K. Ueno<sup>2</sup>
<sup>1</sup>The Institute of Industrial and Scientific Research, Osaka University, Ibaraki 567-0046, Japan

<sup>2</sup>Department of Chemistry, Graduate School of Science and Engineering Saitama University, Saitama 338-8570, Japan

The electronic-excitation dynamics of the material is a key issue for understanding and developing the functional optical device. Transition-metal-dichalcogenides (TMDC) attracts interests of many researchers because of its unique 2D character. Here, we report the photon-energy dependent angle-resolved photoelectron spectroscopy (ARPES) of NbSe<sub>2</sub>(2H), which is one of the most studied TMDC, and examine the band-dispersion of the excited state.

All the experiments were carried out at BL7U of the UVSOR-III. The NbSe<sub>2</sub> sample was cleaved in UHV and the photon-energy-dependent ARPES was measured at 10K. The photon intensity was calibrated by the use of the photodiode.

Figure 1 show the two-dimensional photoelectron intensity map of the normal emission as functions of the binding energy and photon energy. Peaks at the binding energy around -1eV clearly show enhancements in intensity at the photon energy of about 9.6eV. This can be attributed to the resonant enhancement when the photon energy matches the energy-difference between the initial (occupied) and final (empty) bands of the photoexcitation. Therefore, the energy position of the excited (empty) bands can be deduced from the photon-energy-dependent measurement since the initial (occupied) band can be determined from the ordinal (non-resonant) ARPES measurement. The Fig. 2(a) shows the ARPES spectrum along the  $\Gamma$ -K line taken at  $h\nu=11.4\text{eV}$ . We focus the two bands indicated as “upper” and “lower” bands in the figure, and measured their intensity as a function of the photon energy. Then the energy is converted as  $E_f(k)=h\nu+E_B(k)$ , where  $E_f(k)$  denotes the final-state-energy at a specific electron momentum of  $k$ ,  $h\nu$  the photon energy and  $E_B(k)$  the binding energy in the negative scale at  $k$ , which can be derived from the dispersion curves [solid lines in Fig.2 (a)]. The results are shown for several momenta in Figs 2(b) and (c) for upper and lower bands, respectively. The intensity distributions can be well represented by the Lorentzian curves whose peak positions change with the electron momenta. These peak positions should indicates the position of the excited (empty) bands into which the photo-excitation occurs from the upper and lower bands in Fig. 2(a). Figures 2(d, e) show intensity maps of the photoelectron peaks as functions of the final state energy with respect the Fermi level and the electron momentum. The peak positions obtained in Figs. 2(b, c) are shown as solid lines, and these are

dispersions of the excited bands of NbSe<sub>2</sub>.

These experimental results are well explained by the comparison to the 1<sup>st</sup> principles band calculation including the analysis of the photoexcitation selection rules based on the band symmetry.

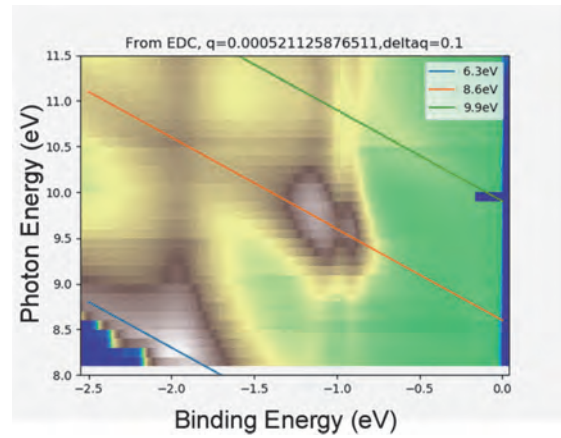


Fig. 1. Photoelectron intensity map of NbSe<sub>2</sub> as functions of photon energy (vertical axis) and binding energy (horizontal axis). Lines indicate the position of the same final state energies.

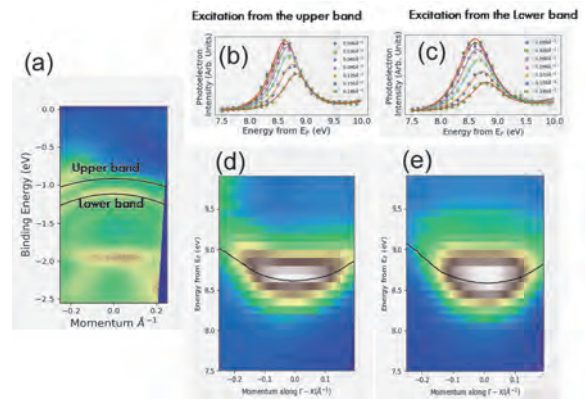


Fig. 2. (a) APRES map of the NbSe<sub>2</sub> at  $h\nu=11.4\text{eV}$ ; (b, c) the intensity of the bands indicated in Fig. 2(a) as a function of the photon energy after the energy conversion; (d, e) the dispersion of the excited state obtained from (b, c).



BL7U

## Temperature Dependence of the Kondo Resonance Peak in Photoemission Spectra of Rare-earth Compound YbMgCu<sub>4</sub>

K. Morikawa<sup>1</sup>, H. Shiono<sup>1</sup>, H. Sato<sup>2</sup>, S. Ideta<sup>3</sup>, K. Tanaka<sup>3</sup>, T. Zhuang<sup>4</sup>,  
K. T. Matsumoto<sup>4</sup>, K. Hiraoka<sup>4</sup> and H. Anzai<sup>1</sup>

<sup>1</sup>Graduate School of Engineering, Osaka Prefecture University, Sakai 599-8531, Japan

<sup>2</sup>Hiroshima Synchrotron Radiation Center, Hiroshima University, Higashi-Hiroshima 739-0046, Japan

<sup>3</sup>UVSOR Synchrotron Facility, Institute for Molecular Science, Okazaki 444-8585, Japan

<sup>4</sup>Graduate School of Science and Engineering, Ehime University, Matsuyama 790-8577, Japan

In rare-earth compounds, the interaction between itinerant conduction and localized-4*f* electrons (*c-f* hybridization) leads to a renormalized quasiparticle. Such a heavy-fermion behavior is characterized by a resonance peak appearing at the energy scales of the Kondo temperature  $T_K$  in electronic excitation spectra. For Yb compounds, the spin-orbit split  $\text{Yb}^{2+} 4f_{7/2}$  state is interpreted as the Kondo resonance peak [1]. The  $\text{Yb}^{2+} 4f_{7/2}$  state near the Fermi level ( $E_F$ ) will provide important clues to the possible mechanism of the heavy-fermion states.

$\text{YbMgCu}_4$  with C15b-type structure is known as a heavy fermion compound with the electronic specific heat coefficient  $\gamma \sim 62 \text{ mJ/K}^2\text{mol}$  [2]. The Kondo temperature is estimated to be  $T_K \sim 855 \text{ K}$  from the magnetic susceptibility measurements [2]. Previous photoemission spectroscopy measurements presented a broad  $\text{Yb}^{2+} 4f_{7/2}$  peak at  $\sim 240 \text{ meV}$ , which deviate considerably from the value of Kondo temperature [3]. To detect the heavy-fermion states in  $\text{YbMgCu}_4$ , it is essential to identify the Yb 4*f* state near  $E_F$ .

Here, we report on a study of the Kondo resonance peak in photoemission spectra of  $\text{YbMgCu}_4$ . The experiments were performed at BL7U of UVSOR. The energy resolution was 16 meV. The samples were cleaved *in situ* and maintained under ultrahigh vacuum ( $8 \times 10^{-9} \text{ Pa}$ ) during the measurements.

Figure 1(a) shows the valence-band spectra at  $T = 8 \text{ K}$ . The spin-orbit splitting of the  $\text{Yb}^{2+} 4f_{7/2}$  and  $\text{Yb}^{2+} 4f_{5/2}$  states are observed at  $|\omega| \sim 0.07 \text{ eV}$  and  $1.36 \text{ eV}$ , respectively [3, 4]. The observability of the  $4f_{7/2}$  state near  $E_F$  is substantially improved by slightly increasing the photon energy from those used in previous studies,  $h\nu \sim 21 \text{ eV}$  [3].

Figure 1(b) shows the temperature dependence of the photoemission spectra near  $E_F$ . We found that a sharp peak of the  $4f_{7/2}$  state survives at even higher temperature,  $T \sim 190 \text{ K}$ , and the peak energy remains unchanged. We determined the peak energies and plotted them as a function of temperature in Fig. 1(c). The peak energy slightly decreases with decreasing temperature from  $T = 187 \text{ K}$  to  $122 \text{ K}$ , and then tends to saturate at low temperatures. The peak energies extrapolated to zero temperature is estimated to be  $\sim 69 \text{ meV}$ . This value corresponds to  $T_K \sim 805 \text{ K}$ , which is approximately consistent with  $T_K$  reported from the magnetic susceptibility measurements [2]. Therefore,

the observed  $4f_{7/2}$  peak can be assigned to the Kondo resonance peak in  $\text{YbMgCu}_4$ . This consistency implies that the observed  $4f_{7/2}$  state in this study is indeed responsible for the heavy-fermion behavior of  $\text{YbMgCu}_4$ .

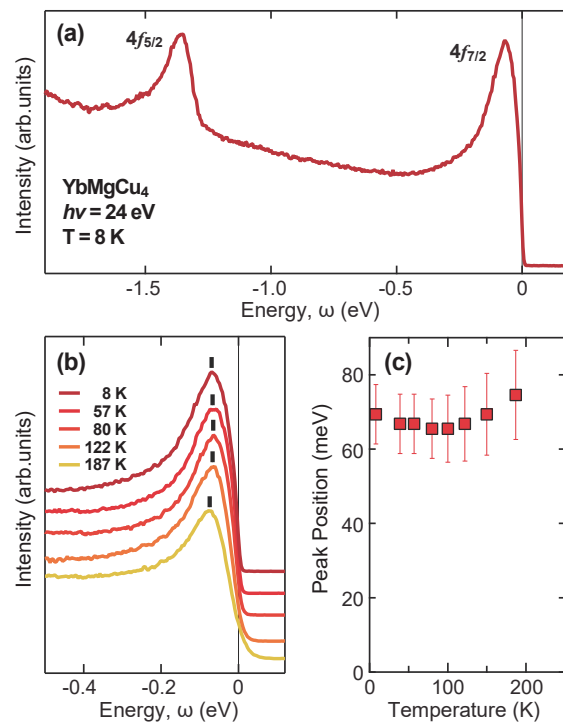


Fig. 1. (a) Valence-band spectra of  $\text{YbMgCu}_4$  taken with photon energy  $h\nu = 24 \text{ eV}$  at  $T = 8 \text{ K}$ . (b) Temperature dependence of the valence-band spectra near  $E_F$ . Vertical bars indicate the peak positions. (c) Energy shift of the  $\text{Yb}^{2+} 4f_{7/2}$  peak in panel (b). The error bars of energies derived from the uncertainty of the peak positions.

- [1] R. I. R. Blyth *et al.*, Phys. Rev. B **48** (1993) 9497.  
[2] J. L. Sarrao *et al.*, Phys. Rev. B **59** (1999) 6857.  
[3] H. Sato *et al.*, J. Synchrotron Rad. **9** (2002) 229.  
[4] F. Reinert *et al.*, Phys. Rev. B **58** (1998) 12808.



BL7U

## ARPES Study of Novel Topological Material Candidates

H. Oinuma<sup>1</sup>, S. Souma<sup>2,3</sup>, D. Takane<sup>1</sup>, T. Nakamura<sup>1</sup>, K. Hori<sup>1</sup>, R. Tsubono<sup>1</sup>, K. Nakayama<sup>1</sup>,  
K. Sugawara<sup>1,2</sup>, T. Takahashi<sup>1,2,3</sup>, A. Ochiai<sup>1</sup> and T. Sato<sup>1,2</sup>

<sup>1</sup>Department of Physics, Tohoku University, Sendai 980-8578, Japan

<sup>2</sup>Center for Spintronics Research Network, Tohoku University, Sendai 980-8577, Japan

<sup>3</sup>WPI Research Center, Advanced Institute for Materials Research, Tohoku University, Sendai 980-8577, Japan

Topological insulators (TIs) are a novel quantum state of matter where gapless edge or surface states (SSs) appear within a bulk-band gap inverted by strong spin-orbit coupling. The SSs of three-dimensional (3D) TIs are characterized by the linearly dispersive Dirac-cone band that can be viewed as a sea of Dirac fermions whose massless nature is guaranteed by the time-reversal symmetry. The search for new topological materials is currently a hot topic in condensed-matter physics.

Recently, it was predicted from the first-principles band-structure calculations [1] that lanthanum (La) monopnictide with rock-salt structure  $LaX$  ( $X = N, P, As, Sb,$  and  $Bi$ ) becomes either topological Dirac semimetal (for  $X = N$ ) or 3D TI (for  $X = P, As, Sb,$  and  $Bi$ ) with Dirac fermions at the surface, due to the band inversion at the X point of bulk fcc Brillouin zone (BZ) [see Fig. 1(a)]. While rare-earth monopnictide  $RX$  ( $R$ : rare earth) was intensively studied in 1980-90's in relation to heavy-fermion physics, this theoretical proposal [1] renewed the interest for  $RX$  in topological aspects and triggered intensive transport, spectroscopic, and theoretical studies. The occurrence of magnetic order in some  $RX$  compounds, e.g., cerium (Ce) monopnictides  $CeX$ , also provides a rare opportunity to investigate the interplay between topological properties and magnetism, which has largely been left unexplored because of the absence of suitable material platform. Therefore, experimental elucidation of the topological properties in  $RX$  compounds is highly desired.

In this study, we performed high-resolution angle-resolved photoemission spectroscopy (ARPES) of  $RX$  family. By utilizing low photon energy and energy-tunable characteristics of BL7U, we determined the bulk and surface band structures and investigated topological properties.

Figures 1(b) and 1(c) show the ARPES spectra measured along a cut crossing the  $\bar{\Gamma}$  point of the surface BZ and the corresponding intensity plot, respectively, obtained in the paramagnetic state of CeBi. We find that at least three hole-like bands cross the Fermi level ( $E_F$ ) near the  $\bar{\Gamma}$  point. Two of them show parabolic dispersions and attributed to the topmost bulk valence bands with the Bi  $6p$  orbital character, consistent with our recent soft-x-ray ARPES measurements on  $RX$  family [5]. The rest hole-like band that shows a linear dispersion is assigned as the topological Dirac-cone SSs with the Dirac point in the close vicinity of  $E_F$ . By performing high-resolution measurements at low

temperatures, we searched for magnetism-induced changes in the topological SSs, and also investigated the topological property of other  $RX$  compounds.

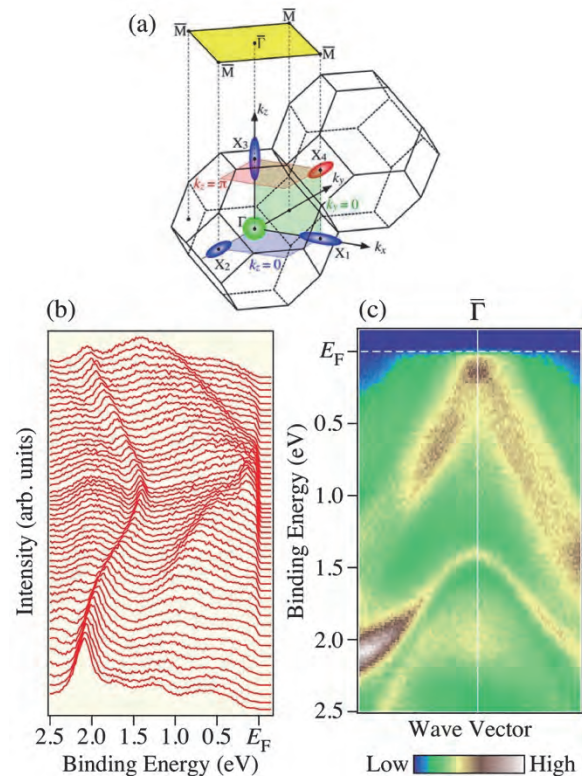


Fig. 1. (a) Bulk and surface BZs with the schematic bulk Fermi surfaces at the  $\bar{\Gamma}$  point (green) and the X point (red and blue). (b) ARPES spectra measured along a momentum cut crossing the  $\bar{\Gamma}$  point of the surface BZ with  $h\nu = 22$  eV. (c) ARPES intensity plot of (b) as a function of binding energy and wave vector.

[1] M. Z. Hasan and C. L. Kane, Rev. Mod. Phys. **82** (2010) 3045.

[2] X.-L. Qi and S.-C. Zhang, Rev. Mod. Phys. **83** (2011) 1057.

[3] Y. Ando, J. Phys. Soc. Jpn. **82** (2013) 102001.

[4] M. Zeng *et al.*, arXiv:1504.03492.

[5] H. Oinuma *et al.*, Phys. Rev. B **96** (2017) 041120(R).

BL7U

## Electronic Structure of Underdoped Triple-layer Cuprate $\text{Bi}_2\text{Sr}_2\text{Ca}_2\text{Cu}_3\text{O}_{10+\delta}$

S. Ideta<sup>1,2</sup>, S. Adachi<sup>3</sup>, N. Sasaki<sup>3</sup>, S. Yamaguchi<sup>3</sup>, T. Watanabe<sup>3</sup> and K. Tanaka<sup>1,2</sup>

<sup>1</sup>National Institutes of Natural Science, Institute for Molecular Science, Okazaki, 444-8585, Japan

<sup>2</sup>The Graduate University for Advanced Studies (SOKENDAI), Okazaki, 444-8585, Japan

<sup>3</sup>Graduate School of Science and Technology, Hirosaki University, Hirosaki 036-8561, Japan

To understand the mechanism of high- $T_c$  superconductivity in cuprates is one of the crucial issues and the energy gap seen in the superconducting (SC) and normal states is believed to be an important piece of evidence for the non-BCS behavior of the SC transition for the underdoped regime in the high- $T_c$  cuprate superconductors. Two different representative energy gaps are present in the SC and normal states, namely, the SC gap and pseudogap in cuprate superconductors [1-3]. Origin of the pseudogap has been considered that it is related to the superconductivity or a phenomenon distinct from superconductivity, and sheds light on its nature to elucidate the mechanism of high- $T_c$  superconductivity.

Triple-layer Bi-based cuprate superconductor,  $\text{Bi}_2\text{Sr}_2\text{Ca}_2\text{Cu}_3\text{O}_{10+\delta}$  (Bi2223), which shows the highest  $T_c$  (110 K) among the Bi-based cuprates, has two inequivalent  $\text{CuO}_2$  planes with different hole carrier [4-6]. In this study, we have investigated the energy gap anisotropy and we found an as-yet-unknown energy gap with a node which is neither the general pseudogap nor the nodeless energy gap in underdoped regime. We observed two bands corresponding to the outer and inner  $\text{CuO}_2$  planes and the hole carrier deduced from the IP and OP FSs suggests that IP is almost zero carrier and OP is underdoped.

High-quality single crystals of underdoped  $\text{Bi}_2\text{Sr}_2\text{Ca}_2\text{Cu}_3\text{O}_{10+\delta}$  (UD Bi2223,  $T_c = 80$  K) were grown by the TSFZ method. Underdoped Bi2223 samples were successfully obtained in the two-step annealing in order to control their doping levels [7]. ARPES experiments were carried out at BL7U of UVSOR-III Synchrotron. Clean sample surfaces were obtained for the ARPES measurements by cleaving single crystals *in-situ* in an ultrahigh vacuum better than  $6 \times 10^{-9}$  Pa. The measurements were performed at 12 K and 95 K.

Figure 1(a) shows the ARPES spectra of UD Bi2223. ARPES intensity mapping integrated within  $\pm 5$  meV centered at  $E_F$  is shown taken at  $h\nu = 18$  eV. Two Fermi surfaces (FSs) are designated as the inner (IP) and outer (OP)  $\text{CuO}_2$  planes reported as previous ARPES studies [4, 5]. The FS momentum ( $k_F$ ) positions for IP (blue dots) and OP (red dots) have been determined by the peak position of momentum-distribution curves in the normal state as shown in Fig. 1(b). The hole carrier for IP and OP deduced from the FS area are 0-2% and 8-10%, respectively, and hence, surprisingly the inner

$\text{CuO}_2$  plane is almost non-doping. To see the momentum dependence of the pseudogap and the SC gap, the energy gap is estimated from the peak position of the energy-distribution curves and plotted as functions of a simple  $d$ -wave order parameter  $|\cos(k_x a) - \cos(k_y a)|/2$  [Figs. 1(c) and 1(d)]. As clearly seen in Fig. 1(c), the energy gap for IP is relatively temperature-independent across  $T_c$  and the FS only remains near node above  $T_c$  as well as that in the SC state. On the other hand, in Fig. 1(d), the energy gaps for OP show a  $d$ -wave-like evolution at 12 K and close the gap and have a Fermi arc around the nodal region at 95 K. To evaluate the validity of the present finding, it is highly desired to demonstrate a further systematic experimental study in the near future.

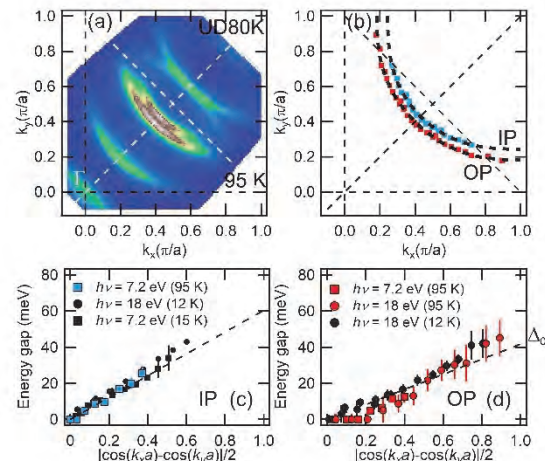


Fig. 1. Electronic structure of underdoped Bi2223. (a) ARPES intensity plots taken at  $T = 95$  K. (b) Fermi momentum plots on the outer (OP) and inner (IP) Fermi surfaces. (c), (d) Temperature dependence of the energy gap for OP and IP plotted as functions of the  $d$ -wave order parameter.

- [1] D. S. Marshall *et al.*, Phys. Rev. B **76** (1996) 4841.
- [2] A. G. Loeser *et al.*, Science **273** (1996) 325.
- [3] H. Ding *et al.*, Nature (London) **382** (1996) 51.
- [4] S. Ideta *et al.*, Phys. Rev. Lett. **104** (2010) 227001.
- [5] S. Ideta *et al.*, Phys. Rev. B **85** (2012) 104515.
- [6] S. Ideta *et al.*, Physica C **470** (2010) S14.
- [7] S. Adachi *et al.*, Physics Procedia **65** (2015) 53.

BL7B

## Photoluminescence and Scintillation of $\text{Rb}_{1-x}\text{Cs}_x\text{CaCl}_3$

K. Takahashi<sup>1</sup>, M. Koshimizu<sup>1</sup>, Y. Fujimoto<sup>1</sup>, T. Yanagida<sup>2</sup> and K. Asai<sup>1</sup>

<sup>1</sup>Department of Applied Chemistry, Graduate School of Engineering, Tohoku University, Sendai 980-8579, Japan

<sup>2</sup>Division of Materials Science, Nara Institute of Science and Technology, Ikoma 630-0192, Japan

Auger-free luminescence (AFL) is caused by the radiative transition of a valence electron to a core hole state. The transition is competitive with the Auger process, which is a much faster process, efficient AFL cannot be observed in many compounds. In other words, efficient AFL has been observed in limited compounds such as alkaline- or alkaline-earth fluorides or CsCl-based compounds.

AFL has been applied to fast scintillators owing to its fast decay. A representative one is  $\text{BaF}_2$ ; however, CsCl-based compounds have an advantage of long emission wavelength appropriate for detection with a photomultiplier tube. Thus far, we have developed fast scintillators based on ternary CsCl-based compounds [1, 2]. In this study, we developed fast scintillators based on quaternary compounds,  $\text{Rb}_{1-x}\text{Cs}_x\text{CaCl}_3$ .

The crystals of  $\text{Rb}_{1-x}\text{Cs}_x\text{CaCl}_3$  was grown in a simple solidification method after heating the mixed raw powders at 400 K to remove the adsorbed water.

Figure 1 shows the X-ray-induced radioluminescence spectra. A prominent band is observed at approximately 450 nm. The excitation spectra for this band exhibited a peak within the band-gap energy of the crystals. Therefore, the band at 450 nm is attributed to the transition at localized levels within the band-gap. Figure 2 shows the X-ray-induced radioluminescence spectra in the UV region. Several emission bands were observed at 250 and 300–400 nm. We obtained the excitation spectra of these bands in the VUV region to discuss the origin of the emission bands. The excitation spectra exhibited a step-like structure at approximately 84 nm, which corresponds to the energy difference between the outermost core level and the bottom of the conduction band. On the basis of this result, the emission bands are attributed to AFL.

Figure 3 shows the pulse-height spectra of the scintillation detectors equipped with the  $\text{Rb}_{1-x}\text{Cs}_x\text{CaCl}_3$  crystals for 662-keV gamma-rays from  $^{137}\text{Cs}$ . Note that the coarse gain (CG) of the main amplifier was different for the  $\text{Rb}_{1-x}\text{Cs}_x\text{CaCl}_3$  crystals and GSO as a reference. Based on the comparison of the full-energy peak channel, the light yields of  $\text{Rb}_{1-x}\text{Cs}_x\text{CaCl}_3$  crystals were estimated to be 520–1200 photons/MeV.

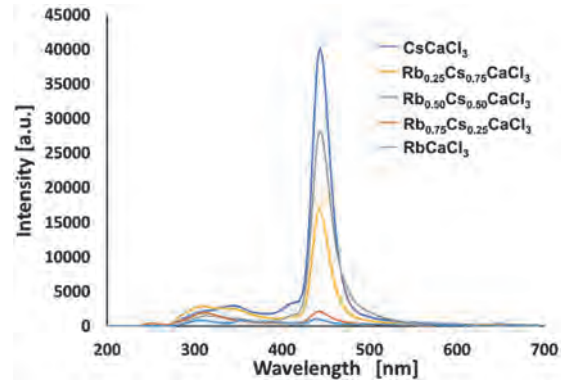


Fig. 1. X-ray-induced radioluminescence spectra of  $\text{Rb}_{1-x}\text{Cs}_x\text{CaCl}_3$  crystals.

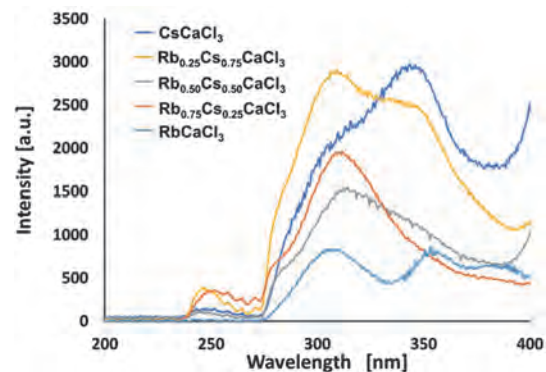


Fig. 2. X-ray-induced radioluminescence spectra of  $\text{Rb}_{1-x}\text{Cs}_x\text{CaCl}_3$  crystals in the UV region.

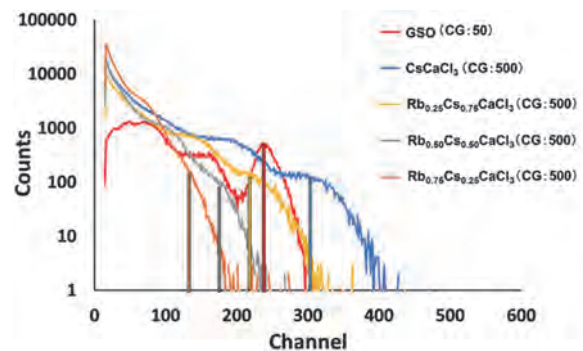


Fig. 3. Pulse-height spectra of the scintillation detectors equipped with the  $\text{Rb}_{1-x}\text{Cs}_x\text{CaCl}_3$  crystals for 662-keV gamma-rays from  $^{137}\text{Cs}$ .

[1] N. Yahaba, M. Koshimizu, Y. Sun, T. Yanagida, Y. Fujimoto, R. Haruki, F. Nishikido, S. Kishimoto and K. Asai, *Appl. Phys. Express* **7** (2014) 062602.

[2] M. Koshimizu, N. Yahaba, R. Haruki, F. Nishikido, S. Kishimoto and K. Asai, *Opt. Mater.* **36** (2014) 1930.



BL7B

## Impurity Luminescences of Bulk and Thin Film AlN

W. Kamihigoshi<sup>1</sup>, Y. Maegawa<sup>1</sup>, K. Fukui<sup>1</sup>, K. Yamamoto<sup>2</sup>, N. Tatemizo<sup>3</sup> and S. Imada<sup>3</sup>

<sup>1</sup>Department of Electrical and Electronics Engineering, University of Fukui, Fukui 910-8507, Japan

<sup>2</sup>Far-infrared region Development Research Center, University of Fukui, Fukui 910-8507, Japan

<sup>3</sup>Faculty of Electrical Engineering and Electronics, Kyoto Institute of Technology, Kyoto 606-8585, Japan

Since AlN has a wide energy band gap of about 6 eV at room temperature, many unintentionally impurity absorption bands are possible in the bandgap. The information in these bands is important for both electrical and optical applications of AlN. Photoluminescence measurement is useful for the study of impurity bands, as the absorption process of these bands often causes a luminescence process. In this report, we focused on the blue - ultraviolet absorption band that makes AlN yellow and the combined excitation emission spectra (CEES) of both bulk crystal and sputtered AlN(film) were measured.

A 0.5 mm thick *c*-plane AlN bulk crystalline substrate (AlN(bulk)) studied in this report was grown in PVT (physical vapor transport) method by CrystaAl-N GmbH. AlN substrate is transparent with yellow dots and has characteristic impurity absorption band of  $\sim 10^{+2}$  cm<sup>-1</sup> from 4.2 eV to 5.2 eV region. The *c*-plane AlN thin film (AlN thin film) was deposited by RF (radio frequency) sputtering on SiO<sub>2</sub> glass, and shows slightly pale yellow color. Film thickness is about 1 μm and there is an absorption band of  $\sim 10^{+4}$  cm<sup>-1</sup> at around same energy region [1]. The CEES measurements were carried out at 10 K, in the order of 10<sup>-6</sup> Pa, and from 2.2 eV to 10.0 eV.

Figure 1 shows the CEES of AlN(bulk) (left) and AlN(film) (right). Each contour plot is normalized at the maximum intensity. Both AlN(bulk) and AlN(film) have similar emission spectra with two peaks at 2.8 eV and around 3.9 eV. However, excitation spectra of the two peaks are different for AlN(bulk) and AlN(film). The CEES of AlN(bulk) is very similar to the results for the AlN(bulk) substrates previously reported by Alden *et al.* [2]. Figure 2 shows the emission spectrum of AlN(bulk) at an excitation energy 4.5 eV. The 3.9 eV emission peak is represented by a single Gaussian fit (UV band), while the 2.8 eV peak is represented by two Gaussian fit (B<sub>H</sub> and B<sub>L</sub> bands). Figure 3 shows integrated excitation spectra of UV, B<sub>H</sub> and B<sub>L</sub> bands. The UV band and the B<sub>H</sub> bands have the same excitation process which is excited only between 4.2 eV and 5.2 eV, but the excitation process of the B<sub>L</sub> band is different and excited up to band gap energy of AlN. On the other hand, both the 2.8 eV and the 3.9 eV peaks of AlN(film) are represented by a single Gaussian fit, and their bandwidth reflecting crystal quality is wider than that of AlN(bulk). Figure 1 suggests that the 2.8 eV peak of AlN(film) is consists only of the B<sub>H</sub> band, since the 2.8 eV excitation spectrum is similar to that of the 3.9 eV peak. Figure 1 also suggests both the UV band and the B<sub>H</sub> bands are

excited above the band gap energy and the excitation spectra of these two bands are similar to the absorption spectrum of AlN. As described above, the absorption coefficient of AlN(film) from 4.2 eV to 5.2 eV is 100 times higher than that of AlN(bulk). This means that in the case of AlN(film), the band-edge tail is able to overlap with this 4.2-5.2 eV absorption band, and the interband transition transfers its energy to both the UV band and the B<sub>H</sub> band emissions.

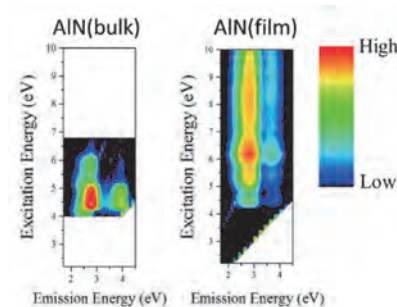


Fig. 1. CEES contour plots of AlN(bulk) and AlN(film).

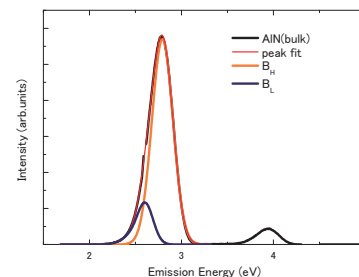


Fig. 2. Emission spectra of AlN(bulk).

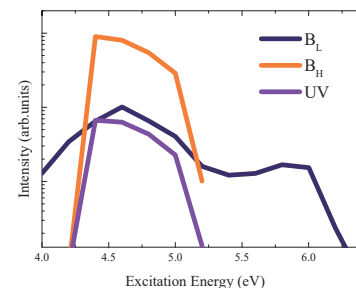


Fig. 3. Excitation spectra of AlN(bulk).

[1] N. Tatemizo *et al.*, *J. Mater. Chem. A* **5** (2017) 20824.

[2] D. Alden *et al.* *Phys. Rev. Applied* **9** (2018) 054036.



BL7B

## Observation of Mott Gap in Pyrochlore Ruthenates $R_2Ru_2O_7$

 R. Kaneko<sup>1</sup>, M. Masuko<sup>1</sup>, R. Yamada<sup>1</sup>, J. Fujioka<sup>2</sup>, K. Ueda<sup>1</sup> and Y. Tokura<sup>1</sup>
<sup>1</sup>Department of Applied Physics, University of Tokyo, Tokyo 113-8656, Japan

<sup>2</sup>Graduate School of Pure and Applied Sciences, University of Tsukuba, Tsukuba 305-8577, Japan

The electronic correlation plays a crucial role on their electronic property in transition metal oxides. A typical example is the Mott transition. Coulomb interaction localizes electrons at each atomic site in a Mott insulator. The effective control of the electron correlation, i.e. bandwidth control, gives rise to a number of exotic phenomena in the vicinity of Mott transitions [1].

The pyrochlore ruthenate  $R_2Ru_2O_7$  (RRO,  $R=Pr, Nd, \dots, Lu$ ) is an insulator which undergoes an antiferromagnetic transition at a low temperature, reminiscent of Mott systems. The effective electronic correlation varies as a change of  $R$  ionic radius through the modulation of Ru-O bond angles which is related to the electron hopping integral (the larger  $R$  gives the smaller  $U_{\text{eff}}$ ). Actually, a specific heat measurement reveals that the Neel temperature  $T_N$ , which is roughly proportional to  $1/U_{\text{eff}}$  in a simple localized-electron picture, increases with an increase of the ion radius of  $R^{3+}$ [2].

What is missing so far is the insight into the electronic band structure. In this experiment, we have aimed to measure optical reflectivity to obtain the optical conductivity which encompasses an important information about the electronic state including the magnitude of the charge gap, interband electronic excitations, and so on.

The optical conductivity can be obtained by Kramers-Kronig (KK) transformation of reflectivity in the whole energy range. Therefore, we measured the reflectivity in a range from 0.01 eV to 5 eV at our laboratory, and from 2 eV to 40 eV at UVSOR. This measurement enables us to discuss the charge dynamics in the energy region of interest. We employed a high-pressure technique for growth of samples which is hard and dense enough to be well polished for the optical measurement.

Figure 1 shows the optical reflectivity for  $R=Pr, Nd, Sm, \text{ and } Y$  compounds. By the KK transformation of the reflectivity, the optical conductivity is obtained as shown in Fig. 2. A charge gap is clearly observed for all samples. We defined the gap size as a value at the crossing point between an energy axis and the extrapolated line from the low-energy slope of each spectrum (dashed lines). The estimated gap size is plotted as a function of the ionic radius of  $R^{3+}$  in Fig. 3. The gap size  $\Delta$  becomes larger as the ionic radius of  $R^{3+}$  decreases, which is consistent with the existing theory. It indicates that the electronic states in the 4d electron system, which is characterized by a weak electron correlation and large spin-orbit coupling compared to those in 3d systems, are mainly governed by the electronic correlation.

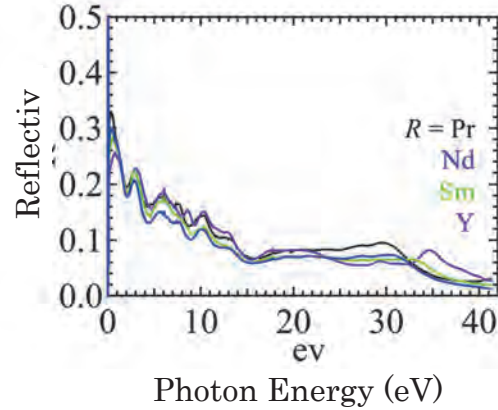


Fig. 1. Optical reflectivity of  $R_2Ru_2O_7$  ( $R=Pr, Nd, Sm, Y$ ) at the room temperature.

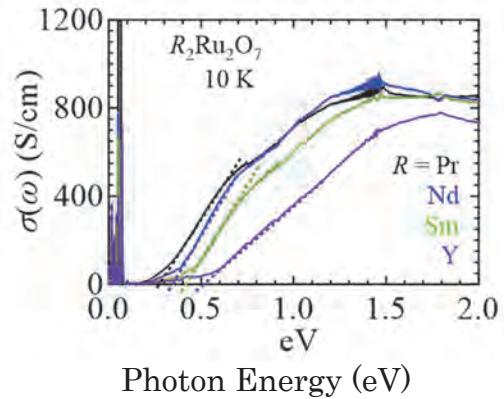


Fig. 2. Optical conductivity of  $R_2Ru_2O_7$  ( $R=Pr, Nd, Sm, Y$ ) at 10 K.

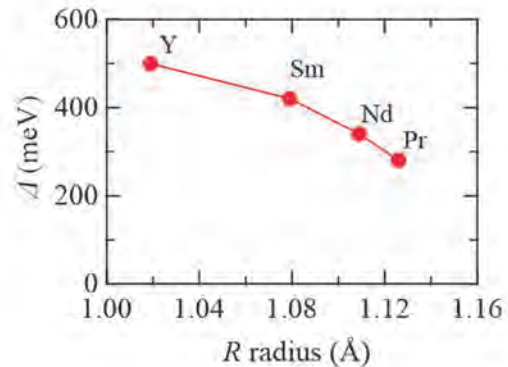


Fig. 3. The magnitude of the charge gap as a function of  $R$  ionic radius.

[1] M. Imada, A. Fujimori and Y. Tokura, Rev. Mod. Phys. **70** (1998) 1039.

[2] M. Ito *et al.*, J. Phys. Chem. Solids **62** (2001) 337.

BL7B

## Evaluation of Electrical Property of CaF<sub>2</sub>-metal Interface and Development of Vacuum Ultraviolet Detector

S. Kato, J. Otani, K. Suzuki and S. Ono

*Nagoya Institute of Technology, Nagoya 466-8555, Japan*

Vacuum ultraviolet light sources are applied in various fields such as surface modification of materials and cleaning of semiconductor substrates. For monitoring such a light source, a detector for stably monitoring vacuum ultraviolet light is required. Therefore, we have focused on the fluoride material which is a wide gap material and has high durability against vacuum ultraviolet light irradiation [1-4]. Using such fluoride material made it possible to develop filterless and durable photodetectors. In this study, we aimed to develop a detector capable of operating at zero bias by selectively bringing the fluoride compound CaF<sub>2</sub> single crystal into contact with metal.

To fabricate the device, a thin film of Au and Al was deposited on both surfaces of a CaF<sub>2</sub> single crystal plate by vacuum deposition method. In order to allow the Au electrode to function as a transparent electrode, the Au electrode was deposited with a thickness allowing vacuum ultraviolet light to pass through (Fig. 1).

In order to investigate a performance of the fabricated device as photodetector, we measured the current value when the device was irradiated with ultraviolet light (photocurrent) and not irradiated (dark current). It was confirmed that the dark current value was about 0.18 pA, the photocurrent value was about 602 pA, and the current value increased more than 3 digits by light irradiation at an applied bias of 100 V. Even at zero bias, the current value increased more than 3 digits by light irradiation. Furthermore, it was confirmed the rectifying property depending on bias direction as shown in Fig. 2.

We measured spectral sensitivity characteristics of the device at zero bias and transmittance of CaF<sub>2</sub> single crystal as shown in Fig. 3. It was confirmed that the wavelength response region of the detector is less than 120 nm and coincide with the transmission end of the CaF<sub>2</sub> single crystal.

In summary, we achieved filterless VUV detector meeting practical performance by applying CaF<sub>2</sub> single crystal and metal interface.

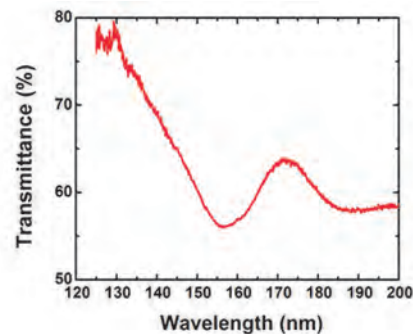


Fig. 1. Transmission spectra of Au electrode.

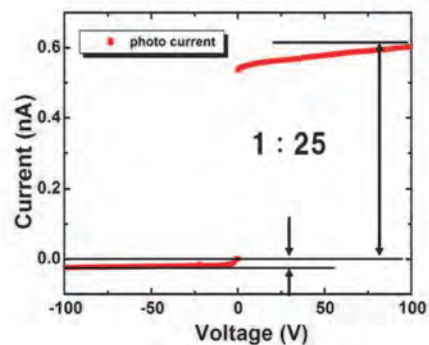


Fig. 2. The rectifying property depending on bias direction.

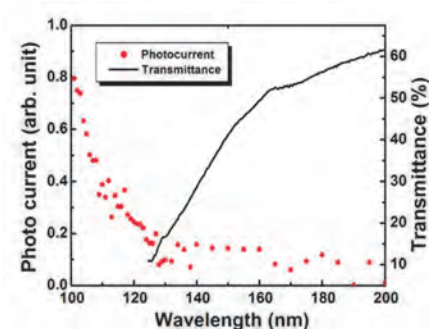


Fig.3. Transmission spectrum and spectral response of the detector.

- [1] M. Ieda, T. Ishimaru, S. Ono, N. Kawaguchi, K. Fukuda, T. Suyama, Y. Yokota, T. Yanagida and A. Yoshikawa, *Jpn. J. Appl. Phys.* **51** (2012) 062202.
- [2] T. Ishimaru, M. Ieda, S. Ono, Y. Yokota, T. Yanagida and A. Yoshikawa, *Thin Solid Films* **534** (2013) 12.
- [3] M. Yanagihara, H. Ishikawa, S. Ono and H. Ohtake, *Testing and Measurement: Techniques and Applications* (2015) 151.
- [4] K. Suzuki, M. C. Raduban, M. Kase and S. Ono, *Optical Materials* **88** (2019) 576.

BL7B

## Optical Study of FeSe Thin Films on LaAlO<sub>3</sub> Substrate

M. Nakajima<sup>1</sup>, K. Yanase<sup>1</sup>, M. Kawai<sup>2</sup>, T. Ishikawa<sup>2</sup>, N. Shikama<sup>2</sup>, F. Nabeshima<sup>2</sup>,  
A. Maeda<sup>2</sup> and S. Tajima<sup>1</sup>

<sup>1</sup>Department of Physics, Osaka University, Osaka 560-0043, Japan

<sup>2</sup>Department of Basic Science, University of Tokyo, Tokyo 153-8902, Japan

In iron-based superconductors, the electronic structure is strongly affected by in-plane strain. In particular, the band structure of FeSe thin films differs from that of bulk FeSe due to the epitaxial strain [1]. The correlation between a superconducting transition temperature ( $T_c$ ) and the magnitude of strain indicates that the band-structure modification definitely altered physical properties [2], but how the electronic state changes with application of strain is still unclear. In this study, we performed optical spectroscopy on thin films of FeSe on LaAlO<sub>3</sub> substrates with a tensile strain and investigated the effect of in-plane strain.

Thin films of FeSe with the thickness of 150 nm were fabricated on LaAlO<sub>3</sub> by the pulsed-laser deposition method [2]. Optical reflectivity measurement was carried out on the FeSe film and the bare LaAlO<sub>3</sub> substrate for the energy range of 0.05–2 eV using the Fourier-transform infrared spectrometer (Bruker Vertex 80v). High-energy reflectivity measurement of LaAlO<sub>3</sub> for 2–40 eV at room temperature was performed at BL7B of the UVSOR synchrotron facility. Dielectric function of LaAlO<sub>3</sub> was derived via the Kramers-Kronig transformation, and the thin-film reflectivity spectrum was fitted using a number of Lorentz oscillators, which gives the dielectric function of FeSe [3].

Figure 1(a) shows the reflectivity spectrum of LaAlO<sub>3</sub> for a wide range of energy up to 40 eV. Three optical phonon modes dominate the low-energy region below 0.1 eV, whereas several peaks associated with interband transitions are present in the high-energy region above 6 eV. In Fig. 1(b), we plot the dielectric function of LaAlO<sub>3</sub> derived from the reflectivity data. The phonon modes are observed at 22.6, 53.0, and 80.8 meV.

The reflectivity spectrum of the FeSe film on LaAlO<sub>3</sub> at room temperature is shown in Fig. 2(a). Due to multiple reflections within the film, the phonon modes of substrate LaAlO<sub>3</sub> makes an impact on the reflectivity spectrum, giving rise to three peaks at corresponding energies. Using the dielectric function of LaAlO<sub>3</sub>, we can remove the substrate contribution and extract the optical conductivity spectrum of FeSe. The result is shown in Fig. 2(b). The peak at 29.6 meV corresponds to an optical phonon mode of FeSe. Compared with the spectrum of FeSe with a compressive strain [3], the low-energy spectral weight is smaller in the present case. The smaller carrier density is likely related to the suppression of  $T_c$ .

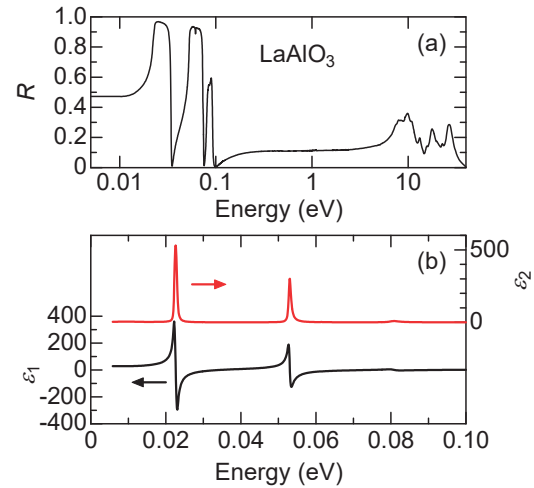


Fig. 1. (a) Reflectivity spectrum of LaAlO<sub>3</sub> at room temperature up to 40 eV. (b) Real and imaginary parts of dielectric function of LaAlO<sub>3</sub> below 0.1 eV.

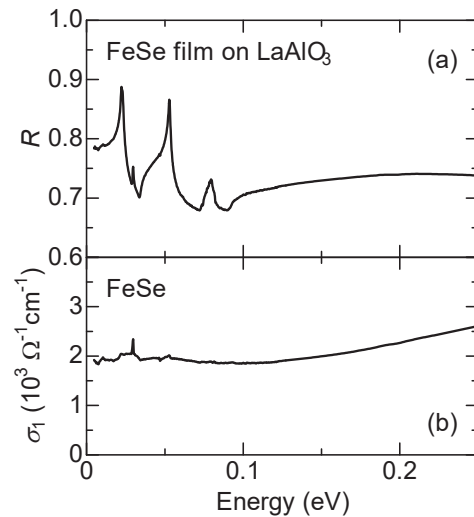


Fig. 2. (a) Reflectivity spectrum of the FeSe thin film on the LaAlO<sub>3</sub> substrate at room temperature. (b) Optical conductivity spectrum of FeSe.

[1] G. N. Phan *et al.*, Phys. Rev. B **95** (2017) 224507.

[2] F. Nabeshima *et al.*, Jpn. J. Appl. Phys. **57** (2018) 120314.

[3] M. Nakajima *et al.*, Phys. Rev. B **95** (2017) 184502.

BL7B

## Optical Investigations of Pr/Ce-doped APLF Glasses as Potential Neutron Scintillators

T. Shimizu, Y. Minami, M. J. F. Empizo, K. Kawano, K. Kuroda, K. Yamanoi, N. Sarukura and T. Murata

*Institute of Laser Engineering, Osaka University, Suita 565-0871, Japan*

Recently, neutron detection is required in inertial confinement fusion research and infrastructure inspection. The ratio of primary neutron and scattered neutron corresponds to the density and radius parameter of fusion plasma. Additionally, neutron detection is considered as one of the nondestructive methods for inspecting the form of infrastructure. Scintillator materials which are able to detect and discriminate neutrons should then be developed to be able to satisfy the technological demand.

Previously, the optical properties of praseodymium ( $\text{Pr}^{3+}$ )-doped and cerium ( $\text{Ce}^{3+}$ )-doped APLF [20Al(PO<sub>3</sub>)<sub>3</sub>-80LiF] glasses was studied as fast response scintillators for neutron detection [1]. The optical properties were characterized using photoluminescence and photoluminescence excitation of the  $\text{Pr}^{3+}$ - and  $\text{Ce}^{3+}$ -doped APLF glass samples for doping concentrations ranging from 0.1 to 3.0 mol%. The APLF glass doped with  $\text{Pr}^{3+}$  revealed rich emission bands under 180, 217, and 430-440 nm excitations. The broad emission from 228 to 371 nm for both excitations were assigned to the interconfigurational 4f5d and intraconfigurational 4f transitions of  $\text{Pr}^{3+}$  ions. The intensity of the emission peaks was observed to increase as a result of increasing  $\text{Pr}^{3+}$  concentration. In contrast, the APLF glass doped with  $\text{Ce}^{3+}$  exhibited intense emission at 340 nm under 240 to 400 nm excitation which originated from the 4f5d transition of  $\text{Ce}^{3+}$  ions. There was no fluorescence from 4f transitions, but the strong emission peak at 340 nm was shifted to shorter wavelengths with decreasing  $\text{Ce}^{3+}$  concentration. The decay times of APLF80+ $\text{Pr}^{3+}$  under 217 nm excitation were constant at different temperatures from 0 K to 300 K and became faster with increased doping concentration from 19 ns (0.5%  $\text{Pr}^{3+}$ ) to 16 ns (3.0%  $\text{Pr}^{3+}$ ). The decay times of APLF80+ $\text{Ce}^{3+}$  glasses were the same in the range from 38 to 41 ns with neutron excitation from a <sup>252</sup>Cf source regardless of Ce concentration. These results highlight that the scintillation decay times from both  $\text{Pr}^{3+}$ - and  $\text{Ce}^{3+}$ -doped APLF glasses are significantly faster than conventional glass scintillators and therefore an advantage for fast-response scintillator applications. Investigation is underway to improve the scintillation decay times and conversion efficiencies by co-doping APLF glass with  $\text{Pr}^{3+}$  and  $\text{Ce}^{3+}$ .

Now, we have developed co-dope APLF glass with Pr

and Ce for improvement of decay times and conversion efficiencies. In this study, we investigated the optical properties of Pr/Ce-doped APLF glasses with different concentrations using the spectroscopy beamline (BL7B) of the Institute of Molecular Science UVSOR Synchrotron Facility. Figure 2 shows the PL spectra of the Pr/Ce-doped APLF glasses. This results are presently under analysis.

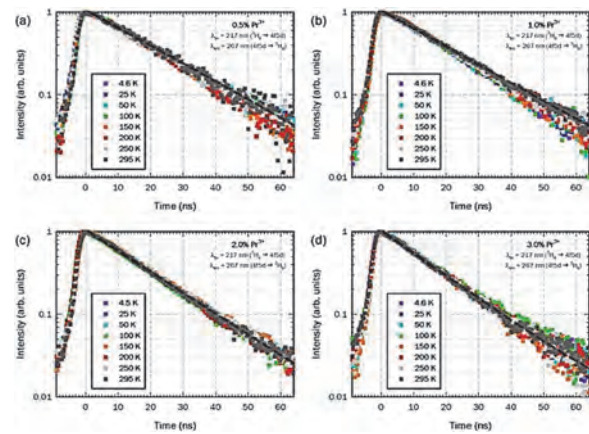


Fig. 1. Decay profiles of the (4f5d → 3H6) emissions of (a) , (b) , (c) , and (d)  $\text{Pr}^{3+}$ -doped APLF glasses at different temperatures under excitation into the 4f5d level [1]

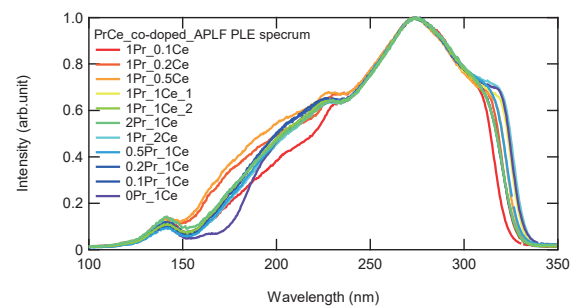
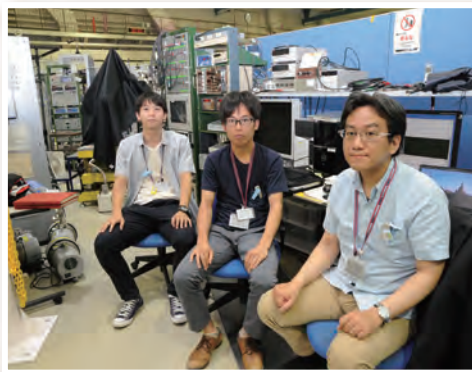
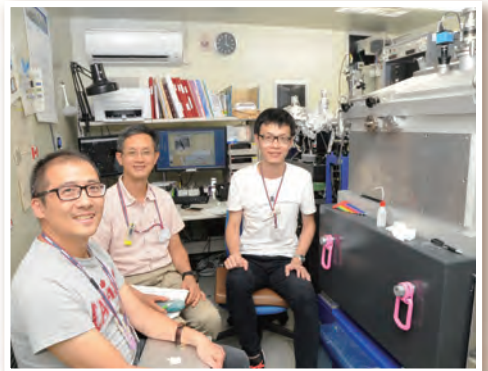
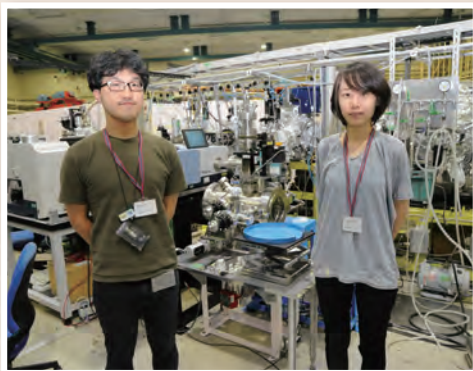
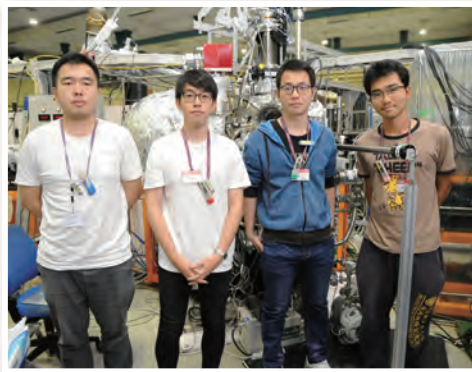
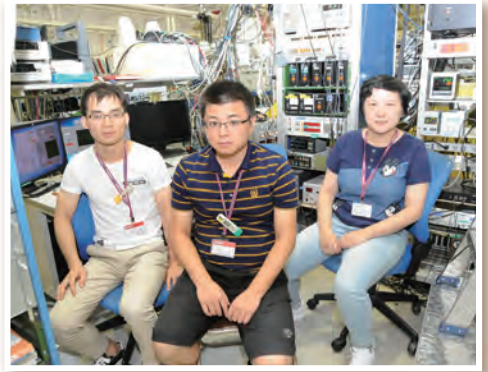
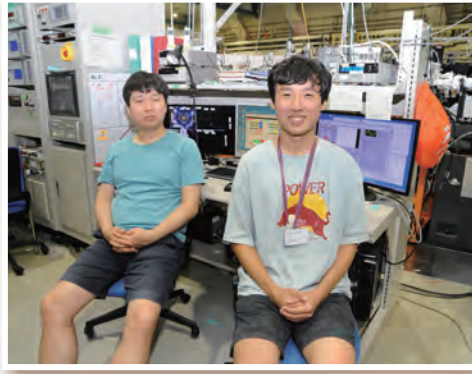
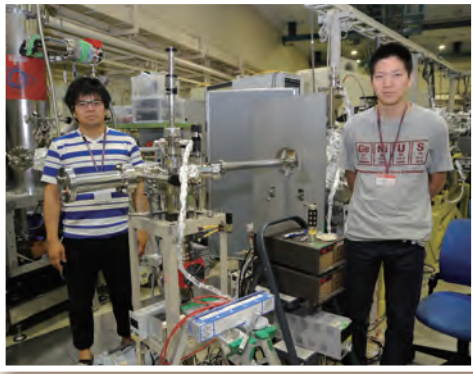


Fig. 2. PLE spectrum of  $\text{Pr}^{3+}$  and  $\text{Ce}^{3+}$  co-doped APLF glass by using UVSOR.

[1] M. J. F. Empizo *et al.*, *J. Lumin.* **193** (2018) 13.



# UVSOR User 3



# III-3

Chemistry





BL1U

## Molecular Orientation Induced by Irradiation Polarized or Optical Vortex Wavelength Selective UV Light to Azo-metal Complexes in Polymer Films

T. Akitsu<sup>1</sup>, S. Yagi<sup>1</sup>, S. Yamazaki<sup>1</sup>, M. Yoshida<sup>1</sup>, T. Haraguchi<sup>1</sup>,  
M. Fujiki<sup>2</sup>, M. Fujimoto<sup>3</sup> and M. Katoh<sup>3</sup>

<sup>1</sup>Faculty of Sciences, Tokyo University of Science, Tokyo 162-8601, Japan

<sup>2</sup>Graduate School of Materials Sciences, NAIST, Nara 630-0192, Japan

<sup>3</sup>UVSOR Synchrotron Facility, Institute for Molecular Science, Okazaki 444-8585, Japan

In recent years, studies on photochemical materials using optical vortex UV light have attracted attention. In contrast to circularly polarized light, a light vortex having a spiral wave front and carrying an orbital angular momentum gives a torque when irradiated on photofunctional materials. In this context, we have attempted molecular orientation control by irradiating linearly and/or circularly polarized (and optical vortex) UV light to polymer films containing (chiral or achiral) dinuclear Schiff base metal complexes [1, 2] with/without azo-dyes exhibiting cis-trans photoisomerization and Weigert effect. Herein, we employed azo-containing mononuclear Schiff base metal complexes (Fig. 1) in PMMA films for molecular orientation phenomenon induced by several types of UV light irradiation.

We prepared them in the common procedures and measured their UV-vis spectra or other data. Among these four complexes, we selected a complex with  $M=Zn(II)$  and  $R=H$  (**PazZn**) appearing intense peak at 380 nm for the following photo-irradiation experiments. We have also checked cis-trans photoisomerization of azo-moiety of ligand by wavelength selective UV light irradiation and Weigert effect, which is linearly polarized light induced anisotropic molecular orientation, and supramolecular chiral arrangement induced by circularly polarized light irradiation.

Based on these experiments using a conventional laboratory light source, the irradiation wavelength of the optical vortex was set to 317 nm,  $\Delta\lambda =$  about 30 nm. Photo-illumination with linearly polarized light (LPL), circularly polarized light (CPL), OV and optical vortex (OV) of UV light was carried out using UVSOR beam line BL1U as listed in Table 1. For example, Fig. 2. depicts typical results of CD spectra.

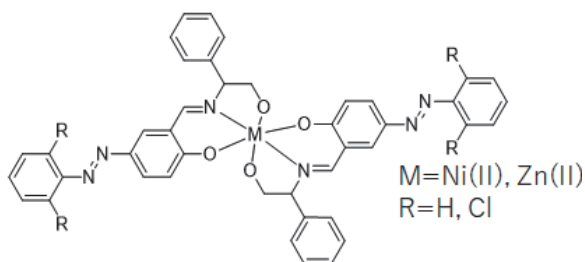


Fig. 1. Molecular structures of metal complexes.

Table 1. Experimental conditions.

	Sample	Light	Time/min	Condensing
1	PazZn	CPL	1	
2	PazZn	CPL	10, 10	
3	PazZn	CPL	10, 65	
4	PazZn	LPL	30	
5	PazZn	CPL	60	
6	PazZn	CPL	60	V
7	PazZn	CPL	60	V
8	PazZn	LPL	180	V
9	PMMA	CPL	60	
10	PazZn	OV	218	
11	PazZn	OV	201, 205	
12	PazZn	OV	267, 195	
13	PazZn	CPL	30, 30	V

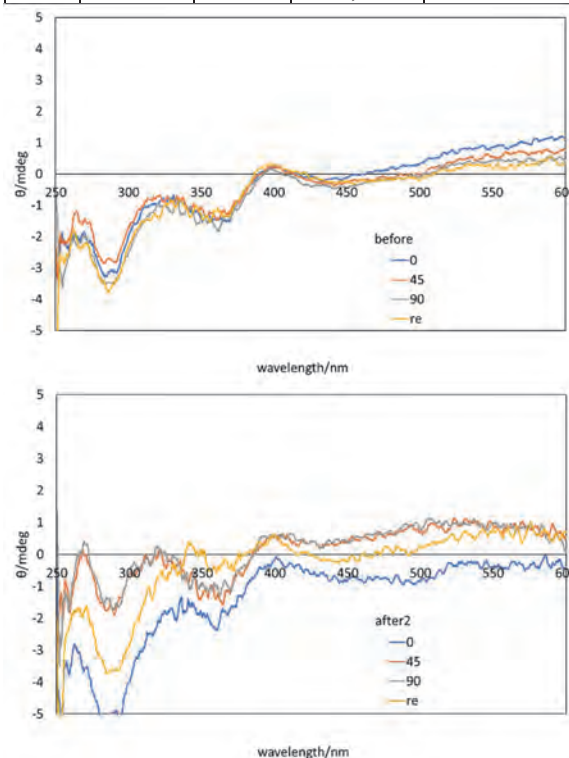


Fig. 2. CD spectra of **PazZn** under the condition 11 after 0 (above) and 205 (below) min.

[1] H. Nakatori, T. Haraguchi and T. Akitsu, *Symmetry* **10** (2018) 147.

[2] M. Takase, S. Yagi, T. Haraguchi, S. Noor and T. Akitsu, *Symmetry* **10** (2018) 760.



BL1U

## Absolute Asymmetric Synthesis with Circularly Polarized Light

J. Yao and C. Yang

Key Laboratory of Green Chemistry & Technology of Ministry of Education, State Key Laboratory of Biotherapy, Sichuan University, Chengdu 610065, China

Circularly polarized light (CPL) is without doubt truly chiral electromagnetic radiation in the sense described above and therefore CPL should in theory be able to induce absolute asymmetric synthesis.[1] We have studied the chiral induction effects of circularly polarized light (CPL) for photo-responsive compounds (Fig. 1). The racemic compounds will be exposure in the CPL and to produce the excess enantiomer by the differential absorption and the process can be detected by CD spectra. We have irradiated 8 samples on these days and the presentationis as follows (Table 1).



Fig. 1. Photo-Responsive Compounds.

Table 1. The Results of CPL Experiments.

Samples	Irradiations	CD spectra
<b>1 (YJB-4-41)</b>	R-CPL 1.6 mW 309 nm 5 min	No signal, Hexane
	R-CPL 1.6 mW 309 nm 35 min	No signal, Hexane (precipitate)
	R-CPL 3.6 mW 359 nm 30 min	No signal, Hexane
	L-CPL 3.6 mW 359 nm 3 min	No signal, Hexane
	L-CPL 3.5 mW 359 nm 10 min	No signal, Hexane
	L-CPL 2.4 mW 359 nm 30 s	No signal, Hexane
	L-CPL 3.5 mW 359 nm 3 min + L-CPL 0.58 mW 510 nm 2 min	No signal, Hexane

Samples	Irradiations	CD spectra
<b>2 (YJB-4-42)</b>	R-CPL 1.6 mW 309 nm 5 min	No signal, Hexane
	R-CPL 3.6 mW 359 nm 20 min	No signal, Hexane
	L-CPL 3.0 mW 359 nm 2 min	No signal, Hexane
	R-CPL 320 nm 3 min	No signal, Hexane
	R-CPL 359 nm 5 min	No signal, Hexane
<b>3 (YJB-4-39D)</b>	R-CPL 1.6 mW 309 nm 5 min	No signal, Hexane
<b>4 (HTT-5B)</b>	R-CPL 2.5 mW 309 nm 5 min	No signal, CHCl <sub>3</sub>
	R-CPL 1.5 mW 280 nm 5 min	No signal, CHCl <sub>3</sub>
<b>5 (HTT-7B)</b>	R-CPL 2.5 mW 309 nm 5 min	No signal, CHCl <sub>3</sub>
<b>6 (ap-BBET)</b>	R-CPL 1.3 mW 280 nm 10 min	No signal, MeCN (color change)
	L-CPL 1.8 mW 280 nm 5 min + L-CPL 0.58 mW 510 nm 7+16 min	No signal, MeCN (color change)
	R-CPL 280 nm 5 min	No signal, MeCN (color change)
<b>7 (Photoreaction)</b>	R-CPL 280 nm 2.5 h + 5.5 h	Unconverted reactants
<b>8 (Photoreaction)</b>	L-CPL 280 nm 3.5 h + 4.5 h	Unconverted reactants

[1] M. Shapiro and P. Brunner, *J. Chem. Phys.* **95** (1991) 8658.

BL3U

## Phase Transitions of Liquid-crystal Materials Studied by X-ray Absorption Spectroscopy

H. Iwayama<sup>1,2</sup>, H. Yuzawa<sup>1</sup> and M. Nagasaka<sup>1,2</sup>

<sup>1</sup>UVSOR Synchrotron Facility, Institute for Molecular Science, Okazaki 444-8585, Japan

<sup>2</sup>School of Physical Sciences, The Graduate University for Advanced Studies (SOKENDAI), Okazaki 444-8585, Japan

In addition to gas, liquid and solid phases, liquid-crystal materials have liquid-crystal phase between solid and liquid phases. In the case of nematic liquid-crystals materials, the rod-shaped organic molecules have no position order, but they self-align to have long-range directional order with their long axes roughly parallel. During a phase transition, certain properties of materials change, often discontinuously, as a result of changes of a local chemical environment. Since X-ray absorption fine structure (XAFS) spectroscopy is sensitive to a local atomic geometry and the chemical state of the atom of one specific element, XAFS spectroscopy is suitable to investigate changes of structures of materials. In this work, we observe discontinuous changes of XAFS spectra for liquid-crystal materials.

Our sample is 4-Cyano-4'-pentylbiphenyl (5cb), which is one of the most popular liquid-crystal materials. A schematic draw of 5cb molecules is shown in Fig. 1. The phase transition temperature of liquid to liquid-crystal and liquid-crystal to solid are 22.5 and 35 °C, respectively. The XAFS measurements were carried out at BL3U [1]. After liquid cell which is composed of two Si<sub>3</sub>N<sub>4</sub> membranes was filled with the liquid sample, the thickness of liquid sample was optimized by controlling the He gas pressure around the cell. The photon energy was calibrated by using the C-K edge XAFS spectrum of the proline thin layer.

Figure 2 shows C K-edge XAFS spectra of 5cb sample at three different temperature, which correspond to liquid, liquid-crystal and solid phases. We observed a strong peak at 285 eV, which correspond to a core excitation of C 1s to  $\pi^*$  orbitals of phenyl group. It seems that the peak at 285 eV has two components, suggesting that  $\pi^*$  orbitals of two benzene rings are different from the viewpoint of binding energies. As shown in Fig.2 intensities of the peak B clearly depend on sample's phases. To evaluate relative intensities of peak B, we performed fitting procedure with using two Gaussian functions.

Figure 3 shows a temperature dependence of peak intensities. We found discontinuous change around 22 °C. This temperature corresponds to the phase transition temperature between solid and liquid-crystal phases. During a phase transition between solid and liquid-crystal, sample lose position order. As a results, local chemical environment change discontinuously. A more detail analysis is now in progress.

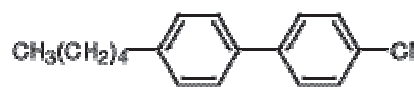


Fig. 1. Schematic draw of 4-Cyano-4'-pentylbiphenyl (5cb) molecules.

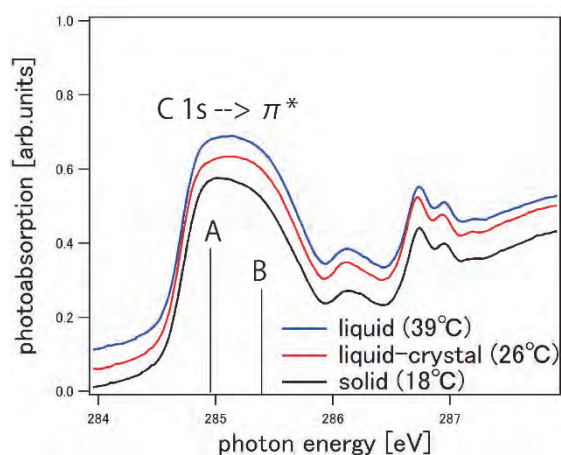


Fig. 2. C K-edge XAFS spectra of 5cb molecules at 18 (solid), 26 (liquid-crystal) and 39 °C (liquid).

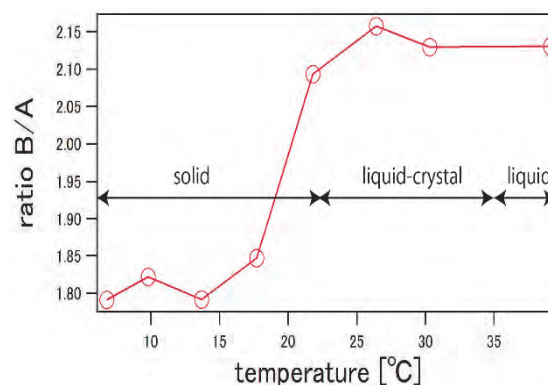


Fig. 3. Temperature dependence of peak B.

[1] M. Nagasaka, H. Yuzawa and N. Kosugi, *J. Spectrosc. Relat. Phenom.* **200** (2015) 293.

BL3U

## Local Structures of Aqueous Acetonitrile Solutions Probed by Soft X-ray Absorption Spectroscopy

M. Nagasaka<sup>1,2</sup>, H. Yuzawa<sup>1</sup> and N. Kosugi<sup>1,2</sup><sup>1</sup>Institute for Molecular Science, Myodaiji, Okazaki 444-8585, Japan<sup>2</sup>The Graduate University for Advanced Studies (SOKENDAI), Myodaiji, Okazaki 444-8585, Japan

Aqueous acetonitrile solution is one of the most basic systems showing the microheterogeneity (MH) state, where two liquids are mixed at macroscopic scale but are not mixed in microscopic scale [1]. It is necessary to observe molecular interactions between acetonitrile and water to discuss the mechanism of the MH state. The previous studies of infrared spectroscopy and X-ray diffraction [2] indicate that acetonitrile molecules form two structures with water: One is hydrogen bond (HB) between N atom of acetonitrile with H atom of water. The other is the dipole (DP) interaction between C≡N group of acetonitrile with water. Recently, Huang *et al.* proposed that the population of DP structure is larger than that of HB structure from O K-edge X-ray absorption spectroscopy (XAS) [3]. However, O K-edge XAS only gives the molecular interactions from the water side. In this study, we have measured XAS of aqueous acetonitrile solutions at both C and N K-edges in order to discuss molecular interactions from acetonitrile side.

The experiments were performed at soft X-ray beamline BL3U. XAS of liquid samples were measured by a transmission-type liquid flow cell [4]. The liquid layers were sandwiched between two 100 nm-thick Si<sub>3</sub>N<sub>4</sub> and SiC membranes for XAS at C and N K-edges, respectively. In order to keep the same X-ray absorbance even at different concentrations, the thickness of the liquid layer was controlled by adjusting the He pressure around the liquid cell.

Figure 1 shows the energy shifts of the C≡N  $\pi^*$  peaks of aqueous acetonitrile solutions at different concentrations  $(\text{CH}_3\text{CN})_x(\text{H}_2\text{O})_{1-x}$  from the neat liquid ( $x = 1.0$ ). In the C K-edge XAS, three concentration regions are found with the borders of  $x = 0.7$  and  $x = 0.2$ . In the acetonitrile-rich region I ( $1.0 > x > 0.75$ ), the  $\pi^*$  peaks in C K-edge shows slightly lower energy shifts by increasing molar fraction of water, and suddenly shows a higher energy shift at  $x = 0.7$ . On the other hand, the  $\pi^*$  peaks in N K-edge show higher energy shifts and show no phase transition-like behavior at  $x = 0.7$ . In the region II ( $0.7 > x > 0.25$ ), the energy shifts of the  $\pi^*$  peaks in both C and N K-edges are gently increased. Note that this concentration region shows the MH behavior [1]. In the water-rich region III ( $0.2 > x > 0.05$ ), the slope of the energy shifts in C K-edge is rapidly increased whereas that in N K-edge is not changed.

We have performed inner-shell calculations of acetonitrile-water mixtures to discuss local structures of acetonitrile at different concentrations in terms of the energy shift in C and N K-edges. As a result, isolated

water molecules disturb the interaction between acetonitrile molecules in the region I. The acetonitrile clusters are surrounded by water molecules with the DP interactions between acetonitrile and water in the region II. Small acetonitrile clusters form the HB interactions with water in the HB network of water in the region III. Since the DP interaction is abundant in the region II, the DP interaction is a key factor to form the MH state in aqueous solutions.

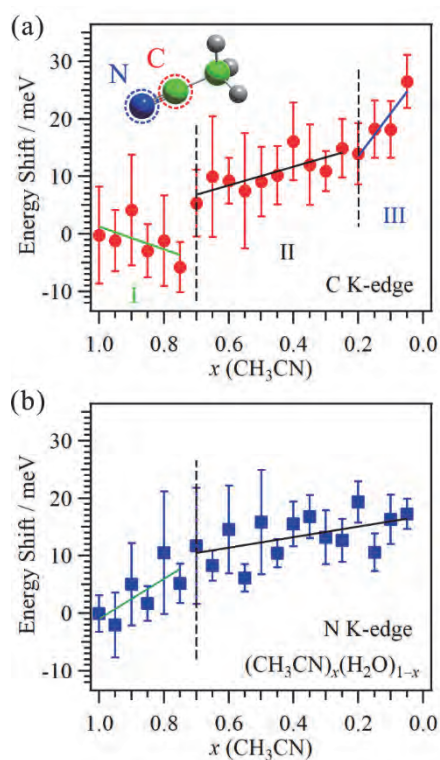


Fig. 1. Energy shifts of the peaks in XAS of aqueous acetonitrile solutions  $(\text{CH}_3\text{CN})_x(\text{H}_2\text{O})_{1-x}$  relative to the peak of neat liquid ( $x = 1.0$ ) at (a) C and (b) N K-edges. Three concentration regions are found with the borders of  $x = 0.7$  and  $x = 0.2$ .

- [1] Y. Marcus, *J. Phys. Org. Chem.* **25** (2012) 1072.  
 [2] T. Takamuku *et al.*, *J. Phys. Chem. B* **102** (1998) 8880.  
 [3] N. Huang *et al.*, *J. Chem. Phys.* **135** (2011) 164509.  
 [4] M. Nagasaka *et al.*, *J. Electron Spectrosc. Relat. Phenom.* **224** (2018) 93.



BL3U

## Effect of Salt Addition on the Electronic Structure of the Hydrated Water of Glycine Betaine Studied by Soft X-Ray Absorption Spectroscopy

S. Ohsawa<sup>1</sup>, N. Fukuda<sup>1</sup>, H. Iwayama<sup>2,3</sup>, H. Yuzawa<sup>2</sup>, M. Nagasaka<sup>2,3</sup> and K. Okada<sup>1</sup><sup>1</sup>Graduate School of Science, Hiroshima University, Higashi-Hiroshima 739-8526, Japan<sup>2</sup>Institute for Molecular Science, Okazaki 444-8585, Japan<sup>3</sup>School of Physical Sciences, The Graduate University for Advanced Studies (SOKENDAI), Okazaki 444-8585, Japan

Most living cells adapt to various environments, such as drought and high salinity, by regulating the concentration of solutes termed osmolytes [1], because an increase in extracellular salinity can cause water efflux and cell shrinkage. Among the most common organic osmolytes is glycine betaine, which is a zwitterionic quaternary ammonium species with  $pK_a = 1.84$ . Its accumulation occurs either by synthesis from choline or by transport from extracellular pools [2]. The amount of glycine betaine has been found to correlate with external salinity for several shoots of halophytes [3] and for halophilic eubacteria [4]. Altering the hydration structure of glycine betaine with the salt concentration presumably plays an important role in protecting the secondary structure of proteins, but the details of interactions of the osmolyte with surrounding water along with salt ions are not yet fully understood.

Photoabsorption spectra at the oxygen K-edge were measured in the transmission mode at room temperature. Aqueous solutions of glycine betaine, sodium chloride, and mixed glycine betaine and sodium chloride were introduced with a tubing pump system into a liquid flow cell installed on the soft X-ray beamline BL3U. The flow cell for this study was equipped with a pair of windows made of thin silicon nitride membrane. Further details of the cell were given elsewhere [5]. The incident photon energy was calibrated to the peak at 530.88 eV of a polymer film [6].

The measured absorption spectra vary from solution to solution. Figure 1 displays the O 1s absorption spectra of glycine betaine, sodium chloride, their mixed aqueous solutions, and liquid water. The broken vertical line corresponds to the resonance energy of the  $4a_1 \leftarrow O\ 1s$  transition of bulk water located at 534.6 eV. For solutions containing glycine betaine, another broad peak appears around 532.2 eV. Because its intensity depends on the osmolyte concentration, the peak is safely assigned to  $\pi^*_{COO} \leftarrow O\ 1s$  of glycine betaine.

The resonance peak top of water is shifted by  $-0.05$  and  $+0.09$  eV for glycine betaine and sodium chloride solutions, respectively. The shift is caused by the change of chemical environment around water. The red shift seen for the glycine betaine solution can be ascribed to the gain of partial negative charge on the oxygen atom of water by making a strong hydrogen

bond with the carboxylate site of glycine betaine.

For the mixed aqueous solutions, an apparent blue shift can be seen for the spectra of samples with the salt concentration greater than or equal to the osmolyte concentration. This observation can be described by the interpretation that the salt is exclusively bound to glycine betaine, and thereby reveals the role of the osmolyte when living cells are exposed to salinity.

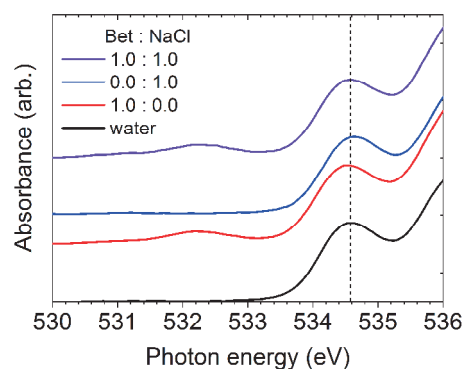


Fig. 1. Enlarged O 1s photoabsorption spectra in the 530–536 eV region of glycine betaine (Bet), sodium chloride, their mixed aqueous solutions, and liquid water. The concentration of each solute is 1.0 mol/L.

- [1] P. H. Yancey, M. E. Clark, S. C. Hand, R. D. Bowlus and G. N. Somero, *Science* **217** (1982) 1214.  
 [2] L. N. Csonka, *Microbiol. Rev.* **53** (1989) 121.  
 [3] R. Storey and R. G. Wyn Jones, *Plant Sci. Lett.* **4** (1975) 161.  
 [4] J. F. Imhoff and F. Rodriguez-Valera, *J. Bacteriol.* **160** (1984) 478.  
 [5] M. Nagasaka, T. Hatsui, T. Horigome, Y. Hamamura and N. Kosugi, *J. Elec. Spectrosc. Relat. Phenom.* **177** (2010) 130.  
 [6] M. Nagasaka, H. Yuzawa, T. Horigome and N. Kosugi, *J. Elec. Spectrosc. Relat. Phenom.* **224** (2018) 93.

BL3U

## X-ray Absorption Measurements Applied to Aqueous Solutions of Glycine at Various pHs, in the Vicinity of the O K-edge Ionization Thresholds

D. Céolin<sup>1</sup>, T. Saisopa<sup>2</sup>, K. Klaipheth<sup>2</sup>, P. Songsiriritthigul<sup>2</sup>, H. Yuzawa<sup>3</sup>, M. Nagasaka<sup>4</sup> and N. Kosugi<sup>4,5</sup>

<sup>1</sup>Synchrotron SOLEIL, L'Orme des Merisiers Saint-Aubin BP 48 91192 Gif-sur-Yvette Cedex, France

<sup>2</sup>Research Network NANOTECH-SUT on Advanced Nanomaterials and Characterization and School of Physics, Suranaree University of Technology, Nakhon Ratchasima 30000, Thailand

<sup>3</sup>UVSOR Synchrotron Facility, Institute for Molecular Science, Okazaki 444-8585, Japan

<sup>4</sup>Institute for Molecular Science, Okazaki 444-8585, Japan

<sup>5</sup>Institute of Materials Structure Science, KEK, Tsukuba 305-0801, Japan

Glycine, the simplest amino acid, is involved in a variety of physiological processes, such as e.g. neurotransmitter in the central nervous system, and is commonly found as a protein precursor. Gas-phase glycine has a neutral form  $\text{H}_2\text{N}-\text{CH}_2-\text{COOH}$  whereas in aqueous solution its structure differs depending on the pH. For pH in the range 2.4-9.6, the zwitterionic form  $^+\text{H}_3\text{N}-\text{CH}_2-\text{COO}^-$  dominates. In acidic medium below pH = 2.4, the protonated form  $^+\text{H}_3\text{N}-\text{CH}_2-\text{COOH}$  is the main one, whereas in basic medium above pH = 9.6, the deprotonated form  $\text{H}_2\text{N}-\text{CH}_2-\text{COO}^-$  prevails (see Fig. 1).

Among our measurements performed at the beamline BL3U using the liquid cell in transmission mode, we obtained the absorption spectra of glycine in aqueous solution at different pH, at a concentration of 0.5 M, and in the vicinity of the O K-edge ionization threshold (see Fig. 2). The idea was to collect spectra in a larger energy window than in the reference [1].

The resonance located at  $h\nu = 535$  eV is associated with the oxygen 1s electron excitation of water to its first empty orbital. On the left side of this structure, we confirm the presence of smaller resonances attributed to the excitation of an oxygen 1s electron of the carboxyl/carboxylate groups of solvated glycine. The  $\text{O}1s \rightarrow \pi^*$  excitation of  $-\text{COO}^-$  leads to a maximum located at 532.75 eV, whereas for  $-\text{COOH}$  the maximum is found at 532.45 eV. For this latter, only the transition involving the  $\text{C}=\text{O}$  group is visible. The one corresponding to the  $-\text{OH}$  excitation is located at a photon energy close to the one of water and is thus not detected in our spectra.

Contrary to the observations presented in reference [1], due to a reduced statistic, we do not highlight a clear asymmetry of the low energy resonance in the acidic solution. However, we can extract some additional information such as the  $-\text{COO}^-/-\text{COOH}$   $\text{O}1s \rightarrow \pi^*$  widths (Gaussian FWHM): 0.85 eV for pH = 1, 1.21 eV for pH = 7 and 1.25 eV for pH = 12, and the corresponding relative areas: 0.52 for pH = 1, normalized to 1 for pH = 7, and 0.77 for pH = 12. Considering that the  $-\text{OH}$  part of the carboxylic group do not resonate in this photon energy region, the lower intensity of the 1<sup>st</sup> structure for the acidic solution is

not surprising. Furthermore, the larger contribution of the same resonances for the two other solutions is due to the possibility of exciting two oxygens instead of only one. Also, the overlap with the 2<sup>nd</sup> large resonance having a maximum at 535 eV increases the uncertainty of the areas estimate especially for the solutions at pH = 7 and 12 since they are located closer in photon energy.

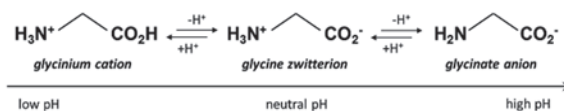


Fig. 1. Structure of glycine in aqueous solution for various pH regions (acidic, neutral, basic).

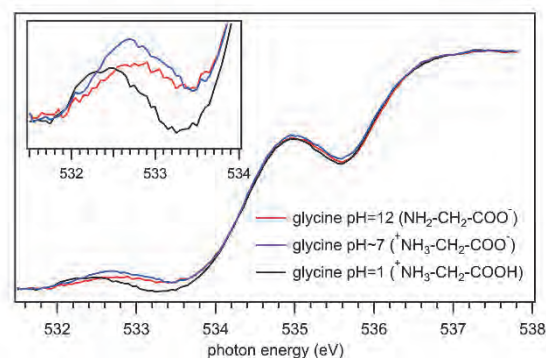


Fig. 2. Normalized X-ray absorption spectra of solvated glycine, recorded for various solutions pH.

[1] B. M. Messer, C. D. Cappa, J. D. Smith, K. R. Wilson, M. K. Gilles, R. C. Cohen and R. J. Saykally, *J. Phys. Chem. B* **109** (2005) 5375.

[2] M. L. Gordon, G. Cooper, C. Morin, T. Araki, C. C. Turci, K. Kaznatcheev and A. P. Hitchcock, *J. Phys. Chem. A* **107** (2003) 6144.

BL3U

## In situ O K-edge X-ray Absorption Spectrum Study of a-Si/SEI in Photocatalytic Water Splitting

J. Ma<sup>1</sup>, H. Yuzawa<sup>2</sup>, H. Ju<sup>1</sup> and R. Long<sup>1</sup>

<sup>1</sup>Hefei National Laboratory for Physical Sciences at the Microscale, iChEM (Collaborative Innovation Center of Chemistry for Energy Materials), School of Chemistry and Materials Science, and National Synchrotron Radiation Laboratory, University of Science and Technology of China, Hefei, Anhui 230026, China

<sup>2</sup>UVSOR Synchrotron Facility, Institute for Molecular Science, Okazaki 444-8585, Japan

Amorphous Si/SEI (a-Si/SEI) nanowire arrays was fabricated and both activity and durability of silicon material for photocatalytic water splitting can be dramatically enhanced. The Si nanoarrays were first loaded in a battery cell, then facilely engineered into active and durable structures, during which lithiation amorphizes silicon and forms a surface protection layer. The photocatalytic hydrogen production was conducted to assess the performance of the as fabricated Si NWs for photocatalytic hydrogen production in ultrapure water. Remarkably, the processed silicon nanowire arrays achieve an apparent quantum efficiency (AQE) of 1.74% in pure water under 450 nm light irradiation with excellent durability. The lithiated Si NWs achieved a hydrogen production rate of  $6.0 \mu\text{mol}\cdot\text{h}^{-1}$  at the first reaction cycle. However, hydrogen production rate was reduced to  $3.4 \mu\text{mol}\cdot\text{h}^{-1}$  in the second reaction cycle and became stable thereafter as indicated by the next 50 h of test.

Then the X-ray photoelectron spectroscopy (XPS) was conducted to characterize surface of the discharged Si NWs which plays a significant role in the photocatalytic hydrogen production. As revealed in Fig. 1, the Si NWs samples before reaction (a), after reaction 4 h (b) and 20 h (c) radiation were measured by in-house XPS.

We can observe the Si at 99 eV binding energy assigned to bulk amorphous silicon, the peak at 103 eV binding energy assigned to surface oxide  $\text{SiO}_2$ , the peak at  $\sim 101.5$  eV binding energy assigned to the lithium orthosilicate  $\text{Li}_4\text{SiO}_4$  and the peak at  $\sim 105$  eV binding energy assigned to the partially fluorinated compound  $\text{SiO}_x\text{F}_y$  located at the extreme surface. The relative intensity of the partially fluorinated compound  $\text{SiO}_x\text{F}_y$  became weaker. And the relative intensity of other Si species changes dramatically after photocatalytic reaction. Indeed the bulk amorphous silicon species relative intensity has significant increase after photocatalytic reaction and stay almost unchanged as the photocatalytic reaction goes on which can be attributed to the change of LiF in solid electrolyte interphase (SEI) during the photocatalytic reaction, and the partially fluorinated compound  $\text{SiO}_x\text{F}_y$  species relative intensity obviously weakens at the begin of the reaction and then keeps constant while the relative intensity of the surface oxide  $\text{SiO}_2$  and the lithium orthosilicate  $\text{Li}_4\text{SiO}_4$  appears no obvious change during the reaction.

To further observe the evolution of the surface

condition during the photocatalytic reaction, the in situ near edge X-ray absorption fine structure (NEXAFS) was conducted at UVSOR Synchrotron Facility. As shown in Fig. 2, the in situ O K-edge XAS was collected before and after illumination in the chamber. We can see that peaks of  $\text{SiO}_2$ ,  $\text{Li}_4\text{SiO}_4$  and  $\text{SiO}_x\text{F}_y$  from the spectra. However, the peaks of  $\text{SiO}_x\text{F}_y$  obviously became weaker assigned to reduction of content, which can be consistent with the X-ray photoelectron spectroscopy. And the peak of  $\text{Li}_4\text{SiO}_4$  almost disappeared after illumination owing to the meager content  $\text{Li}_4\text{SiO}_4$  and weak signal. Overall, the intensity of  $\text{SiO}_x\text{F}_y$  decreases significantly at the reaction starting indicating reduction of  $\text{SiO}_x\text{F}_y$  which we think can well explain the drop of photocatalytic hydrogen production rate at first cycle. The other species remain basically unchanged and these species can reasonably protect the innermost amorphous from photocorrosion.

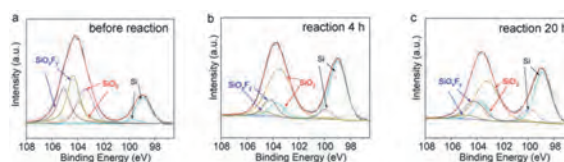


Fig. 1. XPS spectra evolution during reaction.

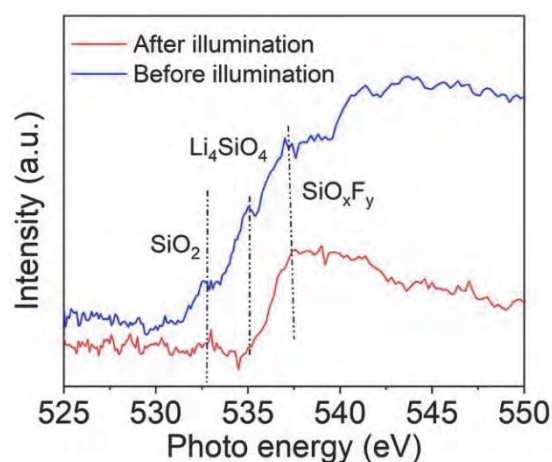


Fig. 2. In situ O K-edge X-ray absorption spectra.



BL3U

## Mechanistic Investigation of Homogeneous Iron-Catalyzed Organic Reactions based on Solution-Phase L-edge XAS

H. Takaya<sup>1</sup>, M. Nagasaka<sup>2</sup> and K. Kashimura<sup>3</sup><sup>1</sup>International Research Center for Elements Science, Institute for Chemical Research, Kyoto University, Uji 611-0011, Japan<sup>2</sup>UVSOR Synchrotron Facility, Institute for Molecular Science, Okazaki 444-8585, Japan<sup>3</sup>Faculty of Engineering, Chubu University, Kasugai 487-8501, Japan

We have found that iron complexes of  $\text{FeX}_2\text{SciOPP}$  ( $\text{X} = \text{Cl}, \text{Br}$ ) bearing bulky phosphine ligand SciOPP showed excellent catalytic activities toward the cross-coupling of organometallic reagents of Mg, B, Al, and Zn with various aryl halides (Eq. 1) [1, 2]. Such iron-based catalysts for organic reactions alternative to the conventional precious metal catalysts has been intensively investigated for the development of future sustainable chemical processes. Solution-phase XAS analysis is highly useful for the mechanistic study of iron-catalyzed organic reactions to identify the catalytically active organoiron species with their electronic and molecular structures, because the conventional solution-phase NMR-based analysis cannot be used due to the paramagnetic nature of organoiron species along with the large paramagnetic shift and peak broadening in NMR spectrum. L-edge XAS of transition-metal catalysts has been expected to be highly useful to investigate the electronic structure of 3d orbitals which provide an essential information to elucidate how to work the catalyst. However, solution-phase L-edge XAS measurement is generally difficult because the measurement has to be performed under low-pressure vacuum condition where the solution sample is evaporated with vigorous boiling. In this project, we used the specially designed flow-cell for the solution-phase L-edge XAS measurement of homogeneous organic solution of iron complex catalysts. In BL3U beamline, a stainless-steel flow cell has been used for various experiments, but we should carefully avoid contamination of iron species from the environment. For this reason Prof. Nagasaka newly designed and prepared PEEK-made flow cell bearing ultra-thin 100 nm  $\text{Si}_3\text{N}_4$  membrane X-ray window as shown in Fig. 1. The solvent-resistant PEEK made body shows an excellent chemical resistance toward the various organic solvents such as THF,  $\text{CH}_2\text{Cl}_2$ , and benzene, these often used in iron-catalyzed cross-

coupling reactions. This flow cell was introduced into the helium-filled chamber which inserted to the X-ray optics line, and connected to syringe pump through a Teflon tube. The THF solution sample of  $\text{FeCl}_2\text{SciOPP}$  was prepared in an argon-filled glovebox, because this type of iron complex in solution is quite sensitive to oxygen and water, and immediately react to give iron oxide and hydroxide. The L-edge XAS experiment was carried out both stop and flow (flow rate: 50 – 500  $\mu\text{L}/\text{h}$ ) conditions to validate the XAS stabilities, base line moving, S/N change etc. As a result, a serious spectrum change and base line jump randomly occurred to interfere the stable XAS measurement by penetration of helium gas in chamber into the cell and made a bubble inside the sample space to cut across X-ray beam. To solve this problem, the Viton O-ring is changed to a fluorosilicone polymer with improving the flow line design and tube connection. This improved cell will be tested in the next experiment scheduled in 2019.

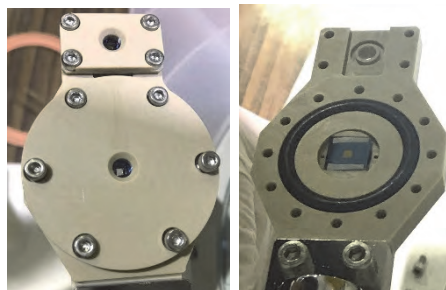
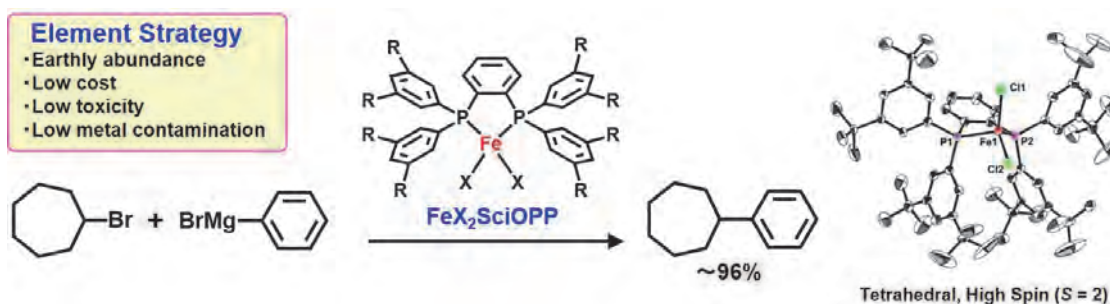


Fig. 1. Photo of the PEEK-made flow.

[1] H. Takaya and M. Nakamura *et al.*, Bull. Chem. Soc. Jpn. **88** (2015) 410.[2] R. Takaya and M. Nakamura *et al.*, Bull. Chem. Soc. Jpn. **92** (2019) 381.



BL3U

## Electronic Structures of Carbon Dots in Aqueous Dispersions Probed by *in-situ* Transmission X-ray Absorption Spectroscopy

J. Ren<sup>1</sup>, D. S. Achilleos<sup>2</sup>, E. Reisner<sup>2</sup> and T. Petit<sup>1</sup>

<sup>1</sup>Institute of Methods for Material Development, Helmholtz-Zentrum Berlin für Materialien und Energie GmbH, Albert-Einstein-Strasse 15, 12489 Berlin, Germany

<sup>2</sup>Christian Doppler Laboratory for Sustainable SynGas Chemistry, Department of Chemistry, University of Cambridge, Lensfield Road, Cambridge CB2 1EW, UK

Carbon dots (CDs) are promising photocatalysts for artificial photosynthesis since they are (1) inexpensive and non-toxic, (2) chemically and photochemically robust, (3) show good water solubility and (4) controlled photocatalytic properties upon pre-designed synthesis. Recently, we reported a facile method to prepare CDs of controlled nanostructures and elemental compositions by varying the organic precursors and the calcination temperatures employed for the synthesis. This approach allows the synthesis of graphitic CDs with (*g*-N-CDs) and without (*g*-CDs) core nitrogen doping, as well as amorphous CDs (*a*-CDs), which all show very distinctive photocatalytic properties.[1]

During this beamtime, colloidal dispersions of these three CDs were successfully characterized by soft X-ray absorption spectroscopy (XAS) at different concentrations. Both the carbon and oxygen K edges were characterized to monitor the impact of hydration on the electronic structure of both CDs and water molecules. Furthermore, these measurements were compared to XAS performed in total electron yield in vacuum and total ionic yield in liquid at BESSY II synchrotron, Germany.

XAS at the C K edge demonstrates that the core of the CDs is poorly influenced by the aqueous dispersion. On the other hand, electronic states associated with C-O bonds from surface groups appear enhanced in dispersion, which is attributed to the formation of hydrogen bonds with water molecules in their solvation shell.

At the O K edge, the signature of the CDs surface groups is screened by the contribution from water molecules (Fig. 1). However, strong changes on the water signature, composed of a pre-, main- and post-edges were found to depend on CDs as well as concentration. We previously observed similar changes in nanodiamonds colloidal dispersions and attributed them to strong changes of the water hydrogen bond network induced by the nanoparticles hydration.[2] These new results suggest that CDs also significantly interact with water molecules in their solvation shells.

These results are the first demonstration that carbon dots interact strongly with their hydration shell and the first *in situ* XAS characterization of CDs. Based on these results, an article has recently been submitted for publication.

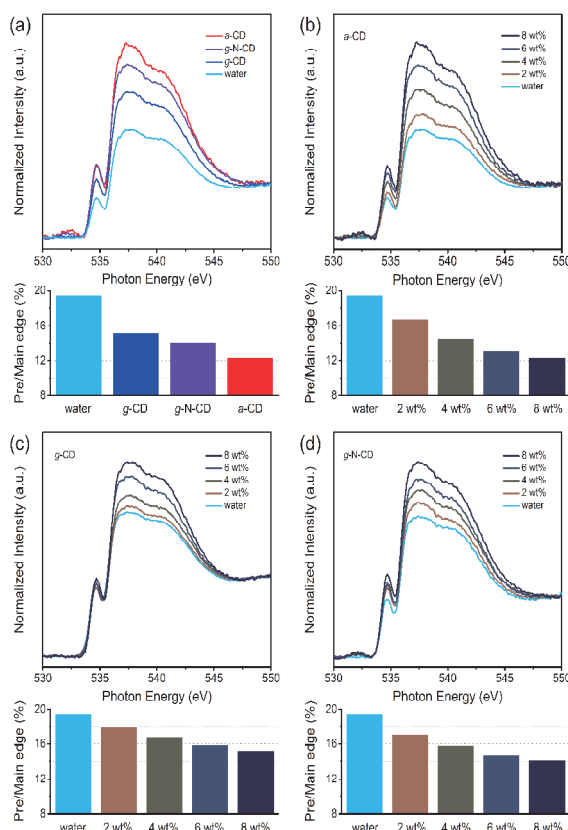


Fig. 1. Transmission mode XA spectra at O K-edge from (a) water and different CDs dispersions (8 wt%) and (b) *a*-CD, (c) *g*-CD, (d) *g*-N-CD at different concentrations. The pre/main-edge ratios for each spectrum are plotted below XA spectra.

[1] B. C. M. Martindale, G. A. M. Hutton, C. A. Caputo, S. Prantl, R. Godin, J. R. Durrant and E. Reisner, *Angew. Chemie Int. Ed.* **56** (2017) 6459.

[2] T. Petit, H. Yuzawa, M. Nagasaka, R. Yamanoi, E. Osawa, N. Kosugi and E. F. Aziz, *J. Phys. Chem. Lett.* **6** (2015) 2909.

BL4U

## P-L<sub>2,3</sub> Absorption Spectra of Phosphates in Plasmid DNA and Cell Nucleus

T. Ejima<sup>1</sup>, M. Kado<sup>2</sup>, T. Ohigashi<sup>3</sup> and S. Tone<sup>4</sup>

<sup>1</sup>IMRAM, Tohoku University, Sendai 980-8577, Japan

<sup>2</sup>Takasaki Adv. Rad. Res. Inst., QST, Takasaki 370-1292, Japan

<sup>3</sup>UVSOR Synchrotron Facility, Institute for Molecular Science, Okazaki 444-8585, Japan

<sup>4</sup>Sch. of Sci & Technol., Tokyo Denki University, Hatoyama 350-0394, Japan

Phosphate PO<sub>4</sub><sup>3-</sup> plays a major role in the structural framework of DNA and RNA. DNA in living cells is mainly present in cell nuclei, and phosphate PO<sub>4</sub><sup>3-</sup> is contained in DNA, RNA, and some phosphorylated proteins among the constituent molecules of cell nuclei [1]. On the other hand, DNA exists alone in bacteria and yeast, and this DNA, called plasmid DNA, is present in the cytoplasm and replicates itself autonomously and independently of genomic DNA [2].

The phosphate PO<sub>4</sub><sup>3-</sup> forms ideally a tetrahedral structure in which four oxygen atoms coordinate equidistantly with a P atom as the center. The absorption spectrum excited at the P-L<sub>2,3</sub> absorption edge shows an electronic structure reflecting the s or d orbitals of the P atoms by the dipolar transition. Furthermore, if the chemical bonding states of a material is changed, the energy position of absorption edge will shift. In this study, the electronic structures and the chemical bonding states of the phosphate are compared by the P-L<sub>2,3</sub> absorption edge structures between the cell nucleus and the plasmid DNA.

As measurement samples, plasmid DNA extracted from *E. coli* and cell nuclei separated from HeLa cells were dispersed in TE solutions, and the solutions of 0.5 μL each were dropped on 50 nm thick SiN membranes and then air-dried as it were. X-ray absorption measurements were performed using STXM beamline of BL4U under the experimental conditions: energy resolution  $E / \delta E = 1000$ , and spatial resolution 50 nm, and under He atmosphere. The obtained spectra are shown in Fig. 1.

The spectral intensity of plasmid DNA increases sharply at around 133 eV, and structures observed are indicated as Peak A ~ D in the figure. Peak intensity increases from Peak A to Peak D and decreases gradually on the higher energy side of Peak D (Fig. 1 (a)). The spectrum shape of the normal cell nucleus likes that of the plasmid DNA, but no explicit peak structures can be seen corresponding to Peak A ~ D observed in the plasmid DNA (Fig. 1 (b)). A broad structure is observed (Peak E) with a broad shoulder structure (Peak F). In the plasmid DNA spectrum, spectral intensities of Peak E and F are weak, and the spectral shape looks as a part of the tail of Peak D.

The similar structures of the spectral shapes can be recognized by the tetrahedral coordination of the phosphate PO<sub>4</sub><sup>3-</sup> in DNA [3]. The different structures will be due to the phosphate PO<sub>4</sub><sup>3-</sup> of the protein molecules other than DNA in the cell nucleus.

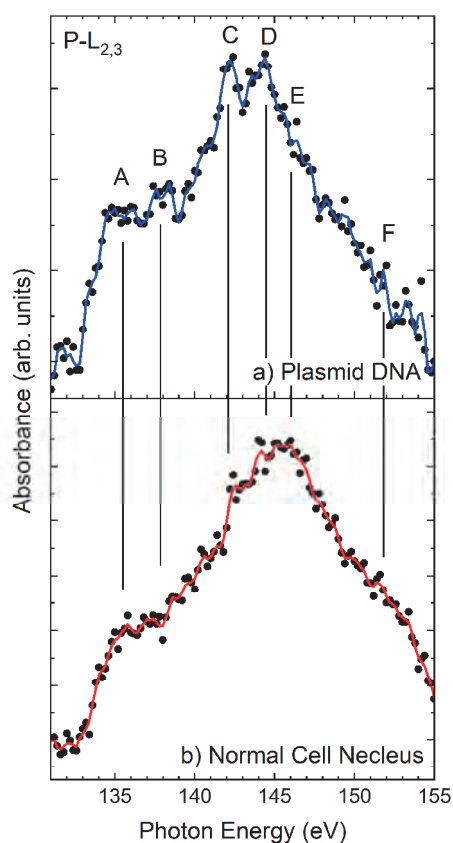


Fig. 1. P-L<sub>2,3</sub> X-ray absorption spectrum of plasmid DNA, (a), and of normal cell nucleus (b). Dots represent the measurement results, curves are 5 point smoothing results of the measurement points for guide to see. Both spectra are normalized by the maximum peak height around 145 eV.

[1] K. Shinohara, S. Toné, T. Ejima, T. Ohigashi and A. Ito, *Cells* **16** (2019) 164.

[2] for example, K. Akasaka and Y. Ohyama, "Principle of Gene Technology", (Syokabo Co. Ltd., 2013, Tokyo, ISBN 978-4-7853-5856-3 C3045).

[3] S. O. Kucheyev, C. Bostedt, T. van Buuren, T. M. Willey, T. A. Land, L. J. Terminello, T. E. Felter, A. V. Hamza, S. G. Demos and A. J. Nelson, *Phys. Rev. B* **70** (2004) 245106.

BL4U

## Heterogeneous Network Structure in Natural Rubber

Y. Higaki<sup>1</sup> and A. Takahara<sup>2</sup><sup>1</sup>*Department of Integrated Science and Technology, Faculty of Science and Technology, Oita University, Oita 870-1192, Japan*<sup>2</sup>*Institute for Materials Chemistry and Engineering, Kyushu University, Fukuoka 819-0395, Japan*

Natural rubber (NR) latex is a liquid rubber product applied for thin rubber sheets and adhesives. The NR latex is a colloid of NR particles dispersed in serum including proteins, lipids, inorganic salts[1]. NR particles consist of a spherical core of poly(cis-1,4-isoprene) and outer shell membrane of a protein-lipid monolayer of approximately 20 nm thickness. The stable dispersion of NR particles is encouraged by the negatively charged substances covered on the surface. Because the NR sheets are produced by the coagulation of the NR particles involving protein and/or lipid shell, the NR sheets would exhibit heterogeneous network with boundary consisting of protein and lipids. In addition, the network structure through C-S, C-S-S bonds produced by vulcanization would be hardly uniform in the rubber matrix. We tried to address the heterogeneous chemical structure distribution in the NR sheets by cross-sectional chemical imaging of the NR sheets by means of scanning transmission X-ray microscopy (STXM) with soft X-ray.

NR particles, of which the averaged particle size is approximately 200 nm, were introduced into a glass dish then dried up subsequently vulcanized with sulfur to produce a vulcanized natural rubber sheet (thickness: 500  $\mu\text{m}$ ). The NR sheet was trimmed without embedding in resin by ultramicrotome to prepare ultra-thin film (setting thickness: 100 nm). The thin films were mounted on a copper grid without collodion supporting membrane (Ohken, Cu 100-A).

STXM experiments were performed at the 4U beamline equipped with a Fresnel zone plate beam-focusing apparatus and a R647P photomultiplier tube detector with a P43 scintillator. The dwell time and the scanning pitch were 2 msec and 0.2  $\mu\text{m}$  step, respectively.

A typical STXM image of the cross-section thin film of the vulcanized natural rubber sheet at 285.2 eV is shown in Fig. 1 (a). Heterogeneous morphology with random domain network was observed. The average domain diameter was approximately 1  $\mu\text{m}$ . The C1s STXM spectra exhibits a sharp absorption peak at 285.2 eV and a broad absorption at 288 eV (Fig. 1 (b)). The absorptions are attributed to C-H $\pi^*$  signals from unsaturated C-C double bonds in poly(cis-1,4-isoprene)[2]. Because the base line absorption is even, the OD contrast would be attributed to the density inhomogeneity nor the uneven thickness. The C-H $\pi^*$  signals in the domains was stronger than that of continuous matrix region. The NR particles would intrinsically involve radial density inhomogeneity. Meanwhile, the protein and lipids in the original NR

latex particles accumulate at the particle boundary leading to the reduction of poly(cis-1,4-isoprene) density in the boundary. The NR particles coalesce in the NR sheet production process to produce the low density continuous network, however, the particle cores would remain without fusion to yield the high density domain regions.

As shown in the above results, we successfully unraveled the density heterogeneity in the NR bulk by means of STXM imaging.

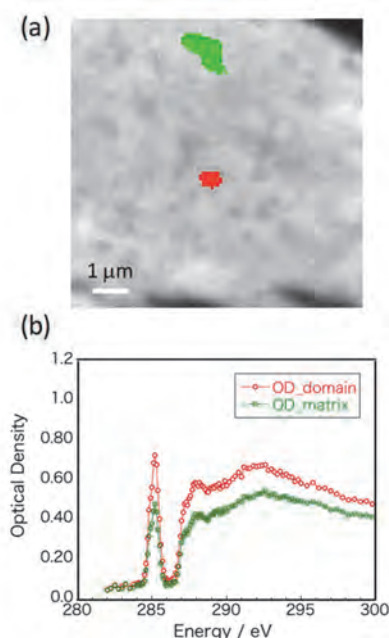


Fig. 1. Cross section of natural rubber sheet. (a) STXM micrograph (10 x 10 mm) at 285.2 eV. (b) C1s absorption spectra of the dark domains (red) and bright matrix (green) regions.

[1] S. Kumarn, N. Churinthorn, A. Nimpaiboon, M. Sriring, C. C. Ho, A. Takahara and J. Sakdapipanich, *Langmuir* **34** (2018) 12730.

[2] S. G. Urquhart, A. P. Hitchcock, A. P. Smith, H. W. Ade, W. Lidy, E. G. Rightor and G. E. Mitchell, *J. Electron Spectros. Relat. Phenom.* **100** (1999) 119.



BL4B

## Multi-electron–Ion Coincidence Spectroscopy Applied to Metastability of Carbonyl Sulfide Dications

Y. Hikosaka<sup>1</sup> and E. Shigemasa<sup>2</sup><sup>1</sup> Institute of Liberal Arts and Sciences, University of Toyama, Toyama 930-0194, Japan<sup>2</sup> Institute for Molecular Science, Okazaki 444-8585 Japan

Carbonyl sulfide is one of the molecules whose dications are known to be stable in the  $\mu\text{s}$  regime. A theoretical calculation predicted that many  $\text{OCS}^{2+}$  electronic states have potential energy surfaces with local minima [1]. In practice, high-resolution Auger spectroscopy [2] and photoelectron-photoelectron coincidence spectroscopy [1,3] have revealed the vibrational structures of several electronic states in  $\text{OCS}^{2+}$ . Kaneyasu et al. have already investigated the metastability and fragmentation of the  $\text{OCS}^{2+}$  states by Auger electron-ion coincidence spectroscopy [4]. However, overlapping Auger structures from the different S2p core-hole states, as well as the moderate energy resolution, obscures the metastability of individual electronic states. In this study, we applied multi-electron-ion coincidence spectroscopy to the S2p Auger decay in OCS and revealed the metastability of each electronic state [5].

The two-dimensional map in Fig. 1 shows correlations between the  $\text{OCS}^{2+}$  dication states and times-of-flight of ions, derived from the triple coincidences among S2p photoelectron, Auger electron, and ion. On this map, coincidence with  $\text{OCS}^{2+}$  ion is remarkably seen for the low-lying dication states around a binding energy of 32 eV. On the other hand, formations of fragment ions are remarkable above a binding energy of 35 eV. These observations basically confirm the findings by Auger electron-ion coincidence spectroscopy [4].

The band around a binding energy of 32 eV consist of three dication states ( $X^3\Sigma^+$ ,  $a^1\Delta$  and  $b^1\Sigma^+$ ) resulting from the removals of two electrons from the  $3\pi$  orbitals. A closer inspection on the coincidence yields reveals that only the highest-lying  $b^1\Sigma^+$  state dissociates into fragments in the  $\mu\text{s}$  regime, though the fraction of the dissociation path is very weak. The calculated potential energy surfaces of these three states have all deep wells, and efficient tunneling dissociation only for the  $b^1\Sigma^+$  state is not likely. The potential energy curve of the  $b^1\Sigma^+$  state along CS stretch intersects that of the  $1^1\Pi$  state [1]. The dissociation of the  $b^1\Sigma^+$  state in the  $\mu\text{s}$  regime possibly results from the conversion into the  $1^1\Pi$  state. Since the crossing point of the two potential energy curves locates around 2 eV above the potential minima of the  $b^1\Sigma^+$  state [1], the heterogeneous predissociation should be extremely inefficient and thus proceeds in the  $\mu\text{s}$  regime.

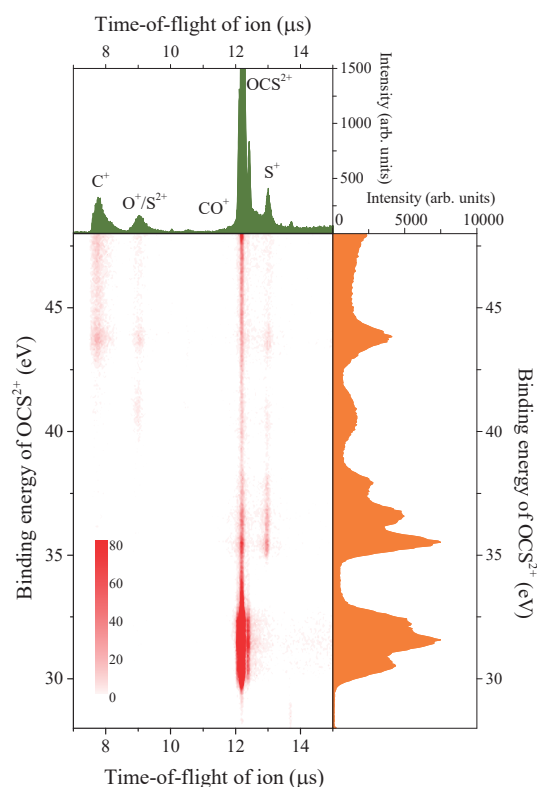


Fig. 1. Two dimensional map showing correlations between the OCS dication states (right panel) and time-of-flights of ions (top panel), derived from the triple coincidences among S2p photoelectron, Auger electron, and ion.

- [1] V. Brites, J. H. D. Eland and M. Hochlaf, *Chem. Phys.* **346** (2008) 23.
- [2] V. Sekushin, R. Püttner, R. F. Fink, M. Martins, Y. H. Jiang, H. Aksela, S. Aksela and G. Kaindl, *J. Chem. Phys.* **137** (2012) 044310.
- [3] J. H. D. Eland, *Chem. Phys.* **294** (2003) 171.
- [4] T. Kaneyasu, M. Ito, Y. Hikosaka and E. Shigemasa, *J. Korean Phys. Soc.* **54** (2009) 371.
- [5] Y. Hikosaka and E. Shigemasa, *Int. J. Mass Spectrom.* **439** (2019) 13.

BL4B

## Pulsed Electron Extraction Introduced into a Magnetic Bottle Time-of-flight Electron Spectrometer

Y. Hikosaka

*Institute of Liberal Arts and Sciences, University of Toyama, Toyama 930-0194, Japan*

Multi-electron coincidence spectroscopy using a magnetic bottle time-of-flight electron spectrometer [1] is one of the most powerful means to study the multi-electron emission processes of atoms and molecules. The magnetic bottle electron spectrometer captures electrons over  $4\pi$ -sr. solid angle by utilizing the magnetic mirror effect, and the electron energy analysis is based on electron time-of-flight measurement. A pulsed light source is thus required for the use of a magnetic bottle spectrometer. The single-bunch operations of synchrotron storage rings provide light pulses applicable to the electron time-of-flight measurement. However, the circumference of the used storage ring limits the periodicity of the light pulses (178 ns for the UVSOR-III ring), and the periodicity is usually shorter than the times-of-flight of slow electrons measured with a magnetic bottle electron spectrometer of a few-meter length. For example, the single bunch operation of the UVSOR-III ring provide light pulses with periodicities of 178 ns, while a slow electron ( $<1$  eV) takes several  $\mu$ s for a few-meter flight.

In this work, a novel method to measure long electron time-of-flight with short-cycle light pulses is established [2]. In the method, a virtual stretch of light pulse intervals is achieved by pulsed extraction of electrons. Here, the observations of electrons are mostly precluded by a DC retardation electric field and are periodically allowed by applying negative voltage pulses to drop the potential at the electron source region.

The performance of the pulsed extraction method was evaluated by measuring electrons emitted from the Xe  $4d_{5/2}^{-1}6p$  resonance at a photon energy of 65.110 eV. Figure 1 shows the time-of-flight spectrum of all the electrons measured with the pulsed extraction method, compared with that by the conventional way (no extraction pulse and no retardation voltage). On the measurement by the pulsed extraction, the negative voltage pulses of -70 eV were applied to the electrodes, under a DC retardation voltage of -70.0 V. The spectrum obtained by the conventional way exhibits cyclic structures resulting from the 178-ns repetition of light pulses. Severe overlaps of slow electrons construct the large background structure lying below the sharp peaks. In contrast, the overlaps are effectively removed in the spectrum measured with the pulsed extraction method, where the absolute times-of-flight of the electrons are determined. Sharp peaks in 300-450 ns result mainly from the spectator Auger decays of Xe  $4d_{5/2}^{-1}6p$  into Xe<sup>+</sup>  $5p^{-2}6p$ , and the broad structure centered at around 500 ns contains slower

electrons emitted on the formation of high-lying Xe<sup>+</sup> states and on their subsequent decay. Weak cyclic peaks, which are noticeable in the region of  $>800$  ns, are due to the valence photoionization by the second-order light. The emitted 5p photoelectrons have a larger kinetic energy than the retardation voltage, and thus the detections cannot be precluded.

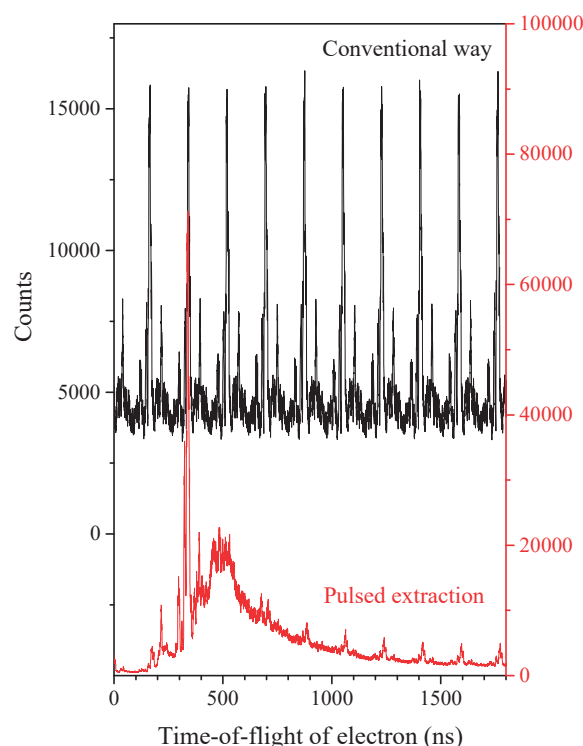


Fig. 1. Time-of-flight spectra of all electrons emitted from Xe at the photon energy for the  $4d_{5/2}^{-1}6p$  resonance (65.110 eV), with the conventional way (in black) and the pulsed extraction method (in red).

[1] J. H. D. Eland, O. Vieuxmaire, T. Kinugawa, P. Lablanquie, R. I. Hall and F. Penent, *Phys. Rev. Lett.* **90** (2003) 053003.

[2] Y. Hikosaka, in preparation.

BL4B

## Double Auger Decay from the Xe $4d_{5/2}^{-1}6p$ Resonance Studied by Multielectron Coincidence Spectroscopy

Y. Hikosaka

*Institute of Liberal Arts and Sciences, University of Toyama, Toyama 930-0194, Japan*

Auger decay is the main decay pathway from inner-shell excited states in light atoms, where two Auger electrons are ejected with a sizable probability. Multielectron coincidence spectroscopy using a magnetic bottle time-of-flight electron spectrometer is a powerful means to investigate the double Auger decay mechanism. In this work, the double Auger decay of the Xe  $4d_{5/2}^{-1}6p$  resonance is studied with multielectron coincidence spectroscopy [1].

Figure 1 shows the coincidences of the two Auger electrons emitted in the resonant double Auger decay. In the two-dimensional map, the formation of individual  $Xe^{2+}$  states by the direct path in the resonant double Auger decay appear as diagonal stripes. This is because the two Auger electrons simultaneously emitted share continuously the available energy which corresponds to the energy difference between the initial Xe  $4d_{5/2}^{-1}6p$  state and a final  $Xe^{2+}$  state. The locations of the diagonal stripes for the formations of the  $Xe^{2+}$   $5p^{-2}$  and  $5s^{-1}5p^{-1}$  states are indicated on the two-dimensional map. Intense spots are exhibited on these diagonal stripes. The cascade path in the resonant double Auger decay produces these spots, where the coordinates of the spots are defined by the discrete kinetic energies of the two Auger electrons. For most spots, the fast electrons are emitted in the first-step decay into  $Xe^+$  states lying above the  $Xe^{2+}$  threshold, and the slow electrons are ejected in the subsequent decay of the  $Xe^+$  states into low-lying  $Xe^{2+}$  states.

The projection of the coincidence counts in the two-dimensional map onto the horizontal axis is potted in the top panel of Fig. 1. The projection spectrum delineates the structure of the  $Xe^+$  states formed intermediately in the cascade path. These  $Xe^+$  structures have been revealed by conventional Auger spectroscopy in some more detail [2]. The sharp peaks lying around 13 eV and 24 eV are assigned to  $5s^{-2}(^1S)6p$  and  $5s^{-1}5p^{-1}(^1P)6p$ , respectively, where the excited electron behaved as a spectator on the Auger electron emission. The structure around 20 eV consists of many  $Xe^+$  states whose dominant configuration is  $5p^{-3}5d6p$ . While conventional Auger spectroscopy locates also the second-step Auger transitions from these intermediate  $Xe^+$  states into final  $Xe^{2+}$  states [2], more unambiguous identifications of the cascade pathways can be made from the features on the two-dimensional map. The decays from  $5s^{-1}5p^{-1}(^1P)6p$  and  $5s^{-3}5d6p$  into  $Xe^{2+}$   $5p^{-2}$  states are exhibited as intense spots lying on the diagonal stripes for the final  $Xe^{2+}$

formations. The intensities of the spots imply that the  $5s^{-1}5p^{-1}(^1P)6p$  state decays with a similar intensity into the  $^3P_2$ ,  $^3P_{0,1}$  and  $^1D_2$  final states, but much weakly into the  $^1S_0$  state. The preference in the decay channels differs among different  $5p^{-3}5d6p$  states.

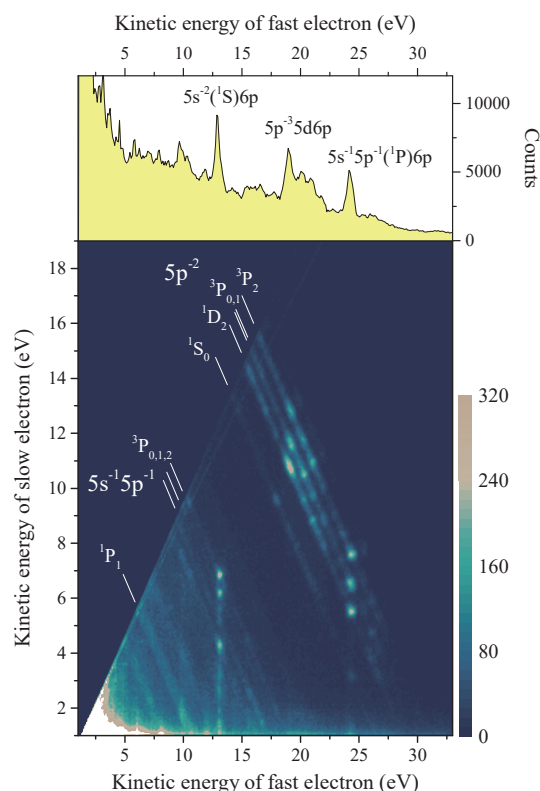


Fig. 1. Energy correlation map between two Auger electrons emitted in the resonant Auger decay from the  $4d_{5/2}^{-1}6p$  resonance in Xe. The projection of the coincidence counts in the two-dimensional map onto the horizontal axis is shown in the top panel. The structures seen in the projection spectrum depict the  $Xe^+$  states formed intermediately in the cascade path of the resonant double Auger decay.

[1] Y. Hikosaka, in preparation.

[2] S. Osmekhin *et al.*, *J. Electron Spectrosc. Relat. Phenom.* **161** (2007) 105, and references therein.

BL4B

## Critical Absorbed Dose of Resinous Adhesive Material Towards Non-Destructive Chemical-State Analysis Using Soft X-Rays

H. Yamane<sup>1</sup>, M. Oura<sup>1</sup>, N. Yamazaki<sup>2</sup>, K. Hasegawa<sup>3</sup>, K. Takagi<sup>4</sup> and T. Hatsui<sup>1</sup>

<sup>1</sup>RIKEN SPring-8 Center, Sayo 679-5148, Japan

<sup>2</sup>Research & Innovation Center, Mitsubishi Heavy Industries, Ltd., Yokohama 220-8401, Japan

<sup>3</sup>Research & Innovation Center, Mitsubishi Heavy Industries, Ltd., Nagoya 455-8515, Japan

<sup>4</sup>Fixed Wing Aircraft Engineering Department, Mitsubishi Heavy Industries, Ltd., Toyoyama 480-0202, Japan

Epoxy resins are the most common matrix materials for high-performance composites and adhesives. Tetraglycidyl-4,4'-diaminodiphenylmethane cured by 4,4'-diaminodiphenylsulfone (TGDDM-DDS) is an archetypal model material for the adhesive bonding. Because the oxygen element plays a crucial role in the chemical interaction and the resultant bonding strength at adhesive interfaces, the O K-edge X-ray absorption spectroscopy (XAS) is one of reliable techniques to understand the chemical interaction at adhesive interfaces. In this work, we performed the quantitative examination of the radiation damage on TGDDM-DDS for the precise analysis of the local chemical state using soft X-rays.

The total-electron-yield (TEY) XAS experiment was performed at BL4B. In the present work, the resolving power ( $h\nu/\Delta E$ ) at  $h\nu = 500$  eV, the photon flux ( $N_{\text{ph}}$ ), and the photon spot size at the surface ( $S$ ) were 2500,  $6 \times 10^9$  ph/s and  $0.847$  mm<sup>2</sup>, respectively. The TGDDM-DDS was obtained by the curing reaction after stirring the uncured TGDDM with the DDS curing agent. To avoid the charging effect in TEY-XAS, we made the conductive path between the sample surface and the ground by pasting the Al- covered carbon tape nearby the measurement spot.

Figure 1 shows the O K-edge TEY-XAS spectra for TGDDM-DDS at 300 K as a function of the X-ray dose time ( $t_{\text{dose}}$ ). The XAS pre-edge structure at  $h\nu = 532.6$  eV was not observable for the uncured TGDDM and DDS, and was found to originate from the curing process of TGDDM-DDS, that is, formation of the OH group and the possible oxidation, as confirmed by the fluorescence-yield XAS. The TEY-XAS spectra show the evidence for the radiation damage; the pre-edge structure at  $h\nu = 532.6$  eV gets weakened with  $t_{\text{dose}}$ . The XAS intensity plot at  $h\nu = 532.6$  eV as a function of  $t_{\text{dose}}$  exhibits the exponential decay, as shown in the inset of Fig. 1. Here, the XAS intensity ( $I_{\text{XAS}}$ ) plot can be fitted by

$$I_{\text{XAS}} = I_{\text{inf}} + C \exp(-t_{\text{dose}}/t_{\text{dose}}^c) \quad (1),$$

where  $I_{\text{inf}}$ ,  $C$ , and  $t_{\text{dose}}^c$  are the XAS intensity at the saturated damage region, a constant, and the critical dose time for the chemical change, respectively [1]. The least-squares fitting using Eq. (1) with  $I_{\text{XAS}} = 1.0$  at  $t_{\text{dose}} = 0$  s gives  $I_{\text{inf}} = 0.853$ ,  $C = 0.147$ , and  $t_{\text{dose}}^c = 4968$  s. The critical flux density ( $N_{\text{ph}} t_{\text{dose}}^c / S$ ) is thus determined as  $3.68 \times 10^{13}$  ph/mm<sup>2</sup>.

The kinetic energy released in materials (kerma,  $K$ ) is expressed as the product between the accumulated

photon flux and the absorbed energy by one photon,

$$K = N_{\text{ph}} t_{\text{dose}} \times h\nu(1 - T)/(\lambda S \rho) \quad (2),$$

where  $T$ ,  $\lambda$ , and  $\rho$  are the transmission probability, the probing depth, and the material density ( $1.05$  g/cm<sup>3</sup> for TGDDM-DDS), respectively. If the photoelectron attenuation length in materials (typically, nm order) is short enough with respect to the photon irradiation area, the charged-particle equilibrium would exist, and the kerma is equal to the absorbed dose ( $D_a$ ),  $D_a/K = 1$ . When  $\lambda$  is 2~10 nm for O K-edge TEY-XAS of polymers, the transmission probability is calculated to be  $T = 0.99265$  ( $\lambda = 6$  nm) by using Ref. [2]. These parameters give the critical absorbed dose ( $D_a^c$ ) of  $3.83 \pm 0.01$  MGy. The small error in  $D_a^c$  of  $\pm 0.01$  (less than 0.3 % for  $D_a^c$ ) indicates that the critical absorbed dose does not depend on the probing depth so much, if the probing depth is sufficiently shallower than the penetration depth of photons.

By using the X-ray emission spectroscopy with the highly-brilliant and well-focused soft X-ray beam at SPring-8 BL17SU ( $N_{\text{ph}} = 3 \times 10^{11}$  ph/s,  $S = 0.001$  mm<sup>2</sup>), we found that the half of  $D_a^c$  is applicable for the non-destructive chemical-state analysis of adhesive materials [3]. These results indicate that the charged-particle equilibrium exists for soft X-rays in the range of at least  $0.001 \sim 0.847$  mm<sup>2</sup> beam spot.

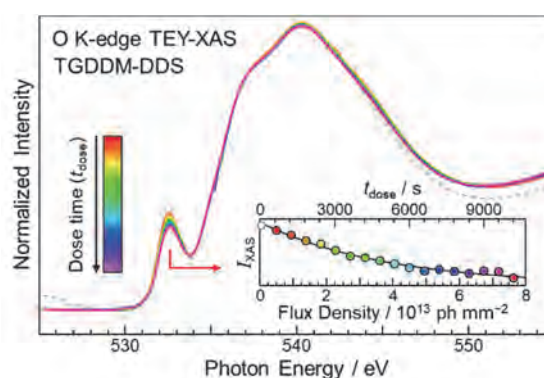


Fig. 1. O K-edge TEY-XAS spectra measured for TGDDM-DDS as a function of the X-ray dose.

[1] X. Zhang *et al.*, J. Vac. Sci. Tech. B **13** (1995) 1477.

[2] [http://henke.lbl.gov/optical\\_constants/](http://henke.lbl.gov/optical_constants/)

[3] H. Yamane *et al.*, J. Electron Spectrosc. Relat. Phenom. **232** (2019) 11.



BL6B

## Redistribution of Molecular Orbital Levels in Platinum-dithiolene Complex

T. Yamamoto<sup>1,2,3</sup>, D. Hiraga<sup>4</sup>, I. Arashi<sup>1</sup>, T. Naito<sup>1,2</sup>, T. Teshima<sup>5</sup>, K. Tanaka<sup>5</sup> and R. Kato<sup>3</sup>

<sup>1</sup>Graduate School of Science and Technology, Ehime University, Matsuyama, 790-8577, Japan.

<sup>2</sup>Geodynamics Research Center, Advanced Research Unit for High-Pressure, and Research Unit for Superconductivity, Ehime University, Matsuyama, 790-8577, Japan

<sup>3</sup>RIKEN, Wako, 351-0198, Japan

<sup>4</sup>Department of Science, Ehime University, Matsuyama, 790-8577, Japan

<sup>5</sup>UVSOR Synchrotron Facility, Institute for Molecular Science, Okazaki 444-8585, Japan

Orbital degrees of freedom in inorganic and multi-functional solids have been attracted attention. In the field of molecular solids, on the other hand, only a few efforts have been devoted to studying the physical properties originating from the orbital degrees of freedom. We have focused on the molecular orbital (MO) of  $X[\text{Pt}(\text{dmit})_2]_2$  ( $\text{dmit} = 1,3\text{-dithiole-2-thione-4,5-dithiolate}$  and  $X =$  monovalent cation). The suppression of the charge disproportionation by the irradiation of near-infrared lights as well as the electric transitions in the infrared and near-infrared regions suggests the proximity of MO levels near Fermi energy [1].

Accumulation of our recent study concerning  $X[\text{Pd}(\text{dmit})_2]_2$  revealed that the  $\text{C}=\text{C}$  stretching modes are useful to studying how electrons occupy orbitals. We have examined the proximity and/or degeneration in the MO levels of  $X[\text{Pt}(\text{dmit})_2]_2$  based on the behavior of the  $\text{C}=\text{C}$  stretching modes. The Raman and IR spectra were observed in Instrumental Center and UVSOR, respectively. Firstly, the polarization dependence of the reflectance spectra in a single crystal was observed by using of the infrared microscope. Secondary, we observed the transmission spectra by using of the KBr pellet method. We confirmed that there is no remarkable difference between the  $\text{C}=\text{C}$  stretching modes in the reflectance spectra and those in the transmission spectra. In the last step, we observed the temperature dependence

of the transmission spectra.

Figure 1 shows the transmission spectra of  $X = \text{Me}_4\text{Sb}$  (left) and  $\text{Me}_4\text{P}$  (right). The phase transition temperature of  $X = \text{Me}_4\text{Sb}$  (180 K) turned out to be lower than that of  $X = \text{Me}_4\text{P}$  (200–220 K). Factor group analysis in the low-temperature phase reveals that the charge-rich dimer ( $[\text{Pt}(\text{dmit})_2]_2^{-1-\Delta}$ ) and the charge-poor dimer ( $[\text{Pt}(\text{dmit})_2]_2^{-1+\Delta}$ ) are alternately arranged in the two-dimensional layer, which indicates no remarkable valence bond ordering in the inter-dimer interaction. This result is in contrast to the charge distributions of  $X[\text{Pd}(\text{dmit})_2]_2$ , where the anti-bonding orbitals of two charge-rich dimers form valence bond. The absence of the inter-dimer valence bond in the low-temperature phase of  $X[\text{Pt}(\text{dmit})_2]_2$  indicates that the redistribution in the MO levels occurs at the phase transition temperature. Furthermore, the mutual exclusion rule cannot be applied to both IR and Raman spectra, which reveal that dimers become asymmetric originating from the disproportionation between two ligands in a monomer. This result is striking because the disproportionation of monomers might explain the conducting properties of the single component metals and superconductors.

[1] T. Ishikawa *et al.*, *Science*. **350** (2015) 1501.

[2] T. Yamamoto *et al.*, *Sci. Rep.* **7** (2017) 12930.

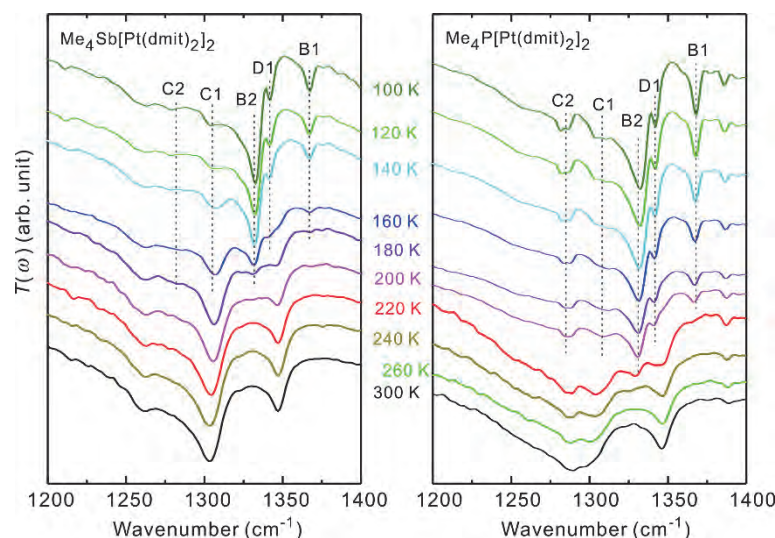
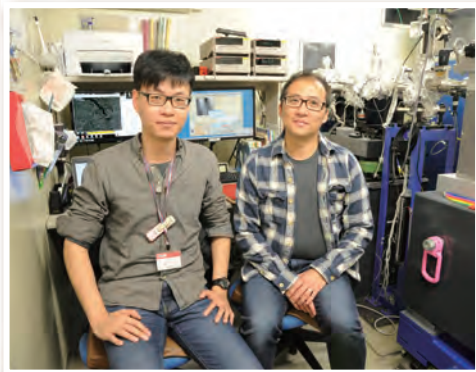
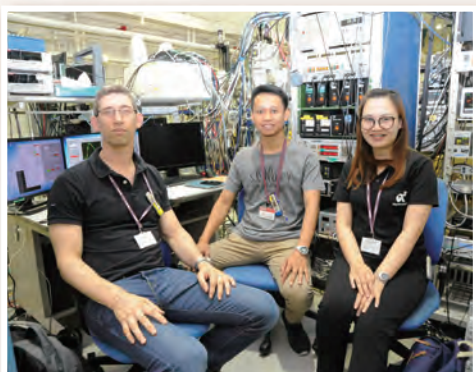
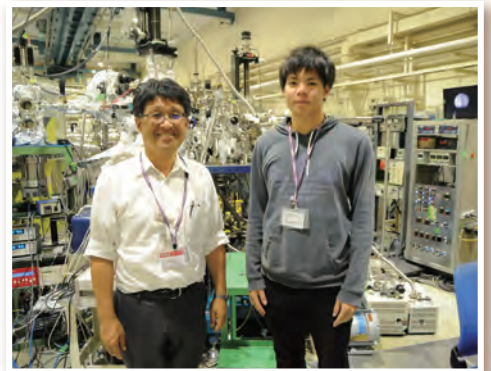
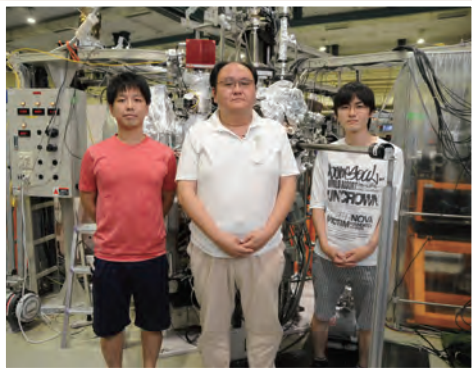
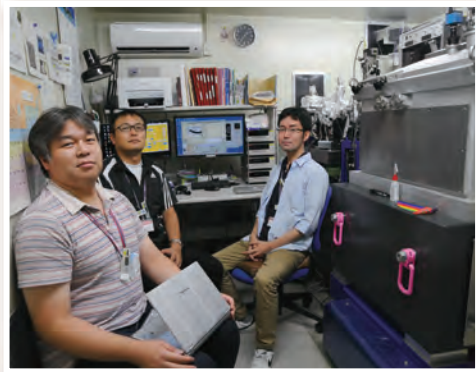
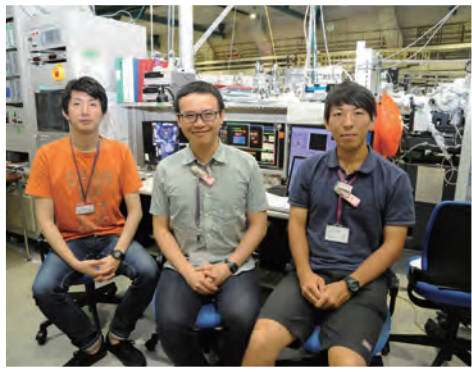
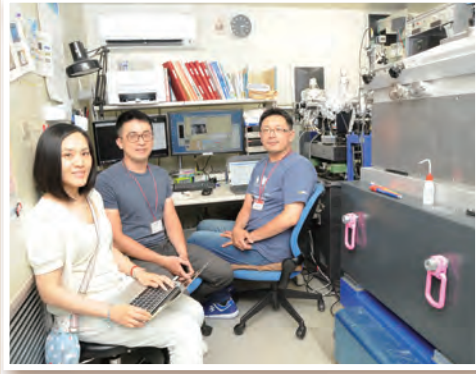
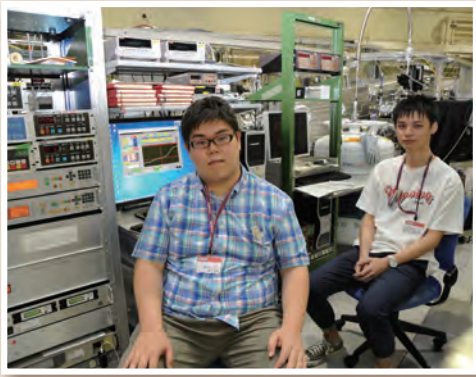


Fig. 1. Transmission spectra of  $X = \text{Me}_4\text{Sb}$  (left) and  $\text{Me}_4\text{P}$  (right).

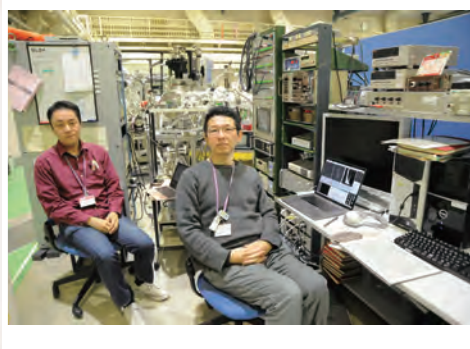
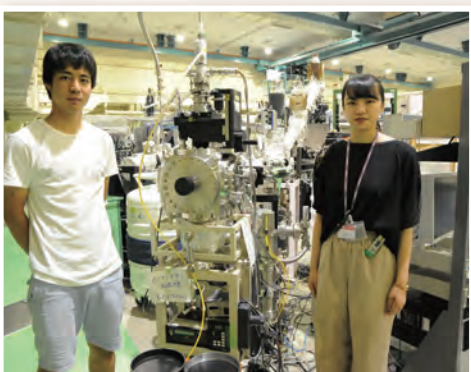
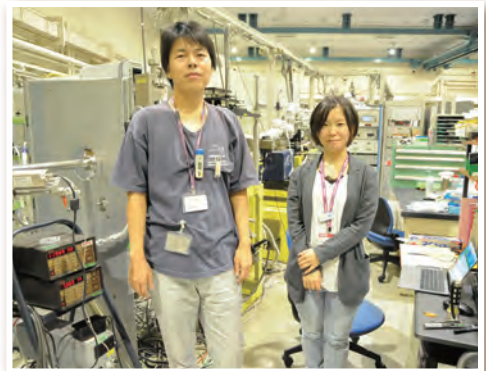
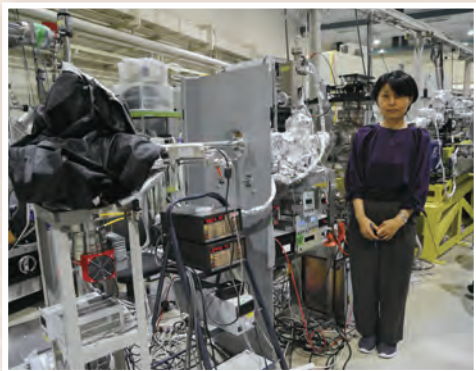
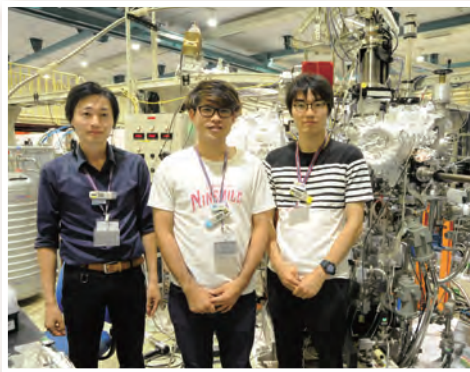
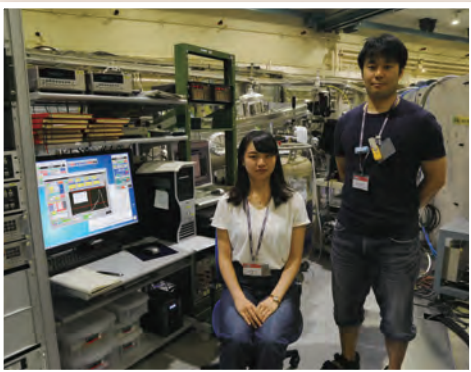
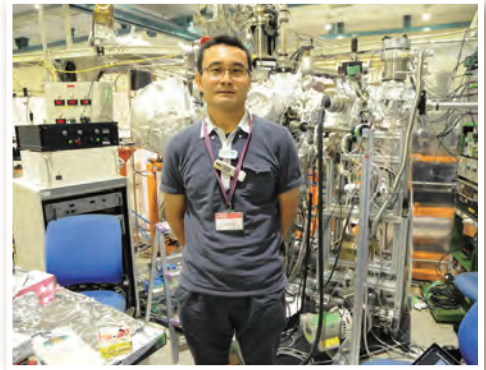
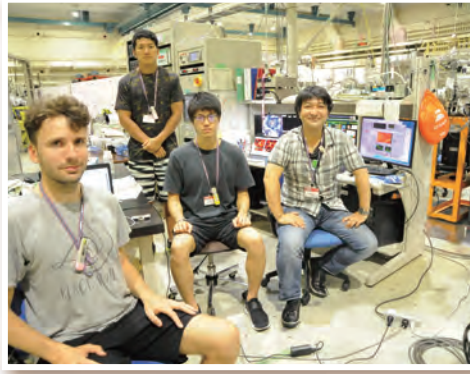
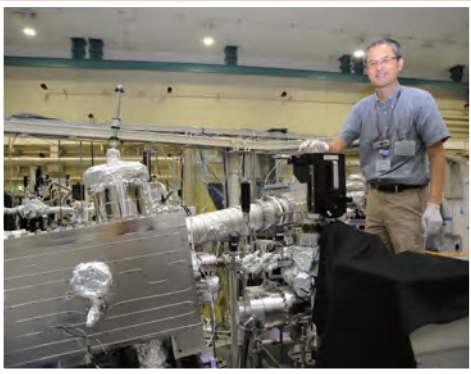


# UVSOR User 4





# UVSOR User 5



# III-4

Surface,  
Interface and  
Thin Films





BL6U

## Bulk and Surface Band Dispersion Mapping of the Au(111) Surface by Newly-developed Acceptance-cone Tunable PES System

F. Matsui<sup>1</sup>, H. Yamane<sup>2</sup>, T. Ueba<sup>1</sup>, T. Horigome<sup>1</sup>, S. Makita<sup>1</sup>, K. Tanaka<sup>1,3</sup>, S. Kera<sup>1,3</sup> and N. Kosugi<sup>3,4</sup>

<sup>1</sup>UVSOR Synchrotron Facility, Institute for Molecular Science, Okazaki 444-8585, Japan

<sup>2</sup>RIKEN SPring-8 Center, Sayo 679-5148, Japan

<sup>3</sup>The Graduate University for Advanced Studies (SOKENDAI), Okazaki 444-8585, Japan

<sup>4</sup>Institute of Materials Structure Science, KEK, Tsukuba 305-0801, Japan

Two-dimensional angle-resolved photoelectron (PE) spectroscopy is a powerful method to study the electronic structure of crystal surfaces. The initial state binding energy ( $E$ ) and the wave vector ( $\mathbf{k}$ ) can be determined from the kinetic energy and the direction of the detected PE. The latest version of ARPES analyzer was installed (MB Scientific AB, A-1 analyzer Lens#5) at BL6U (in-house beamline). This PE spectrometer consists of a hemispherical electron analyzer with a mechanical deflector and a mesh electrostatic lens near the sample to make the acceptance cone tunable. A constant energy PE angular distribution of the valence band dispersion cross section in the large  $\mathbf{k}$  range can be efficiently obtained by applying a negative bias voltage to the sample and using the mechanical deflector. Details of the specifications will be reported elsewhere [1].

Here, we introduce three-dimensional band dispersion mapping of the Au single crystal to show the performance of the current PE spectroscopy end station. The Au(111) surface was cleaned by repeating the cycle of Ar<sup>+</sup> sputtering and annealing. The cleanliness of the reconstructed Au surface was confirmed by LEED and XPS. ARPES measurement was made at approximately 20 K. The incident photon axis, the electric vector, the normal direction and the  $\bar{\Gamma}\bar{M}$  direction of the sample surface and the analyzer entrance slit were all in the horizontal plane. The incident photon axis was offset 60° from the surface normal direction.

Figure 1 shows the bias-voltage-dependent band dispersion map in the  $\bar{\Gamma}\bar{M}$  plane. The photon energy was 90 eV. A well-known Au surface state across the Fermi level is observed at  $\bar{\Gamma}$  point. The acceptance angle was  $\pm 16^\circ$ , which corresponding to  $\pm 1.2 \text{ \AA}^{-1}$ . The detection range was expanded to  $\pm 3.0 \text{ \AA}^{-1}$  by applying a negative bias to the sample.

Figure 2 shows the photon-energy-dependent Fermi surface maps with simulated cross sections of bulk Fermi surface. Photon energies of 60, 90, and 120 eV were used for excitation. The bias voltage applied to the sample was fixed to -400 V. The Au(111) surface state at the  $\bar{\Gamma}$  point was observed at the center. The hexagonal cross section of the bulk Fermi surface was observed in the angular distribution excited with photon energies of 90 and 120 eV. Note that the observed patterns are more six-fold symmetric, although a three-fold symmetric feature is expected for the second

adjacent Brillouin zone. This is probably due to the PE scattering at the surface reconstructed structure. One can not notice such a phenomenon just by measuring the band dispersion at a high symmetry plane.

We greatly acknowledge Dr. P. Baltzer and Ms. M. Matsuki (MB Scientific AB) for their contribution in the construction of the BL6U PE end station.

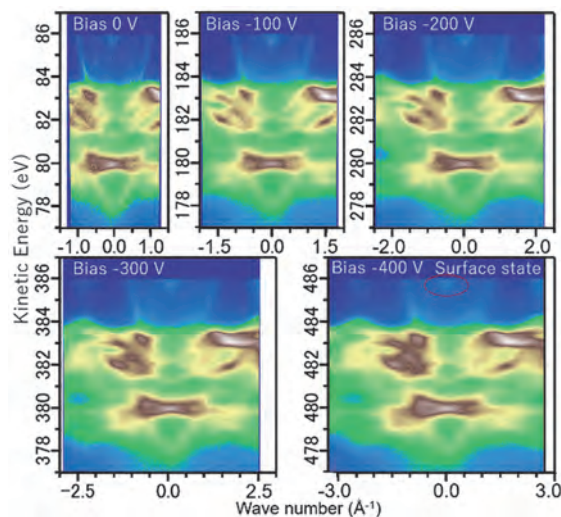


Fig. 1. Band dispersion of the Au(111) surface along  $\bar{\Gamma}\bar{M}$  direction. Photon energy was 90 eV. Various negative bias was applied to the sample.

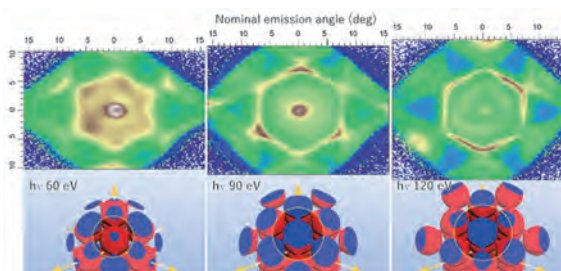


Fig. 2. Fermi surface of the Au(111) surface. Photon energy was varied from 60 eV to 120 eV. Bias voltage of -400 V was applied to the sample.

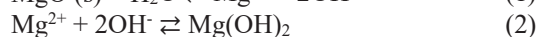
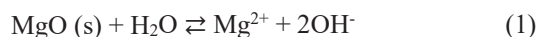
[1] H. Yamane, F. Matsui, T. Ueba, T. Horigome, S. Makita, K. Tanaka, S. Kera and N. Kosugi, Rev. Sci. Instrum. in Press (2019).

BL2A

## Kinetics Investigation to Form Magnesium Hydroxide from Low Crystalline Magnesium Oxide in the Solution

T. Kato<sup>1</sup>, K. Takahashi<sup>1</sup>, Y. Sawamura<sup>1</sup>, M. Kadokura<sup>2</sup> and C. Tokoro<sup>3</sup><sup>1</sup>Graduate School of Creative Science and Engineering, Waseda University, Tokyo 169-8555, Japan<sup>2</sup>School of Creative Science and Engineering, Waseda University, Tokyo 169-8555, Japan<sup>3</sup>Faculty of Science and Engineering, Waseda University, Tokyo 169-8555, Japan

The low crystalline magnesium oxide, which is produced by heating at 600 degree in 1 hour, has the capacity to remove toxic elements, such as the boron (B), fluorine (F) and so on [1]. In the solution, a part of low crystalline magnesium oxide forms to magnesium hydroxide by the reaction described in equations (1) and (2).



When a part of low crystalline magnesium oxide precipitates as magnesium hydroxide in the solution, it is suggested that the toxic elements, such as B, F and so on, remove by co-precipitation with magnesium hydroxide. However, the ratio of magnesium hydroxide in the low crystalline magnesium oxide after experiments is not clarified because the structure of precipitation is amorphous. To achieve the quantitative modeling for toxic elements removal by low crystalline magnesium oxide, it is desired that the ratio of magnesium hydroxide in the low crystalline magnesium oxide after experiments evaluates. Thus, the objective of this study is to evaluate the ratio of magnesium hydroxide in the low crystalline magnesium oxide after experiments using x-ray absorption fine structure (XAFS) analysis in magnesium K-edge.

The precipitation after experiments, which the low crystalline magnesium oxide reacted in the solution after 0, 1, 5, 10, 20 and 120 min, was analyzed by XAFS analysis in magnesium K-edge by fluorescence method (Fig. 1). The XAFS spectra of magnesium oxide in magnesium K-edge has two peaks while that of magnesium hydroxide has three peaks in the range of 1300 – 1320 eV [2]. Thus, the x-ray absorption near edge structure (XANES) analysis was performed in the range of 1300 – 1320 eV to evaluate the ratio of magnesium hydroxide in the low crystalline magnesium oxide (Table 1). From XANES results, it was confirmed that almost low crystalline magnesium oxide was precipitated as magnesium hydroxide after 20 min. Using above results, we can construct the quantitative model for toxic elements by low crystalline magnesium oxide.

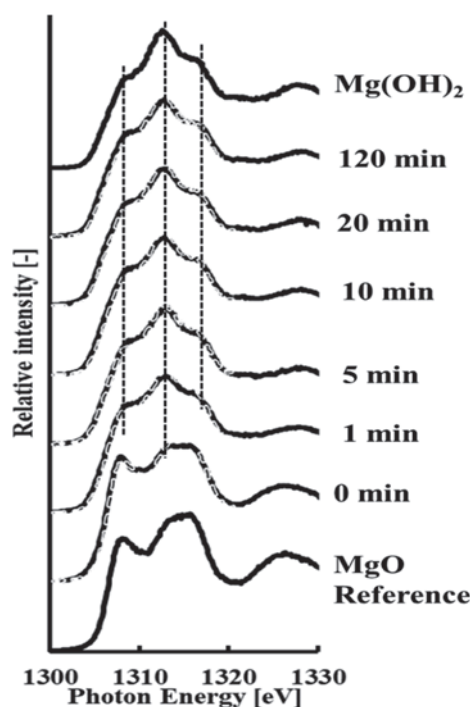


Fig. 1. Magnesium K-edge x-ray absorption fine structure spectra corresponding to x-ray absorption spectra near edge structure region of 0, 1, 5, 10, 20 and 120 min samples, showing resolved components of magnesium oxide and hydroxide based on magnesium oxide and hydroxide reference spectra, respectively.

Table 1. Concentration of magnesium oxide and hydroxide in 0, 1, 5, 10, 20 and 120 min samples, based on x-ray absorption near edge structure analysis in magnesium K-edge [%]

Reaction time [min]	Concentration of MgO	Concentration of Mg(OH) <sub>2</sub>
0	100	0
1	29.1	70.9
5	16.4	83.6
10	10.1	89.9
20	6.2	93.8
120	0	100

[1] H. Fukuda, S. Hobo, G. Granata, C. Tokoro, Y. Toba and M. Eguchi, Proceedings of the Conference of Metallurgists (2017) 9408.

[2] T. Yoshida, T. Tanaka, H. Yoshida, T. Funabiki and S. Yoshida, J. Phys. Chem. **100** (1996) 2302.



BL2B

## Molecular Orientation of DNTT Thin Film on TES-derivatives Deposited Au Substrate

K. K. Okudaira and A. Murafuji

Association of Graduate Schools of Science and Technology, Chiba University, Chiba 263-8522, Japan

Organic devices such as organic light-emitting diodes, organic thin-film transistors (OTFTs), and organic photovoltaic cells, have been attracting interest concerning both fundamental research and practical application for low-cost, large-area, lightweight and flexible devices. Recently, OTFT's with field-effect mobility and on/off current ratio comparable to hydrogenated amorphous silicon thin-film transistors.

Since source and drain contact resistance has been identified as a major limitation in OTFTs, control of this interface is important. Several surface treatments have been reported to improve charge injection from metal electrodes into organic semiconductors. A single molecular layer, for example self-assembled monolayer (SAM), has been purposely introduced on top of the electrode as well as insulator surfaces [1]. SAM spontaneously forms by dipping the substrate in a solution of an appropriate reactive surfactant. For the case of application of SAM to the bottom-contact OTFT, where the substrates consist of not only electrodes such as Au but also insulator, it is necessary to use of two types of SAMs for the suitable surfaces of substrates. 6-(3-(triethoxysilyl) propylamino)-1,3,5-triazine-2,4-dithiol monosodium (TES) derivatives have been reported as molecular adhesion, which are able to form the chemical bonds with both insulator such as plastic and metal. TES can be considered as a kind of SAM, which is available to form the chemical bonding (anchoring) to two different substrates.

The characteristics of OTFT such as mobility are considered to be dependence on not only the electronic structure but also the molecular orientation of organic molecule.

In this work we deposited a TES derivative on Au and examined the molecular orientation of dinaphtho[2,3-b:2',3'-f]thieno[3,2-b]thiophene (DNTT) thin films thermally deposited on the TES-derivate surface by angle-resolved ultraviolet photoelectron spectroscopy (ARUPS) measurements. In the ARUPS take-off angle dependence of HOMO peak for  $\pi$ -conjugated organic molecule provides an important information on the molecular orientation [2].

ARUPS measurements were performed at the beam line BL2B of UVSOR III at the Institute for Molecular Science. The take-off angle ( $\beta$ ) dependencies of photoelectron spectra were measured with the photon energy ( $h\nu$ ) of 28 eV. The Au coated substrate was prepared by depositing Au thin films on natural-oxide Si(001) wafer. We used TES derivatives as coupling agent. The TES layer on Au substrates was prepared using a dipping method at room temperatures. DNTT

thin film was deposited on TES.

We observed take-off angle ( $\beta$ ) dependence of HOMO peak in UPS of DNTT thin film (thickness of about 6.0 nm on TES-derivates prepared on Au substrate (Fig.1). The peaks originated from  $\pi$ -orbitals including HOMO do not show take-off angle dependence. On the contrary, the intensities of photoelectrons from the  $\sigma$ -states become large as increase take-off angle. For the case of flat-lying molecular orientation of  $\pi$ -conjugated aromatic molecules such as phthalocyanine, the  $\pi$ -peaks show strong take-off angle dependence [3]. It indicates that DNTT molecules have the orientation (not parallel orientation) on TES-derivates Au substrate.

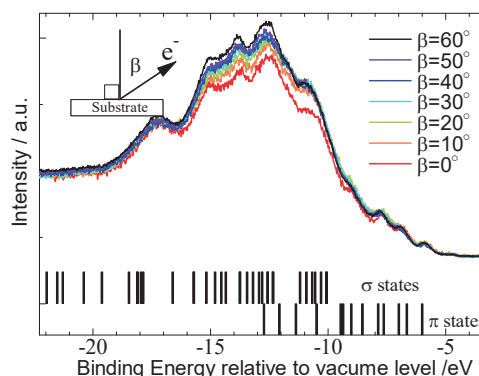


Fig.1. Take-off angle ( $\beta$ ) dependences of ultraviolet photoelectron spectra DNTT (6.0nm)/TES/Au.

- [1] P. Marmont *et al.*, *Org Electron.* **9** (2008) 419, Y. Horii *et al.*, *Thin Solid Films* **518** (2009) 642.
- [2] K. Mori and K. Abe, *Hyomen Gijutsu* **59** (2008) 299, K. Mori *et al.*, *J. Soc. Rubber Sci. Technol.* **83** (2010) 71.
- [3] N. Ueno *et al.*, *J. Chem. Phys.* **99** (1993) 7169.

BL2B

## Electronic Structure of Disordered Molecular Heterointerfaces

K. Akaike<sup>1</sup>, A. Onishi<sup>1</sup>, Y. Wakayama<sup>2</sup> and K. Kanai<sup>1</sup>

<sup>1</sup>Department of Physics, Faculty of Science and Technology, Tokyo University of Science, Noda 278-8510, Japan

<sup>2</sup>International Center for Materials Nanoarchitectonics (WPI-MANA), National Institute for Materials Science (NIMS), Tsukuba 305-0044, Japan

Intended design of organic heterointerfaces is crucial to control functionality in organic devices based on multi-stacked organic layers. Formation of the heterointerfaces via either vacuum deposition or solution process leads to a variety of interfacial structure; molecular exchange, molecular reorientation, and mixed heteromolecular arrangement. The formation of a well-defined heterointerface is a typically expected consequence, but it is not a sole case. The complicated molecular rearrangement that have been found should introduce structure disorder into the system, but its molecular origin is elusive.

Previously, using scanning tunneling microscopy (STM), we directly observed the disorder formed upon the formation of sexithiophene (6T)/perfluorinated copper phthalocyanine (F<sub>16</sub>CuPc) interface on a cleaned Ag(111) surface [1]. Deposition of 6T onto an epitaxially grown F<sub>16</sub>CuPc monolayer perturbed the arrangement of F<sub>16</sub>CuPc along [1–2] direction. The adsorbed 6T molecules adapted various bent shapes and were randomly mixed with F<sub>16</sub>CuPc molecules. The bent molecules are originated from *cis-trans* isomerization, in which neighboring thiophene rings rotate. The various molecular shapes of 6T significantly reduced short- and long-range orders.

The STM results prompted us to characterize the electronic structure of such a disordered heterointerfaces, because the Gaussian broadening and tailing of the frontier orbitals are often correlated with structural disorder [2]. In this research, we performed ultraviolet photoelectron spectroscopy (UPS) in BL2B to investigate the energy distribution of the occupied states of 6T/F<sub>16</sub>CuPc interface.

Figure 1 shows the evolution of the UPS spectra for the interface as a function of 6T coverage in secondary electron cutoff (a) and valence band regions (b). Photon energy of 28 eV was used to acquire the spectra at room temperature. Photoelectron emission angle was fixed to be 45°. The formation of F<sub>16</sub>CuPc monolayer on Ag(111) reduced work function (WF) by 0.5 eV. This originates from the push-back effect. The highest occupied molecular orbital (HOMO) peak appeared at the binding energy of ~2.1 eV. At the same time, a broad feature was observed just below the Fermi level. The electronic states should be originated from partial occupation of the lowest unoccupied molecular orbital (LUMO) of F<sub>16</sub>CuPc upon the adsorption on the silver surface.

Increasing coverage of 6T lowered WF by less than 0.1 eV. The WF reduction accompanies with the shift of

the F<sub>16</sub>CuPc HOMO toward lower binding energy. The analysis of the STM images suggested that the nominal coverage of the organic layer reduced upon the deposition of 6T. Therefore, because the bare silver surface has a larger WF, the WF increased upon the interface formation. Unexpectedly, the shape of the HOMO was not broadened by the structural disordering.

Comparable UPS measurements were also carried out for 6T/CuPc/Ag(111) interface. The interface states, formed upon the adsorption of CuPc on the silver surface, shifted toward higher binding energy with increasing 6T coverage. STM images of 6T/CuPc interface suggested the formation of phase-separated binary structure. However, further investigation is necessary to elucidate what molecular arrangement led to the shift of the interface states.

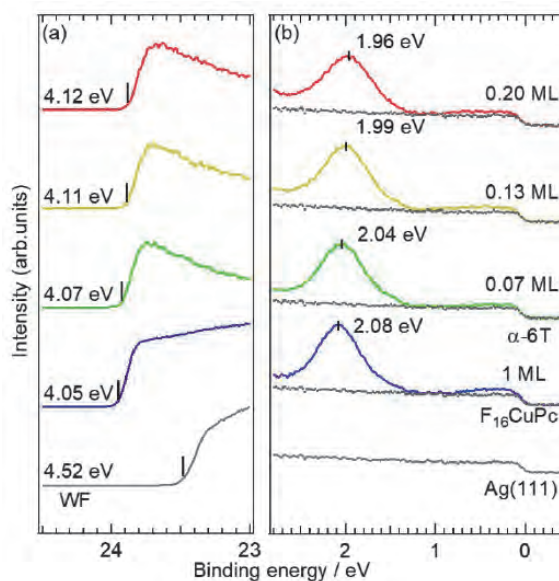


Fig. 1. Evolution of UPS spectra for 6T/F<sub>16</sub>CuPc interface as a function of 6T coverage.

[1] K. Akaike, A. Onishi, Y. Wakayama and K. Kanai, *J. Phys. Chem. C*, in press.

[2] J.P. Yang, F. Bussolotti, S. Kera and N. Ueno, *J. Phys. D: Appl. Phys.* **50** (2017) 423002.

BL3U

## Cobalt Oxide Catalyst in Carbonate Aqueous Solution Studied by Operando C K-edge XAFS Measurement

K. Yamada<sup>1</sup>, T. Hiue<sup>2</sup>, M. Nagasaka<sup>3</sup>, H. Yuzawa<sup>3</sup>, H. Kondoh<sup>2</sup>, Y. Sakata<sup>1</sup> and M. Yoshida<sup>1,4</sup>

<sup>1</sup>Faculty of Engineering, Yamaguchi University, Ube 755-8611, Japan

<sup>2</sup>Graduate School of Science and Technology, Keio University, Yokohama 223-8522, Japan

<sup>3</sup>Institute for Molecular Science, Okazaki 444-8585, Japan

<sup>4</sup>Blue energy center for SGE technology (BEST), Yamaguchi University, Ube 755-8611, Japan

In these days, the system to produce hydrogen by water electrolysis utilizing renewable energy such as solar, wind, and salinity concentration gains significant attention due to increasing global awareness of environmental issues. However, the efficiency of water electrolysis is not enough for commercial use, because of the high overvoltage on the oxygen evolution electrocatalyst. In this situation, Takanabe and co-workers reported that cobalt oxide catalyst electrodeposited in carbonate aqueous solution (Co-C<sub>i</sub>) could function as the efficient oxygen evolution reaction (OER) catalyst in 2014 [1]. On the other hand, our group find out the function of similar OER catalysts by operando observation using X-ray absorption fine structure (XAFS) technique [2]. Herein, we examined the operando XAFS measurements for Co-C<sub>i</sub> catalysts to reveal the function of carbonate species in the Co-C<sub>i</sub>.

A Teflon electrochemical cell was equipped with a Pt counter electrode and an Ag/AgCl reference electrode for all electrochemical experiments. The Co-C<sub>i</sub> thin films were electrodeposited on Au thin film in potassium carbonate aqueous solution (K-C<sub>i</sub>) containing Co(NO<sub>3</sub>)<sub>2</sub> at 1.7 V vs. RHE. The operando C K-edge XAFS spectra for Co-C<sub>i</sub> were taken under electrochemical control with transmission mode at BL3U in the UVSOR Synchrotron, according to the previous works [3].

First, we measured C K-edge XAFS for saturated K<sub>2</sub>CO<sub>3</sub> aqueous solution as reference sample (Fig. 1), in order to find out the absorption peak of carbonate species. The absorption peak was estimated around 290.3 eV, corresponding with a previous research about carbonate material [4].

Next, we measured operando C K-edge XAFS spectrum for Co-C<sub>i</sub> electrocatalyst. An absorption peak assigned to carbonate adsorbed on the Co-C<sub>i</sub> catalyst was observed around 290.4 eV. Moreover, when the electrode potential was changed from 0.5 V to 1.0 V, a new peak was observed around 290.6 eV. In our previous work about operando O K-edge XAFS spectra, we revealed that the CoO<sub>2</sub> structure was generated by the oxidation of CoOOH at higher electrode potential. Therefore, we think the new peak in the C K-edge XAFS is assigned to the carbonate species adsorbed on the CoO<sub>2</sub> structure and functions as the active site for OER process.

In conclusion, we found that the carbonate species were adsorbed on the CoO<sub>2</sub>/CoOOH structure in the Co-C<sub>i</sub> electrocatalyst by operando C K-edge XAFS and the interface of carbonate/CoO<sub>2</sub> was likely to work as efficient OER site.

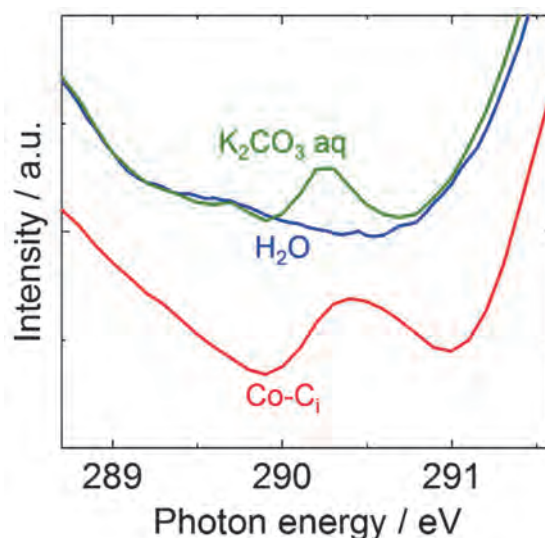


Fig. 1. Operando C K-edge XAFS spectra for the saturated K<sub>2</sub>CO<sub>3</sub> aqueous solution (green line) and Co-C<sub>i</sub> at 1.7 V vs. RHE (red line).

[1] K. Takanabe *et al.*, *Adv. Energy Mater.* (2014) 1400252.

[2] M. Yoshida *et al.*, *J. Phys. Chem. C* **121** (2017) 255.

[3] (a) M. Nagasaka *et al.*, *J. Phys. Chem. C* **117** (2013) 16343.

(b) M. Yoshida *et al.*, *J. Phys. Chem. C* **119** (2015) 19279.

[4] Chris Jacobsen *et al.*, *J. Synchrotron Rad.* **17** (2010) 676.



BL3B

## Evaluation of Optical Basic Properties of Ultra-Violet Emitting Zinc Aluminate Phosphor

H. Kominami<sup>1</sup>, M. Ohkawa<sup>1</sup>, Y. Kato<sup>1</sup>, M. Arimura<sup>1</sup>, K. Imagawa<sup>1</sup>, K. Warita<sup>2</sup>,  
S. Takahashi<sup>2</sup>, K. Higashi<sup>2</sup> and S. Nishibori<sup>2</sup>

<sup>1</sup>Graduate School of Integrated Science and Technology, Shizuoka University, Hamamatsu, 432-8651 Japan

<sup>2</sup>Faculty of Engineering, Shizuoka University, Hamamatsu, 432-8651 Japan

The UV light is used for various applications depending on the wavelength as well as the sterilization described above. The lights of 200-280 nm (UV-C) region as for the sterilization, 280-320 nm (UV-B) region as the treatment of the skin disease, 320-400 nm (UV-A) region as application of purification of water and air, and photocatalysts. Recently, from the viewpoint of consideration to the environment, the mercury free UV emission devices have been demanded for the application of catalyst and medical situations. In our previous work, it was clarified that  $\text{ZnAl}_2\text{O}_4$  phosphor was suitable for the UV field emission lamp because of its stability and luminescent property. It shows strong UV emission peaked around 250 nm which suitable for sterilization.

We are exploring the physical properties of  $\text{ZnAl}_2\text{O}_4$ , because the optical properties of  $\text{ZnAl}_2\text{O}_4$  have not been cleared. We tried the evaluation of  $\text{ZnAl}_2\text{O}_4$  using the powder phosphor. However, it is difficult to evaluate because of the influence of surface scattering, such as the absorption coefficient and refractive index reflectance. Therefore, we thought that the thin film analysis was suitable for correct measurements of the fundamental properties. In previous work,  $\text{ZnAl}_2\text{O}_4$  thin film prepared by thermal diffusion process using ZnO film on sapphire substrate. However, the optical measurement was difficult, because the composition of the film and each interface was not uniform.

In this study, to avoid the inarticulate interface of each layer, the multilayer film containing constituent elements was formed by sputtering on sapphire substrate, and tried to prepare the  $\text{ZnAl}_2\text{O}_4$  thin film by thermal diffusion.

In this experiment, we used an RF magnetron sputtering system. Fig.1 shows the experimental procedure of the  $\text{ZnAl}_2\text{O}_4$  film formation. ZnO layer was deposited on a, c, and m-plane sapphire substrates at room temperature. Next,  $\alpha\text{-Al}_2\text{O}_3$  thin layer was covered with ZnO to avoid re-evaporation by thermal diffusion process because of high evaporation pressure of Zn. All ZnO layer was sandwiched by  $\alpha\text{-Al}_2\text{O}_3$  layers. The films were annealed at 1000 °C for several hours in air to enhance thermal diffusion of Zn and Al atoms in the film. The films were evaluated by X-ray diffraction (XRD), scanning electron microscope (SEM), cross-sectional EPMA, and photo- and cathodoluminescence (PL, CL) systems were used.

Figure 1 shows transmittance spectra of  $\text{ZnAl}_2\text{O}_4$  thin film prepared on sapphire substrates annealed at 1000 °C for 100 hours. The absorption edge of  $\text{ZnAl}_2\text{O}_4$  on a-substrate was sifted to shorter wavelength. For comparison, Fig. 2 shows transmittance spectra of substrates. The change of absorption edge indicates that  $\text{ZnAl}_2\text{O}_4$  film on a-plane substrate was formed Al-rich  $\text{ZnAl}_2\text{O}_4$  spinel structure. From the figure, the interference fringes were also obtained. Now we try to calculate the refractive index from the spectra. We are expecting that the optical parameters of  $\text{ZnAl}_2\text{O}_4$  are obtain from the UVSOR measurement.

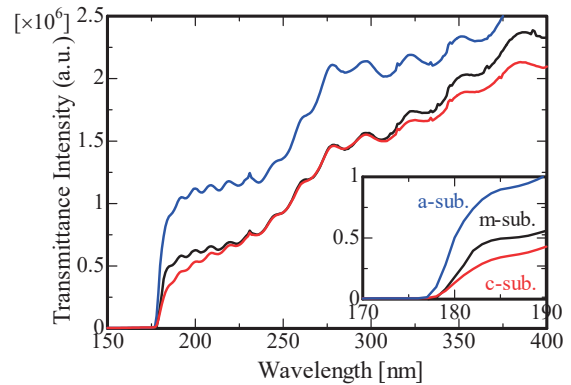


Fig. 1. Transmittance spectra of  $\text{ZnAl}_2\text{O}_4$  thin film prepared on several -plane sapphire substrates annealed at 1000 °C for 100 hours.

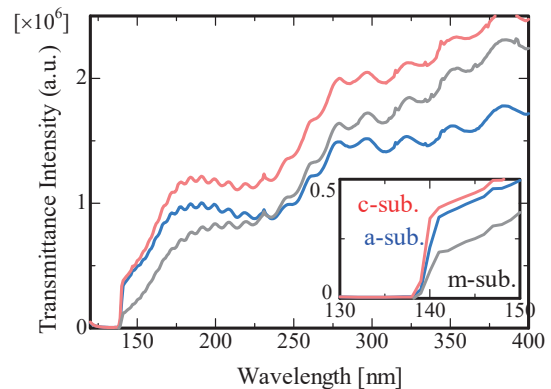


Fig. 2. Transmittance spectra of sapphire substrate.

BL4B, BL5B

## Observation of Photoinduced Phenomenon in Amorphous Chalcogenide Thin Films by Ultraviolet Synchrotron Orbital Radiation

K. Hayashi

*Department of Electrical, Electronic and Computer Engineering, Gifu University, Gifu 501-1193, Japan*

It is well known that amorphous semiconductor materials are very sensitive to the light and show a variety of photoinduced phenomena [1-3]. Therefore, amorphous semiconductor are very expected as materials for optoelectronic devices, such as solar cells, thin film transistors, light sensors, and optical memory devices etc. These applications require an understanding of the physical properties of amorphous materials. In our recent study, we observed interesting photoinduced change in the photoconductivity of amorphous chalcogenide films by the irradiation of the visible light with the energy corresponding to the optical bandgap. To obtain a wide knowledge of the photoinduced phenomena, we are trying to investigate photoinduced effects in the vacuum ultraviolet region by the transmission spectra. In the previous report, we have reported the transmission spectrum of amorphous arsenic selenium thin film measured at beamline BL5B [4, 5]. The inner core level absorption of this material is observed in the wavelength region between 16nm and 30nm. Amorphous thin films for transmission spectrum measurement can be easily prepared by conventional evaporation technique. The aluminum thin film used as a filter for removing higher order light from the monochromator in this wavelength region was used as a substrate for transmission spectrum measurement. However, beamline BL5B does not have very good wavelength accuracy and spectral resolution. Beamline BL4B has better wavelength accuracy and spectral resolution than BL5B, but it is not suitable for measurement in the lower energy region. In this report, we try to measure the transmission spectra of other materials that have absorption levels in the higher energy region and compare the results of BL4B and BL5B.

The metal thin films were prepared onto Corning 7059 glass plates with a pinhole of the diameter of 2.0mm. The transmission spectrum was measured through this pinhole. The metal thin film was used as a filter to eliminate the higher order light from the monochromator in the VUV region and also as a substrate of amorphous film. A gold thin film was used in the wavelength region between 5nm and 12nm, and an aluminum thin film was used in the wavelength region between 16nm and 36nm. A silicon photodiode was used as a detector in the wavelength region. The measurement of the transmission spectra in the VUV region was performed at room temperature at BL4B and BL5B of the UVSOR facility of the Institute for Molecular Science.

Figure 1 shows the transmitted light intensity of

metal thin films (Au and Al) measured at BL4B and BL5B by a silicon photodiode. As can be seen in the figure, the transmitted light intensity in the high energy region at BL4B is stronger than at BL5B, which is advantageous for the measurement of the transmission spectrum. In fact, the transmission spectra of amorphous films prepared on gold thin film substrates were able to be measured with higher resolution when measured with BL4B than with BL5B. On the other hand, the transmitted light intensity of the aluminum thin film in the low energy region near 30nm was not much different between the two beamlines. In the measurement of the transmission spectrum in the low energy region, the SN was lower in BL4B than in BL5B.

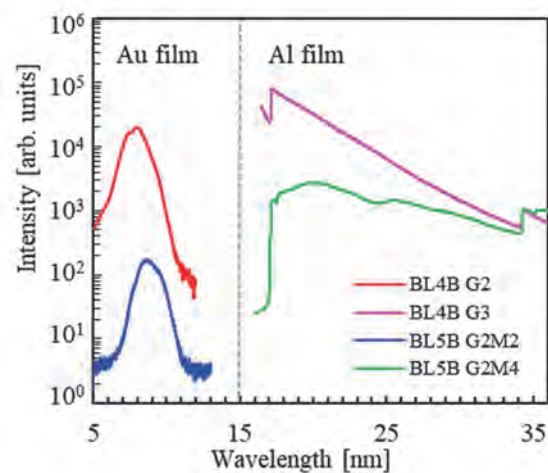


Fig. 1. Transmitted light intensity of thin metal films (Au and Al) measured at BL4B and BL5B by a silicon photodiode.

- [1] K. Tanaka, *Rev. Solid State Sci.* **4** (1990) 641.
- [2] K. Shimakawa, A. Kolobov and S. R. Elliott, *Adv. Phys.* **44** (1995) 475.
- [3] K. Tanaka, *Encyclopedia of Nanoscience and Nanotechnology* **7** (2004) 629.
- [4] K. Hayashi, *UVSOR Activity Report 2013* **41** (2014) 140.
- [5] K. Hayashi, *UVSOR Activity Report 2014* **42** (2015) 134.

BL4B

## Electronic and Magnetic Properties of FeNi Alloy Thin Films Grown on a Monatomic Layer Magnetic Nitride

T. Miyamachi<sup>1</sup>, K. Kawaguchi<sup>1</sup>, T. Hattori<sup>1</sup>, T. Koitaya<sup>2,3</sup>, T. Yokoyama<sup>2,3</sup> and F. Komori<sup>1</sup>

<sup>1</sup>*Institute for Solid State Physics (ISSP), The University of Tokyo, Kashiwa 277-8581, Japan*

<sup>2</sup>*Department of Materials Molecular Science, Institute for Molecular Science, Okazaki 444-8585, Japan*

<sup>3</sup>*Department of Structural Molecular Science, The Graduate University for Advanced Studies (SOKENDAI), Okazaki 444-8585, Japan*

L1<sub>0</sub>-ordered alloy thin films fabricated by the alternating deposition of magnetic or noble elements attract great attention for their strong uniaxial magnetic anisotropy. Especially, L1<sub>0</sub>-ordered FeNi alloy thin films, composed of cheap and abundant materials, raise the hope for rare-earth free permanent magnets compatible with NdFeB-based rare earth magnets. Previous studies revealed the close relationship between the strength of the uniaxial magnetic anisotropy and structural ordering. However, the order parameter *S* reported so far still remains low (up to ~ 40 %) for L1<sub>0</sub>-ordered FeNi alloy thin films and the magnetic easy axis is still along in-plane direction. The low *S* values could be caused by the atomic-scale disorder at the Fe/Ni interface during the fabrication processes, but the lack of the appropriate experimental method with high spatial resolution hampered the intrinsic improvement of structural and resulting electronic and magnetic properties of FeNi alloy thin films.

Toward realizing high quality FeNi alloy thin films, we here focus on the fabrication method utilizing nitrogen surfactant effects in a monatomic layer magnetic nitride. In this method, high lateral lattice stability, which is characteristic of a monatomic layer magnetic nitride [1, 2], and surfactant nitrogen during the deposition of Fe and Ni layers can effectively suppress the interdiffusion at the Fe/Ni interface, leading to atomically flat and homogeneous surface and interface of FeNi alloy thin films.

In this work, we investigate structural, electronic and magnetic properties of 1 monolayer (ML) Fe on a monatomic layer nickel nitride (Ni<sub>2</sub>N) grown on Cu(001), the initial stage for the fabrication of FeNi alloy thin films by means of nitrogen surfactant effects, using scanning tunneling microscopy (STM) combined with x-ray absorption spectroscopy/x-ray magnetic circular dichroism (XAS/XMCD). This complementary experimental approach allows to link macroscopic observations of element specific and quantitative electronic and magnetic properties by XAS/XMCD with microscopic origins of the Fe/Ni interface characteristics revealed by STM [3].

The growth of the Ni<sub>2</sub>N on Cu(001) was checked by STM before XAS/XMCD measurements. Likewise the fabrication process of a monatomic layer iron nitride (Fe<sub>2</sub>N) [1,2], N<sup>+</sup> ions with an energy of 500 eV were firstly bombarded to the Cu(001) substrate and 1 ML

Ni was deposited at room temperature. By subsequent annealing at ~ 670 K, well-ordered and flat 1 ML Ni<sub>2</sub>N was grown on the surface [4]. 1 ML Fe was thereafter deposited at a low temperature (~ 150 K).

XAS/XMCD measurements were performed at BL4B in UVSOR by total electron yield mode at  $B = \pm 5$  T and  $T = 7.1$  K. The XMCD spectra are obtained at the normal (NI:  $\theta = 0^\circ$ ) and the grazing (GI:  $\theta = 55^\circ$ ) geometries by detecting  $\mu_+ - \mu_-$ , where  $\mu_+$  ( $\mu_-$ ) denotes the XAS recorded at Ni and Fe L adsorption edges with the photon helicity parallel (antiparallel) to the sample magnetization. Note that  $\theta$  is the angle between the sample normal and the incident x-ray.

We find no clear Ni L<sub>3</sub> XMCD signal for bare Ni<sub>2</sub>N both in the NI and GI geometries, reflecting its paramagnetic character as previously reported [5]. However, the Ni magnetization is induced by adding 1 ML Fe as a consequence of the formation of Fe<sub>2</sub>N/Ni/Cu(001) via nitrogen surfactant effects. The electronic hybridization at the Fe/Ni interface modifies the strong in-plane magnetic anisotropy of Fe<sub>2</sub>N [2] toward an out-of-plane direction, but the uniaxial magnetic anisotropy has not yet been achieved.

In future work, combining STM and XAS/XMCD, we will further improve structural ordering of FeNi alloy thin films by annealing and discuss the impacts of surface/interface quality on their electronic and magnetic properties at the atomic scale.

[1] Y. Takahashi *et al.*, Phys. Rev. Lett. **116** (2016) 056802.

[2] Y. Takahashi *et al.*, Phys. Rev. B **95** (2017) 224417.

[3] S. Nakashima *et al.*, Adv. Funct. Mater. **29** (2019) 1804594.

[4] Y. Hashimoto *et al.*, Surf. Sci. **604** (2010) 451.

[5] F. Tanaka *et al.*, J. Appl. Phys. **120** (2016) 083907.



BL4B

## Magnetic Coupling at the Interface of Ferromagnetic Iron and Nickel Nitride Monatomic Layers

T. Miyamachi<sup>1</sup>, K. Kawaguchi<sup>1</sup>, T. Gozłinski<sup>1,2</sup>, T. Koitaya<sup>3,4</sup>,  
W. Wulfhekel<sup>2</sup>, T. Yokoyama<sup>3,4</sup> and F. Komori<sup>1</sup>

<sup>1</sup>*Institute for Solid State Physics (ISSP), The University of Tokyo, Kashiwa 277-8581, Japan*

<sup>2</sup>*Physikalisches Institut, Karlsruhe Institute of Technology (KIT), Karlsruhe D-76161, Germany*

<sup>3</sup>*Department of Materials Molecular Science, Institute for Molecular Science, Okazaki 444-8585, Japan*

<sup>4</sup>*Department of Structural Molecular Science, The Graduate University for Advanced Studies (SOKENDAI), Okazaki 444-8585, Japan*

L1<sub>0</sub>-ordered FeNi alloy thin films attract great attention as rare-earth free permanent magnets compatible with NdFeB-based magnets for their expected uniaxial magnetic anisotropy. Previous studies revealed the importance of structural ordering of FeNi alloy thin films on the emergence of the strong uniaxial magnetic anisotropy. However, the order parameter  $S$  of up to  $\sim 0.4$  reported so far still remains low. The atomic scale disorder could result in the low  $S$  values, but the details have been overlooked due to the lack of the appropriate experimental method with high spatial resolution. Toward achieving FeNi alloy thin films with high  $S$  values, we intend to utilize nitrogen surfactant effects in a monatomic layer magnetic nitride, which can effectively suppress the interdiffusion at the Fe/Ni interface and keep atomically flat surface/interface of FeNi alloy thin films.

For this purpose, we have recently performed scanning tunneling microscopy (STM) and x-ray absorption spectroscopy/x-ray magnetic circular dichroism (XAS/XMCD) measurements on a monatomic layer nickel nitride (Ni<sub>2</sub>N) on Cu(001) with 1 Fe overlayer, which is the initial stage for the fabrication of FeNi alloy thin films by means of nitrogen surfactant effects. The combined STM and XAS/XMCD study gives the comprehensive information on structural, electronic and magnetic properties of the system both from microscopic and macroscopic points of view. The results demonstrated that nitrogen surfactant effects lead to the formation of a monatomic layer iron nitride (Fe<sub>2</sub>N: [1]) on the surface [Ni<sub>2</sub>N/Cu(001)→Fe<sub>2</sub>N/Ni/Cu(001)], and the strong in-plane magnetic anisotropy of the Fe<sub>2</sub>N [2] is partially modified toward the out-of-plane direction. In this work, we further investigate the impacts of annealing on the Fe/Ni interface structures and magnetic properties of the system by STM and XAS/XMCD.

The Ni<sub>2</sub>N was grown on Cu(001) by following processes. First, N<sup>+</sup> ions with an energy of 500 eV were bombarded to the Cu(001) substrate and 1 ML Ni was deposited at room temperature. By subsequent annealing at 670 K, well-ordered and flat 1 ML Ni<sub>2</sub>N was grown on the surface [3]. The quality of the Ni<sub>2</sub>N surface was prechecked by STM and LEED before XAS/XMCD measurements. 1 ML Fe was then

deposited on the Ni<sub>2</sub>N at 150 K. This “as-deposited sample” was finally annealed up to 420 and 570 K.

XAS/XMCD measurements were performed at BL4B in UVSOR by total electron yield mode at  $T = 6.1$  K and  $B = 0-5$  T. The XMCD spectra are obtained at the normal (NI:  $\theta = 0^\circ$ ) and the grazing (GI:  $\theta = 55^\circ$ ) geometries by detecting  $\mu_+ - \mu_-$ , where  $\mu_+$  ( $\mu_-$ ) denotes the XAS recorded at Ni and Fe L adsorption edges with the photon helicity parallel (antiparallel) to the sample magnetization. Note that  $\theta$  is the angle between the sample normal and the incident x-ray.

We observed that the XMCD intensity at Fe L<sub>3</sub> edge of the as-deposited sample, Fe<sub>2</sub>N/Ni/Cu(001), increases by annealing at 420 K. Furthermore, the magnetization curves of Fe<sub>2</sub>N recorded in the NI and GI geometries reveals the enhancement of the magnetic anisotropy. Taking results of atomically resolved STM observations into account, these changes could be attributed to the promotion of the structural ordering at the Fe/Ni interface by annealing at an optimal temperature. In contrast, we found that annealing the as-deposited sample at 570 K degrades magnetic properties of the system. At this annealing temperature, the surface segregation of substrate Cu atoms is activated, locally weakening the magnetic coupling at the Fe/Ni interface.

In the future, we will grow high-quality thicker FeNi alloy thin films by additional alternating Fe and Ni depositions with controlled post-annealing processes, and investigate their structural, electronic and magnetic properties by STM and XAS/XMCD.

[1] Y. Takahashi *et al.*, Phys. Rev. Lett. **116** (2016) 056802.

[2] Y. Takahashi *et al.*, Phys. Rev. B **95** (2017) 224417.

[3] Y. Hashimoto *et al.*, Surf. Sci. **604** (2010) 451.

BL5U

## Valence-Band Electronic Structures of Ultra-Thin Co Layers on Rashba-Split Au (111) Surfaces

J. Okabayashi<sup>1,\*</sup>, K. Tanaka<sup>2</sup> and S. Mitani<sup>3</sup>

<sup>1</sup>Research Center for Spectrochemistry, The University of Tokyo, Tokyo 113-0033, Japan

<sup>2</sup>UVSOR synchrotron Facility, Institute for Molecular Science, Okazaki, 444-8585, Japan

<sup>3</sup>National Institute for Materials Science, Tsukuba 305-0047, Japan

When ferromagnetic transition metals (TMs) are deposited on the Rashba-type spin-orbit coupled surface, novel properties such as perpendicular magnetic anisotropy (PMA) are emerged at the interfaces, which are derived from the symmetry broken spin-orbit effects. The gold Au (111) surfaces have been investigated extensively by means of scanning tunneling microscopy and angle-resolved photoemission spectroscopy (ARPES) because this surface exhibits the large Rashba-type spin-orbit splitting. Large spin-orbit interaction in the heavy element of gold provides the wide varieties for the topological physics and spin-orbit coupled sciences at the surfaces and interfaces. The Rashba splitting of 110 meV in Au (111) surface was reported firstly by LaShell *et al.* [1]. Recently, the interfaces between Au(111) and other heavy elements such as Bi or Ag have been extensively investigated [2, 3]. Here, we focus on the interfaces between ferromagnetic materials and Au(111) interfaces because the thin Fe layers on the heavy elements are expected to exhibit the PMA induced by the Rashba-type spin-orbit interaction.

The spin-orbit coupling between the ferromagnetic 3d TMs Fe or Co and 5d heavy TM elements of non-ferromagnetic materials such as Pt and Au has been utilized for the PMA through the proximity at the interfaces. It is believed that the future researches concerning not only spins but also orbitals are recognized as the *spin-orbitronics*. Therefore, to clarify the origin of the PMA at these interfaces is a crucial role. The relationship between Au (111) Rashba-type spin-orbit interaction and PMA in 3d TMs has not been clarified explicitly. In order to investigate the orbital-resolved states in the Fe films showing the PMA, ARPES at the interfaces becomes powerful techniques through the photon-energy and polarization dependences in each 3d orbital. By using ARPES, we aim to understand the orbital-resolved electronic structures at the magnetic interfaces on the Rashba-type Au (111) surface in order to develop the researches of novel PMA using spin-orbit coupled interfaces.

We prepared the clean Au (111) surface for the Co deposition. The commercialized single-crystalline 100-nm-thick Au (111) films on Mica were used. At the beamline BL5U in UVSOR, we repeated the Ar-ion sputtering at 1 kV accelerating voltage and subsequent annealing at 400 °C under the high vacuum conditions. After the sample preparation, the Co layer was deposited at room temperature and then annealed. By *in-situ* transferring the samples into the ARPES chamber, we performed ARPES at 10 K using the

photon energies of 60 and 120 eV because of the large cross-section of Au (111) surface states and detections of Co 3s and Au 4f intensity ratios, respectively.

Figure 1 displays the Co deposition dependence on Au (111). As shown in Fig. 1a, the intensity ratio between Co 3s and Au 4f peaks systematically changes. The Au (111) surface clearly exhibits the Rashba-type surface states. The Co 3d states appear near the Fermi level ( $E_F$ ) and the surface states disappear. As shown in Fig. 1b,  $k_x$ - $k_y$  plots taken by horizontal and vertical polarized beams exhibit asymmetric feature, which can be explained by the Co 3d orbital resolved states through the overlap between Co and Au. Furthermore, we confirmed the PMA at Co/Au interface by x-ray magnetic circular dichroism. Therefore, the interfacial chemical reaction between Co and Au brings the novel properties on the ultrathin Co electronic structures.

We acknowledge Dr. S. Ideta in IMS for technical supports of data analyses. This work was in part supported by KAKENHI Kiban(S) project.

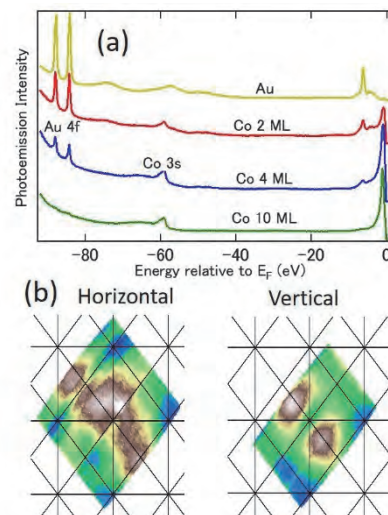


Fig. 1. (a) Photoemission spectra for various Co deposited layers taken at 120 eV. (b) Polarization-dependent  $k_x$ - $k_y$  Fermi surface mapping of Co 4 ML taken at 60 eV.

- [1] S. LaShell *et al.*, Phys. Rev. Lett. **77** (1996) 3419.  
 [2] C. Tusche *et al.*, Ultramicroscopy **159** (2015) 620.  
 [3] B. Yan *et al.*, Nature Commun. **6** (2015) 10167.

\*e-mail: jun@chem.s.u-tokyo.ac.jp

BL5U

## Effects of P Segregation on the Surface Electronic Structure of Fe<sub>2</sub>P(0001)

N. Maejima<sup>1,2</sup>, Y. Sugizaki<sup>1</sup>, Y. Shimato<sup>1</sup>, T. Yoshida<sup>1</sup> and K. Edamoto<sup>1,2</sup>

<sup>1</sup>Department of Chemistry, Rikkyo University, Tokyo 171-8501, Japan

<sup>2</sup>Research Center for Smart Molecules, Rikkyo University, Tokyo 171-8501, Japan

Transition metal phosphides (TMPs) are good candidates for the catalyst in the next generation for hydrodesulfidation. Although Ni<sub>2</sub>P shows the highest catalytic activity among TMPs, Fe<sub>2</sub>P, which have the same crystal structure as that of Ni<sub>2</sub>P, shows the lowest catalytic activity.[1] One of possible origins of the activity difference is the difference in the surface electronic structures of these catalysts. We have reported that surface segregation of P atoms in Ni<sub>2</sub>P induces the change of surface electronic structure in the vicinity E<sub>F</sub>. [2, 3] On the other hand, P segregation in Fe<sub>2</sub>P(10-10) had little effect on the surface electronic structure around E<sub>F</sub>. [4] In this study, we investigated the process of P segregation induced by annealing and its effect on the electronic structure of Fe<sub>2</sub>P(0001) using photoelectron spectroscopy (PES) at BL5U, and the results will be compared with those of Ni<sub>2</sub>P.

Figure 1 shows the peak intensity ratio of P<sub>LMM</sub> to Fe<sub>MVV</sub> obtained by Auger electron spectroscopy (AES) in various conditions of annealing temperature. The ratio decreased by annealing at temperatures lower than 400 °C and increased with annealing at higher than 400 °C. It indicates that the surface segregation induced by the annealing at higher than 400 °C. The P segregation process was studied in detail by P 2p PES. Figure 2 show the results of the fitting of the P 2p spectrum of Fe<sub>2</sub>P(0001) clean surface. The spectrum can be fit with seven P components. The inspection of annealing temperature dependence of each peak shows that a,b,d,f and g components are increased in intensity by annealing at higher than 350 °C, while those of c and e components are decreased by annealing at higher than 350 °C. PES and AES results indicate that segregation and desorption of P atoms compete at 350 °C and segregation exclusively proceeds at higher than 400 °C. Finally, we studied the change of surface electronic structure by the heating treatment. Figure 3 shows the valence band spectra of Fe<sub>2</sub>P(0001) annealed at various temperatures at 300 – 700 °C. All spectra are normalized by the peak top intensity at 0.2 eV. Although the spectral line shape in the range of 1 - 4 eV is changed by annealing, the peak in the vicinity of the E<sub>F</sub> did not show any shifts. These results indicate that segregated P atoms have little effect on the surface electronic structure around E<sub>F</sub> of Fe<sub>2</sub>P(0001). Although the Ni 3d states are stabilized through the segregating P atoms for the Ni<sub>2</sub>P, the Fe 3d states are not changed by P segregation for Fe<sub>2</sub>P, which would be one of the possible origins of the stark contrast in the catalytic activities of these materials.

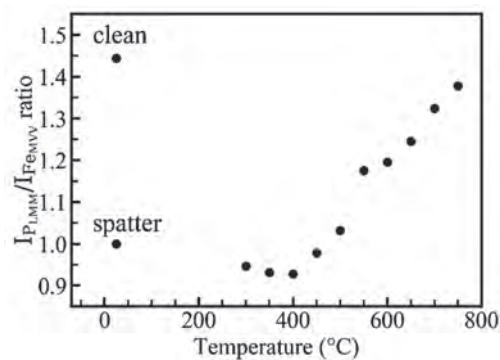


Fig. 1. The results of Auger electron intensity ratio at each annealing temperature.

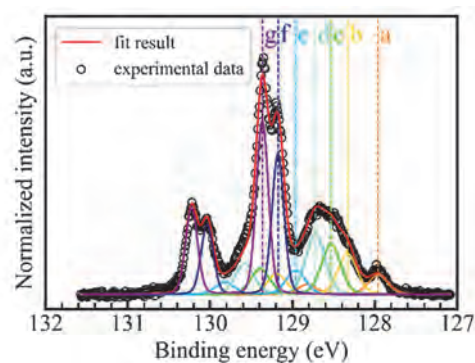


Fig. 2. Fitting result of P 2p spectra obtained from clean surface of Fe<sub>2</sub>P(0001).

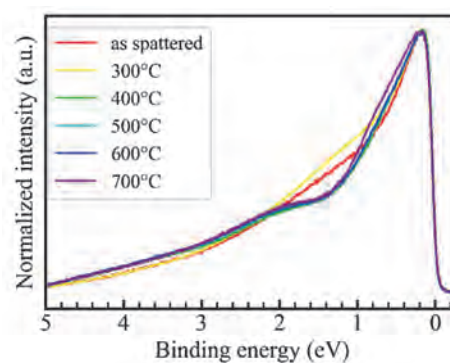


Fig. 3. The change of valence band spectrum obtained from the sample annealed at each temperature.

- [1] S. T. Oyama *et al.*, *Catal Today* **143** (2009) 94.
- [2] K. Edamoto *et al.*, *Appl. Surf. Sci.* **269** (2013) 7.
- [3] S. Ishida *et al.*, *e-J. Surf. Sci. Nanotech.* **13** (2015) 93.
- [4] Y. Sugizaki *et al.*, *Jpn. J. Appl. Phys.* **57** (2018) 115701.



BL5U

## Measuring the Berry Curvature of Dresselhaus Semiconductor by Circular Dichroism ARPES

 S. Cho<sup>1</sup>, D. Oh<sup>2,3</sup>, K. Tanaka<sup>4</sup>, S. R. Park<sup>5</sup> and C. Kim<sup>2,3</sup>
<sup>1</sup>*Institute of Physics and Applied Physics, Yonsei University, Seoul 03722, Korea*
<sup>2</sup>*Center for Correlated Electron Systems, Institute for Basic Science (IBS), Seoul 08826, Republic of Korea*
<sup>3</sup>*Department of Physics and Astronomy, Seoul National University (SNU), Seoul 08826, Republic of Korea*
<sup>4</sup>*UVSOR Synchrotron Facility, Institute for Molecular Science, Okazaki 444-8585, Japan*
<sup>5</sup>*Department of physics, Incheon National University, Incheon 406-772, Korea*

Recently, Datta and Das [1] proposed that spin-field-effect transistor (spin-FET) can be shown by in light of controllability of spin precession motion of electrons of zinc blende semiconductors (ZBS) [2, 3, 4]. The ZBS have unique features; broken inversion symmetry and strong spin orbit coupling (SOC). The features lead to an effective momentum dependent magnetic field which lifts the spin degeneracy of the electrons in the materials. The helical spin structure can be described successfully by Rashba and Dresselhaus model at a constant energy contour of the valence band [5]. The unique spin structure lead to the noble spin transport, spin Hall effect, and this was shown by Kerr rotation measurement in GaAs with zinc blende structure generally imply that there is a transvers velocity which proportional to the Berry curvature [6, 7]. Understanding the Berry curvature of the ZBS is considered important to develop the spin-FET.

In this study, we try to investigate the Berry curvature of HH and LH band of ZBS. We note that the semiconductor with zinc blende structure generally have the three hole bands which consist of 2-fold degenerate ( $j = 1/2$ ) and 4-fold degenerate ( $j = 3/2$ ) state, resulting from the SOC and a negligible crystal field. The  $j = 3/2$  state split into heavy- ( $m_j = \pm 3/2$ ) (HH) and light hole ( $m_j = \pm 1/2$ ) (LH) bands near the Fermi level. The  $j = 1/2$  state, called split-off band, is located at a higher binding energy about the energy splitting ( $\Delta$ ) than  $j = 3/2$  state. This splitting  $\Delta$  is determined by the magenitude of the spin-orbit interaction. Since the HH and LH state have different value of  $m_j$ , it is expected that the Berry curvature have different behavior [8].

To show the Berry curvature of Bloch state in the ZBS, we note a recent proposal, based on the study on the relation bewteen Berry curvature and circular dichroism (CD)-ARPES, that the CD-signal is approximatly

proportional to the Berry curvature in 2H-WSe<sub>2</sub> [9]. It implied that CD-ARPES can show the Berry curvature of Bloch state in momentum space. From the previous study, it is expected that the diffetent behavior of the Berry curvature between HH and LH state can be shown by CD-ARPES measurement.

Figures 1(a) and (b) show the ARPES intensity map of InSb at a binding energy 0.6 eV obtained from right- (RCP) and left (LCP) circularly polarized light. Then, we can have CD-signal, as shown in Fig. 1(c), from the difference between the intensity map taken from RCP and LCP light. In our result as depicted in Fig. 1(c), outer (inner) band indicate the CD-intensity map of HH (LH) band. But, they seem to illustrate a similar CD-pattern. We think that our CD-intensity map reflected the final state effect because CD-ARPES data of HH and LH band were taken with 2nd Brillouin zone (BZ). In that experiments, since the ARPES intensities with RCP and LCP light in first BZ were too low, we chose the 2nd BZ.

- [1] S. Datta *et al.*, Appl. Phys. Lett. **56** (1990) 665
- [2] Y. A. Bychkov *et al.*, JETP Lett. **39** (1984) 78.
- [3] J. Schliemann *et al.*, Phys. Rev. Lett. **90** (2003) 146801.
- [4] X. Cartoixa *et al.*, Appl. Phys. Lett. **83** (2003) 1462.
- [5] G. Dresselhaus, Phys. Rev. **100** (1955) 2.
- [6] S. Murakami *et al.*, Science **301** (2003) 1348.
- [7] Y. K. Kato *et al.*, Science **306** (2004) 1910.
- [8] M.-C. Chang and Q. Niu, J. Phys.: Condens. Matter **20** (2008) 193202.
- [9] S. Cho *et al.*, PRL **121** (2018) 186401.

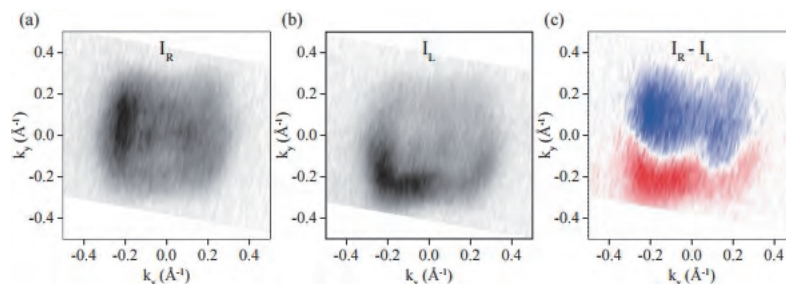


Fig. 1. ARPES intensity map of InSb at a binding energy 0.6 eV taken with (a) right and (b) left circularly polarized 70 eV light. (c) Circular dichroism (CD) intensity obtained from the difference between (a) and (b).

BL6U

## Arpes Study of $(\text{Bi}_x\text{Sb}_{1-x})_2\text{Se}_3$ Topological Insulators

 L. Yashina<sup>1</sup> and F. Matsui<sup>2</sup>
<sup>1</sup>Chemistry Department, Moscow State University, Moscow 119991, Russian Federation

<sup>2</sup>UVSOR Synchrotron Facility, Institute for Molecular Science, Okazaki 444-8585, Japan

Band structure of crystals of a series of solid solutions  $(\text{Bi}_x\text{Sb}_{1-x})_2\text{Se}_3$  ( $x=1 - 0.7$ ) between prototypical topological insulator (TI)  $\text{Bi}_2\text{Se}_3$  [1] and trivial insulator (BI)  $\text{Sb}_2\text{Se}_3$  was studied by means of ARPES. In the  $\text{Bi}_2\text{Se}_3$ - $\text{Sb}_2\text{Se}_3$  system, topological phase transition was predicted theoretically. In this project we have aimed on revealing its relevant aspects: spontaneous destroying or gap formation in Dirac cone and  $x$  composition corresponding to topological phase transition. For better surface sensitivity photon energy  $h\nu=60$  eV was chosen.

Increasing an antimony content leads to Dirac point shifting towards bulk valence band at range  $x=1-0.8$ . This trend breaks at  $(\text{Bi}_{0.7}\text{Sb}_{0.3})_2\text{Se}_3$  composition (Fig.1a). In case of its electronic structure, Dirac point

is located approximately at the same energy that in  $\text{Bi}_2\text{Se}_3$  (Fig.1a). However, exact energy position of Dirac point in  $(\text{Bi}_{0.7}\text{Sb}_{0.3})_2\text{Se}_3$  is hard to estimate. Bisthmus-like band structure near Dirac point allowed us to suggest, that backscattering channels starts to open near the  $(\text{Bi}_{0.7}\text{Sb}_{0.3})_2\text{Se}_3$  composition, but no energy gap in topological surface state was not observed (Fig.1b).

[1] Y. Xia *et al.*, Nat. Phys. **5** (2009) 398.

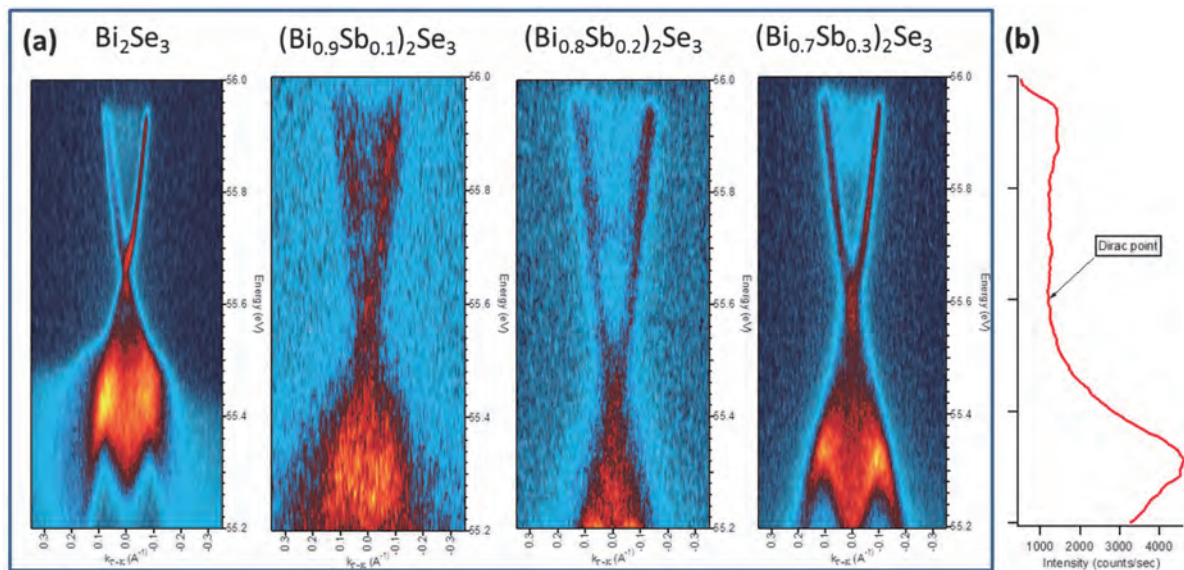


Fig. 1. a) Energy dispersion curves along  $\text{K}-\Gamma-\text{K}$  direction as a function of crystal composition. b) Constant momentum cross-section at  $k_{\Gamma-\text{K}}=0$  for  $(\text{Bi}_{0.7}\text{Sb}_{0.3})_2\text{Se}_3$  compound.

BL6U

## Reversible and Irreversible Metal-insulator Transition of VO<sub>2</sub>

T. Zhai<sup>1</sup>, J. Yang<sup>1</sup>, F. Matsui<sup>2</sup> and S. Duhm<sup>1</sup><sup>1</sup>Institute of Functional Nano & Soft Materials (FUNSOM), Soochow University, Suzhou 215123, P. R. China<sup>2</sup>UVSOR Synchrotron Facility, Institute for Molecular Science, Okazaki 444-8585, Japan

Vanadium Dioxide (VO<sub>2</sub>) is widely known for its first order metal-insulator transition (MIT) property. The MIT goes along with a structural change from a monoclinic phase to a rutile phase at 340 K, while the conductivity increases 5 orders of magnitude comparing to the insulating phase. Moreover, also oxygen vacancies [1] or soft X-ray irradiation [2] can lead to a metallic state.

Figure 1 shows the electronic structure of insulating and metallic VO<sub>2</sub> based on a previous photoelectron spectroscopy (PES) study [3]. For insulating VO<sub>2</sub> the occupied V 3d derived orbital (termed as  $d_{||}$ ) is located below the Fermi level, while the other two V 3d orbitals,  $d_{||}^*$  and  $\pi^*$ , are unoccupied and provide a 0.6 eV band gap. In the metallic phase the  $d_{||}$  and  $\pi^*$  orbitals are partially filled. Interestingly, non-stoichiometric VO<sub>2- $\delta$</sub>  shows a similar behavior. However, the details of the electronic structure are not clarified yet. Especially the unoccupied DOS of VO<sub>2- $\delta$</sub>  is largely unexplored. Thus, we performed X-ray absorption spectroscopy (XAS), resonant photoemission (RPES) and ultraviolet photoelectron spectroscopy (UPS) experiments at BL6U.

VO<sub>2</sub> thin films were fabricated by pulsed laser deposition (PLD) [1,3] and cleaned by sputtering and annealing cycles in the ultra-high vacuum (UHV) preparation chamber of the BL6U endstation. The stoichiometry can be controlled by annealing at 423 K in UHV (base pressure:  $\sim 8 \times 10^{-10}$  mbar) or in partial oxygen atmosphere ( $\sim 9 \times 10^{-5}$  mbar).

The XAS spectra in Fig. 2 show the V L-edge and the O K-edge regions of pristine, stoichiometric VO<sub>2</sub> at room temperature (RT), the sample after an exposure to X-rays of 180 min and a pristine VO<sub>2</sub> sample at 388 K. The peak shift at the V L<sub>3</sub> edge at  $\sim 511.6$  eV is ascribed to the weight increase of  $t_{2g}$  due to the irradiation, which also narrows the band gap; the  $t_{2g}$  of O K-edge region from irradiation induced VO<sub>2</sub> exhibits weight loss. In the meantime the energy interval between the  $t_{2g}$  and  $e_g$  becomes smaller. UPS (not shown) confirms a metallic state of irradiated VO<sub>2</sub>. The irradiation induced phase is different to the temperature induced metallic phase. In particular, the main absorption peak at the V L-edge shift does not show an apparent shift. The O K-edge absorption features reveal that there is almost no oxygen loss during the temperature induced reversible MIT.

In conclusion, our preliminary data analysis confirms that X-ray exposure of VO<sub>2</sub> leads to a non-reversible phase transition and to a metallic state at RT. Analyzing the additional XAS data and the RPES and UPS data measured at BL6U, will allow us to understand the mechanism leading to this phase transition. Moreover, our data will also shed light on the electronic structure

of VO<sub>2</sub> upon the temperature and the oxygen vacancy induced MIT.

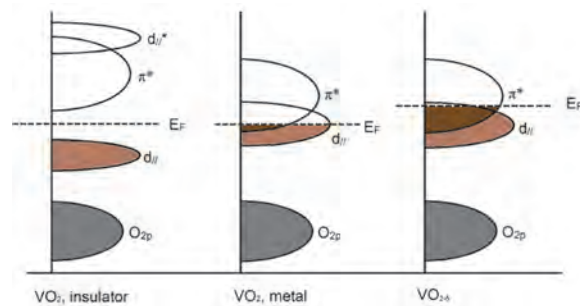


Fig. 1. Electronic structure of stoichiometric VO<sub>2</sub> (insulating and metallic phase) and VO<sub>2- $\delta$</sub> . In the insulating state a gap opens between the V 3d derived  $d_{||}^*$ ,  $\pi^*$  and  $d_{||}$  orbitals. Taken from Ref. [3].

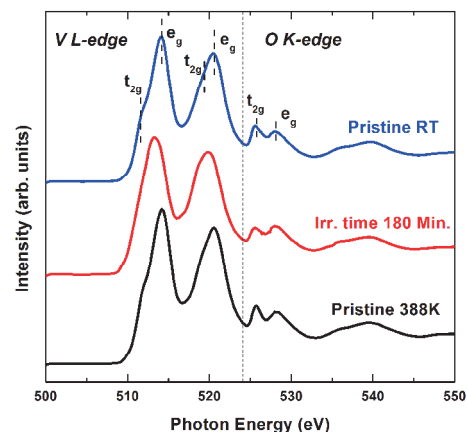


Fig. 2. XAS spectra for pristine VO<sub>2</sub> at RT, the same sample after 180 minutes of X-ray exposure and pristine VO<sub>2</sub> at 388 K. In all cases, the V L-edge region and the O K-edge region are shown. The peaks are labeled according to Ref. [4].

[1] R.-B. Wang, T. Katase, K.-K. Fu, T.-S. Zhai, J.-C. Yang, Q.-K. Wang, H. Ohta, N. Koch and S. Duhm, *Adv. Mater. Interfaces* **5** (2018) 1801033.

[2] V. R. Singh, V. Jovic, I. Valmianski, J. G. Ramirez, B. Lamoureux, I. K. Schuller and K. E. Smith, *Appl. Phys. Lett.* **111** (2017) 241605.

[3] K.-K. Fu, R.-B. Wang, T. Katase, H. Ohta, N. Koch and S. Duhm, *ACS Appl. Mater. Interfaces* **10** (2018) 10552.

[4] R. Zimmermann, R. Claessen, F. Reinert, P. Steiner and S. Hüfner, *J. Phys.: Condens. Matter* **10** (1998) 5697.



BL6U

## Resonant Photoemission Spectroscopy of Aligned Graphene Nanoribbons

D. Usachov<sup>1</sup>, B. Senkovskiy<sup>2</sup> and F. Matsui<sup>3</sup>

<sup>1</sup>Saint Petersburg State University, 7/9 Universitetskaya Nab., St. Petersburg 199034, Russia

<sup>2</sup>II. Physikalisches Institut, Universität zu Köln, Zùlpicher Strasse 77, 50937 Köln, Germany

<sup>3</sup>UVSOR Synchrotron Facility, Institute for Molecular Science, Okazaki 444-8585, Japan

Absence of a band gap in graphene prevents its wide use in electronic devices. This problem can be overcome by reducing dimensionality from 2D to 1D. Due to quantum confinement graphene nanoribbons (GNRs) have a notable band gap and a tunable electronic structure, and therefore they are a promising material for optoelectronic applications. Furthermore, thanks to the bottom-up nanofabrication technique it is possible to synthesize atomically precise GNRs with defined electronic properties. GNRs also represent significant fundamental interest because of being an intermediate system between a 2D crystal and molecules. Their valence band is formed by a set of subbands possessing dispersion along the ribbon axis, while in perpendicular direction the wave function is trapped in a narrow quantum well [1]. Bottom-up synthesis allows atomically precise fabrication of GNRs of fixed width. The present work is devoted to resonant photoemission study of 7-atom-wide armchair-edge GNRs (7-AGNRs) aligned on a stepped Au(788) surface.

The C K-edge NEXAFS spectrum of 7-AGNR contains fine features, which can be associated with different unoccupied subbands [2]. Therefore, it was expected that photoemission from different subbands could be selectively enhanced by tuning the photon energy near the absorption resonance.

Figure 1 shows preliminary results of our study. The upper row corresponds to such tilting angle of sample, at which the topmost valence subband (indicated by the arrow) has maximal intensity. At the photon energy of 284.6 eV, which is just below the absorption edge, this subband is not visible because of low photoemission cross section. When the photon energy is increased to 285 eV the subband is resonantly enhanced (shown with white arrow). However, already at 285.8 eV it disappears.

The second row corresponds to the second subband. We have found that its behavior is different from the first one. While it is resonantly enhanced at 285 eV, it does not disappear at 285.8 eV. For the third subband (shown in the third row) the resonance seems to be shifted to higher photon energies. This is a clear indication that different valence subbands are selectively excited with photons of different energy at the C absorption K-edge. Further theoretical calculations will be performed to understand this effect in more detail.

Another result of our study was the discovery of the fact that 7-AGNRs undergo radiation damage when the photon energy is set to the C K-edges absorption resonance. The valence bands rapidly vanish under the photon beam. We suppose that photoexcited

nanoribbons undergo dehydrogenation and become chemically active due to formation of carbon dangling bonds. Such active edge carbon atoms may react with adsorbates. This opens a possibility for chemical functionalization of GNRs by means of photostimulated reactions. This possibility will be explored in more detail in the future experiments.

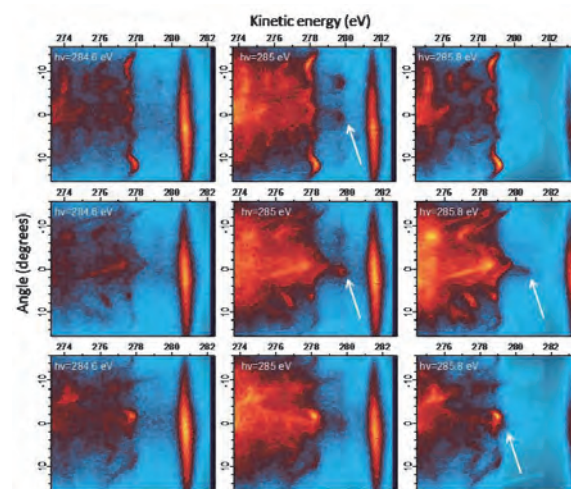


Fig. 1. Resonance photoemission of 7-AGNR at the carbon K-edge. Different rows correspond to different sample orientations at which different subbands exhibit the highest intensity.

- [1] B. V. Senkovskiy *et al.*, 2D Mater. **5** (2018) 035007.  
 [2] B. V. Senkovskiy *et al.*, ACS Nano **12** (2018) 7571.

BL6U

## Photoemission Tomography of Organic Monolayer: Substrate-assisted Intermolecular Dispersion of PTCDA on Cu(100)

A. Haags<sup>1,2</sup>, M. Meissner<sup>3</sup>, X. Yang<sup>1,2</sup>, F. Matsui<sup>3</sup>, S. Soubatch<sup>1,2</sup>, F. S. Tautz<sup>1,2</sup> and S. Kera<sup>3</sup><sup>1</sup>Peter Grünberg Institut (PGI-3), Forschungszentrum Jülich, 52425 Jülich, Germany<sup>2</sup>Jülich Aachen Research Alliance, Fundamentals of Future Information Technology, 52425 Jülich, Germany<sup>3</sup>UVSOR Synchrotron Facility, Institute for Molecular Science, Okazaki 444-8585, Japan

The transport properties of electronic materials are crucial for device performances. This is particularly important for organic-based electronics [1, 2], because charge mobility in molecular films is usually restricted due to a hopping transport, while exclusively band-like transport along the  $\pi$  stacking direction is expected in well-structured films. However, recently several reports have been published about intermolecular band dispersion of occupied states in the organic monolayers on metal in the lateral direction. Since there is no significant overlap of  $\pi$  states, the rise of dispersion in these cases has been attributed to molecule-substrate hybridization. An example is the strong intermolecular dispersion of the former lowest unoccupied molecular orbital (f-LUMO) of perylene-tetracarboxylic dianhydride (PTCDA) on Cu(100) [3]. Upon PTCDA adsorption on Cu(100), its LUMO becomes occupied due to the charge transfer from copper and forms a dispersive band whose momentum-space ( $k$ -space) pattern clearly reflects the symmetry of the PTCDA/Cu(100) interface [3].

An intriguing aspect in this context is the  $k$ -space character of the hybridized molecular electronic states. Recently it has been shown by means of photoemission tomography that the  $k$ -space patterns of particular molecular states usually retain their shapes despite hybridization and charge transfer [4]. Only in case of the dispersive mixed state, the modified symmetry of wavefunctions becomes apparent in the  $k$ -space patterns as an additional fine-structure [3, 5]. So far it remains unclear, why the symmetry of the hybridized molecular states changes in some cases and remains intact in others. To shed light on this issue, a combined experimental and theoretical approach is required. The experimental setups used so far for photoemission tomography, such as  $k$ -space imaging photoemission microscopes and a toroidal electron spectrometer, suffer from poor energy and  $k$ -space resolution, which is particularly needed for a characterization of dispersive bands. On the other hand, the analytical tools providing state-of-the-art resolution, for example hemispherical analyzers, do not have the  $k$ -space imaging option.

To address this issue, we initiated a series of experiments using the two-dimensional (2D) angle-resolved photoemission end-station based on an MBS A-1 hemispherical electron analyzer with modified lens system at the BL6U beamline of UVSOR. The 2D  $k$ -space resolution in this case is achieved by a mechanical deflection of the lens system perpendicular to the

entrance slit of the analyzer. Correspondingly, the photoemission distribution is recorded as a set of energy distribution maps depending on the deflection angle resulting in a three-dimensional dataset  $I(E_{kin}, \varphi, \theta)$ .

To demonstrate the capability of the setup for photoemission tomography applications, we grew a commensurate monolayer of PTCDA on Cu(100) and carried out angle-resolved photoemission spectroscopy at room and low temperature. To visualize the experimental results, we developed a python-based software. The 2D angle-space resolved photoemission patterns measured at the binding energy corresponding to the f-LUMO, clearly resemble the contrast of the major LUMO emission lobes as well as substrate-related features - copper  $sp$ -bands.

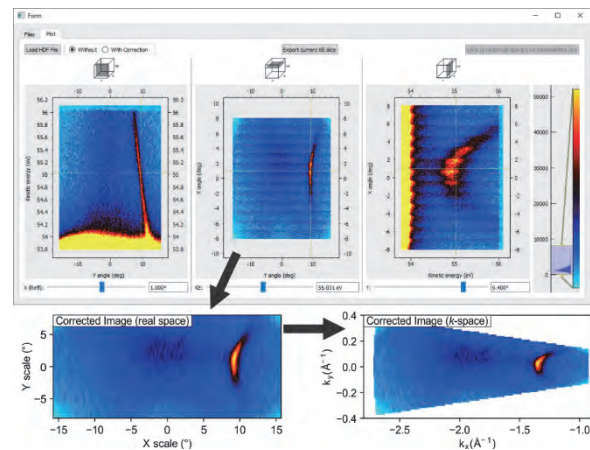


Fig. 1. Screenshot of the python-based software for data evaluation. Top: slicing in different axes of the 3D data cube  $I(E_{kin}, \varphi, \theta)$  measured on PTCDA/Cu(100); Bottom Left: corrected  $I(\varphi, \theta)$  image for  $E_{kin} = 55$  eV; Bottom Right: corresponding image converted to reciprocal space.

- [1] M. Schwarze *et al.*, Nat. Mat. **18** (2019) 242.
- [2] N. Ueno and S. Kera, Prog. Surf. Sci. **83** (2008) 490.
- [3] D. Lüftner *et al.*, Phys. Rev. B **96** (2017) 125402.
- [4] S. Weiss *et al.*, Nat. Commun. **6** (2015) 8287.
- [5] T. Ules *et al.*, Phys. Rev. B **90** (2014) 155430.

BL7U

## Fabrication of $\text{Bi}_1\text{Te}_1$ Ultrathin Films and the Surface Electronic Structure

S. Kusaka<sup>1</sup>, K. Yokoyama<sup>1</sup>, S. Ideta<sup>2</sup>, K. Tanaka<sup>2</sup>, S. Ichinokura<sup>1</sup> and T. Hirahara<sup>1</sup>

<sup>1</sup>Department of Physics, Tokyo Institute of Technology, Tokyo 152-8551, Japan

<sup>2</sup>UVSOR Synchrotron Facility, Institute for Molecular Science, Okazaki 444-8585, Japan

A typical example of a compound composed of Bi and Te is  $\text{Bi}_2\text{Te}_3$  (Te-Bi-Te-Bi-Te), which is known as a strong topological insulator (TI), but compounds having different composition ratios also exist. One of them,  $\text{Bi}_1\text{Te}_1$ , is a superlattice (Te-Bi-Te-Bi-Te - Bi-Bi-Te-Bi) in which two  $\text{Bi}_2\text{Te}_3$  quintuple layer (QL) and one bilayer (BL) of Bi stack alternately [1]. There can be three types of terminations for this material, namely 1QL and 2QL  $\text{Bi}_2\text{Te}_3$  terminations or a BL-Bi termination. It is called a dual TI and has a surface state of a topological crystal insulator (TCI) which is protected by the mirror symmetry of a crystal and a surface state of a weak topological insulator protected by time reversal symmetry. They are located at different surface orientations. Thus it has been predicted that  $\text{Bi}_1\text{Te}_1$  can realize novel exotic properties by breaking individual symmetries protecting different topologies by applying a magnetic field or a lattice distortion and inducing a gap in the respective surface Dirac cone [2].

In the previous study,  $\text{Bi}_1\text{Te}_1$  was prepared by depositing Bi and Te at a ratio of 1:1 with molecular beam epitaxy (MBE), and its electronic structure was reported [2]. However, the surface termination seemed to be mixed between 1QL and 2QL  $\text{Bi}_2\text{Te}_3$ . Therefore, for a better understanding of  $\text{Bi}_1\text{Te}_1$ , establishment of a stable sample preparation method with a well-defined surface termination is required. Therefore in the present study, we tried to fabricate a  $\text{Bi}_1\text{Te}_1$  thin film with controlled termination by a different method. Namely, first we fabricated  $\text{Bi}_2\text{Te}_3(111)$  films by depositing Bi and Te at a ratio of 1:5 with MBE (Fig. 1 (a)) and then annealed it to get rid of Te layers. The samples thus prepared showed three different band

dispersions as shown in Fig. 1 (b-d) before breaking. We found through comparison with *ab initio* calculations for  $\text{Bi}_1\text{Te}_1$  with different surface terminations that (b) showed similarities with the 2QL- $\text{Bi}_2\text{Te}_3$  terminated  $\text{Bi}_1\text{Te}_1$ , whereas (d) was similar to the 1QL- $\text{Bi}_2\text{Te}_3$  terminated  $\text{Bi}_1\text{Te}_1$ , although there was no quantitative match [2]. (c) was identified as an intermediate state of (a) and (b). Furthermore, we also observed a Dirac point in the direction perpendicular to  $\Gamma$ -M at a wavenumber not equal to zero ( $\Gamma$  point). This was also seen in the theoretical calculation and thus this (111) surface was identified as the surface possessing the TCI Dirac cone.

We are now trying to investigate the real atomic structure of this system with low-energy electron diffraction (LEED) as well as cross sectional transmission emission microscopy (X-TEM). There is a possibility that they are not actually  $\text{Bi}_1\text{Te}_1$ , but rather more complex structures composed of BL-Bi and  $\text{Bi}_2\text{Te}_3$ , such as  $\text{Bi}_4\text{Te}_5$ ,  $\text{Bi}_6\text{Te}_7$ ,  $\text{Bi}_4\text{Te}_3$ ,  $\text{Bi}_2\text{Te}$ ,  $\text{Bi}_7\text{Te}_3$  [3]. In any case, the combination of ARPES, *ab initio* calculations, and structure analysis should be very useful in studying the topological properties of Bi-Te compounds.

[1] T. Hirahara *et al.*, Phys. Rev. Lett. **107** (2011) 166801.

[2] M. Eschbach *et al.*, Nat. Comm. **8** (2017) 14976.

[3] O. Concepcion *et al.*, Inorg. Chem. **57** (2018) 10090.

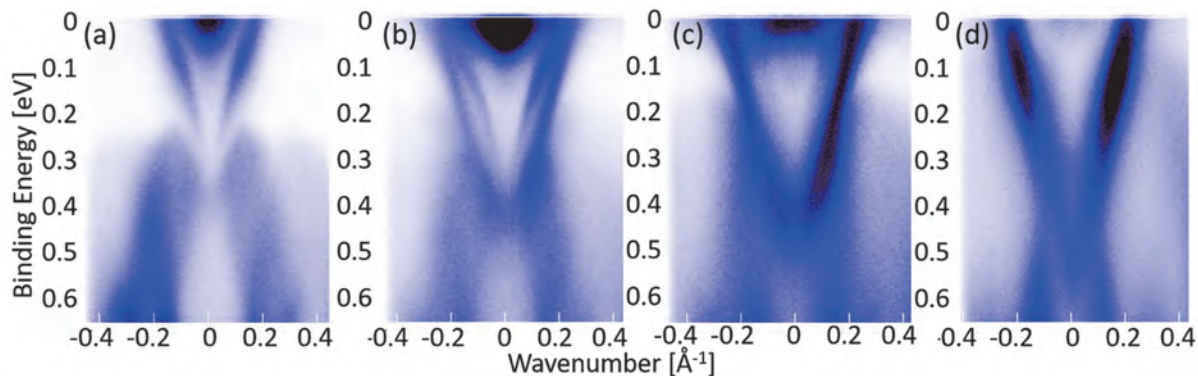


Fig. 1. Band dispersion of  $\text{Bi}_2\text{Te}_3$  (a) and that obtained by annealing it (b-d), which is likely  $\text{Bi}_1\text{Te}_1$  with different surface terminations. The measurements were performed along the  $\Gamma$ -M direction.



BL7U

## Photoelectron Angular Distribution of Pentacene/Graphite Interface Investigated by Low-energy Angle-resolved Photoelectron Spectroscopy

T. Yamaguchi<sup>1,2</sup>, M. Meissner<sup>2</sup>, S. Ideta<sup>1,3</sup>, K. Tanaka<sup>1,3</sup> and S. Kera<sup>1,2,3</sup><sup>1</sup>*School of Physical Sciences, The Graduate University for Advanced Studies (SOKENDAI), Okazaki 444-8585, Japan*<sup>2</sup>*Department of Photo-Molecular Science, Institute for Molecular Science, Okazaki 444-8585, Japan*<sup>3</sup>*UVSOR Synchrotron Facility, Institute for Molecular Science, Okazaki 444-8585, Japan*

Ultraviolet photoelectron spectroscopy (UPS) is a very useful technique for studying the electronic structure of surfaces and interfaces. However, the origin of UPS features obtained by low-energy photon excitation is not well established theoretically and experimentally because of the complicated photoemission process. Tanaka et al. demonstrated resonance excitation between initial states and final states which causes unexpected scattering due to the relatively long lifetime of low-energy electrons potentially trapping them in intermediate states at the interface [1]. A similar behavior was found for organic monolayers on graphite, giving rise to inelastic energy-loss features [2-4]. In addition, the lifetime of photogenerated holes may also lead to interesting phenomena. Franck-Condon anomalies, where the vibronic progression does not follow that of the gaseous phase and shows a strong angular anisotropy, and photoemission matrix anomalies, where high intensity appears at the surface normal, were observed for monolayers of flat-lying organic molecules on graphite [2-4]. Moreover, anomalous bands have been reported, caused by conduction bands in the secondary electron emission (SEE) background [5]. Therefore, despite the weak interaction of physisorbed molecules with the substrate, the corresponding wavefunctions may connect strongly at the interface; and the combination of these effects could be used to study the impact on the electronic states. In this work, we investigated the photoelectron angular distribution (PAD) of the highest occupied molecular orbital (HOMO) for pentacene (PEN), using low-energy angle-resolved UPS (LE-ARUPS) to clarify those phenomena.

Highly oriented pyrolytic graphite (HOPG) as the substrate was cleaned by annealing at 600 K for 2 h. A PEN film of 4 Å was deposited on HOPG at room temperature in a custom UHV chamber designed for organic layer deposition.

Figure 1(a) shows a LE-ARUPS map taken at  $h\nu = 7.7$  eV and  $T = 15$  K. In the HOMO region (1.6 ~ 2.0 eV) some features stand out: (i) Strong photoemission intensity around the  $\Gamma$  point which is unexpected for p-polarized excitation of weakly bounded, flat-lying, pi-conjugated molecules, (ii) the first vibronic satellite has a higher intensity at  $\Gamma$  than the HOMO (dashed oval in Fig. 1(a)), which deviates from the spectral shape found for higher photon energies such as HeI light, and (iii) a faint background in form of a strongly

dispersed dark band and/or bright bands with constant kinetic energy is detected (dashed straight lines). The latter can be seen more clearly when averaging LE-ARUPS maps for different photon energies (here 7.4 ~ 7.8 eV) and normalizing the averaged map by its horizontally and vertically integrated profiles separately (Fig. 1(b)). This way, a constant-kinetic-energy feature becomes more prominent while molecular occupied states move in energy and “scan” the unoccupied features.

In conclusion, we clearly observed an unusual evolution of PAD in a photon energy range of  $h\nu = 7$  eV ~ 8 eV which is caused by non-trivial multi-particle photoemission events at weakly bounded interfaces. Multiple scattering theory will be helpful to understand the origin of the PAD and hence to reveal the modification of the molecular orbital upon weak interactions.

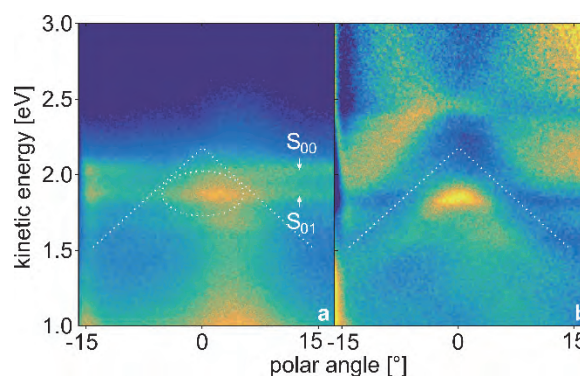


Fig. 1. (a) LE-ARUPS intensity map for PEN(0.3 nm)/HOPG taken at 15 K and normal emission using  $h\nu = 7.4$  eV; and (b) the average of 5 maps using  $h\nu = 7.4$  eV ~ 7.8 eV, normalized by its horizontally and vertically integrated profiles.

- [1] S. Tanaka *et al.*, *Sci. Rep.* **3** (2013) 3031.
- [2] T. Yamaguchi *et al.*, *UVSOR Activity Report* 2015 **43** (2016) 135.
- [3] T. Yamaguchi *et al.*, *UVSOR Activity Report* 2016 **44** (2017) 151.
- [4] T. Yamaguchi *et al.*, *UVSOR Activity Report* 2017 **45** (2018) 142.
- [5] S. K. Mahatha *et al.*, *Phys. Rev. B* **84** (2011) 113106.

BL7U

## Band Structure Modification of 2D TMDCs Using a Molecular Dopant

S. Park, T. Schultz, P. Amsalem, X. Xu and N. Koch

*Humboldt-Universität zu Berlin, Institut für Physik, Brook-Taylor-Str. 6, 12489 Berlin, Germany*

The aim of the proposed experiments was to achieve a deep understanding of the microscopic phenomena occurring upon interface formation between a MoS<sub>2</sub> monolayer and a strong electron acceptor molecule, F<sub>6</sub>TCNNQ, which can be employed for p-doping of semiconductors [1]. In the initially planned experiments, several substrates including sapphire, HOPG and silver, were to be employed as support for the MoS<sub>2</sub> film.

During the experiments at BL7U, we first encountered charging issues when using sapphire as support, though the very same sample could be successfully measured in-house by photoemission using a standard helium discharge lamp. Most of the remaining time was then dedicated to high resolution measurements of MoS<sub>2</sub>/HOPG with and without F<sub>6</sub>TCCNQ and at different temperatures ranging from 7 K to 300 K. For this system, we first observed by angle-resolved photoemission (ARPES) that the electronic band structure could be nicely resolved, as exemplified in Fig. 1, though the MoS<sub>2</sub> monolayer is azimuthally disordered. Such an observation is enabled by selective high photoemission intensity along  $\Gamma$ -K and  $\Gamma$ -M of the single crystal which singles out these features also after azimuthal integration. These first results are included in a manuscript that has been submitted for publication [2].

Regarding the initial aim of this project, we could successfully demonstrate that p-doping of the MoS<sub>2</sub> film on HOPG occurs upon F<sub>6</sub>TCCNQ deposition. This is shown in Fig. 1 in which the MoS<sub>2</sub> valence band (VB) features are seen to shift to lower binding energies by up to 0.26 eV upon molecular adsorption. Interestingly, we also observed that the MoS<sub>2</sub> VB shifts are temperature-dependent and p-doping is found less effective at low temperatures. The measurements indicate that p-doping results from charge transfer to the F<sub>6</sub>TCNNQ, giving rise to partial filling of the lowest unoccupied molecular orbital (LUMO). Further high-resolution measurements of the low binding energy region corresponding to the partially-filled LUMO states, revealed temperature-dependent magnitude of the charge transfer with a critical temperature of ca. 100 K as shown in Fig. 2. Deep understanding of the charge transfer mechanisms as unraveled in this experiment will lead to strong insight into the physics involved in TMDC doping by adsorption of small organic molecules with strong electron acceptor properties.

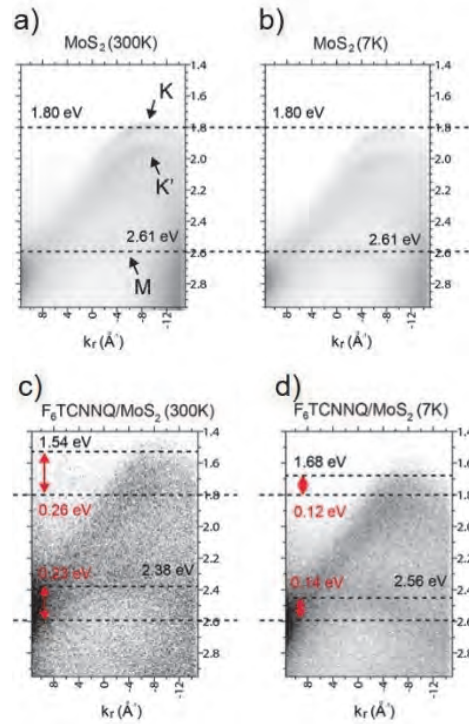


Fig. 1. a) and b) ARPES spectra of clean MoS<sub>2</sub>/HOPG around the K point of the Brillouin zone at 300 K and 7 K, respectively. c) and d) corresponding ARPES spectra after deposition of F<sub>6</sub>TCNNQ. ( $h\nu = 21$  eV)

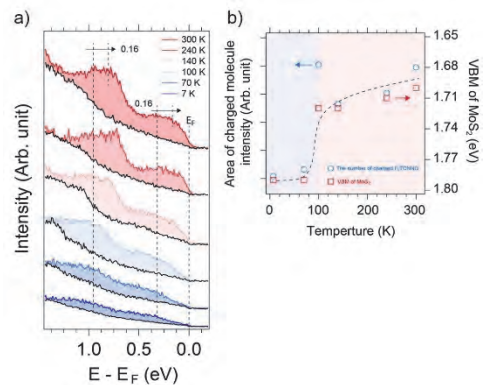


Fig. 2. a) Temperature-dependent energy distribution curve of MoS<sub>2</sub>/HOPG near the Fermi-level, before (black) and after (colored) F<sub>6</sub>TCNNQ deposition. The additional density of states after molecular deposition is due to charged molecules only. b) Area of the signal due to charged molecules and energy shift of the MoS<sub>2</sub> VB as a function of temperature. The critical temperature occurs at ca. 100 K.

- [1] T. Schultz *et al.*, Physical Review B **93** (2016) 125309.  
 [2] S. Park *et al.*, Comm. Phys. (submitted).

BL7U

## UPS Measurement of Valence Electronic States in Dinaphtho[2,3-b:2',3'-f]thieno[3,2-b]thiophene Single Crystals

R. Takeuchi<sup>1</sup>, S. Izawa<sup>2</sup>, R. Tsuruta<sup>1</sup>, S. Yamanaka<sup>1</sup>, M. Iwashita<sup>1</sup>, K. Tonami<sup>1</sup>, S. Ideta<sup>2</sup>,  
K. Tanaka<sup>2</sup>, M. Hiramoto<sup>2</sup> and Y. Nakayama<sup>1</sup>

<sup>1</sup>Department of Pure and Applied Chemistry, Tokyo University of Science, Noda 278-8510, Japan

<sup>2</sup>UVSOR Synchrotron Facility, Institute for Molecular Science, Okazaki 444-8787, Japan

Dinaphtho[2,3-b:2',3'-f]thieno[3,2-b]thiophene (C<sub>22</sub>H<sub>12</sub>S<sub>2</sub>, DNTT, Fig. 1) attracts attention as a high-mobility p-type organic semiconductor material [1]. One of the problems of organic semiconductor materials such as pentacene is their low stability in the atmosphere. DNTT is proposed to be more robust against oxidation than pentacene [2], and has been regarded as a promising material for applications. However, the valence electronic structure that contributes to its charge transport is not fully understood, and researches using the single crystals are necessary to obtain knowledge about the fundamental electronic structure [3]. In this study, the valence electron structure of the single crystal of DNTT was measured by ultraviolet photoelectron spectroscopy (UPS).

DNTT single crystals were prepared by a physical vapor transport (PVT) technique. The crystals were attached to gold-coated silicon substrates using silver paste in order to avoid sample charging. UPS measurements were conducted at BL7U, UVSOR, using an electron spectrometer A-1 (MBS) or at an offline apparatus equipped with DA-30 (Scienta-Omicron). For the offline UPS measurements, He-II $\alpha$  light source ( $h\nu = 40.81$  eV) was used, and the work function value of the electron spectrometer was determined to be 4.37 eV from the Fermi edge position. In this study, a 375 nm laser was irradiated at the same time in order to avoid sample charging. All UPS measurements were conducted at room temperature.

Figure 2 shows a UPS spectrum of a DNTT single crystal taken at  $h\nu = 10$  eV. Whereas three components were barely recognized in the binding energy (BE) range of  $-3.5 \sim -0.5$  eV, the highest occupied molecular orbital (HOMO)-derived peak was not resolved clearly.

In contrast, UPS results taken at  $h\nu = 40.81$  eV clearly exhibited the HOMO-derived peak as shown in Fig. 3 (left), which allowed the determination of the valence band maximum (VBM) of the DNTT single crystal to be  $-0.69$  eV. Figure 3 (right) shows a photoemission spectrum in the secondary electron cutoff region from the sample being biased at  $-5$  V, where the abscissa is rescaled to indicate the work function. The work function of the DNTT single crystal was determined to be 4.30 eV from the onset position. From these results, the ionization energy of the DNTT single crystals is determined to be 4.99 eV, which is significantly smaller than that reported previously for the DNTT thin film (5.44 eV [2]).

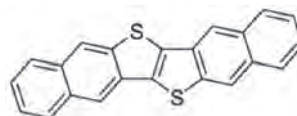


Fig. 1. Molecular structure of DNTT.

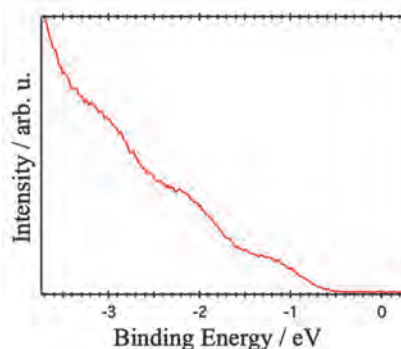


Fig. 2. UPS spectrum of the DNTT single crystal taken at BL7U ( $h\nu = 10$  eV).

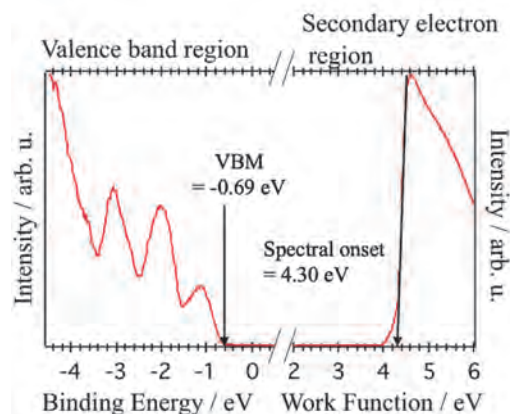


Fig. 3. UPS spectra of the DNTT single crystal in the HOMO region (left) and secondary electron cutoff region (right) taken with He-II $\alpha$  excitation.

[1] T. Yamamoto and K. Takimiya, *J. Am. Chem. Soc.* **129** (2007) 2224.

[2] H. Yagi *et al.*, *Chem. Phys. Lett.* **563** (2013) 56.

[3] X. Wei *et al.*, *Adv. Mater.* **25** (2013) 3478.



BL7U

## Two-Dimensional Nature of Topological Surface States on SmB<sub>6</sub>(111) Clarified by Synchrotron-Radiation Angle-Resolved Photoelectron Spectroscopy

Y. Ohtsubo<sup>1,2</sup>, Y. Yamashita<sup>2</sup>, T. Nakamura<sup>2</sup>, S. Ideta<sup>3</sup>, K. Tanaka<sup>3</sup>, W. Hirano<sup>4</sup>, F. Iga<sup>4</sup> and S. Kimura<sup>1,2</sup>

<sup>1</sup>Graduate School of Frontier Biosciences, Osaka University, Suita 565-0871, Japan

<sup>2</sup>Department of Physics, Graduate School of Science, Osaka University, Toyonaka 560-0043, Japan

<sup>3</sup>UVSOR Synchrotron Facility, Institute for Molecular Science, Okazaki 444-8585, Japan

<sup>4</sup>College of Science, Ibaraki University, Mito 310-8512, Japan

Topological Kondo Insulators (TKI) are gathering much attention in these days as a promising playground to study the concert effect of the spin-polarized topological surface states and strong electron correlation resulting in the metal-insulator transition of Kondo insulators [1]. SmB<sub>6</sub> is the first and the most extensively studied candidate of TKI. It has been revealed that the (001) surface of the cleaved SmB<sub>6</sub> single crystal hosts the metallic and spin-polarized surface states as expected from topological classification [1, 2]. However, the topological order of SmB<sub>6</sub> itself is still under debate because of the multiple possible interpretations of the metallic surface bands [3].

We have studied the surface electronic structure of SmB<sub>6</sub> in these years to reveal its topological order as well as the non-conventional electronic phenomena driven by strong electron correlation [4, 5]. Before this project, we have already discovered the metallic electronic states with spin polarization on the (111) surface of SmB<sub>6</sub> [4, 5]. However, its dimensionality, two-dimensional (2D) surface-derived ones or three-dimensional (3D) bulk bands, had not been clear yet.

In this project, we performed angle-resolved photoelectron spectroscopy (ARPES) measurements on the SmB<sub>6</sub>(111) surface and carefully traced the incident photon energy dependence of the metallic band S1 and the other band lying just below S1, namely S2, as shown in Fig. 1 (a), to elucidate  $k_z$ -dependent band dispersions, if it exists.

Figures 1(b) and 1(c) show the ARPES momentum distribution curves (MDCs) corresponding to S1 and S2, respectively. As evidently shown there, the S1 peak positions shown in Fig. 1(b) are independent from the incident photon energy, indicating its 2D nature, implying to originate from the surface electronic structure. As for S2 in Fig. 1(c), the behavior is similar to S1, suggesting the common 2D origin. However, one can find broad humps changing its center positions depending on the photon energies, such as that at +0.3 Å<sup>-1</sup> with  $h\nu = 20$  eV. Because of these photon-energy-dependent features, we cannot exclude possible 3D character for S2 from these data.

Based on the current data, we could conclude that the metallic electronic state at the Fermi level, S1, is from the surface electronic structure without any ambiguity. Together with the former results, we propose the topologically non-trivial picture of SmB<sub>6</sub> [4, 5].

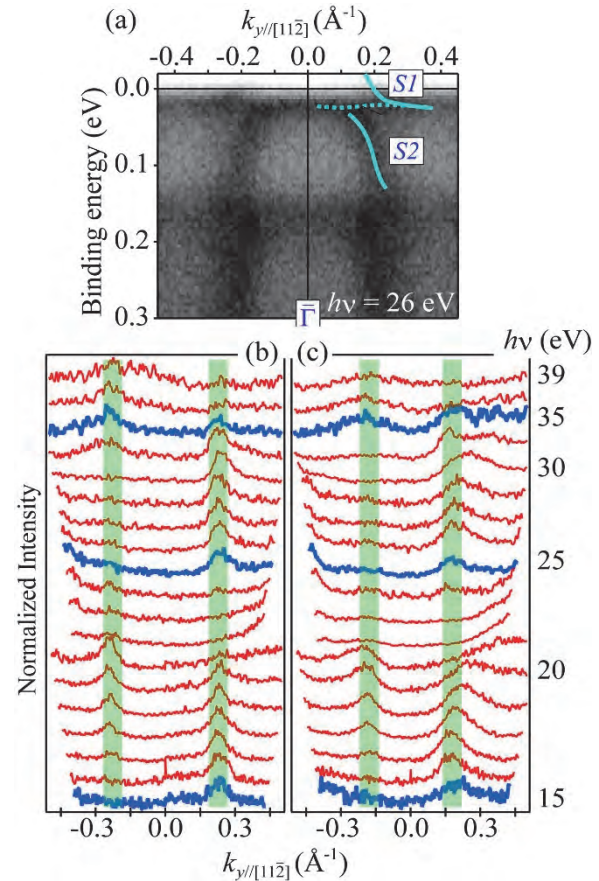
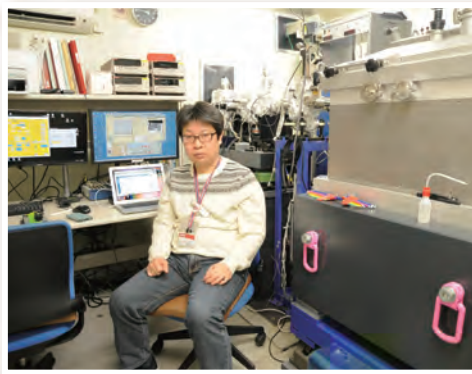
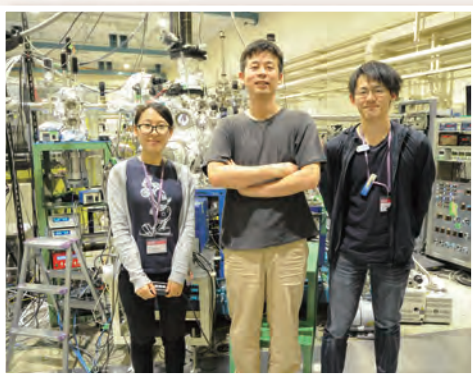
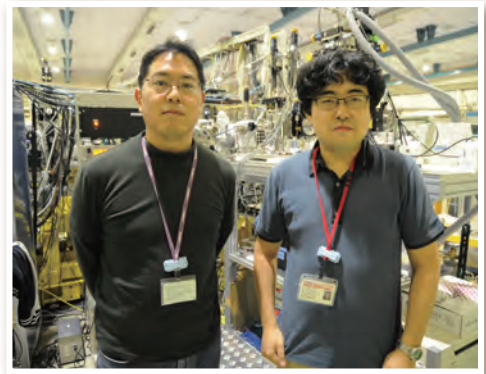
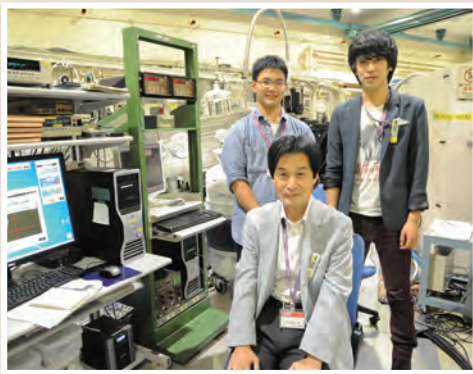
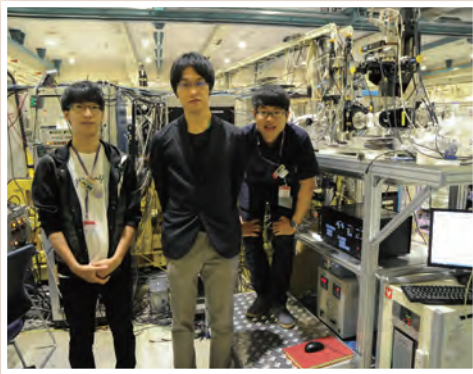
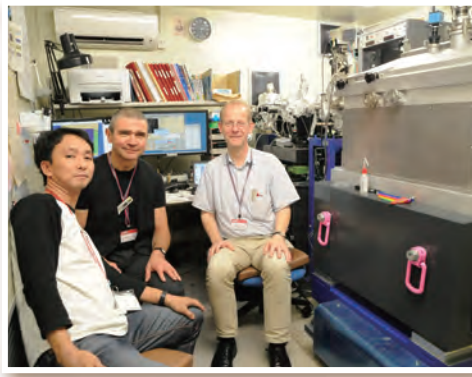
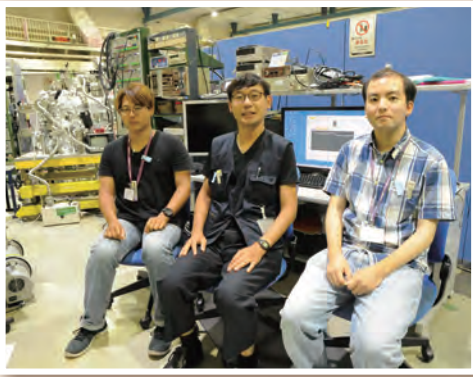



Fig. 1. (a) ARPES intensity plot of SmB<sub>6</sub>(111) taken at  $h\nu = 26$  eV and 15 K. (b, c) ARPES MDCs at 15 K with elevating photon energies. The binding energies are (b) 0 meV (Fermi level) and (c) 60 meV, corresponding to the bands S1 and S2 in (a), respectively.

- [1] M. Dzero *et al.*, Phys. Rev. Lett. **104** (2010) 106408.
- [2] N. Xu *et al.*, J. Phys.: Condens. Matt. **28** (2016) 363001 and references therein.
- [3] P. Hlawenka *et al.*, Nat. Commun. **9** (2018) 517.
- [4] Y. Ohtsubo *et al.*, arXiv: 1803.09433 (2018).
- [5] Y. Ohtsubo *et al.*, UVSOR Activity Report 2016 **44** (2017) 138.



# UVSOR User 6



The background is a solid purple color with several abstract geometric elements. A large, semi-transparent circular graphic is centered on the right side, featuring concentric rings and a dotted border. Diagonal lines and a grid of small dots are also visible in the lower-left quadrant.

# III-5

Life, Earth and  
Planetary Sciences





BL4U

## Different Distribution of DNA and RNA in Chromosome Revealed by Spectromicroscopy with STXM

A. Ito<sup>1</sup>, K. Shinohara<sup>1</sup>, H. Yuzawa<sup>2</sup> and T. Ohigashi<sup>2,3</sup>

<sup>1</sup>School of Engineering, Tokai University, Hiratsuka 259-1292, Japan

<sup>2</sup>UVSOR Synchrotron Facility, Institute for Molecular Science, Okazaki 444-8585, Japan

<sup>3</sup>SOKENDAI (The Graduate University for Advanced Studies), Okazaki 444-8585, Japan

Spectromicroscopy using scanning transmission X-ray microscope (STXM) has been applied to study the difference in the distributions of DNA and protein in biological specimens such as chromosome and sperm at the C-K absorption edge [1, 2]. In the previous reports, we developed an image processing procedure for quantitative mapping of biomolecules, and successfully applied to the distribution of DNA and proteins in mammalian chromosomes using combined NEXAFS at the C, N and O-K absorption edges [3, 4].

In the present study, we extended our method to the discrimination of two kinds of nucleic acids, DNA and RNA which have similar chemical composition with slightly different structure: DNA is double-stranded, while RNA is single-stranded. RNA has a uracil base with hydrogen at the 5 position, instead of a thymine base in DNA with a methyl residue at the same position. In addition, DNA is missing an oxygen at the 2' position in a ribose sugar.

Figure 1 shows NEXAFS of DNA and RNA at the C, N and O-K absorption edges by the analysis using aXis 2000 software. Although very similar spectra were obtained as expected, slightly but significantly different profile at the C-K edge was observed.

To discriminate the distribution of such closely related molecules, we introduce the SVD method into the present method. At first, by using the SVD method, relative distributions of DNA, RNA and other molecules including proteins are obtained. The amount of total nucleic acids was estimated from the height of the unique peak of nucleic acids in the NEXAFS at the N-K edge. Quantitative distributions of DNA and RNA with absolute amount were then calculated by distributing the total amount of nucleic acids to each component, DNA and RNA in the images of relative amounts.

We used a chromosome for the discrimination of DNA and RNA. Chromosome was prepared from cultured Chinese Hamster Ovary (CHO) cells as described previously [3].

Figure 2 represents RGB maps that demonstrate the different distribution of DNA (red) and RNA (green). Molecules other than nucleic acids, mainly composed of proteins, are shown by blue.

Interesting observations are as follows:

- 1) RNA in addition to DNA is also present in chromosomes.
- 2) RNA distribution was clearly separated from that of DNA. RNA was preferentially located in the outer area of a chromosome.

Detailed analysis was reported recently [5]. These observations should be supported by other methods to detect RNA. The proposed procedure is being successfully applied to RNA distribution in mammalian cells [6], and in apoptotic nuclei [5].

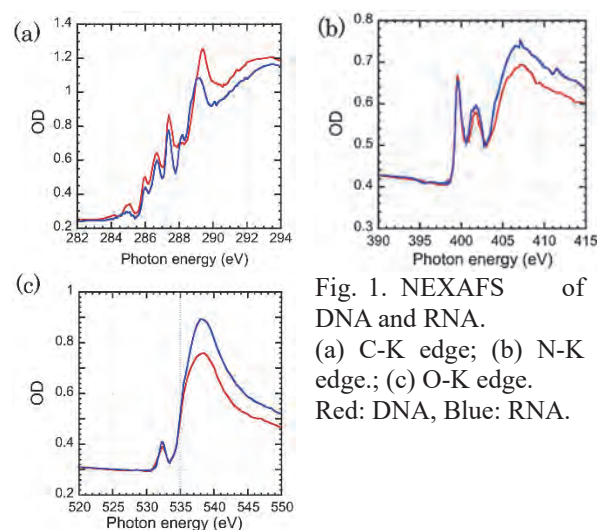


Fig. 1. NEXAFS of DNA and RNA. (a) C-K edge; (b) N-K edge.; (c) O-K edge. Red: DNA, Blue: RNA.

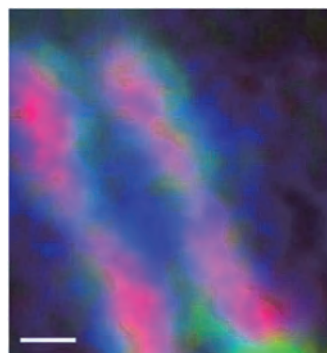


Fig. 2. Distribution of DNA, RNA and other molecules in a CHO chromosome. Red: DNA; Green: RNA; Other molecules: Blue. Bar: 0.5  $\mu$ m

- [1] H. Ade *et al.*, *Science* **258** (1992) 972.
- [2] X. Zhang *et al.*, *J. Struct. Biol.* **116** (1996) 335.
- [3] A. Ito, K. Shinohara, T. Ohigashi, S. Tone, M. Kado, Y. Inagaki and N. Kosugi, *UVSOR Activity Report 2017* **45** (2018) 156.
- [4] K. Shinohara, T. Ohigashi, S. Tone, M. Kado and A. Ito, *Ultramicrosc.* **194** (2018) 1.
- [5] K. Shinohara, S. Tone, T. Ejima, T. Ohigashi and A. Ito, *Cells* **8** (2019) 8.
- [6] K. Shinohara, A. Ito, T. Ohigashi, M. Kado and S. Tone, *J. X-Ray Sci. Technol.* **26** (2018) 877.

BL1U

## Optical Activity Emergence in Amino-Acid Films by Vacuum-Ultraviolet Circularly-Polarized Light Irradiation (II) - Irradiation Experiments -

J. Takahashi<sup>1</sup>, T. Sakamoto<sup>1</sup>, Y. Izumi<sup>2</sup>, K. Matsuo<sup>2</sup>M. Fujimoto<sup>3</sup>, M. Katoh<sup>3</sup>, Y. Kebukawa<sup>1</sup> and K. Kobayashi<sup>1</sup><sup>1</sup>Faculty of Engineering, Yokohama National University, Yokohama 250-8501, Japan<sup>2</sup>Hiroshima Synchrotron Radiation Center, Higashi-Hiroshima 739-0046, Japan<sup>3</sup>UVSOR Synchrotron Facility, Institute for Molecular Science, Okazaki 444-8585, Japan

The origin of homochirality in terrestrial bioorganic compounds (L-amino acid and D-sugar dominant) remains one of the most mysterious problems in the research for the origins of life. One of the most attractive hypotheses in the context of astrobiology is “Cosmic Scenario” [1] as below.

(1) Prebiotic simple molecules were densely accumulated on interstellar dust surfaces in dense molecular cloud circumstances.

(2) “Chiral radiations” in space induced asymmetric reactions and produced chiral complex organic materials including amino-acid precursors as “chiral seeds”.

(3) The “chiral seeds” were transported with meteorites or asteroids to primitive Earth resulting in terrestrial biological homochirality through some kind of “chiral amplification” mechanism.

As for ground experiments to validate the scenario, we already have reported optical activity emergence in solid-phase films of racemic mixture of alanine (DL-alanine) by irradiation of left- or right-handed circularly polarized light (L- or R-CPL). The CPL irradiation experiments were carried out in the air at atmospheric pressure using wavelengths 215 nm from free electron laser (FEL) of UVSOR-II [2] and 230, 215, 203 nm from undulator beamline BL1U of UVSOR-III [3].

We are mainly using circular dichroism (CD) spectroscopy to detect optical activity emergence because CD spectra sensitively reflects the steric structures of chiral molecules with a high degree of accuracy. Theoretical calculation of CD spectrum of alanine molecule has revealed that the circular dichroism chromophores derived from characteristic electronic transitions ( $n\text{-}\pi^*$ ,  $\pi\text{-}\pi^*$  for carboxyl group and  $n\text{-}\sigma^*$ ,  $\pi\text{-}\sigma^*$  for amino group) are corresponding to several different wavelengths in 120 ~ 230 nm region [4]. From this point of view, it is suggested that the expecting aspects of optical activity emergence by asymmetric photochemical reactions strongly depends on the CPL irradiation wavelength.

We are presently carrying out CPL irradiation experiments using vacuum-ultraviolet (VUV) light at undulator beamline BL1U of UVSOR-III. In case of VUV-CPL irradiation of shorter wavelengths than 200 nm, the DL-alanine film samples were set in a vacuum sample chamber to prevent the attenuation due to

photon absorption band by oxygen molecules in the air [5]. On the undulator beam entrance side of the vacuum sample chamber, a gate valve with a vacuum-sealed MgF<sub>2</sub> or LiF window was mounted. The irradiated CPL wavelengths were selected to 180 and 155 nm corresponding to the circular dichroism chromophores of alanine molecule [4].

CD spectra of the CPL irradiated DL-alanine film samples were measured at synchrotron radiation CD beam line BL-12 of Hiroshima Synchrotron Radiation Center (HiSOR) to clarify the optical activity emergence by the CPL irradiation. Preferential structural changes between the two enantiomers in racemic amino-acid mixtures introduced by the CPL irradiation can be detected by using CD spectroscopy. In Fig. 1, CD spectra of DL-alanine films after irradiation with L- and R-CPL at 180 nm (Fig.1(a)) and 155 nm (Fig.1(b)) in wavelength are shown. Detailed analysis of CD spectra are in progress to clarify full mechanism of the optical activity emergence, which potentially has relevance to the origin of terrestrial bioorganic homochirality stimulated by “chiral radiation”.

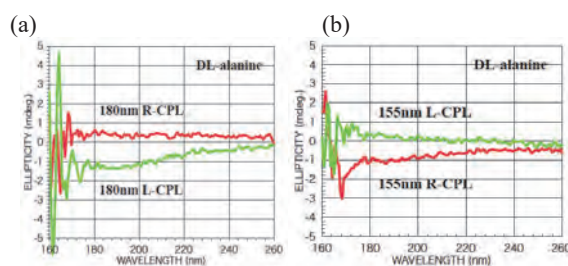


Fig. 1. CD spectra of the L- or R-CPL irradiated DL-alanine films measured at BL-12 of HiSOR. The CPL irradiation wavelengths were (a) 180 nm and (b) 155 nm at BL1U of UVSOR-III.

[1] W. A. Bonner, Orig. Life Evol. Biosph. **21** (1991) 407.

[2] J. Takahashi *et al.*, Int. J. Mol. Sci. **10** (2009) 3044.

[3] K. Matsuo *et al.*, UVSOR Activity Report 2016 **44** (2017) 157.

[4] F. Kaneko *et al.*, J. Phys. Soc. Jpn. **78** (2009) 013001.

[5] J. Takahashi *et al.*, UVSOR Activity Report 2017 **45** (2018) 147.



BL2B

## Impacts of Ambient Conditions on the Electronic States of a Molecular Semiconductor Bis(1,2,5-thiadiazolo)-*p*-quinobis(1,3-dithiole)

Y. Nakayama<sup>1</sup>, K. Sudo<sup>1</sup> and Y. Watanabe<sup>2</sup><sup>1</sup>Department of Pure and Applied Chemistry, Tokyo University of Science, Noda 278-8510, Japan<sup>2</sup>Department of Mechanical and Electrical Engineering, Suwa University of Science, Chino 391-0292, Japan

Bis(1,2,5-thiadiazolo)-*p*-quinobis(1,3-dithiole) (BTQBT) is a promising molecular material for organic electronics applications because of its widely dispersed intermolecular valence bands in the crystalline thin films [1] and good performance in use of vertical field effect transistor devices [2]. On the other hand, the degradation under the ambient conditions has been a common problem for the organic semiconductor materials. In this study, evolution of the electronic states of BTQBT thin films grown on Au substrate were tracked before and after exposure to ambient conditions by means of photoelectron spectroscopy (PES).

BTQBT was deposited on Au-coated Si substrates in ultra-high vacuum conditions. PES measurements were conducted at BL2B, UVSOR, by using an electron spectrometer R3000 (VG-Scienta). The photon energy was fixed at 120 eV in this work. All measurements were done at room temperature.

Figure 1 shows PES spectra of the Au substrate and 10 nm-thick BTQBT film plotted together with a simulated density-of-states (DOS) curve being expected from a molecular orbital energy distribution derived from quantum chemical calculation. This suggests that, whereas the spectral profiles of the present BTQBT film have to be regarded as superposition of the DOS of BTQBT and signals from the Au substrate, at least the highest-occupied molecular orbital (HOMO)-derived component of BTQBT can be separated from the 5d bands of Au.

Evolution of the BTQBT HOMO-derived PES peak and work function upon exposure to the ambient conditions is shown in Figs. 2(a) and 2(b), respectively. While the energy positions of the HOMO and vacuum level were substantially unchanged in ultra-high vacuum ( $10^{-7}$  Pa) condition for more than one month, an exposure of the BTQBT film to the ambient air in dark only for 5 minutes brought about a significant (ca. 0.2 eV) decrease and increase in the hole injection barrier and work function, respectively. Further exposure induced extra spectral shifts in the same direction. Interestingly, additional exposure to air with the ambient light made a change in the opposite direction, i.e., increase in the hole injection barrier and decrease in the work function. This implies a possibility that the presence/absence of the ambient light may lead to different degradation paths of the BTQBT-based electronic devices.

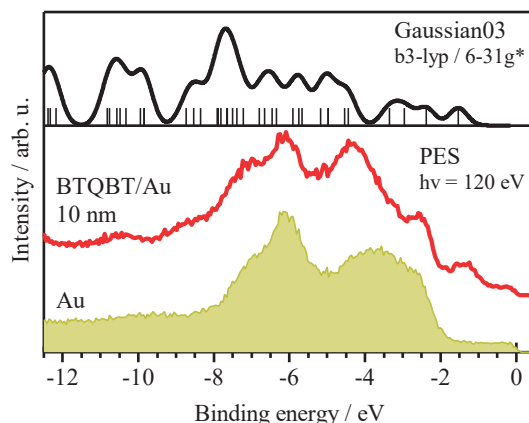


Fig. 1. PES spectra of the Au substrate (orange) and BTQBT film (red). A simulated DOS curve derived from the calculated molecular orbital pattern (vertical bars) is also displayed in the upper panel.

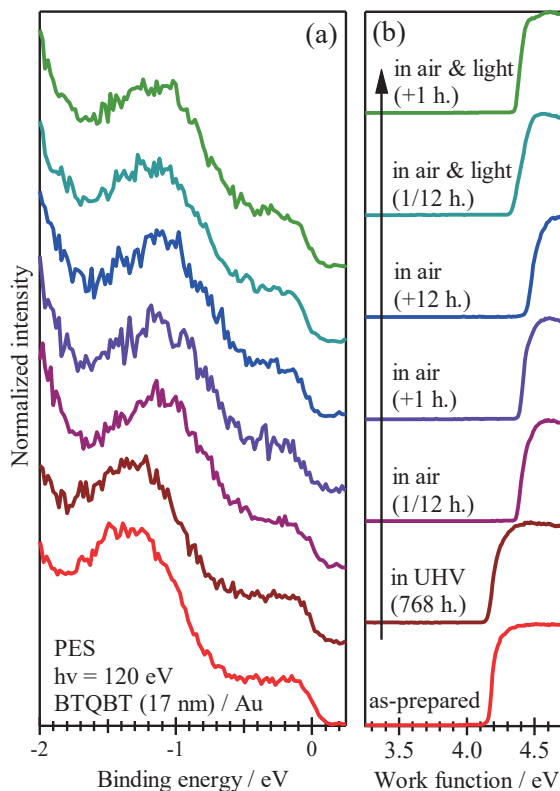


Fig. 2. Evolution of the PES spectra in the (a) HOMO and (b) secondary electron cutoff regions of the 17 nm-thick BTQBT induced by the ambient exposure.

[1] S. Hasegawa *et al.*, *J. Chem. Phys.* **100** (1994) 6969.

[2] H. Fukagawa *et al.*, *AIP Adv.* **6** (2016) 045010.

BL3U

## X-ray Absorption Spectroscopy Measurement of Lipid Bilayer Membranes in Aqueous Solutions

R. Tero<sup>1</sup>, S. Nakamura<sup>1</sup>, Y. Sano<sup>1</sup> and M. Nagasaka<sup>2</sup>

<sup>1</sup>Toyohashi University of Technology, Toyohashi, 441-8580, Japan

<sup>2</sup>Institute for Molecular Science, Okazaki 444-8585, Japan

The lipid bilayer is a self-assembled structure of amphiphilic lipid molecules, and is the fundamental structure of biomembranes such as cell membranes. Lipid bilayer provides reaction fields for transporting materials, information and energy into and out of cells. Internal structures of lipid bilayers, e.g. two dimensional domains and hydrophobic thickness, and physical properties affect the transportation reactions. All these physiological reactions proceeds in the presence of ions. Ions in the aqueous solution significantly influence to these structures and properties of lipid bilayers. Phosphatidylcholine (PC) (Fig. 1) is the major component of eukaryotic cells. Cations bind to the phosphate and carbonyl groups of PC. However, affinity of cations to PC, and also other lipids, are still controversy especially in the fields of theoretical simulations [1]. In this study, we aim to determine the binding affinity of cations to the phosphate and carbonyl groups experimentally. This year we started X-ray absorption spectroscopy (XAS) measurement of a PC bilayer in aqueous solution, to detect the chemical shifts of O 1s binding energy.

We prepared a suspension of dioleoyl-PC (DOPC) vesicles in a buffer solution using a tip-type sonicator. We introduced the suspension into the XAS flow cell consisting of Si<sub>3</sub>N<sub>4</sub> membranes [2]. Planar DOPC bilayers were formed on the Si<sub>3</sub>N<sub>4</sub> membranes (Fig. 2) through the process of vesicle fusion method [3]. Fluorescence microscope imaging and fluorescence recovery after photobleaching method showed that the Si<sub>3</sub>N<sub>4</sub> membranes were fully covered with planar DOPC bilayers.

Figure 3 shows an O K-edge spectrum the Si<sub>3</sub>N<sub>4</sub> membrane flow cell with DOPC bilayers on its inner surface. We improved the experimental, and obtained a peak comprising of several components at 530-533 eV. It was isolated from the peaks of bulk water, which appeared above 533 eV. The components were attributed to the phosphate and carbonyl groups of DOPC, and to the native oxide layer on Si<sub>3</sub>N<sub>4</sub>. After subtracting the blank spectrum of Si<sub>3</sub>N<sub>4</sub> without the DOPC bilayer, we found that at least two O 1s components originating from PC, and also that from molecular oxygen that was dissolved in the hydrophobic core of the bilayer membrane. The DOPC bilayer existed stably after repeated solution exchange. We showed that O K-edge spectra of lipid bilayers can be measured in aqueous solution the XAS flow cell. Next year we will measure PCs without phosphate or carbonyl groups, to identify the PC-originated peaks.

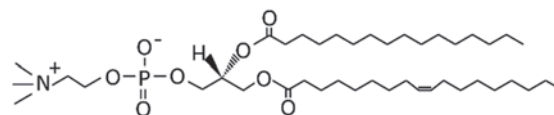


Fig. 1. Molecular structure of a representative phosphatidylcholine.

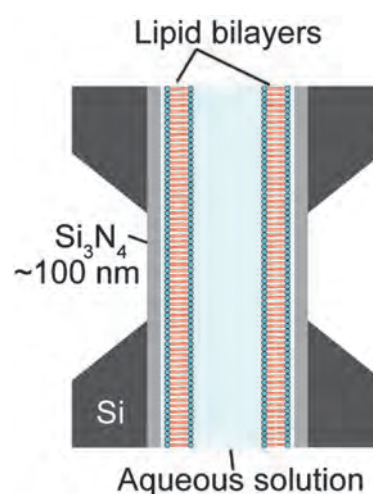


Fig. 2. Schematic of a lipid bilayer sample in the flow cell for XAS measurement.

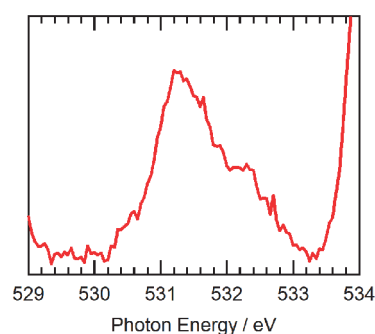


Fig. 3. O K-edge spectrum in absorbance of the Si<sub>3</sub>N<sub>4</sub> membrane covered with a DOPC planar bilayer.

[1] T. B. Woolf, *Biophys. J.* **104** (2013) 746.

[2] M. Nagasaka, H. Yuzawa, T. Horigome and N. Kosugi, *J. Electron Spectros. Relat. Phenomena* **224** (2018) 93.

[3] R. Tero, *Materials* **5** (2012) 2658.

BL3U

## Study of Micelle Formation in Aqueous Solutions of Fatty Acids Using Soft X-ray Absorption Spectroscopy

J. J. Lin<sup>1</sup>, G. Michailoudi<sup>1</sup>, R. R. Kamal<sup>1</sup>, H. Yuzawa<sup>2</sup>, M. Nagasaka<sup>3,4</sup> and N. L. Prisle<sup>1</sup>

<sup>1</sup>Nano and Molecular Systems research unit, University of Oulu, P.O. Box 3000, 90014 University of Oulu, Finland

<sup>2</sup>UVSOR Synchrotron Facility, Institute for Molecular Science, Okazaki 444-8585, Japan

<sup>3</sup>Institute for Molecular Science, Okazaki 444-8585, Japan

<sup>4</sup>School of Physical Sciences, The Graduate University for Advanced Studies (SOKENDAI), Okazaki 444-8585, Japan

Atmospheric aerosols have a key role in global climate as they interact with solar radiation and take part in cloud formation [1]. Fatty acids and their salts are found both in urban and marine environments, and are well-known surfactants, meaning that they accumulate at the liquid/gas interface, including that of water droplets in the atmosphere. With a hydrophilic head (carboxyl group) and a hydrophobic tail (aliphatic chain), surface active molecules can form films on the surface of an aqueous solution, with the heads oriented towards the water. Above the critical micelle concentration (CMC), these molecules can self-assemble into structures called micelles, which in turn can impact both chemical and physical properties of the solutions, including surface tension which play an important role in cloud microphysics [2, 3].

At BL3U, we studied binary systems of fatty acids in aqueous solutions and also ternary water–fatty acid–salt solutions with varying concentrations above and below the respective CMC values, using X-ray absorption spectroscopy (XAS) on a liquid flow cell [4]. XAS is highly sensitive to the chemical environment of different components in solution and provide information about the bulk properties of dissolved compounds.

The studied liquid samples were aqueous solutions of sodium hexanoate ( $C_5H_{11}COONa$ ) at 0.75, 1, 2, 3, 4 and 5 CMC (CMC = 0.9 M) and ternary solutions of sodium hexanoate and sodium chloride salt ( $H_2O-C_5H_{11}COONa-NaCl$ ) at 5.3 M of NaCl and approximately 1.5 times the ternary CMC for  $C_7H_{15}COONa$ . This value is not well-known and basing the concentration on a multiple of CMC involves estimating the dependency of CMC on solution salt content. Spectra of pure hexanoic acid ( $C_5H_{11}COOH$ ) and aqueous  $C_5H_{11}COOH$  solution (7.3 M) were also measured as a reference.

The thickness of the liquid cell was optimized for better absorption and the sample temperature was set at 25°C. We monitored solution properties of surfactant molecules and their micelle formation by scanning the C *K*-edge from 280 to 300 eV, in energy steps of 0.02 eV from 285 to 290 eV and 0.1 eV for the remainder of the range.

Figure 1 presents a preliminary analysis at the C *K*-edge XAS spectra for binary and ternary solutions, after normalization at the peak position. A background

spectrum of absorption from water was subtracted, removing also signal from carbon contamination on the liquid cell membranes. Solutions with highest concentration resemble the pure acid. Furthermore, the ratio of the pre-peak feature to main peak changes with the concentration of the surfactant relative to the CMC. From such changes and energy shifts on peak position of our spectra, we expect to extract information about the structures present in each solution.

Further analysis is needed to fully interpret the spectra, including an appropriate fitting procedure and identifying underlying peaks from the occurring excitations in the C *K*-edge from comparison to theoretical predictions. Model predictions for these and similar systems are the focus of ongoing work.

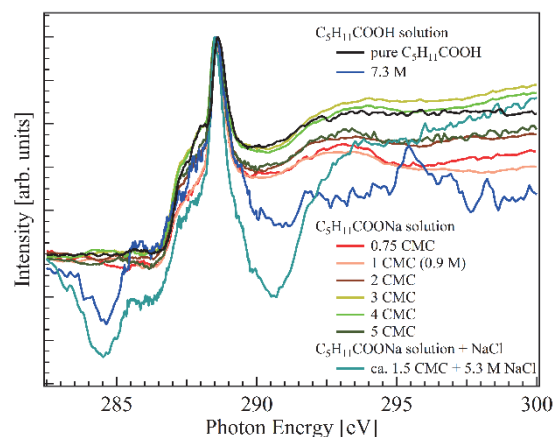


Fig. 1. C *K*-edge XAS spectra of pure  $C_5H_{11}COOH$ , aqueous  $C_5H_{11}COOH$  and aqueous  $C_5H_{11}COONa$  solutions at various multiples of the CMC value, and of  $H_2O-C_7H_{15}COONa-NaCl$  ternary solution.

[1] Intergovernmental Panel on Climate Change: *Climate Change 2013: The Physical Science Basis*, Cambridge University Press, New York, USA, 2013.

[2] P.S. Gill *et al.*, *Rev. Geophys.* **21** (1983) 903.

[3] M.C. Facchini *et al.*, *Atmos. Environ.* **34** (2000) 4853.

[4] M. Nagasaka *et al.*, *J. Electron Spectrosc. Relat. Phenom.* **224** (2018) 93.



BL4U

## Estimation of the Thickness of Fe(III)-oxides Layer near the Magnetite (111) Surface after Hydrothermal Treatment

T. Tamura, A. Kyono and I. Kinebuchi

Division of Earth Evolution Sciences, Graduate School of Life and Environmental Sciences, University of Tsukuba, Tsukuba 305-8572, Japan

Since the discovery of hydrothermal chimneys and black smoker vents in 1979 [1], a great variety of hydrothermal vents has been found all over the world [2-4]. Some of them are characterized by hydrothermal fluids enriched in molecular hydrogen ( $H_2$ ) [5]. Previous studies have shown that the hydrogen generation can be induced by water-magnetite interaction [6, 7]. Furthermore, it has been reported that the reaction is accompanied by oxidation of magnetite ( $Fe_3O_4$ ) to maghemite ( $\gamma-Fe_2O_3$ ) [7], but the mechanism has been still unknown. In the study, we employed a scanning transmission X-ray microscopy (STXM) to estimate the thickness of maghemite layer.

About 0.02 g of synthesized magnetite crystals were introduced into the 28 ml Teflon-lined stainless steel autoclave. Ultrapure water was in advance sufficiently bubbled with  $N_2$  gas to remove dissolved  $O_2$ . 14 ml of the deoxidized water were added into the Teflon container. The autoclave was tightly sealed and then heated at 200 °C for 24 hours. After the hydrothermal treatment, the magnetite crystals were removed from the Teflon container and dried at room temperature. After amorphous carbon was deposited on the sample surface, a cross-section was prepared with a JEOL JEM-9320FIB focused ion beam (FIB) system using a 30 keV Ga ion source. The FIB cross-section was analyzed using a STXM at UVSOR branch line 4U.

The Fe  $L_{23}$  edges provide chemical information about valence-specific multiplet structures of iron which can be used as valence fingerprints. In the study, the Fe  $L_3$  and  $L_2$  edges were clearly observed at around 709 and 722 eV, respectively (Fig. 1). The  $L_3$  edge shape obtained at a depth of 100 nm seemed to be split, which suggesting that hematite is formed at the surface. With increasing the depth, the split peaks of  $L_3$  edge were merged into one broad peak. The Fe  $L_2$  edge peaks at 721.0 and 722.5 eV were, on the other hand, continuously observed up to a depth of 800 nm, but a new peak at 721.5 eV became dominant from 900 nm (Fig. 1). The result implies that maghemite ( $\gamma-Fe_2O_3$ ) is dominantly distributed between 100 nm and 800 nm. Therefore, we can conclude that during hydrothermal reaction magnetite is oxidized to hematite through maghemite.

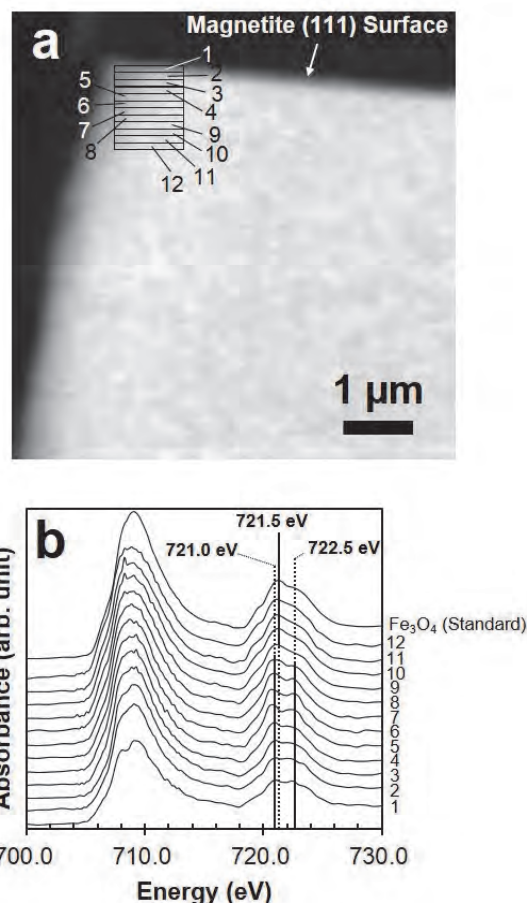


Fig. 1 (a) Fe distribution map of cross-section perpendicular to hydrothermally treated (111) magnetite surface. The box size is 100 nm of depth. (b) Fe  $L_{23}$  edge XANES spectra of hydrothermally treated magnetite resulting from the image stack on the area depicted in (a). Reference spectra of as grown magnetite is also shown for comparison.

- [1] Corliss *et al.*, *Science* **203** (1979) 1073.
- [2] Hekinian *et al.*, *Science* **219** (1983) 1321.
- [3] Azuende *et al.*, *J. Geophys. Res.* **101** (1996) 17995.
- [4] Connelly *et al.*, *Nat. Commun.* **620** (2012) 1.
- [5] Kelley *et al.*, *Science* **307** (2005) 1428.
- [6] Mayhew *et al.*, *Nat Geosci.* **6** (2013) 478.
- [7] Tamura *et al.*, *J. Mineral. Petrol. Sci.* **113** (2018) 310.
- [8] Almeida *et al.*, *Nat. Commun.* **5154** (2014) 1.

BL4U

## Investigating the Effect of Space Exposure Experiment on Carbonaceous Dust Based on XANES/STXM Analysis

I. Sakon<sup>1</sup>, I. Endo<sup>1</sup>, H. Yabuta<sup>2</sup> and T. Noguchi<sup>3</sup>

<sup>1</sup>Department of Astronomy, Graduate School of Science, University of Tokyo, Tokyo 113-0033, Japan

<sup>2</sup>Graduate School of Science, Hiroshima University, Higashi-Hiroshima 739-8526, Japan

<sup>3</sup>Division for Experimental Natural Science, Faculty of Arts and Science, Kyushu University, Fukuoka 819-0395, Japan

We have carried out the space exposure experiment of various kinds of carbonaceous solids using International Space Station (ISS) Japanese Experiment Module 'Kibo' ExHAM (See the top panel of Fig. 1). The major goal of this project is to understand how the carbonaceous dust particles synthesized in the stellar ejecta from evolved stars are chemically and physically altered in nature in the circumstellar environment until it becomes a member of the interstellar medium. In particular, we aim to investigate the properties of 'astronomical' polycyclic aromatic hydrocarbons (PAHs), the carrier of the unidentified infrared (UIR) bands, which have been observed ubiquitously in various astrophysical environments [1]. So far, we have brought three experiment samples to the ISS. Each experiment sample has a 10cm x 10cm exposure surface and has 64 slots for exposure experiment materials. In total, more than 40 kinds of materials including filmy quenched carbonaceous composites (filmy-QCCs [2]), nitrogen-included carbonaceous composites (NCCs [3]), anthracite, graphite, and silicates are installed in the experiment samples. Among the three samples, two of them (EE64-I and EE64-II) were attached on ExHAM-1 and were exposed in the space exposure environment for 384 days from 26 May 2015 to 13 June 2016. The final sample (EE64-III) was attached on ExHAM-1 and was exposed for 386 days from 29 June 2016 to 19 July 2017. All the samples are now collected back on earth and the difference in properties of our exposure experiment materials between before and after the experiment is investigated based on infrared micro-spectroscopy.

The bottom panel of Fig. 1 shows the comparison of the infrared spectra of the filmy-QCC before and after the experiment. In addition to the presence of new features at 2.95  $\mu\text{m}$ , attributed to O-H stretching with moderate hydrogen-bonding, and at 5.95  $\mu\text{m}$ , attributed to C=O stretching of conjugated ketone and/or aldehyde, a broad bump structure in 8-10  $\mu\text{m}$  has been recognized. In order to identify the effect of space exposure on the filmy-QCC, we have carried out the XANES/STXM analyses of TEM samples made by FIB processing of filmy-QCC (U-02 in EE64-I) and non-exposed filmy-QCC as a reference.

Our beamtime using the BL4U STXM beamline of the UVSOR was scheduled on July 24-25 in 2018, however, we still have not yet obtained the conclusive results of the XANES/STXM measurement due to beam trouble that has happened in July 2018. We have

proposed an another try in this semester (first half of 2019) and the beamtime was allocated in this June and July.

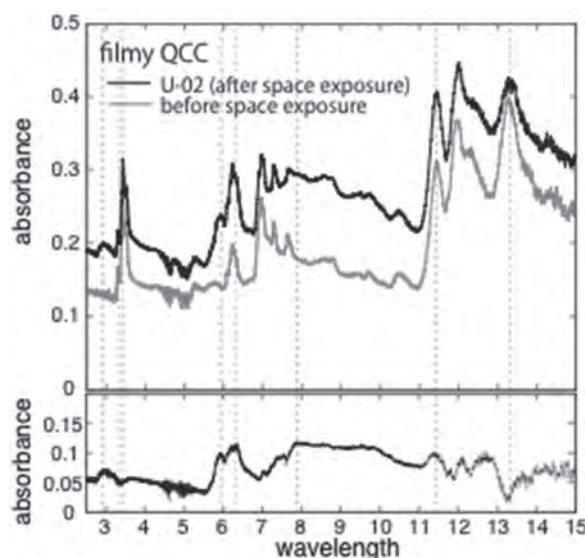
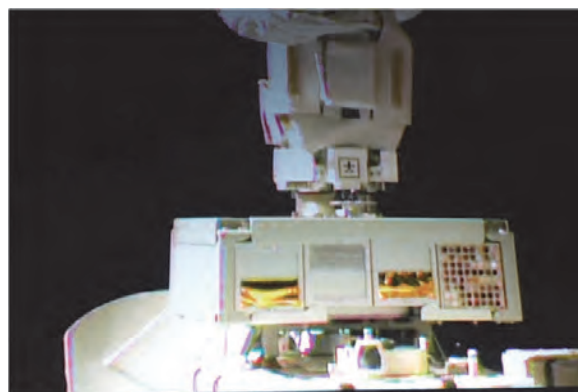


Fig. 1. [Top] A photo of space exposure experiment of EE64-I and EE64-II attached to ExHAM (credit: JAXA/NAXA), [Bottom] The comparison of the infrared spectra of the filmy-QCC before and after the space exposure experiment.

- [1] A. T. Tokunaga, ASP Conf. Ser. **124** (1997) 149.
- [2] A. Sakata *et al.*, Nature **301** (1983) 493.
- [3] I. Sakon *et al.*, Asian Journal of Physics **24** (2015) 1143.

BL4U

## Investigation of Origin and Evolution of Organic Material inside the Extraterrestrial Material with a Series of in-situ Analyses: Construction of System for the Inter-facility Collaboration for the Analysis of Hayabusa2 Returned Samples

M. Uesugi<sup>1</sup>, M. Ito<sup>2</sup>, K. Tomioka<sup>2</sup>, Y. Kodama<sup>3</sup>, T. Ohigashi<sup>4,5</sup>, H. Yuzawa<sup>4</sup>, K. Uesugi<sup>1</sup>, A. Yamaguchi<sup>6</sup>, N. Imae<sup>6</sup>, Y. Karouji<sup>7</sup>, N. Shirai<sup>8</sup>, T. Yada<sup>9</sup> and M. Abe<sup>9</sup>

<sup>1</sup>Japan synchrotron radiation research institute (JASRI/SPring-8), Sayo 679-5198, Japan

<sup>2</sup>Kochi Institute for Core Sample Research, Japan Agency for Marine-Earth Science Technology (JAMSTEC), Nankoku 783-8502, Japan

<sup>3</sup>Marine Works Japan Ltd., Yokosuka 237-0063, Japan

<sup>4</sup>UVSOR Synchrotron Facility, Institute for Molecular Science, Okazaki 444-8585, Japan

<sup>5</sup>School of Physical Sciences, The Graduate University for Advanced Studies (SOKENDAI), Okazaki 444-8585, Japan

<sup>6</sup>Antarctic Meteorite Research Center, National Institute of Polar Research, Tachikawa 190-8518, Japan

<sup>7</sup>Space Exploration Innovation Hub Center, Japan Aerospace Exploration Agency (JAXA), Sagami-hara 252-5210, Japan

<sup>8</sup>Department of Chemistry, Graduate School of Science, Tokyo Metropolitan University, Hachioji 192-0397, Japan

<sup>9</sup>Institute of Space and Astronautical Science, Japan Aerospace Exploration Agency (JAXA), Sagami-hara 252-5210, Japan

Hayabusa2 spacecraft successfully touched down on the surface of asteroid Ryugu, in Feb. 2019. It is scheduled that the spacecraft will return back to the Earth in 2020, with the sample of Ryugu [1]. Reflectance spectrum of the surface of Ryugu suggested that the sample would have water and carbonaceous materials, those similar to carbonaceous chondrites found on the Earth.

We started the development of techniques and devices for the handling, transfer and analysis of samples returned by Hayabusa2 spacecraft from 2015, by organizing a special team constituting of members of Japan Aerospace Exploration Agency (JAXA), Japan Agency for Marine-Earth Science and Technology (JAMSTEC), Institute for Molecular Sciences (IMS), SPring-8 and National Institute of Polar Research (NIPR) [2]. The team, called Phase 2 team Kochi, will also analyze the Hayabusa2 returned samples from 2021.

Rehearsal of the analysis of Hayabusa2 returned samples was started in 2017 using Antarctic micro-meteorites (AMMs) which simulated the small returned particles. 10 AMMs, with diameter around 100 $\mu$ m, provided by NIPR were observed by synchrotron radiation computed tomography (SR-CT) and x-ray diffraction (XRD) at SPring-8, high resolution field emission scanning electron microscopy and energy dispersive spectroscopy (FE-SEM-EDS) system at IMS. Through the series of non-destructive analysis, we selected two AMMs those having characteristics similar to carbonaceous chondrites, and extracted thin sections by focused ion beam (FIB) for the analysis of organic materials by scanning transmitted x-ray microscopy and x-ray absorption near edge structure (STXM-XANES) at BL4U.

We found two different phases of organic matter in AMMs, spotty particles with high carbon density and broad distribution of organics with low density of carbon, in C-XANES analysis. They also show different C-XANES spectrum, suggesting different origin or evolutionary history. Though spatial resolution is not enough to resolve precise structure of those phases, high resolution analysis by transmission electron microscopy (TEM) at JAMSTEC revealed that the spotty particles are hollow organic globules (HOG) those are previously reported by literatures [3][4]. However, the number density of the HOG is almost ten times higher than previous result obtained by TEM [3]. This means that wide-area observation of organics by STXM-XANES, with spatial resolution less around 0.1  $\mu$ m, is important for analysis of extraterrestrial organic material, and also characterization of parent extraterrestrial material.

In future works, we will examine other extraterrestrial materials, such as hydrated and/or heated carbonaceous chondrites with same manner.

[1] S. Tachibana *et al.*, *Geochemical Journal* **48** (2014) 571.

[2] M. Ito *et al.*, LPSC conf. (2019) abstract#1394.

[3] K. Nakamura-Messenger *et al.*, *Int. J. Astrobiol.* **1** (2002) 179.

[4] L.A. Garvie, P. R. Buseck *Earth. Planet. Sci. Lett.* **224** (2004) 431.



BL4U

## Aqueous Alteration Scenario in Martian Meteorite Based on Chemical Speciation

N. Shiraishi<sup>1</sup>, H. Suga<sup>1</sup>, M. Miyahara<sup>1</sup>, T. Ohigashi<sup>2</sup>, Y. Inagaki<sup>2</sup>, A. Yamaguchi<sup>3</sup>,  
N. Tomioka<sup>4</sup>, Y. Kodama<sup>5</sup> and E. Ohtani<sup>6</sup>

<sup>1</sup>*Department of Earth and Planetary Systems Science, Graduate School of Science, Hiroshima University, Higashi-Hiroshima 739-8526, Japan*

<sup>2</sup>*UVSOR Synchrotron Facility, Institute for Molecular Science, Okazaki 444-8585, Japan*

<sup>3</sup>*National Institute of Polar Research, Tokyo 190-8518, Japan*

<sup>4</sup>*Kochi Institute for Core Sample Research, Japan Agency for Marine-Earth Science and Technology, Nankoku 783-8502, Japan*

<sup>5</sup>*Marine Works Japan, Nankoku 783-8502, Japan*

<sup>6</sup>*Department of Earth Sciences, Graduate School of Science, Tohoku University, Sendai 980-8578, Japan.*

Previous studies showed that Martian meteorite clan nakhlite has evidence for a rock-fluid reaction occurred on the Mars. One of the representative fingerprints for the rock-fluid reaction is “iddingsite”, which is the alteration texture formed in and around the olivine grains of nakhlites. Iddingsite is the assemblages of any kinds of secondary minerals. The mineral species, compositions, and chemical species of the iddingsite depend on the varied parameters such as temperature and pH of the fluid contributing to the reaction [e.g., 1]. Accordingly, the secondary minerals in the iddingsite allow us to elucidate the physicochemical properties of the fluid in ancient Martian subsurface and its origin.

In this study, we clarified the mineral species, chemical compositions, and chemical species of the secondary minerals in the iddingsite of the nakhlite Yamato 000749 (Y 000749) using a combined SEM-Raman-FIB-TEM-STXM technique. In particular, FIB-STXM measurement is a unique point of this study. We performed two-dimensional chemical state analysis using X-ray absorption near edge structure (XANES).

TEM images revealed that the iddingsite in Y 000749 had a layer structure (oxidized olivine: laihunite–ferrihydrite–low crystalline silica minerals in Fig. 1a). Fe-XANES spectra revealed that most irons in the original olivine and iddingsite were divalent and trivalent, respectively (Fig. 1b). Based on O-XANES spectra (Fig. 1c) and TEM observations, most of the iron oxides in the iddingsite of Y000749 were identified as ferrihydrite. In addition, S-XANES spectra and TEM observations revealed that a small amount of iron sulfate mineral coexisted with ferrihydrite.

On the basis of the occurrences and formation conditions of the secondary minerals, we expect that Y 000749 experienced three different alteration events at least. The alteration of Y000749 was initiated by the formation of ferrihydrite subsequent to the formation of laihunite, which occurred under high-temperature and high-pH conditions [2]. Then, silicon dissolved in the fluid precipitated as low-crystalline silica minerals. Thus, by combining the FIB-STXM analysis of secondary minerals with the conventional model calculations, we can disclose more detailed environmental evolution processes on Mars.



Ol: Olivine, Laih: Laihunite, Ferri: Ferrihydrite, Low sili: Low crystalline silica mineral

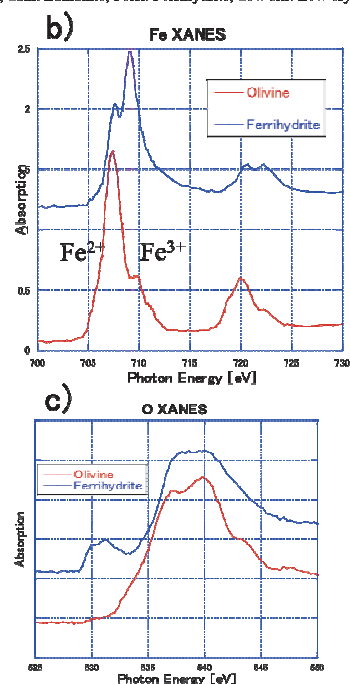


Fig. 1. a) HAADF-STEM image, b) Fe-XANES, c) O-XANES of the iddingsite in Y 000749.

[1] Bridges J.C. and Grady M.M., *Earth Planet. Sci. Lett.* **176** (2000) 267.

[2] Treiman A.H., *Chem Erde-Geochem* **65** (2005) 203.

BL4U

## Sulfur Map in Organics in Meteorites by STXM-XANES and NanoSIMS

M. Ito<sup>1</sup>, R. Nakada<sup>1</sup>, H. Suga<sup>2</sup>, T. Ohigashi<sup>3</sup>, Y. Kodama<sup>4</sup> and H. Naraoka<sup>5</sup>

<sup>1</sup> Kochi Inst. for Core Sample Res., JAMSTEC, Nankoku 783-0086, Japan

<sup>2</sup> The University of Tokyo, Tokyo 113-8654, Japan

<sup>3</sup> UVSOR Synchrotron Facility, Institute for Molecular Science, Okazaki 444-8585, Japan

<sup>4</sup> Marine Works Japan, Yokosuka, 237-0063, Japan

<sup>5</sup> The Kyushu University, Fukuoka, 812-0053, Japan

Organic matter in carbonaceous chondrites is composed of an insoluble macromolecule (aka insoluble organic matter: IOM) and complex soluble organic molecules (OM). The total organic content is around 4 wt% in chondrites (IOM of ~75 wt%) [1]. The proposed composition of IOM is  $C_{100}H_{70}O_{22}N_3S_7$  [1] or  $C_{100}H_{48}N_{1.8}O_{12}S_2$  [2].

The STXM studies were carried out to identify functional groups of C, N and O in organics of extraterrestrial materials (IOM in chondrites [3], cometary returned sample [4], organics in Hayabusa Category-3 particles [5], organics in IDPs [6], and organics extracted from halite in the Monahans LL chondrite [7]). However, sulfur study by XANES in the extraterrestrial organics is very rare [8, 9].

In our experiments at Inst. Mole Sci. UVSOR synchrotron BL4U, we have reported nine sulfur  $L_{3-}$  edge spectra from sulfur bearing terrestrial organics; sodium lauryl sulfate, sodium methanesulfonate, dibenzothiophene, thianthrene, DL-methionine, DL-methionine sulfone, L-cysteic acid, L-cystine, and L-cystine showing different absorption curves (e.g., sulfate, sulfone, thiol) [10].

In this study, we report preliminary results of sulfur speciation measurements by S-XANES in the FIB sections of the Murchison and the Tagish Lake meteorites using scanning transmission X-ray microscope (STXM) at the BL4U. The purpose of this study is understanding of sulfur speciation, its distribution and isotopic compositions ( $^{33}S/^{32}S$ ,  $^{34}S/^{32}S$ ,  $^{36}S/^{32}S$ ) within organics in a carbonaceous chondrite which may provide the secondary alteration processes of thermal metamorphism and aqueous alteration in the parent body.

We successfully obtained high resolution S-STXM image of FIB sections from the Murchison (147 x 187 pixels, 22 x 28  $\mu m^2$ ; spatial resolution = 150 nm) and the Tagish Lake meteorites (01L section = 132 x 132 pixels, 33 x 33  $\mu m^2$  and spatial resolution = 250 nm). Figure 1a shows S-STXM (Red: 173.6 eV assigned to sulfate) image together with IOM (Green) and diffused OM (Blue) images in the Murchison FIB section. Figure 1b is a representative S-XANES spectra in the Murchison FIB section. First and second strong peaks in Fig. 1b may be related to sulfate based on our previous sulfur  $L_{3-}$  edge spectra for organic standards [10]. We might find small peak around 181 eV which assigned to sulfonate in Fig. 1b, and difficult to assign 164 eV peak which is related to organic sulfide. The S-STXM spectra of Tagish Lake is slightly different peaks

and peak-top shape. We found several  $\mu m$ -sized spots having the S-STXM spectra in the Tagish Lake section.

We, then, conducted S (red), C (green), and O (blue) elemental imaging with the JAMSTEC NanoSIMS for the Murchison FIB section in comparison with the STXM image (red: Sulfate, green: IOM, blue: DiffOM) of the same FIB section (Fig. 2). Note that the green area in both images are almost identical each other implying NanoSIMS C-image are relate to the IOM. However, S regions from both sections show completely different locations within the entire section. S distributions observed by STXM is an organic component, but S image obtained by NanoSIMS might be inorganic components (i.e., FeS).

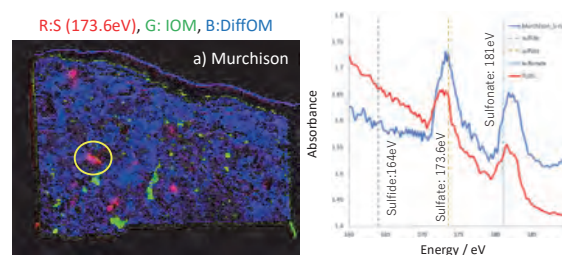


Figure 1. a) STXM image of Murchison FIB section, and b) S-XANES spectra of the Murchison and Tagish Lake meteorites

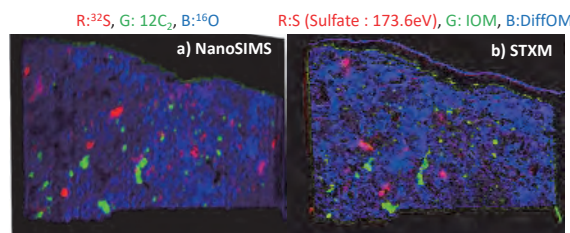


Figure 2. Comparison a) NanoSIMS elemental image and b) STXM image

- [1] Remusat, EPJ Web of Conferences **18** (2011) 05002.
- [2] Gilmour, In Meteorit., comets and planets, Treatise on Geochemistry, (2005) 269.
- [3] Kebukawa *et al.* 2019. Scientific Reports, **9**:3169.
- [4] Sanford *et al.*, Science **314** (2006) 1720.
- [5] Yabuta *et al.*, EPS **66** (2014) 156.
- [6] Flynn *et al.*, Geochim Cosmochim Acta **67** (2003) 4791.
- [7] Chan *et al.*, Science Advance **4** (2018) eaao3521.
- [8] Orthous-Daunay *et al.*, EPSL **300** (2010) 321.
- [9] Bose *et al.*, Meteor Planet Sci. **52** (2017) 546.
- [10] Ito *et al.*, UVSOR activity report 2017 **45** (2018) 84.

BL4U

## Hyperspectral Imaging by Scanning X-ray Microscopy: Probing the Penetration of Rapamycin in Fixed Human Skin

G. Germer<sup>1</sup>, T. Ohigashi<sup>2</sup>, H. Yuzawa<sup>2</sup>, F. Rancan<sup>3</sup>, A. Vogt<sup>3</sup> and E. Rühl<sup>1</sup>

<sup>1</sup>Physical Chemistry, Freie Universität Berlin, Arnimallee 22, 14195 Berlin, Germany

<sup>2</sup>UVSOR Synchrotron Facility, Institute for Molecular Science, Okazaki 444-8585, Japan

<sup>3</sup>Charité Universitätsmedizin, 10117 Berlin, Germany

Progress in hyperspectral imaging using scanning X-ray microscopy is reported. This is facilitated by using a custom-made Ni-coated zone plate for investigations in the O 1s-regime, which provides higher photon flux and improved spatial resolution compared to previous beam times. This substantial improvement allowed us to take for fixed human skin sample stacks of images, which cover multiple photon energies in the O 1s regime (520 – 560 eV, 134 energy steps) in areas of a size of 20  $\mu\text{m}$  x 5  $\mu\text{m}$  with 100 nm step width as well as high resolution maps with 30 nm step width (size: 4  $\mu\text{m}$  x 2  $\mu\text{m}$ ). This provides substantially more detailed information than in our previous work, where X-ray micrographs were taken at a few pre-selected photon energies [1]. These were chosen according to characteristic changes in absorption of the species under study, allowing for determining the location of the penetrating drug. The present developments go beyond, so that the spectral shapes in the near-edge regime as well as their differences can also be used for identifying highly dilute species in a given compartment of biological matter. This is of importance for identifying local changes induced by topical drug delivery. We have investigated for the first time the skin penetration of the anti-inflammatory drug rapamycin (sirolimus) ( $\text{C}_{51}\text{H}_{79}\text{NO}_{13}$ ,  $M=914.13$  g/mol), a well-known mTOR inhibitor. Skin penetration of rapamycin is expected to be inefficient due to its high molecular mass [2], if not properly formulated. The present studies were performed at the O 1s-edge, where the drug is selectively probed at the O 1s $\rightarrow\pi^*$ -resonance near 531 eV, which is characteristically shifted in energy compared to the matrix of fixed human skin. The skin was partially treated before drug penetration by serine protease [3], enhancing the drug penetration. This was verified for rapamycin dissolved in ethanol, where the drug was only observed in the stratum corneum in the lipophilic membranes between the corneocytes after long penetration times, reaching up to 1000 min (see Fig. 1). In contrast, intact skin samples do not provide evidence for such drug penetration, underscoring the successful use of primary serine protease treatment as a prerequisite for drug penetration. Figure 1(a) shows a high resolution micrograph of such skin sample. Clearly visible is the stratified structure of the stratum corneum (SC). Distinct changes in local composition are visible at the locations A and B. The raw spectra (Fig. 1(b)) show only minor differences in shape, but when the contribution of a reference skin sample is subtracted

(see Fig. 1(c)), then evidence is found for the local abundance of rapamycin (location A), whereas in corneocytes (location B) only enhanced intensity in the O 1s continuum is observed (see Fig. 1(c)). This progress will be systematically exploited for subsequent studies involving redox nanocarriers for bringing the drug efficiently in viable skin layers.

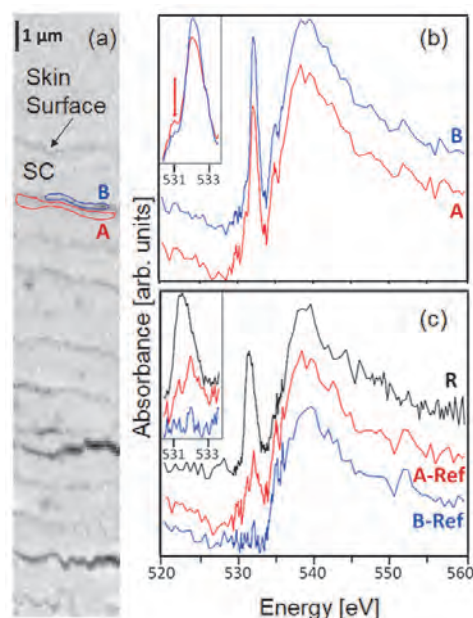


Fig. 1. (a) X-ray micrograph of fixed human skin treated with serine protease and subsequently exposed for 1000 min with rapamycin (R), SC: stratum corneum, A: lipophilic lamella; B: corneocyte; (b) X-ray absorption spectra at the locations A and B at the O 1s-edge; (c) reference spectrum of rapamycin and at the locations A and B subtracted by the contribution of reference skin (A-Ref; B-Ref). The insets in (b) and (c) show the O 1s $\rightarrow\pi^*$ -bands in greater detail.

[1] K. Yamamoto *et al.*, *Anal. Chem.* **87** (2015) 6173; *Eur. J. Pharm. Biopharm.* **118** (2017) 30; *Eur. J. Pharm. Biopharm.* **139** (2019) 68.

[2] J. D. Bos *et al.*, *Exp. Dermatol.* **9** (2000) 165.

[3] J. Frombach *et al.*, *Z. Phys. Chem.* **232** (2018) 919.



BL4U

## Ultrastructural Features in Mice Liver Samples Imaged Using STXM

M. Patanen<sup>1,2</sup>, H. Yuzawa<sup>3</sup>, T. Ohigashi<sup>3</sup>, T. Mansikkala<sup>1,2</sup>, I. Miinalainen<sup>2</sup>, S. M. Kangas<sup>2,4</sup>, A. E. Hiltunen<sup>2,4</sup>, E.-V. Immonen<sup>1,4</sup>, R. Hinttala<sup>2,4</sup>, J. Uusimaa<sup>2,4</sup>, N. Kosugi<sup>3</sup> and M. Huttula<sup>1</sup>

<sup>1</sup>Nano and Molecular Systems Research Unit, PO Box 3000, 90014 University of Oulu, Finland

<sup>2</sup>Biocenter Oulu, PO Box 5000, 90014 University of Oulu, Finland

<sup>3</sup>UVSOR Synchrotron Facility, Institute for Molecular Science, Okazaki 444-8585, Japan

<sup>4</sup>PEDEGO Research Unit and Medical Research Center Oulu, and Oulu University Hospital, PO Box 5000, 90014 University of Oulu, Finland

In this work, we have used scanning transmission X-ray microscopy (STXM) technique at BL4U beamline to study liver tissue samples of control (healthy) mice and mice with a mutation in *NHLRC2* gene. The *NHLRC2* gene encodes an NHL repeat containing protein 2 ubiquitously present in various types of tissues, from animals to bacteria. Recently, we have characterized a novel, fatal cerebropulmonary disease in children with fibrosis, neurodegeneration and cerebral angiomatosis (FINCA disease) [1]. FINCA disease has been linked to mutations in *NHLRC2*, but the functional role of the *NHLRC2* is still unknown. Transmission Electron Microscopy (TEM) images of analysis of immortalized cell cultures from FINCA patients demonstrated multi lamellar bodies and distinctly organized vimentin filaments, and based on thorough multitechnique characterization, it was suggested that *NHLRC2* dysfunction enhances tissue fibrosis [2]. Previously, we have also reported an STXM study of human FINCA patient tissue samples which were in line with TEM results [3].

Recently, we have created a knock-in mouse model for FINCA disease utilizing the CRISPR-Cas9 technology. This mouse model enables us to investigate the changes in ultrastructural features as the disease progresses. For the present study, liver sections from control mice and knock-in mice were collected from 13 weeks old mice. Tissue samples were fixed in 4% paraformaldehyde and 2.5% glutaraldehyde in 0.1 M phosphate-buffered saline. Prior to embedding in resin some samples were stained with 1% OsO<sub>4</sub> and/or uranyl acetate. Some samples were left without staining in order to investigate its effects. The 100 nm thick sections of resin-embedded sample were measured first with STXM, and then further imaged at Biocenter Oulu using a Tecnai G2 Spirit 120kV TEM (FEI, Eindhoven, The Netherlands) equipped with a Quemesa CCD camera (Olympus Soft Imaging Solutions GmbH, Münster, Germany).

Figure 1 shows examples of a FINCA mouse liver section without block staining imaged with STXM and after with TEM. Radiation damage seems to thin the sample, as the STXM imaged regions are clearly visible as lighter regions in TEM images. However, no ultrastructural changes in sample due to radiation were observed. The average STXM image taken over the O K-edge is presented in optical density, in contrast to transmission mode of TEM images. A cluster analysis of STXM image stacks (Figs. 1c & f) was performed

using a MANTiS software [4]. Even with the resin-embedded unstained samples, the cluster analysis was able to differentiate cell components rather consistently based on their spectral information. For example, the Figs. 1b-d contain a cell nucleus with a nucleolus, which the cluster analysis also catches, and in Fig. 1f mitochondria (orange) are well separated from the surrounding endoplasmic reticulum (green). The result shows great promise in ultrastructural characterization of unstained tissue samples using STXM.

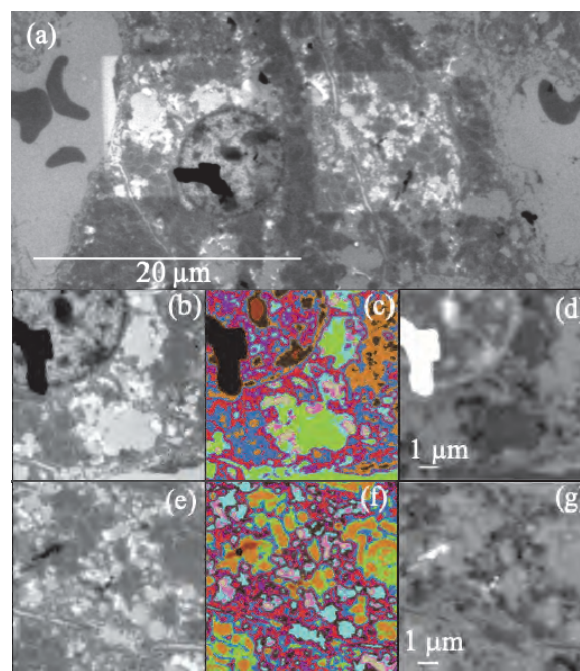


Fig. 1. (a) TEM image of the FINCA mouse sample studied after STXM. (b) & (e) Higher resolution TEM images of the studied areas. (c) & (f) Cluster analysis of the STXM image stacks. (d) & (g) Average STXM image recorded over O K-edge.

- [1] J. Uusimaa *et al.*, *Acta Neuropathol.* **135** (2018) 727.  
 [2] T. Paakkola *et al.*, *Hum. Mol. Gen.* **27** (2018) 4288.  
 [3] E.-V. Immonen *et al.*, *UVSOR Activity Report 2017* **45** (2018) 161.  
 [4] M. Lerotic *et al.*, *J. Synchr. Rad.* **21** (2014) 1206.

BL4U

## The Molecular Structures and Distributions of Organic Matter Depending on the Lithologies of the Tagish Lake Meteorite Examined by C- and Fe-XANES

K. Kiryu<sup>1</sup>, Y. Kebukawa<sup>2</sup>, T. Ohigashi<sup>3</sup> and K. Kobayashi<sup>2</sup>

<sup>1</sup>Graduate School of Engineering Science, Yokohama National University, Yokohama 240-8501, Japan

<sup>2</sup>Faculty of Engineering, Yokohama National University, Yokohama 240-8501, Japan

<sup>3</sup>UVSOR Synchrotron Facility, Institute for Molecular Science, Okazaki 444-8585, Japan

The Tagish Lake meteorite is an anomalous carbonaceous chondrite (CC) and contains abundant organic matter (OM) which has been affected by aqueous alteration in the parent bodies [1]. In the process of aqueous alteration, specific minerals may be involved in the reaction of OM. In fact, the distributions of OM overlap with these of phyllosilicates and partially carbonates in Tagish Lake [2]. Phyllosilicates are known to adsorb OM [e.g., 3], and thus they possibly serve as catalysts of the reactions of OM [e.g., 4, 5]. Tagish Lake is known to consist of various lithologies [1, 6]. Therefore, we aim to evaluate the relationships between minerals and OM through microscopic analyses of various lithologies of the Tagish Lake meteorite.

Fragments from three different lithologies of Tagish Lake (“Pristine”, “KN2”, and “Degraded” samples) were observed using a scanning electron microscope (SEM) and energy dispersive X-ray spectroscopy (EDS). We selected four areas randomly and two areas based on the EDS (a Mg-rich region and a carbonate region). Six ultrathin sections (~100 nm thick) were prepared using focused ion beam (FIB). We analyzed these sections by scanning transmission X-ray microscope (STXM) and obtained C- and Fe-X-ray absorption near-edge structure (XANES) from C-rich regions in the FIB sections. The C-XANES spectra of Tagish Lake showed peaks at 287.3 eV (aliphatic C), 285.2 eV (aromatic C), 288.5 eV (carboxyl and/or ester) and 290.3 eV (carbonate) (Fig. 1), and the Fe-XANES spectra showed peaks at 706.8 eV (Fe<sup>2+</sup>) and 708.5 eV (Fe<sup>3+</sup>) (Fig. 2).

To compare molecular structures of OM in various fragments from Tagish Lake, C-XANES peak intensities were normalized to the intensity at 291.5 eV (ionization potential). The normalized intensities of aliphatic C were KN2 (carbonate region) > Pristine ≥ KN2 (Mg-rich region) > KN2 > Degraded. The Fe<sup>2+</sup>/Fe<sup>3+</sup> ratios were lower in the OM rich regions compared to the OM poor regions. These results indicate that the molecular structure of OM varies among lithologies of Tagish Lake, possibly related to chemical compositions of coexisting minerals.

Acknowledgements: We thank Dr. M. E. Zolensky and Dr. W. Fujiya for providing the Tagish Lake meteorite samples, and Dr. M. Ito for preparing the FIB sections.

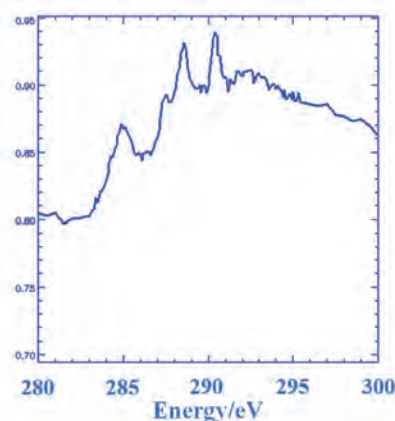


Fig. 1. C-XANES obtained from a FIB section of Tagish Lake “KN2”.

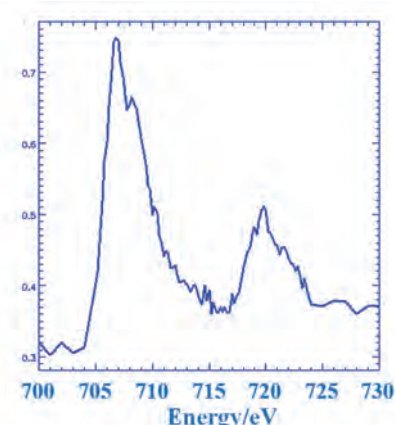


Fig. 2. Fe-XANES obtained from a FIB section of Tagish Lake “KN2” (same region to Fig. 1).

- [1] C. D. K. Herd *et al.*, *Science* **332** (2011) 1304.
- [2] M. Yesiltas and Y. Kebukawa, *Meteoritics & Planetary Science* **51** (2016) 584.
- [3] M. Kahle *et al.*, *Organic Geochemistry* **35** (2004) 269.
- [4] L. B. Williams *et al.*, *Geology* **33** (2005) 913.
- [5] J. S. Watson and M. A. Sephton, *Astrobiology* **15** (2015) 787.
- [6] M. E. Zolensky *et al.*, *Meteoritics & Planetary Science* **37** (2002) 737.

BL4U

## Composition of Carbon Functional Group of Soil Organic Matter in Clay Size Fraction in Initial Forming Stage of Volcanic Ash Soils in Japan

M. Asano<sup>1</sup>, V. F. Eseese<sup>2</sup>, H. Shimada<sup>2</sup>, K. Tamura<sup>1</sup> and T. Ohigashi<sup>3,4</sup>

<sup>1</sup>Faculty of Life and Environmental Sciences, University of Tsukuba, Tsukuba 305-8572, Japan

<sup>2</sup>Graduate School of Life and Environmental Sciences, University of Tsukuba, Tsukuba 305-8572, Japan

<sup>3</sup>UVSOR Synchrotron Facility, Institute for Molecular Science, Okazaki 444-8585, Japan

<sup>4</sup>School of Physical Sciences, The Graduate University for Advanced Studies (SOKENDAI), Okazaki 444-8585, Japan

Soil is the largest terrestrial carbon reservoir in the World. Soil organic matter (SOM) accounts for a major portion of terrestrial C and is considered to be stabilized against microbial degradation due partly to its interaction with soil minerals. These organo-mineral interactions contribute to the formation of heterogeneous organo-mineral particles at various space scales down to submicron level [1]. Volcanic ash soil tend to accumulate large amounts of carbon as SOM in comparison to other soil type. The abundance of Short Range Order minerals and secondary Al, Fe and Si-humus complexes are common in developed volcanic ash soil (Andosols) which contributes to its SOM accumulation capacity [2]. On the other hand, the changing of organo-mineral interactions with weathering process on fresh volcanic ash during soil forming is remain unclear. The research on initial soil forming process on fresh volcanic ash under natural environment is important to understand the development of Andosols and carbon dynamics in volcanic region.

Here we focused on the carbon functional groups within the organo-mineral particle in the initial soil forming stages using scanning transmission X-ray microscopy (STXM) and near-edge X-ray absorption fine structure (NEXAFS) at UVSOR BL4U. We compared top soil from different soil ages, immature volcanic ash soil (Regosol) and mature volcanic ash soil (Andosol). The smaller than 2  $\mu\text{m}$  fraction was separated by particle size fractionation method [3].

The C-NEXAFS spectrum of organo-mineral particles showed clear difference between Regosol and Andosol. To show the C chemical composition map, we split the C K-edge spectra three energy regions, 284–286 eV (aromatic C), 286–287 eV (phenol and aliphatic C), and 287–289 eV (amid and carboxyl C) (Figs. 1 and 2). The C functional group map of Regosol was dominated by carboxylic C with minimal Aliphatic C and Aromatic C (Fig. 1). The C functional group map of Andosol shows also dominated by carboxyl C, but Aromatic C and Aliphatic C appeared clear than Regosol (Fig. 2). Those results indicated amide and carboxylic C, potentially labile C, was accumulated in both immature and mature soils.

We will further examine microstructure, diffraction

pattern, and elemental composition of specific regions within the tested organo-mineral particles in this report by transmission electron microscope (TEM) to discuss organo-mineral interactions.

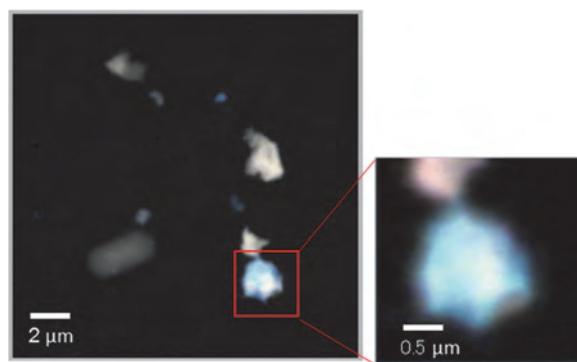


Fig. 1. Carbon functional group map of immature soil (Regosol). red: 284–286eV (aromatic C), blue: 286–287 eV (phenol and aliphatic C), and green: 287–289 eV (amide and carboxyl C).

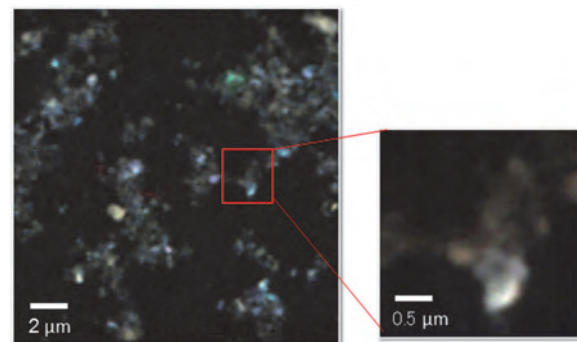


Fig. 2. Carbon functional group map of mature soil (Andosol). red: 284–286eV (aromatic C), blue: 286–287 eV (phenol and aliphatic C), and green: 287–289 eV (amide and carboxyl C).

[1] M. Asano *et al.*, *Soil Systems* **2** (2018) 32.

[2] R. A. Dahlgren *et al.*, *Adv. Agron.* **82** (2004) 113.

[3] M. Asano and R. Wagai, *Geoderma* **216** (2014) 62.



BL4U

## STXM-XANES Analysis of Carbonaceous Matter in ~3.95 Billion-year-old Sedimentary Rocks

M. Igisu<sup>1</sup>, T. Ohigashi<sup>2,3</sup>, H. Yuzawa<sup>2</sup> and T. Komiya<sup>4</sup>

<sup>1</sup>Department of Subsurface Geobiological Analysis and Research, Japan Agency for Marine-Earth Science and Technology (JAMSTEC), Yokosuka 237-0061, Japan

<sup>2</sup>UVSOR Synchrotron Facility, Institute for Molecular Science, Okazaki 444-8585, Japan

<sup>3</sup>School of Physical Sciences, The Graduate University for Advanced Studies (SOKENDAI), Okazaki 444-8585, Japan

<sup>4</sup>Department of Earth Science and Astronomy, The University of Tokyo, Meguro 153-8902, Japan

Carbonaceous matter (CM) in Archean (approximately 4-2.5 billion years ago) sedimentary rocks provides important insights into understanding the physiological and phylogenetic characteristics of life on early Earth [1]. The presence of life on Earth has been inferred primarily from morphologically preserved microscopic fossils, stromatolites, molecular biomarkers, and stable isotopic compositions in sedimentary rocks. Recently, <sup>13</sup>C-depleted CM was found in ~3.95 billion-year-old metasedimentary rocks in Labrador, Canada, which provides the oldest evidence of life on Earth [2]. The carbon isotopic signatures provide potential chemical evidence of microbial activity in the environment at the time. However, they do not necessarily offer clues for distinguishing whether the products are derived from the microbial functions of the bacterial and/or archaeal populations. In this study, we characterized the molecular structure of CM in order to obtain insights into its origin.

The C-K and N-K X-ray absorption near edge structure (XANES) spectra of CM in sedimentary rocks were acquired using a scanning transmission X-ray microscope (STXM) at the BL4U, UVSOR. Analyzed sedimentary rocks were a pelitic rock (LAF497) and a conglomerate (LAD849A), both containing CM. Before XANES analyses, Raman microspectroscopic analysis was performed on the petrographic thin sections to identify the presence of CM and examine its graphitization degree [3]. The Raman spectra revealed that the CM in the pelitic rock was less graphitized as compared to that in the conglomerate. Thin cross-sectional foils (about 100-150 nm thick) containing CM were then prepared by focused ion beam (FIB) milling for thin sections of both pelitic and conglomerate rocks.

Figure 1 shows an example of a C-XANES spectrum of the CM in the conglomerate. Absorption peaks at 285 eV and at 292 eV correspond to  $1s \rightarrow \pi^*$  of electronic transitions in aromatic C=C bonds, and  $1s \rightarrow \sigma^*$  exciton of graphite, which are typical for graphitized carbon [4]. The CM in the pelitic rock has similar C-XANES spectra to that in the conglomerate, regardless of the difference in their graphitization degrees. N-XANES spectra for the CM did not exhibit clear absorption peaks. Figure 2 reveals submicron-scaled heterogeneity of carbon within one CM grain. Although one possible explanation for this heterogeneity is the orientation of the graphite layer,

further examination of the microstructure of the CM is required for further validation.

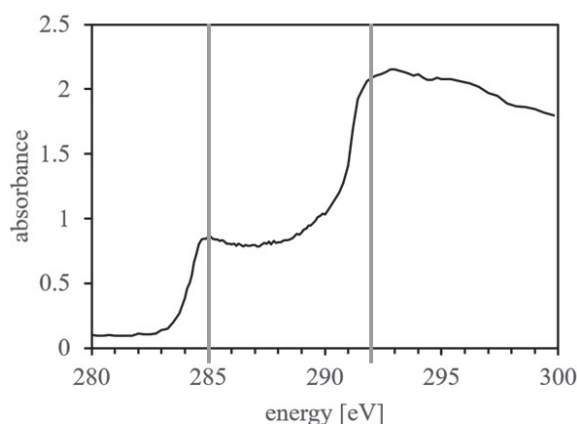


Fig. 1. Carbon-XANES spectrum of the CM (LAD849A).

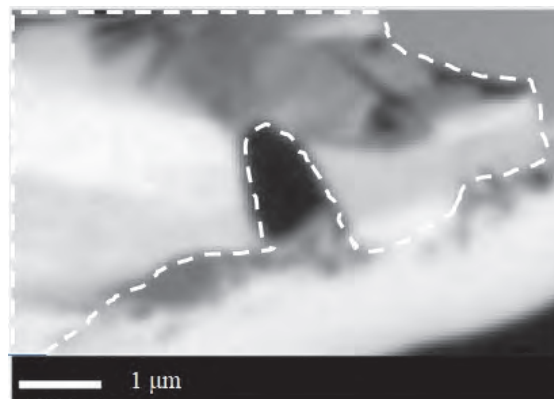


Fig. 2. A STXM image at 285 eV of the analyzed foil (LAD849A).

[1] J. J. Brocks, *Emerging Topics in Life Sciences* **2** (2018) 181.

[2] T. Tashiro *et al.*, *Nature* **549** (2017) 516.

[3] O. Beyssac *et al.*, *J. Metamorph. Geol.* **20** (2002) 859.

[4] G. D. Cody *et al.*, *Earth Planet. Sci. Lett.* **272** (2008) 446.

BL4U

### 3-Dimensional Spectroscopy of an Isolated Cell Nucleus by Using a Scanning Transmission X-ray Microscope

T. Ohigashi<sup>1,2</sup>, H. Yuzawa<sup>1</sup>, S. Toné<sup>3</sup>, K. Shinohara<sup>4</sup> and A. Ito<sup>4</sup>

<sup>1</sup>UVSOR Synchrotron Facility, Institute for Molecular Science, Okazaki 444-8585, Japan

<sup>2</sup>School of Physical Sciences, The Graduate University for Advanced Studies (SOKENDAI), Okazaki 444-8585, Japan

<sup>3</sup>Graduate School of Advanced Science and Technology, Tokyo Denki University, Hatoyama 350-0394, Japan

<sup>4</sup>School of Engineering, Tokai University, Hiratsuka 259-1292, Japan

Apoptosis is a programmed cell death which is frequently observed in many biological processes such as developmental process. Then, nuclear condensation and DNA fragmentation occur during process of apoptosis, and this process is classified into 3 stages regarding to morphology of nucleus. Apoptosis is generally observed by using fluorescence microscope with staining process but high resolution image, chemical compositions and 3-dimensional (3D) structure of apoptosis are still unclear. Then, scanning transmission X-ray microscopy (STXM) with computer tomography (CT) is a promising tool to elucidate these issues with 3-dimensional (3D) distribution of chemical states. In the previous report, we performed STXM-CT of an isolated cell nucleus at N K-edge since DNA and protein have remarkable spectral features at N K-edge [1]. However, qualities of 3D distributions of DNA and protein were not good mainly due to saturation of X-ray absorption [2]. In this report, we tried STXM-CT of the cell nucleus by using O K-edge.

The isolated cell nucleus of HeLa S3 cell at stage 0 (i.e. a normal cell) was used as a sample. After fixation by glutaraldehyde, the cell nucleus was performed critical point drying. The cell nucleus was glued on a tip of a tungsten needle (TP-005, Micro Support Co., Ltd.) with a crystal bond and the tungsten needle was fixed on a CT sample cell [3]. As data acquisition, 50 image stacks, each of which is consisted of 48 STXM images around O K-edge region from 528 to 538 eV, were obtained manually with rotating the sample 3.6° each (in total 180° rotation) to obtain complete projection data. Their measurement conditions are as follows; scan area is 8×8 μm<sup>2</sup> composed of 50×50 pixels, and the dwell time is 1s per a pixel. This measurement condition was determined to keep radiation damage on the sample minimum.

As a pre-process of reconstruction, position shifts in the image stacks were aligned and were converted to optical density (OD) images by using aXis2000 program. By extracting the OD images of same energies from each image stack, sinograms were obtained. Cross-sectional images were reconstructed from these sinograms by home-made filtered-back projection algorithm.

3D reconstructed image (volume projection by using ImageJ software) and, for an example, a cross sectional image of the isolated cell nucleus at the X-ray energy of 528 eV are shown in Fig. 1. With noticing structures of nucleoli and filaments, X-ray

absorption spectra are extracted from the areas in Fig. 1b (Fig. 2). Peaks of π\* resonance of the spectra (around 532 eV) resemble those of DNA and protein in their position and shape.

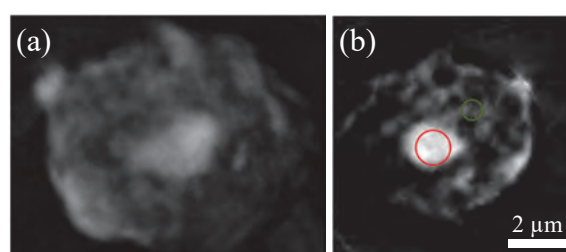


Fig. 1. (a) 3D volume projection image and (b) a cross sectional image of the isolated cell nucleus of the X-ray energy of 528 eV.

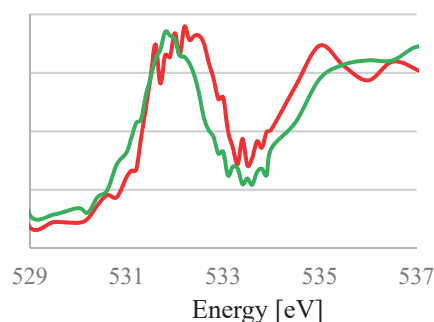


Fig. 2. Spectra extracted from reconstructed energy stack. Colors of the spectra correspond to the areas indicated in Fig. 1(b).

[1] T. Ohigashi, A. Ito, K. Shinohara, S. Tone, M. Kado, Y. Inagaki, Y-F. Wang and N. Kosugi, AIP Conf. Proc. **1696** (2016) 020027.

[2] T. Ohigashi, A. Ito, K. Shinohara, S. Toné, Y. Inagaki, H. Yuzawa and N. Kosugi, Microsc. Microanal. **24** (2018) 400.

[3] T. Ohigashi, Y. Inagaki, A. Ito, K. Shinohara and N. Kosugi, J. Phys.: Conf. Ser. **849** (2017) 012044.

BL4U

## Study on the Mechanism of Microbial Weathering of Oceanic Crust by in situ Observation of the Basalt-cell Interface

S. Mitsunobu, S. Urano and J. Fukudo

*Department of Agriculture, Ehime University, Matsuyama 790-8566, Japan*

The weathering of oceanic basalts is one of the most crucial water-rock interaction ubiquitously occurring in the vast oceanic crust. The weathering of oceanic basalt has a significant impact on Earth's climate on a geological timescale by providing a sink for atmospheric CO<sub>2</sub> through carbonization of oceanic basalts [1]. The fresh basalt rock contains abundant Fe (about 10 wt.%) and its major species is ferrous iron (Fe(II)) and initial Fe(II)/Fe<sub>total</sub> ratio in fresh basalt ranges between 82 and 90% [2]. Hence, when the oceanic basalts are exposed to oxidative conditions, the Fe(II) in basalts is gradually oxidized to Fe(III) in the weathering process on a geological timescale even at low temperature in deep seafloor [3]. Recent previous studies have reported that oceanic microorganisms (mainly bacteria) would play a significant role to the oxidation of Fe(II) in the basalt. Also, it is indicated that bacterial Fe(II) oxidation would promote the whole weathering process of oceanic crust [3], as the rate of microbial Fe(II) oxidation is generally more rapid than that of chemical oxidation by dissolved O<sub>2</sub>. There have been considerable efforts to investigate chemical and biological mechanism of the oxidation of Fe(II) involved in the oceanic basalt. However, little is known on the mechanism of microbial Fe(II) in the basalt alteration, because direct chemical speciations of Fe and biomolecules at rock-microbe interface has been difficult due to a short of spatial resolution in the analysis.

Here, we examined the mechanisms of the Fe(II) oxidation in basalt weathering by using direct scanning transmission X-ray microscopy (STXM)-based NEXAFS analyses at UVSOR BL4U. The basalt sample used in the study was prepared by in situ incubation of fresh basalt glass for 12 months at deep seafloor (water depth: 700-800 m) in Izu-Ogasawara bonin.

STXM-based merged Fe/C image and C 1s NEXAFS were shown in Fig. 1. The NEXAFS clearly showed that the spectrum obtained at bacterial cell-basalt interface (area 3) in the incubated basalt glass contains a strong peak corresponding for acidic polysaccharides (alginate), addition to the other biomolecules of protein, DNA, and lipid. The spectral features were not observed in those of whole cell area. These finding indicates that the sessile bacteria attached on the basalt glass largely produced the polysaccharide-rich extracellular polymeric substances at the cell-basalt interface. The biogenic polysaccharides are likely to form a strong complex with Fe(II) under wide pH region [3]. Thus, our finding from C NEXAFS analysis

suggests that the sessile bacteria produce the polysaccharides on the basalt glass to enhance the dissolution of basalt by the complexation between the cell and basalt surface. These findings would be an important knowledge to understand mechanism of bacteriogenic weathering of oceanic crust.

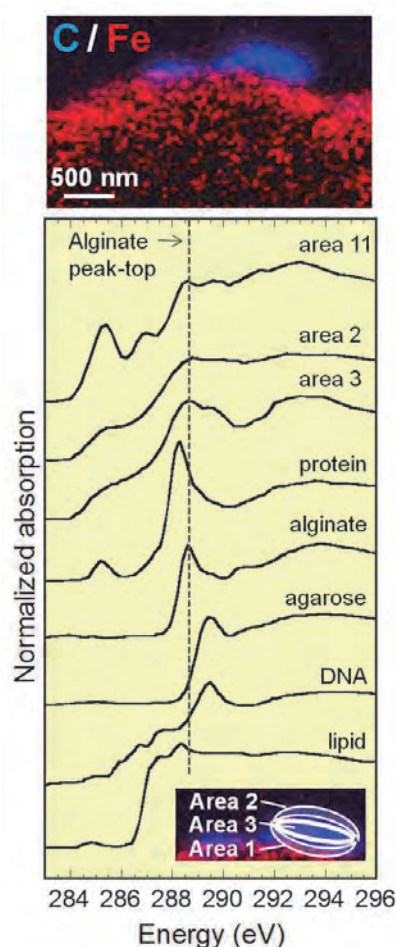


Fig. 1. STXM-based C and Fe images (upper) and C 1s NEXAFS spectra (bottom).

- [1] H. Staugigel *et al.*, *Geochim. Cosmochim. Acta* **53** (1989) 3091.
- [2] A. Bezos and E. Humler, *Geochim. Cosmochim. Acta* **69** (2005) 711.
- [3] W. Bach and K.J. Edwards, *Geochim. Cosmochim. Acta* **67** (2003) 3871.



BL4U

## Chemical Mapping of Individual Atmospheric Nanoparticles

R. R. Kamal<sup>1</sup>, J. J. Lin<sup>1</sup>, G. Michailoudi<sup>1</sup>, H. Yuzawa<sup>2</sup>, T. Ohigashi<sup>2</sup> and N. L. Prisle<sup>1</sup>

<sup>1</sup>Nano and Molecular Systems Research Unit, University of Oulu, Oulu 90041, Finland

<sup>2</sup>UVSOR Synchrotron Facility, Institute for Molecular Science, Okazaki 444-8585, Japan

Chemical maps were drawn for three types of aerosol samples. 1) Laboratory-generated aerosols with 150 nm diameter, produced by atomization of solutions of sodium n-decanoate and sodium chloride with different mixing ratios. 2) Urban aerosol samples collected in Beijing during a winter campaign from October 2017 to January 2018 jointly operated by Peking University and the University of Gothenburg. Sampling was carried out at the Peking University Atmosphere Environment Monitoring Station on the roof of a six-floor building on the campus of Peking University located in the northwestern urban area of Beijing. A SKC 4-stage cascade impactor was used to collect particles with cut-off sizes of 250 and 500 nm that were impacted onto Formvar films. 3) Plastic reference samples prepared from industrial grade plastics sliced as thinly as possible to ensure good transmission of X-rays. Slices were made of 100 and 60 nm polyethylene and 150 and 100 nm polypropylene using microtome. Spectra are to our knowledge first of their kind and will serve as reference for characterizing microplastic collected in nature.

Based on chemical formula, plastic samples should only contain C-C bonds, and the absorption region from 280 to 320 eV was studied. Along with uniform presence of expected C-C, as seen in selected region of Fig 1 (a), plastic samples also showed presence of K<sup>+</sup> group. Occurrence of K was only around the sample edges, indicating potential contamination during cutting and slicing of the plastics. The spectrum in (c) also shows a small peak at 285 eV corresponding to C=C [1], and further analysis is required to confirm what contributes to that peak.

The urban aerosol samples were examined at the absorption edges of carbon, nitrogen, sulfur, silicon, chlorine, calcium, iron, vanadium, and titanium, to identify their possible origins from e.g. organic sources, mineral dust, or traffic emission. Figure 2 shows the optical density of one particle probed at the carbon (a), sulfur (b), and calcium (c) edges and the spectra obtained are shown in panels (d), (g), and (e) respectively. For comparison, panel (f) shows spectra from literature of laboratory-generated soot coated by  $\alpha$ -pinene (in red) and naphthalene SOA (in black) [2]. We did not observe similar peak features between 285 and 300 eV, but find peaks corresponding to K<sup>+</sup> (296 eV), sulfate (170-180 eV) and calcium (345-350 eV), suggesting that this particular particle examined most likely originates from mineral dust. Other particles in the same sample show indicators of different origins, comprising carbon, nitrogen, or heavy metal peaks. Detailed analysis is required for more accurate conclusions. Chemical mapping of single particles is

still extremely rare, and these experiments give a first glimpse into the heterogeneity of samples previously assumed to be uniform.

Laboratory-generated samples were mapped with focus on spatially resolved chemical characterization. Detailed analysis will reveal presence of biases in sampling procedures.

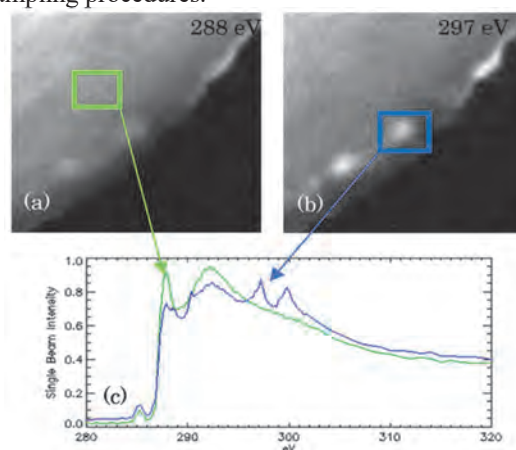


Fig. 1. Optical density of plastic sample at various photon energies. Bright areas indicate where excited functional groups are located. (a) Regions with C-C bonds; (b) Presence of K; (c) Spectra obtained from selected regions showing peaks corresponding to of C-C (288 eV), C=C (285 eV), and K (296 eV).

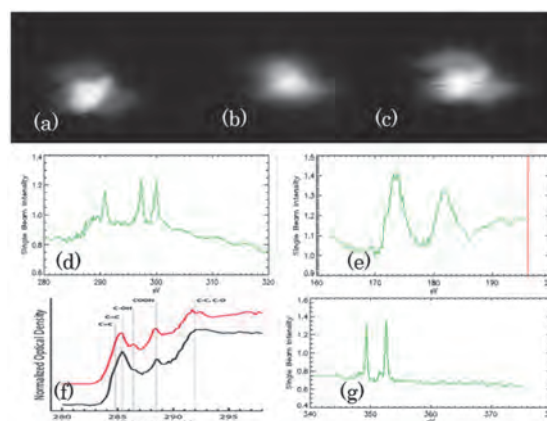


Fig. 2. Urban aerosol at different absorption edges and literature reference of organic aerosol absorption spectra.

[1] R. C. Moffet, A.V. Tivanski and M.K. Gilles, *Fundamentals and Applications in Aerosol Spectroscopy* (CRC Press; Boca Raton, FL, 2011).

[2] J. C. Charnawskas *et al.*, *Faraday Discussions* **200** (2017) 165.

BL4U

## STXM-XANES Analysis of Carbonaceous Matter of the Ediacara Biota-type Fossils from the Early Cambrian Chengjiang Section

T. Komiya<sup>1</sup>, T. Ohigashi<sup>2,3</sup>, D. Shu<sup>4</sup>, J. F. H. Cuthill<sup>5,6</sup> and J. Han<sup>4</sup>

<sup>1</sup>Department of Earth Science and Astronomy, The University of Tokyo, Meguro 153-8902, Japan

<sup>2</sup>UVSOR Synchrotron Facility, Institute for Molecular Science, Okazaki 444-8585, Japan

<sup>3</sup>School of Physical Sciences, The Graduate University for Advanced Studies (SOKENDAI), Okazaki 444-8585, Japan

<sup>4</sup>Early Life Institute & Department of Geology, Northwest University, 229 Taibai Road, Xi'an 710069, P.R. China

<sup>5</sup>Earth-Life Science Institute, Tokyo Institute of Technology, Tokyo 152-8550, Japan.

<sup>6</sup>Department of Earth Sciences, University of Cambridge, Downing Street, Cambridge, CB2 3EQ, UK

The Ediacara biota is one of the enigmatic organism groups through geologic history. The biota occurred in the late Ediacaran from 580 to 543 Ma, namely during the early evolution of the Metazoan. Their sizes and complexity indicate that they should be multi-cellular animals, but it is still controversial which phylum/phyla the Ediacara biota belong to. Seilacher (1989) proposed a new stem group of Vendobionta, independent of all living-Metazoa. On the other hand, recent reappraisals suggest that each organism of the Ediacaran biota should belong to a stem group of each closely-related phylum of the living organisms (e.g. Xiao & Laflamme, 2009). Because some of the biota have similar morphology to extant cnidarians and molluscs, their classification into the phyla is plausible, but most of them have quite different morphology from the extant and even extinct Metazoa; thus the identification does not work for most of them.

Generally speaking, each organism has its own organic molecules, related to the function, such as chitin and hemocyanin for arthropods and molluscs. Therefore, detection of the unique organic molecules is useful to identify the precursor organisms of the fossils. We tried detecting the organic molecules from carbonaceous matter (CM) in four Ediacara biota-type fossils from the Chengjiang area, South China.

The C-K X-ray absorption near edge structure (XANES) spectra of the CM were acquired using a scanning transmission X-ray microscope (STXM) at the BL4U, UVSOR. Raman microspectroscopic analysis on the fossils was performed in order to identify the CM before the XANES analyses.

Figure 1A shows four analytical points on an STXM image of the Sample 4. Figure 1B shows C-XANES spectra of the CM in the Sample 4 along with typical spectra of chitin and collagen. The spectra are different among the analytical points, suggesting that the CM is heterogeneous. The Chitin has two distinguished peaks at 285.1 and 288.56. The spectra of the sample 4, as well as other samples 1–3, are dissimilar to those of chitin and collagen. The absorption peaks around 285 eV and at 292 eV possibly correspond to  $1s$  to  $\pi^*$  of electronic transitions in aromatic C=C bonds, and  $1s$  to  $\sigma^*$  exciton of graphite, respectively, which are typical for graphitized carbon.

This study can detect neither chitin nor collagen

from the Ediacara Biota-type fossils from South China. Analysis of better-preserved specimen is required to identify the precursor organisms from the fossils.

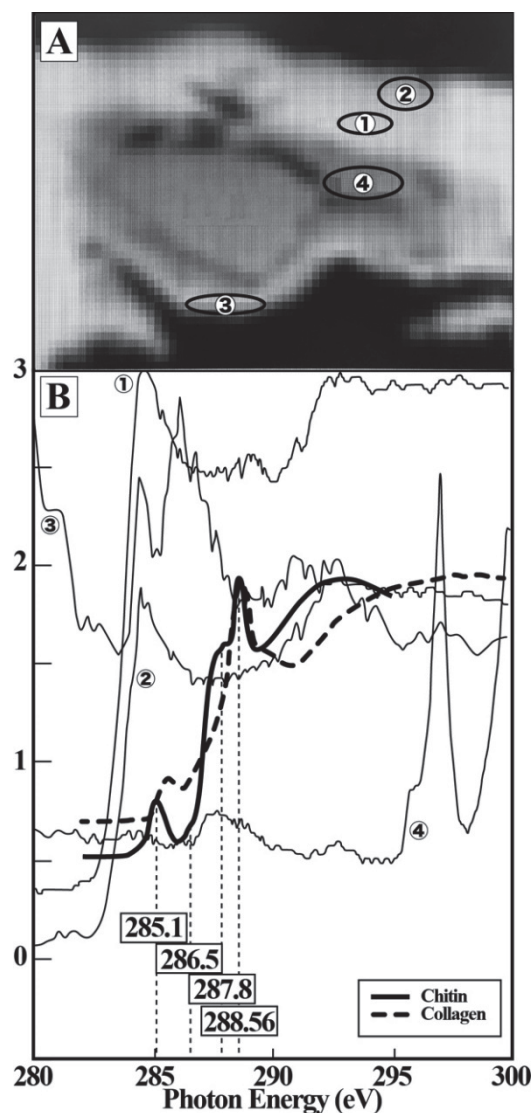


Fig. 1. (A) Analytical points on Sample 4. (B) Carbon-XANES spectra of the analytical points on the Sample 4 (A), and organic molecules of chitin and collagen.

BL4B

## Preliminary Study on Nitrogen K-edge XANES on Martian Meteorites

R. Nakada<sup>1</sup> and M. Koike<sup>2</sup>

<sup>1</sup>Kochi Institute for Core Sample Research, Japan Agency for Marine-Earth Science and Technology (JAMSTEC), Nankoku 783-8502, Japan

<sup>2</sup>Institute of Space and Astronautical Science (ISAS), Japan Aerospace Exploration Agency (JAXA), Sagamihara 252-5210, Japan

Surface environment of terrestrial planet varies to a large degree. The understanding on the diversity and universal property of planetary surface environment is one of the most important study for the planetary science and is related to the habitability. Volatile elements such as hydrogen, carbon, and nitrogen circulate through inner and surface of a planet and determine the evolution of the planetary environment. However, the behavior and cycles of volatile elements in the other planet than the Earth is largely unknown. Mars had experienced a great environmental change; it held a large body of liquid water on the surface in ~4 billion years ago, while presents a cold and dry environment today [1]. This study focuses on the nitrogen on Mars and examines species and stable isotope ratio (ratio between <sup>15</sup>N and <sup>14</sup>N) of nitrogen in the Martian surface environment by analyzing the Martian meteorites.

In general, nitrogen in the planetary surface circulates through (i) atmosphere, (ii) rocks, water, and biosphere, and (iii) planetary interior by changing its species. Modern atmospheric nitrogen (N<sub>2</sub>) on Mars is 0.15 mbar, though its <sup>15</sup>N/<sup>14</sup>N ratio 1.6 times heavier than the atmospheric N<sub>2</sub> on the Earth [2]. Such a thin and heavy N<sub>2</sub> can be a result of the atmospheric escape. A model calculation suggests that the Mars had a dense atmosphere in the past [3]. On the other hand, recent exploration reported the presence of nitrate on the Martian surface [4]. Destructive analyses on impact melt glass of Martian meteorites showed the presence of nitrate with the remarkably lighter <sup>15</sup>N/<sup>14</sup>N ratios than Martian atmosphere [5, 6]. These studies suggest the importance of the nitrogen fixation on Martian surface environments. It is necessary to determine the <sup>15</sup>N/<sup>14</sup>N ratios of individual nitrogen species to understand the Martian nitrogen cycle. However, nitrogen abundance in Martian meteorites is typically around 10 ppm [7, 8], which might be difficult to determine the nitrogen species by X-ray absorption near edge structure (XANES) analysis.

We have performed preliminary study on nitrogen K-edge (402 eV) XANES measurements on Martian meteorite at BL4B of UVSOR. NaNO<sub>3</sub> and NH<sub>4</sub>Cl reagents were measured in total electron yield mode, while meteorites and epoxy resin were measured in fluorescence mode.

Small but clear X-ray absorption was observed for some samples (Fig. 1). However, it should also be noted that nitrogen X-ray absorption also occurs for

epoxy resin, which is generally used to make thin section of a meteorite. In contrast, any absorption was observed from indium which is also used for sample mounting. Regarding the nitrogen K-edge XANES spectra of Martian meteorites, possible contribution of contaminant during preparation procedure should be checked in future.

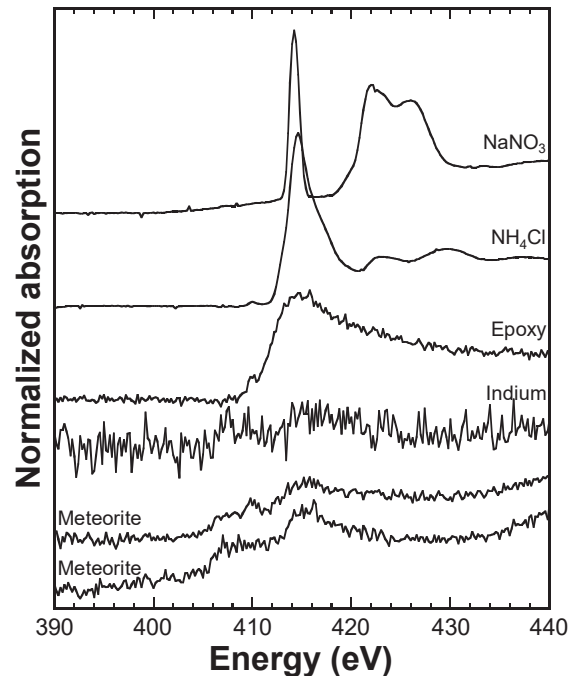


Fig. 1. Nitrogen K-edge XANES spectra of standards and samples.

- [1] V. R. Baker, *Nature* **412** (2001) 228.
- [2] M. H. Wong *et al.*, *Geophys. Res. Lett.* **40** (2013) 6033.
- [3] H. Kurokawa *et al.*, *Icarus* **299** (2018) 443.
- [4] J. C. Stern *et al.*, *PNAS* **112** (2015) 4245.
- [5] M. M. Grady *et al.*, *J. Geophys. Res.* **100** (1995) 5449.
- [6] S. P. Kounaves *et al.*, *Icarus* **229** (2014) 206.
- [7] Y. N. Miura *et al.*, *GCA* **59** (1995) 2105.
- [8] K. Mathew and K. Marti, *J. Geophys. Res.* **106** (2001) 1401.



BL5B

## Evaluation of the Hydrogen Absorption Cell Imager for Planetary Explorations

M. Kuwabara<sup>1</sup>, M. Taguchi<sup>2</sup>, K. Yoshioka<sup>3</sup>, T. D. Kawahara<sup>4</sup>, S. Kameda<sup>2</sup>,  
S. Komoriya<sup>2</sup>, S. Yonemoto<sup>3</sup>, Y. Shirafuji<sup>2</sup> and S. Kawase<sup>2</sup>

<sup>1</sup>*Institute of Space and Astronautical Science, Japan Aerospace Exploration Agency, Sagamihara 252-5210, Japan*

<sup>2</sup>*College of Science, Rikkyo University, Tokyo 171-8501, Japan*

<sup>3</sup>*Graduate School of Frontier Sciences, The University of Tokyo, Chiba 277-8561, Japan*

<sup>4</sup>*Faculty of Engineering, Shinshu University, Nagano 380-8553, Japan*

In the planetary lower atmosphere, H<sub>2</sub>O generate mainly hydrogen atoms through photodissociation by sunlight. The generated hydrogen atoms ascend to the exopause and only those atoms which have higher kinetic energy than gravitational potential energy there escape to interplanetary through thermal dissipation. Understanding the dissipation process in the present environment gives us some information to estimate planetary atmospheric evolution.

Hydrogen atoms in the planetary exosphere resonantly scatter the solar H Lyman-alpha radiation (121.567 nm) and form the planetary hydrogen corona. Imaging of this emission gives us to obtain the spatial structure of the corona because its brightness depends on the number density of the hydrogen atoms.

An absorption cell technique is efficient for remote sensing for the density and temperature distributions of the exospheric hydrogen atoms in the planet. In addition, the absorption cell technique has some advantages over others from the point of view of geometrical size, weight, simplicity, and durability. Thus, the technique is suitable for future missions with small size spacecraft.

An absorption cell photometer was mounted on the first Japanese Mars mission [1, 2], NOZOMI, but the parameter optimization for the absorption cell was insufficient due to the limitation of the development time. Therefore, further optimization and study have been required for future space missions. We evaluated the performances which depend on filament shape, applied power to the filament, enclosed gas pressure, optical path length of the cell, and position of the incident light using an ultra high resolution Fourier transform spectrometer installed on the DESIRS beamline of Synchrotron SOLEIL in France in 2016 and 2018. However, additional evaluations of the performances, such as an endurance test of the filaments, confirmation of absorption stability, have been needed. See Kuwabara *et al.* [2018] for more details [3].

In this experiment, we evaluate the stability of the absorption performance of the cell using the SOR beam with high intensity and stability. Figure 1 shows the configuration of the experiment. A prototype of hydrogen absorption cell imager consists of an absorption cell, MgF<sub>2</sub> band-pass filter, and photon detector. Microchannel plates and a resistive anode

encoder are assembled and used as the photon detector. The absorbance of the cell for the hydrogen Lyman-alpha radiation (121.567 nm) is measured with a repeat of turning on and off filaments at 0.3 Hz through approximately 60 hours.

The result is shown in Fig. 2. The absorbance seems to be stable and its value is  $4.95\% \pm 0.92$ . The errors are caused by the measurement system. For the next step, further long-term stability should be investigated.

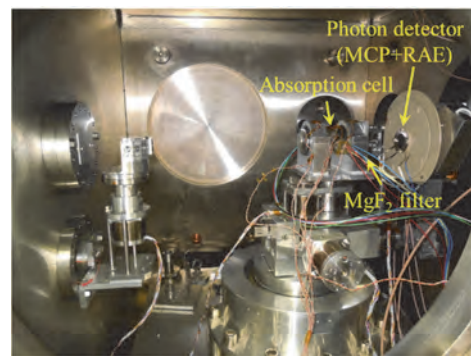


Fig. 1. Photo of the prototype of the new imager.

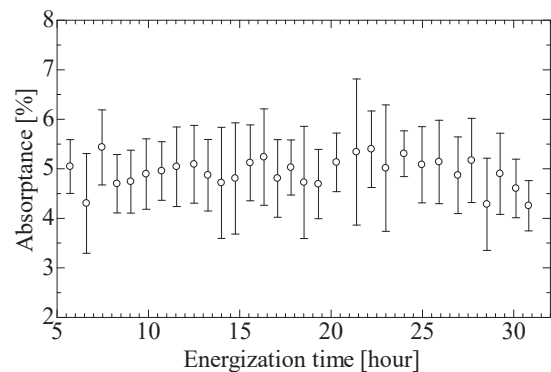


Fig. 2. Temporal variation of the absorbance of the prototype of the new imager.

[1] T. D. Kawahara *et al.*, *Applied Optics* **36** (1997) 2229.

[2] M. Taguchi *et al.*, *Earth, Planets and Space* **52** (2000) 49.

[3] M. Kuwabara *et al.*, *Rev. Sci. Instrum.* **89** (2018) 023111.

BL7B

## Effect of Space Weathering on Identification of Organic Matter on Celestial Body Surface Using Ultraviolet Wavelength Region Spectrum

S. Arao<sup>1</sup>, I. Yoshikawa<sup>1,2</sup>, K. Yoshioka<sup>1,2</sup>, I. Sakon<sup>3</sup>, R. Hikida<sup>1</sup>, R. Katsuse<sup>2</sup> and I. Endo<sup>3</sup>

<sup>1</sup>Department of Earth and Planetary Science, Graduate School of Science, The University of Tokyo, Tokyo 113-0033, Japan

<sup>2</sup>Department of Complexity Science and Engineering, Graduate School of Frontier Sciences, The University of Tokyo, Chiba 277-8561, Japan

<sup>3</sup>Department of Astronomy, Graduate School of Science, The University of Tokyo, Tokyo 113-0033, Japan

Analysis of reflection spectrum is a conventional means for identifying compositions of the celestial body's surface, but in the ultraviolet region, it has rarely been conducted. Analysis of spectrum suggests the existence of polycyclic aromatic hydrocarbon (PAH) in interstellar dust and on the surface of Mars' moon Phobos, but the replication study is insufficient. A comparison of the spectra of natural terrestrial PAH mixtures with that of interstellar dust or the Phobos surface suggests that there are similarly shaped absorption bands around wavelengths of 210 nm and 217.5 nm respectively. This similarity is the basis of the hypothesis that PAH is present in interstellar dust and the Phobos surface. However, considering the gap of peak wavelength, there are also many negative opinions on the hypothesis. Thus, there has been no definitive conclusion until now.

One of the phenomena that may have a description for this problem is change in the absorption spectrum due to space weathering. The absorption band of PAH around the wavelength of 210 nm is caused by the transition of aromatic  $\pi$  electrons and their orbital area relates to the absorption peak wavelength. If the hydrogen atoms bonded to the aromatic rings of PAH molecules are desorbed by space weathering, it is suggested theoretically that the orbital area of aromatic  $\pi$  electrons is broadened and the absorption band's peak wavelength may approach 217.5 nm.

In this experiment, to evaluate the influence of space weathering on the optical properties of PAH, we prepared several PAH (coronene and chrysene) samples which had been exposed to the space environment for about 1 year on orbit of the International Space Station (ISS). Then, we compared the reflection characteristics of these samples with those of non-exposure samples in a wavelength region of 160-300 nm.

As a result, all the samples experienced space weathering reflected the light in 160-300 nm wavelength region more weakly than non-exposure samples did. Furthermore, reflection characteristics of coronene sample exhibited a broad dip around 235 nm wavelength and showed a trend in 210-280 nm wavelength region that the attenuation of the reflected light is more significantly at longer wavelengths (Fig. 1). This trend suggests that the wavelength which corresponds to the bottom of the dip may shift to the

direction of longer wavelength due to space weathering.

As another research, to detect the main factor of space weathering, we are going to irradiate non-exposure PAH samples with UV light or radial ray simulating the environment on the flight orbit of the ISS, and compare their reflection characteristics with those of space weathered sample.

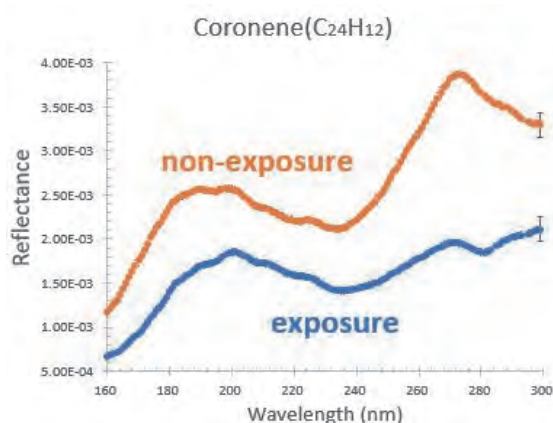


Fig. 1. Reflection characteristics of coronene sample in a wavelength region of 160-300 nm. Each curve shows an average of measured values upon three different incident points on the sample. Typical errors are added on the plots at 300 nm wavelength.

[1] Bertaux *et al.*, Proceedings of the EPSC-DPS Joint Meeting. 2011.

[2] Hendrix *et al.*, Meteoritics & Planetary Science **51** (2016) 105.

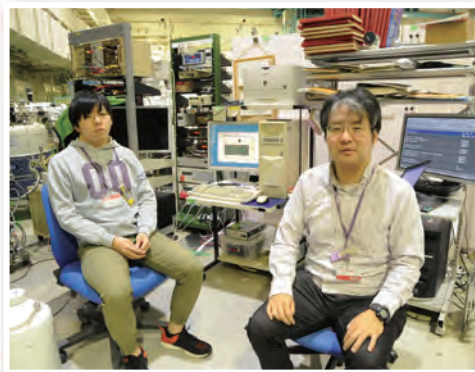
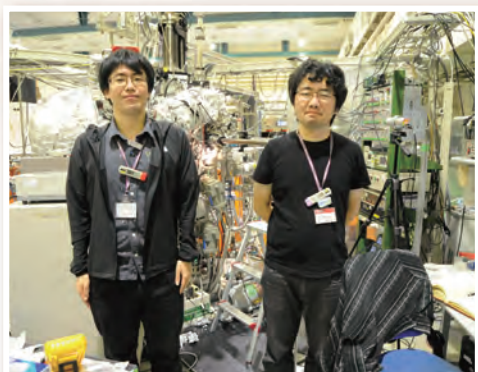
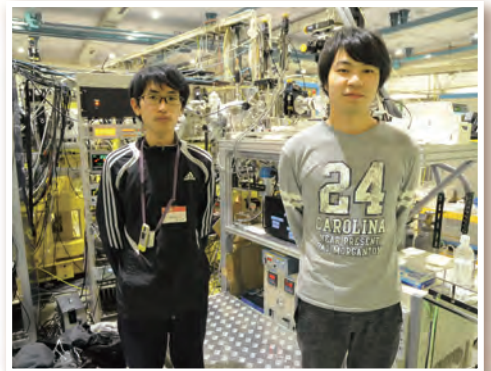
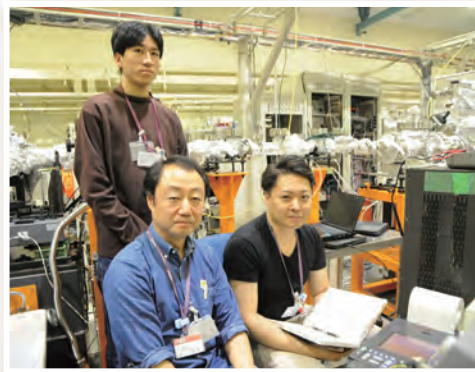
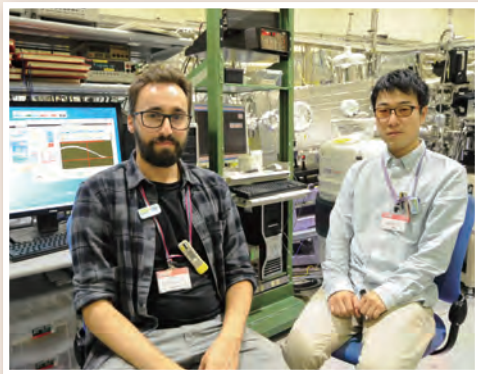
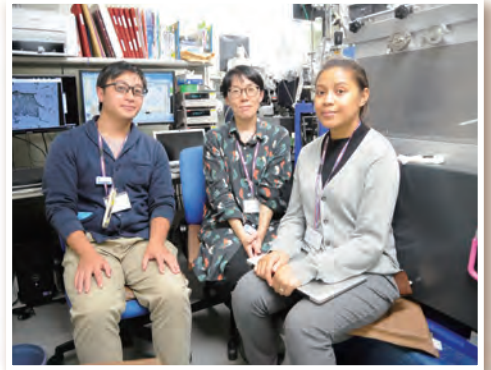
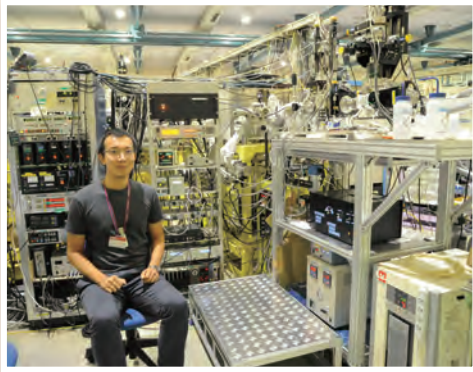
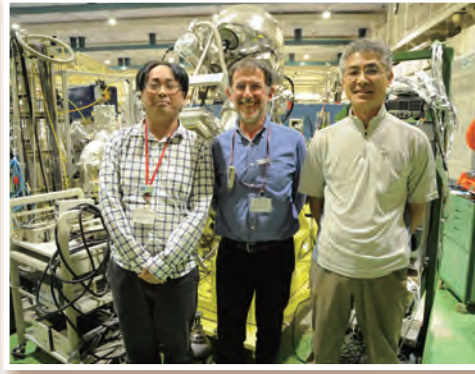
[3] Joblin *et al.*, The Astrophysical Journal **393** (1992) L79.

[4] Sakata *et al.*, Nature **301** (1983) 493.

[5] Steglich *et al.*, The Astrophysical Journal **742** (2011) 2.

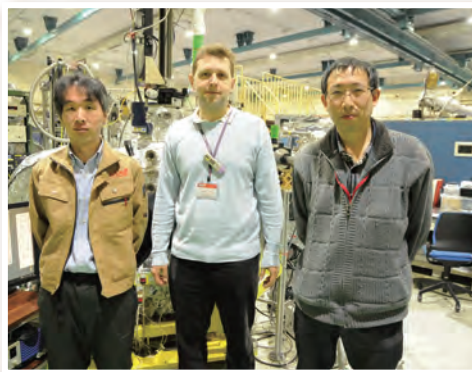
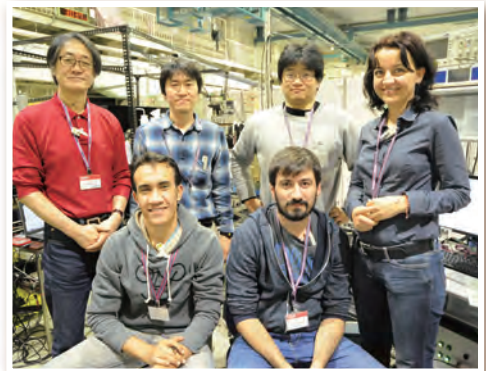
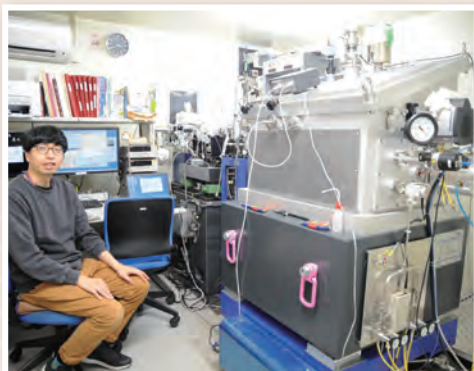
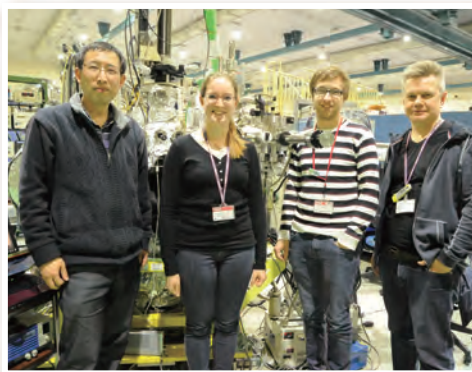
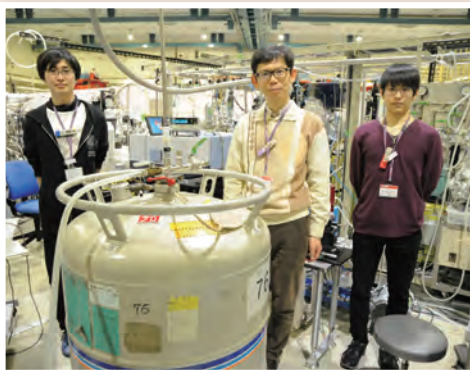
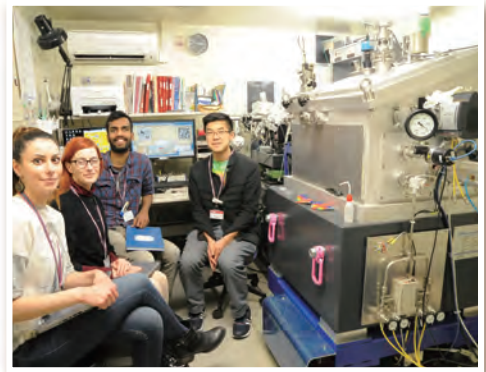
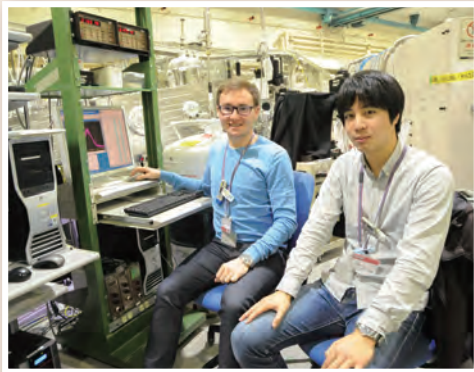
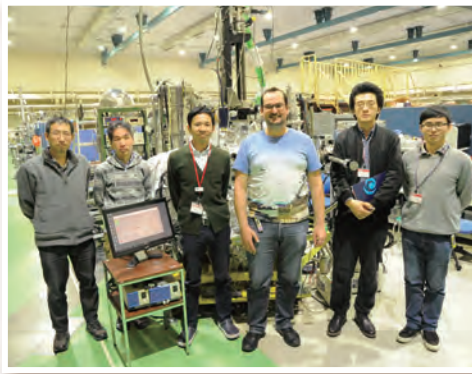
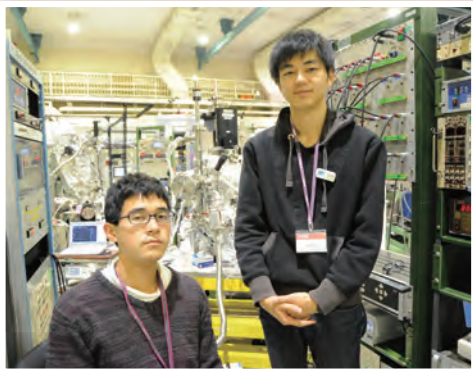


# UVSOR User 7





# UVSOR User 8



The background is a vibrant red color. It features several abstract geometric elements: a large, semi-transparent white circle with a dashed border and a ring of small white dots around its perimeter; several diagonal lines of varying thickness and opacity; and a grid of small white dots in the lower-left corner. The Roman numeral 'IV' is centered in the upper half of the page in a large, white, serif font.

# IV

## List of Publications





## List of Publications

- K. Asami, J. Ueda, K. Yasuda, K. Hongo, R. Maezono, M. G. Brik and S. Tanabe  
**“Development of Persistent Phosphor of  $\text{Eu}^{2+}$  Doped  $\text{Ba}_2\text{SiO}_4$  by  $\text{Er}^{3+}$  Codoping Based on Vacuum Referred Binding Energy Diagram”**, *Opt. Mater.*, **84** (2018) 436.
- L. Guo and M. Katoh  
**“*pn*-type Substrate Dependence of  $\text{CsK}_2\text{Sb}$  Photocathode Performance”**, *Phys. Rev. Accel. Beams*, **22** (2019) 033401.
- A. Hara and T. Awano  
**“Ground State of Ultrashallow Thermal Donors in Silicon”**, *Jpn. J. Appl. Phys.*, **57** (2018) 101301.
- Y. Hikosaka and E. Shigemasa  
**“Metastability of Carbonyl Sulfide Dications Studied by Multi-Electron–Ion Coincidence Spectroscopy”**, *Int. J. Mass Spectrom.*, **439** (2019) 13.
- M. Huttula, M. Patanen, R. Piispanen, T. Ohigashi, N. Kosugi, S. Swaraj, R. Belkhou, A. Pranovich, T. Jyske, P. Kilpeläinen, A. Kärkönen, R. Korpinen, T. Laakso, S. Valkonen and P. Saranpää  
**“STXM Chemical Mapping of Norway Spruce Knotwood Lignans”**, *Microsc. Microanal.*, **24** (2018) 482.
- H. Iwayama and J. R. Harries  
**“Resonant-Auger-State-Selected Dissociation Dynamics and Dissociation Limits of  $\text{N } 1s \rightarrow \pi^*$  core Excited  $\text{N}_2$  Molecules Studied Using a Two-Dimensional Auger-Electron-Photoion Coincidence Method”**, *J. Electron Spectrosc., Relat. Phenom.* **232** (2019) 40.
- S. Kamei, J. Hibi, Y. Ohtsubo, H. Watanabe and S. Kimura  
**“Infrared Evaluation of Enantiometric Amount and Application to Racemization at the Interface Between L- and D-Alanine”**, *Applied Spectrosc.*, **72** (7) (2018) 1074.
- T. Kawai, T. Hirai and K. Bando  
**“Optical Studies on the Conversion from  $\text{Ag}^+$  to  $\text{Ag}^-$  Centers by the Electrolytic Coloration in  $\text{NaCl}$  and  $\text{KCl}$  Crystals”**, *Opt. Mater.*, **77** (2018) 30.
- T. Kawai and A. Iguchi  
**“Energy Transfer Processes from  $\text{I}^-$  Centers to  $\text{In}^+$  Centers at Room Temperature in Co-Doped  $\text{NaCl}:\text{I}^-, \text{In}^+$  Crystals”**, *J. Lumin.*, **207** (2019) 58.
- M. Kitaura, S. Watanabe, K. Kamada, K. J. Kim, M. Yoshino, S. Kurosawa, T. Yagihashi, A. Ohnishi and K. Hara  
**“Shallow Electron Traps Formed by  $\text{Gd}^{2+}$  Ions Adjacent to Oxygen Vacancies in Cerium-Doped  $\text{Gd}_3\text{Al}_2\text{Ga}_3\text{O}_{12}$  Crystal”**, *Appl. Phys. Lett.*, **113** (2018) 041906.
- S. Kurosawa, T. Horiai, R. Murakami, Y. Shoji, J. Pejchal, A. Yamaji, S. Kodama, Y. Ohashi, Y. Yokota, K. Kamada, A. Yoshikawa, A. Ohnishi and M. Kitaura  
**“Comprehensive Study on Ce-Doped  $(\text{Gd}, \text{La})_2\text{Si}_2\text{O}_7$  Scintillator”**, *IEEE Trans. Nucl. Sci.*, **65** (2018) 2136.
- M.-H. Li, H.-H. Yeh, Y.-H. Chiang, U.-S. Jeng, C.-J. Su, H.-W. Shiu, Y.-J. Hsu, N. Kosugi, T. Ohigashi, Y.-A. Chen, P.-S. Shen, P. Chen and T.-F. Guo  
**“Highly Efficient 2D/3D Hybrid Perovskite Solar Cells via Low-Pressure Vapor-Assisted Solution Process”**, *Adv. Mater.*, **30** (2018) 1801401.

- S. Matsuba, K. Kawase, A. Miyamoto, S. Sasaki, M. Fujimoto, T. Konomi, N. Yamamoto, M. Hosaka and M. Katoh  
**“Generation of Vector Beam with Tandem Helical Undulators”**, Appl. Phys. Lett., **113** (2018) 021106.
- Z. Mita, H. Watanabe and S. Kimura  
**“Giant Thermal Effect of Vibration Modes of Single-Crystalline Alanine”**, Infrared Phys. Tech., **96** (2019) 7.
- M. Nagasaka, H. Yuzawa and N. Kosugi  
**“Intermolecular Interactions of Pyridine in Liquid Phase and Aqueous Solution Studied by Soft X-ray Absorption Spectroscopy”**, Z. Phys. Chem., **232** (2018) 705.
- M. Nagasaka, H. Yuzawa, K. Mochizuki, E. Rühl and N. Kosugi  
**“Temperature-Dependent Structural Changes in Liquid Benzene”**, J. Phys. Chem. Lett., **9** (2018) 5827.
- T. Ohigashi, A. Ito, K. Shinohara, S. Tone, Y. Inagaki, H. Yuzawa and N. Kosugi  
**“3-Dimensional Chemical Structures of an Isolated Cell Nucleus by a Scanning Transmission X-ray Microscope”**, Microsc. Microanal., **24** (2018) 400.
- J. Okabayashi, Y. Miura and H. Munekata  
**“Anatomy of Interfacial Spin-Orbit Coupling in Co/Pd Multilayers Using X-ray Magnetic Circular Dichroism and First-Principles Calculations”**, Scientific Reports, **8** (2018) 8303.
- J. Okabayashi, S. Miyasaka, M. Takahashi and S. Tajima  
**“Local Electronic and Magnetic Properties of Ferro-Orbital-Ordered FeV<sub>2</sub>O<sub>4</sub>”**, Jpn. J. Appl. Phys., **57** (2018) 0902BD.
- J. Okabayashi  
**“Tailoring Spins and Orbitals in Spin-Orbitronic Interfaces Probed by X-Ray Magnetic Circular Dichroism”**, Progress in Photon Science, (2019) 471. Springer (review book).
- T. Sakai, M. Koshimizu, Y. Fujimoto, D. Nakauchi, T. Yanagida and K. Asai  
**“Evaluation of the Scintillation and Thermally Stimulated Luminescence Properties of Cs<sub>2</sub>CdCl<sub>4</sub> Single Crystals”**, Sensors and Materials, **30** (2018) 1564.
- K. Shinohara, T. Ohigashi, S. Toné, M. Kado and A. Ito  
**“Quantitative Analysis of Mammalian Chromosome by Scanning Transmission Soft X-ray Microscopy”**, Ultramicroscopy, **194** (2018) 1.
- K. Shinohara, S. Toné, T. Ejima, T. Ohigashi and A. Ito  
**“Quantitative Distribution of DNA, RNA, Histone and Proteins Other than Histone in Mammalian Cells, Nuclei and a Chromosome at High Resolution Observed by Scanning Transmission Soft X-Ray Microscopy (STXM)”**, Cells, **8** (2019) 164.
- M. M. Shirolkar, Y.-F. Wang, Y. C. Shao, K.-H. Chen, H.-T. Wang, X.-S. Qiu, J.-S. Yang, J.-J. Wu, J.-W. Chiou, T. Ohigashi, N. Kosugi and W.-F. Pong  
**“Probing the Electronic Structure of BiVO<sub>4</sub> Coated ZnO Nanodendrite Core-Shell Nanocomposite Using X-ray Spectroscopic and Spatially Resolved Scanning Transmission X-ray Microscopy Studies”**, Microsc. Microanal., **24** (2018) 468.
- Y. Sugizaki, H. Motoyama, K. Edamoto and K. Ozawa  
**“Electronic Structure of the VO Film Grown on Ag(100): Resonant Photoelectron Spectroscopy Study”**, e-J. Surf. Sci. Nanotech., **16** (2018) 236.
- Y. Sugizaki, H. Motoyama, Y. Shimato, T. Yoshida, T. Takano and K. Edamoto  
**“Valence and Core-Level Photoelectron Spectroscopy Studies of Fe<sub>2</sub>P(10 $\bar{1}$ 0):Effect of P Segregation on the Surface Electronic Structure”**, Jpn. J. Appl. Phys., **57** (2018) 115701.

Y. Taira and M. Katoh

**“Generation of Optical Vortices by Nonlinear Inverse Thomson Scattering at Arbitrary Angle Interactions”**, *Astrophys. J.*, **860:45** (2018).

K. Takahashi, M. Koshimizu, Y. Fujimoto, T. Yanagida and K. Asai

**“Auger-Free Luminescence Characteristics of  $\text{Rb}_{1-x}\text{Cs}_x\text{CaCl}_3$ ”**, *J. Ceram. Soc. Jpn.*, **126** (2018) 755.

Y. Takamori, T. Morimoto, N. Fukuda and Y. Ohki

**“Effects of Ultraviolet Photon Irradiation and Subsequent Thermal Treatments on Solution-Processed Amorphous Indium Gallium Zinc Oxide Thin Films”**, *AIP Advances*, **8** (2018) 115304.

A. Takemori, T. Hajiri, S. Miyasaka, Z. H. Tin, T. Adachi, S. Ideta, K. Tanaka, M. Matsunami and S. Tajima

**“Change of Fermi Surface States Related with Two Different  $T_c$ -raising Mechanisms in Iron Pnictide Superconductors”**, *Phys. Rev. B*, **98** (2018) 100501.

M. Uesugi, M. Ito, H. Yabuta, M. Naraoka, F. Kitajima, Y. Takano, H. Mita, Y. Kebukawa, A. Nakato and Y. Karouji

**“Further Characterizations of Carbonaceous Materials in Hayabusa-returned Samples to Understand Their Origin”**, *Meteorit. Planet. Sci.*, **54** (2019) 638.

Y. F. Wang, Y. C. Shao, S. H. Hsieh, Y. K. Chang, P. H. Yeh, H. C. Hsueh, J. W. Chiou, H. T. Wang, S. C. Ray, H. M. Tsai, C. W. Pao, C. H. Chen, H. J. Lin, J. F. Lee, C. T. Wu, J. J. Wu, Y. M. Chang, K. Asokan, K. H. Chae, T. Ohgashi, Y. Takagi, T. Yokoyama, N. Kosugi and W. F. Pong

**“Origin of Magnetic Properties in Carbon Implanted ZnO Nanowires”**, *Scientific Reports*, **8** (2018) 7758.

F. B. Wiggers, A. Fleurence, K. Aoyagi, T. Yonezawa, Y. Yamada-Takamura, H. Feng, J. Zhuang, Y. Du, A.Y. Kovalgin and M. P. de Jong

**“Van der Waals Integration of Silicene and Hexagonal Boron Nitride”**, *2D Mater.*, **6** (2019) 035001.

H. Yamane, A. Carlier and N. Kosugi

**“Orbital-Specific Electronic Interaction in Crystalline Films of Iron Phthalocyanine Grown on Au(111) Probed by Angle-Resolved Photoemission Spectroscopy”**, *Mater. Chem. Front.*, **2** (2018) 609.

H. Yamane, M. Oura, K. Sawada, T. Ebisu, T. Ishikawa N.Yamazaki, K. Hasegawa, K. Takagi and T. Hatsui

**“Critical Absorbed Dose of Resinous Adhesive Material towards Non-Destructive Chemical-State Analysis Using Soft X-Rays”**, *J. Electron Spectrosc. Relat. Phenom.*, **232** (2019) 11.

H. Yamane and N. Kosugi

**“Photoelectron Angular Distribution Induced by Weak Intermolecular Interaction in Highly Ordered Aromatic Molecules”**, *J. Phys. Chem. C*, **122** (2018) 26472.

J.-P. Yang, M. Meissner, T. Yamaguchi, X.-Y. Zhang, T. Ueba, L.-W. Cheng, S. Ideta, K. Tanaka, X.-H. Zeng, N. Ueno and S. Kera

**“Band Dispersion and Hole Effective Mass of Methylammonium Lead Iodide Perovskite”**, *Sol. RRL*, **2** (2018) 1800132.

H. Zen, H. Ohgaki, Y. Taira, T. Hayakawa, T. Shizuma, I. Daito, J. Yamazaki, T. Kii, H. Toyokawa and M. Katoh

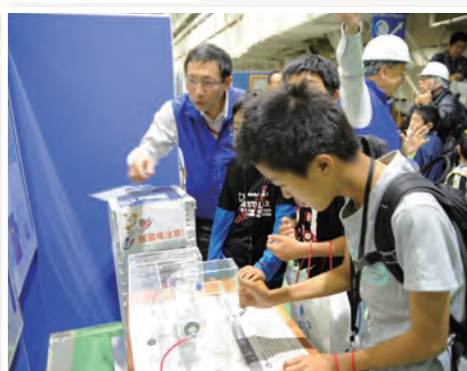
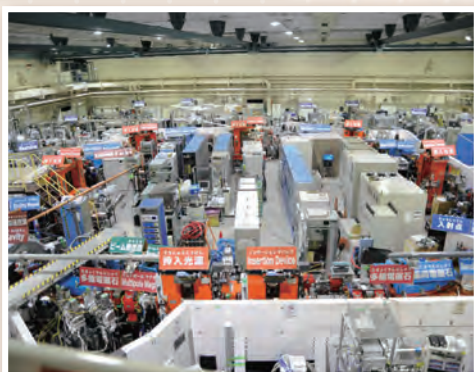
**“Demonstration of Tomographic Imaging of Isotope Distribution by Nuclear Resonance Fluorescence”**, *AIP Advances*, **9** (2019) 035101.

H. Zen, T. Hayakawa, E. Salehi, M. Fujimoto, T. Shizuma, J. K. Koga, T. Kii, M. Katoh and H. Ohgaki

**“Generation of 1-MeV Quasi-Monochromatic Gamma-ray for Precise Measurement of Delbrück Scattering by Laser Compton Scattering”**, *J. Phys.: Conf. Ser.*, **1067** (2018) 092003.

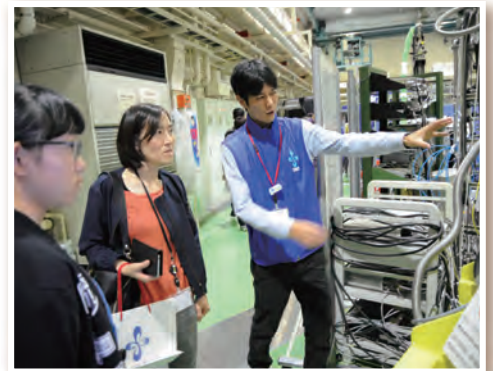
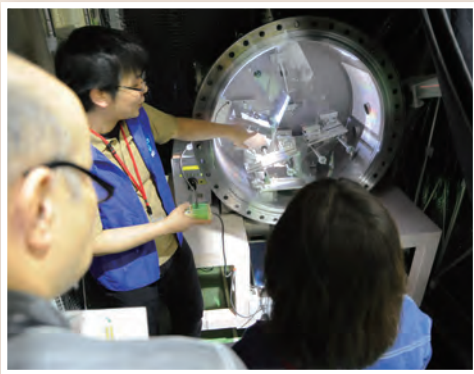
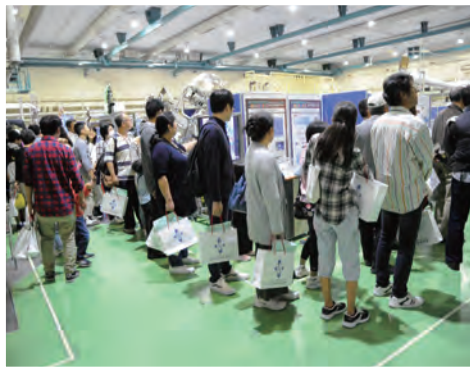


# IMS Open to the public 1



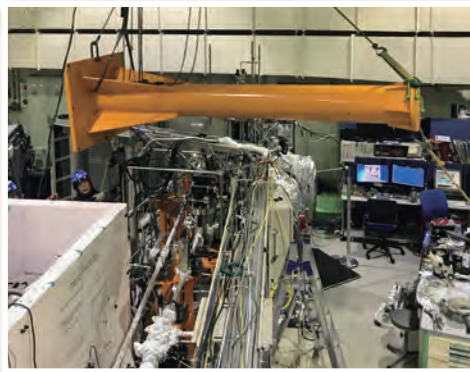
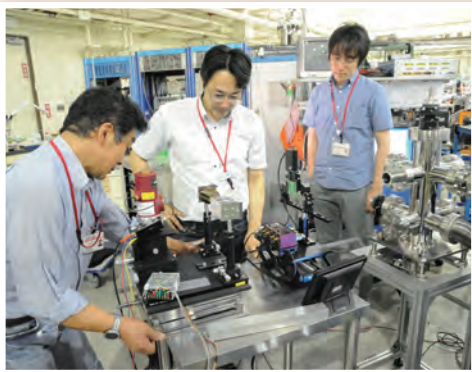
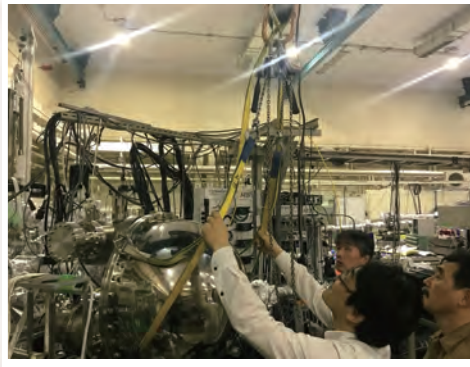
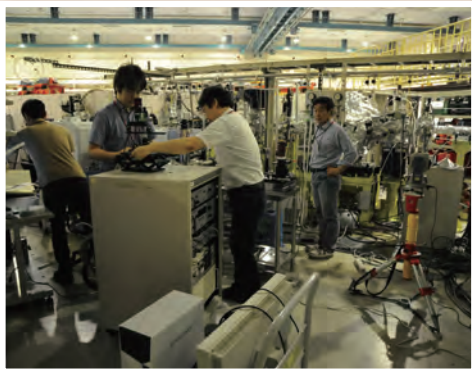


# IMS Open to the public 2





# UVSOR Staff Works & Year End Party





A large, stylized white letter 'V' is centered within a circular graphic element. The 'V' has a slight shadow effect, making it stand out against the background. The circular element it sits in is composed of several concentric rings with different patterns, including a dashed line and a dotted line. The background of the entire page is a warm, brownish-orange color with abstract, flowing lines and a grid of small dots at the bottom.

Workshops



# The first international workshop on Momentum Microscopy & Spectroscopy for Materials Science

Date: October 22-23, 2019

Place: Okazaki Conference Center

## **February 22<sup>nd</sup> (Fri.)**

9:00 – 9:20 Registration

9:20 – 9:30 Opening: **Satoshi KERA** (IMS, Director of UVSOR)

<Chair: **F. Matsui** (UVSOR)>

9:30 – 10:15 KEYNOTE LECTURE: **Shigemasa SUGA** (Osaka Univ.)

Frontier of Spin- & Angle-Resolved Photoelectron Spectroscopy by Momentum Microscopy

10:15 – 10:50 **Fumihiko MATSUI** (IMS)

The Momentum Microscope Project at UVSOR

10:50 – 11:05 — Coffee —

11:05 – 11:40 INVITED: **Yoshihiro KUBOZONO** (Okayama Univ.)

Pressure-induced superconductivity in metal doped topological materials and two-dimensional materials

11:40 – 12:25 INVITED: **Lada YASHINA** (Lomonosov Moscow State Univ.)

Gap opening and spin dynamics in topological insulators

12:25 – 13:40 — Lunch —

<Chair: **K. Tanaka** (UVSOR)>

13:40 – 14:15 INVITED: **Koji HORIBA** (KEK PF)

Synchrotron-based ARPES study at VUV-SX combination beamline KEK-PF BL-2 MUSASHI

14:15 – 14:50 INVITED: **Taichi OKUDA** (Hiroshima Univ.)

Recent activities and future prospects of spin- and angle-resolved photoemission spectroscopy at HiSOR

14:50 – 15:25 INVITED: **Kazuyuki SAKAMOTO** (Chiba Univ.)

Spin-polarized bands at solid surfaces

15:25 – 15:45 — Coffee —

<Chair: **S. Kera** (UVSOR)>

15:45 – 16:30 INVITED: **Sergey SUBACH** (Forschungszentrum Julich PGI-3)

Dependence of the adsorption height of graphenelike adsorbates on their dimensionality

16:30 – 17:05 INVITED: **Yoichi YAMADA** (Tsukuba Univ.)

STM and photoelectron spectroscopy of well-ordered organic systems: Doping and interfaces

17:05 – 17:40 **Satoshi Kera** (IMS, Director of UVSOR)

Imaging of electron delocalization upon assembling the molecules

17:40 – 17:50 Workshop Photo

17:50 – 20:00 Poster session with Buffet-style dinner



## February 23<sup>rd</sup> (Sat.)

8:30 – 9:00 — BF —

<Chair: **F. Matsui** (UVSOR)>

- 9:00 – 9:35 INVITED: **Peter KRÜGER** (Chiba Univ.)  
Theoretical advances in angle-resolved photoelectron and resonant Auger electron spectroscopy
- 9:35 – 10:10 INVITED: **Yoshitada MORIKAWA** (Osaka Univ.)  
First-principles Theoretical Study on Atomic Geometries, Electronic Properties, and Chemical Reactivity of Active Sites at Graphene
- 10:10 – 11:45 INVITED: **Yukiaki ISHIDA** (The Univ. Tokyo, ISSP)  
“Slit-less” ARPES analyzers: Some utilities and prospects in surface photo-electronics
- 10:45 – 11:05 — Coffee —
- 11:05 – 11:40 INVITED: **Tomohiro MATSUSHITA** (SPring-8, Riken)  
Determination of dopant structure by photoelectron holography
- 11:40 – 12:15 INVITED: **Masato KOTSUGI** (Tokyo Univ. Sci.)  
Topological data analysis of labyrinth magnetic domain
- 12:15 – 12:30 Closing  
*Optional* 12:30-14:00: Lunch & 14:00-16:00 tour & discussion at UVSOR

## POSTERS:

- P1 Electronic structure of the half-metallic ferrimagnet  $Mn_2VAl$  probed by resonant inelastic soft X-ray scattering under magnetic field  
**Hidenori FUJIWARA**, (Osaka Univ.)
- P2 Circular dichroism in ARPES mapping of Bi thin films  
**Kazutoshi TAKAHASHI**, (Saga Univ.)
- P3 Energy level alignment at molecule/metal and molecule/insulator/metal interfaces using k-space imaging orbital tomography  
**Anja HAAGS**, (Forschungszentrum Jülich PGI-3)
- P4 Dependence of the adsorption height of graphenelike adsorbates on their dimensionality  
**Sergey SOUBATCH**, (Forschungszentrum Jülich PGI-3)
- P5 Mn 2p core-level electronic structure of a new material for a spacecraft radiator  $La_{0.775}Sr_{0.225-x}Ca_xMn_{1-y}Ga_yO_3$  studied by hard x-ray photoemission spectroscopy  
**H. IIO**, (Tokyo Univ. of Science)
- P6 Multiple scattering calculation of photoelectron angle distribution of ARPES  
**Misa NOSAKI**, (Chiba University)
- P7 Orbital tomography of a strong hole-vibration coupling molecule  
**Matthias MEISSNER**, (IMS)
- P8 Electronic structure of  $Pr_{1-x}Y_xCoO_3$  showing a unique magnetic state  
**Daisuke KANAI**, (Tokyo Univ. of Science)
- P9 Unsubstituted and Fluorinated Cu-phthalocyanine Overlayers on  $Si(111)-(\sqrt{7}\times\sqrt{3})$ -In Surface: Adsorption Geometry, Charge Polarization, and Effects on Superconductivity  
**Naoya SUMI**, (Tsukuba Univ.)

- P10 Germanene epitaxial growth by segregation method on Ag(111) thin films  
**Junji YUHARA**, (Nagoya Univ.)
- P11 Pressure dependence of superconductivity in a new type of superconductor  
**Xiaofan YANG**, (Okayama Univ.)
- P12 Ultrafast carrier dynamics at well-ordered organic P-N interfaces  
**Masato IWASAWA**, (Tsukuba Univ.)
- P13 Core levels and frontier orbitals of K-doped sumanene monolayer  
**Chunyang ZHANG**, (Tsukuba Univ.)
- P14 Development of simple two-dimensional electron analyzer using variable-deceleration-ratio wide-acceptance-angle  
**Hiroyuki MATSUDA**, (Nara Institute of Science and Technology)
- P15 Screening at the metal/organic interface  
**Takumi AIHARA**, (Chiba Univ.)
- P16 Developing angle resolved low energy inverse photoelectron spectroscopy apparatus  
**Haruki Sato**, (Chiba Univ.)
- P17 Study on effect of impurity doping on transport properties in topological insulator  $\text{Bi}_2\text{Se}_3$   
**Takaki UCHIYAMA**, (Okayama Univ.)
- P18 Enhancement of signal intensity for inverse photoelectron spectroscopy by grating-coupled surface plasmon resonance  
**Koki SHIBATA**, (Chiba Univ.)
- P19 Thin-film structure and electronic state of anthradithiophene monolayer on graphite  
**Keishi TAKAHASHI**, (Chiba Univ.)
- P20 Epitaxial growth of pn heterointerface on organic single crystal  
**Ryohei TSURUTA**, (Tokyo Univ. of Science)
- P21 Measurement for the dispersion of the excited states in the transition metal dichalcogenide by the use of photon-energy-dependent ARPES  
**Shinichiro TANAKA**, (Osaka Univ.)
- P22 Current Status of BL6U at UVSOR  
**Seiji MAKITA**, (IMS)
- P23 Current Status of Beamline 5U at UVSOR  
**Kiyohisa TANAKA**, (IMS)
- P24 Current Status of Beamline 7U at UVSOR  
**Shinichiro IDETA**, (IMS)

# NINS Joint Research Program

## Workshop on next generation nondestructive analytical method utilizing a quantum beam physics: Applications to Earth and Planetary sciences

Date: October 12, 2018

Place: Uji Obaku Plaza, Kyoto University

10:00 – 10:30      Opening Remark  
                         **M. Ito** (JAMSTEC)

<Session 1, Chair: **H. Zen** (Kyoto Univ.)>

10:30 – 11:10      Non-destructive isotope CT imaging by using LCS gamma-ray  
                         **H. Ohgaki** (Kyoto Univ.)

11:10 – 11:50      Generation of Quantum Beams from Electron Storage Rings  
                         **M. Katoh** (UVSOR)

11:50 – 12:30      Precise isotope analysis of Pb for cosmo- and geochemistry  
                         **Y. Fukami** (JAMSTEC)

12:30 – 13:30      Lunch

13:30 – 14:30      Poster Session

<Session 2, Chair: **T. Ohigashi** (UVSOR)>

14:30 – 15:10      Non-destructive inspection by neutron beam  
                         **T. Shinohara** (JAEA/J-PARC)

15:10 – 15:50      Current status and future development of synchrotron radiation imaging technique for Earth and Planetary materials at SPring-8  
                         **M. Uesugi** (JASRI/SPring-8)

15:50 – 16:00      Coffee break

<Session 3, Chair: **R. Nakata** (JAMSTEC)>

16:00 – 16:40      The contribution of X-ray microscopic analysis in the planetary material science, and its future possibilities  
                         **H. Suga** (Univ. Tokyo)

16:40 – 17:20      What does future solar system exploration request from next-generation analytical tools?  
                         **T. Usui** (JAXA/ISIS)

17:20 – 17:50      Panel Discussion  
                         **M. Ito** (JAMSTEC)

17:50 – 18:00      Closing Remark  
                         **T. Ohigashi** (UVSOR)

18:00 – 20:00      Banquet



<Poster Presentation>

- P1 Secondary mass-dependent isotopic fractionation in the ion source of TIMS: Application for high-precision Nd isotopic analysis  
**R. Fukai** (Tokyo Tech Univ.)
- P2 Reconstruction by simultaneous algebraic reconstruction technique (SART) for cosmic dust samples.  
**J. Matsuno** (Kyoto Univ.)
- P3 Dissolved species controlling isotope effect for cerium during adsorption and precipitation  
**R. Nakada** (JAMSTEC)
- P4 Non-destructive elemental analysis method for interior of a material by muonic X-ray measurement  
**K. Ninomiya** (Osaka Univ)
- P5 Current status of STXM beamline BL4U in UVSOR Synchrotron  
**T. Ohigashi** (UVSOR)
- P6 The occurrence of perchlorate salt in and round the Taklimakan Desert, China  
**H.B. Qin** (Univ. Tokyo)
- P7 Elucidation of aqueous alteration of Martian meteorite, Yamato 000749, using multi-probe microscopic observation  
**N. Shiraishi** (Hiroshima Univ.)
- P8 Martian water environment of iddingsite formation in Yamato 000593 studied by the detail analysis of secondary minerals  
**K. Suzuki** (Univ. Tokyo)
- P9 Mineralogical and H isotope study of jarosites in Yamato 000593 nakhlite  
**A. Takano** (Hiroshima Univ.)
- P10 Molecular geochemistry of rubidium: a possibility of its stable isotope to estimate water-rock ratio  
**H. Tsuboi** (Univ. Tokyo)
- P11 High energy CT system detecting 10um order size defects which is unable by Linac or SLS  
**H. Yamada** (MIRRORCLE Analysis Center)
- P12 Measurement of 2D Isotope Distribution by LCS Gamma-ray  
**H. Zen** (Kyoto Univ.)
- P13 Source of dissolved methane in the western Arctic Ocean  
**K. Kudo** (Tokyo Inst. Tech.)
- P14 Analytical of structure of water in poly(vinyl alcohol) hydrogel  
**K. Kudo** (Kobe Univ.)
- P15 Investigation of the organic matter in the Martian meteorite Northwest Africa 7034 (Black beauty)  
**H. Suga** (Univ. Tokyo)
- P16 Computational study of the isotopic fractionation in pressure using the ab initio path integral molecular dynamics  
**T. Kawatsu** (Riken)
- P17 Study of the effect of space exposure on the carbonaceous dust based on XANES/STXM analysis  
**I. Sakon** (Univ. Tokyo)

# UVSOR Symposium 2018

Date: November 10-11, 2018

Place : Okazaki Conference Center

## November 10<sup>th</sup> (Sat.)

<Session 1, Chair: **T. Ohigashi** (UVSOR)>

- 13:00 – 13:05      Opening Remark  
                         **T. Ohigashi** (UVSOR)
- 13:05 – 13:25      UVSOR of past 35 years and future 20 years  
                         **S. Kera** (UVSOR)
- 13:25 – 13:45      Quantitative Mapping of Biomolecules in Biological Specimens using STXM  
                         **A. Ito** (Tokai Univ.)
- 13:45 – 14:05      Development of Analytical Method of Extraterrestrial Organic Matter for Analysis of Hayabusa2 Returned Samples –an Application to Cosmic Dust Showing High Density of Organic Globules-  
                         **M. Uesugi** (JASRI/SPring-8)
- 14:05 – 14:25      Coffee Break
- 14:25 – 15:30      Short Presentation for Poster Session

<Session 2, Chair: **S. Kera** (UVSOR)>

- 15:30 – 15:50      Achievements and Outlook of the Solid Photoelectron Spectroscopy Station at BL6U  
                         **F. Matsui** (UVSOR)
- 15:50 – 16:35      [Invited Talk] Detailed Study of the Formation of Organic-Inorganic Interfaces and of the Growth of Organic Layers  
                         **E. Umbach** (Univ. of Wuerzburg)
- 16:40 – 18:30      Poster Session
- 18:30 – 20:00      Banquet

## November 11<sup>th</sup> (Sun.)

<Session 3, Chair: **S. Kimura**(Osaka Univ.)>

- 9:00 – 9:20          Surface Electronic Structure Analysis of Fe<sub>2</sub>P by Photoelectron Spectroscopy  
                         **N. Maejima** (Rikkyo Univ.)
- 9:20 – 9:40          Surface Electronic Structure of Topological Kondo Insulators  
                         **Y. Ohtsubo** (Osaka Univ.)
- 9:40 – 10:00        Soft X-ray Absorption Spectroscopy of Liquid-crystal Materials in Transmission Mode  
                         **H. Iwayama** (UVSOR)
- 10:00 – 10:20      Coffee Break

<Session 4, Chair: **J. Okabayashi** (Univ. Tokyo)>

- 10:20 – 10:40      FOXSI-3 Succeeded in Focusing Imaging Spectroscopic Observation in Soft X-rays from the Sun for the First Time in the World!  
                         **N. Narukage** (National Astronomical Observatory of Japan)

10:40 – 11:00 Measurement of 2D Isotope Distribution by LCS Gamma-ray 3  
**H. Zen** (Kyoto Univ.)

11:00 – 12:00 Discussion and Closing Remark

### Poster Session

- P1 Zeeman Quantum Beat of Helium Atoms by XUV Vector Beam  
**T. Kaneyasu** (SAGA-LS)
- P2 Visualizing Vacancy-Type Defects in Solids by Measurement of Positron Annihilation Lifetime Spectra with Laser-Compton-Scattering Gamma-Rays  
**K. Fujimori** (Yamagata Univ.)\*
- P3 Optical Vortex UV Light Irradiation to Dinuclear Zn(II) Complex-PVA Hybrid Materials  
**S. Yamazaki** (Tokyo Univ. Science)\*
- P4 Generation of 1-MeV Gamma-ray by Laser Compton Scattering for Precise Measurement of Delbrück Scattering  
**H. Zen** (Kyoto Univ.)
- P5 Optical Properties of Mercury Lamp Irradiated Amorphous Carbon Nitride  
**K. Imamura** (Univ. Fukui)\*
- P6 CEES Measurements of the 3d-transition Metal Doped AlN Films II  
**W. Kamihigoshi** (Univ. Fukui)\*
- P7 Temperature Dependence of Dielectric Function in Widegap Oxide Epilayers  
**T. Makino** (Univ. Fukui)
- P8 Emission Properties and Electronic States of Ce Doped  $\text{Ba}_3\text{Y}_2\text{B}_6\text{O}_{15}$   
**M. Yoshino** (Nagoya Univ.)
- P9 Optical Properties of Ag- centers Doped in NaI Crystals  
**S. Watanabe** (Osaka Prefecture Univ.)\*
- P10 VUV Excitation Processes of Rare-Earth Ions in  $\text{Lu}_3\text{Al}_5\text{O}_{12}$  Crystals  
**R. Tarukawa** (Yamagata Univ.)\*
- P11 Energy Transfer Phenomena from  $\text{I}^-$  Centers to  $\text{Tl}^+$  Centers in Codoped NaCl:  $\text{I}^-$ ,  $\text{Tl}^+$  Crystals  
**T. Kawai** (Osaka Prefecture Univ.)
- P12 Optical Properties of  $\text{Tl}^+$ -doped  $\text{CsCaCl}_3$  Single Crystals  
**K. Kubota** (Osaka Prefecture Univ.)\*
- P13 Report on Scintillation Properties for Scintillators with UVSOR beam (FY2018)  
**S. Kurosawa** (Tohoku Univ.)
- P14 Soft X-ray Absorption Spectroscopy of Liquid Mixtures in Microfluidics  
**M. Nagasaka** (IMS)
- P15 Effect of Salt Addition to Glycine Betaine Aqueous solutions on the electronic structure of water studied by soft X-ray absorption spectroscopy  
**S. Ohsawa** (Hiroshima Univ.)\*
- P16 Observation of Cobalt-carbonate Electrocatalyst for Oxygen Evolution Using Operando C K-edge XAFS  
**T. Hiue** (Keio Univ.)\*
- P17 Electron-Ion Coincidence Spectroscopy Using a Magnetic Bottle Electron Analyzer  
**Y. Hikosaka** (Univ. Toyama)



- P18 Sulfur speciation high-spatial resolution map in extraterrestrial organics utilizing STXM-XANES  
**M. Ito** (JAMSTEC)
- P19 Vacuum Ultra-Violet Absorption Spectra of Amorphous Chalcogenide Thin Films  
**K. Hayashi** (Gifu Univ.)
- P20 Band dispersion of Bi<sub>2</sub>Te<sub>3</sub> with Mn and Te deposition and its temperature dependence  
**K. Yokoyama** (Tokyo Inst. Tech.)\*
- P21 Polarization-dependent Angle-resolved Photoemission Study of MAX Phase Compound V<sub>2</sub>AlC  
**M. Ikemoto** (Nagoya Univ.)\*
- P22 Electronic Structure of NEA Surface of a Photo-cathode Material  
**H. Matsumoto** (Osaka Univ.)\*
- P23 High-resolution ARPES studies of transition-metal dichalcogenides NbSe<sub>2</sub> and NbS<sub>2</sub>  
**K. Sugawara** (Tohoku Univ.)
- P24 Magnetic and Electronic Structures in Co/Au Interfaces  
**J. Okabayashi** (Univ. Tokyo)
- P25 Change of Electron Trap Levels in Ce:GAGG Mixed Crystals  
**T. Yagihashi** (Yamagata Univ.)\*
- P26 Derivation of Complex Refractive Index by Spectroscopic Ellipsometry for VIS-VUV and Kramers-Kronig Analysis  
**S. Takashima** (Univ. Fukui)\*
- P27 Development of Measurement Device of Complex Refractive Index for VIS-VUV  
**D. Imai** (Univ. Fukui)\*
- P28 Evaluation of Electric Property of CaF<sub>2</sub>-metal interface and Development of Vacuum Ultraviolet Detector  
**K. Suzuki** (Nagoya Inst. Tech.)\*
- P29 Electronic Structure of Iron-based Superconductor Ba<sub>1-x</sub>K<sub>x</sub>Fe<sub>2</sub>As<sub>2</sub> Using Angle-Resolved Photoemission Spectroscopy  
**S. Ideta** (UVSOR)
- P30 Spin-polarized Quasi-one-dimensional Electronic Structure on Bi/GaSb(110)-(2×1)  
**T. Nakamura** (Osaka Univ.)\*
- P31 Electronic Structures of Methyl Ammonium Lead Triiodide Single Crystals Probed by Low Energy Photoemission  
**S. Yamanaka** (Tokyo Univ. Sci.)\*
- P32 Effects of Film Structure on Electronic Structure for Pentacene Monolayer on Graphite  
**T. Yamaguchi** (IMS)\*
- P33 Fabrication of Bi<sub>1</sub>Te<sub>1</sub> Ultrathin Films and the Surface Electronic Structure  
**S. Kusaka** (Tokyo Inst. Tech.)\*

(\*: student)

# UVSOR Symposium 2018





# MM Workshop













Editorial Board : T. Ohigashi H. Iwayama M. Sakai H. Hagiwara I. Inagaki







**Institute for Molecular Science  
National Institutes of Natural Sciences  
Okazaki 444-8585, Japan**

**Tel: +81-564-55-7402**

**Fax: +81-564-54-7079**

**<http://www.uvsor.ims.ac.jp>**



**ISSN 0911-5730**